A Novel Chemical Looping Based Air Separation Technology for Oxy-Fuel Combustion of Coal

2014

Final Report

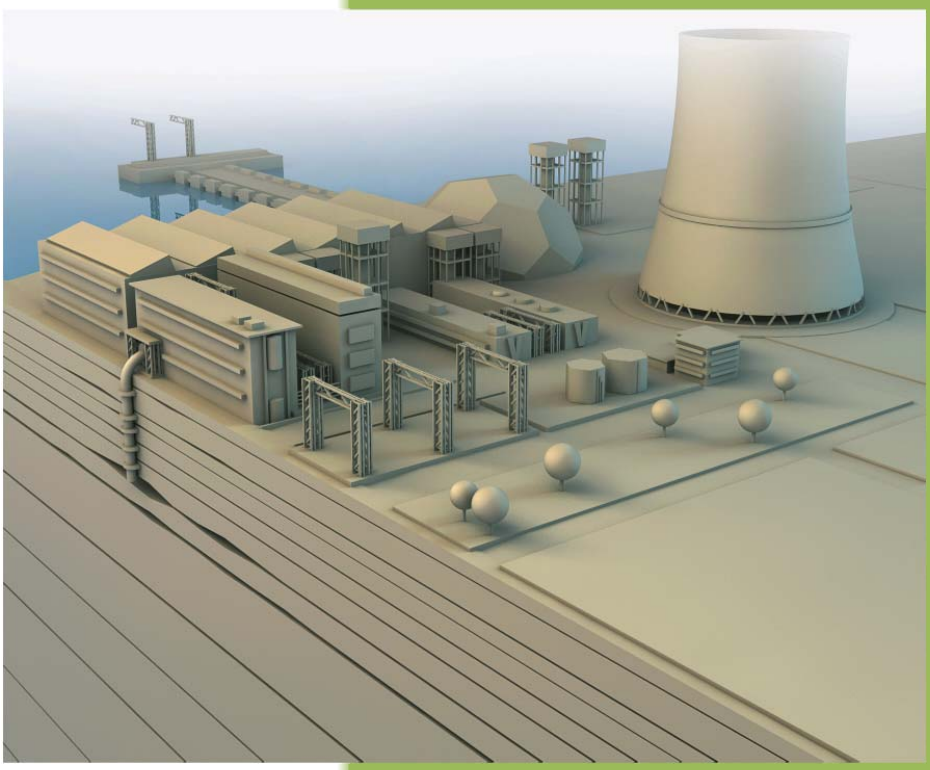

Behdad Moghtaderi

University of Newcastle

30 May 2014

Project Leader:	Prof Behdad Moghtaderi
Chief Investigators:	Prof Behdad Moghtaderi and Prof Terry Wall
Project Duration:	23 Dec 2010 to 22 Dec 2013 (official start and end date)
Report Period:	24 Jan 2011 to 21 March 2014 (actual project dates)
Sponsor/Scheme:	Coal Innovation NSW
Sponsor ID:	MOC10/1067
Institution Ref. Number:	G1000643

I, the undersigned, being a person duly authorised by the Grantee, certify that:

(a) the above information is true and complete;

(b) the expenditure of the Funding received to date has been solely on the Project;

(c) there is no matter or circumstances of which I am aware, that would constitute a breach by I&I NSW or, if applicable the End Recipient, of any term of the Funding Agreement between I&I NSW and the Grantee dated that has not been notified by the Grantee.

Signature: B Moghtaderi

Position: Project Leader (Head, Chemical Engineering, The University of Newcastle)

Name: Professor Behdad Moghtaderi

Date: 30 May 2014

EXECUTIVE SUMMARY

This final report details the key outputs and findings of the project titled "*A Novel Chemical Looping Based Air Separation Technology for Oxy-Fuel Combustion of Coal; Project ID: MOC10/1067*". The project, supported by generous funding from the NSW Coal Innovation, was conducted over the period between 24 Jan 2011 and 31 Dec 2014 by a team of researchers from the University of Newcastle. The project MOC10/1067 was concerned with the development of a novel chemical looping based air separation process named CLAS (and its variant named ICLAS) to facilitate the commercial-scale deployment of oxy-fuel combustion across the power generation sector in NSW. The project was part of a larger program of study at the University of Newcastle on alternative air separation technologies and specifically complemented two other relevant projects funded by the ANLEC-R&D [1] and Glencore (formerly Xstrata Coal [2]), respectively. The emphasis of the project MOC10/1067, though, was mainly on fundamental studies at bench-scale and pilot-scale under controlled laboratory settings.

As detailed below the project MOC10/1067 reached all its milestones and successfully met its key targets. More importantly, the project produced the scientific evidence that confirms the viability of the chemical looping air separation process from both technical and economic points of view.

The technical aims of the project were to:

1. Examine the redox behaviour of metallic oxide oxygen carriers under conditions pertinent to high temperature air separation.
2. Determine the fundamental science underpinning the oxygen decoupling phenomenon during the spontaneous reduction stage.
3. Once the underpinning science has been fully investigated, to determine the cost and energy penalty of the technology when applied to retrofitted power stations of the NSW fleet and to identify plant characteristics and age for economic viability.

To achieve the broad objectives of the project the team designed, constructed and commissioned several innovative experimental setups at bench-scale, pilot-scale and demonstration scale. These included a fixed-bed chemical looping reactor, a 10 kW_{th} pilot-scale prototype of the CLAS / ICLAS process and a large-scale demonstration unit. The team also employed an extensive array of conventional laboratory equipment and analytical / characterisation instruments.

As far as Aim (1) was concerned, the team concentrated its focus on two main fronts, namely: (i) identification of the most suitable oxygen carriers for chemical looping based air separation processes and (ii) development of a cost effective method for mass production of oxygen carriers to be used in the pilot-scale and large-scale investigations associated with the project.

On the former front, we made the final selection of the most suitable metal oxide species for CLAS based applications after a combined series of theoretical (e.g. thermodynamic assessment) and experimental research involving thermo-gravimetric analysis, packed-bed and pilot-plant experiments. Cu-oxide on SiO_2 support was found to have the highest performance characteristics. The CuO/SiO_2

oxygen carrier also exhibited higher stability than other metal oxides over repeated oxygen sorption-desorption cycles. Moreover, it was found that compare with other oxygen carriers the performance characteristics of CuO/SiO_2 oxygen carrier species can be enhance to a greater extent by additives. On this basis CuO/SiO_2 oxygen carrier species was selected as the preferred metal oxide for our future studies.

On the latter front the team managed to adapt the spray drying technique for production of high quality metal oxides that were particularly suited to pilot-scale studies. This method proved to be very effective and has now been adopted as our standard production method. Significant quantities of spray dried metal oxides (approximately 6 kg) were produced for pilot-scale experiments and the relevant tasks which were due in mid-2013 were completed ahead of the schedule.

As far as Aim (2) was concerned, one of major tasks completed during the period covered by this report was the commissioning of the 10 kW_{th} pilot-plant. The plant was initially used in a series of preliminary tests to identify its weaknesses. A few procedural and instrumental issues were identified which were subsequently resolved. The upgraded version of the pilot-plant was then employed in a number of different investigations under a wide range of operational scenarios to firstly better understand the plant operational envelop but more importantly to gain insight into the science underlying the oxygen decoupling process. In this context, one of the most important experimental campaigns undertaken in the project was the manifold switching (MS) experiments where the feed gas streams were systematically switched rather than solids being circulated. The importance of the MS experiments was twofold; firstly MS experiments allowed us to decouple the solid circulation and particle attrition issues from the reaction kinetics behaviour of oxygen carrier particles, thus focusing on the oxygen decoupling phenomenon; secondly MS experiments enabled us to assess the effectiveness of the manifold switching concept as a means of resolving the issues associated with the particle transport.

The experimental results obtained from the MS investigation confirmed that the most important parameter that underpins the oxygen decoupling process during the reduction phase was the oxygen partial pressure in the reduction reactor. The accurate control of the partial pressure in this reactor was the key is achieving the desired level of the oxygen purity in the product gas stream. Moreover, the results of the MS experimental campaign revealed that adequate levels of control over the partial pressure of oxygen can be achieved with either steam or CO_2 and in that sense the results were insensitive to the reduction gas.

The manifold switching experiments also confirmed the strengths of the concept and its usefulness for CLAS based applications. But the results also highlighted several shortcoming of the MS concept including the formation of undesirable hot spots in both reduction and oxidation reactors and the complexity of accurately controlling the process especially during the switch over phase.

Achieving project Aims (1) and (2) also required a great deal of theoretical, mathematical modelling and numerical simulations. In this context, we developed a two-dimensional (2D) CFD-DEM model for a numerical study of the mixing and segregation behaviour of binary mixtures of particles with different sizes and densities in a bubbling fluidized bed under conditions pertinent to the fuel reactor of

a cold-flow model (i.e. a non-reacting replica) of the 10 kW_{th} chemical looping pilot-plant. The work was motivated by the findings from other components of the project that showed the performance of chemical looping combustion processes can be improved drastically by enhancing the overall redox characteristics of the system through the use of binary mixtures of oxygen carriers; provided that particles of different species remains in the mixture for prolong period of operation. Results of the numerical investigation showed that as the size ratio of the binary mixture of particles reduced, the mixing index increased indicating better mixing conditions. The agreement between the CFD-DEM model predictions and the experimental data were found to be satisfactory. The optimum conditions for mixing of binary mixtures appeared to be a function of bubble size, bubble rising rate and bubbling dynamics (e.g. splitting and coalescence).

As part of modelling studies, we also developed a three-dimensional (3D) CFD-DEM model given that the 2D version lacked chemical reaction, energy balance and heat transfer sub-models and hence was more suited for examination of non-reacting systems like the bench-scale cold-flow setup. The 3D model was employed to: (i) study the performance characteristics of the 10 kW_{th} pilot-plant, (ii) assisting with the scale-up rule studies and (iii) assisting with the engineering design of CLAS / ICLAS processes particularly in regards to the sensitivity of the design geometry to inlet velocities for the reduction reactor, the air reactor and the loop seals. The 3D model was validated by comparing the predicted solid circulation rate with the experimental data collected from the bench-scale cold-flow model as well as those from the 10 kW_{th} pilot-plant and proved to be a very useful tool.

One of the other key outcomes of the theoretical / modelling studies was the establishment of a set of scale-up rules which allow designers in the future to design industry-scale versions of the CLAS system based on the knowledge gained experimentally in this study from the small-scale laboratory and pilot-scale prototypes of CLAS.

We also carried out a detailed techno-economic assessment of the NSW fleet of coal-fired power plants for oxy-fuel conversion and determined the extent to which the economic viability of oxy-fuel operations is enhanced by integration of the chemical looping based air separation processes into such operations. The assessment: (i) confirmed the technical and economic superiority of the CLAS process over the conventional cryogenic systems and (ii) revealed that while the rollout of oxy-fuel technology fitted with cryogenic air separation across the State's major coal-fired power plants will likely to be uneconomic, by integrating CLAS based air separation units the rollout might become viable. Based on our analysis the normalised capital cost of a chemical looping based oxy-fuel retrofit in NSW can be as low as \$2,300/kW while the corresponding levelised cost of electricity and the cost of CO_2 abatement are \$92/MWh and \$41/tCO_2, respectively. These figures, as discussed in details in the report, are among the lowest values reported in the literature for low emission technologies and are quite comparable with those associated with cost effective technologies such as supercritical pulverised fuel (black coal) and combined cycle gas turbine. However, further feasibility studies and more importantly new experimental investigations are required to demonstrate the effectiveness of the chemical looping based air separation at scale.

In addition to the techno-economic assessment, a LCA study was also carried out to assess the environmental impact and/or benefits of the chemical looping air separation. The comparative LCA

study demonstrated the domination of black coal feed as an energy and emissions source within the overall LCA. The large quantity of feed required results in the annual operational emissions to be far larger than that of power station set-up. This breakdown implies the importance of using the feed as efficiently as possible (on a tonne coal/MWh sent out to the grid basis) for optimal environmental performance (which is an intuitive outcome). It was found that the ICLAS version of the chemical looping air separation can significantly achieve better performance than current methods (cryogenic distillation) by reducing the parasitic load required by the power station for oxy-fuel combustion. It should be noted that chemical looping air separation may additionally have significant safety and associated cost benefits over current methods as well (while not explored in this study).

From the outset of this study, the benefit of the lower energy requirement for oxygen production indicated an improvement for energy and emissions, though it was unknown how the use of the metal substrate oxygen carrier (and associated processes and activities) may ameliorate this benefit. Due to the large contribution of black coal in operations, the use of the metal substrate oxygen carrier is negligible, contributing less than 1% additional energy and emissions in power station set-up (using conservative assumptions) and in operational phase still showing a substantial benefit (over 13% reduction in carbon emissions equivalent) even when the ICLAS metal substrate processes and activities are included. The use of ICLAS in place of cryogenic distillation could substantially reduce required energy and emissions. Using this study's model, it would be equivalent to saving:

- 120 PJ or over 33,300,000 MWh of embodied energy saved
- 20,700,000 tCO_2e (equivalent to taking almost 200,000 new passenger vehicles off the road for every year of the 20 year operation of the facility [using 5 metric tonnes of CO_2 equivalent per new passenger vehicle per year]).

Table of Contents

	Page Number
EXECUTIVE AUMMARY	3
1. INTRODUCTION	21
1.1 BACKGROUND	22
1.2 PROJECT AIMS AND OBJECTIVES	25
1.3 APPROACH AND METHODOLOGY	27
2. EXPERIMENTAL METHODS & TECHNIQUES	28
2.1 EXPERIMENTAL SETUPS	28
2.1.1 Bench-Scale Cold-Flow Setup	28
2.1.2 Bench-Scale Fixed-Bed Setup	30
2.1.3 Thermo-Gravimetric Analyser (TGA)	31
2.1.4 Dimensional Analysis and Pilot-Plant Design	32
2.1.5 Dual Fluidised-Bed 10 kW_{th} Pilot-Plant	33
2.1.6 Cold-Flow Demonstration Setup	37
2.2 METAL OXIDES	38
2.2.1 Preparation and Production of Metal Oxides	38
2.2.2 Characterisation of Metal Oxides Using Analytical Techniques	40
3. SELECTION OF METAL OXIDES	42
3.1 THERMODYNAMIC APPROACH	42
3.1.1 Thermodynamic Assessment of Single Species Metal Oxides	42
3.1.2 Review of Mixed Metal Oxide Thermodynamics	53
3.2 Reaction Kinetics Approach	59
3.2.1 Summary	59
3.2.2 Metal Oxide Samples	59
3.2.3 Reactivity and Stability Measurements Using TGA	60
3.2.4 Reactivity and Stability Measurements Using the Bench-Scale Fixed-Bed Setup	70
3.2.5 Reactivity and Stability Measurements Using the 10 kW_{th} Pilot-Plant	77
3.3 ASSESSMENT AND CONCLUSIONS	86
3.3.1 Mono-species Metal Oxides	86
3.3.2 Bimetallic Cu/Ni, Cu/Co, Cu/Mn and Cu/Fe Based Metal Oxides	87
4. PARTICLE TRANSPORT AND HYDRODYNAMICS	89
4.1 HYDRODYNAMIC EXPERIMENTS (BENCH-SCALE)	89
4.1.1 Fluidisation Velocities	89
4.1.2 Segregation	90
4.1.3 Pressure Profiles	99
4.2 COMPUTATIONAL FLUID DYNAMICS / DISCRETE ELEMENT MODELLING (CFD-DEM)	104
4.2.1 Summary	104
4.2.2 The Mathematical Model	104
4.2.3 Approach and Methodology	108

4.2.4 Results and Discussion 113
4.2.5 Conclusions 126
5. PILOT-SCALE STUDIES ON REACTOR CONFIGURATION 128
5.1 MANIFOLD SWITCHING REACTOR (MSR) CONCEPT 128
5.2 EXPERIMENTAL METHODS & TECHNIQUES 129
5.2.1 Sample Preparation 129
5.2.2 Procedure 129
5.3 RESULTS AND DISCUSSION 130
5.4 CONCLUDING REMARKS 133
6. DETERMINATION OF SCALE-UP RULES 134
6.1 OVERVIEW 134
6.2 MAIN CHALLENGES IN SCALING-UP FLUIDISED BED REACTORS 134
6.3 SCALE-UP METHODOLOGY AND PROCEDURES 136
6.4 HYDRODYNAMIC SCALE-UP 137
6.5 CHEMICAL REACTION SCALE-UP 140
6.6 SCALE-UP RULES 141
7. MATHEMATICAL MODELLING 142
7.1 OVERVIEW 142
7.2 DESCRIPTION OF THE 3D CFD-DEM MODEL 143
7.2.1 Governing Equations for the Fluid-Flow and Particle Transport 143
7.2.2 Governing Equations for the Energy Balance, Heat Transfer and Chemical Reactions 143
7.3 NUMERICAL SIMULATIONS 144
7.3.1 Numerical Procedure 144
7.3.2 Simulation Results 145
8. TECHNOECONOMIC ASSESSMENT 147
8.1 BACKGROUND 147
8.2 METHODOLOGY 148
8.2.1 Overview 148
8.2.2 Technical Assessment Methodology 149
8.2.3 Economic Assessment Methodology 154
8.3 RESULTS AND DISCUSSION 158
8.3.1 Plant Technical Assessment 158
8.3.2 Plant Economic Assessment 166
8.4 CONCLUSIONS 176
9. LIFE CYCLE ASSESSMENT 177
9.1 BACKGROUND 177
9.2 METHODOLOGY 177
9.3 LCA CALCULATIONS 180
9.4 RESULTS AND DISCUSSION 181
9.5 CONCLUSIONS 189
10. OVERALL CONCLUSIONS AND RECOMMENDATIONS 191

FOR FUTURE RESEARCH
10.1 OVERALL CONCLUSION 191
10.2 RECOMMENDATIONS FOR FUTURE WORK 191
11. PROJECT ADMINISTRATION OVERVIEW 193
11.1 BUDGET AND ACTUAL SPEND 193
11.2 TIMELINE 193
11.3 HUMAN RESOURCES 193
11.4 PROJECT MANAGEMENT 194
11.5 PUBLICATIONS 194
REFERENCES 196
ACKNOWLEDGEMENTS 199
APPENDIX A: SEM AND XRD RESULTS 200
APPENDIX B: BIMETALLIC CU-BASED RESULTS
APPENDIX C: LCA CALCULATIONS

LIST OF FIGURES

Figures in Main Body of the Report

Figure 1: Schematic of the CLAS process.
Figure 2: Schematic of the ICLAS process.
Figure 3: Schematic of an oxy-fuel coal-fired power plant retrofitted with an ICLAS unit.
Figure 4: Relationship between the existing projects related to the CLAS process.
Figure 5: Simplified version of the project plan.
Figure 6: Schematic of the cold-flow setup showing key dimensions (not to scale); (a) complete system; (b) upper loop-seal, and (c) lower loop seal, as well as (d) photo of the setup.
Figure 7: Locations of pressure measuring points in the cold-flow setup.
Figure 8: Bench-scale fixed-bed setup; (a) schematic, and (b) photos.
Figure 9: TGA units; (a) Rubotherm pressurised MSB-Aus-2004-00188 unit and (b) TA Instruments Q50 unit.
Figure 10: Schematic of the pilot-scale setup; (a) 2D view, and (b) 3D view.
Figure 11: Pilot plant; (a) Perspex version; (b) SS version, (c) control box and (d) internal view of the control box.
Figure 12: Pilot plant; (a) basic configuration, (b) particle and gas flow arrangement corresponding to various operational modes.
Figure 13: Selection of operational modes/parameters and pilot plant control through the graphical LabView interface.
Figure 14: The 7 m high demonstration unit (minus auxiliary systems).
Figure 15: Optical microscope image of spray dried particles sintered for; (a) 12h at 1100°C in air and (b) 24h at 1100°C in air.
Figure 16: SEM images of fresh (a) and reacted (b) spray dried CuO samples.
Figure 17: XRD pattern of reacted spray dried CuO samples after 42 redox cycles.
Figure 18: Ellingham diagram of different metal oxide systems (the diagram does not show metal oxide systems having ΔG lower than -2000 KJ and temperature >1500^{0}C).
Figure 19: Equilibrium partial pressure of oxygen for different metal oxide systems at elevated temperatures (the diagram only shows metal oxide systems which need EPP of O_2 between 0.01 to 1 % and temperature < 2000 ^{0}C).
Figure 20: Steam/CO_2 requirement calculations for Mn_2O_3/Mn_3O_4 oxide system at elevated temperature.
Figure 21: Ellingham diagram from investigating hydroxide and carbonate formation during reduction with steam and/or CO_2.
Figure 22: Equilibrium calculations for O_2 release for Mn_2O_3 at elevated temperature under different CO_2.
Figure 23: Equilibrium calculations for O_2 release for CuO at elevated temperature under different CO_2.
Figure 24: Thermodynamic cycle at 850^{0}C Mn-Oxides with Al_2O_3 support.
Figure 25: Equilibrium calculations for the redox cycle of Mn-Oxides with Al_2O_3 support.
Figure 26: Oxygen carrier inventory and steam/CO_2 requirement calculations for oxy-fuel firing thermal power plant (*HOS= Higher oxidation state and *LOS= Lower oxidation state).

Figure 27: Gibbs free energy for mixed metal oxides.
Figure 28: A typical Ellingham diagram for mixed metal oxides selection.
Figure 29: TGA results showing the weight variations over 5 desorption and adsorption cycles for Mn_2O_3, CuO and Co_2O_3 800°C.
Figure 30: Conversion of different pure metal oxides at 800°C; (a) reduction and (b) oxidation.
Figure 31: TGA results showing the cyclic weight variations during desorption and adsorption cycles for 30%CuO/SiO_2 at 800°C (reduction time = 90 min, oxidation time = 30 min).
Figure 32: TGA results showing the cyclic weight variations during desorption and adsorption cycles for 30%CuO/SiO_2 at 950°C (reduction time = 30 min, oxidation time = 30 min).
Figure 33: Conversion corresponding to the fifth cycles for 30%CuO/SiO_2 at 800°C, 875°C and 950°C; (a) reduction (b) oxidation.
Figure 34: TGA results showing the cyclic weight variations during desorption and adsorption cycles for CuO/Al_2O_3-4IWP at 800°C (reduction time = 60 min, oxidation time = 30 min).
Figure 35: TGA results showing the cyclic weight variations during desorption and adsorption cycles for CuO/Al_2O_3-4IWP at 850°C (reduction time = 50 min, oxidation time = 30 min).
Figure 36: TGA results showing the cyclic weight variations during desorption and adsorption cycles for CuO/Al_2O_3-4IWP at 950°C (reduction time = 30 min, oxidation time = 30 min).
Figure 37: TGA results showing the cyclic weight variations during desorption and adsorption cycles for Co_3O_4/Al_2O_3- 4IWP at 800°C (reduction time = 60 min, oxidation time = 30 min).
Figure 38: TGA results showing the cyclic weight variations during desorption and adsorption cycles for Co_3O_4/Al_2O_3- 4IWP at 900°C (reduction time = 30 min, oxidation time = 30 min).
Figure 39: TGA results showing the cyclic weight variations during desorption and adsorption cycles for Co_3O_4/Al_2O_3- 4IWP at 950°C (reduction time = 30 min, oxidation time = 30 min).
Figure 40: Conversion corresponding to the fifth cycles for Co_3O_4/Al_2O_3-4IWP at 800°C, 875°C and 950°C; (a) reduction (b) oxidation.
Figure 41: TGA results showing the cyclic weight variations during desorption and adsorption cycles for Co_3O_4/SiO_2-4IWP at 800°C (reduction time = 60 min, oxidation time = 30 min).
Figure 42: TGA results showing the cyclic weight variations during desorption and adsorption cycles for Co_3O_4/SiO_2-4IWP at 900°C (reduction time = 30 min, oxidation time = 30 min).
Figure 43: Comparison of conversions corresponding to the fifth cycles for Co_3O_4/Al_2O_3-4IWP and Co_3O_4/Al_2O_3-4IWP at 800°C and 850°C; (a) reduction (b) oxidation.
Figure 44: Variations of weight fraction over 41 continuous redox cycles for 60%CuO/SiO_2.
Figure 45: Fraction of maximum weight variation in every cycle versus cycle number over 41 continuous redox cycles for 60%CuO/SiO_2 (n is the cycle number).
Figure 46: Effect of cycle numbers on (a) reduction (b) oxidation conversion for the experiments conducted at 900°C for 60%CuO/SiO_2.
Figure 47: Arrhenius plot of 30%CuO/SiO_2 reduction (experiments: ◆ and the trendline: solid line) for the calculations of activation energy E.
Figure 48: Photograph of the quartz tube reactor loaded with a metal oxide sample.
Figure 49: The variation of oxygen concentration tested with silica after (a) switching gas from mixing gas with 5% O_2 to nitrogen; and (b) from nitrogen to mixture gas.
Figure 50: The variation of oxygen partial pressure during (a) desorption and (b) process at 800°C.
Figure 51: The variation of oxygen partial pressure during (a) desorption and (b) process at 850°C.
Figure 52: The variation of oxygen partial pressure during (a) desorption and (b) process at 900°C.

Figure 53: The variation of oxygen partial pressure during (a) desorption and (b) process at 950°C.
Figure 54: Images of SiO_2 particles with magnifications; (a) 140x, (b) 350x and (c) 1440x.
Figure 55: Images of Al_2O_3 particles with magnifications; (a) 140x, (b) 350x and (c) 1440x.
Figure 56: Images of Fresh 48%-CuO-SiO_2 (by single impregnation) particles with magnifications; (a) 140x, (b) 350x and (c) 1440x.
Figure 57: Images of Fresh CuO-Al_2O_3 (by 4IWP cycles) particles with magnifications; (a) 140x, (b) 350x and (c) 1440x.
Fresh Mn_2O_3-SiO_2 (4IWP) Images:
Figure 58: Images of Fresh Mn_2O_3-SiO_2 (by 4IWP cycles) particles with magnifications; (a) 140x, (b) 350x and (c) 1440x.
Figure 59: Images of Fresh Mn_2O_3- Al_2O_3 (by 4IWP cycles) particles with magnifications; (a) 140x, (b) 350x and (c) 1440x.
Figure 60: Images of Fresh Co_3O_4-SiO_2 (by 4IWP cycles) particles with magnifications; (a) 140x, (b) 350x and (c) 1440x.
Figure 61: SEM images of (a) fresh, (b) fully reacted, (c) enlarged-view fully-reacted, CuO particles on silica support.
Figure 62: Weight change profiles for five continuous oxygen desorption-sorption cycles for
Figure 63: Weight change profiles for five continuous oxygen desorption-sorption cycles for Mn_2O_3/SiO_2, Co_3O_4/SiO_2 and CuO/SiO_2 at temperatures of 800, 850, 900 and 950°C.
Figure 64: Conversion of Co_3O_4/Al_2O_3 during oxygen desorption (a) and sorption (b) at temperatures between 800~950°C for the fifth cycle.
Figure 65: Conversion of CuO/SiO_2 during oxygen desorption (a) and sorption (b) at temperatures between 800~950°C for the fifth cycle.
Figure 66: Weight change profile for Co_3O_4/Al_2O_3 at 880°C during continuous 41-cycle oxygen desorption-sorption tests.
Figure 67: Weight change profile for CuO/SiO_2 at 900°C during continuous 41-cycle oxygen desorption-sorption tests.
Figure 68: Cyclic conversion of Co_3O_4/Al_2O_3 at 880°C during oxygen desorption (a) and sorption (b) for continuous 41-cycle desorption-sorption tests.
Figure 69: Cyclic conversion of CuO/SiO_2 at 900°C during oxygen desorption (a) and sorption (b) for continuous 41-cycle desorption-sorption tests.
Figure 70: SEM images of fresh and used (after 41 cycles in TGA) Co_3O_4/Al_2O_3 and CuO/SiO_2 oxygen carriers.
Figure 71: Oxygen concentration profile at the outlet of the pilot-plant reactor loaded with CuO/SiO_2 oxygen carriers: (a) 750°C~900°C; (b) 950°C.
Figure 72: Bimetallic CuO-based metal oxide oxygen carriers on silica support.
Figure 73: Oxygen transport capacity (OTC) change during 41 continuous oxygen desorption-sorption cycles in TGA at 900°C for mixed metal oxides oxygen carriers.
Figure 74: Air reactor gas velocity vs. mass flux.
Figure 75: Particle concentration for components of the rig for an initial mixture of 10 % 212-255 μm microlene in 90-106 μm glass beads.
Figure 76: Particle concentration for components of the rig for an initial mixture of 20% 300-355 μm microlene in 90-106 μm glass beads.

Figure 77: Particle concentration for components of the rig for an initial mixture of 10 % 212-255 µm microlene in 106-125 µm glass beads.
Figure 78: Particle concentration for components of the rig for an initial mixture of 10 % 300-355 µm microlene in 90-106 µm glass beads.
Figure 79: Particle concentration for components of the rig for an initial mixture of 20% 212-255 µm microlene in 125-150 µm glass beads.
Figure 80: Particle concentration for components of the rig for an initial mixture of 5 % 212-255 µm microlene in 90-106 µm glass beads.
Figure 81: Particle concentration for components of the rig for an initial mixture of 20% 300-355 µm microlene in 106-125 µm glass beads.
Figure 82: Height segregation in the air reactor across three experiments at 0.41 m/s reactor velocity on an initial mixture of 20 % 300-355 µm microlene particles in 90-106µm glass beads.
Figure 83: Microlene weight percentage vs. bed height for an initial mixture of 10 % 300-355 µm microlene in 90-106 µm glass beads.
Figure 84: Pressure profile in the air reactor and riser for a 20 wt % concentration of 212-255 µm Microlene in 125-150 µm glass beads
Figure 85: Pressure profile in the air reactor and riser for a 20 wt % concentration of 300-355 µm Microlene in 106-125 µm glass beads.
Figure 86: Pressure profile in the fuel reactor for a 20 wt % concentration of 212-255 µm Microlene in 125-150 µm glass beads.
Figure 87: Pressure profile in the fuel reactor for a 20 wt % concentration of 300-355 µm Microlene in 106-125 µm glass beads.
Figure 88: Pressure profile in the air reactor/riser section of the rig for different mixtures of particles at 0.45 m/s air reactor velocity.
Figure 89: Pressure profile in the air reactor/riser section of the rig for different concentration of the same mixture of particles at 0.45 m/s air reactor velocity.
Figure 90: Pressure profile in the fuel reactor for varying particle mixtures and concentrations.
Figure 91: Adjustable sampling boxes for calculation of mixing index.
Figure 92: Mixing process with initial segregated particles arrangement (U_{ex} = 0.04 m/s, X_L=0.1, ρ_1 = 2462 kg/m^3, ρ_2 = 939 kg/m^3, d_1 = 116 µm, d_2 = 328 µm, A_D = 15 × 150 mm^2).
Figure 93: Influence of (a) vertical column width and (b) fixed particle number in each sampling box on mixing index (U_{ex} = 0.04 m/s, X_L = 0.1, ρ_1 = 2462 kg/m^3, ρ_2 = 939 kg/m^3, d_1 = 116 µm, d_2 = 328 µm, A_D = 15 × 150 mm^2).
Figure 94: Influence of sampling box size on mixing index using conventional Lacey's and Feng's methods (U_{ex} = 0.04 m/s, X_L=0.1, ρ_1 = 2462 kg/m^3, ρ_2 = 939 kg/m^3, d_1 = 116 µm, d_2 = 328 µm, A_D = 15 × 150 mm^2).
Figure 95: Sensitivity of mixing index to domain size (U_{ex} = 0.04 m/s, X_L=0.1, ρ_1 = 2462 kg/m^3, ρ_2 = 939 kg/m^3, d_1 = 116 µm, d_2 = 278 µm).
Figure 96: Sensitivity of bed expansion to domain size (U_{ex} = 0.04 m/s, X_L=0.1, ρ_1 = 2462 kg/m^3, ρ_2 = 939 kg/m^3, d_1 = 116 µm, d_2 = 278 µm).
Figure 97: Sensitivity of mixing index to initial packed bed height (U_{ex} = 0.04 m/s, X_L=0.1, ρ_1 = 2462 kg/m^3, ρ_2 = 939 kg/m^3, d_1 = 116 µm, d_2 = 328 µm, A_D = 20 × 200 mm^2).
Figure 98: Sensitivity of mixing index to initial particle position (U_{ex} = 0.04 m/s, X_L=0.1, ρ_1 = 2462 kg/m^3, ρ_2 = 939 kg/m^3, d_1 = 116 µm, d_2 = 328 µm, A_D = 15 ×150 mm^2).

Figure 99: Snapshots of solids mixing status at different particle size ratios (t = 10.84 s, U_{ex} = 0.04 m/s, X_L=0.1, ρ_1 = 2462 kg/m^3, ρ_2 = 939 kg/m^3, A_D = 20 × 200 mm^2).
Figure 100: Influence of particle size ratio on mixing index (U_{ex} = 0.04 m/s, X_L=0.1, ρ_1 = 2462 kg/m^3, ρ_2 = 939 kg/m^3, A_D = 20 × 200 mm^2).
Figure 101: Snapshots of solids mixing status at different particle density ratios (t = 10.84 s, U_{ex} = 0.04 m/s, X_L=0.1, d_1 = 116 µm, d_2 = 328 µm, A_D = 20 × 200 mm^2).
Figure 102: Influence of particle density ratio on mixing index (U_{ex} = 0.04 m/s, X_L=0.1, d_1 = 116 µm, d_2 = 328 µm).
Figure 103: Snapshots of solids mixing status at different excess gas velocities (t = 10.84 s, X_L=0.1, ρ_1 = 2462 kg/m^3, ρ_2 = 939 kg/m^3, d_1 = 116 µm, d_2 = 328 µm, A_D = 20 × 200 mm^2).
Figure 104: Influence of excess gas velocities on mixing index (X_L=0.1, ρ_1 = 2462 kg/m^3, ρ_2 = 939 kg/m^3, d_1 = 116 µm, d_2 = 328 µm, A_D = 20 × 200 mm^2).
Figure 106: Schematic representation of the evolution of the normalised fields for (a) concentration of product gases and (b) bed temperature within a typical MSR unit.
Figure 107: Temporal and spatial evolution of the normalised oxygen concentration within a typical MSR unit.
Figure 108: Temporal and spatial evolution of the temperature within a typical MSR unit.
Figure 109: Variation of the reactor outlet temperature as a function of time within a typical MSR unit.
Figure 110: Plots of maximum temperature rise as a function of the axial position for a typical MSR unit.
Figure 111: Flowchart of the procedure implemented in this project for determining scale-up rules.
Figure 112: Initial particle loading in each component of the large-scale demonstration unit.
Figure 113: Pressure profiles for the demonstration plant for d_p= 120µm GB [Case1: P_{in}=37.6 kPa, Case2: P_{in}=40.60 kPa and Case3: P_{in}=38.60 kPa].
Figure 114: A typical pressure profile for the 10 kW$_{th}$ pilot-plant prototype.
Figure 115: Comparison of pressure profiles of the demonstration unit and 10 kW$_{th}$ pilot-plant.
Figure 116: Flow chart of the CFD-DEM two way coupling.
Figure 117: Contour plots of oxygen concentration in the simulated 10 kW$_{th}$ pilot-plant.
Figure 118: Contour plots of (a) N_2 and (b) water in the simulated 10 kW$_{th}$ pilot-plant.
Figure 119: Contour plots of (a) temperature and (b) particle distribution in the simulated 10 kW$_{th}$ pilot-plant.
Figure 120: Flowchart of TAS.
Figure 121: Flowchart of CAS.
Figure 122: Bar char plots of gross oxygen demand for coal-fired power plants in NSW.
Figure 123: Bar char plots of normalised oxygen demand for coal-fired power plants in NSW.
Figure 124: Bar char plots of gross CO_2 avoided for coal-fired power plants in NSW.
Figure 125: Bar char plots of normalised CO_2 avoided for coal-fired power plants in NSW.
Figure 126: Bar char plots of ASU power demand for coal-fired power plants in NSW.
Figure 127: Bar char plots of CPU power demand for coal-fired power plants in NSW.
Figure 128: Bar char plots of combined parasitic load for coal-fired power plants in NSW.
Figure 129: Bar char plots of plant capacity loss for coal-fired power plants in NSW.
Figure 130: Bar chart plots of thermal efficiency for the NSW fleet of coal-fired power plants.
Figure 131: Bar chart plots of thermal efficiency penalty for the NSW fleet of coal-fired power plants.

Figure 132: Bar chart plots of thermal efficiency penalty for the NSW fleet of coal-fired power plants as a function of efficiency penalty due to ASU and CPU power demands.
Figure 133: Bar chart plots of EOP for the NSW fleet of coal-fired power plants.
Figure 134: Bar chart plots of the gross capital cost for the retrofit of NSW fleet of coal-fired power plants.
Figure 135: Bar chart plots of the normalised capital cost for the retrofit of NSW fleet of coal-fired power plants.
Figure 136: Breakdown of capital cost items for the Bayswater power plant (cryogenic option).
Figure 137: Breakdown of capital cost items for the Bayswater power plant (ICLAS [S] option).
Figure 138: Breakdown of capital cost items for the Bayswater power plant (ICLAS [FG] option).
Figure 139: Relative costs of ASU and CPU with respect to their combined capital cost.
Figure 140: Benchmarking of the normalised capital cost for the NSW coal-fired power plants retrofitted for oxy-firing (with ICLAS [FG] and CCS) against the normalised capital cost for 22 alternative low emission technologies.
Figure 141: Bar charts of LCOE for NSW coal-fired power plants retrofitted for oxy-firing operation.
Figure 142: Benchmarking of the LCOE for the NSW coal-fired power plants retrofitted for oxy-firing (with ICLAS [FG] and CCS) against the LCOE for 22 alternative low emission technologies [46].
Figure 143: Bar char plot of rises in the cost of generating electricity (no carbon tax).
Figure 144: Bar char plot of rises in the cost of generating electricity (carbon tax included).
Figure 145: Bar char plot of cost of abatement for NSW coal-fired power plants (no carbon tax).
Figure 146: Bar char plot of cost of abatement for NSW coal-fired power plants (carbon tax included).
Figure 147: Flowchart of inputs, components and output for the ICLAS [FG] process.
Figure 148: Flowchart of inputs, components and output for the cryogenic process.
Figure 149: Emissions of both scenarios over the 20 year lifetime of the power plant.
Figure 150: Energy of both scenarios over the 20 year lifetime of the power plant.
Figure 151: Emissions of all sources.
Figure 152: Emissions of all sources (resized for non-feed sources).
Figure 153: Energy of all sources.
Figure 154: Energy of all sources (resized for non-feed sources).
Figure 155: Comparison of all annual emissions for both scenarios of ICLAS and CD.
Figure 156: Comparison of all annual energy for both scenarios of ICLAS and CD.

Figures in Appendix A

Figure A1. SiO_2 images at the magnification of 200X, 2000X, 5000X and 10000X.
Figure A2. Al_2O_3 images at the magnification of 200X, 2000X, 5000X and 10000X.
Figure A3. Fresh sample images of 30%CuO/SiO2 at the magnification of 200X, 2000X, 5000X and 10000X.
Figure A4. Sample images of 30%CuO/SiO_2 after 41 continuous desorption-sorption cycles test in TGA at 800^{o}C for the magnification of 200X, 2000X, 5000X and 10000X.
Figure A5. Sample images of 30%CuO/SiO_2 after continuous five desorption-sorption cycles test in TGA at 800 for the magnification of 200X and 5000X.
Figure A6. Fresh sample images of 60%CuO/SiO_2 at the magnification of 200X, 2000X, 5000X and 10000X.
Figure A7. Sample images of 60%CuO/SiO_2 after 18 continuous desorption-sorption cycles test in

TGA at 900°C for the magnification of 200X, 2000X, 5000X and 10000X.
Figure A8. Sample images of 60%CuO/SiO_2 after 41 continuous desorption-sorption cycles test in TGA at 900°C for the magnification of 200X, 2000X, 5000X and 10000X.
Figure A9. Sample images of 60%CuO/SiO_2 after packed-bed test at 800°C for the magnification of 200X, 2000X, 5000X and 10000X.
Figure A10. Fresh sample images of CuO/Al_2O_3 at the magnification of 200X, 2000X, 5000X and 10000X.
Figure A11. Sample images of CuO/Al_2O_3 after five continuous desorption-sorption cycles test in TGA at 800°C for the magnification of 200X, 2000X, 5000X and 10000X.
Figure A12. Fresh sample images of Co_3O_4/Al_2O_3 at the magnification of 200X, 2000X, 5000X and 10000X.
Figure A13. Sample images of Co_3O_4/Al_2O_3 after five continuous desorption-sorption cycles test in TGA at 800°C for the magnification of 200X
Figure A14. Sample images of Co_3O_4/Al_2O_3 after packed-bed test at 800°C for the magnification of 200X, 2000X, 5000X and 10000X.
Figure A15. Fresh sample images of Co_3O_4/SiO_2 at the magnification of 200X, 2000X, 5000X and 10000X.
Figure A16. Sample images of Co_3O_4/SiO_2 after five continuous desorption-sorption cycles test in TGA at 800°C for the magnification of 200X, 2000X, 5000X and 10000X.
Figure A17. Fresh sample images of Mn_2O_3/Al_2O_3 at the magnification of 200X, 2000X, 5000X and 10000X.
Figure A18. Sample images of Mn_2O_3/Al_2O_3 after five continuous desorption-sorption cycles test in TGA at 800°C for the magnification of 200X, 2000X, 5000X and 10000X.
Figure A19. Fresh sample images of Mn_2O_3/SiO_2 at the magnification of 200X, 2000X, 5000X and 10000X.
Figure A20. Sample images of Mn_2O_3/SiO_2 after five continuous desorption-sorption cycles test in TGA at 800°C for the magnification of 200X, 2000X, 5000X and 10000X.
Figure A21. Fresh sample images of CuO-MgO-9-1/SiO_2 at the magnification of 200X, 2000X, 5000X and 10000X.
Figure A22. Sample images of CuO-MgO-9-1 /SiO_2 after 41 continuous desorption-sorption cycles test in TGA at 900°C for the magnification of 2000X and 5000X.
Figure A23. Fresh sample images of CuO-MgO-4-1/SiO_2 at the magnification of 200X, 2000X, 5000X and 10000X.
Figure A24. Sample images of CuO-MgO-4-1 /SiO_2 after 41 continuous desorption-sorption cycles test in TGA at 900°C for the magnification of 5000X and 10000X.
Figure A25. Fresh sample images of CuO-MgO-7-3/SiO_2 at the magnification of 5000X and 10000X.
Figure A26. Sample images of CuO-MgO-7-3 /SiO_2 after 41 continuous desorption-sorption cycles test in TGA at 900°C for the magnification of 5000X and 10000X.
Figure A27. Fresh sample images of CuO-MgO-1-1/SiO_2 at the magnification of 5000X and 10000X.
Figure A28. Sample images of CuO-MgO-1-1 /SiO_2 after 41 continuous desorption-sorption cycles test in TGA at 900°C for the magnification of 5000X and 10000X.
Figure A29. Fresh sample images of CuO-NiO-9-1/SiO_2 at the magnification of 200X, 2000X,

5000X and 10000X.
Figure A30. Sample images of CuO-NiO-9-1 /SiO_2 after 41 continuous desorption-sorption cycles test in TGA at 900^{o}C for the magnification of 5000X and 10000X.
Figure A31. Fresh sample images of CuO-NiO-4-1/SiO_2 at the magnification of 200X, 2000X, 5000X and 10000X.
Figure A32. Sample images of CuO-NiO-4-1 /SiO_2 after 41 continuous desorption-sorption cycles test in TGA at 900^{o}C for the magnification of 5000X and 10000X.
Figure A33. Fresh sample images of CuO-NiO-7-3/SiO_2 at the magnification of 200X, 2000X, 5000X and 10000X.
Figure A34. Sample images of CuO-NiO-7-3 /SiO_2 after 41 continuous desorption-sorption cycles test in TGA at 900^{o}C for the magnification of 200X, 2000X, 5000X and 10000X.
Figure A35. Fresh sample images of CuO-Co_3O_4-9-1/SiO_2 at the magnification of 200X, 2000X, 5000X and 10000X.
Figure A36. Sample images of CuO-Co_3O_4-9-1 /SiO_2 after 41 continuous desorption-sorption cycles test in TGA at 900^{o}C for the magnification of 200X, 2000X, 5000X and 10000X.
Figure A37. Fresh sample images of CuO-Co_3O_4-4-1/SiO_2 at the magnification of 200X, 2000X, 5000X and 10000X.
Figure A38. Sample images of CuO-Co_3O_4-4-1 /SiO_2 after 41 continuous desorption-sorption cycles test in TGA at 900^{o}C for the magnification of 200X, 2000X, 5000X and 10000X.
Figure A39. Fresh sample images of CuO-Co_3O_4-7-3/SiO_2 at the magnification of 200X, 2000X, 5000X and 10000X.
Figure A40. Fresh sample images of CuO-Fe_2O_3-4-1/SiO_2 at the magnification of 200X, 2000X, 5000X and 10000X.
Figure A41. Sample images of CuO- Fe_2O_3-4-1 /SiO_2 after 41 continuous desorption-sorption cycles test in TGA at 900^{o}C for the magnification of 200X, 2000X, 5000X and 10000X.
Figure A42. Fresh sample images of CuO-Mn_2O_3-4-1/SiO_2 at the magnification of 200X, 2000X, 5000X and 10000X.
Figure A43. Sample images of CuO- Mn_2O_3-4-1 /SiO_2 after 41 continuous desorption-sorption cycles test in TGA at 900^{o}C for the magnification of 200X, 2000X, 5000X and 10000X.
Figure A44. XRD pattern of SiO_2
Figure A45. XRD pattern of Al_2O_3
Figure A46. XRD pattern of CuO/SiO_2
Figure A47. XRD pattern of CuO/Al_2O_3
Figure A48. XRD pattern of Co_3O_4/Al_2O_3
Figure A49. XRD pattern of Co_3O_4/SiO_2
Figure A50. XRD pattern of Mn_2O_3/ Al_2O_3
Figure A51. XRD pattern of Mn_2O_3/ SiO_2
Figure A52. XRD pattern of CuO-NiO-9-1 / SiO_2
Figure A53. XRD pattern of CuO-NiO-4-1 / SiO_2
Figure A54. XRD pattern of CuO-NiO-7-3 / SiO_2
Figure A55. XRD pattern of CuO-Mn_2O_3-4-1 / SiO_2
Figure A56. XRD pattern of CuO-Fe_2O_3-4-1 / SiO_2
Figure A57. XRD pattern of CuO-MgO-9-1 / SiO_2
Figure A58. XRD pattern of CuO-MgO-4-1 / SiO_2

Figure A59. XRD pattern of CuO-MgO-7-3 / SiO_2
Figure A60. XRD pattern of CuO-MgO-1-1 / SiO_2

Figures in Appendix B

Figure B1: The effect of adding MgO and its weight ratio on oxygen desorption conversion of CuO/SiO_2 at 900°C.
Figure B2: The effect of adding MgO and its weight ratio on oxygen sorption conversion of CuO/SiO_2 at 900°C.
Figure B3: The effect of adding Co_3O_4 and its weight ratio on oxygen desorption conversion of CuO/SiO_2 at 900°C.
Figure B4: The effect of adding Co_3O_4 and its weight ratio on oxygen sorption conversion of CuO/SiO_2 at 900°C.
Figure B5: The effect of adding NiO and its weight ratio on oxygen desorption conversion of CuO/SiO_2 at 900°C.
Figure B6: The effect of adding NiO and its weight ratio on oxygen sorption conversion of CuO/SiO_2 at 900°C.
Figure B7: The effect of adding different metal oxides at 25 wt. % on oxygen desorption conversion of CuO/SiO_2 at 900°C.
Figure B8: The effect of adding different metal oxides at 25 wt. % on oxygen sorption conversion of CuO/SiO_2 at 900°C.
Figure B9: Weight change of 60 wt.%CuO/40 wt.%SiO_2 during 41 continuous oxygen desorption-sorption cycles in TGA at 900°C. Desorption time = 15min; Sorption time = 15min.
Figure B10: Weight change of CuO-MgO-9-1/SiO_2 during 41 continuous oxygen desorption-sorption cycles in TGA at 900°C. Desorption time = 15min; Sorption time = 30min.
Figure B11: Weight change of CuO-MgO-4-1/SiO_2 during 41 continuous oxygen desorption-sorption cycles in TGA at 900°C. Desorption time = 15min; Sorption time = 30min.
Figure B12: Weight change of CuO-MgO-7-3/SiO_2 during 41 continuous oxygen desorption-sorption cycles in TGA at 900°C. Desorption time = 15min; Sorption time = 30min.
Figure B13: Weight change of CuO-MgO-1-1/SiO_2 during 41 continuous oxygen desorption-sorption cycles in TGA at 900°C. Desorption time = 15min; Sorption time = 30min.
Figure B14: Weight change of CuO-Co_3O_4-9-1/SiO_2 during 41 continuous oxygen desorption-sorption cycles in TGA at 900°C. Desorption time = 15min; Sorption time = 30min.
Figure B15: Weight change of CuO-Co_3O_4-4-1/SiO_2 during 41 continuous oxygen desorption-sorption cycles in TGA at 900°C. Desorption time = 15min; Sorption time = 30min.
Figure B16: Weight change of CuO-Co_3O_4-7-3/SiO_2 during 41 continuous oxygen desorption-sorption cycles in TGA at 900°C. Desorption time = 15min; Sorption time = 30min.
Figure B17: Weight change of CuO-NiO-9-1/SiO_2 during 41 continuous oxygen desorption-sorption cycles in TGA at 900°C. Desorption time = 15min; Sorption time = 30min.
Figure B18: Weight change of CuO-NiO-4-1/SiO_2 during 41 continuous oxygen desorption-sorption cycles in TGA at 900°C. Desorption time = 15min; Sorption time = 30min.
Figure B19: Weight change of CuO-NiO-7-3/SiO_2 during 41 continuous oxygen desorption-sorption cycles in TGA at 900°C. Desorption time = 15min; Sorption time = 30min.
Figure B20: Weight change of CuO-Mn_2O_3-4-1/SiO_2 during 41 continuous oxygen desorption-

sorption cycles in TGA at 900°C. Desorption time = 15min; Sorption time = 30min.
Figure B21: Weight change of CuO-Fe_2O_3-4-1/SiO_2 during 41 continuous oxygen desorption-sorption cycles in TGA at 900°C. Desorption time = 15min; Sorption time = 30min.

LIST OF TABLES

Table 1: Basic design specifications obtained from dimensional analysis for pilot-scale unit(s)
Table 2: Properties of metal oxides
Table 3: Values of R^2 for linear fitting of all models employed in the reduction of 30%-CuO/SiO_2 at 800°C, 875°C and 950°C
Table 4: Physical characteristics of the fresh oxygen carriers
Table 5: *OTC* and *ROT* values at 30% conversion for selected oxygen carriers
Table 6: Settling velocities of the particles used in this experiment
Table 9: Influence of top sampling boxes on mixing index
Table 10: Simulation conditions and parameters
Table 11: Particles properties in experiments
Table 12: Properties of CuO on alumina support
Table 13: Initial solid inventory calculations
Table 14: Scale-up Rules
Table 15: Basic plant data for 8 major coal-fired power plants in NSW [45]
Table 16: Fuel properties for 8 major coal-fired power plants in NSW [45]
Table 17: Components of capital cost.
Table 18: Properties of reference coal used in determining unit costs listed in Table 17
Table 19: Components of the fixed operating and maintenance cost
Table 20: Components of the variable operating and maintenance cost
Table 21: Emissions of both scenarios over the 20 year lifetime of the power plant (tabulated form)
Table 22: Energy of both scenarios over the 20 year lifetime of the power plant (tabulated form)

Chapter 1

INTRODUCTION

1.1 BACKGROUND

Oxygen is the second largest-volume chemical produced in the world with a 30% share of the global industrial gas market. The global demand for oxygen in 2011 is forecast to be 950 billion cubic meters with an annual growth rate of about 6%. It has major commercial applications in metallurgical industry, chemical synthesis, glass manufacturing, pulp and paper industry, petroleum recovery / refining, and health services. Emerging markets for oxygen include advanced power generation systems, such as integrated gasification combined cycle (IGCC), oxy-fuel combustion and solid oxide fuel cells, SOFC. Among these, oxy-fuel combustion is particularly an attractive low emission technology because of its inherent ability for in-situ separation of CO_2. However, oxy-fuel combustion requires oxygen and, thereby, an air separation unit (ASU) to function effectively. Conventional ASU units (e.g. cryogenic systems) may consume between 10% and 40% of the gross power output of a typical oxy-fuel plant and constitute 40% of the total equipment cost (about 14% of the total plant cost).

Oxygen is commonly produced at industrial scales by air separation using cryogenic distillation and adsorption based technologies (pressure swing adsorption, PSA, and vacuum-PSA or VPSA). Advanced technologies such as membrane separation (e.g. ion-transport membrane, ITM) and in-situ air separation are also being developed for small-volume point-of-use oxygen generation. Cryogenic processes are generally expensive owing to the energy intensity of their air compression sub-process. Similar to the cryogenic methods, air compression is a key step in the adsorption based air separation methods and as such the specific power consumptions of PSA and VPSA plants are not much lower than their cryogenic counterparts. Membranes have been in commercial use for several decades but much of their past applications have been in liquid-liquid and liquid-solid separation. The use of membranes for large volumetric gas flow rates, such as those in air separation, has not been demonstrated yet. Membrane systems also suffer from high cost of manufacture. There is a need for a more simple and cost effective air separation technology with much smaller energy footprint and lower capital cost than conventional and emerging air separation methods.

In recognition of this need and after a comprehensive literature review our group has been developing two chemical looping based methods for air separation. The first method known as chemical looping air separation (CLAS) is a general technique for tonnage production of high purity oxygen while the second method (integrated chemical looping air separation, ICLAS) is a modified version of the CLAS process specifically tailored for oxy-fuel applications.

By incorporating the concept of oxygen decoupling into the two-step redox reaction, CLAS is able to separate oxygen from normal air. As Figure 1 illustrates, the CLAS process works in a cyclic fashion by continuous recirculation of metal oxide particles between a set of two interconnected rectors, where oxidation (O_2 coupling, see R1) and reduction (O_2 decoupling, R2) of carrier particles take place, respectively. During this cyclic process, oxygen is taken from air in one reactor, carried by particles and then released in a second reactor. The system therefore consists of two reactors linked together through a loop-seal to prevent gas leakage from one reactor to another. Air is fed into the oxidation reactor so that the incoming reduced carrier particles can be regenerated to a higher oxidation state. The regenerated carrier particles, in turn, are transported back to the reduction reactor where oxygen decoupling occurs in the presence of steam. The mixture of steam and oxygen exiting from the reduction reactor is passed through a condenser so that steam can be fully separated from O_2. The product oxygen can be then compressed for storage and delivery or directly fed to another process for on-site use.

Me_xO_{y-2} (s) + O_2 (g) → Me_xO_y (s) *Oxidation or O_2 coupling* (R1)

Me_xO_y (s) → Me_xO_{y-2} (s) + O_2 (g) *Reduction or O_2 uncoupling* (R2)

From energy efficiency point of view the CLAS process is quite efficient because of its low energy demands. This is partly due to the fact that the theoretical net heat released over reactions (R1) and (R2) is zero. Therefore, in theory the heat transported by the incoming carrier particles into the reduction reactor must be sufficient to support the endothermic reaction (R2). Furthermore, under steady state operation much of the heat required for production of steam and pre-heating of air is offset by the heat contents of the superheated steam stream leaving the reduction reactor and the reduced air stream exiting from the oxidiser. As Figure 1 shows, this is achieved by exchanging: (i) the sensible heat between various streams in a series of heat exchangers, and (ii) the latent heat of phase change in a combined steam condenser/boiler unit. The additional thermal energy required to carry out the CLAS process can be provided by electrical power. Our mass and energy balance calculations[15] carried out using the HYSYS process simulation package suggest that the heat/power demand for the CLAS process is much lower than that required in cryogenic systems. The specific power for the CLAS process varies between 0.041 and 0.053 kWh/m^3_n with an average value of 0.045 kWh/m^3_n. This is about 11% of the specific power of a conventional cryogenic system (i.e. 0.4 kWh/m^3_n). More advanced cryogenic systems due to enter the market by 2012, however, are expected to approximately reach a specific power of 0.3 kWh/m^3_n. Such specific powers are still 7 times greater than the average specific power for the CLAS process.

The integrated chemical looping air separation (ICLAS) process is a step-change improvement over the CLAS process and has been specifically tailored for ease of integration with oxy-fuel type power plants running on organic (e.g. biomass) or fossil-based (e.g. coal, gas, oil, etc) fuels. For example consider an oxy-fuel coal-fired power plant where coal, oxygen (from the ASU) and recycled flue gas are co-fed into the boiler and the mixture is combusted at high temperatures. The heat generated from the combustion process runs a steam cycle which in turn converts the thermal energy into electricity. The use of recycled flue gas here is an important and integral part of the oxy-fuel combustion process because firing pure oxygen in a boiler would result in excessively high flame temperatures which may damage the boiler. Therefore, the mixture must be diluted by mixing with recycled flue gas before it

can be fed into the boiler. Given the need for recycled flue gas in oxy-fuel combustion and considering the high energy demand for steam generation in a CLAS type process, recycled flue gas rather than steam is employed in the ICLAS process during the reduction phase (Figures 2 and 3). This innovative use of the recycled flue gas in the ICLAS process: (i) lowers the overall energy footprint of the air separation process and hence operational costs to levels well below those of the CLAS process, (ii) simplifies the hardware required for chemical looping air and thereby reduces the capital cost for the air separation unit in an oxy-fuel power plant, and (iii) leads to a more effective integration of the ASU with the oxy-fuel plant due to better use of material and energy streams (see Figure 3).

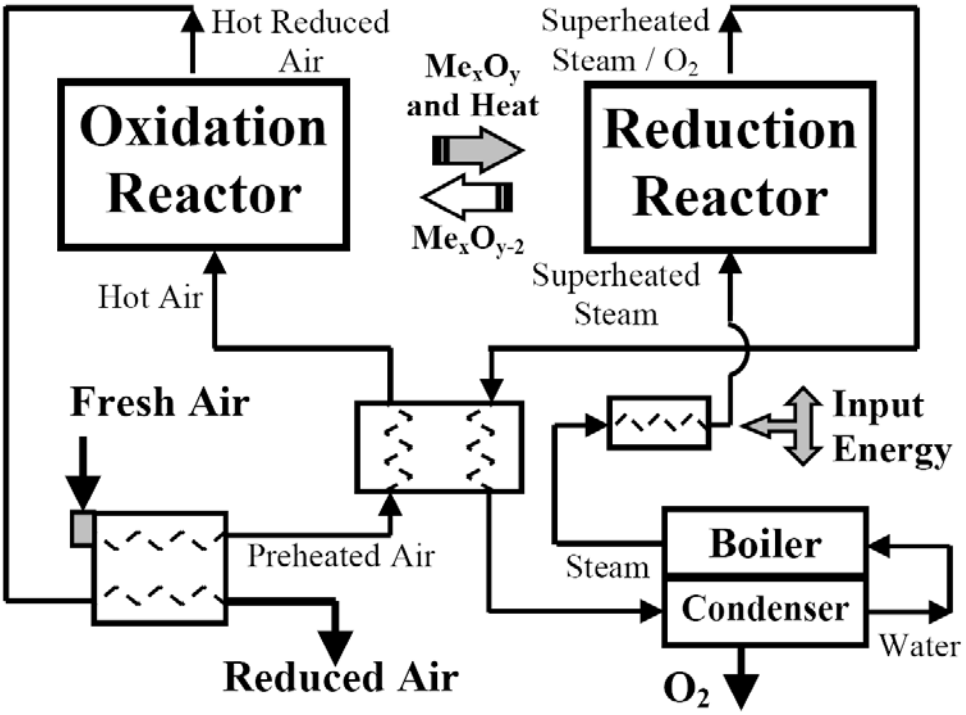

Figure 1: Schematic of the CLAS process.

The working principle of the ICLAS process is similar to that of the CLAS process but the ICLAS process is executed is a distinctly different way. Both CLAS and ICLAS processes works in a cyclic fashion by continuous recirculation of metal oxide particles between a set of two interconnected rectors, where oxidation (R1, O_2 coupling) and reduction (R2, O_2 decoupling) of carrier particles take place, respectively. In both processes air is first fed into the oxidation reactor for separation of oxygen from air through the oxygen coupling process (i.e. regeneration of reduced carrier particles) and then the oxidised (i.e. regenerated) particles are reduced in a reduction reactor to release oxygen via the oxygen decoupling reaction. However, in the ICLAS process the reduction and hence oxygen decoupling process takes place in the presence of recycled flue gas not steam. The mixture of oxygen and recycled flue gas exiting the reduction reactor is then directly fed into the boiler of the oxy-fuel plant (Figure 3). The use of flue gas rather than steam not only eliminates the need for steam generation but also implies

that condenser units for separation of O_2 from steam are no longer required. This reduces the number of unit operations and thereby capital cost as well as operational and running costs.

From the energy efficiency point of view the heat transported by the incoming carrier particles into the reduction reactor is sufficient to support the endothermic oxygen decoupling process. In practice, though, some heat must be supplied to the reduction reactor to compensate for heat losses to the surrounding. However, unlike the CLAS process no additional heat is also required for generation of superheated steam in the ICLAS process. Moreover, much of the required heat duty is offset by utilising the flue gas stream which is already hot. Our preliminary calculations suggest that the heat demand for the ICLAS process is ≈0.03 kWh per cubic meters of oxygen produced (i.e. 0.03 kWh/m^3_n) which is about 30% and 90% less than those of the equivalent CLAS and cryogenic type process, respectively.

The successful execution of the CLAS and ICLAS processes largely depends on oxygen carriers capable of reacting reversibly with gaseous oxygen at high temperatures. This additional thermodynamic constraint is a means of differentiating oxygen carriers feasible for the CLAS and ICLAS processes from those only suitable for common redox applications. Numerous studies have been carried out on oxides of transitional metals, such as Fe, Cu, Co, Mn and Ni as potential candidates for redox applications. Thermodynamically, oxides of Cu, Mn and Co are more promising for oxygen decoupling (i.e. CLAS and ICLAS processes) because of their ability to reversibly react with oxygen. But any other metal oxide, solid oxides, or their mixtures with reversible oxygen decoupling properties can be employed in the CLAS and ICLAS processes.

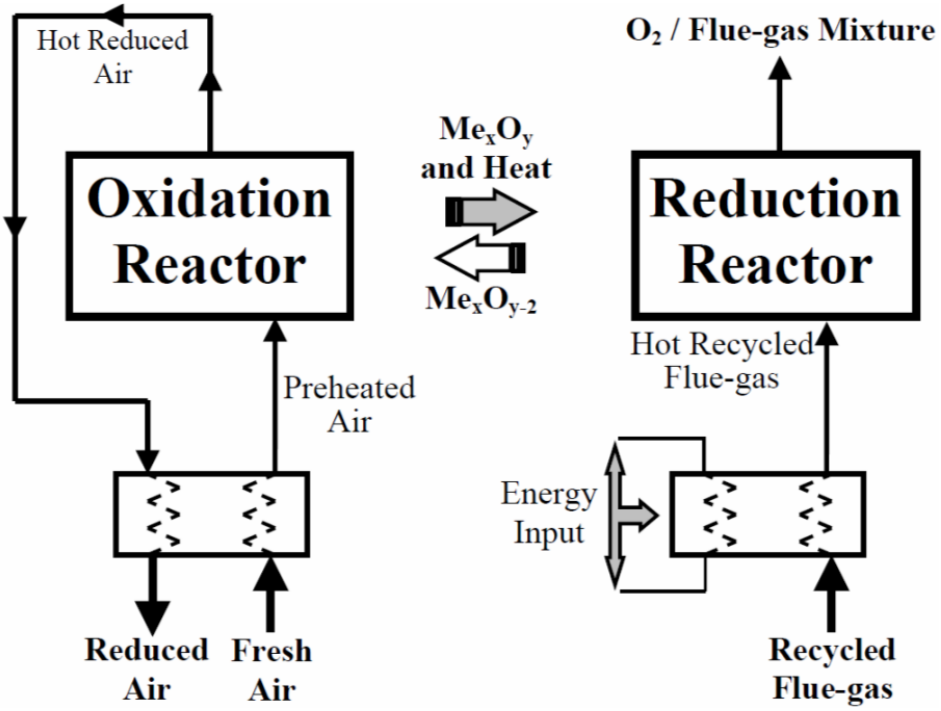

Figure 2: Schematic of the ICLAS process.

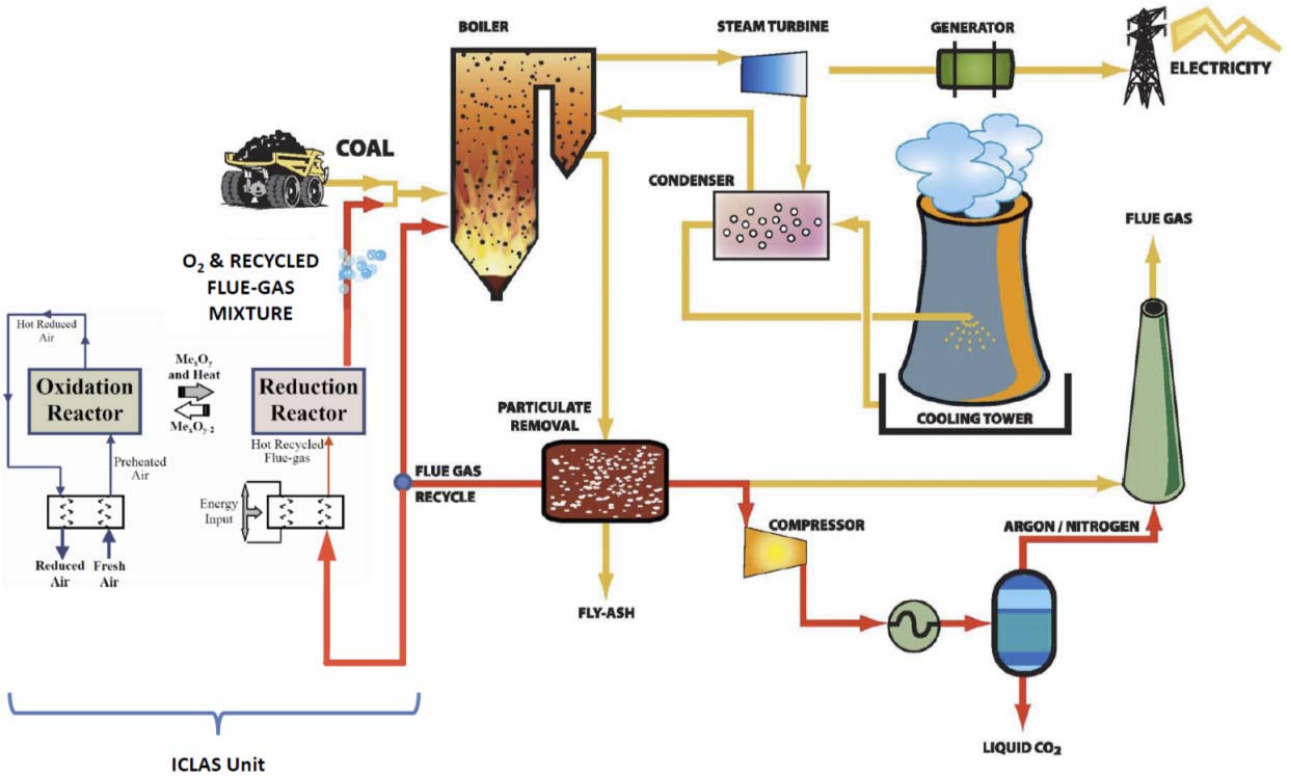

Figure 3: Schematic of an oxy-fuel coal-fired power plant retrofitted with an ICLAS unit.

1.2 PROJECT AIMS AND OBJECTIVES

As noted earlier oxygen is the second largest-volume chemical produced in the world with a 30% share of the global industrial gas market. Emerging markets for oxygen include advanced power generation systems, such as solid oxide fuel cells, integrated gasification combined cycle (IGCC) and oxy-fuel combustion which is the focus of this NSW government funded project (Project ID: MOC10/1067).

Project MOC10/1067 was concerned with the development of a novel air separation process to facilitate the commercial-scale deployment of oxy-fuel combustion across the power generation sector in NSW. Project MOC10/1067 was part of a larger program of study at the University of Newcastle on alternative air separation technologies and specifically complemented two other relevant projects funded by the ANLEC-R&D [1] and Glencore (formerly Xstrata Coal [2]), respectively.

As Figure 4 shows, the major research elements of this alternative air separation program were: (i) fundamental studies, (ii) integration & adaptation studies, and (iii) demonstration. The emphasis of the NSW Coal Innovation and Glencore (formerly Xstrata) funded projects was mainly on fundamental studies at bench-scale and pilot-scale under controlled laboratory settings whereas the ANLEC-R&D project exclusively focused on practical issues related to integration and adaptation of CLAS into an oxy-fuel type coal-fired power plant.

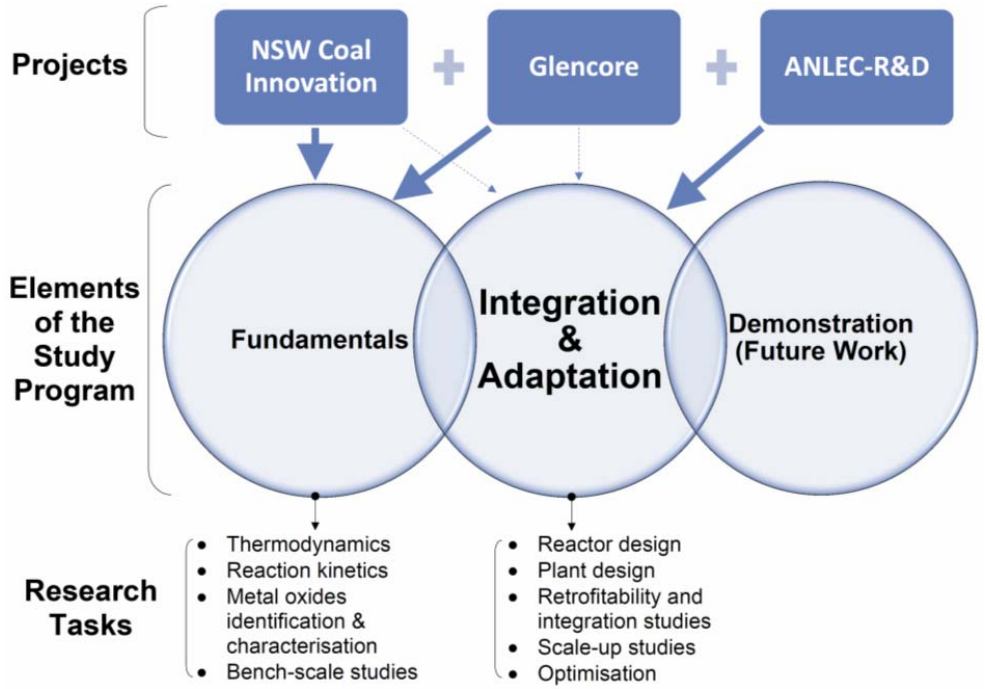

Figure 4: Relationship between the existing projects related to the CLAS process.

The technical aims of the project were to:

4. Examine the redox behaviour of metallic oxide oxygen carriers under conditions pertinent to high temperature air separation.
5. Determine the fundamental science underpinning the oxygen decoupling phenomenon during the spontaneous reduction stage.
6. Once the underpinning science has been fully investigated, to determine the cost and energy penalty of the technology when applied to retrofitted power stations of the NSW fleet and to identify plant characteristics and age for economic viability.

To achieve the technical aims 1 and 2, one needs to understand the mechanism of oxygen transport from metal oxides to the bulk (i.e. reacting environment) and vice versa. It was hypothesised in our proposal to the NSW government that the migration of Me^{y+} ions provide paths for oxygen vacancies to migrate from surface to the bulk during oxygen decoupling and from the bulk to the surface during oxygen coupling, in turn, leading to a degree of oxygen vacancy diffusion. It was also highlighted that very likely the above mechanism would be influenced by the particle transformation phenomena such as structural, morphological, and compositional changes during the course of a given redox reaction. In this context, the following key focusing questions were identified and formed the basis of our combined experimental / theoretical investigations: (i) how do the reaction conditions; e.g. *P*, *T*, and heating rate; affect the particle transformation and, in turn, the mechanism outlined above for the diffusion of oxygen vacancies?, (ii) what is the combined effect of reaction conditions and particle transformation on the reactivity, conversion and selectivity of redox products? and; (iii) are there any synergistic effects when particles of different metal oxides are mixed?

1.3 APPROACH AND METHODOLOGY

Ideally, the focusing questions listed above should be answered by direct measurements of the microscopic features of the oxygen carrier particles during their redox reactions. Unfortunately, the full in-situ characterisation of the microscopic features of porous media such as metal oxides is beyond the current technological capabilities. Therefore, innovative methods were needed. What we proposed to the NSW government was a novel approach whereby experimental and theoretical techniques could be integrated so that a more mechanistic picture of the system was obtained. We postulated that if the changes in macroscopic features were followed experimentally and the data was fed into appropriate models with microscopic features, the particle transformation phenomena could be accurately reconstructed. Driven by the above philosophy, the proposed research consisted of experimental and theoretical (including modelling) programs aimed at investigating the redox behaviour of metal oxide oxygen carriers in the chemical looping air separation followed by techno economic assessment of the proposed air separation method. The plan of work consisted of a number of closely linked components. Figure 5 illustrates an updated version of the overall project plan demonstrating how various components of the project fit together (please refer to the original grant application for a more detailed version of the project plan). As can be seen, the research program consists of two parallel but closely linked research strands, namely: experimental and theoretical / modelling. Each strand, in turn, comprises several overlapping sets of studies.

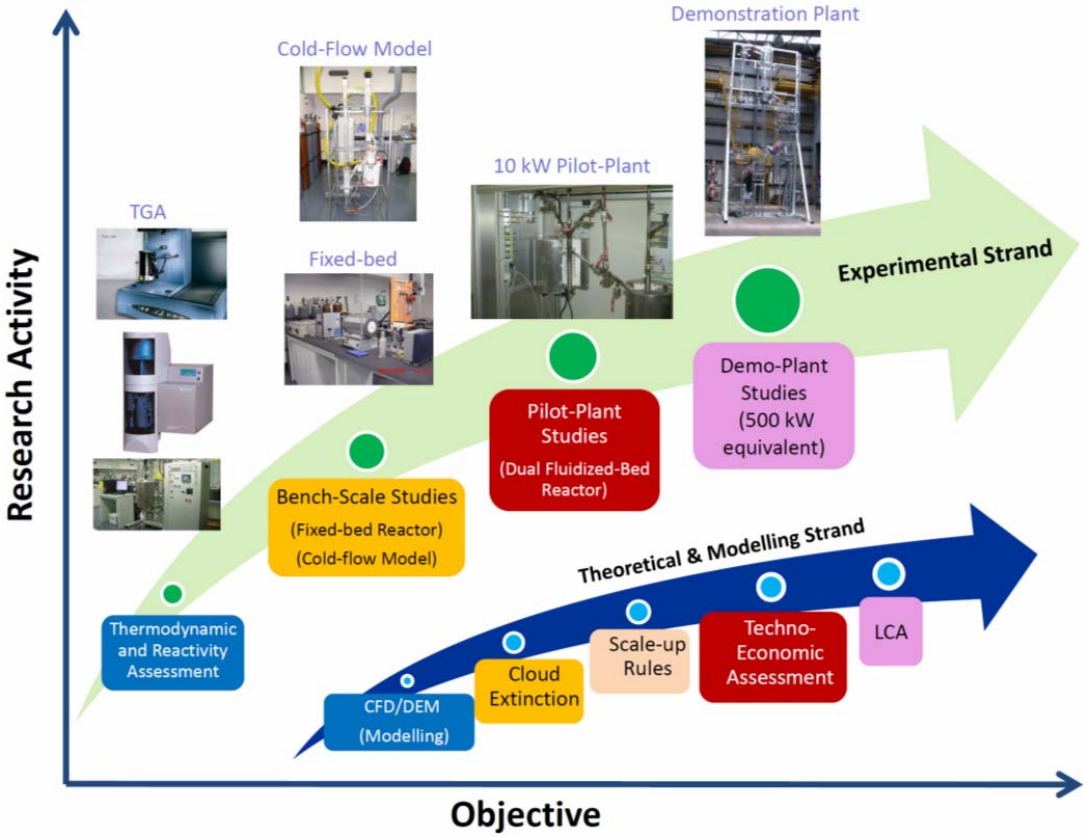

Figure 5: Simplified version of the project plan.

Chapter 2

EXPERIMENTAL METHODS & TECHNIQUES

2.1 EXPERIMENTAL SETUPS

To achieve the broad objectives of the project, particularly in the "Experimental Strand", a number of experimental setups and instruments were employed. Some of these units were deigned, constructed and commissions in-house as part of the project while a number of other necessary units were existing laboratory instruments acquired earlier by our group through other projects and/or funding schemes. This Section provides a brief description of experimental setups.

2.1.1 Bench-Scale Cold-Flow Setup

The bench-scale cold-flow setup is a model of chemical looping air separation system. The setup allows us to gain insight into the pressure profiles, the solids circulation rate, gas leakage, and the residence time distribution of the real system without necessarily carrying out any redox reactions. In addition, the hydrodynamics of mechanical mixing of particles with different density can be examined and as such the segregation behaviour of particle mixtures can be quantified. The cold-flow setup employed in the present study is constructed primarily of acrylic and consists of two fluidised beds and two fluidised bed loop seals. The dimensions (in mm) of these components system are detailed in Figures 6a, 6b, 6c and 6d. Figure 6 details the key components of the cold-flow setup used in the bench-scale hydrodynamic experiments. The apparatus consists of two main fluidised beds (FBa and FBb) and two loop seals. FBa and FBb respectively represent the air and reduction reactors in a real CLAS system. FBa and FBb as well as the two loop seals are bubbling type fluidised bed. FBa has a particle bed depth of 70-100 mm and a diameter of 76 mm. Above FBa is a riser which is a pipe of diameter of 40 mm that rises a 110 mm. The particles are forced up the riser and across a horizontal section 300 mm long. At the end of the section the particles enter a cyclone, which is used to separate the particles from the gas. The cyclone has a diameter of 80 mm with a top exit of 40 mm and a bottom exit of 33 mm. At the bottom of the cyclone the particles fall down through a downcomer that is approximately 220 mm long into the upper loop seal. The upper loop seal as shown in Figure 6b is 56 mm wide and has a baffle clearance of 40 mm. As the loop seal is a fluidised bed, the overflow of the loop seal due to particles falling from the cyclone fall into the fuel reactor. FBb has a bed height of around 40 mm and a bed diameter of 80 mm. Particles exit the FBb by overflow due to the influx of particles from the loop seal. The overflow of particles enters an opening around 20 mm above the top of the bed. This opening then allows particles to fall into the lower loop seal. The lower loop seal as outlined in Figure 6c is also 56 mm wide with a baffle clearance lower than that of the upper loop seal of 40 mm. The particles exit the lower loop seal similarly to the FBb and upper loop seal, by over flow.

The overflow of particles from the lower loop seal falls back down into the air reactor to complete the loop.

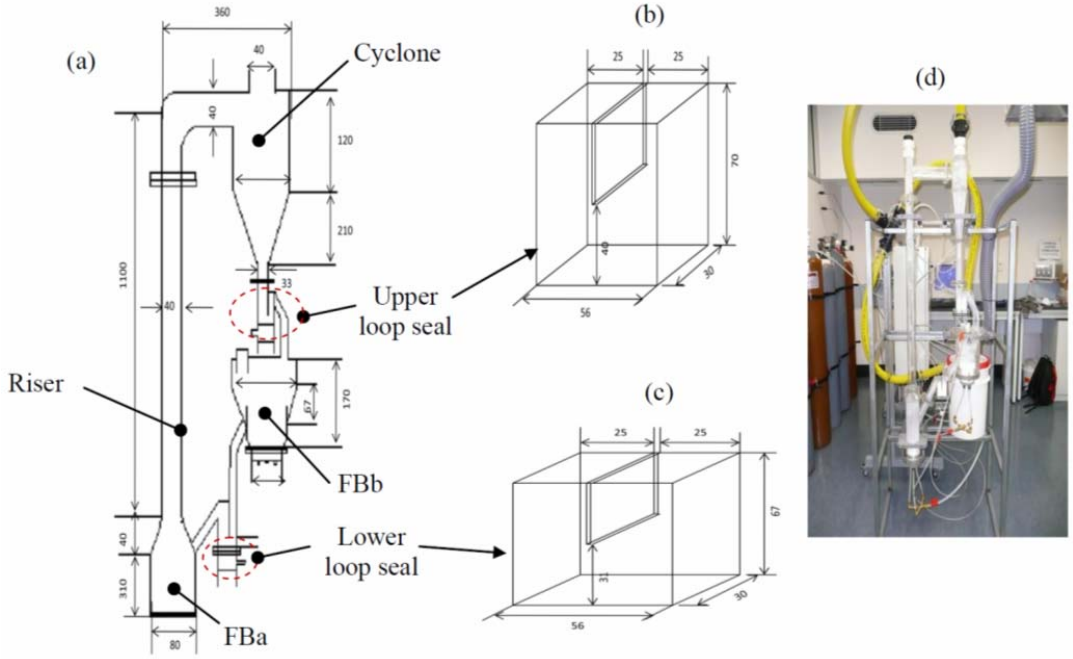

Figure 6: Schematic of the cold-flow setup showing key dimensions (not to scale); (a) complete system; (b) upper loop-seal, and (c) lower loop seal, as well as (d) photo of the setup.

The flowrates in the system are controlled via computer. The FBb and the two loop seal flowrates are controlled through the LabView user interface while FBa is controlled via the computer program called Flow DDE V4.58. The rig is connected to a control box which is in turn connected to a computer from which the entire system can be controlled and the pressure drops of the system can be recorded. The control box has four flow controllers which controlled the flow in each of the loop seals and fluidised beds and twenty pressure transducers which record the pressure at different points in the system. To go with the four flow controllers there are four flow sensors to measure the flow in each section of the rig. Pressure measurements are taken at 20 points around the rig. The pressures are sensed by pressure transducers which were connected to a computer interface. The pressure readings in the system are recorded in the LabView program.

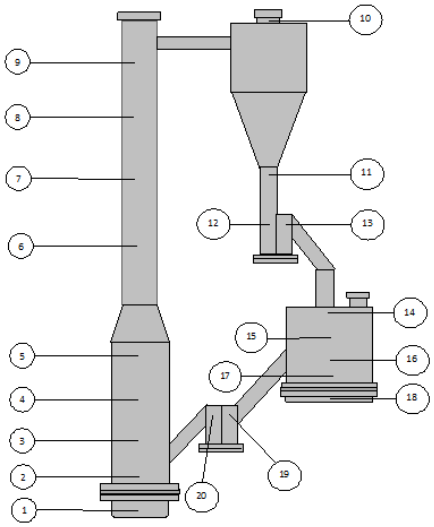

Figure 7: Locations of pressure measuring points in the cold-flow setup.

Figure 7 shows the points at which in the system the pressure is recorded. The pressure measuring devices that are located in the control box are Honeywell type micro switch whilst the flowrate controllers and measuring devices are Bronkhurst brand and are capable of controlling and reading flowrates of 5-200 L/min of feed gas to each component of the system. Sampling height segregation in

the FB reactor is done using as custom designed cylinder that was designed to fit inside of the FBa and hold the sample. The cylinder has markings at 1 cm intervals along its side so the height can be measured as samples are being taken out for sieving. The cylinder has been constructed out of Perspex and is designed to fit as tightly as possible into the FBa section.

2.1.2 Bench-Scale Fixed-Bed Setup

The bench-scale fixed-bed setup is used in reaction reactivity studies (i.e. reaction kinetics). More specifically, the fixed-bed setup is used to experimentally determine the pre-exponential factors and reaction orders by fitting the experimental values of reaction times associated with 50% and 100% conversion. As shown in Figure 8, the fixed-bed setup consists of: (a) a quartz tube reactor externally heated by a tube furnace, (b) a steam generator; (c) a data acquisition system; (d) a gas analysis train comprising a micro-GC, a drying tower and a vent; and (e) a gas inlet manifold which includes several mass flow controllers, three-way valves, regulators and gas bottles.

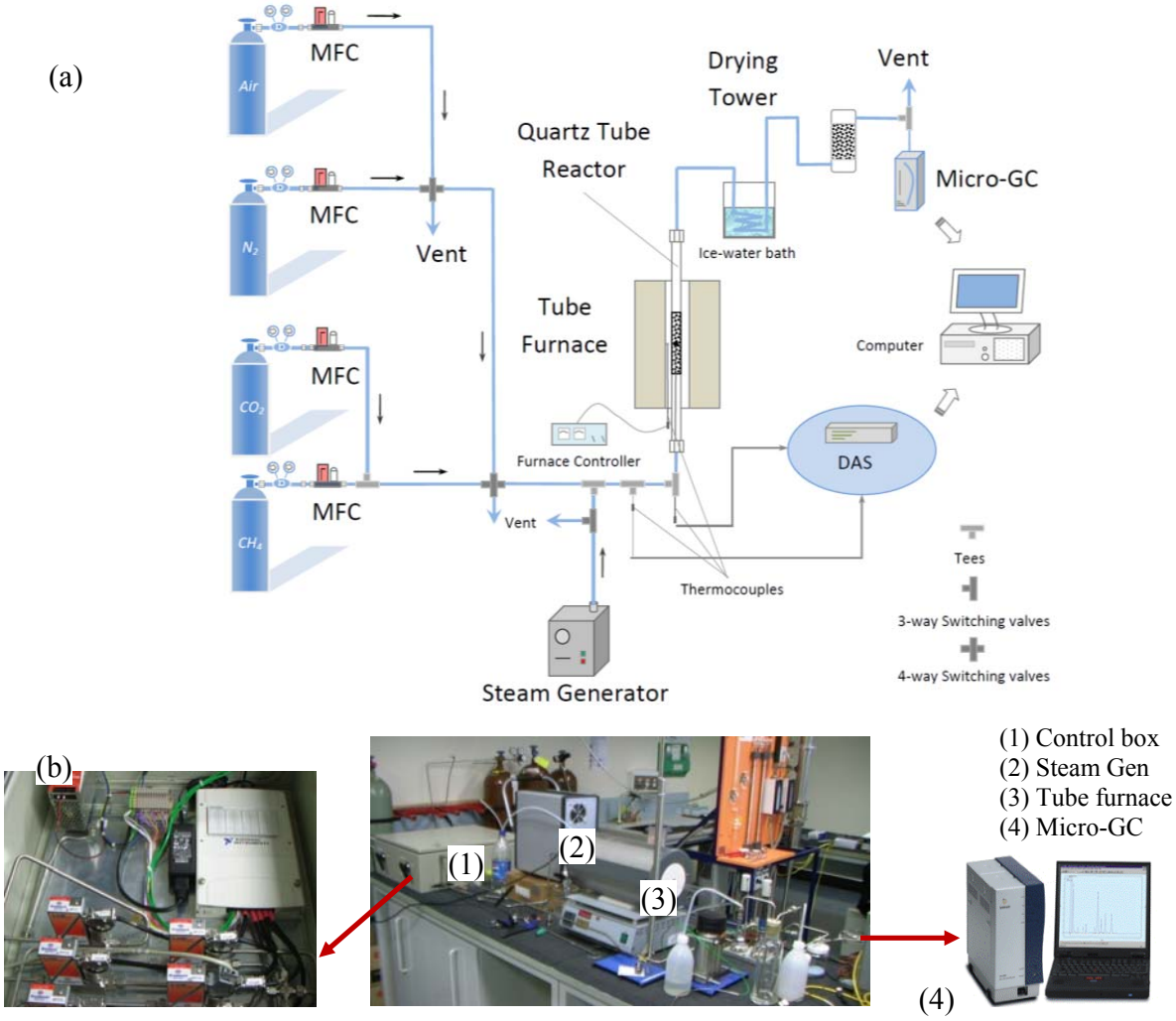

Figure 8: Bench-scale fixed-bed setup; (a) schematic, and (b) photos.

2.1.3 Thermo-Gravimetric Analyser (TGA)

Complete thermodynamic equilibrium cannot be generally achieved in a chemical process like CLAS since it is profoundly affected by the diffusion limited transport of heat and mass. Consequently, the yield and composition of products as well as the overall performance of the process is underpinned by reaction kinetics. The relevant reaction properties can be measured using a thermogravimetric analyser (TGA) which measures weight changes in a material (e.g. metal oxides) as a function of temperature (or time) under a controlled atmosphere. The reaction properties of the material (e.g. activation energy, per-exponential factor, reaction order) can then be extracted from the weight loss curves using a series of reaction kinetics models. Apart from kinetic properties, conversion and selectivity can be also quantified using the data from TGA. TGA based techniques for reactivity assessments, especially the non-isothermal temperature-programmed approach, have been widely reported in the literature. However, the heating rates used in TGA measurements are several orders of magnitude smaller than those of real reactors making it difficult to extrapolate the measured data. On the other hand instruments such as the bench-scale fixed-bed setup described in Section 2.1.2 can provide more realistic heating rates but they suffer from heat and mass diffusion limitations. A combined method is proposed used in this study to avoid the drawbacks of both TGA and bench-scale methods. In this method, the intrinsic activation energies corresponding to redox reactions, which are independent of the heating rate are determined using TGA instruments(s) while, a s noted before, the pre-exponential factors and reaction orders are determined using bench-scale fixed-bed setup by fitting the experimental values of reaction times associated with 50% and 100% conversion.

In the present study we make use of two TGA instruments. The first unit is a pressurised Rubotherm Magnetic Suspension Balance TGA (MSB-Aus-2004-00188) which is used for investigating the effect of pressure on redox properties (see Figure 9a). The second unit is an atmospheric TGA (Q50) manufactured by TA Instruments (see Figure 9b). This unit is used in temperature-programmed mode to determine the intrinsic activation energies. Both TGA units have been modified and couple with a steam generator as part of the current project so that reactions can be studied under steam environment.

Figure 9: TGA units; (a) Rubotherm pressurised MSB-Aus-2004-00188 unit and (b) TA Instruments Q50 unit.

2.1.4 Dimensional Analysis and Pilot-Plant Design

Dimensional analysis is a powerful theoretical method allowing the performance characteristics of an engineering system to be related with the characteristics of its scaled model run under a different set of operating conditions. Using dimensional analysis we have been able to relate the experimental data collected from the cold-flow and fixed-bed setups and determine the design specifications (e.g. size, geometry, operating temperature, etc) of the 10 kW_{th} pilot-plant (see Section 2.1.5). This has been achieved by maintaining identical values of several key dimensionless parameters in bench- and pilot-scale units. The dimensions of the pilot-scale unit were calculated from those of the bench-scale setup. The key dimensionless parameters used in this analysis were:

$$\frac{u^2}{g.L},\quad \frac{\rho_p}{\rho_f},\quad \frac{\rho_p.u.d_p}{\eta^2},\quad \frac{\rho_f.u.L}{\eta},\quad \frac{G_s}{\rho_p.u},\quad bed\_geometry,\quad \Phi,\quad PSD \qquad (2.1)$$

where u is superficial gas velocity, g the acceleration of gravity, L characteristic length, ρ_p particle density, ρ_f gas density, d_p particle diameter, η dynamic viscosity of the gas, G_s solid circulation rate, Φ particle sphericity, and PSD the particle size distribution.

The original plan was to design and construct a 100 kW_{th} pilot-plant. However, dimensional analysis revealed that the overall footprint of such unit would be about 10×6×8 m; with a capital cost much greater than what was allocated in the budget for the construction of the pilot-plant. For this reason, a new set of dimensional analyses was carried out to assist with the design of a smaller 10 kW_{th} pilot-plant with an approximate footprint of 2.5×1.5×2. The smaller unit size enabled us to design and construct (see next section for details) two versions of the pilot plant, namely: (i) the Perspex version for carrying out hydrodynamic and particle transport studies at pilot-scale, and (ii) the stainless steel or SS version for conducting redox reactions at pilot-scales. Both Perspex and SS versions have identical geometry and dimensions. The design specifications for these pilot-scale units are given in Table 1.

Table 1: Basic design specifications obtained from dimensional analysis for pilot-scale unit(s)

Design Parameter	**Unit**	**Design Specs** (Perspex unit)	**Design Specs** (SS unit)
Thermal power	kW	--	100
Operating temperatures	^oC	Room Temp	650 - 1100
Operating pressure	bar	1	1 - 4
Particle density	kg/m^3	500-2000	2500 - 5400
Mean particle diameter	μm	300 - 400	100 - 200
Dimensionless gas velocity in the riser	--	4 -10	4 -10
Dimensionless gas velocity(oxidation reactor)	--	1-3	1-3
Dimensionless gas velocity (reduction reactor)	--	5-15	5-15
Dimensionless gas velocity in the loop seal	--	1.2 - 4	1.2 - 4
Riser diameter	m	0.05	0.05
Riser height	m	0.5	0.5
Oxidation reactor diameter	m	0.05	0.05
Oxidation reactor height	m	0.15	0.15
Reduction reactor diameter	m	0.05	0.05
Reduction reactor height	m	0.85	0.85
Total system height	m	2.0	2.0

2.1.5 Dual Fluidised-Bed 10 kW_{th} Pilot-Plant

The design and construction of the dual 10 kW_{th} pilot-plant has been a vital component of the work completed to date. The plant, as shown schematically in Figure 10, consists of: (a) a dual fluidised bed reactor (essentially a pair of interconnected fluidised bed reactors) externally heated by two tube furnaces, (b) steam generator, (c) inlet gas manifold comprising gas bottles, mass flow controllers, three-way valves and piping & fittings, (d) gas analysis train comprising a condenser, drying tower, a micro-GC and a vent, (e) cyclones and feeders, and (f) control box.

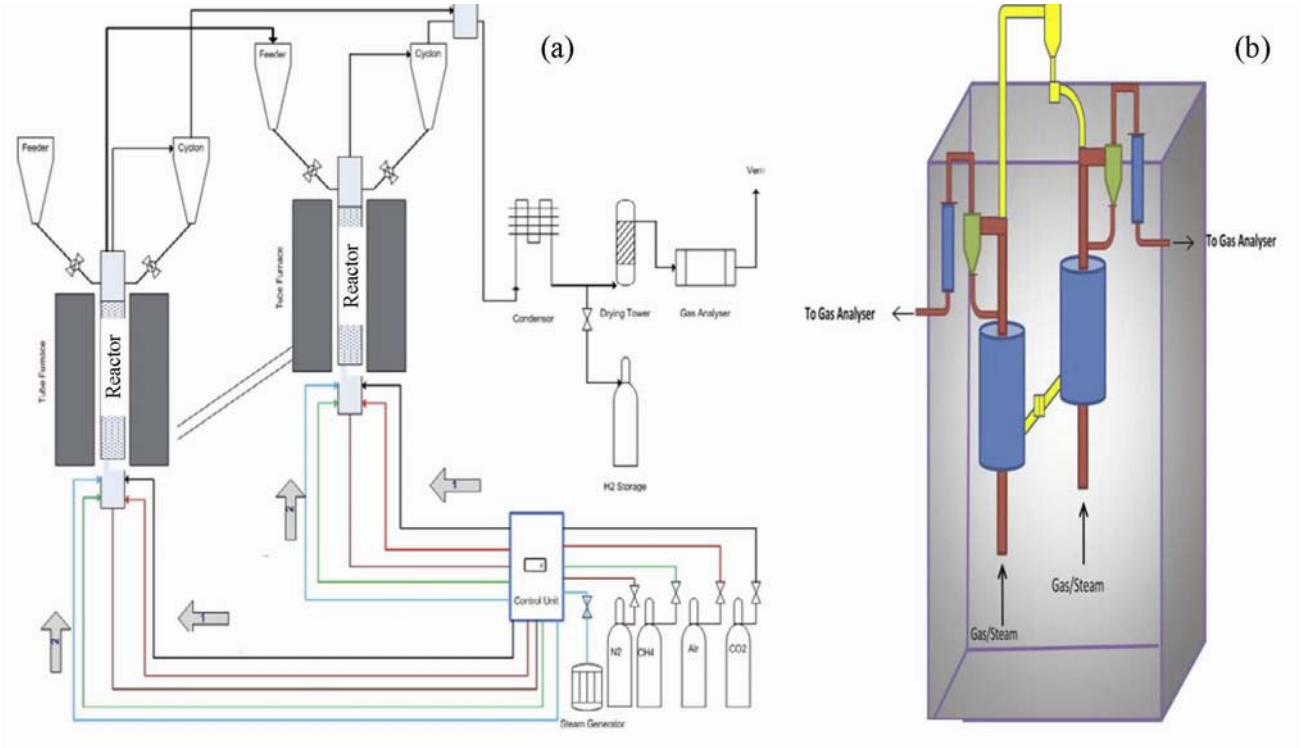

Figure 10: Schematic of the pilot-scale setup; (a) 2D view, and (b) 3D view.

As noted earlier in Section 2.1.4, two different versions of the pilot-plant were constructed as part of this study, namely Perspex and SS. The two versions of the pilot-plant have identical components, geometry, configuration and size and only differ in the material of construction for the dual fluidised bed components. In the Perspex version (Figure 11a) the reactor vessels are fabricated from acrylic materials whereas in the SS version the reactor vessels are constructed from stainless steel. The relevant tasks for construction of the Perspex version of the pilot-plant were completed ahead of the agreed schedule in late Oct, 2011. The Perspex vessels within this version were replaced by new reactors fabricated from stainless steel (SS) when pilot-scale hydrodynamic experiments were completed in 2012 (hence SS version of the pilot-plant). We completed our preliminary pilot-scale experiments in early 2012 as part of the commissioning of the 10 kW_{th} pilot-plant setup. This highlighted several minor issues in the electronics and instrumentation of the system which were

resolved in preparation for the full pilot-scale experimental campaign in 2013. The final version of the SS pilot-plant which is shown in Figure 11b can operate:

- In fixed or fluidized bed modes
- In single or dual reactor configuration
- In the manifold switching mode where gases rather than particles are circulated
- Over a range of temperatures between 25-1200˚C and pressures up to 20 bar

Figure 11: Pilot plant; (a) Perspex version; (b) SS version, (c) control box and (d) internal view of the control box.

The operation of the pilot-plant in dual fluidised bed or manifold switching modes is achieved by manipulating a series of three-way and solenoid valves attached to the system. Figure 12 illustrates the basic configuration of the pilot-plant and how various functionalities can be achieved.

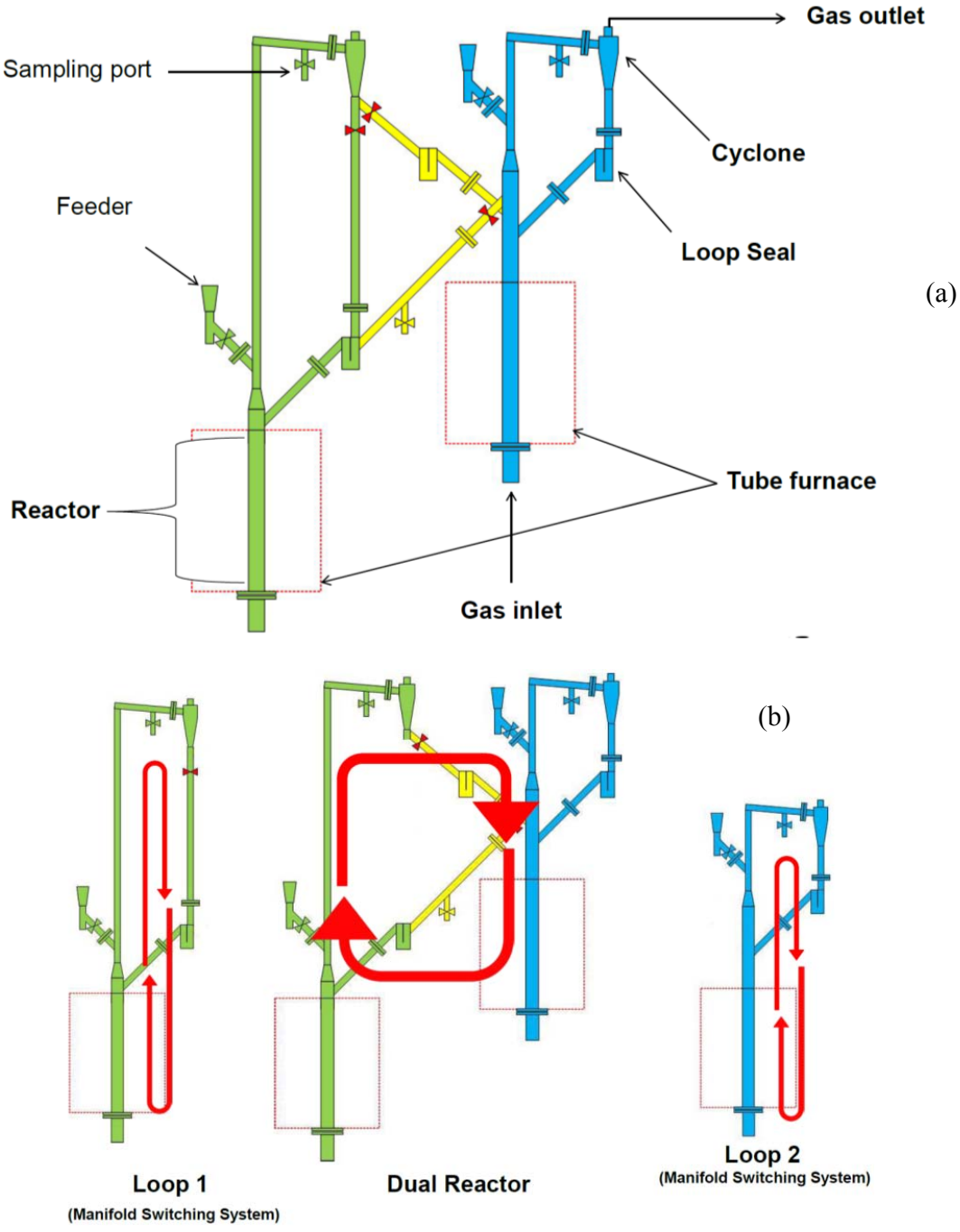

Figure 12: Pilot plant; (a) basic configuration, (b) particle and gas flow arrangement corresponding to various operational modes.

The operational parameters and configuration of the pilot-plant can be easily set to match any desired mode of operation by selecting the relevant system parameters through the LabView user friendly interface which is entirely graphical. Some of the pop-up menus of the LabView interface designed by our team for the 10 kW_{th} pilot-plant are shown in Figure 13.

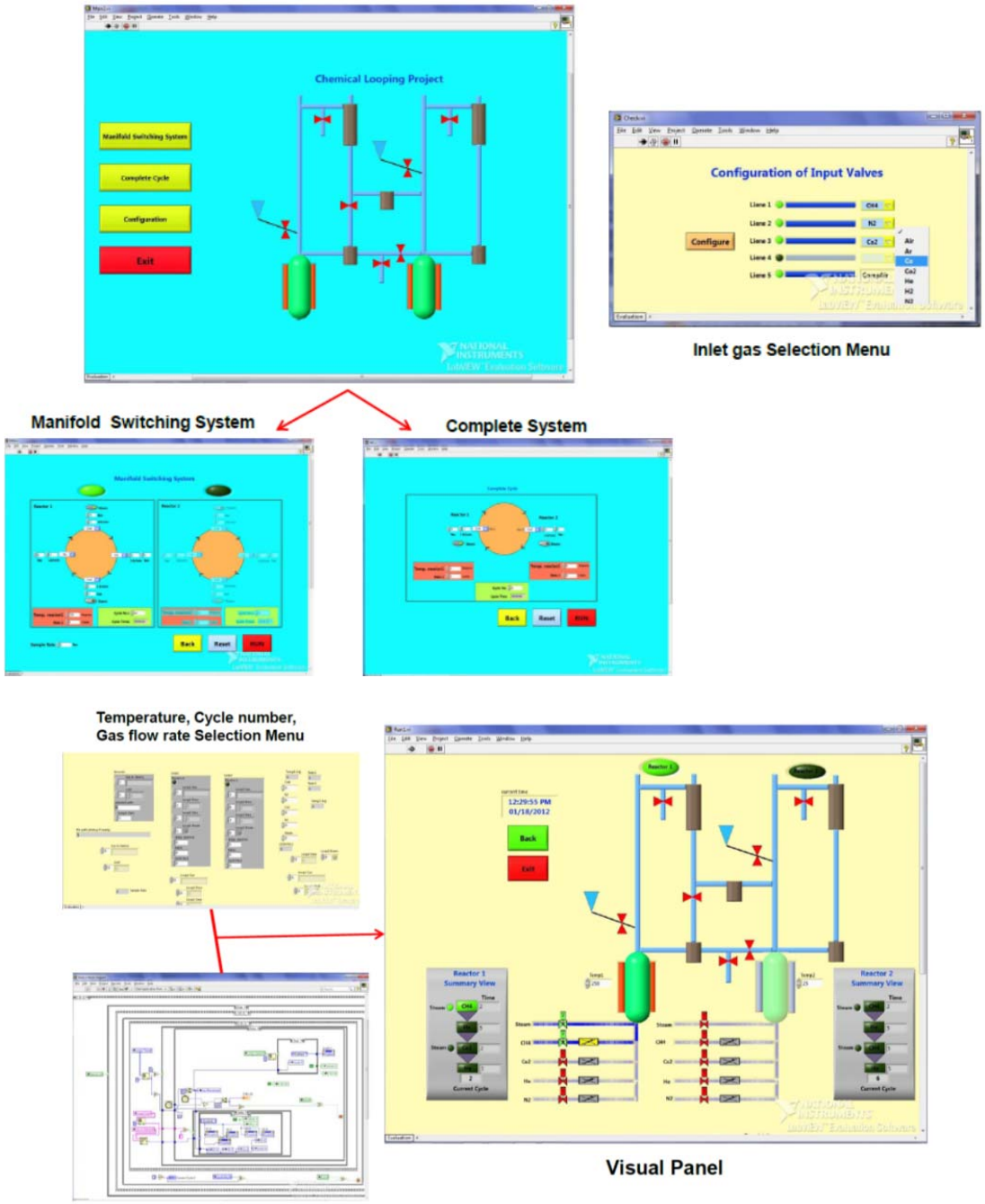

Figure 13: Selection of operational modes/parameters and pilot plant control through the graphical LabView interface.

2.1.6 Cold-Flow Demonstration Setup

We have also completed the design and fabrication of the 7 m high cold-flow demonstration unit (equivalent of a 500 kW CLAS system, see Figures 14) and have installed the unit in our high space shed at the NIER (Newcastle Institute for Energy & Resources) precinct. This unit was fitted with auxiliary systems (e.g. compressed air system, sensors and instruments, control system, etc) in the early 2013 and was commissioned over the period of May-June 2013.

It should be highlighted that while the demonstration unit has not been explicitly listed in the agreed Milestone Schedule, it represents a vital component of scale-up studies. It would be extremely difficult if not impossible to develop accurate scale-up rules without carrying out a range of comprehensive particle transport experiments using a large-scale demonstration unit similar to that shown in Figure 14.

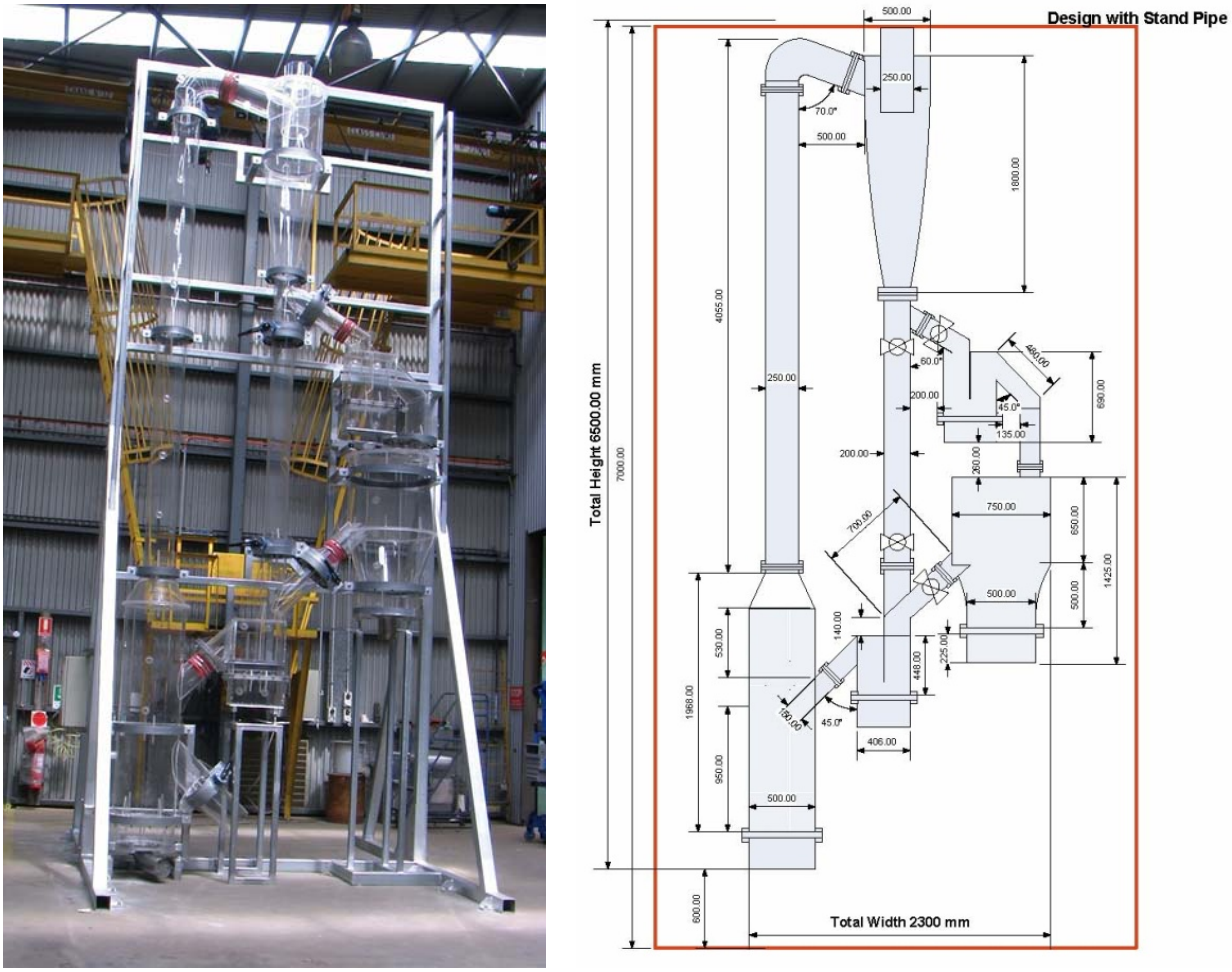

Figure 14: The 7 m high demonstration unit (minus auxiliary systems).

2.2 METAL OXIDES

2.2.1 Preparation and Production of Metal Oxides

Dry / Wet Impregnation Method

The preparation of mono-species metal oxide samples by impregnation method begun by the direct mixing of commercial oxides (e.g. CuO, Fe_2O_3, etc) with alumina powder (Sigma-Aldrich) at a 3:2 carrier/support weight ratio. Distilled water was then added to the carrier/support mix to form a paste. The paste was dried in an oven at 105°C for 36 hours to free up the capillary water. The dry paste was then calcined for 5 hours under nitrogen in a high temperature furnace at a set temperature of 750°C for CuO samples and 900°C for Fe_2O_3 and NiO samples. The calcined sample was pulverised in a ball mill and sieved to a particle size range of 90-106 μm (mesh 170 < particle size < mesh 140[§]).

The quality of the final products were evaluated using X-Ray fluorescence (XRF) and X-Ray Diffraction (XRD) methods to determine the distribution of metal active sites on the surface and within the carrier particles, respectively. The internal structure of samples were characterised by mercury porosimetry and BET (Brunauer-Emmer-Teller) surface area measurements. In particular, the grain radius was determined from porosity and surface area measurements while for Cu-based samples which show platelike grains the thickness of the CuO layer was also determined from the weight fraction of CuO in the sample and the active surface area data. In the case of mixed metal oxide systems, the binary mixtures were prepared by physical mixing of parent samples (prepared using the method outlined above) at desired proportions. Binary mixtures were prepared over a range of blending ratios but typically blending ratios of 25:75, 50:50, and 75:25 were implemented.

Spray Drying Method

In an attempt to produced metal oxides with higher qualities especially for pilot-scale studies, in addition to dry and wet impregnation some oxygen carriers were made using the spray drying method. This method proved to be very effective (see the characterisation results shown below) and has now been adopted as our standard production method. Significant quantities of spray dried metal oxides (approximately 6 kg) have now been produced for current and future pilot-scale experiments.

The particle preparation was performed in the following manner; a powder mixture of the desired metal oxide and support material (60 wt% - 40 wt%) was dispersed in deionised water containing polyethyleneoxide and/or polyvinylalcohol and/or polyethyleneglycol as organic binders and Darvan C or Dolapix as dispersant. The suspension was homogenised by milling and the water-based suspension was continuously stirred with a propeller blade mixer while being pumped to the 2-fluid spray-dry nozzle. Sintering of the oxygen carriers was performed in air at top temperatures in the range of 1100°C, for 12-24 hours. The organic agents added during the slurry preparation, are all burnt out during the calcinations and sintering, and do not have a large influence on the final product. They are required to enable the spray drying step. The quality of spray dried and sintered materials were evaluated using the "Strength Test", "Optical Microscopy", SEM and XRD methods. In order to

[§] *ASTM-E11 standard*

evaluate the strength of the green particles (i.e. before sintering), the particles were put in a sample holder and loaded to a Retsch analytical sieve shaker AS200 at maximum amplitude (3 mm) for 14 h. The particles were evaluated afterwards for any deformation or shape change. No breaking of the particles or dust formation was observed. This indicative test suggests that the green particles are very likely to survive repeated redox cycles.

The samples were also imaged with an optical microscope. The spray dried particles were found to be all in the right size range and were built up from a homogeneous mixture of support material (white) and metal oxide (black). Some particles were found to be hollow and contain a number of satellites (Figure 15). There was no clear difference between particles sintered for 12 h versus particles sintered for 24 h (e.g. Figures 15a vs Figure 15b). For this reason 12 h sintering was adopted as the standard.

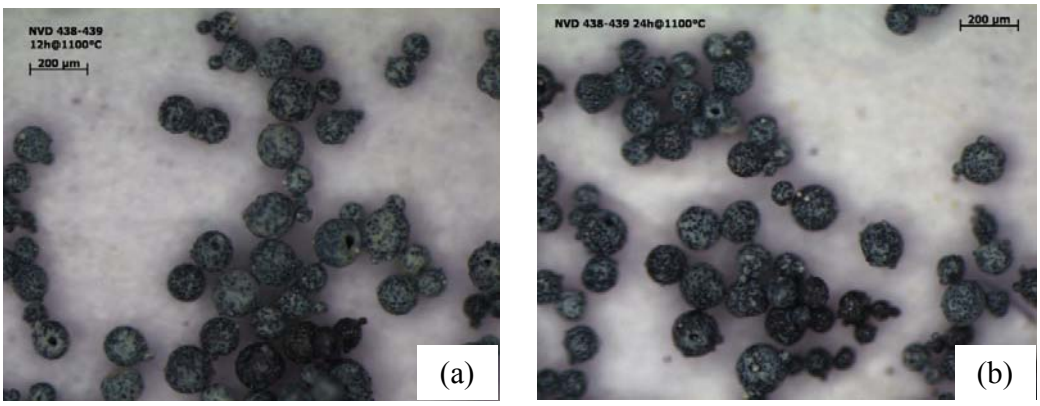

Figure 15: Optical microscope image of spray dried particles sintered for; (a) 12h at 1100°C in air and (b) 24h at 1100°C in air.

A sample set of data collected using SEM (Scanning Electron Microscopy) and XRD (X-ray Diffraction) analytical methods is also shown in Figures 16 and 17 for selected spray dried samples of CuO (see Appendix A for a more comprehensive set of SEM and XRD data). These data highlight the better distribution of active site in spray dried samples and show that even after many repeated redox cycles the spray dried samples maintain their mechanical integrity and chemical stability.

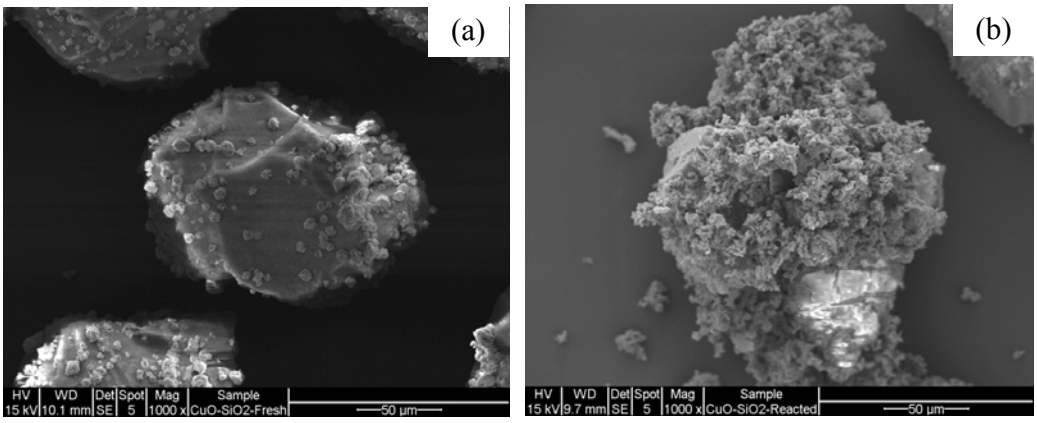

Figure 16: SEM images of fresh (a) and reacted (b) spray dried CuO samples.

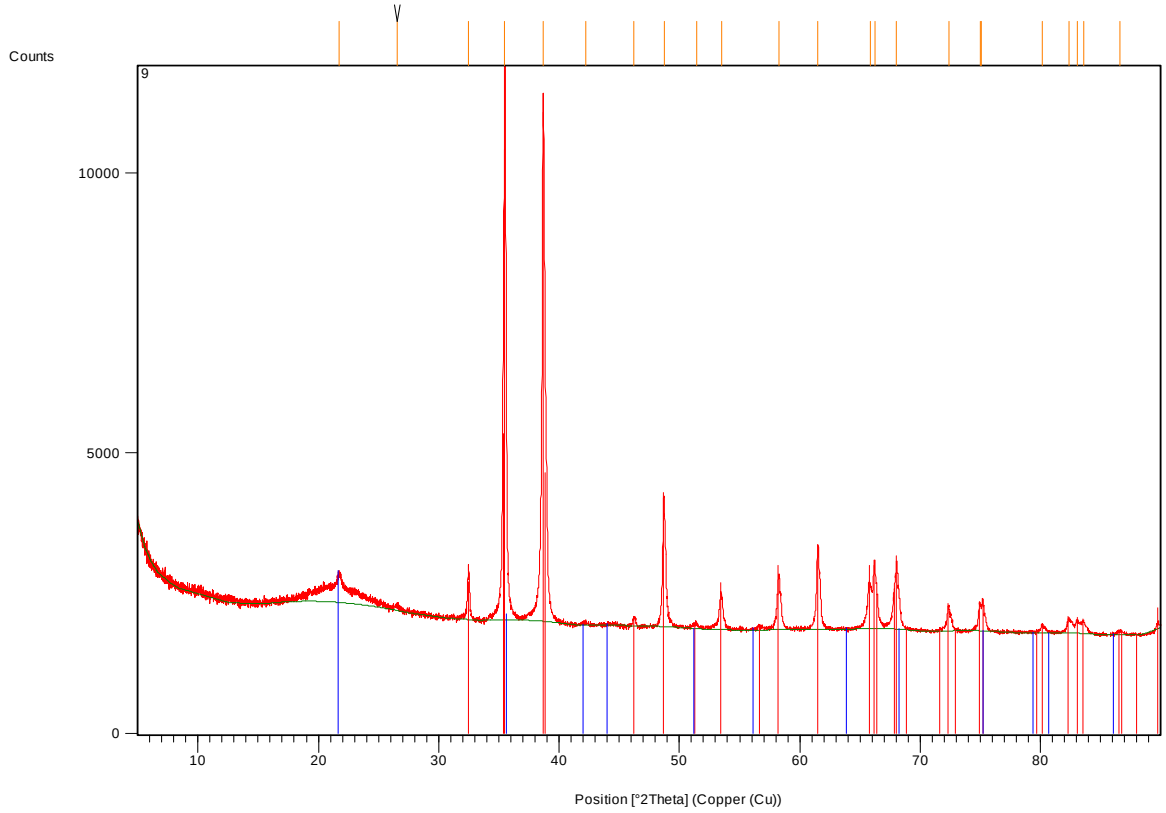

Figure 17: XRD pattern of reacted spray dried CuO samples after 42 redox cycles.

2.2.2 Characterisation of Metal Oxides Using Analytical Techniques

The analyses of fresh, partially-reacted, and fully-reacted metal oxide samples were carried out by conventional analytical techniques as well as advanced methods. The techniques employed included elemental analysis, total internal surface and porosity measurements, X-ray fluorescence analysis (XRF), X-ray diffraction analysis (XRD), and high-resolution transmission electron microscopy (HRTEM).

Elemental analyses were carried out using a LECO-CHN-600 (Amdel Laboratory, Newcastle) system to examine the decrease in Me/O ratio as an indicator of aromatic units, the loss of reactive edge sites and aliphatic materials, as well as, dehydrogenation and preferential oxidation reactions.

The XRF analyses were employed to quantify the extent of major inorganic elements (e.g. CaO, MgO, SiO_2, Al_2O_3, and TiO_2) in the metal oxide samples. These analyses were carried out at Amdel Laboratory, Newcastle using a Philips PW-1400 spectrometer. Additionally, we adopted and modified a newly developed chemical fractionation (CF) technique which is more suited for analysis of inorganic

elements. This method uses selective extraction of elements based on solubility which reflects their association in the samples. The process consists of three successive extractions. The first is by water and is intended to remove water-soluble elements such as sodium. The second extraction uses ammonium acetate to remove elements such as sodium, calcium, and magnesium that are ion exchangeable. The third extraction uses hydrochloric acid to remove acid-soluble species such as alkaline earth sulfates, carbonates, etc. The residual material typically consists of silicates, oxides, and sulfides. This wet-chemistry technique can be biased by incomplete penetration of the fuel by the solutions and partially soluble compounds. However, when carefully performed, it would be both accurate and precise, nearly within the limits of XRF-based procedures. Procedural modifications were implemented to enhance the capabilities of the CF technique for identifying the mode of occurrence of inorganic elements. The extent and nature of modifications, where necessary, was determined after consultation with experts who pioneered the technique.

Despite its usefulness, chemical fractionation alone cannot provide sufficient information for a complete description of thermal behaviour of the inorganic matter during redox reactions. The Computer Controlled Scanning Electron Microscopy (CCSEM) based techniques together with the chemical fractionation results can enable a better prediction of the fate of inorganic material during the pyrolysis of biomass materials. For this reason in a selected number of characterisation tests we employed an advanced CCSEM-based technique known as QemSCAN for analysis of the nature, grain size distribution and type of minerals matter in the metal oxide samples. QemSCAN is an automated image analysis system that uses backscattered electron and energy dispersive x-ray signals from a scanning electron microscope (SEM) to create digital mineral images in which each pixel corresponds to the mineral species in a small region under the electron beam. Once an individual particle section has been located, a grid is defined on the particle with cell size 2-5 microns. The X-ray photons emanating from each grid point on the particle are used to identify the elements present and thus classify the mineral species present. Each pixel in each particle section image is assigned a number that is a representative of the species at that point in the section. The detailed analysis of the images provides comprehensive statistical information on particle compositions and mineral associations / distributions.

Measurements of the internal surface area by CO_2-BET and the pore size distribution and the pore volume by the mercury porosimetry were also undertaken to provide insight into the ultra-fine structure of metal oxide samples. In addition, a modified SEM-based technique was used to measure the porosity/density and sample thickness. The porosity was estimated by counting the number of pixels corresponding to the pores in a char particle. However, thickness distribution was estimated by removing a pixel from all the surface of a char particle.

Furthermore, XRD data in conjunction with Bragg's law will be employed to obtain information on turbostratic crystallite dimensions, such as, average crystallite diameter, aromatic layer stacking height and inter-planer spacing. HRTEM was employed in some cases to determine the volume fraction of these crystallite entities. XRD measurements were performed using a Rigaku diffractometer with an 18-kW high intensity rotating anode. Similarly he HRTEM analyses were conducted using a JEOL 3000 F electron microprobe equipped with a 300 kV field emission gun capable of producing high resolution imaging.

Chapter 3

SELECTION OF METAL OXIDES

3.1 THERMODYNAMIC APPROACH

3.1.1 Thermodynamic Assessment of Single Species Metal Oxides

Summary: The increasing demand for oxygen combined with the need for improved economic performance necessitates the search for alternative methods of oxygen production. Chemical Looping Air Separation (CLAS) is one of these alternatives with a relatively small energy footprint. The present paper describes the results of a comprehensive thermodynamic study conducted by our group to identify suitable oxygen carriers for CLAS at medium to low temperatures. The thermodynamic simulations were carried out using Fact-Sage 6.1 for twenty different metal oxides forming forty oxygen carrier systems. An Ellingham diagram was developed to relate the Gibbs free energy of the relevant reactions to temperature for all metal oxide systems. Furthermore, the equilibrium partial pressure of oxygen was calculated at elevated temperatures. The mass balance calculations were also performed for identifying the steam/CO_2 requirements for the reduction reactor. Based on the comprehensive thermodynamic study, oxides of manganese, cobalt and copper have been found most suitable for the CLAS process. Additionally, the possibility of carbonate and hydroxide formation during the reduction with CO_2 and steam respectively was calculated. The formation of the mixed oxide phases or the spinel structures between the metal oxides and various supports (such as SiO_2 and Al_2O_3) has also been thermodynamically investigated. Several other important factors were also qualitatively assessed. The Cu-Oxides with SiO_2 and the Co-Oxides with Al_2O_3 were found to be the most suitable oxygen carriers for the CLAS.

Statement of the Problem: The advantages of the CLAS process over other known processes are the simplicity of its hardware and operation but more importantly its low energy footprint due to its thermal process heat integration and reversible chemical reaction of metal oxide systems at relatively low operating temperatures and pressures. However, the CLAS process also faces many challenges of which identification of effective oxygen carrier materials is perhaps the most difficult task. The particular challenge arises from the fact that an ideal oxygen carrier must meet two conflicting requirements to be effective in the CLAS process. More specifically, an ideal oxygen carrier should be able to undergo reversible redox reactions at low/medium temperatures ($100^oC < T < 1000^oC$) so that the overall energy footprint of the oxygen production can be minimised. However, by operating at lower temperatures the rate of redox reactions may be also slowed down requiring larger system volumes. This, in turn, would increase the capital and operating costs of a CLAS based air separation system which is not desirable. None of the oxygen carriers employed in the CLAS process so far (e.g.

CuO/Cu_2O, Mn_2O_3/Mn_3O_4, and Co_3O_4/CoO) can effectively satisfy the above requirements and unfortunately there is a limited capacity to optimise their performance given that our knowledge about the properties/characteristics of these oxygen carriers under conditions pertinent to the CLAS process is quite inadequate. Thus, there is a compelling case for further research on oxygen carrier systems suitable for use in the CLAS based air separation processes. Motivated by this, our group has undertaken a large program of study aimed at developing novel oxygen carriers for the CLAS process. The work presented here is part of this program of study and specifically focuses on developing a thermodynamic approach for identification/selection of suitable oxygen carriers. Our ongoing work on reaction kinetic properties of these oxygen carriers will be reported in future milestone reports.

Thermodynamic Modelling: The Fact-Sage 6.1 (Thermodynamic chemical equilibrium software) was used in this study to investigate thermodynamic properties of different metal oxides as potential oxygen carriers for the CLAS process. Forty different metal oxide systems were studied from twenty elements selected from the periodic table including transition metal elements (e.g. K, Ca, Ce, Cr, Mn, Fe, Co, Ni, Cu, Zn, Ru, Rh, Pd, Pt, Cd, Re, Os, Ir, Pb, Bi) at different oxidation states. The study was limited to metal oxides only as sulphides, chlorides, nitrides, carbides may generally not be suitable for high purity oxygen production using the CLAS process. Based on equilibrium results an Ellingham diagram was developed. The equilibrium partial pressure of oxygen and the steam/CO_2 requirements were also calculated at elevated temperatures for all metal oxide systems. Possibilities of the formation of hydroxide and carbonate during the reduction with steam and/or CO_2 were thermodynamically investigated. For higher mechanical strength and oxygen transport capacity, formation of mixed oxide phases or spinel structures between the metal oxides and various supports was also studied.

Results & Discussion: The standard Gibbs free energy (ΔG) of the reaction for each metal oxide system has been calculated using Fact-sage 6.1 to construct the Ellingham diagram. The ΔG indicated in equation (3.1) of a reaction is a measure of the thermodynamic driving force that makes the reaction to proceed. The Gibbs free energy is related to the reaction temperature, enthalpy and entropy through the following expression:

$$\Delta G = \Delta H - T\,\Delta S \tag{3.1}$$

where ΔH is the enthalpy, T is absolute temperature, and ΔS is entropy. ΔG for any chemical reaction can be calculated from equation (3.2) as a difference between ΔG of products minus ΔG of reactants. A negative value for ΔG indicates that a reaction can proceed spontaneously without external inputs.

$$\Delta G = \Delta G_{\text{products}} - \Delta G_{\text{reactants}} \tag{3.2}$$

Further in detail for CLAS, the ΔG for oxidation reactions can be determined as shown in equation (3.3) and (3.4) for different reacting systems. Reactant X/ X-O represents the metal/ metal oxides which are oxidized by oxygen to produce a higher oxidation state for a given metal oxide in the oxidation reactor. Alternatively, higher metal oxide states such as XO_2/XO_3 may reduce to lower oxidation states under reducing conditions in the reduction reactor. The arrow (←→) sign suggests reversible reaction.

$$\underbrace{X + O_2}_{\text{Reactants}} \leftrightarrow \underbrace{XO_2}_{\text{Products}} \qquad \Delta G = \Delta G_{XO2} - \Delta G_{X} - \Delta G_{O2} \tag{3.3}$$

$$\underbrace{X\text{-}O + O_2}_{\text{Reactants}} \leftrightarrow \underbrace{XO_3}_{\text{Products}} \qquad \Delta G = \Delta G_{XO3} - \Delta G_{X\text{-}O} - \Delta G_{O2} \qquad (3.4)$$

Figure 18 shows the Ellingham diagram constructed for different metal oxide systems for CLAS as a function of temperature. The Ellingham diagram qualitatively suggests whether a given metal oxide system will oxidise or reduce at elevated temperatures. However, it does not quantify the rate of the reaction. It can be assumed that the reaction will qualitatively occur more rapidly as temperature increases or as the conditions for reduction or oxidation deviate farther from equilibrium conditions. The Ellingham diagram approach is normally used in pyro-metallurgical and its information is easily available in the literature. As noted earlier, generally medium to low operating temperatures are preferred in the CLAS process although given that low temperatures often lead to slow reactions medium temperatures appear to be more suitable. Furthermore, negative ΔG is needed for the reaction to occur. The more negative the value of ΔG on the Ellingham diagram, the more likely that the forward reaction (i.e. oxidation, see equation 3.3 and 3.4) will proceed while for less negative ΔG values the reduction will occur more easily. Therefore, as Figure 18 indicates the oxides of Ca, Cr, Pb (i.e. PbO/PbO_2 and Pb_3O_4/PbO_2) and the higher oxidation state of Mn-O (MnO_2/Mn_2O_3) are easier to reduce and more difficult to oxidize as their corresponding ΔG values are not highly negative (i.e. closer to zero). In contrast, oxides of Pd, Cu, Co and the lower Mn oxidation state (Mn_2O_3/Mn_3O_4) are more difficult to reduce but easier to oxidize. Furthermore, given that temperatures greater than 1000^0C are not suitable due to high operating norms and fabrication issues of relevant CLAS reactors, Os, Fe and the lower oxidation state of lead (Pb/PbO) may also not be suitable for the CLAS process. Hence, oxides of Ca, Cr, Pb, Mn, Pd, Cu and Co may be suitable for temperatures between 100 and 1000^0C.

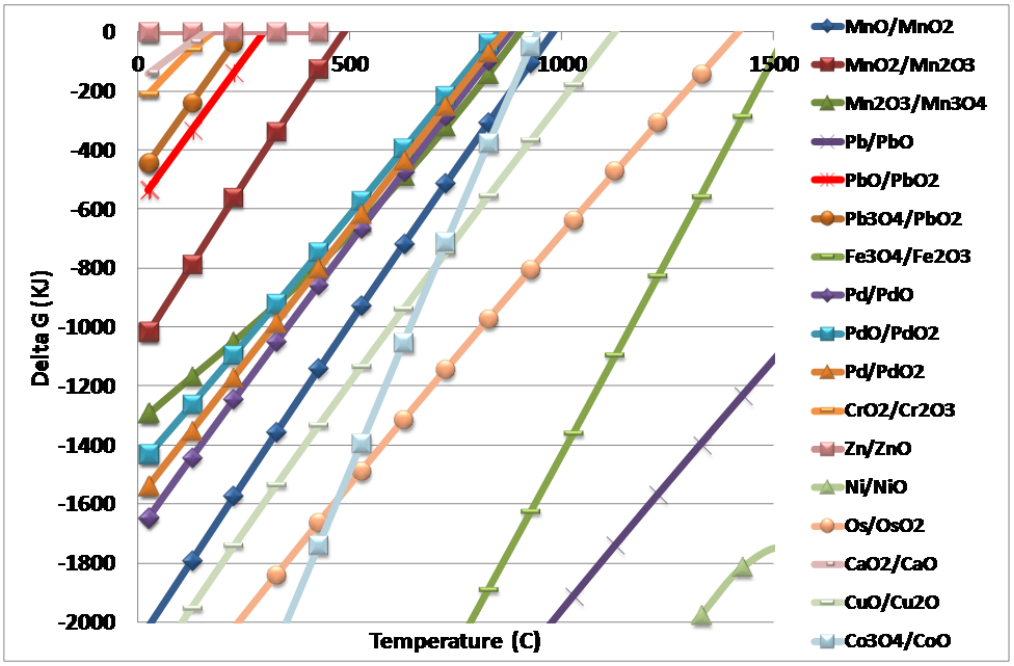

Figure 18: Ellingham diagram of different metal oxide systems (the diagram does not show metal oxide systems having ΔG lower than -2000 KJ and temperature >1500^0C).

To assess the suitability of these oxides we carried out a range of additional thermodynamic analyses. In this context, the equilibrium partial pressures (EPP) of oxygen for different metal oxide systems were calculated using equation (3.7) over the temperature range of ($100^{o}C < T < 1000^{o}C$) and results have been plotted in Figure 19. The dotted zone displays suitable metal oxide systems which can perform effectively at the desired range of operating temperatures between 100 and 1000 ^{0}C.

$$P_{O2} = Exp\left(\frac{\Delta G}{RT}\right) \tag{3.5}$$

According to Le Châtelier's principle, if the equilibrium of a reacting system is disturbed by changing its equilibrium partial pressure or temperature, the system will try to restore equilibrium. For CLAS, the equilibrium can be disturbed by increasing the actual partial pressure of oxygen above its equilibrium value by providing the system with normal air which will allow oxidation to take place. In contrast, the oxygen-releasing step (reduction) can be realized by creating the reducing environment using inert gases (steam/CO_2). The reason for the selection of steam/CO_2 for reduction of metal oxide is mainly for the purpose of oxygen purity as the majority of the metal oxides in their solid states do not react with steam/CO_2. However, CO_2 can only be used for oxygen production in an oxy-fuel firing plant where it is recycled in the furnace along with O_2 to maintain the desired flame temperature. From Figure 19, it can be observed that for any metal oxide system, the equilibrium partial pressure of O_2 changes with the temperature which can be a limiting factor in the selection of metal oxide system for the CLAS. For example, the Mn_2O_3/ Mn_3O_4 system cannot work thermodynamically beyond $900^{0}C$ as it needs a higher oxygen concentration than air for re-oxidizing back to the higher oxidation state due to higher EPP of O_2 beyond $900^{0}C$. Similarly, it can also not work below $560^{0}C$ as the EPP of O_2 at this temperature will be around 1.0E-04 % which needs very high steam/CO_2 in the reduction reactor.

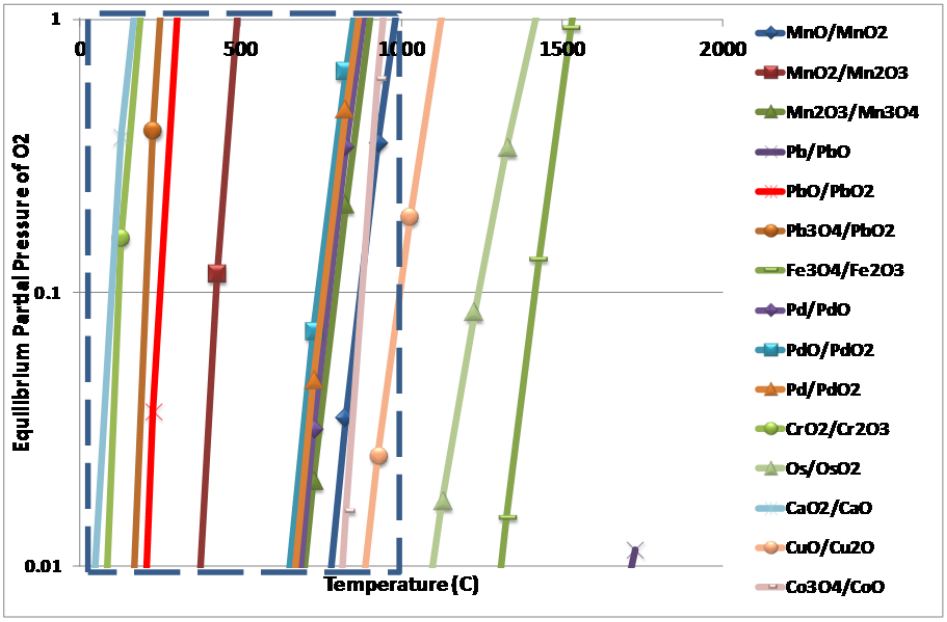

Figure 19: Equilibrium partial pressure of oxygen for different metal oxide systems at elevated temperatures (the diagram only shows metal oxide systems which need EPP of O_2 between 0.01 to 1 % and temperature < 2000 ^{0}C).

The oxides of Ca, Cr, Pb, Mn, Pd, Cu and Co can be operated between temperature ranges of 100 to 1000 ^{o}C. The Pd oxides being the rarest element and highly expensive have not been studied further. The lead (Pb) oxides are also not studied due to their high density which may not be favourable for the chemical looping systems.

The steam/CO_2 requirements for reduction have been calculated by mass balance calculations assuming that the actual partial pressure was 10% higher and 10% lower than the equilibrium partial pressures of oxygen in the oxidation and reduction reactors respectively for the all selected metal oxide systems and plotted against the equilibrium partial pressure of oxygen in Figure 20 for the Mn_2O_3/Mn_3O_4 system given in equation (3.6).

$$6Mn_2O_3 \leftrightarrow 4Mn_3O_4 + O_2 \quad (3.6)$$

It can be observed from Figure 20 that running the system at lower temperatures will decrease the equilibrium partial pressure which will significantly increase the inert gas (steam/CO_2) requirement in the reduction reactor. For example at around 450^{o}C, steam requirement is 1.0E+05 kg/kg of air while at nearly 750^{o}C it is only 1.0E+01. Furthermore, the kinetics will be slow at lower temperature. Alternatively, running the system at high temperature will reduce the oxygen throughput due to increased partial pressure and will also increase the energy foot prints.

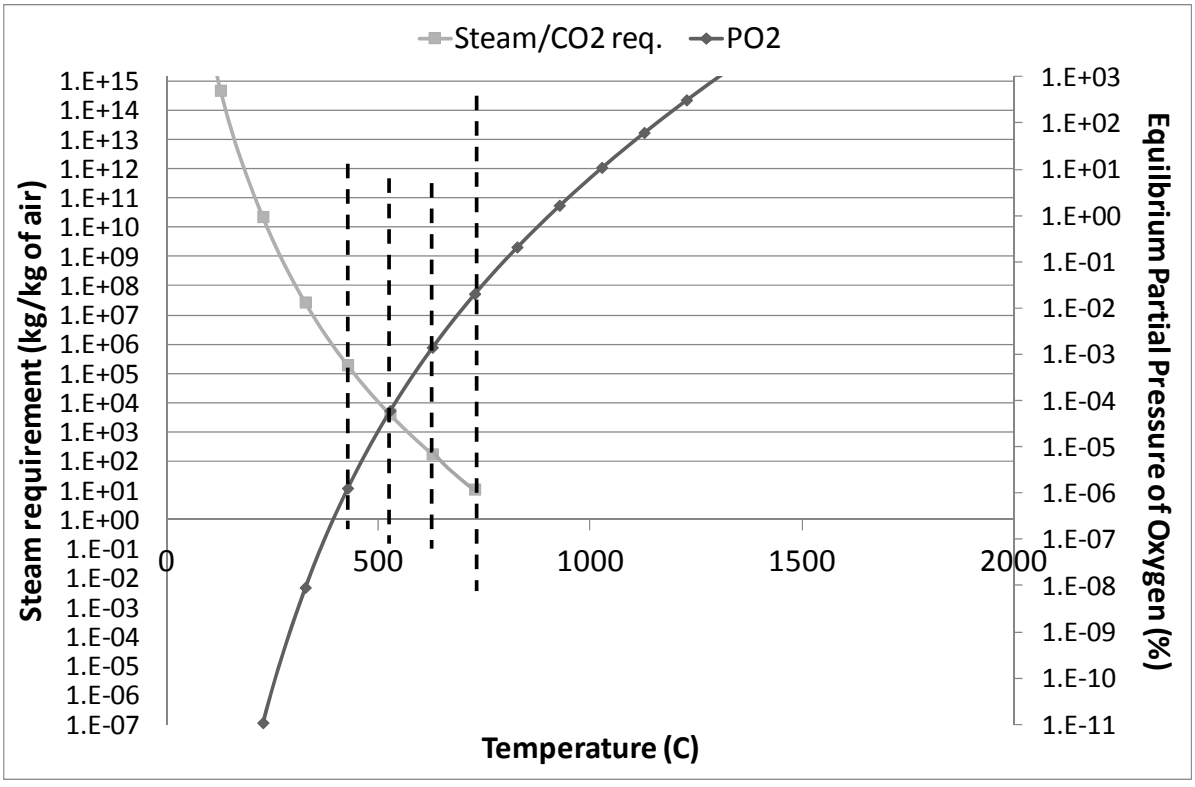

Figure 20: Steam/CO_2 requirement calculations for Mn_2O_3/Mn_3O_4 oxide system at elevated temperature.

As proposed in Figure 20, metal oxides are reduced in the reduction reactor with CO_2/steam in CLAS process. However during reduction, these metal oxides can react with CO_2/ steam to produce metal carbonates and/or hydroxides respectively as shown in equation (3.7) and (3.8) which can reduce the oxygen transport capacity.

$$\underbrace{XO_2 + CO_2}_{\text{Reactants}} \rightarrow \underbrace{XCO_3 + 0.5\ O_2}_{\text{Products}} \qquad \Delta G = \Delta G_{XCO3} - \Delta G_{0.5O2} - \Delta G_{XO2} - \Delta G_{CO2} \qquad (3.7)$$

$$\underbrace{XO_2 + H_2O}_{\text{Reactants}} \rightarrow \underbrace{X(OH)2 + 0.5\ O_2}_{\text{Products}} \qquad \Delta G = \Delta G_{X(OH)2} - \Delta G_{0.5O2} - \Delta G_{XO2} - \Delta G_{H2O} \qquad (3.8)$$

Gibbs free energy calculations for the reactions producing carbonates, hydroxides and oxygen (reduction step) have been performed and plotted in Figure 21 for the desired temperature ranges for different oxygen carrier systems. Positive values of Gibbs free energy indicate that no such reaction would occur while negative values suggest a reaction will take place. The results clearly indicate that only Ca-Oxides can potentially react with CO_2 and H_2O to form $CaCO_3$ and $Ca(OH)_2$ respectively. Therefore, it can be concluded that even though the redox mechanism can be achieved at the lowest temperatures, its reactivity with the reduction gases limit the use of the Ca-Oxides as a potential oxygen carrier in the CLAS and so has not been studied further. The rest of the metal oxides will not react with the reduction gases under the desired temperature ranges. Moreover, Cr-oxides are also not studied further due to the health issues associated with them.

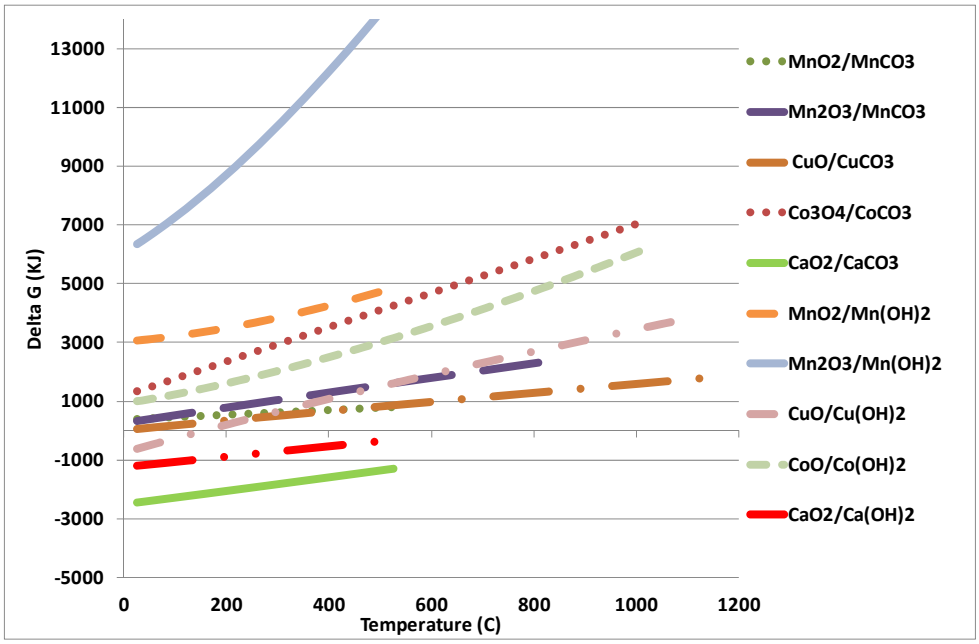

Figure 21: Ellingham diagram from investigating hydroxide and carbonate formation during reduction with steam and/or CO_2.

The reaction rate for the solid-gas (metal oxides and gases) reactions depends on a number of parameters such as particle size, size distribution, packing density, contact areas and porosity. Solids are normally impregnated on supports such as Al_2O_3 and SiO_2 which are normally believed to be non-reacting with the gases and help in increasing the mechanical strength and the contact area between them. However, it has been noted in the literature that some pure supports react with the metal oxides to form mixed phases or spinel structures which may reduce the oxygen storage/transport capacity of the metal oxides and also be responsible for lowering the mechanical strength due to possible sintering. To avoid the sintering of the metal oxides with pure alumina or silica oxides (support/binders), the use of metal oxide aluminates and silicates as support is also mentioned in the literature. During the preparation, oxygen carriers are normally sintered at high temperatures (> 900-1100^{0}C) for long period to ensure complete formation of metal oxide aluminates and silicates. It is found from the kinetic experiments that metal oxide aluminates or silicates may work better as support in some cases.

The main aim in the current exercise was to study the chemical equilibrium of the different oxygen carriers and their support at elevated temperatures in CLAS environment. Secondly, the attention was also given to find out the best metal oxides and support which do not form any mixed phases or spinel structures together under CLAS environment. The chemical equilibrium calculations have been performed using Fact-Sage 6.1 for the oxidation and the reduction of Cu, Co and Mn metal oxides with Al_2O_3 and SiO_2 supports in air and CO_2 respectively for the CLAS operation. Results of the Cu and Mn are only discussed here for detailed explanation.

Figures 22 and 23 show that the increasing CO_2 concentrations during reduction step helps in releasing the O_2 from the Mn and Cu metal oxides even at lower temperature. However, the presence of an active Al_2O_3 in the Mn based oxygen carriers have increased the release of oxygen significantly which indicates that the Al_2O_3 may take part in the reaction under the desired temperature range. To investigate the effect of Al_2O_3, thermodynamic equilibrium calculations were performed at constant temperature (850^{0}C) for the redox cycles and presented in the Figures 24 and 25.

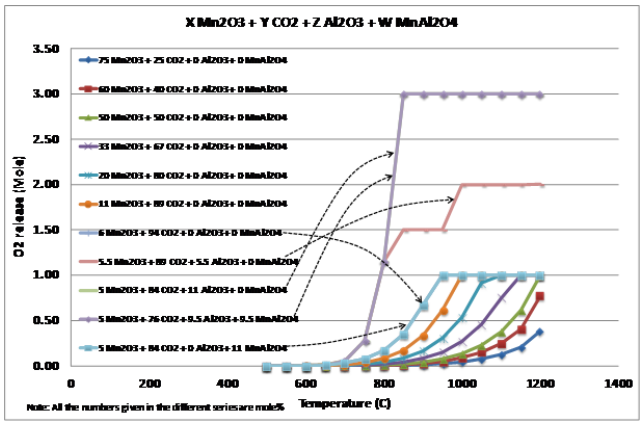

Figure 22: Equilibrium calculations for O_2 release for Mn_2O_3 at elevated temperature under different CO_2.

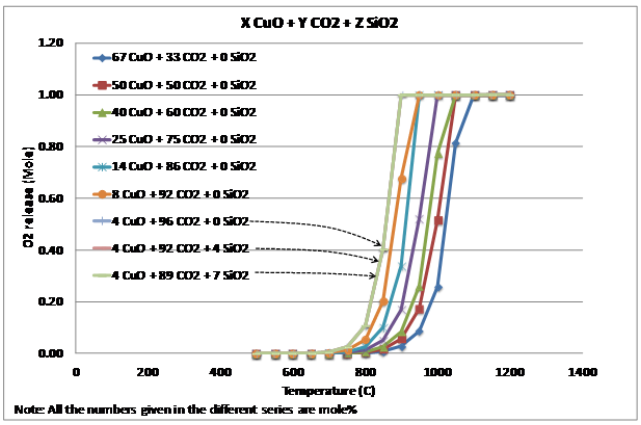

Figure 23: Equilibrium calculations for O_2 release for CuO at elevated temperature under different CO_2.

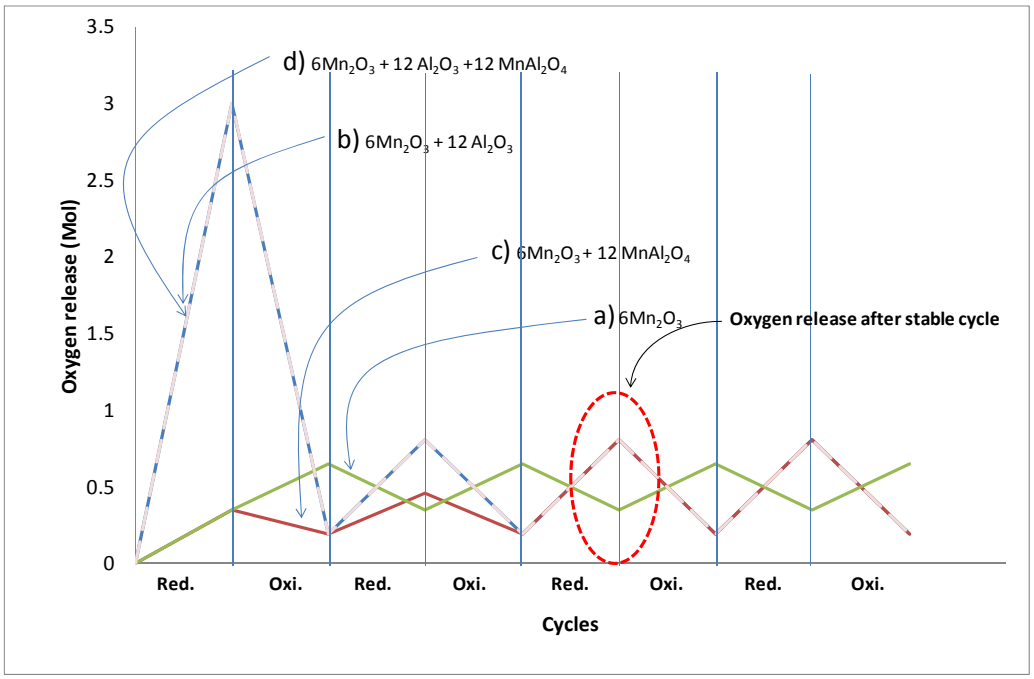

Figure 24: Thermodynamic cycle at 850^{0}C Mn-Oxides with Al_2O_3 support.

Four cases were selected for the thermodynamic calculations based on the existing literature. It has been cited in the literature that to avoid the stability and sintering issues during the redox cycles, metal-oxide-aluminates can be used as support in some cases where metal oxides are found to react with alumina oxides. Therefore, the selected four cases were: (a) Mn_2O_3 (b) Mn_2O_3 + Al_2O_3 (c) Mn_2O_3 + $MnAl_2O_4$ (d) Mn_2O_3 + Al_2O_3 + $MnAl_2O_4$. There is no support used in Case a. In Case b, Al_2O_3 is used as a support. Case c considers the use of the metal-oxide-aluminates as support. And, Case d assumes that some active Al_2O_3 still remained in the sample along with metal-oxide-aluminates supports. The oxidation gas was the Air (1 mole O_2 + 3.76 mole N_2) and the reduction gas was CO_2 (96 moles). From Figure 20, it can be seen that the oxygen release was quite stable from the first cycle with Mn_2O_3 (Case a) oxidation and reduction. However in rest of the cases, the oxygen release was decreased (Case b and d) or increased (Case c) in the first one/two cycles before finally stabilized. It can be observed that release of oxygen was found to increase when Al_2O_3 or $MnAl_2O_4$ were used as support (Case b, c and d). To answer the above, detailed compositions of solid and gases during thermodynamic equilibrium calculations were calculated and presented in Figure 25. It can be observed from Figure 25 that no Mn_3O_4 was found to thermodynamically exist except for Case a. Moreover, any Al_2O_3 present (Case b and d) was eventually reduced and converted to $MnAl_2O_4$ during the reduction with CO_2 and the newer equilibrium values were reached. To avoid this, number of literatures recommended use of $MnAl_2O_4$ as a support. However, aluminates (i.e.) $MnAl_2O_4$ has a higher density than alumina (i.e. Al_2O_3) and consequently, needs larger reactor volumes which may increase the capital as well as operating costs. Alternatively, any $MnAl_2O_4$ present (Case d) was eventually converted to Mn_2O_3 and Al_2O_3 during the oxidation with air under the newer equilibrium. The experiments, however, suggests that decomposition of $MnAl_2O_4$ may be very slow and not achieve equilibrium in the controlled lab scale experiments with switching gas environment. On the other hand, in fluidized bed reactors, it is often

observed that large particles may not be circulated between the two reactors and only expose to the same gaseous environment where equilibrium for decomposition reaction will be achieved for long run which may be responsible for fragmentation, agglomeration and/or reactivity loss for particles. Thus it can be stated that $Al_2O_3/MnAl_2O_4$ may take part in the reaction under equilibrium condition which may change the purpose of them being used as a support to provide the high contact area between the oxygen carriers and the gas. The overall oxygen release was found to increase with the use of oxide supports such as $Al_2O_3/MnAl_2O_4$. However, reaction with such reactive supports may be responsible for the reduction in the mechanical strength and also raise serious sintering issues during redox cycle for long term operation.

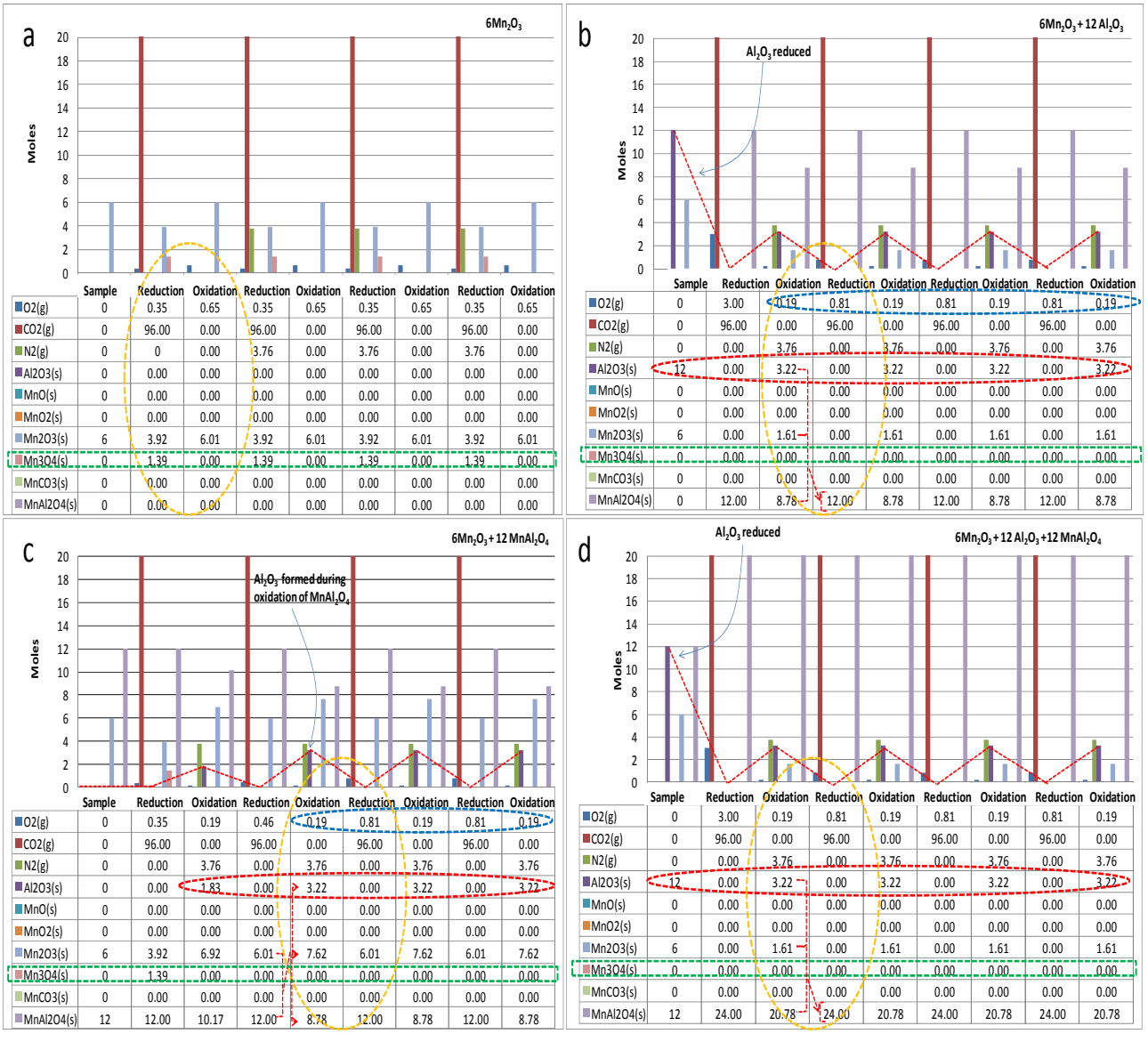

Figure 25: Equilibrium calculations for the redox cycle of Mn-Oxides with Al_2O_3 support.

From Figure 23, it was observed that the Cu-Oxides do not react with SiO_2 to form any spinel structures and therefore may have stable performance during repeated redox cycles. Figure 20 represents the thermodynamic cycles where full decline in the oxygen release was observed only in the first or second cycle before the final equilibrium was achieved while in the actual kinetic experiments, the declining trend may be observed gradually with the higher number of cycles in the long time operation as the reaction proceeds towards equilibrium or may not be observed at all if the declining reaction rates are very slow. Further kinetic experiments are needed to confirm the present findings.

It has been found in this comprehensive thermodynamic study that the majority of the metal oxides react with these two supports to form spinel structures such as $MnAl_2O_4$, $MnSiO_3$, $CoSiO_3$ and $CuAl_2O_4$. However, no spinel structures are thermodynamically found to be formed between Co-Oxides and Al_2O_3 and Cu-Oxides and SiO_2 supports as per the Fact-Sage 6.1 database which may be good choice for potential oxygen carriers. Such thermodynamic study may be helpful sometimes in justifying the decline in the oxygen release during kinetic experiments where XRD analyses fail to detect the formation of such complex structures. Apart from the thermodynamic suitability, other factors are also needed to be considered for the efficient process design and operation. Factors that have been qualitatively compared and discussed in this study are shown in Tables 2(a) and 2(b) for selected metal oxide systems (i.e. Ca-O, Cr-O, Mn-O, Co-O, Cu-O). It can be seen that the oxides of Cr, Pb and Mn are suitable for the redox process at temperatures below than 500 ^{0}C. However, lead oxides due to their higher density and toxic nature will be unfavorable for gas-solid circulation (chemical looping) systems. From the literature and the thermodynamic study presented earlier in this Section, it was found that calcium peroxide at lower temperatures may be highly unstable and forms carbonates and hydroxides during reduction with steam and CO_2 respectively. Some oxidation states of chromium oxide are also found to be toxic. For an intermediate temperature range (650-1150 ^{0}C), oxides of Pd, Mn, Co and Cu appear to be promising in delivering a redox mechanism. However, Pd is a rare element and very expensive. Molecules such as O and Fe are good at high temperatures (>1150 ^{0}C) which may lead to high energy footprints and capital investment. Moreover, Os is also the rarest element and highly expensive. From the comparison made in Tables 2(a) and 2(b), it can be seen that the oxides of Mn, Co and Cu can be efficient oxygen carriers for the CLAS operation. However, Mn-Oxides may form aluminates or silicates with Al_2O_3 and SiO_2 supports. Therefore, Cu-Oxides with SiO_2 and Co-Oxides with Al_2O_3 support may be a good choice for the CLAS. Detailed kinetic experiments are needed to confirm this.

The oxygen carrier inventory and the steam/CO_2 requirement are calculated and presented in Figure 26 for Mn-Oxide systems. The steam/CO_2 requirements have been assumed and fixed as 2 kg per 1 kg of air using Figure 18 and 19 for calculation purpose in Figure 26. It can be read from the Figure 26 that for such an assumption, the steam/CO_2 requirement (~4300 MT for 500 MWe) is significant. The amount can be reduced further by increasing the reduction temperature (see Figure 20) but it will reduce the oxygen throughput due to increased partial pressure (see Figure 19).

Therefore, it can be stated that the reduction temperature and steam/CO_2 requirement are crucial parameters and need to be optimised for efficient oxygen production. Inventory calculations for MnO_2/Mn_2O_3 (HOS) and Mn_2O_3/Mn_3O_4 (LOS) systems suggest that higher oxidation states may be favourable even though having slower reaction kinetics in terms of inventory and energy foot prints due to their lower molar values and lower operating temperature.

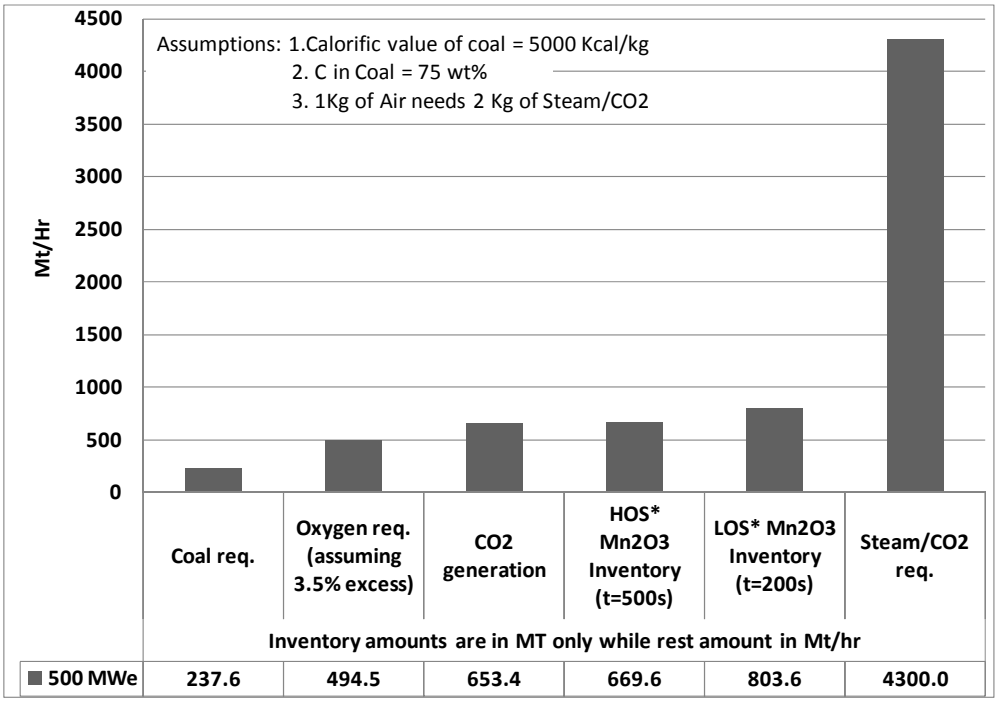

Figure 26: Oxygen carrier inventory and steam/CO_2 requirement calculations for oxy-fuel firing thermal power plant (*HOS= Higher oxidation state and *LOS= Lower oxidation state).

Table 2: Properties of metal oxides

(a)

	Details	1 CaO/ CaO_2	2 CrO_2/ Cr_2O_3	3 PbO_2/Pb_3O_4	4 PbO/ PbO_2	5 PdO /PdO_2	6 Pd/PdO_2	7 Pd/ PdO
1	Price	Low	Medium	Low	Low	High	High	High
2	Physical Properties							
	Density (g/ml)	3.35 / 2.92	NA / 5.21	9.37 / 9.10	9.53/9.38	8.70 / Not known	11.40 / Not known	11.40 / 8.70
	Molecular weight (gm/mol)	56.07 / 72.07	83.99 / 151.99	239.2/ 685.6	223.2/ 239.2	122.42 / 138.41	106.42 / 138.41	106.42/ 122.41
3	Risk (Health and Safety)	Low to Moderate	Moderate	High (Poisonous and Carcinogenic)		Low		
4	Operating Temperature*	35-150	127-200	200-250	227-300	627-875	627-875	627-875
5	Reaction kinetics	Slow	Slow	Slow	Slow	Medium		
6	Mechanical Strength	Poor	Medium	High	High	High		
7	Solid inventory	Small-Medium	Small-Medium	Small-Medium	Small-Medium	Small-Medium		
8	Reactor Size	High	High	High	High	Medium		
9	Steam Separation Unit	Small	Small	Small	Small	Medium		
10	Operating Cost	Low	Low	Low	Low	Medium		
11	Special Remarks	CaO_2 is highly unstable and may react with steam or CO2	Poisonous and Slower kinetics	Poisonous, High density and Lower kinetics		Too expensive and high density		

* The actual partial pressure (APP) is considered 10% higher and 10% lower than the equilibrium partial pressures (EPP) of oxygen in the oxidation and reduction reactors respectively for calculating operating temperatures of the metal oxide system

(b)

	Details	8 MnO_2/ Mn_2O_3	9 Mn_2O_3/ Mn_3O_4	10 CoO/ Co_3O_4	11 CuO/ Cu_2O	12 Os/ OsO_2	13 Fe_2O_3/ Fe_3O_4	14 Pb/PbO
1	Price	Medium	Medium	Medium	Medium	Expensive	Low	Low
2	Physical Properties							
	Density (g/ml)	5.03 / 4.30	4.30 / 4.86	6.45 / 6.07	6.40 / 6.00	22.48 / 11.37	5.23 / 5.20	11.34/ 9.53
	Molecular weight (gm/mol)	86.93 / 157.87	157.87 / 228.81	74.93 / 240.79	79.54 / 143.09	190.2 / 222.20	159.69 / 231.53	207.2 / 223.2
3	Risk (Health and Safety)	Low to Moderate						High (Poisonous and Carcinogenic)
4	Operating Temperature*	327-500	627-900	750-950	827-1127	1027-1400	1227-1550	> 1627
5	Reaction kinetics	Slow	Medium	Medium	Medium	Fast	Fast	Fast
6	Mechanical Strength	Medium	Medium	Medium	Medium	High	Medium	High
7	Solid inventory	Small-Medium	Medium - Large	Medium-Large	Small-Medium	Small-Medium	Medium - Large	Medium-Large
8	Reactor Size	High	Medium	Medium	Medium	High	High	High
9	Steam Separation Unit	Small	Medium	Medium	Medium	Large	Large	Large
10	Operating Cost	Low	Medium	Medium	Medium	High	High	High
11	Special Remarks	Good but possible slower Reaction Kinetics	Good for CLAS operation			Too expensive and high density	High Temperature	High Temperature and high density

* The actual partial pressure (APP) is considered 10% higher and 10% lower than the equilibrium partial pressures (EPP) of oxygen in the oxidation and reduction reactors respectively for calculating operating temperatures of the metal oxide system

Summary of Major Findings:

- Comprehensive thermodynamic scoping study was carried out for the selection of the most suitable oxygen carriers for the CLAS. Several other critical factors apart from the thermodynamic suitability are also qualitatively compared. Of the twenty metals with their different oxidation states examined in this study, MnO_2/Mn_2O_3, Mn_2O_3/Mn_3O_4, CoO/Co_3O_4 and CuO/Cu_2O appear to be potentially suitable for the CLAS process.
- It was found that Ca-Oxides may not be suitable as oxygen carriers for CLAS due to their reactivity with steam and CO_2 (based on thermodynamic study) despite the fact that they may run at lower temperature.
- It was also observed that thermodynamically Mn, Co and Cu may form spinel structures or mixed phases of silicates and aluminates with Al_2O_3 and SiO_2 such as $MnAl_2O_4$, $MnSiO_3$, $CoSiO_3$, $CuAl_2O_4$. However, detailed kinetic experiments are needed further to confirm the presence of the spinel structures as it may not be observed largely in the experiments if the kinetics of such phases are slower. It was found that thermodynamically Cu-Oxides do not react with SiO_2 and Co-Oxides do not react with Al_2O_3 which may be a good choice as oxygen carriers.
- The temperature of the system, steam/CO_2 requirement, reaction kinetic properties and oxygen throughput are the crucial parameters in the selection of most suitable oxygen carriers for the CLAS system.
- It was also found that the higher oxidation states may generally be more favourable as they may operate at lower temperatures with much smaller solid inventories.
- The Ellingham diagram (normally used for pyro-metallurgical operations) approach suggested here can be effectively used to determine the efficient metal oxide systems for any chemical looping / redox systems.

3.1.2 Review of Mixed Metal Oxide Thermodynamics

We are currently carrying out a range of thermodynamics and experimental studies of mixed metal oxides for chemical looping air separation applications. The results will be reported in future milestone reports. What is presented in this section provides a review of relevant literature.

Summary: The mixed oxide systems work as catalysts are normally used to increase the reactivity and selectivity of the oxidation or reduction reactions. In the metallurgical operations also metal/metal oxides are often used to reduce or oxidise the other metal/ metal oxides (i.e. pyrometallurgy or hydrometallurgy). A number of researchers have applied the concept of mixed metal oxides for newly developed chemical looping processes. There are several important factors that have to be carefully examined before oxides can be mixed for catalysis, metallurgical or chemical looping based processes. Effects of mass ratio of mixed oxides, their sintering temperature, porosity, surface area, density, rate index, crushing strength and methods of preparation, reactivity and selectivity are among these factors. However, the causes for the basic change in the reactivity, selectivity or ionic activity of oxygen with mixed metal oxides are still remain uncertain and a matter of debate in the literature due to the level of

complexity associated with mixed metal oxide particles at micro level. The current review provides a brief critical assessment of mixed metal oxides for applications in catalysis, metallurgical operations and chemical Looping. The aim of this review is to understand/ derive the essential steps in selecting the best mixed metal oxides combination for Chemical Looping Air Separation (CLAS) process. The review confirms that thermodynamics of mixed metal oxides at given operating conditions is a first key step to find out the potential mixed oxides and their optimum compositions. Based on the derived approach more specifically designed mixed metal oxides will be prepared and tested in TGA, fixed bed and fluidised bed rigs at the University of Newcastle in future.

General Background:

(a) Application of mixed metal oxides at micro scale (catalysts industry)

- Plays an important role in chemistry, physics, materials, environmental science and geochemistry.
- Technological applications: microelectronic circuits, piezoelectric devices and importantly as catalysts etc.
- Nobel metals (i.e. Pt, Pd, Au) are easy to reduce and as they sit up on the Ellingham diagram. Therefore, they are normally used as a catalyst in the oxidation of several hydrocarbons at low temperature (i.e. when any process needs oxygen, these metals easily releasing their oxygen). In contrast, Ce, Ni, Fe and many other metal/metal oxides sitting lower on the Ellingham diagram can be worked as a catalyst to enhance reduction reaction at high temperature (i.e. they are easy to oxidize so can be used to store the oxygen). Normally, it is found that metal/metal oxides sitting higher on Ellingham diagram work better at lower temperature applications while Ce, Ni and Fe parked at bottom on Ellingham diagram work better at high temperatures. Often, metal oxides are mixed in catalysis processes. Mixing oxides may change the overall reaction path and therefore changes the activation energy for the reaction which enhances the reaction rate considerably.
- Points of interest: Mixed metal oxides are used as active catalysts for the selective hydrogenation and isomerization of olefins, water-gas shift reaction, dehydrogenation of alcohols, the oxidation of CO and alkenes, NO reduction, SO_2 destruction, pyrolysis.
- Recent development: Flue gas cleaning, chemical looping combustion, gasification and reforming.

(b) General literature review for mixed metal oxides as a catalysts in DeNOx and DeSOx, CO and hydrocarbon removal operations (Jose et. al. Catalysis today 85 (2003); 177-192)

- PbTiO3 and PbZrxTi1-xO2 (x<0.6) generates catalytic effects and works 7-12 times faster for SO_2 reduction than its individuals
  - $SO_2 + 2H_2S \rightarrow 2H_2O + 3S$
  - $SO_2 + CO \rightarrow 2CO_2 + S$

  This is possibly due to the change in the activation energy.

- Due to its redox properties, CeO_2 is used as catalysts in reduction of CO, NOx and hydrocarbon from automobile exhaust for high temperature application. To enhance its reactivity, CeO_2 is often doped with stabilized ZrO2 which possibly provides high oxygen vacancies for the catalysts surface. It is generally believed that mixing/doping X metal oxides with Y metal oxides having lower valences, increase the oxide vacancies in the structure. In opposite to that, bonding with metal oxides with higher valences, decrease the oxide vacancies.

  Higher the oxide vacancy → Higher porosity → Higher O_2 activity → Higher reaction rate

- For cerium based mixed oxides: CeO_2-CaO (+2), CeO_2-CuO (+2) showed better reactivity than CeO_2-Mn_2O_3 (+3), CeO_2-Fe_2O3 (+3), CeO_2-Nb_2O_5 (+5). This may even be true for identifying suitable support for catalysts and oxygen carriers. However, the literature suggests selection of Al_2O_3 (+3), $MnAl_2O_4$ (+8/3), SiO_2 (+4), ZrO_2 (+4), TiO_2 (+4) as support for oxygen carriers mainly increases surfaces area, avoids interactions between the metal and support and improves mechanical strength. So far, catalytic effects (higher oxide vacancies) of support/binder in oxygen carriers for chemical looping applications have not been studied in details.

(c) Applications of mixed metal oxides at large scale (metallurgy)

- Play important role in metallurgical operations. Normally one metal/metal oxides can reduce/oxidize other metal/metal oxides. In principle, the metal/metal oxides sitting lower on the Ellingham diagram (being stronger oxidizer) can reduce the metal/metal oxides parked on upper side (stronger reducer) of the Ellingham . (Thermit process – Sacrificial method)

  $$\underset{\text{(Strong oxidiser)}}{2Al} + \underset{\text{(strong reducer)}}{Fe_2O_3} \rightarrow Al_2O_3 + 2Fe$$

  The reverse reaction is not possible thermodynamically.

- Points of interest: Such mixed oxides if applied as oxygen carriers may alter the oxygen transport path and activation energy which will enhance/reduce the reactivity. For example, mixed oxides (Cu-Ni) may deliver redox mechanism more efficiently than individuals

Oxidation (in air)	Reduction (with inert)
$2Cu_2O + O_2 \rightarrow 4CuO$	$2NiO \rightarrow 2\,Ni + 2\,O^*$ $2Ni + 4\,CuO \rightarrow 2Cu_2O + 2NiO$

  This may enhance the reduction reaction which is often found slow with Cu-O and Ni-O alone. Higher Ni-O is desired for high temperature application.

Mixed Metal Oxides in Chemical Looping Combustion

(a) To increase the operating temperature of the chemical looping system

- For example, Mn-Fe mixed oxides are used as mixed metal oxides to increase the operating temperature of chemical looping combustion. The oxidation of Mn_3O_4 to Mn_2O_3 at 900_oC is not feasible due to thermodynamic limitations. However, Fe_3O_4 can be oxidized easily at and above 900^oC being lower on the Ellingham diagram. Therefore, combination of Mn-Fe will work as below:

Oxidation (in air)	Reduction (with inerts)
$4Mn_3O_4 + O_2 \rightarrow 6Mn_2O_3$	$6\ Fe_2O_3 \rightarrow 4Fe_3O_4 + O_2$
$4Fe_3O_4 + O_2 \rightarrow 6Fe_2O_3$	$4Fe_3O_4 + 6\ Mn_2O_3 \rightarrow 6\ Fe_2O_3 + 4\ Mn_3O_4$

  Note: Higher Fe loading is essential to achieve higher temperature of system. The Mn-Fe forms spinel structures ($MnO.Fe_2O_3$) which will also change its thermodynamic property. The system should work even if spinels are not formed based on thermit process theory.

(b) To reduce the sintering effect and reactivity loss by avoiding interactions between the metal oxide and its support

- For example, Mn-$MgAl_2O_4$ is used instead Mn-Al_2O_3, Mn-$MnAl_2O_4$ to reduce the possible interactions between Mn_2O_3 and Al_2O_3. MgO and Al_2O_3 have higher affinity towards each other compare to Mn_2O_3 and Al_2O_3 as shown in Figure 27.

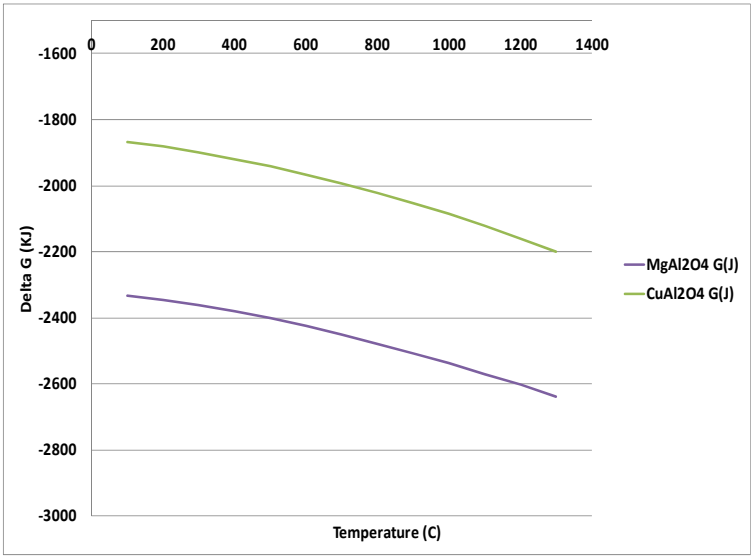

Figure 27: Gibbs free energy for mixed metal oxides.

(c) To increase the reactivity/selectivity of the metal oxides (where the second metal oxide will catalyze the reaction) - this way higher conversion can be achieved at marginally lower temperatures.

The concept applied so far in catalysts industry has been applied in chemical looping. For example, perovskites (ABO_3) are found to be useful in chemical looping combustion.

Mixed Metal Oxides in Chemical Looping Air Separation

(a) The same logic applied for increasing the operating temperature in CLC as discussed earlier can be useful inversely to decrease the temperature for CLAS system as lower operating temperature will reduce the operating cost.

For example, Pb-Mn mixed oxides can be used. Oxidation and Reduction of Pb-oxides can be achieved thermodynamically at lower temperatures (i.e. 400^{o}C) compare to Mn-oxides.

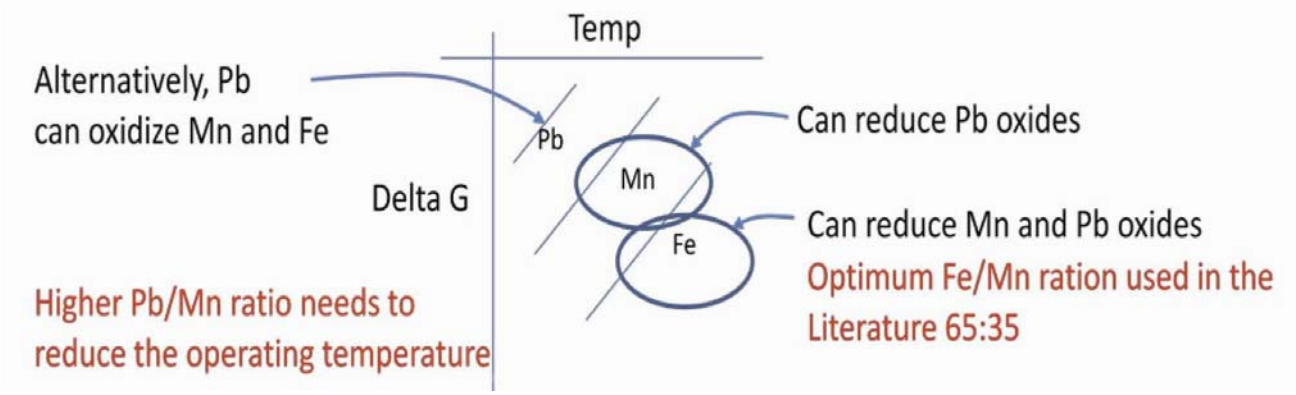

Figure 28: A typical Ellingham diagram for mixed metal oxides selection.

However, Pb-oxides are toxic and so its quantity can be reduced by adding some Mn oxides with them. The Pb-Mn oxides may work as per below redox mechanisms. Pb-oxide can be easily reduced but difficult to re-oxidize. It may need higher time to re-oxidize at low temperature. Therefore, higher Mn-Oxides loading may be desired. This combination may enhance the reduction process for the Mn-oxides quickly at medium to high temperature.

Oxidation (in air)	Reduction (with inert)
$4PbO + O_2 \rightarrow 2Pb_2O_3$	$6\ Mn_2O_3 \rightarrow 4Mn_3O_4 + O_2$
$4Mn_3O_4 + O_2 \rightarrow 6\ Mn_2O_3$	$2Pb_2O_3 + 4\ Mn_3O_4 \rightarrow 4\ PbO + 6\ Mn_2O_3$

(b) To reduce the sintering effect and reactivity loss by avoiding interactions between the active metal oxide and its support

Number of studies is available in the existing literature. Few studies will be discussed later in this report.

(c) To increase the reactivity/selectivity of the metal oxides (where the second metal oxide will catalyze the reaction or work as per Thermit process) - this way higher conversion can be achieved at marginally lower temperatures.

One study on Me-Ce and Me-Ce-Gd is done recently at Chalmers University (2011) which improved oxidation reactivity. For Cu-O, oxidation with air is slower than reduction with fuel for CLC. Therefore,

adding metal oxides lower on ED normally gave further improvement in the performance. For CLAS, oxidation with air is faster than reduction with CO_2/steam/N_2 and therefore, adding metal oxides higher on Ellingham diagram will enhance reduction reaction.

Oxygen Carrier Replacement Cost

Production cost for CLAS will increase as the operating temperature of the system increases oxygen carrier replacement costs depends on

C = 24 RMC* OPC* SCR * NOD / NCY

RMC= Raw material cost
OPC = Oxygen carrier preparation cost
SCR = Solid circulation rate
NOD = Number of days of operation
NCY = Number of cycles

Important: Solid circulation rate depends on active metal oxide loading in prepared oxygen carrier and kinetics at given temperature. Now, mixing two/three metal oxides may reduce the active metal content loading in the prepared oxygen carriers which will increase the SCR and thus oxygen carrier replacing cost. On the other hand, cyclic performance can be sometimes improved by mixing oxides. Therefore, this equation will help in optimizing the oxygen carrier preparation and selection.

Important Considerations When Mixing Metal Oxides

- preparation methods
- supports/mixed oxides (i.e. their ratio, and composition of different single/ mixed phases)
- thermodynamics of the oxidation and reduction
- sintering temperature
- crushing strength
- porosity/surface area

Supports can work as inert (increase porosity and mechanical strength) or mixed oxides (produce catalytic effect and reduce sintering).

- Oxygen carrier preparation method
    - mechanical mixing
    - freeze granulation
    - dry and wet impregnation
    - co- precipitation (good for less porous material)
    - sol-gel

- Morphology control, rigidity and curing methods
  - Drying
    - Thermal treatment,
    - Spray drying
    - Freeze drying
  - Product formation and morphology control
    - Manual grinding
    - Ball mill grinding
    - Standard granulation techniques such as fluidized bed, mixer, freeze granulation
  - Calcination and product curing

3.2 Reaction Kinetics Approach

3.2.1 Summary

We found previously that CuO, Mn_2O_3 and Co_3O_4 are the most thermodynamically suitable metal oxides for CLAS applications. In 2012, reactivity and stability of these metal oxides were further analysed in thermogravimetric analyser (TGA) as well as the packed-bed and pilot-plant reactors to make the final selection of suitable oxygen carriers. A total of six oxygen carrier samples were prepared by dry impregnation method on either SiO_2 or Al_2O_3 supports. The redox behaviours of these metal oxide samples were investigated using weight change profiles obtained at four different temperatures of 800°C, 850°C, 900°C and 950°C. Temperature programmed oxygen desorption and sorption were applied for five continuous cycles using air and nitrogen, respectively. All oxygen carriers exhibited good reactivity but CuO/Cu_2O on SiO_2 support and Co_3O_4/CoO on Al_2O_3 support were found to be most stable and effective carriers. Furthermore, oxygen transport capacity - *OTC* (%) and rate of oxygen transport - *ROT* (%min^{-1}) were calculated. It was found that Cu-oxide on SiO_2 had the highest *OTC* of 4.77% as well as the highest *ROT* of 5.1%min^{-1} and 10.9 %min^{-1} for oxygen desorption and sorption respectively at 950°C. The CuO/SiO_2 oxygen carriers also exhibited better stability over 41 continuous redox cycles test with only 10.3 % *OTC* loss in comparison to 22.3 % for Co_3O_4/Al_2O_3. Moreover, it was found that compare with other oxygen carriers the performance characteristics of CuO/SiO_2 oxygen carriers can be enhance to a greater extent by mixing them with additives (e.g. other metal oxides). On this basis CuO/SiO_2 oxygen carriers were selected as the preferred metal oxide for our future studies. This section details how we arrived at this conclusion.

3.2.2 Metal Oxide Samples

A total of six oxygen carrier samples were prepared in the laboratory using the sample preparation techniques outlined in Section 2.2.1. Commercially available Al_2O_3 and SiO_2 support materials and precursors of Mn, Co and Cu nitrates were used in sample preparation. Silica was purchased from Grace Davison, while the other binder alumina and precursory nitrates of copper trihydrate, cobalt hexahydrate and manganese tetrahydrate were obtained from Sigma Aldrich.

3.2.3 Reactivity and Stability Measurements Using TGA

The reactivity and stability of all oxygen carrier samples were examined through TGA method at different temperatures between 800°C and 950°C using a TA-Q50 instrument. Typically, around 10 mg of oxygen carrier sample were loaded into a platinum pan of 10 mm inner diameter and 1 mm height. The sample holder was then placed in the furnace via a thin platinum wire. The sample holder assembly was heated from the room temperature to desired process temperature at a heating rate of 10°C/min under normal air. Following that, the repeated desorption and sorption cycles at isothermal conditions were performed by switching the regeneration gas and air respectively. Nitrogen was used for regeneration of metal oxide particles during the reduction process for all oxygen carriers. The flow rate of the reactive purge gas was kept at 180 ml/min throughout all experiments. Also, a separate nitrogen / stream mixture with a flow rate of 40 ml/min was used as the balance gas for protecting the weighing mechanisms of the TGA instrument. The residence time for the oxygen sorption half cycle was generally kept constant at about 30 min while for the residence time for the desorption half cycle was varied depending on the test temperature; for example 60 min for 800°C, 50 min for 850°C and 30 min for both 900°C and 950°C. The complete set of results is presented below.

TGA Results for Pure Metal Oxides (no support):

Figure 29 shows cyclic weight loss variations of pure Mn, Co and Cu oxides (i.e. no support) at 800°C. The oxygen transport capacity is found to be very low for Mn_2O_3. Copper and cobalt oxide, however, may transport much larger amount of oxygen than Mn_2O_3, as indicated by their larger weight variation ratio compared to Mn_2O_3 (see Figure 29).

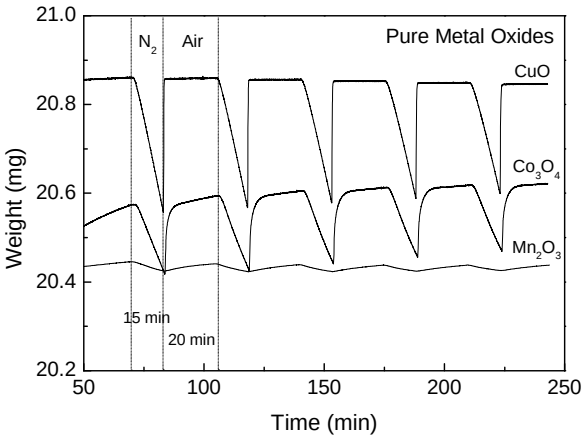

Figure 29: TGA results showing the weight variations over 5 desorption and adsorption cycles for Mn_2O_3, CuO and Co_2O_3 800°C.

The TGA results for oxygen adsorption and desorption tests (i.e. redox reactions) for pure Mn_2O_3, CuO and Co_2O_3 show that copper oxide exhibits the fastest reaction rate in both adsorption and desorption. Within 10 min, 10% of CuO weight was lost due to release of oxygen and within approximately 1 min to reduced metal could be completely re-oxidized. At a reduction rate slightly lower than that of CuO, Co_2O_3 takes about 620 s to achieve 10% conversion. However, full oxidation of CoO is attained at an

oxidation rate 5 times slower than Cu_2O. As shown in Figures 29 and 30 the thermal decomposition of manganese oxide are undoubtedly the slowest among the three metal oxides studied here for both reduction and oxidation. As can be seen from Figure 30, manganese oxide achieves only around 2% conversion at the end of desorption and requires approximately 20 min to be fully re-oxidized during oxidation phase.

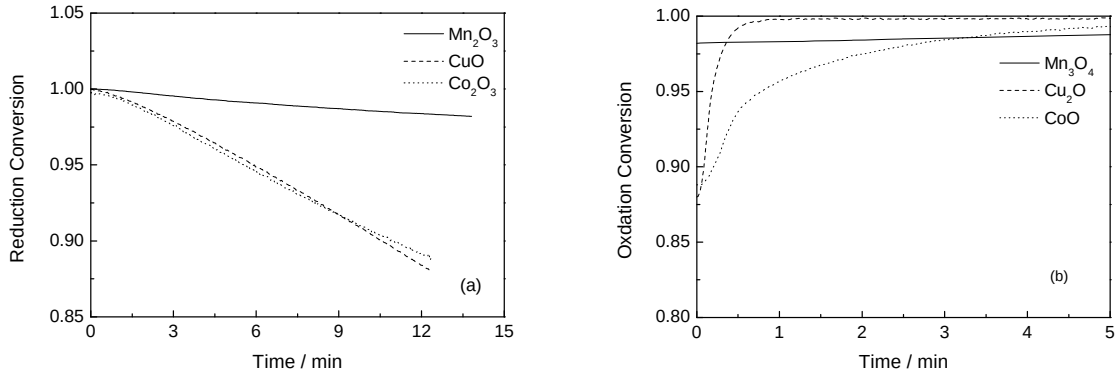

Figure 30: Conversion of different pure metal oxides at 800°C; (a) reduction and (b) oxidation.

TGA Results for Copper Oxide on Silica Support:

Figures 31 and 32 show the TGA results for cyclic weight variation of copper oxide during experiments carried out with 30%CuO/SiO_2 at 800°C and 950°C, respectively. It is obvious that the rate of reduction increases with increasing temperature. Full reduction at 950°C is achieved within roughly 2 min which is much faster than the 30 min reduction time associated with 50% reduction (i.e. 50% conversion) at 800°C (see Figure 33a). On the other hand, the rate of oxidation decreases as the temperature is increased (see Figure 33b). This is possibly because of the thermodynamic limitations of oxidation reaction. For copper the oxidation reaction is slightly endothermic and thus it will not benefit from increasing temperature. The product layer formed during oxidation may also partly contribute to the decrease of the oxidation rate.

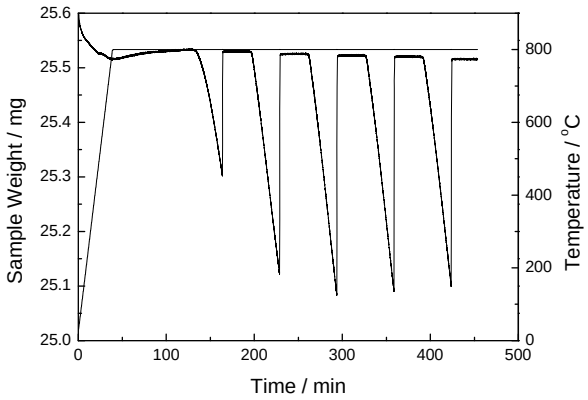

Figure 31: TGA results showing the cyclic weight variations during desorption and adsorption cycles for 30%CuO/SiO_2 at 800°C (reduction time = 90 min, oxidation time = 30 min).

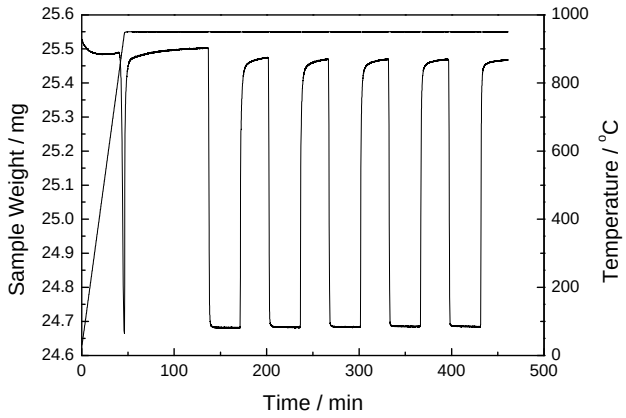

Figure 32: TGA results showing the cyclic weight variations during desorption and adsorption cycles for 30%CuO/SiO_2 at 950°C (reduction time = 30 min, oxidation time = 30 min).

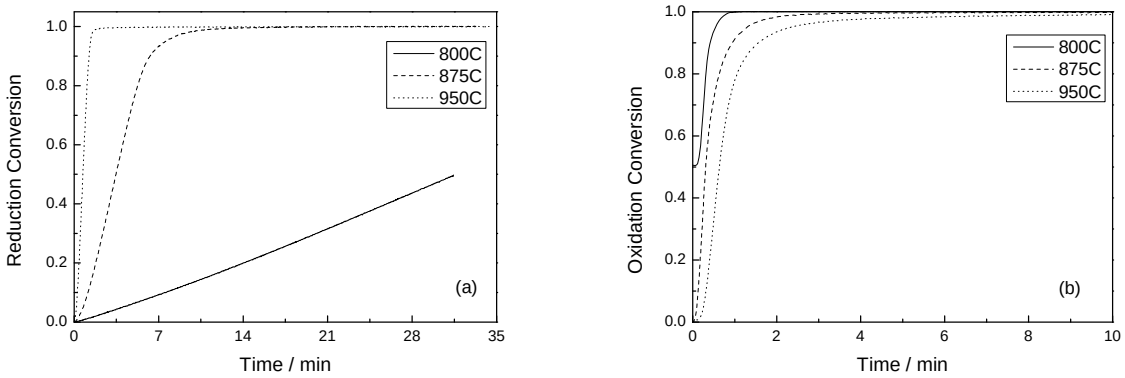

Figure 33: Conversion corresponding to the fifth cycles for 30%CuO/SiO_2 at 800°C, 875°C and 950°C; (a) reduction (b) oxidation.

TGA Results for Copper Oxide on Alumina Support (CuO/Al_2O_3-4IWP)

The cycle weight variations for copper oxide on alumina support are shown in Figures 34-36. The abbreviation "IWP" refers to the metal oxide preparation method of incipient wet impregnation. The weight variations clearly show that CuO with alumina as support is not the most suitable oxygen carrier over the range of temperatures of interest for chemical looping air separation. The formation of Aluminates during TGA tests which was also confirmed by thermodynamic calculation represents a technical challenge. By overcoming this challenge through proper modifications, it might be still possible to use CuO/Al_2O_3 in CLAS process.

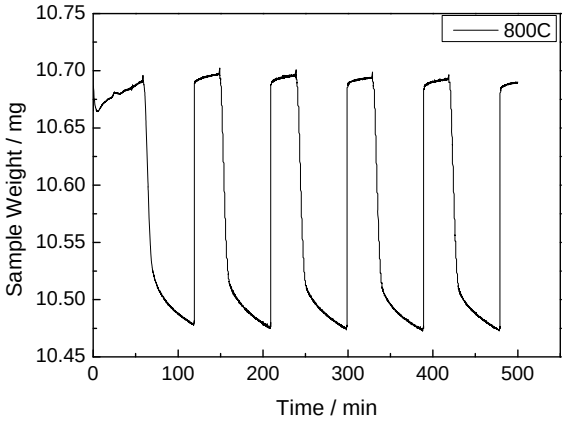

Figure 34: TGA results showing the cyclic weight variations during desorption and adsorption cycles for CuO/Al_2O_3-4IWP at 800°C (reduction time = 60 min, oxidation time = 30 min).

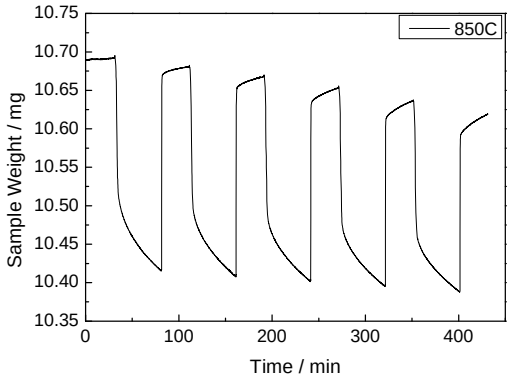

Figure 35: TGA results showing the cyclic weight variations during desorption and adsorption cycles for CuO/Al_2O_3-4IWP at 850°C (reduction time = 50 min, oxidation time = 30 min).

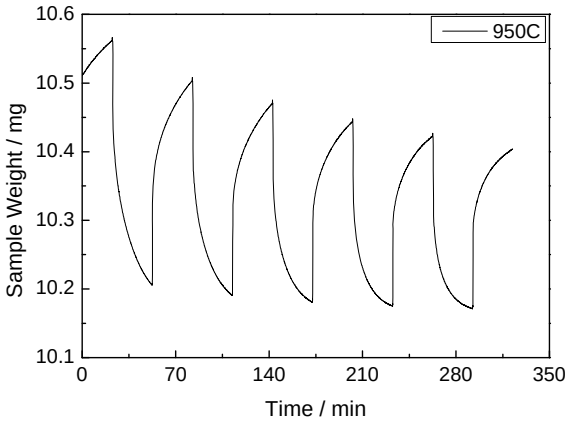

Figure 36: TGA results showing the cyclic weight variations during desorption and adsorption cycles for CuO/Al_2O_3-4IWP at 950°C (reduction time = 30 min, oxidation time = 30 min).

TGA Results for Cobalt Oxide on Alumina Support (Co_3O_4/Al_2O_3-4IWP)

Figures 37-40 show the TGA results for cobalt oxide on alumina support. The variation of reaction rate with temperature for Co_3O_4/Al_2O_3 follows a similar trend to that shown earlier for 30%-CuO/SiO_2. However, as shown in Figures 37-39 the cyclic weight variations for Co_3O_4/Al_2O_3 samples is quite small particularly during the oxidation phase due to the high equilibrium partial pressure of oxygen required for cobalt conversion. The fully reduced samples are oxidized back to Co_3O_4/Al_2O_3 achieving around 100% conversion at 900°C, but for the experiment at 950°C only a small amount of reduced particles can be oxidized. This is because the partial pressure needed for oxidation of CoO at high temperature is greater than 21% used in the experiment. According to thermodynamic calculations, equilibrium partial pressure of oxygen reaches 31.8% at 900°C, which means in the air CoO is hardly oxidized. However, the actual concentration of oxygen needed for oxidation of CoO/Al_2O_3 at 900°C may be less than 31.8%.

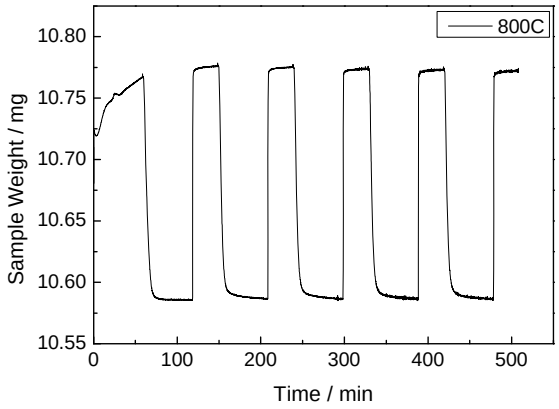

Figure 37: TGA results showing the cyclic weight variations during desorption and adsorption cycles for Co_3O_4/Al_2O_3- 4IWP at 800°C (reduction time = 60 min, oxidation time = 30 min).

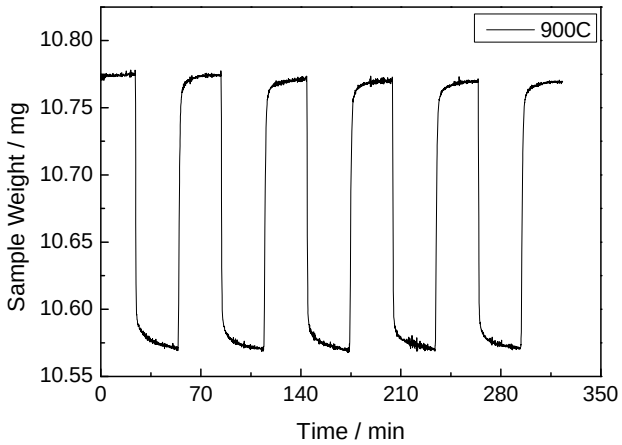

Figure 38: TGA results showing the cyclic weight variations during desorption and adsorption cycles for Co_3O_4/Al_2O_3- 4IWP at 900°C (reduction time = 30 min, oxidation time = 30 min).

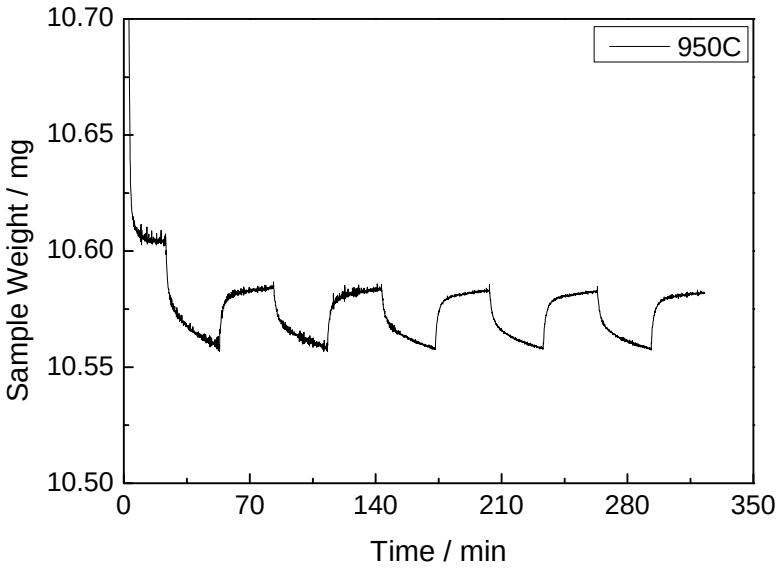

Figure 39: TGA results showing the cyclic weight variations during desorption and adsorption cycles for Co_3O_4/Al_2O_3- 4IWP at 950°C (reduction time = 30 min, oxidation time = 30 min).

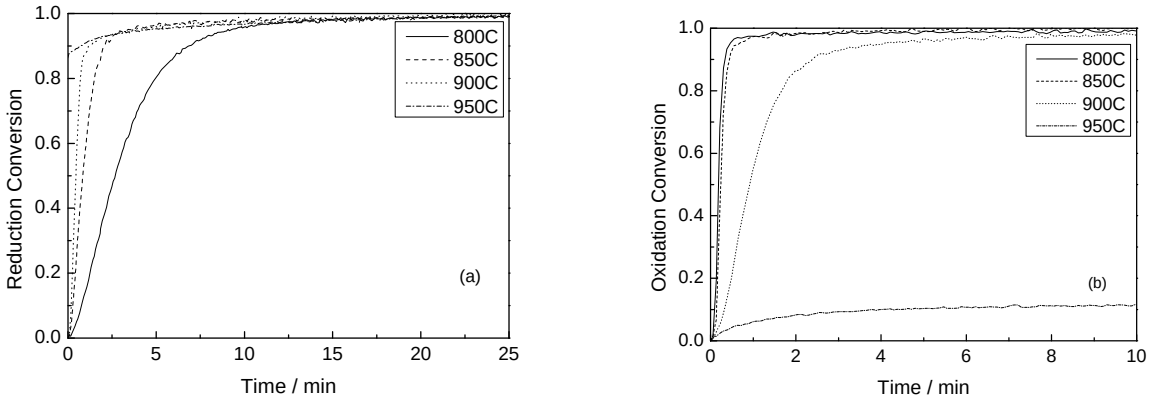

Figure 40: Conversion corresponding to the fifth cycles for Co_3O_4/Al_2O_3-4IWP at 800°C, 875°C and 950°C; (a) reduction (b) oxidation.

TGA Results for Cobalt Oxide on Silica Support (Co_3O_4/SiO_2-4IWP)

Figures 41-43 show the TGA results for cobalt oxide on silica support. As cyclic weight variation plots indicate (Figure 41 and 42), when using SiO_2 as support the oxidation of CoO at 900°C is difficult to be completed compared with those corresponding to Al_2O_3 support. Also, as can be seen from these figures, for both desorption and adsorption half cycles, cobalt oxides on Al_2O_3 support appear to be more reactive than those on SiO_2 support.

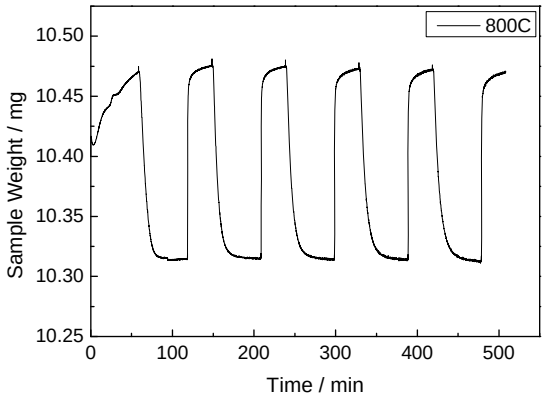

Figure 41: TGA results showing the cyclic weight variations during desorption and adsorption cycles for Co_3O_4/SiO_2-4IWP at 800°C (reduction time = 60 min, oxidation time = 30 min).

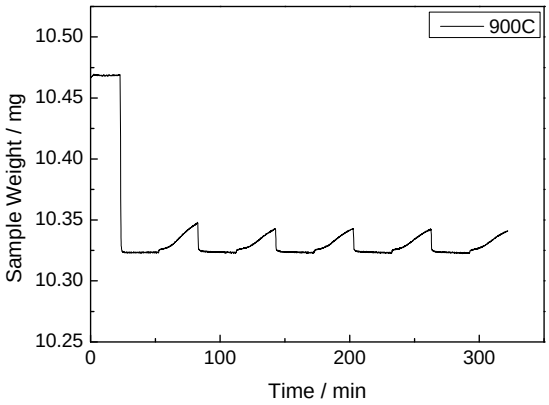

Figure 42: TGA results showing the cyclic weight variations during desorption and adsorption cycles for Co_3O_4/SiO_2-4IWP at 900°C (reduction time = 30 min, oxidation time = 30 min).

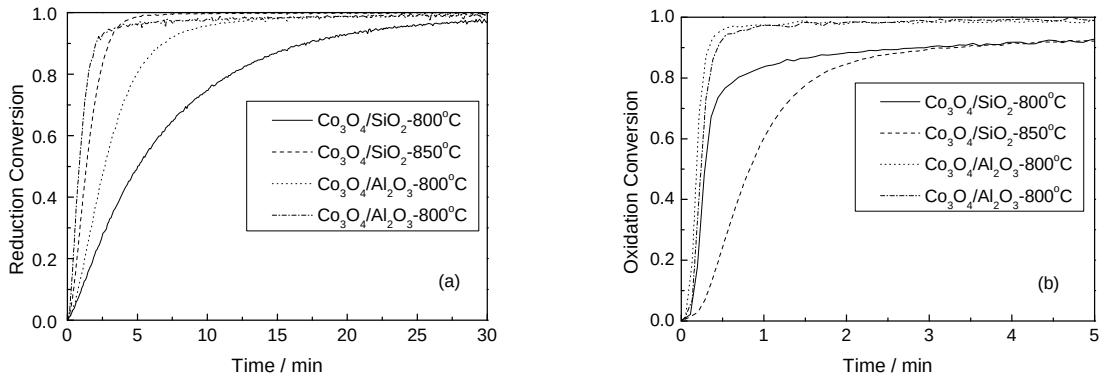

Figure 43: Comparison of conversions corresponding to the fifth cycles for Co_3O_4/Al_2O_3-4IWP and Co_3O_4/Al_2O_3-4IWP at 800°C and 850°C; (a) reduction (b) oxidation.

TGA Results for 60%CuO/SiO_2 over Prolonged Operations

Figures 44-46 show the TGA results for 60%CuO/SiO_2 over 41 redox cycle corresponding to about 1200 min of continuous operation. As Figure 44 shows, there is a gradual decline of the cyclic weight variation over prolonged operations. This is very likely the result of sinter formation due to the low melting point of copper oxide. Also as Figure 45 illustrates, initially, the oxygen transport capacity of 60%CuO/SiO_2 is about 4.7%. However, after 41redox cycles the oxygen transport capacity drops to a value of 4.25% indicating that only 0.45% is lost during the TGA redox test. Yet again this can be assigned to the sintering issue. Moreover, as can be seen from Figure 46, the rates of both oxidation and reduction decrease with increasing the number of redox cycles, especially for the initial 5 cycles. After the 10^{th} cycle, the rates are found to be relatively stable.

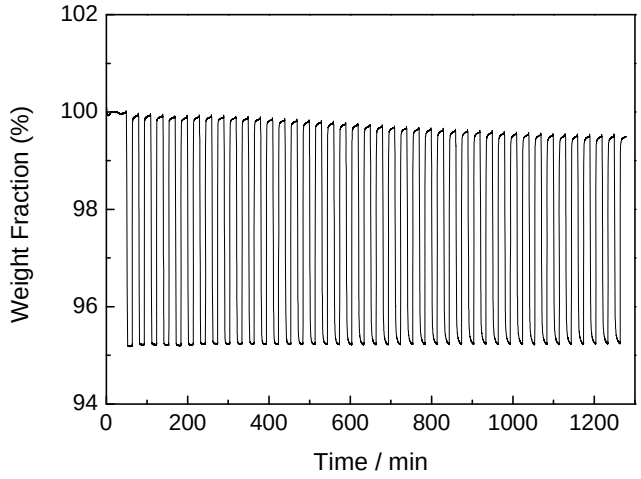

Figure 44: Variations of weight fraction over 41 continuous redox cycles for 60%CuO/SiO_2.

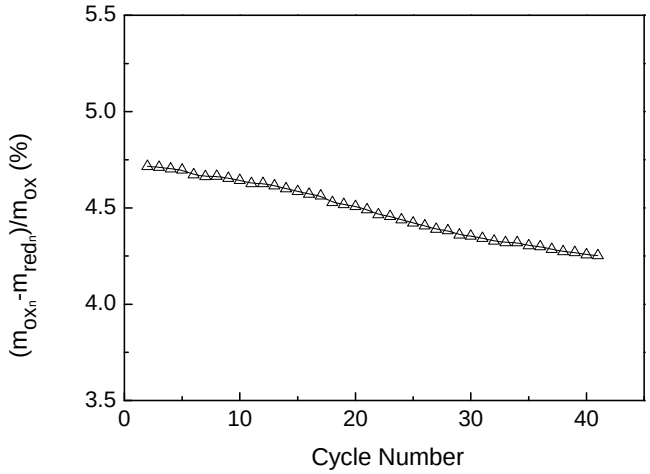

Figure 45: Fraction of maximum weight variation in every cycle versus cycle number over 41 continuous redox cycles for 60%CuO/SiO_2 (n is the cycle number).

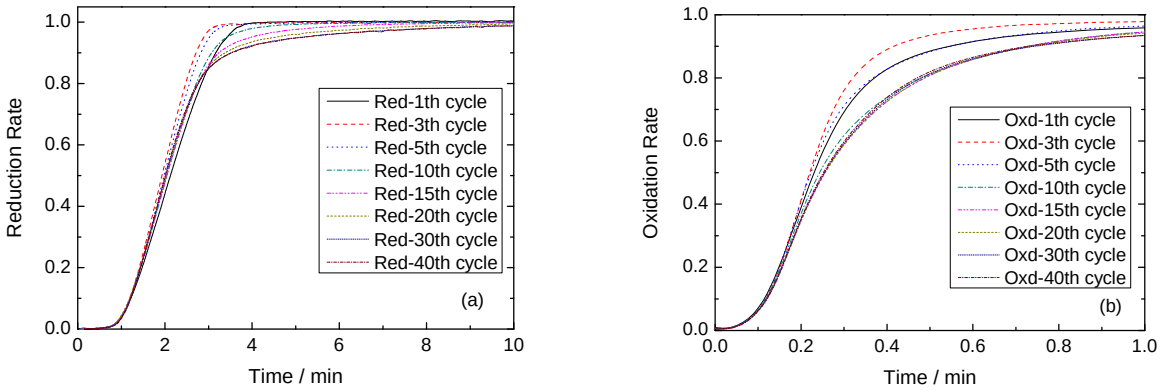

Figure 46: Effect of cycle numbers on (a) reduction (b) oxidation conversion for the experiments conducted at 900°C for 60%CuO/SiO_2.

Determination of Activation Energy for 60%CuO/SiO_2

The rate of chemical reaction for a solid material like a metal oxide can be expressed by the well-known generalized kinetic equation:

$$d\alpha/dt=kf(\alpha) \quad (3.9)$$

where

$$\alpha= (m_o-m_t)/(m_o-m_\infty) \quad (3.10)$$

Here the reaction rate constant k follows the Arrhenius type behaviour:

$$k=A \exp(-E/RT) \quad (3.11)$$

By integrating equation 10, it can be shown that:

$$g(\alpha)=\int 1/f(\alpha)d\alpha=\int kdt=kt \quad (3.12)$$

g(α) could be found from the literature according to different reaction mechanism:

D1:	α^2
D2:	$(1-\alpha)\ln((1-\alpha)+\alpha$
D3:	$[1-(1-\alpha)^{1/3}]^2$
D4:	$1-2\alpha/3-(1-\alpha)^{2/3}$
C1:	$-\ln(1-\alpha)$
C2:	$(1-\alpha)^{-1}-1$
A2:	$[-\ln(1-\alpha)]^{1/2}$

A3: $[-\ln(1-\alpha)]^{1/3}$
R2: $1-(1-\alpha)^{1/2}$
R3: $1-(1-\alpha)^{1/3}$
P1: α
P2: $\alpha^{1/2}$
P3: $\alpha^{1/3}$
P4: $\alpha^{1/4}$
Prout: $-\ln[\alpha/(1-\alpha)]$
Tompkins: $\ln[\alpha/(1-\alpha)]=k\ln t$

where

D1: one dimensional diffusion; D2: two dimensional diffusion; D3: three dimensional diffusion (Jandar function); D4: three dimensional diffusion (G-B function); An: Avrami-Erofe'ev random nucleation and subsequence growth, where n = 2,3; Rn, phase boundary reaction, where n = 1,2,3; Pn, Mampel Power Law, where n = 1,2,3; Cn: second order chemical reaction, where n=1,2

The values of R^2 for linear fitting of all models listed above are shown in Table 3. For the reduction at 875°C and 950°C, model A2 fits experimental results very well. As for the results of experiments at 800°C, P1 model may well predict. From Arrhenius plot shown in Figure 47, the free activation energy is calculated to be 272 kJ/mol.

Table 3: Values of R^2 for linear fitting of all models employed in the reduction of 30%-CuO/SiO_2 at 800°C, 875°C and 950°C

R^2	D1	D2	D3	D4	C1	C2	A2	A3	R2	R3	P1	P2	P3	P4
800°C	0.9694	0.7935	0.7652	0.7841	0.9654	0.9149	0.8812	0.3486	0.9829	0.9777	0.9943	0.7714	0.0605	0.0351
875°C	0.9211	0.889	0.8103	0.8668	0.9061	0.5935	0.9896	0.8186	0.9735	0.079	0.9454	0.6454	0.0296	0.857
950°C	0.905	0.8621	0.756	0.8317	0.8378	0.4841	0.9937	0.9212	0.958	0.9332	0.9533	0.7387	0.2384	0.531

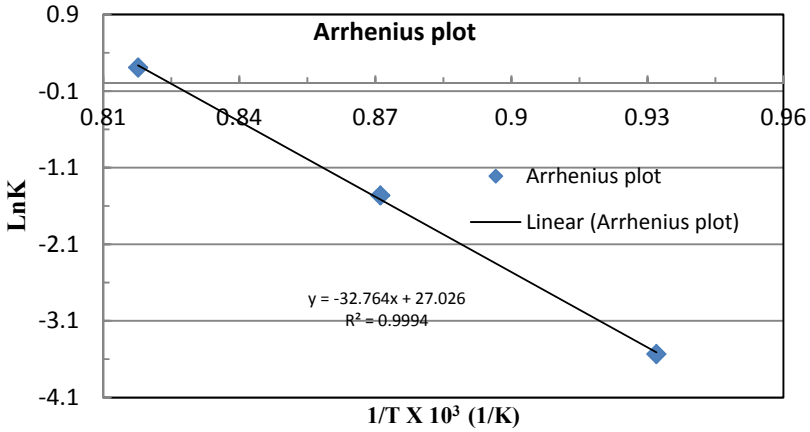

Figure 47: Arrhenius plot of 30%CuO/SiO_2 reduction (experiments: ◆ and the trendline: solid line) for the calculations of activation energy E.

3.2.4 Reactivity and Stability Measurements Using the Bench-Scale Fixed-Bed Setup

Methods and Procedures (48%CuO/SiO_2 Sample):

The weight of oxygen carrier samples used for fixed bed tests was about 2.5 g. The samples were first loaded into the middle of the quartz tube reactor with outside diameter 7 mm and 1mm wall thickness (see Figure 48). A small amount of quartz wool was then packed to the front and back ends of the sample to fix the sample in place. The tube furnace was employed to heat the samples up to desired temperature at a flow of 40 ml/min air in order to ensure all the particles completely oxidized under isothermal conditions. Once the desired temperature reached, gases were manually switched through four way valves between nitrogen during desorption and a mixture gas with 5% oxygen concentration from air and nitrogen for adsorption process. The gas flow rate for both adsorption and desorption was set to 40 ml/min. The low concentration of oxygen was chosen during adsorption for avoiding the high temperature variation caused by the exothermic oxidizing reaction under air. Moreover, this value was also kept greater than the equilibrium partial pressure. This is essential to oxidize the reduced copper oxides at 950^{o}C based on thermodynamic calculations (4.53% by HSC Chemistry Software 6.0). Experiments were carried out in temperature range between 800^{o}C and 950^{o}C. Micro gas chromatograph from Varian equipped with a column of 5A molecule sieve was used to analyse the gases from the outlet of the reactor. The summary of major findings is presented below.

Figure 48: Photograph of the quartz tube reactor loaded with a metal oxide sample.

Fixed-Bed Results for 48%CuO/ SiO_2:

Before carrying out the actual tests, a series of experiments was conducted using silica (inert support) to find out if this inert material influences the oxygen adsorption/desorption process in any shape or form. As shown in Figure 49, for this case a small quantity of oxygen with concentration around 0.21% remains in the reactor when switching the reacting gas from 5% O_2 to nitrogen at all temperatures of interest from 700^{o}C to 950^{o}C. Given the long residence times needed for complete removal of this residual oxygen and considering that the influence of such minute quantities of oxygen on the

desorption process are negligible in the actual tests the process of desorption was considered complete when an oxygen concentration of 0.21% was reached.

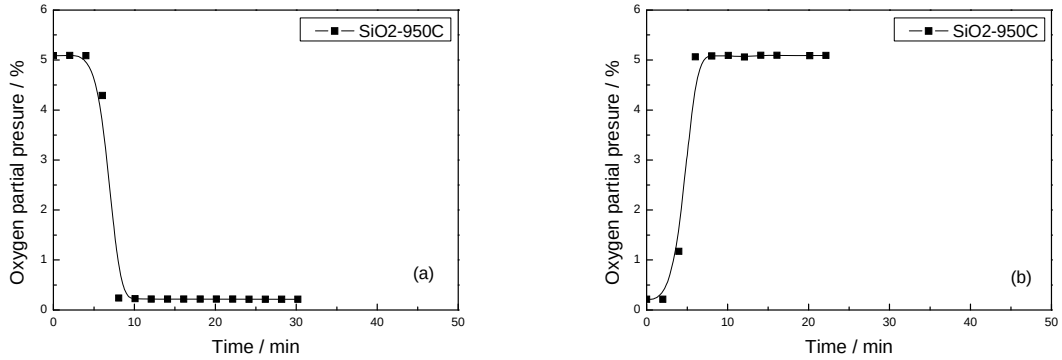

Figure 49: The variation of oxygen concentration tested with silica after (a) switching gas from mixing gas with 5% O_2 to nitrogen; and (b) from nitrogen to mixture gas.

The impact of oxygen partial pressure on adsorption and desorption processes at temperatures of 800°C, 850°C, 900°C and 950°C are shown in Figures 50 to 53, respectively. The results indicated that the desorption process at the testing temperatures between 850°C and 950°C reached the corresponding partial pressures of 0.69%, 1.72% and 4.7% which are closed to the values of 0.46%, 1.51% and 4.53% obtained from thermodynamic calculations. The weight of loading sample is large enough to release sufficient quantity of oxygen to maintain partial pressure at 850°C and 900°C over the time frame associated with the desorption process. But as can be observed from the desorption process at 950°C (Figure 53), the partial pressure remains constant for a short while at the initial stage of the oxygen desorption process and then dramatically drops to the concentration equal to 0.21%. This may attribute to the high partial pressures required for oxygen release which may not be provided by the sample loaded. For the experiments carried out at temperature of 800°C, oxygen content reach 0.32% at the end of desorption without attaining any stabilised partial pressure

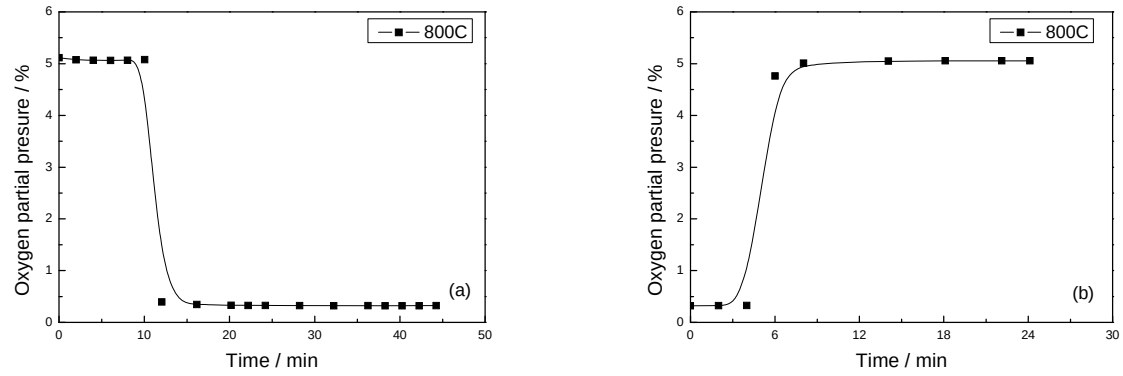

Figure 50: The variation of oxygen partial pressure during (a) desorption and (b) process at 800°C.

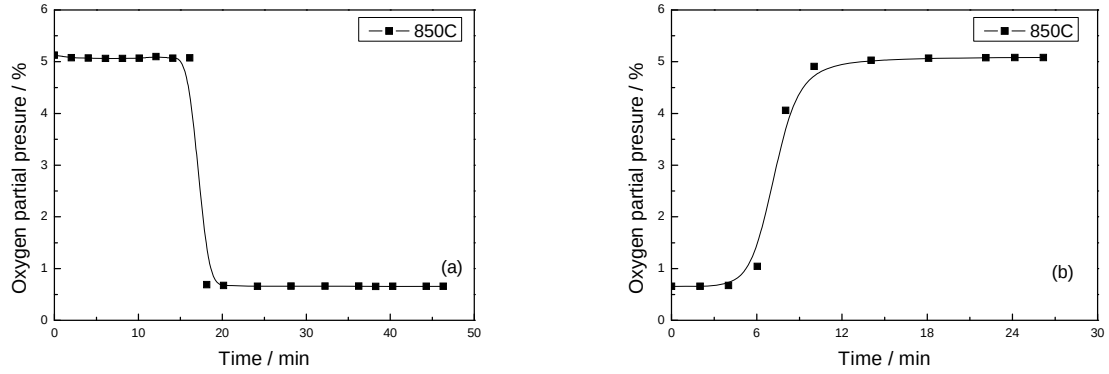

Figure 51: The variation of oxygen partial pressure during (a) desorption and (b) process at 850°C.

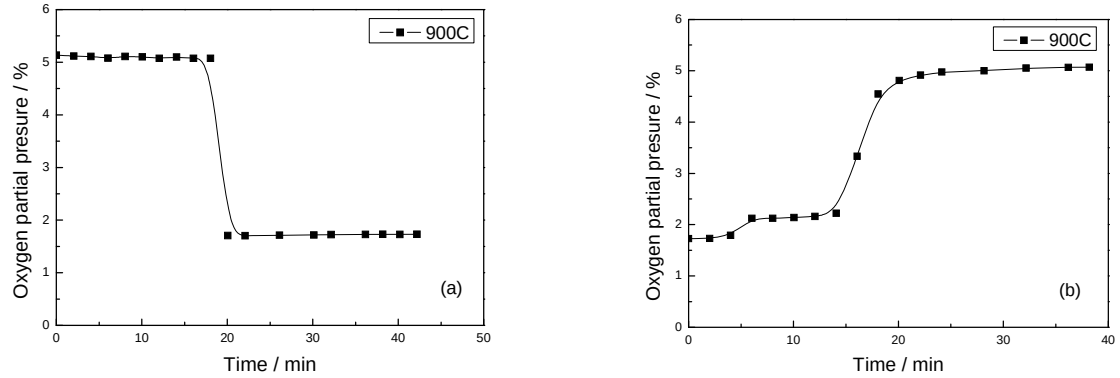

Figure 52: The variation of oxygen partial pressure during (a) desorption and (b) process at 900°C.

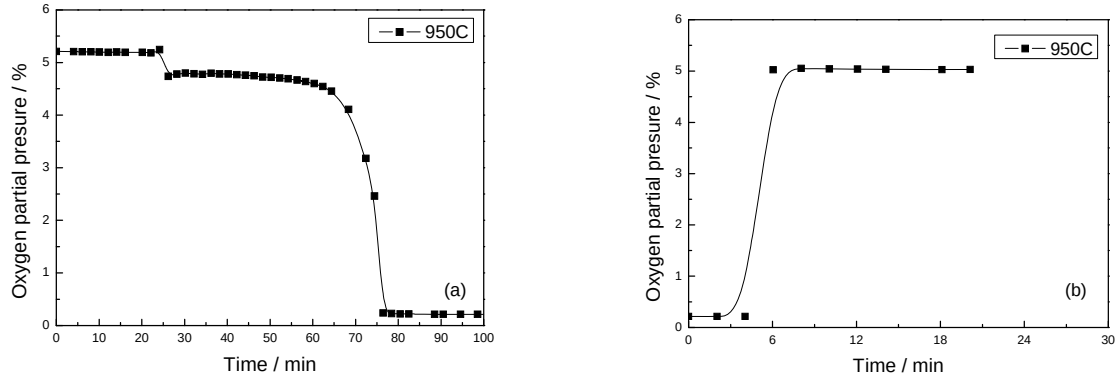

Figure 53: The variation of oxygen partial pressure during (a) desorption and (b) process at 950°C.

Characterisation of Oxygen Carrier Samples Obtained from the Fixed-Bed Setup

SiO_2 Images:

Figures 54a to 54c show the optical images of SiO_2 particles at different magnifications. It is clear from these figures that silica is a transparent material capable of transmitting the light of microscope lamp. Furthermore, while the surfaces of particles appear to be smooth, most of the particles shown in these figures have relatively sharp edges. This, in some circumstances, may lead to a poor fluidness when the particles used in fluidised bed.

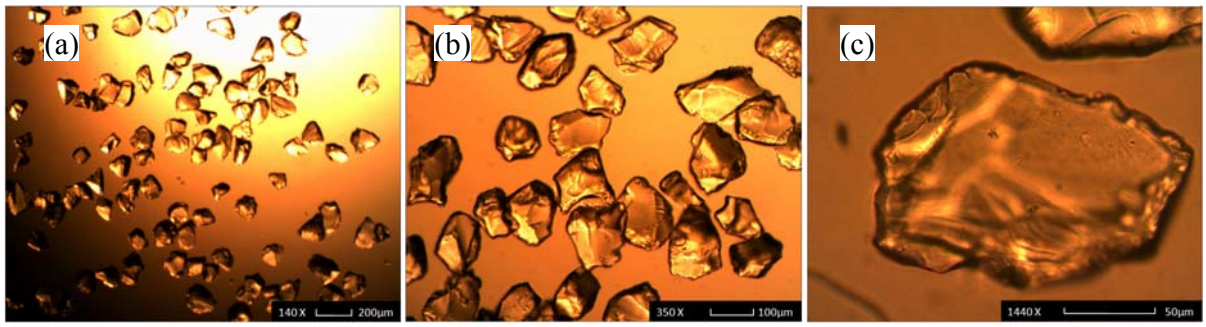

Figure 54: Images of SiO_2 particles with magnifications; (a) 140x, (b) 350x and (c) 1440x.

Al_2O_3 Images:

Figures 55a to 55c show the optical images of Al_2O_3 particles at different magnifications. Unlike silica, the particles of alumina do not transmit light emitted by the microscope and hence all alumina particles in these figures appear as black grains. As a result, the surface texture of alumina particles cannot be determined from these optical images. The edges of the majority of alumina particles appear to be round and no sharp edges are observed.

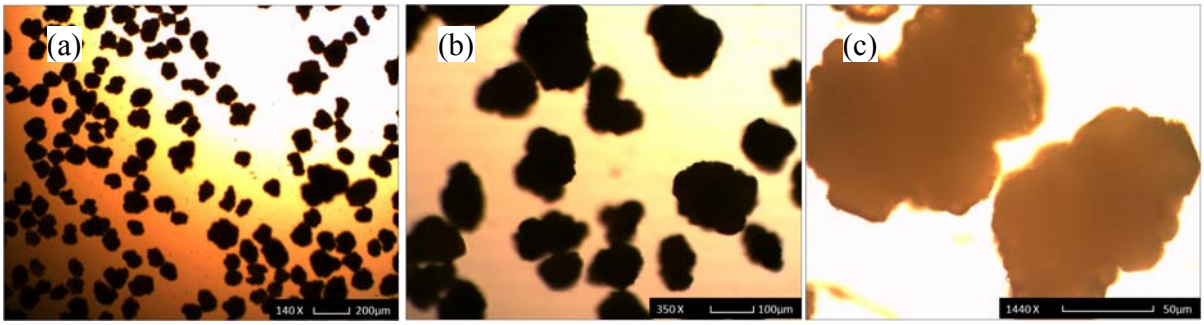

Figure 55: Images of Al_2O_3 particles with magnifications; (a) 140x, (b) 350x and (c) 1440x.

Fresh 48%-CuO-SiO_2 (by single impregnation) Images:

Figures 56a to 56c show the optical images of Fresh 48%-CuO-SiO_2 (by single impregnation) particles at different magnifications. Many fine particles which fell off the silica are observed from the Figure 56a. This may be partly caused by the smooth surface of the silica that provides a poor contact with copper oxides and may also be related to the fact that no reactions occurs between copper and silica (this has been confirmed by our thermodynamic calculations). These figures clearly show that most of the copper oxide particles deposit at the surface of silica particles but the surface coverage is not complete since part of the composite particle surface still transmits light. Increasing the number of impregnation cycles may be essential for better coverage of composite particles by metal oxides.

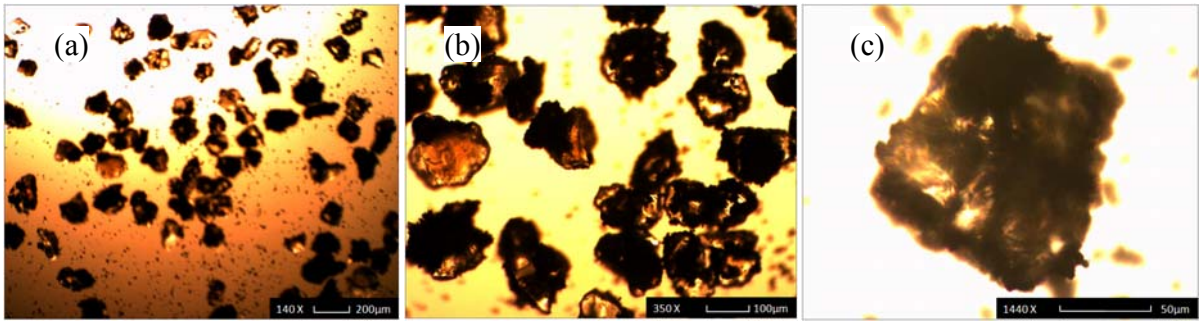

Figure 56: Images of Fresh 48%-CuO-SiO_2 (by single impregnation) particles with magnifications; (a) 140x, (b) 350x and (c) 1440x.

Fresh CuO/Al_2O_3 (4IWP) Images:

Figures 57a to 57c show the optical images of Fresh CuO-Al_2O_3 (by 4IWP cycles) particles at different magnifications. The samples were prepared by 4IWP cycles because of the low pore volume of Al_2O_3 and the fact that copper aluminates may form during the preparation process. Many fine particles fell off Al_2O_3 due to the high loading of copper oxide and the low pore volume of Al_2O_3 which may keep CuO remaining at the surface of the support rather than getting inside it. As shown in these figures compared with the surface of inert material (i.e. Al_2O_3) the coarse surfaces are obvious in CuO/Al_2O_3.

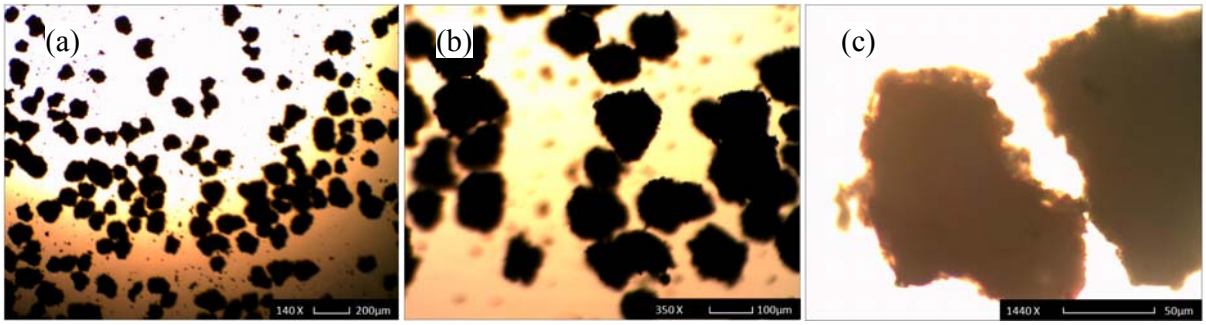

Figure 57: Images of Fresh CuO-Al_2O_3 (by 4IWP cycles) particles with magnifications; (a) 140x, (b) 350x and (c) 1440x.

Fresh Mn_2O_3-SiO_2 (4IWP) Images:

Figures 58a to 58c show the optical images of Fresh Mn_2O_3-SiO_2 (by 4IWP cycles) particles at different magnifications. Unlike the results shown earlier for CuO/SiO_2, the surface coverage of composite particles by Mn_2O_3 particles appear to be complete. This indicates that in the case of Mn by increasing the impregnation cycles better dispersion of metal oxide around inert materials can be achieved. Moreover, the surface of Mn_2O_3/SiO_2 becomes coarser compared with silica, however, to better understand the distribution of Mn_2O_3 inside silica more evidence from cross sectional SEM images are required.

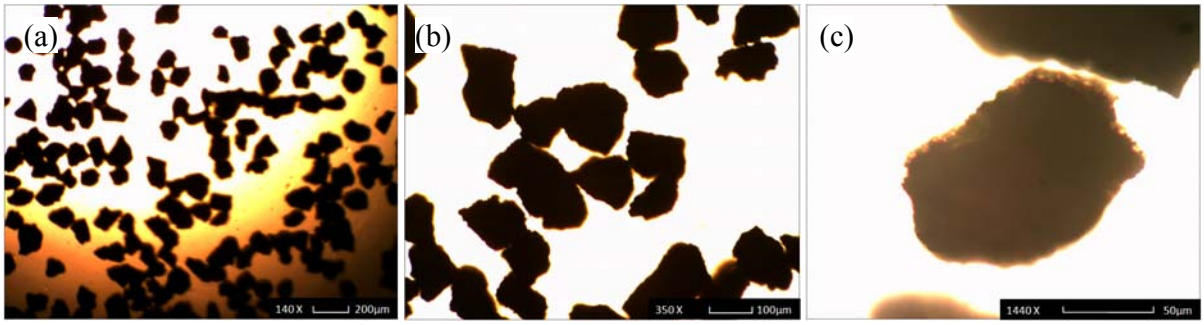

Figure 58: Images of Fresh Mn_2O_3-SiO_2 (by 4IWP cycles) particles with magnifications; (a) 140x, (b) 350x and (c) 1440x.

Fresh Mn_2O_3-Al_2O_3(4IWP) Images:

Figures 59a to 59c show the optical images of Fresh Mn_2O_3-Al_2O_3 (by 4IWP cycles) particles at different magnifications. The composite particles are very similar to inert material images shown earlier for Al_2O_3. Some particles, however, show sharp edges. There are almost no falling fine particles from manganese oxides used with either silica or alumina as support. The reasons for this are not fully understood at this stage. It may probably be caused by the well dispersion of manganese oxide.

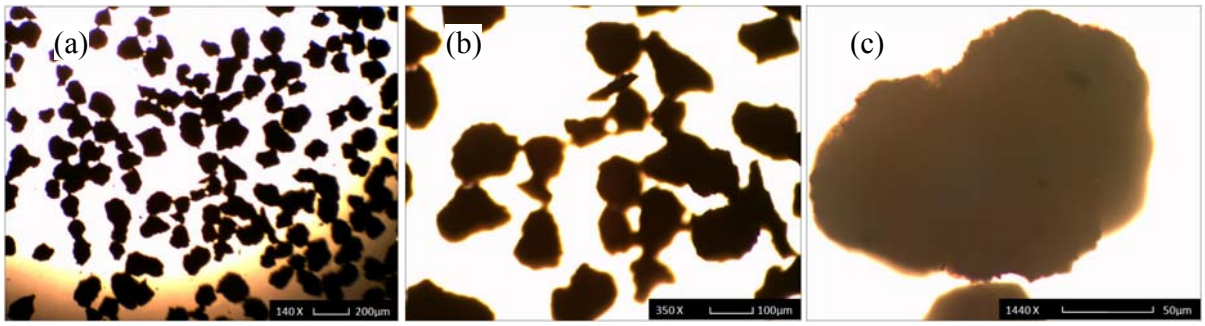

Figure 59: Images of Fresh Mn_2O_3- Al_2O_3 (by 4IWP cycles) particles with magnifications; (a) 140x, (b) 350x and (c) 1440x.

Fresh Co_3O_4-SiO_2-4IWP Images:

Figures 60a to 60c show the optical images of Fresh Co_3O_4-SiO_2 (by 4IWP cycles) particles at different magnifications. The surface of the cobalt oxide covered composite particles appears to be quite coarse and some fine particles have fallen off silica support due to high loading of cobalt oxide. The colour of particles shows a level of pinkish contrast which is possibly the evidence of cobalt silicates formation.

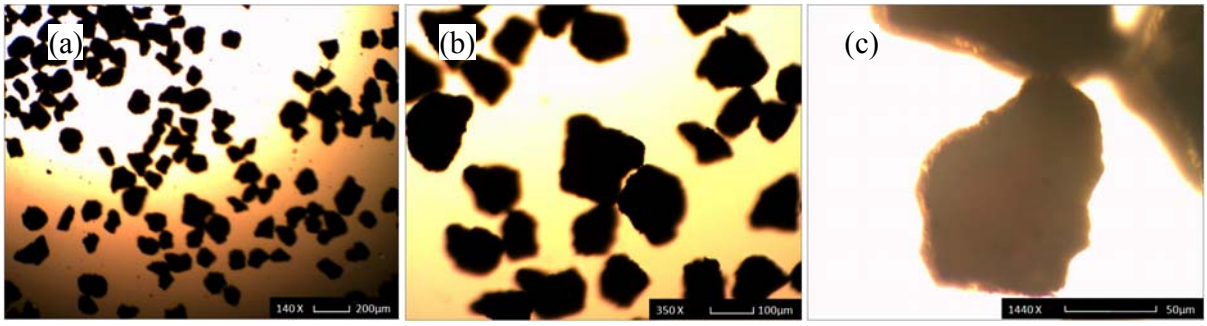

Figure 60: Images of Fresh Co_3O_4-SiO_2 (by 4IWP cycles) particles with magnifications; (a) 140x, (b) 350x and (c) 1440x.

Images of Reacted CuO Particles:

Figures 61a and 61b show the SEM images of CuO particles on silica support before and after reduction, respectively. Figure 61c also depicts the magnified view of a fully reacted (i.e. reduced) CuO particle. As can be seen from these figures, the dense surfaces of fresh CuO/SiO_2 particles become coarser after reduction.

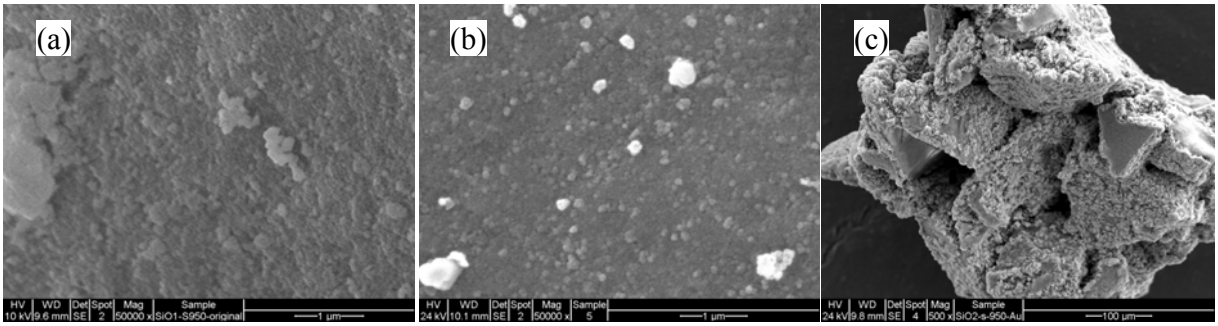

Figure 61: SEM images of (a) fresh, (b) fully reacted, (c) enlarged-view fully-reacted, CuO particles on silica support.

3.2.5 Reactivity and Stability Measurements Using the 10 kW_{th} Pilot-Plant

Methods and Procedures

The oxygen concentration profile during desorption and sorption process was determined in a dual fluidised-bed reactor (i.e. 10 kW_{th} pilot-plant). Approximately 4 g of oxygen carrier sample was charged to the reactor. The experiments were carried out under isothermal conditions at temperatures between 800 and 950^{o}C. Analogous to TGA experiments, nitrogen was used as oxygen regeneration gas during desorption half cycle. The oxygen concentration for sorption was set 5% to avoid the influence of the heat released during sorption process. Based on thermodynamic calculations, such 5% typical oxygen concentration was well above its equilibrium value and also sufficient enough to oxidize the reduced samples at 950^{o}C. The gas flow rate was set to 40 ml/min for both reduction and oxidation processes. The oxygen concentration was analysed at the outlet of the reactor using Varian Micro Chromatograph equipped with 13X molecule sieve column.

The surface morphology of metal oxide samples before and after tests was analysed using a Philip XL30 Scanning Electron Microscope (SEM) for identifying the scattering, clustering and/or agglomeration metal particles. The crystalline structures were also identified using the X-ray Diffraction (XRD) method (Appendix A details some of the SEM images and XRD patterns). Furthermore, a Shimpo forge gauge (FGE-10X) was used for determining the crushing strength of oxygen carrier particles. The density of the oxygen carriers was measured by a calibrated density bottle.

The fifth desorption-sorption cycle was used for data evaluation and quantification given the typical performance degradation in the first 4 cycles. The conversion for desorption and sorption process was calculated according to the following equations:

$$X_{red} = \frac{m_{ox} - m}{m_{ox} - m_{red}} \tag{3.13}$$

$$X_{ox} = \frac{m - m_{red}}{m_{ox} - m_{red}} \tag{3.14}$$

where, X_{red} and X_{ox} represent the conversion of oxygen desorption and sorption respectively; m_{ox} and m_{red} denote the mass corresponding to the complete oxidation and reduction state respectively, while m is the instantaneous weight during test.

Moreover, two other parameters (i.e. oxygen transport capacity, *OTC*, and rate of oxygen transport *ROT*) were introduced for quantifying and comparing the performance of various oxygen carriers. They are defined as where d*X*/d*t* is the conversion rate calculated from Equations 1 and 2:

$$OTC = \frac{m_{ox} - m_{red}}{m_{ox}} \tag{3.15}$$

$$ROT = OTC \times \frac{dX}{dt} \tag{3.16}$$

Results and Discussion:

The active metal oxide content determined from the fifth desorption-sorption cycle in TGA experiment at 850°C as well as the apparent density and crushing strength are summarized in Table 4 for all prepared oxygen carriers. Furthermore, the crystalline phase identified by X-ray diffraction (XRD) is also listed in Table 4. From the XRD analysis of the fresh oxygen carriers, it can be seen that silicate or aluminate phases were formed in the majority of these oxygen carriers except for CuO/SiO_2 and Mn_2O_3/Al_2O_3. Most of these silicates or aluminates were found to be thermodynamically stable at temperatures lower than 1000°C and as a result the oxygen transport capacity (*OTC*) determined by the active metal oxide content is reduced. Although certain candidates e.g. $CuAl_2O_4$ may possibly decompose to release oxygen, the oxygen desorption rate was found to be significantly lower than the precursory metal oxide [5-6]. Regarding the mechanical strength, all oxygen carriers shown greater values than 1 N except for CuO/Al_2O_3. Generally, minimum mechanical strength of 1 N has been reported as a primary requirement for oxygen carriers to potentially diminish attrition issues [5, 7].

Table 4: Physical characteristics of the fresh oxygen carriers

Oxygen carriers	Active metal oxide content (wt. %)	Density of particle (kg/m^3)	Crushing strength (N)	Crystalline phase
CuO/SiO_2	47.7	2900	1.2 ± 0.3	CuO, SiO_2
Mn_2O_3/SiO_2	32.4	3100	1.5 ± 0.4	Mn_2O_3, Mn_3O_4, Mn_7SiO_{12}
Co_3O_4/SiO_2	21.8	4000	2.6 ± 0.3	Co_3O_4, Co_2SiO_4
CuO/Al_2O_3	25.8	4100	0.9 ± 0.2	CuO, $CuAl_2O_4$
Mn_2O_3/Al_2O_3	21.6	3800	1.7 ± 0.5	Mn_2O_3, Mn_3O_4, Al_2O_3
Co_3O_4/Al_2O_3	26.5	4700	3.5 ± 0.5	Co_3O_4, Co_2AlO_4, Al_2O_3

As noted earlier, the thermodynamic property of Mn_2O_3/Mn_3O_4 meal oxides system can be varied while certain metal oxide is used as support [8-9, 21-22]. To evaluate whether SiO_2 or Al_2O_3 has similar effects on thermodynamic properties of Co_3O_4/CoO and Mn_2O_3/Mn_3O_4 meal oxides systems, the experiments were conducted in the temperature range 800-950°C for all prepared oxygen carriers despite the thermodynamic limitations of pure CoO and Mn_3O_4 for oxidation at high temperature under air environment. The weight change results for twenty four set of TGA runs each comprising five desorption-sorption cycles for CuO/Cu_2O, Mn_2O_3/Mn_3O_4 and Co_3O_4/CoO with Al_2O_3 and SiO_2 supports are summarised in Figures 62 and 63, respectively. Among all studied oxygen carriers, only CuO/SiO_2 shows a relatively stable performance for all tested temperatures.

Oxygen desorption-sorption cycles appear to be unstable by increasing the temperature for all oxygen carriers with Al_2O_3 support as shown in Figure 62. Although, Co_3O_4/Al_2O_3 and CuO/Al_2O_3 have shown some stability within the five cycle test at lower temperatures of 800~850°C and 800°C respectively, the rest of the experimental profiles were found to be unstable. The reason for instability of Mn_2O_3/Al_2O_3 at low temperatures, i.e. 800°C and 850°C may be the slow oxidation rate during oxygen sorption process. Additionally, agglomeration effects due to possible $MnAl_2O_4$ formation (although not observed in our XRD analysis) during desorption process mentioned in the literature cannot be ignored [10]. However, the major reason for low *OTC* at 900°C and 950°C for Mn_2O_3/Al_2O_3 could be

aluminates formations and a higher oxygen partial pressure requirement at this temperature (i.e. higher than 21% oxygen partial pressure in normal air).

Similarly, the reason for stable cyclic performance of Co_3O_4/Al_2O_3 at lower temperatures may be partly due to free Co-oxide that remains in the oxygen carriers after the formation of $Co_2Al_2O_4$ and partly due to low agglomeration tendency of the free Co-oxide. Moreover, it may also be possible that cobalt aluminates formed during sintering process were highly stable and not decomposed back to Co_3O_4 and Al_2O_3. However, oxidation is found to be limited at 900-950°C for Co-oxide and the reason is the same as Mn-oxide (i.e. requirement of higher oxygen partial pressures at temperatures of 900°C and 950°C for oxidation).

Unlike Co-oxides, thermodynamically Cu-oxides do not require high oxygen partial pressures for oxidation process even at 950°C and therefore the reason for the instability of Cu base oxides at elevated temperatures could be only the decomposition of $CuAl_2O_4$ and formation of agglomerates at these temperatures [5].

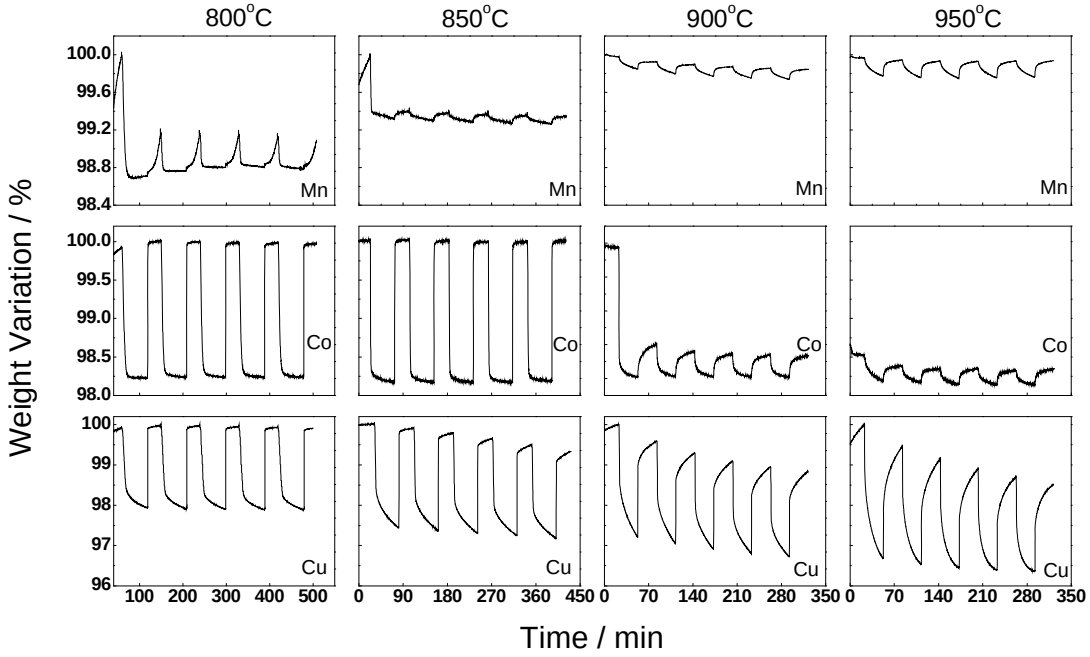

Figure 62: Weight change profiles for five continuous oxygen desorption-sorption cycles for Mn_2O_3/Al_2O_3, Co_3O_4/Al_2O_3 and CuO/Al_2O_3 at temperatures of 800, 850, 900 and 950°C.

The trend observed for the weight variations of oxygen carriers with Al_2O_3 support is also exhibited by SiO_2 as shown in Figures 8. Similar with Al_2O_3 support, silica does not show improved performance for either Mn_2O_3 or Co_3O_4 at high temperatures due to the expected thermodynamic limitations as explained earlier. The reason for the instability of Mn_2O_3/SiO_2 at low temperatures, i.e. 800°C and 850°C, may be the slow oxidation rate during oxygen sorption process as well as Mn_7SiO_{12} formation. It is worth noting that for Mn_2O_3/SiO_2 there is an increase in the extent of oxygen desorption with

increasing cycle numbers at 900°C and 950°C as illustrated in Figure 63. This could be possibly caused by the decomposition of Mn_7SiO_{12}. For Co-oxide oxygen carriers with SiO_2 as support, thermodynamic limitations similar to Mn-oxide and cobalt silicate formation at high temperatures could be the reason for unstable cyclic performance at 900~950°C. However, the stable activity at lower temperatures for Co-oxides is likely due to the existence of two distinct phases, i.e. Co_3O_4 and CoO, during desorption and sorption along with the stable cobalt silicate phase.

Among all oxygen carriers studied here, Cu-oxide with SiO_2 showed excellent stability at all temperatures. The main reason is the low agglomeration tendency of Cu-oxide on SiO_2 surface. Most importantly, unlike the majority of the investigated oxygen carriers, Cu-oxide does not react with the SiO_2 support and thus more Cu-oxide can be made available for the oxygen transport.

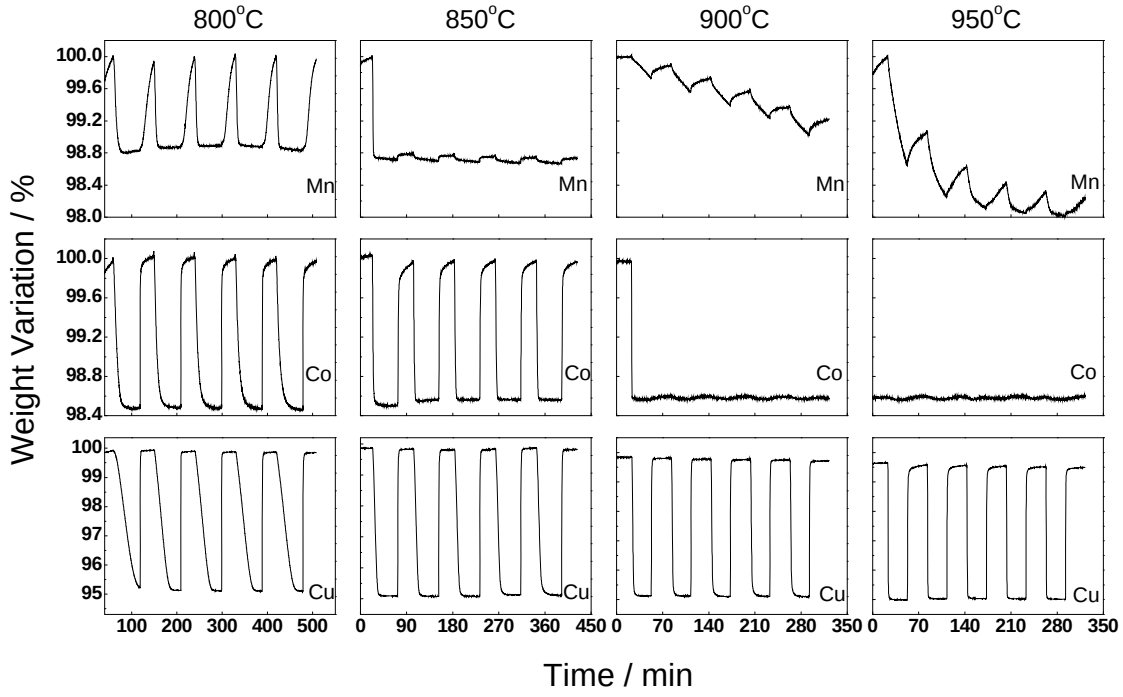

Figure 63: Weight change profiles for five continuous oxygen desorption-sorption cycles for Mn_2O_3/SiO_2, Co_3O_4/SiO_2 and CuO/SiO_2 at temperatures of 800, 850, 900 and 950°C.

The higher oxygen transport capacity (*OTC*) and higher rate of oxygen transport (*ROT*) are considered as the imperative measures for identifying suitable oxygen carriers. The *OTC* is defined as the difference in the mass fraction between the fully oxidized and reduced form of the oxygen carrier which can be used for oxygen transport. The formula for *OTC* has already been given in Equation (3.15). However, *OTC* alone is not sufficient to measure the oxygen transport capability of a given oxygen carrier as it does not account for the rate of oxygen transport. Therefore, *ROT* is often recommended in the literature for this purpose. The *ROT* combines *OTC* with conversion rate and as such provides a better explanation of the oxygen transport potential of a given metal oxide system. The formula for *ROT* has been provided in Equation (3.16).

Table 5: *OTC* and *ROT* values at 30% conversion for selected oxygen carriers

Oxygen carrier	*OTC* (%)	Temperature (°C)	*ROT* (%min^{-1})	
			Desorption	Sorption
CuO/SiO_2	4.77	800	0.125	25.2
		850	0.468	17.4
		900	1.65	14.7
		950	5.1	10.9
Mn_2O_3/SiO_2	1.1	800	0.122	0.0261
Co_3O_4/SiO_2	1.44	800	0.165	0.945
		850	0.491	0.755
Co_3O_4/Al_2O_3	1.75	800	0.334	3.47
		850	1.01	2.68

The *OTC* and *ROT* values obtained from TGA experiments for the selected oxygen carriers having relatively stable cyclic performance at corresponding temperatures have been summarised in Table 5. It should be noted that for comparison, *ROT* has been calculated for typical conversion of X = 30% for both oxygen desorption and sorption half cycles. As can be seen from Table 5, for desorption the *ROT* tends to increase with increasing temperature, however, it decreases in the case of sorption half cycle. Clearly, Mn_2O_3/SiO_2 has the lowest *ROT* at 800°C for both oxygen desorption and sorption among all studied oxygen carriers. In particular, it shows an extremely low value of *ROT* for sorption, i.e. 0.0261%min^{-1}. The reason for low *ROT* can be partially attributed to the lowest *OTC* value of 1.1%. However, lower oxygen sorption rate also can be the reason for the low *ROT* for sorption. At the same operating temperatures Co_3O_4/CoO on Al_2O_3 support exhibits higher *ROT* than Co_3O_4/CoO on SiO_2 support. From Table 5, it can be seen that the highest *OTC* is obtained for CuO/SiO_2 which suggests the lower requirement of oxygen carrier inventory for the CLAS reactors. Secondly, unlike in the case of Co_3O_4/Al_2O_3, CuO/SiO_2 can be used at higher temperatures without any thermodynamic limitations where the highest values of *ROT* can still be obtained, e.g. 5.1 and 10.9 %min^{-1} corresponding to desorption and sorption at 950°C.

The oxygen desorption and sorption conversion for Co_3O_4/Al_2O_3 and CuO/SiO_2 oxygen carriers have also been calculated and depicted in Figures 64 and 65, respectively. As shown in these figures, increasing temperature generally results in a significant increase in the conversion rate for oxygen desorption but little or no decrease in oxygen sorption. Furthermore, it can be observed that the oxygen sorption process for both Co_3O_4/Al_2O_3 and CuO/SiO_2 is comparatively faster than desorption. Due to the thermodynamic limitations as shown in Figure 64, around 10% conversion is attained for Co_3O_4/Al_2O_3 at temperatures of 900 and 950°C. No such thermodynamic limitation is observed for CuO/SiO_2 as shown in Figure 65. Interestingly, the conversion rates for oxygen desorption at temperatures of 800 and 850°C are found to be higher for Co_3O_4/Al_2O_3 (Figure 64a) compared to CuO/SiO_2 (Figure 10a). The corresponding value at X=30% was calculated as 0.19 and 0.58 min^{-1} for Co_3O_4/Al_2O_3 (see Figure 9a) which was much higher than 0.03 and 0.1 min^{-1} for CuO/SiO_2 (Figure 65a). However, CuO/SiO_2 exhibits the highest conversion rate of 2.29 min^{-1} at 950°C.

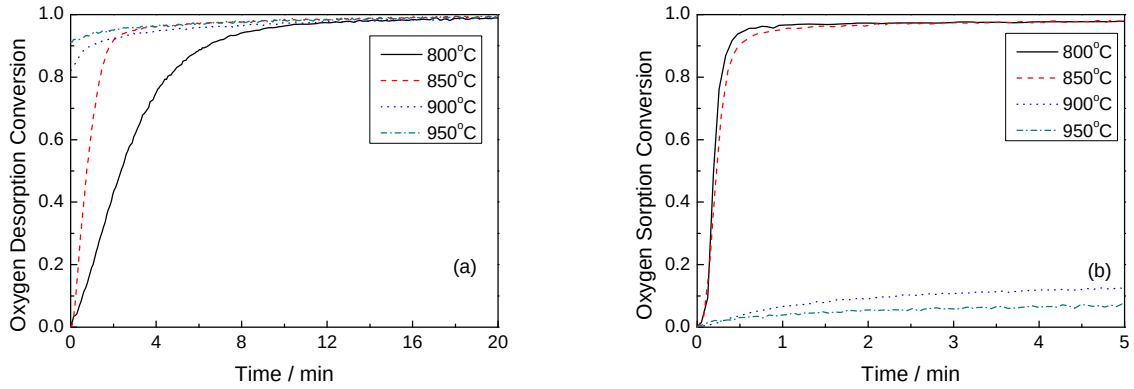

Figure 64: Conversion of Co_3O_4/Al_2O_3 during oxygen desorption (a) and sorption (b) at temperatures between 800~950°C for the fifth cycle.

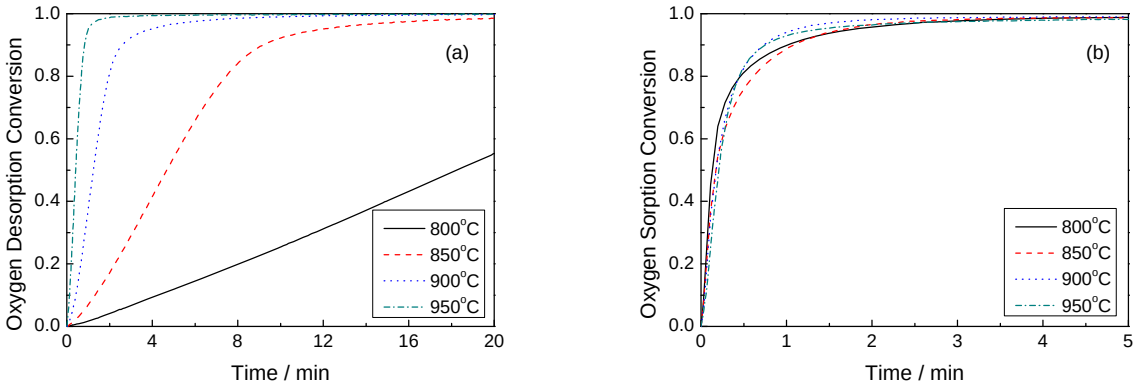

Figure 65: Conversion of CuO/SiO_2 during oxygen desorption (a) and sorption (b) at temperatures between 800~950°C for the fifth cycle.

To determine the long term stability, a continuous set of 41 oxygen desorption-sorption cycles was conducted on Co_3O_4/Al_2O_3 and CuO/SiO_2 in TGA. The weight change results for the Co_3O_4/Al_2O_3 and CuO/SiO_2 are shown in Figures 66 and 67, respectively. The temperature was set to 880°C for Co_3O_4/Al_2O_3 to avoid the thermodynamic oxidation limitations and to 900°C for CuO/SiO_2. After 41 repeated cycles both oxygen carriers showed a decline in their *OTC*. Approximately, 22.3% and 10.3% reduction in *OTC* was noted for Co_3O_4/Al_2O_3 and CuO/SiO_2, respectively. The corresponding rates of conversion for oxygen desorption / sorption half cycles are presented in Figures 68 and 69 for Co_3O_4/Al_2O_3 and CuO/SiO_2, respectively. Clearly, with increasing cycle number the oxygen desorption for both Co_3O_4/Al_2O_3 and CuO/SiO_2 does not proceed to a complete oxidation state due to the uncompleted oxygen sorption in previous cycles (e.g. see the conversion values at time = 0 min in Figures 68a and 69a. Moreover, it can also be realised from Figures 69a and 69b that the declining trend for both conversion rates in particular for sorption process is mainly observed for Co_3O_4/Al_2O_3. However, in comparison with Co_3O_4/Al_2O_3 oxygen carriers, CuO/SiO_2 shows relatively lower declining trend as shown in Figures 69a and 69b.

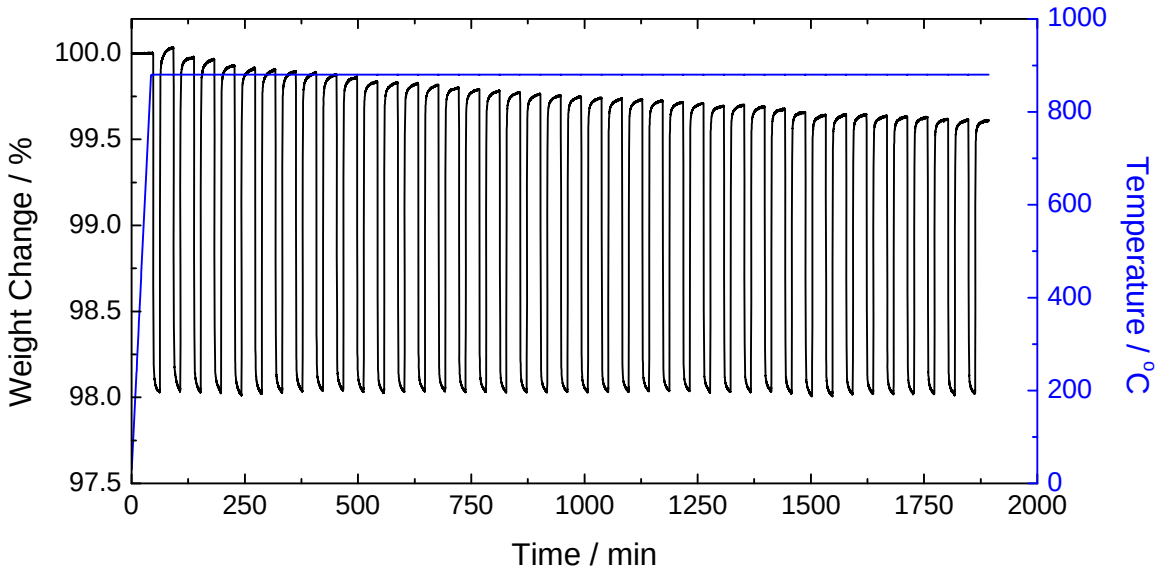

Figure 66: Weight change profile for Co_3O_4/Al_2O_3 at 880°C during continuous 41-cycle oxygen desorption-sorption tests.

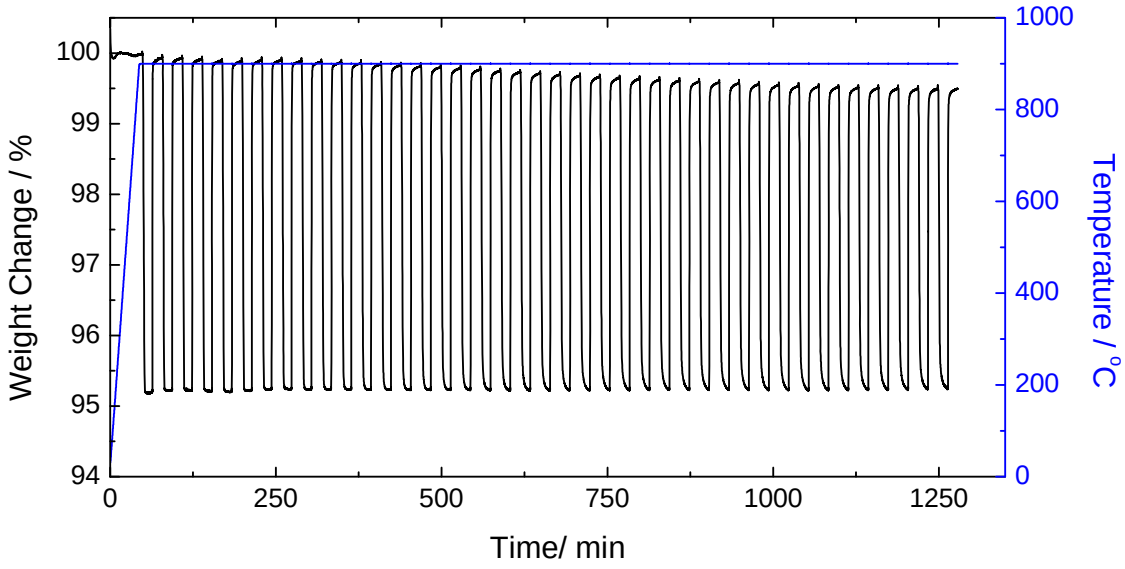

Figure 67: Weight change profile for CuO/SiO_2 at 900°C during continuous 41-cycle oxygen desorption-sorption tests.

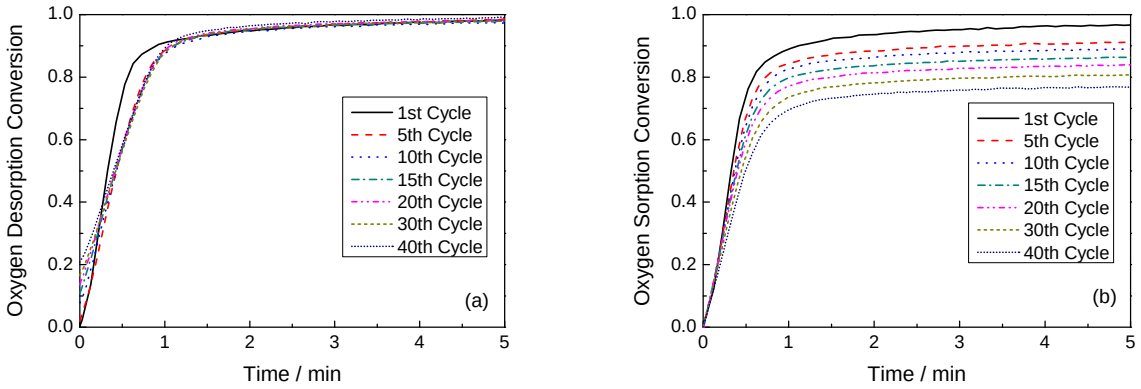

Figure 68: Cyclic conversion of Co_3O_4/Al_2O_3 at 880°C during oxygen desorption (a) and sorption (b) for continuous 41-cycle desorption-sorption tests.

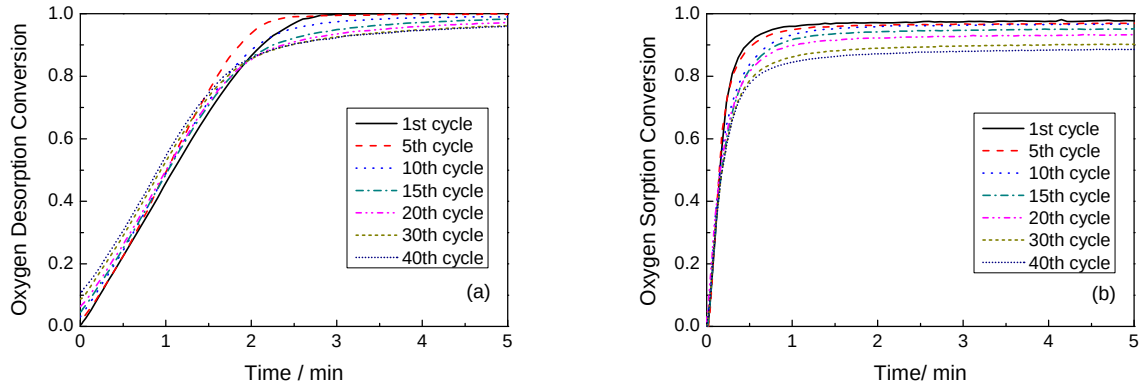

Figure 69: Cyclic conversion of CuO/SiO_2 at 900°C during oxygen desorption (a) and sorption (b) for continuous 41-cycle desorption-sorption tests.

Additionally, the surface morphology was also determined for both fresh and tested oxygen carrier samples of Co_3O_4/Al_2O_3 and CuO/SiO_2. The SEM images are given in Figure 70. It is evident from the this figure that the active metal oxides were dispersed and weakly bonded mostly around the surface of the support materials forming a very thin shell for both fresh samples of Co_3O_4/Al_2O_3 and CuO/SiO_2. However after 41 repeated cycles, the cluster of active metal oxides appears to grow more irregularly. At the surface of reacted Co_3O_4/Al_2O_3, a well dispersed micro pore structure can be observed following the cluster growth. Conversely, reacted CuO/SiO_2 exhibits more serious cluster growth. The higher cluster growth can potentially reduce the active surface area of the oxygen carrier particles and thus is possibly responsible for lowering the reactivity over the repeated cycles. Therefore, it can be suggested that the loss of *OTC* after 41 cycles for Co_3O_4/Al_2O_3 and CuO/SiO_2 is partially caused by such cluster growth mechanism. Interestingly, it is still unclear that how CuO/SiO_2 could still perform better and has lower losses in *OTC* compared to Co_3O_4/Al_2O_3 despite the fact that they were strongly affected by the cluster growth.

Co_3O_4/Al_2O_3	Fresh	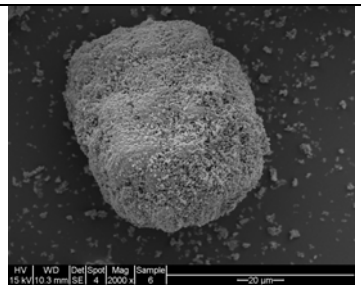	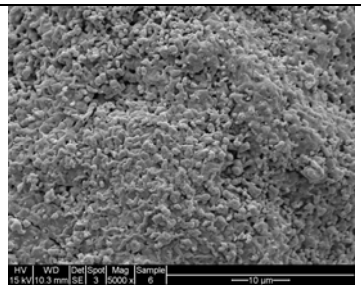
	After test (880°C)	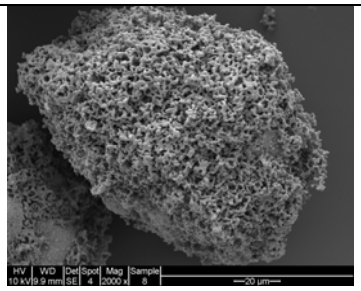	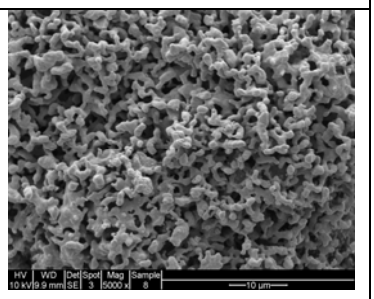
CuO/SiO_2	Fresh	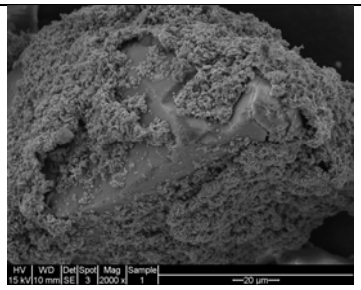	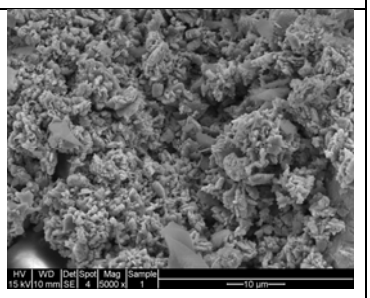
	After test (900°C)	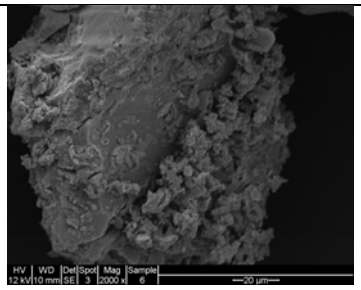	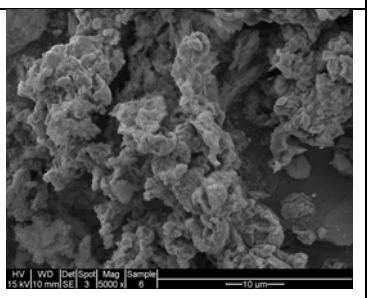
		200X	5000X

Figure 70: SEM images of fresh and used (after 41 cycles in TGA) Co_3O_4/Al_2O_3 and CuO/SiO_2 oxygen carriers.

From above analysis, CuO/SiO_2 showed better performance over Co_3O_4/Al_2O_3 in terms of lower solid inventory, higher stability and the highest rate of oxygen desorption and sorption. Therefore, the oxygen concentrations in the gas product streams during desorption and sorption processes were only measured for CuO/SiO_2 in the pilot-plant experiments. Figures 16a and 16b illustrate the oxygen profile at the outlet of pilot-plant reactor. The oxygen desorption and sorption times were set as 25 min and 30 min at temperatures of 800, 850 and 900°C. As shown in Figure 71a, oxygen desorption starts at

approximate 5 min after the gas is switched to oxygen regeneration gas, i.e. N_2. The oxygen concentration in the product stream during desorption process is found to be 0.33%, 0.63% and 1.67% corresponding to the temperatures of 800°C, 850°C and 900°C, which is in good agreement with the equilibrium concentration of 0.12%, 0.46% and 1.5% respectively for pure CuO-Cu_2O system. For oxygen sorption process, oxidation reaction is found to be completed more rapidly as oxygen concentration reached back to 5% at lower temperatures compared to higher temperatures. This is possibly due to low quantities of oxygen released during oxygen desorption process along with reasonably higher oxidation rate. The rate for oxygen sorption was found to be 2.84 $\%min^{-1}$ at 900°C which is in accordance with the rate obtained in TGA experiments, i.e. 3.08 $\%min^{-1}$.

Figure 71b shows the oxygen concentration profile for 80 min oxygen desorption and 25 min sorption at 950°C for CuO/SiO_2 oxygen carriers. The oxygen concentration profile is found to be similar with the ones corresponding to low temperatures. However, the oxygen concentration during desorption at such high temperature is observed to be close to 4.5% for around 40-50 min and then gradually drops off to zero. The oxygen concentration declining to zero could be due to the full release of the stored oxygen from oxygen carriers during desorption half cycle. The sorption at 950°C is found to be completed in 20-25 min. It can be concluded from the pilot-plant experiments at low temperatures that the oxygen concentration and release are very consistent with the equilibrium values at the higher temperatures studied before.

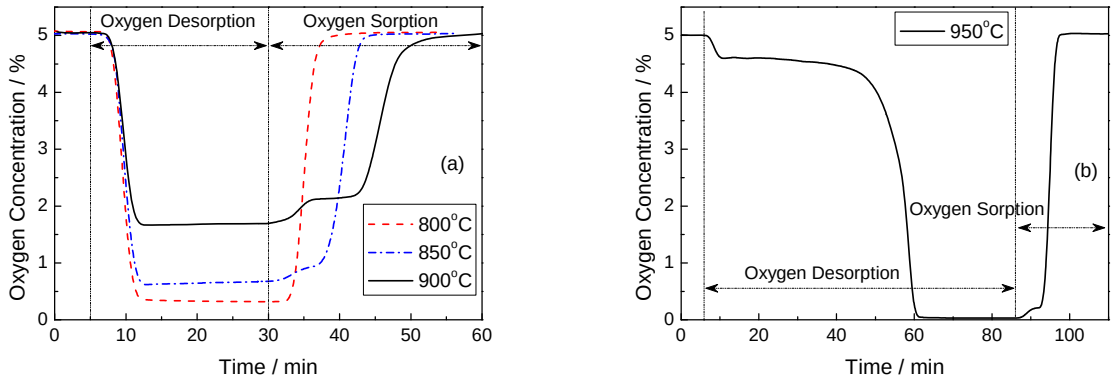

Figure 71: Oxygen concentration profile at the outlet of the pilot-plant reactor loaded with CuO/SiO_2 oxygen carriers: (a) 750°C~900°C; (b) 950°C.

3.3 ASSESSMENT AND CONCLUSIONS

3.3.1 Mono-species Metal Oxides

Chemical looping air separation (CLAS) is a relatively new process which differs from the chemical looping combustion (CLC) so that the oxygen carriers suitable for CLC may or may not be suitable for CLAS. The current study was aimed at investigating the reactivity and stability of the most thermodynamically favourable oxygen carriers i.e. Mn_2O_3/Mn_3O_4, Co_3O_4/CoO and CuO/Cu_2O with

either Al_2O_3 or SiO_2 support for CLAS. Their redox behaviours were investigated in a range of instruments / setup where temperature-programmed sorption and desorption were typically considered for five cycles using air and nitrogen respectively. The experiments were conducted at four different temperatures, i.e. 800°C, 850°C, 900°C and 950°C at which the oxygen carriers had shown good reactivity. However, CuO/Cu_2O with SiO_2 and Co_3O_4/CoO with Al_2O_3 were found to be most stable. Furthermore, Oxygen storage capacity - *OTC* (%) and Rate of oxygen transport - *ROT* (%min^{-1}) were calculated. It was found that Cu-oxide with SiO_2 has the highest *OTC* of 4.77% and *ROT* of 5.1%min^{-1} and 10.9 %min^{-1} for oxygen desorption and sorption respectively at 950°C. The CuO/SiO_2 oxygen carriers also exhibited better stability over 41 continuous cycles test with only 10.3 % *OTC* loss in comparison to 22.3 % for Co_3O_4/Al_2O_3. The cluster growth mechanism was found to be the critical cause of the loss of *OTC*. The oxygen concentration in the outlet streams for CuO/SiO_2 oxygen carriers was measured in pilot-plant experiments at different temperatures. It was observed that the oxygen concentration at the outlet of the reactor was consistent with the equilibrium values at the higher temperatures studied. Overall, CuO on SiO_2 support appears to be the most effective oxygen carrier for CLAS applications. Its performance characteristics can be further enhanced by introducing additives. This is briefly discussed in the next section.

3.3.2 Bimetallic Cu/Ni, Cu/Co, Cu/Mn and Cu/Fe Based Metal Oxides

We have also examined the redox behaviour of bimetallic Cu/Ni, Cu/Co, Cu/Mn and Cu/Fe based metal oxides over prolonged operations. Secondary metal oxides, e.g. NiO, Co_3O_4, Mn_2O_3, MgO and Fe_2O_3 were added into CuO/SiO_2 through co-impregnation method (Figure 72). These bimetallic oxide samples were generally prepared to lower the sintering tendency of CuO-based metal oxide oxygen carriers for chemical looping air separation applications. The bimetallic samples were subjected to 41 cycles of sorption / desorption at a temperature of 900°C. The results have been summarised in Appendix B. The key findings are:

- The continuous 41 sorption-desorption cycles test results corresponding to CuO/SiO_2 oxygen carriers clearly show the loss of oxygen transport capacity with increasing cycle numbers.
- Interestingly, both desorption and sorption conversion rate increased after adding the secondary metal oxides into the primary oxide CuO/SiO_2. However, the increase of desorption rate is found to be more significant than oxygen sorption rate.
- The weight content of the added metal oxides is a key factor in determining the reactivity of mixed metal oxides oxygen carriers.
- The addition of 30 wt% and 50 wt% of MgO in CuO/SiO_2, i.e. oxygen carriers of CuO-MgO-7-3/SiO_2 and CuO-MgO-1-1/SiO_2 largely eliminated the loss of performance (i.e. the oxygen transport capacity); potentially allowing the metal oxide samples to be used perpetually.
- CuO-MgO-1-1/SiO_2 exhibits faster oxygen desorption rate.
- Increasing content of Co_3O_4, however, leads to a decline of reaction rate, in particular in oxygen desorption process.
- In the case of adding NiO, no obvious change in reaction rate was observed with varying NiO content.

- In addition to the percentage content of the secondary metal oxides, the metal oxides type was also found to dramatically influence the reactivity of bimetallic oxygen carriers
- Higher reactivity was obtained through mixing CuO/SiO_2 with Fe_2O_3, MgO and NiO than with Co_3O_4 and Mn_2O_3.
- In terms of the oxygen transport capacity (OTC) which is probably the most important factor underpinning the cost effective operation of a CLAS process, mixtures of Cu/Co and Cu/Fe provide the best combination of cyclic stability and high OTC (see Figure 73).

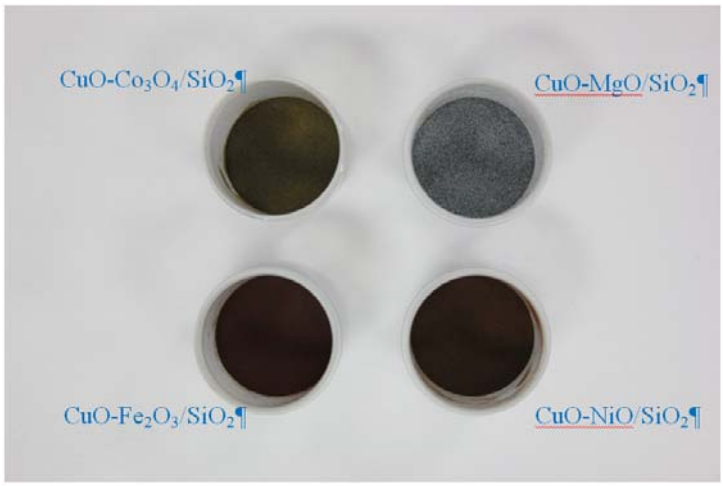

Figure 72: Bimetallic CuO-based metal oxide oxygen carriers on silica support.

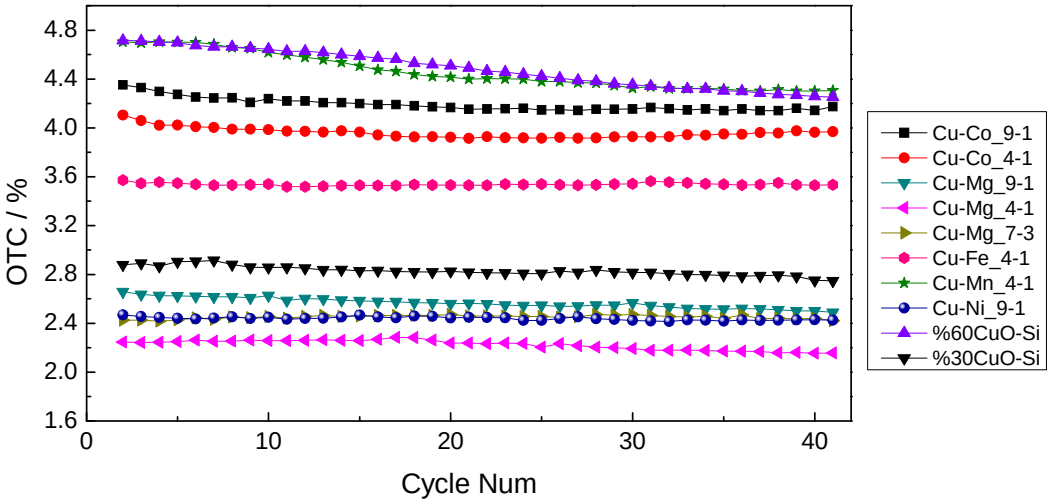

Figure 73: Oxygen transport capacity (OTC) change during 41 continuous oxygen desorption-sorption cycles in TGA at 900°C for mixed metal oxides oxygen carriers.

Chapter 4

PARTICLE TRANSPORT AND HYDRODYNAMICS

4.1 HYDRODYNAMIC EXPERIMENTS (BENCH-SCALE)

4.1.1 Fluidisation Velocities

One of the key parameters noticed when running experiments using this rig was the differences in the required gas flow rates to reach the desired mass fluxes for different combinations of particles. This was identified when the air reactor flow rate had to be altered for each set of particles to gain the desired mass fluxes in the system. Figure 74 shows the mass flux vs. fluid velocity for the different sets of particles used in this experiment.

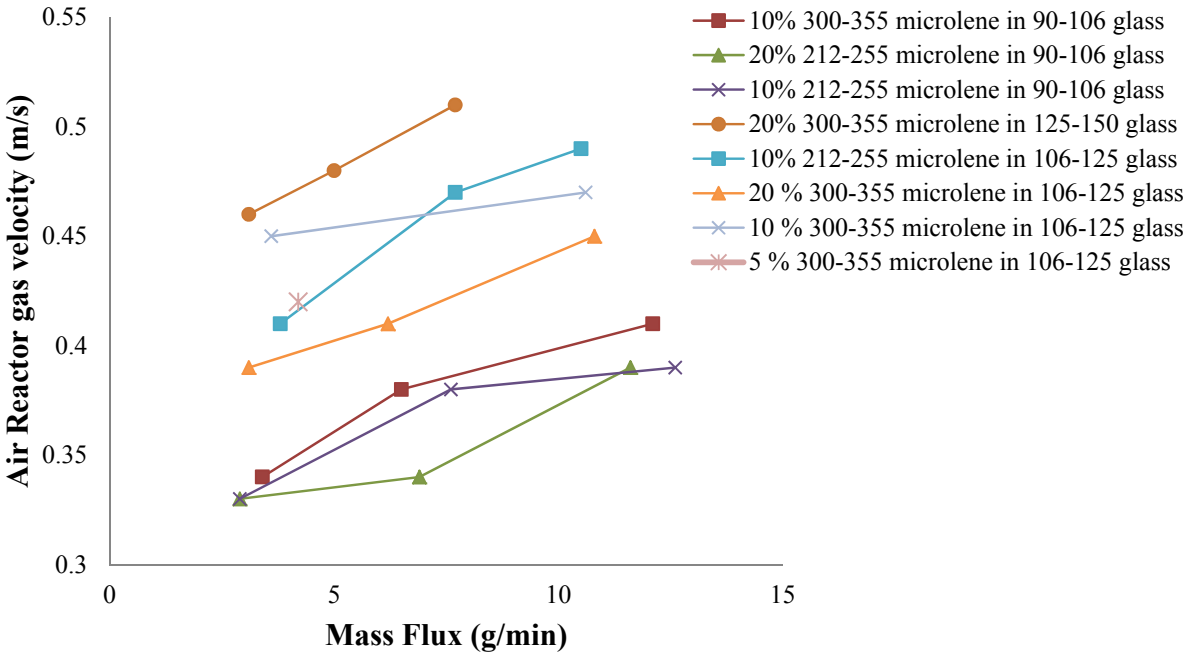

Figure 74: Air reactor gas velocity vs. mass flux.

It can be seen in Figure 74 that as the particle size gets larger the gas velocity required to reach the required mass fluxes increases. It can also be seen that as the concentration of Microlene in the particle

mixture increases the required gas velocity to reach required flow-rates decreases. It can be seen that glass beads are primarily responsible for the difference in required gas velocities. As glass beads make up the majority of the particle bed (minimum 80 %), the majority of the influence on the required flow-rate comes from the glass beads. It can be seen that as the concentration of the glass beads in the mixture increases the overall density of the bed increases and hence the higher the required mass velocity is to reach the same flow-rate. These trends indicate that generally, as the particles in the bed increase, the higher the required gas velocity is if the required mass fluxes of the system are to be reached. This trend also indicates that if the concentration of lower density particles in the bed increases the required gas velocity to obtain the correct mass fluxes in the system are lowered due to overall bed density decrease.

4.1.2 Segregation

Particle Segregation

The terminal settling velocities of the different particles used in this experiment are detailed in Table 6. These values will be used in the examination of the segregation of particles.

Table 6: Settling velocities of the particles used in this experiment

Material	Size Range	Settling Velocity (m/s)
Microlene	212-255 µm	2.28
Microlene	300-355 µm	2.72
Glass Beads	90-106 µm	2.42
Glass Beads	106-125 µm	2.61
Glass Beads	125-150 µm	2.85

The settling velocity values were calculated using the relevant particle transport equations. It was found that under all experimental conditions in this project the Reynolds number was between 1000 and 350,000. It must also be noticed that all velocities published in Table 6 are single particle velocities, for hindered velocities must be used to get a corrected value of settling velocity as a function of void fraction. For all particle mixtures examined in this experiment particle segregation of some kind was found.

Figure 75 shows an example of particle segregation. From Figure 75, it can be seen that there is segregation occurring in the rig. Examining Figure 75, it is seen that after the experiment has run the concentrations of microlene in the various sections of the rig have deviated from their initial concentrations (indicated by the dashed line). Due to the segregation of particles in all experiments, patterns in the segregation of particles were studied to identify common trends. Microlene particles were concentrated upon as the particle being segregated. Glass segregation could also be studied by subtracting the Microlene segregation from 1. Studying the microlene segregation however allowed the degrees of segregation to be more easily identified due to the lower values of concentration. Due to sample size and the significance to the rig the two key areas to take note of are the air and fuel reactors

as these are the two sections in which the reactions would be taking place in for a real system. The loop seal concentrations are still important however but not to the extent of the air and fuel reactors. One of the first questions that arose after the data was collated into excel was to find the primary cause of the segregation of one type of particle or another. This was further investigated to find the major contributors to particle segregation.

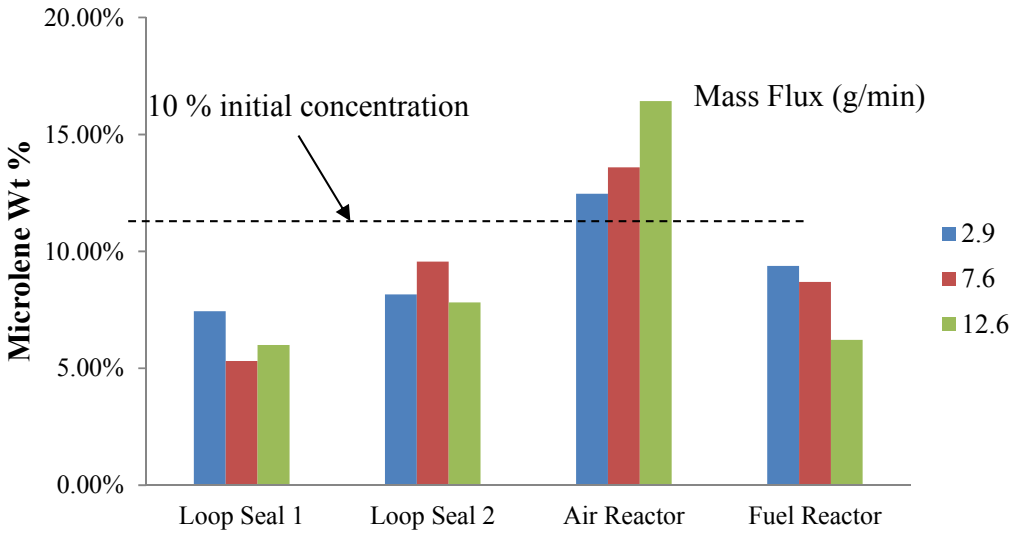

Figure 75: Particle concentration for components of the rig for an initial mixture of 10 % 212-255 µm microlene in 90-106 µm glass beads.

The first thing that was investigated was the effect of the difference in particle settling velocity upon segregation as suggested by Rowe et al. (1975). As outlined previously Rowe et al. (1975) suggested that if the fluid velocity in the bed is in between the settling velocities of the two particles in the bed segregation will occur. The average bed void fraction across all the experiments was found to be around 0.45. Using this value and the values listed in Table 6 the actual settling velocity of each particle in the bed can be estimated. The results of these calculations can be seen in Table 7.

Table 7: Actual settling velocities of the particles in the bed

Material	Size Range	Settling Velocity (m/s)
Microlene	212-255 µm	0.31
Microlene	300-355 µm	0.37
Glass Beads	90-106 µm	0.33
Glass Beads	106-125 µm	0.36
Glass Beads	125-150 µm	0.39

The minimum velocities of gases in the air reactor used in this experiment was around 0.35 m/s and was above 0.40 m/s for the majority of the experiments. It can hence be seen that segregation is caused by fluid velocity in the air reactor. As it can be seen that segregation is not due to the gas velocity in the air reactor fluidised bed, other reasons for segregation of particles in the system must be investigated.

The section after the air reactor is the riser. This section thins from an internal diameter of 80 mm to an internal diameter of 40 mm. By reducing the cross sectional area of the column and keeping the flow rate constant the gas velocity will increase. With the size difference in the two sections in this rig the gas velocity will increase by around 3.6 times greater than in the air reactor.

At the base of the riser the solids concentration is estimated to be around 10-15% hence the void fraction in this section is around 0.85-0.9. The altered fluid velocities of the particles will be impacted upon by the change in void fraction and hance the gas velocity in the riser may lie between the particles and cause one particle to settle out and the other to be carried upward through the riser. This will be shown as an example further into the results section as a reason for segregation. A good example of this phenomena being the primary cause of the segregation of particles in the system is shown in Figure 76.

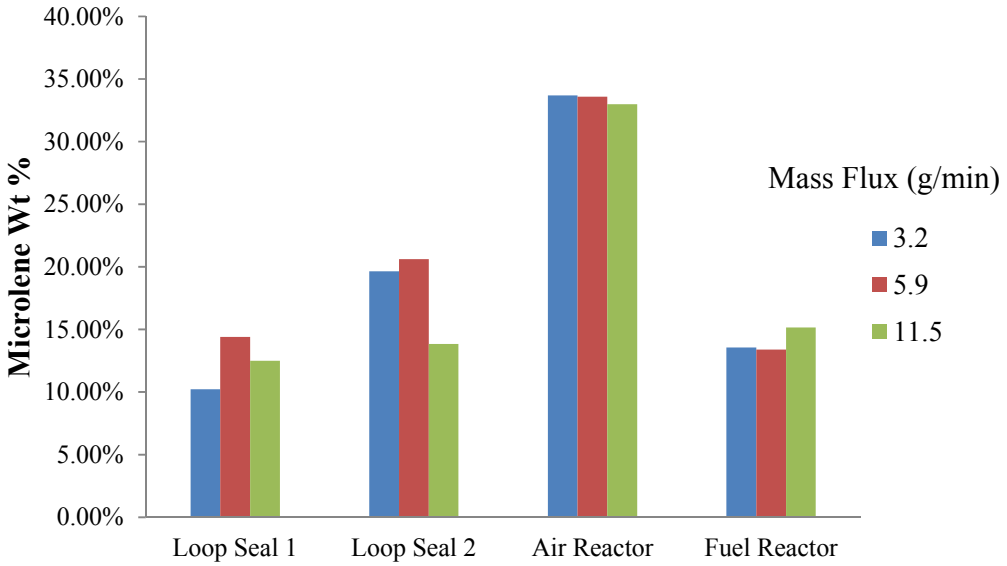

Figure 76: Particle concentration for components of the rig for an initial mixture of 20% 300-355 µm microlene in 90-106 µm glass beads.

For this case it can be seen in Figure 76 that the degrees of segregation in the fuel and air reactors remain constant at all mass fluxes tested hence size and density segregation is not occurring in the air reactor bed itself. This indicates that the segregation is not affected by gas velocity. If the segregation in the system cannot be identified to be due to segregation in the air reactor fluidised bed the segregation has to be put down to the velocity of the gas in the riser. If the gas velocity in the riser is lower than the settling velocity of one of the particles but not the other one particle will settle out and the other will be carried on upwards.

In the case of the particles the riser fluid velocity for the three mass fluxes is 1.38 m/s, 1.52 m/s and 1.65 m/s. If the solids concentration is estimated at between 15 and 20 % at the base of the riser the actual terminal velocities of the particles can be calculated. For this case the terminal settling velocity of the microlene particles is between 1.56 and 1.81 m/s whilst the glass beads have a settling velocity of 1.38.1.60 m/s. It can be seen in this case that the source of segregation is due to the velocity of the gas in the riser being in between the settling velocities of the glass and microlene.

A trend arose in the data analysis and it was found that for all except one combination of particles that the segregation favoured microlene build up in the air reactor. Two examples of microlene build up in the air reactor are shown in Figures 76 and 77.

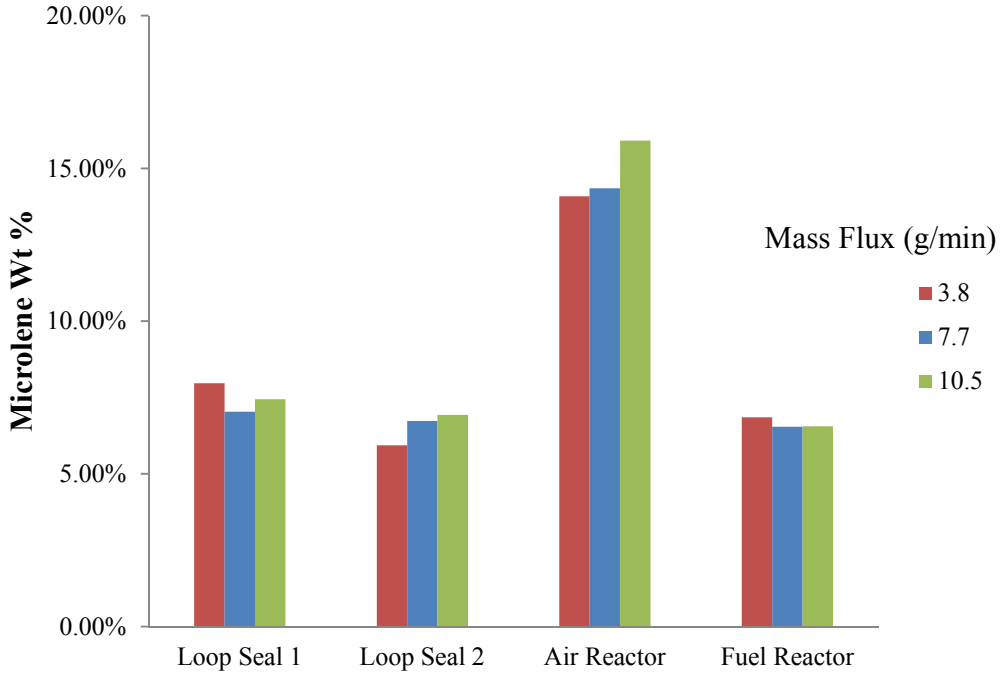

Figure 77: Particle concentration for components of the rig for an initial mixture of 10 % 212-255 µm microlene in 106-125 µm glass beads.

As can be seen from Figures 77 and 78 particle segregation shows a build-up of microlene in the air reactor with the final concentration being higher in the air reactor than initially and lower in the loop seals and the fuel reactors. The only combination of particles where the segregation of microlene favoured the fuel reactor was with the largest and hence heaviest glass particles were coupled with the smallest and hence lightest microlene particles. This segregation is shown in Figure 79. It must also be noted that the degree of segregation does not change with the increase in mass flux indicating that this segregation is most likely due to the difference in density of the particles with little influence from particles size.

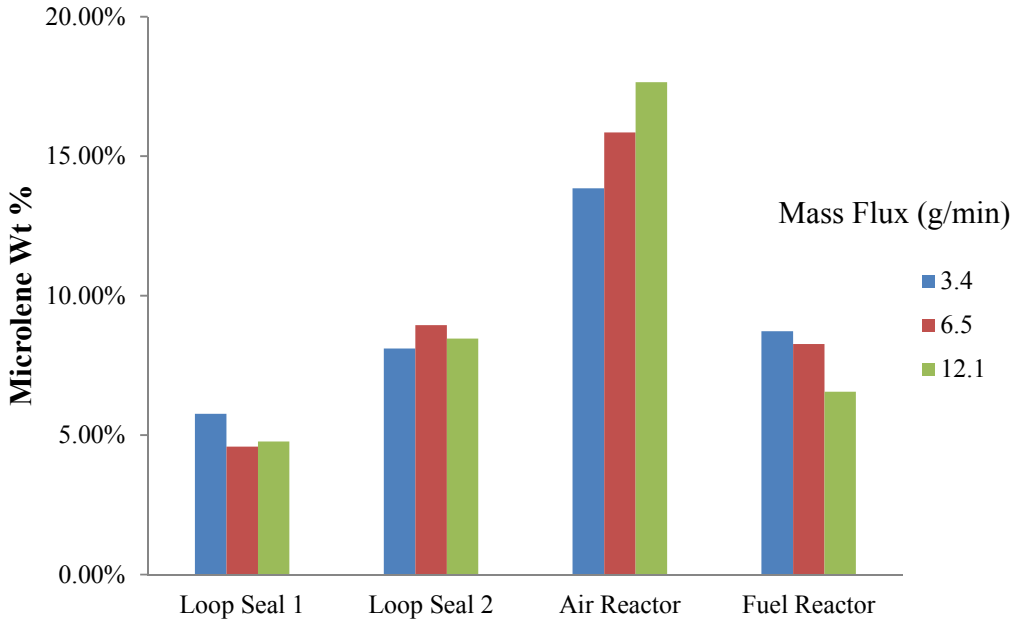

Figure 78: Particle concentration for components of the rig for an initial mixture of 10 % 300-355 µm microlene in 90-106 µm glass beads.

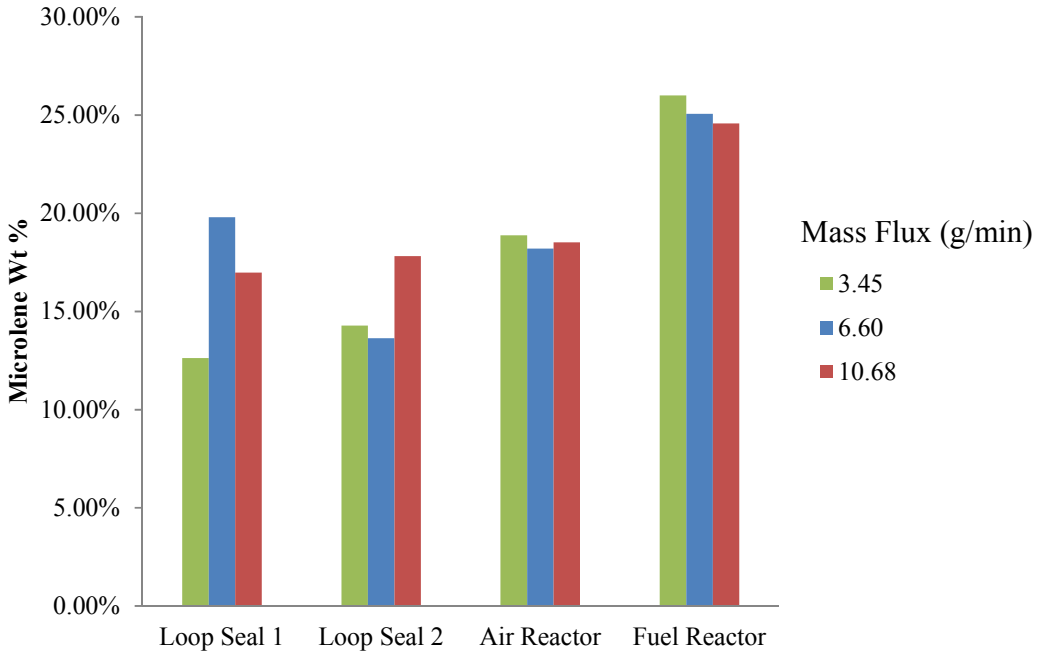

Figure 79: Particle concentration for components of the rig for an initial mixture of 20% 212-255 µm microlene in 125-150 µm glass beads.

Segregation was found to show different trends dependent upon particle concentration, particle size and mass flux. Segregation of particles in the system was found at times to increase in magnitude with increase in mass flux. Figure 80 below shows the increase in the magnitude of the particle segregation as mass flux in the system increases for a mixture of particles. From Figure 80 it can be seen that as the mass flux increases in the system (due to increase in the air reactor gas velocity), the degree of segregation towards the air reactor increased. It must be noted that this same trend of increasing the degree of segregation towards the air reactor for all concentrations of microlene of this particle combination, 5, 10 and 20 %. These degrees of segregation towards the air reactor can possibly be explained in terms of larger particles that will migrate to the bottom of the bed due to bubbling action and not be carried off the top of the bed by the gas. In this situation the microlene particles are much larger than the glass beads (212-255 µm compared to 90-106 µm) and the segregation seems to follow the prediction reported in the literature. As the particles that circulate the system are forced up from the top of the bed it can be seen that as the larger microlene particles are in less concentration at the very top of the bed hence segregation of microlene in the air reactor will occur.

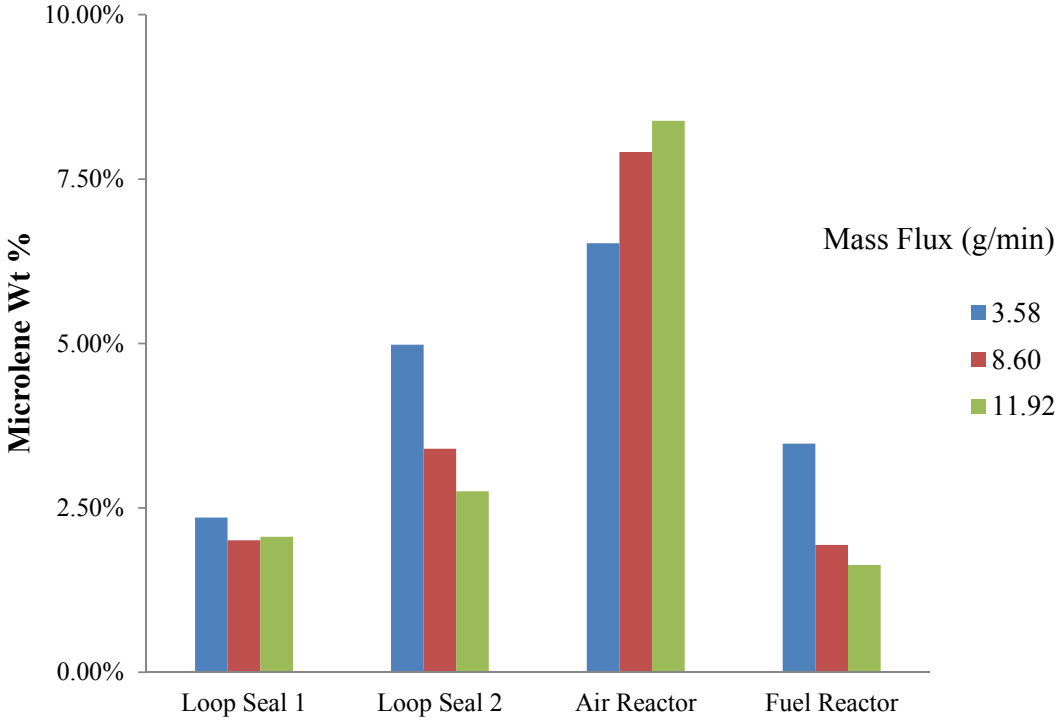

Figure 80: Particle concentration for components of the rig for an initial mixture of 5 % 212-255 µm microlene in 90-106 µm glass beads.

The increasing degree of segregation as the mass flux increases can be put down to a greater bubbling rate in the bed and hence greater segregation favouring the air reactor. Segregation in other case was found to decrease with the increase mass flux. Figure 65 shows the decrease in the degree of particle segregation as mass flux increases for a single set of particles. It can be seen in Figure 81 that the segregation of microlene favours the fuel reactor rather than the air reactor. This segregation trend can

be put down to the drag/unit weight ratio of the glass being higher than the microlene. The microlene particles have a large surface area and are low density whilst the glass beads have a small surface area and have a large density. As stated before as the particles that pass up the riser and around the system are at the top of the air reactor, less microlene is given the opportunity to pass up the riser due to this segregation.

It can also be seen that in this case as the mass flux and hence the fluid velocity in the air reactor increase, the segregation of particles becomes closer to parity in the fuel and air reactors. This is most likely due to the increasing gas velocity overcoming the differences in the drag/unit weight ratio of the particles.

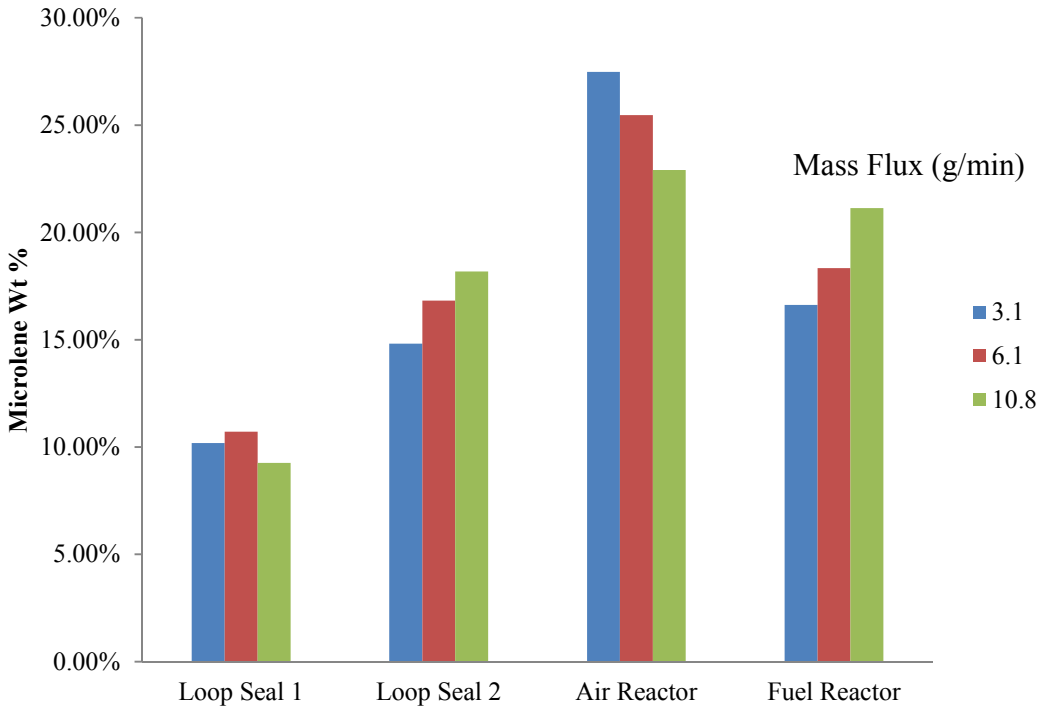

Figure 81: Particle concentration for components of the rig for an initial mixture of 20% 300-355 µm microlene in 106-125 µm glass beads.

Reasons for particle segregation in the system either favouring the build-up of microlene in the air reactor or the fuel reactor vary depending upon the particles in the system. The major cause for segregation was identified to be due to gas velocity in the riser being between the settling velocities of the two particles in the system. This segregation would occur under these conditions in a fluidised particle system. In this system it was found that the increase in gas velocity due to the riser having a smaller diameter than that of the air reactor and the lower particle concentration of at the base of the riser than in the bed the settling velocities of the particles would vary. Often these changes in gas velocity and particle settling velocity led to one type of particle being carried away by the stream of air and the other settling back out into the bed.

These segregation patterns could be minimised if the riser diameter was decreased. Currently the cross sectional area of the air reactor bed is 3.6 times larger than the cross sectional area of the riser. This results in a 3.6 times greater velocity in the riser than in the air reactor. The air reactor velocities varied from 0.33 m/s to 0.53 m/s. These velocities then varied in the riser from 1.33 m/s to 2.11 m/s. Coupled with altered settling velocities of particles in the bed these velocities will potentially lay between the settling velocities of different particles in this binary mixture. To overcome the variation in riser velocity contributing to system particle segregation the riser diameter could be decreased. An example of this could be decreasing the riser internal diameter from 40 mm to 30 mm would give a riser velocity/air reactor velocity around 6.5. This difference in riser velocity would allow the problem of segregation in the system due to riser velocity to be overcome.

Other trends in particle segregation that arose were the degree of segregation increasing or decreasing with variation in mass flux. The degree of segregation increasing with increases in mass flux (as seen in Figure 80) can be attributed to the effects of a bubbling bed. In this type of segregation, smaller particles are carried upwards by bubbles whilst the larger particles are not able to be lifted and hence never reach the top of the bed.

If the degree of segregation decreases with the increase in mass flux in the system the majority of the segregation can be put down to the drag/unit weight ratio differences in the particle. An example of this is seen in Figure 81. Particles will segregate if the drag/unit weight of a particle is different to the other particles in a bed. The decrease in the degree of segregation in the bed as mass flux increases can be attributed to the gas velocity in the bed being large enough to overcome the drag/unit weight ratio issues.

The trend in the changing degree of segregation depended upon the particles in the system. If the effect of the drag/unit weight ratio had a more of an effect the bubbling effect the segregation would decrease with increasing mass flux. If the effect of bubbling was more prominent than the effect of drag/unit weight ratio of the particles the segregation would increase with increase in mass flux due to increased bubbling.

Height Segregation

The air reactor was sampled at different height intervals to examine if height segregation occurred in the air reactor fluidised bed at different flow rates. This was done using the method outlined before. Height segregation was plotted with microlene weight percentage in the bed versus the height of the bed. Height segregation in the air reactor was found to show no particular. Height segregation was examined to test consistency across a number of experiments for the same particle mixture at the same flow rate. These results can be seen in Figure 82. It can be seen that the height segregation in the air reactor was consistent across all experiments. The results varied seemingly randomly but the overall microlene weight percentage in the bed was consistent.

Changing the flow rate in the air reactor was also examined to study if height segregation occurred in the air reactor due to varying gas velocity. Figure 83 shows the height segregation vs. bed height for an initial 10 % mixture of 300-355 μm microlene in 90-106 μm glass beads.

Examining Figure 83, it is evident that the overall concentration of the bed varies as was outlined earlier. Disregarding the differences in overall concentration and concentrating on the variations of microlene concentration with variation in bed height is evident that there is no general trend of height segregation in the bed with only small variations in the height. These variations can be seen as random as there is no real predictability in the microlene weight percentage at a given height in the bed.

This pattern of unpredictability of height segregation was consistent for all experiments analysed. There was no general trend of microlene segregation in the air reactor favouring one section or another.

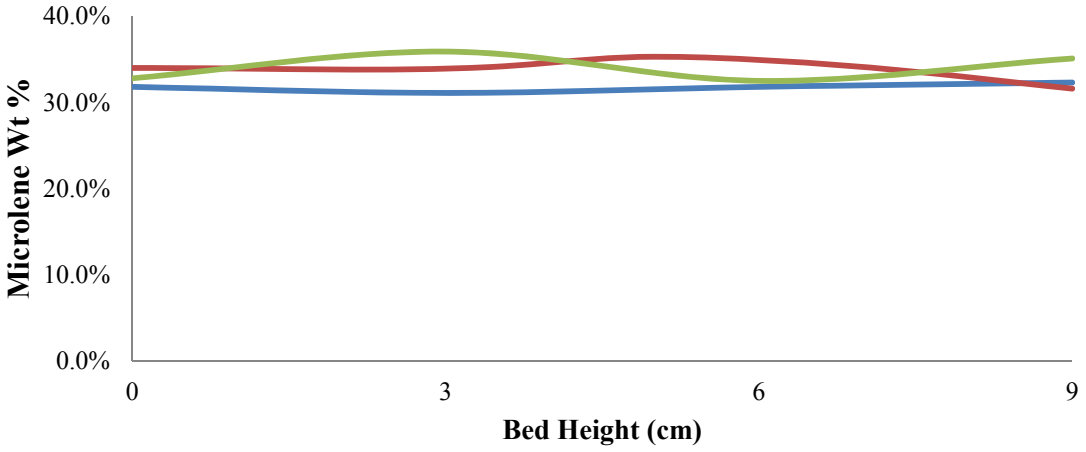

Figure 82: Height segregation in the air reactor across three experiments at 0.41 m/s reactor velocity on an initial mixture of 20 % 300-355 µm microlene particles in 90-106µm glass beads.

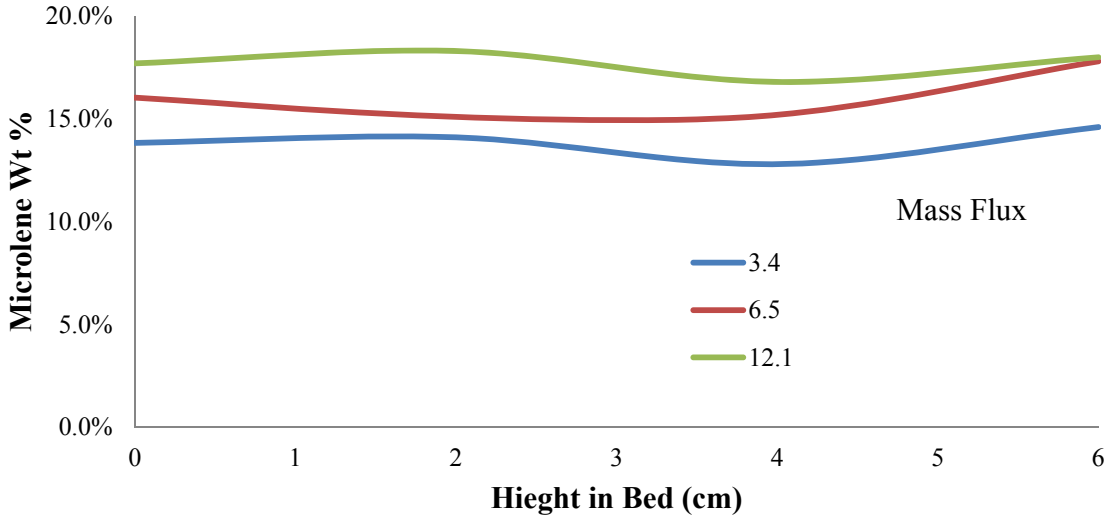

Figure 83: Microlene weight percentage vs. bed height for an initial mixture of 10 % 300-355 µm microlene in 90-106 µm glass beads.

4.1.3 Pressure Profiles

Figures 84 and 85 are pressure profiles in the air reactor and the riser. The plots indicate the superficial fluid velocity and the measured mass flux rate in the system when the air reactor is running at that gas velocity.

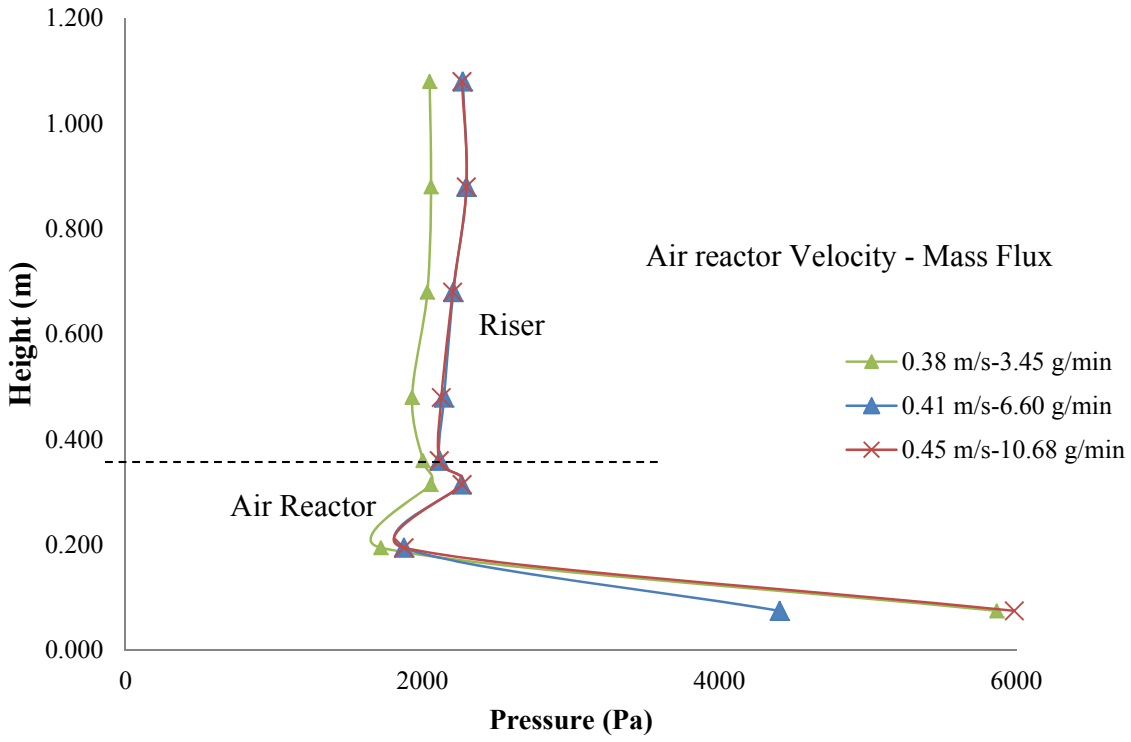

Figure 84: Pressure profile in the air reactor and riser for a 20 wt % concentration of 212-255 µm Microlene in 125-150 µm glass beads.

It can be seen that the pressure is greatest at the base fluidised bed of the air reactor decreasing closer to the top of the air reactor bed. Higher up into the riser the pressure is constant all the way up the riser. This pressure profile agrees with the expected outcomes of pressure profile in the air reactor and riser reported by others. Fluctuations in the pressure profile around the top of the air reactor are most likely due to flow interference from the air reactor sampling cylinder.

Also in the riser the pressure is larger as the flow rate of the air reactor is increased and hence the pressure drop in the riser is larger as mass fluxes are increased. The trend of pressure drop in Figure 68 is similar to the trend produced in Figure 85 however for a different mixture of particles. The trend again is similar to what is expected and reported in the literature for similar systems. The trend measured is that the pressure is highest at the base of the bed and decreases closer to the top and being continuous above the height of the particle bed.

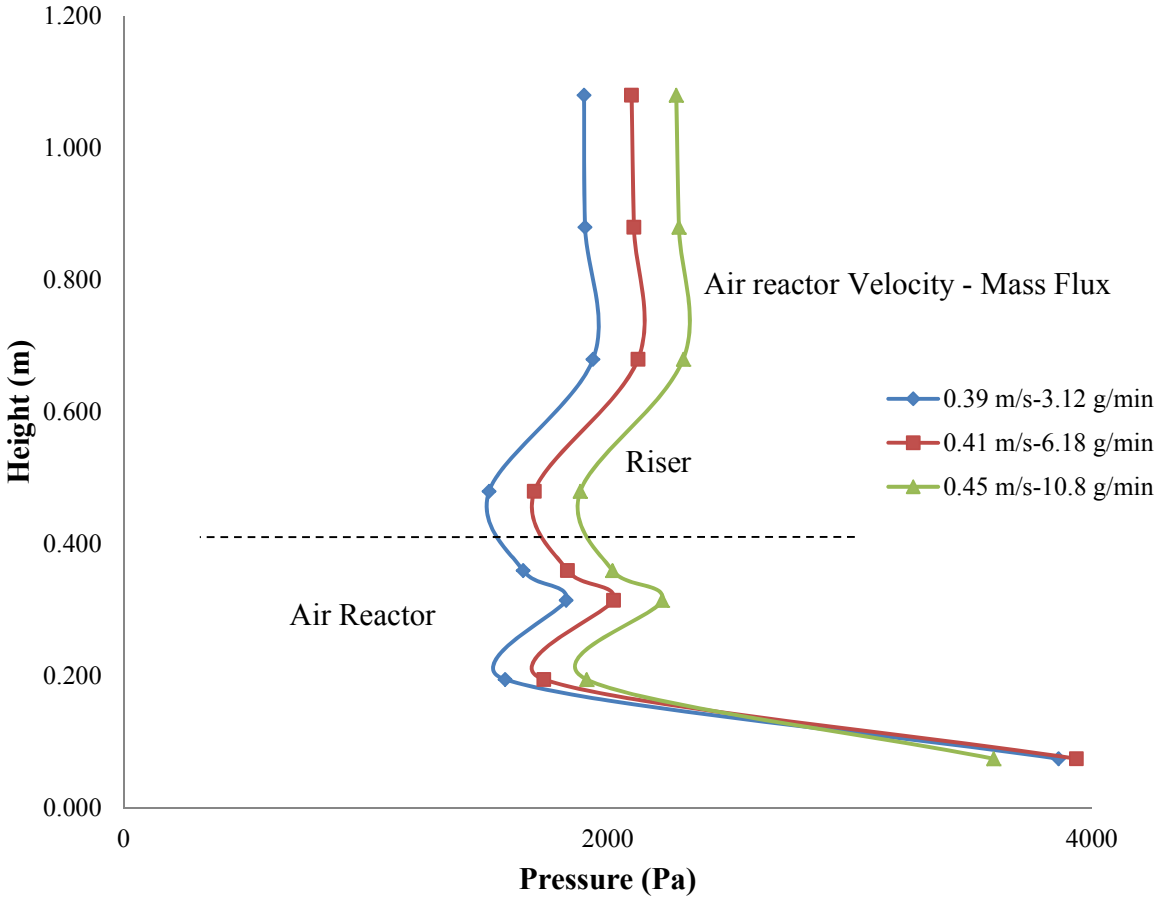

Figure 85: Pressure profile in the air reactor and riser for a 20 wt % concentration of 300-355 µm Microlene in 106-125 µm glass beads.

Figures 86 and 87 show the pressure profiles attained from the rig under different operating conditions. From Figure 71 it can be seen that the pressure profile is as predicted by others. The pressure is highest at the bottom of the bed decreasing closer to the top of the bed and staying constant above the particle bed. The pressure drop remains constant can be seen to remain constant in the fuel reactor across all mass fluxes. This is what should be expected as only the residence of the particles in the fuel reactor is being changed. The mass of particles in the bed and the fluid velocity are kept constant.

Figure 86 shows the same trend as in Figure 87 for pressure in the fuel reactor. The pressure is highest at the base of the fuel reactor bed, decreasing closer to the top and staying constant above the particle bed. As it was found that the trends in pressure profiles were the same for different particle mixtures, what must be examined now is the effect that particle size and concentration have upon the magnitude of pressure in the air reactor/riser section of the rig and the pressure in the fuel reactor.

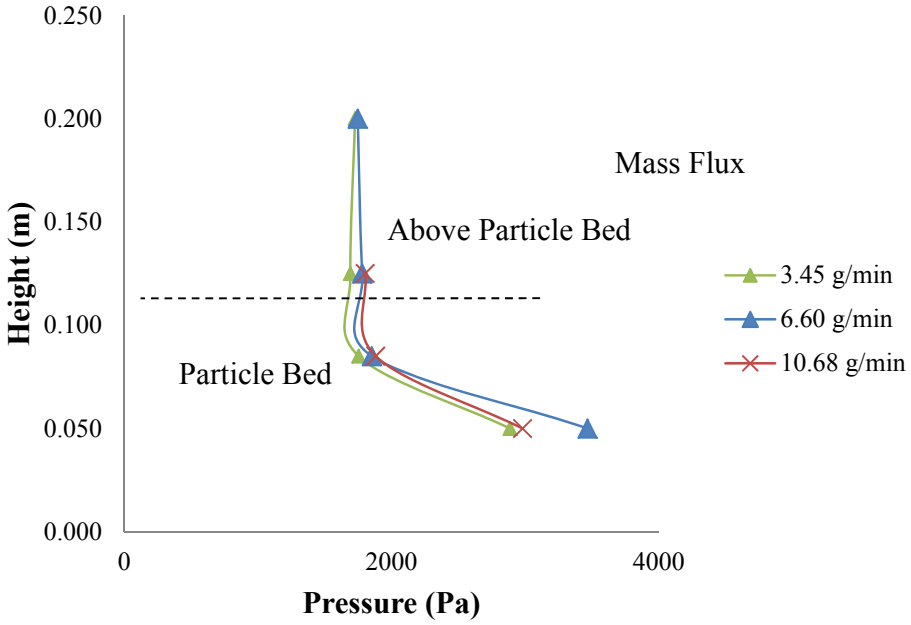

Figure 86: Pressure profile in the fuel reactor for a 20 wt % concentration of 212-255 µm Microlene in 125-150 µm glass beads.

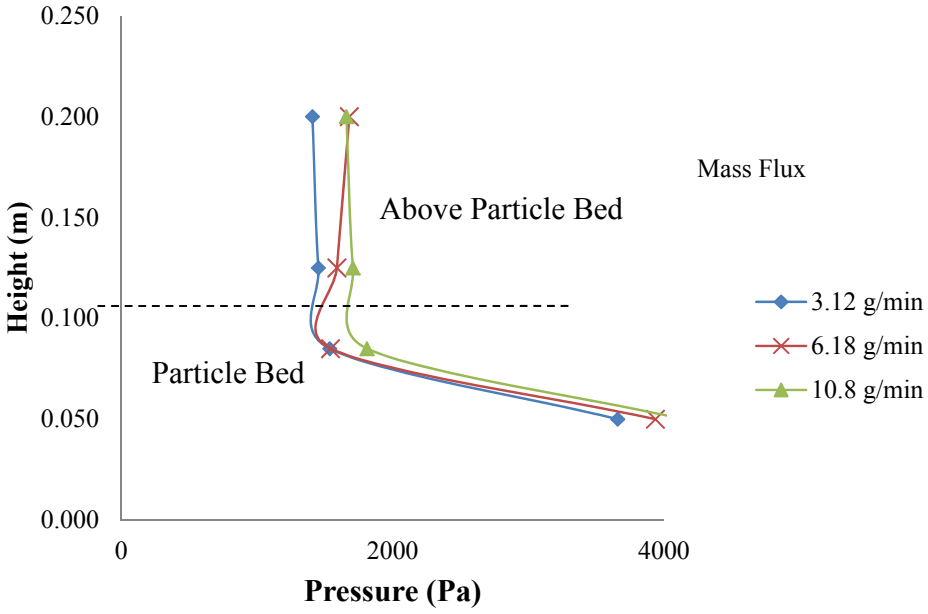

Figure 87: Pressure profile in the fuel reactor for a 20 wt % concentration of 300-355 µm Microlene in 106-125 µm glass beads.

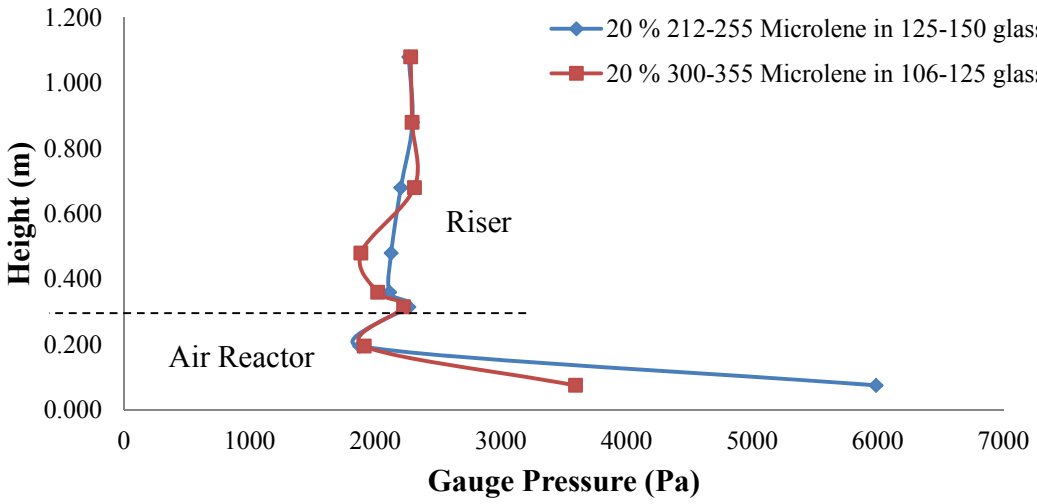

Figure 88: Pressure profile in the air reactor/riser section of the rig for different mixtures of particles at 0.45 m/s air reactor velocity.

Figure 88 shows the pressure profiles for different mixtures of particles at the same gas velocity in the air reactor. It can be seen that the pressure profile for the different particle mixtures in the air reactor is different. At the base of the bed it can be seen that the pressure is around 6000 Pa for a mixture of 20% 212-255 µm Microlene in 1125-150 µm glass beads whilst the pressure at the base of the bed for a mixture of 20% 300-355 µm Microlene in 106-125 µm glass beads was around 3900 Pa. However the pressure profile in the riser remains the same for both particle combinations as the particles have little or no impact upon the pressure in the riser with the pressure resulting from the gas flowing through the pipe. The 125-125 µm glass beads have a much larger mass per particle than glass beads of size 106-125 µm (0.048 g per particle rather than 0.034 g per particle). Due to the glass beads making up the majority of the bed it can be seen that the increase in glass bead size is the reason for pressure increase in the air reactor bed.

As the concentration of particles was varied in these experiments pressure profile differences were also noticed. Figure 89 shows how particle concentration in the mixture affected the pressure profile in the bed. Examining Figure 89, it is clear that as concentration of Microlene decreases for the same combination of particles the pressure in the air reactor increases. It can be seen that the pressure at the base of the air reactor almost doubles as the concentration decreases from 20 % to 10 %.

The same examinations of variations in pressure profile were carried out for the pressure profiles in the reduction reactor. Figure 90 shows the difference in pressure in the fuel reactor with various combinations. It can be seen that similarly to the case in the air reactor as the size of the glass beads in the particle bed increase so does the pressure in the system. It is also seen that as was the case of the air reactor as the concentration of Microlene decreases the pressure in the bed increases indicating that the glass is the main cause of the pressure increase in both the fuel and air reactor. Differences in pressure above the height of the bed are attributed to gas flow rate. In Figure 90 it can be seen that the pressure

above the bed height was around 1000 Pa larger for a 5 % Microlene concentration of particle size 300-355 µm in 106-125 µm glass beads than for a concentration of 20 % of the same particle mixture. This difference is due to the higher flow rate in the fuel reactor to fluidise the lower concentration of Microlene.

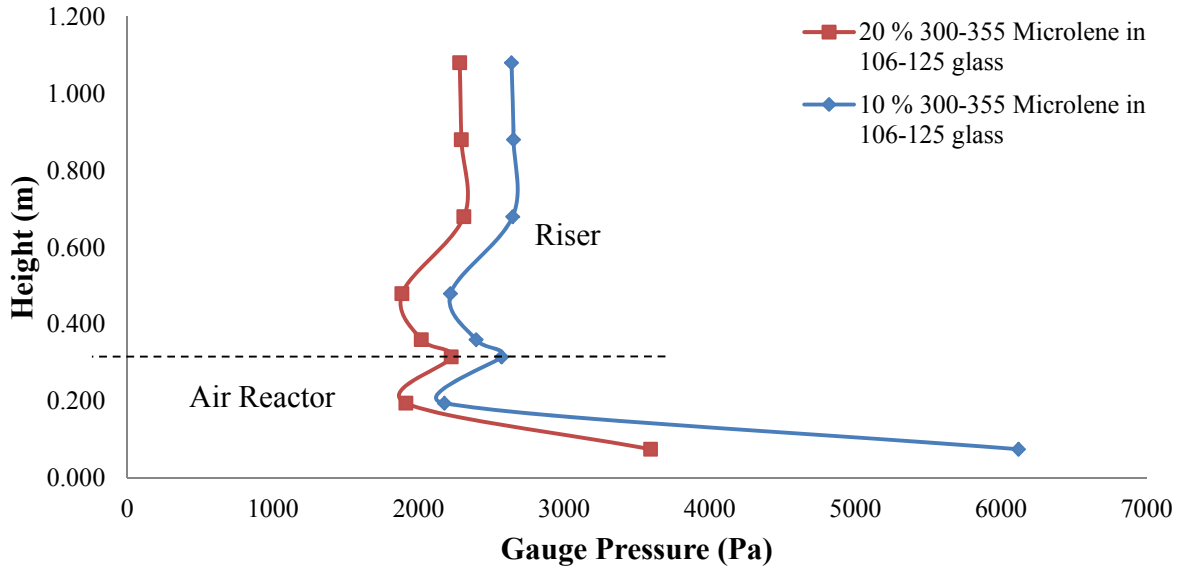

Figure 89: Pressure profile in the air reactor/riser section of the rig for different concentration of the same mixture of particles at 0.45 m/s air reactor velocity.

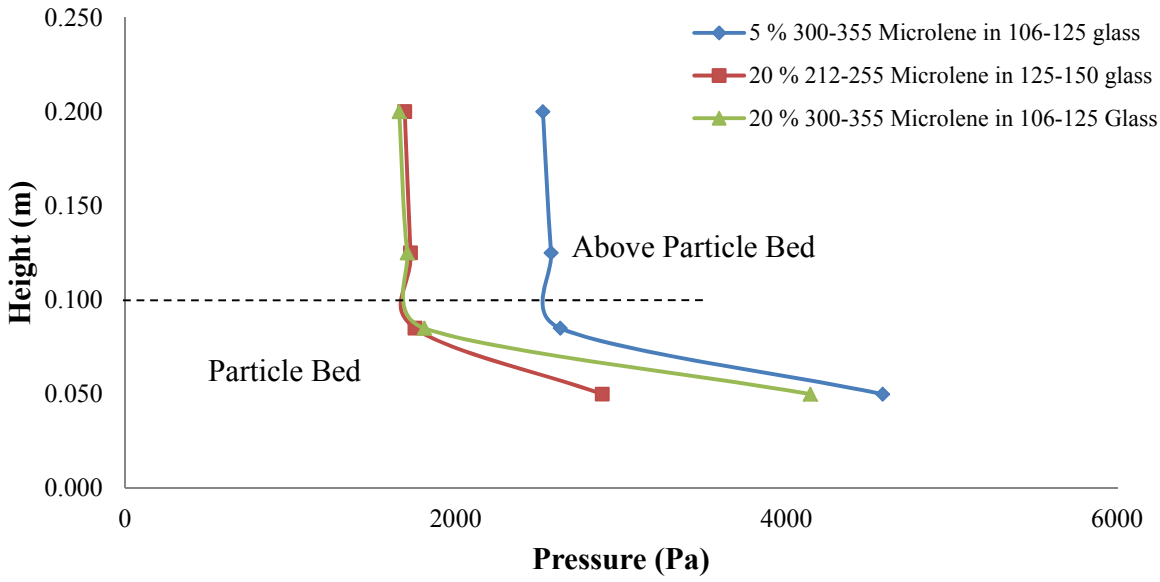

Figure 90: Pressure profile in the fuel reactor for varying particle mixtures and concentrations.

4.2 COMPUTATIONAL FLUID DYNAMICS / DISCRETE ELEMENT MODELLING (CFD-DEM)

4.2.1 Summary

As shown in Chapter 3 the performance of chemical looping combustion processes can be improved drastically by enhancing the overall redox characteristics of the system through the use of binary mixtures of oxygen carriers. However, binary mixtures of oxygen carrier particles are often found to differ in both size and density and therefore have the tendency to segregate under certain operating conditions.

In this work, a numerical study was conducted to investigate the mixing and segregation behaviour of binary mixtures of particles with different sizes and densities in a bubbling fluidized bed under conditions pertinent to the fuel reactor of a cold-flow model (i.e. a non-reacting replica) of a 10 kW_{th} chemical looping pilot-plant (i.e. the setup used in Section 4.1). The motion of particles was tracked individually by discrete element model (DEM), whilst the gas flow was modelled by computational fluid dynamics (CFD). Gas-particle interactions were considered by a two-way coupling method. Further, a modified version of Lacey's method was developed to calculate the mixing index, taking into account both the heterogeneity of solids spatial distribution and particle size differences.

Results showed that the modified Lacey's method provided very consistent and stable mixing indexes, proving to be effective for an in-situ quantitative description of mixing. It was also found that as the size ratio of the binary mixture of particles reduced, the mixing index increased indicating better mixing conditions. The agreement between the CFD-DEM model predictions and the experimental data were found to be satisfactory. The optimum conditions for mixing of binary mixtures appeared to be a function of bubble size, bubble rising rate and bubbling dynamics (e.g., splitting and coalescence). Application of the CFD-DEM model for prediction of layer inversion phenomenon in gas-solid fluidised beds was also demonstrated.

4.2.2 The Mathematical Model

Discrete Solid Phase

Particles were differentiated according to their sizes and densities. The trajectories of particles were solved based on the DEM approach. In this approach the motion of each particle is tracked individually using Newtonian equation of motion, with the position, linear and angular velocities of i^{th} particle being defined as,

$$\frac{d\boldsymbol{s}_{\mathrm{t}}^{i}}{dt} = \boldsymbol{v}_{\mathrm{t}}^{i}, \tag{4.1}$$

$$m^{i}\frac{d\boldsymbol{v}_{\mathrm{t}}^{i}}{dt} = \boldsymbol{F}_{\mathrm{t}}^{i} = \boldsymbol{F}_{\mathrm{f}}^{i} + \sum_{j}\boldsymbol{F}_{\mathrm{c}}^{ij} + m^{i}\mathbf{g}, \tag{4.2}$$

$$I^i \frac{d\boldsymbol{\omega}_{\mathrm{t}}^i}{dt} = \sum_j \left(n \times \boldsymbol{F}_{\mathrm{t}}^{ij}\right) L_i \,, \tag{4.3}$$

where, m and I are the particle mass and inertia moment; $\boldsymbol{F}_{\mathrm{f}}$ is the fluid forces; $\boldsymbol{F}_{\mathrm{c}}$ is the collision contact forces; $\boldsymbol{s}$, $\boldsymbol{v}$ and $\boldsymbol{\omega}$ are particle position, translation and angular velocities, respectively. Subscript t represents the transient time.

Contact Forces

Interactions between two colliding particles were modelled using a linear spring model with velocity-dependent damping (i.e., the spring-dashpot interaction) and static friction [11-13]. In this model the implementation of contact forces, both normal and tangential components, is based on a reduced version of that employed by Walton and Braun [12]. Specifically, the hysteretic effects between loading or unloading normal contacts are ignored, and the frictional directions are not differentiated at the same contact point at different time steps. The static friction is implemented by keeping track of elastic tangential displacement throughout the lifetime of a contact. Normal and tangential components of the contact force are calculated as,

$$\boldsymbol{F}_{\mathrm{n}} = -k_{\mathrm{n}}\delta_{\mathrm{n}}\boldsymbol{n} - \eta_{\mathrm{n}}\left(\boldsymbol{v}_{\mathrm{r}} \cdot \boldsymbol{n}\right)\boldsymbol{n}, \tag{4.4}$$

$$\boldsymbol{F}_{\mathrm{t}} = -k_{\mathrm{t}}\delta_{\mathrm{t}} - \eta_{\mathrm{t}}\left(\boldsymbol{v}_{\mathrm{r}} \cdot \boldsymbol{t}\right)\boldsymbol{t}, \tag{4.5}$$

where, k_{n} and k_{t} are the normal and tangential stiffness; η_{n} and η_{t} are the normal and tangential damping coefficient determined by the particle restitution coefficient e; δ_{n} is the normal displacement between two colliding particles i and j, $\delta_{\mathrm{n}}=(r_i+r_j)-d_{\mathrm{s}}$; r is the particle radius and d_{s} is the centre-to-centre distance between two particles. The normal unit, $\boldsymbol{n}$, is given as,

$$\boldsymbol{n} = \frac{\boldsymbol{s}_i - \boldsymbol{s}_j}{\left|\boldsymbol{s}_i - \boldsymbol{s}_j\right|}, \tag{4.6}$$

$\boldsymbol{v}_{\mathrm{r}}$ is the relative velocity, which is the combination of linear and angular relative velocities between colliding particles,

$$\boldsymbol{v}_{\mathrm{r}}^{ij} = \boldsymbol{v}^i - \boldsymbol{v}^j + \left(\boldsymbol{\omega}^i L^i + \boldsymbol{\omega}^j L^j\right) \times \boldsymbol{n}, \tag{4.7}$$

where L is the distance from the particle centre to the contact point. $\boldsymbol{t}$ is the tangential unit calculated as,

$$t = \frac{\boldsymbol{v}_{\mathrm{t}}^{ij}}{\left|\boldsymbol{v}_{\mathrm{t}}^{ij}\right|}, \tag{4.8}$$

where $\boldsymbol{v}_{\mathrm{t}}$ is the tangential component of relative velocity given as,

$$\boldsymbol{v}_{\mathrm{t}}^{ij} = \boldsymbol{v}_{\mathrm{r}}^{ij} - (\boldsymbol{v}_{\mathrm{r}} \cdot \boldsymbol{n})\boldsymbol{n}, \tag{4.9}$$

$\boldsymbol{\zeta}_{\mathrm{t}}$ is the tangential displacement. At the initiation of the contact, the tangential displacement is calculated as,

$$\boldsymbol{\zeta}_{\mathrm{t}} = \boldsymbol{v}_{\mathrm{t}} \min\left(\frac{|\delta_{\mathrm{n}}|}{\boldsymbol{v} \cdot \boldsymbol{n}}, \Delta t\right), \tag{4.10}$$

At time $t+\Delta t$, the tangential displacement is updated by,

$$\boldsymbol{\zeta}_{\mathrm{t}}(t+\Delta t) = \boldsymbol{\zeta}_{\mathrm{t}}(t) + \boldsymbol{v}_{\mathrm{t}}\Delta t, \tag{4.11}$$

To ensure that the tangential displacement lies in the current tangent plane, the tangential displacement is corrected by subtracting the normal component,

$$\boldsymbol{\zeta}_{\mathrm{t}}(t+\Delta t) = \boldsymbol{\zeta}_{\mathrm{t}}(t+\Delta t) - (\boldsymbol{\zeta}_{\mathrm{t}}(t+\Delta t) \cdot \boldsymbol{n})\boldsymbol{n}, \tag{4.12}$$

For the case of finite Coulomb friction between particles, if the following holds at any time during the contact,

$$\left|\boldsymbol{F}_{\mathrm{t}}^{ij}\right| > \mu_{\mathrm{f}}\left|\boldsymbol{F}_{\mathrm{n}}^{ij}\right|, \tag{4.13}$$

then sliding is assumed to occur. Subsequently the tangential contact force is calculated as,

$$\boldsymbol{F}_{\mathrm{t}}^{ij} = \begin{cases} -\mu_{\mathrm{f}}\left|\boldsymbol{F}_{\mathrm{n}}^{ij}\right| t & \text{if } t \neq 0 \\ -\mu_{\mathrm{f}}\left|\boldsymbol{F}_{\mathrm{n}}^{ij}\right| \dfrac{\boldsymbol{F}_{\mathrm{t}}^{ij}}{\left|\boldsymbol{F}_{\mathrm{t}}^{ij}\right|} & \text{if } t = 0, \left|\boldsymbol{F}_{\mathrm{t}}^{ij}\right| \neq 0, \\ 0 & \text{otherwise} \end{cases} \tag{4.14}$$

The total contact force between particle i and j is the sum of normal and tangential components,

$$\boldsymbol{F}_{\mathrm{c}}^{ij} = \boldsymbol{F}_{\mathrm{n}}^{ij} + \boldsymbol{F}_{\mathrm{t}}^{ij}, \tag{4.15}$$

Fluid Forces

Considering that complex flow patterns, such as bubble splitting and coalescence, wakes drifting, and particle circulation are present in the bed, various fluid forces were considered in the simulation:

$$\boldsymbol{F}_{\mathrm{f}} = \boldsymbol{F}_{\mathrm{D}} + \boldsymbol{F}_{\mathrm{S}} + \boldsymbol{F}_{\mathrm{A}} + \boldsymbol{F}_{\mathrm{P}} \tag{4.16}$$

Equations for calculation of these forces are summarised in Table 8.

Table 8: Major fluid forces

Fluid forces	Governing equations
Drag force, $\boldsymbol{F}_{\mathrm{D}}$	$\dfrac{0.75C_{\mathrm{g}}C_{\mathrm{D}}\lvert\boldsymbol{v}_{\mathrm{r}}\rvert\boldsymbol{v}_{\mathrm{r}}\varepsilon^{(-\gamma+1)}}{d_{\mathrm{p}}}$
Spin lift force, $\boldsymbol{F}_{\mathrm{S}}$	$\dfrac{0.75C_{\mathrm{g}}C_{\mathrm{S}}\lvert\boldsymbol{v}_{\mathrm{r}}\rvert\boldsymbol{v}_{\mathrm{r}}}{d_{\mathrm{p}}}$
Added mass force, $\boldsymbol{F}_{\mathrm{A}}$	$C_{\mathrm{g}}C_{\mathrm{A}}\dfrac{d\boldsymbol{v}_{\mathrm{r}}}{dt}$
Pressure gradient force, $\boldsymbol{F}_{\mathrm{P}}$	$0.5\left(\dfrac{d\boldsymbol{v}_{\mathrm{f}}}{dt}-\mathbf{g}\right)$
Coefficients and exponents: $C_{\mathrm{g}}=\dfrac{\pi\rho_{\mathrm{f}}d_{\mathrm{p}}^3}{6}$, $C_{\mathrm{D}}=(0.63+\dfrac{4.8}{\sqrt{Re_{\mathrm{p}}}})^2$, $\gamma=3.7-0.65\exp(-\dfrac{(1.5-\log(\mathrm{Re}_{\mathrm{p}}))^2}{2})$, $C_{\mathrm{S}}=\begin{cases}0.45+(2\varpi-0.45)\exp(-0.075\varpi^{0.4}Re_{\mathrm{p}}^{0.7}) & Re_{\mathrm{p}}\le 140\\ 0.5\varpi & Re_{\mathrm{p}}>140\end{cases}$, $\varpi=\dfrac{1}{2}d_{\mathrm{p}}\boldsymbol{\omega}_{\mathrm{p}}\Big/\lvert\boldsymbol{v}_{\mathrm{r}}\rvert$, $C_{\mathrm{A}}=0.5$	

Continuous Gas Phase

The gas phase was treated as a continuum and modelled in a way very similar to the one widely used in the conventional two fluid model. The continuity and momentum equations are,

$$\frac{\partial(\varepsilon\rho_{\mathrm{g}})}{\partial t}+\nabla\cdot(\varepsilon\rho_{\mathrm{g}}\boldsymbol{u})=0\,, \tag{4.17}$$

$$\frac{\partial(\varepsilon\rho_{\mathrm{g}}\boldsymbol{u})}{\partial t}+\nabla\cdot(\varepsilon\rho_{\mathrm{g}}\boldsymbol{u}\boldsymbol{u})=-\nabla\cdot(\varepsilon\overline{\overline{\tau}})-\nabla\varepsilon p+\boldsymbol{F}_{\mathrm{pf}}+\varepsilon\rho_{g}\mathbf{g}\,, \tag{4.18}$$

where $\boldsymbol{u}$, p, ρ_{g} are the velocity, pressure, density of the gas phase. $\boldsymbol{F}_{\mathrm{pf}}$ is the returning force from the particles by Newtonian's third law.

ε is the local void fraction in each computational cell. The accurate calculation of local void fraction plays a vital role in determining the accuracy of the prediction of a CFD-DEM model. At each time step, particle locations were obtained from the discrete particle model. Based on the cell geometrical information (i.e., cell centroid coordinate, dimensions and cell faces), the local void fraction was calculated by the area (projected) occupied by the particles that were overlapping with the cell. For a

particle that overlapped multiple cells, the particle area was proportionally partitioned amongst the cells involved. However, this two dimensional local void fraction (ε_{2D}) is inconsistent with the applied empiricism for the original development of drag closures, which were developed based on real three-dimensional systems. To correct for this inconsistency the calculated area based void fraction (ε_{2D}) was converted to a three-dimensional void fraction (ε_{3D}). Xu and Yu [14] adopted a fictitious domain with a depth equal to a particle diameter to directly calculate ε_{3D} based on the volume fraction of gas in a cell. However, in a system of different sized particles, the approach of Xu and Yu [14] encounters an inconsistency in the depth of the fictitious 3D domain. For this reason, the correlation proposed by Hoomans et al. [15] was used to convert ε_{2D} (area-based) to a 3D value,

$$\varepsilon = 1 - \frac{2}{\sqrt{\pi\sqrt{3}}}\left(1-\varepsilon_{2D}\right)^{1.5} \tag{4.19}$$

This correlation was derived on the basis of geometrical relations between a hexagonal lattice and an FCC unit cube, and hence is independent of the fictitious domain depth making it suitable for 2D polydispersed particle systems. However, it should be noted that the correlation over-predicts the packing density in the dense region and hence to some extent under-predicts the minimum fluidisation velocity.

After the calculation of the motion of discrete particles, the fluid forces are returned to the conservative equations of momentum of fluid as a source term. $\boldsymbol{F}_{pf}$ in Eq. (4.18) for each computational cell is then calculated as a sum of the fluid forces acting on each particle which is fully residing or partially covering the cell,

$$F_{pf} = -\sum_{i=1}^{n_c} \frac{F_{fp}^{i}}{\Delta V_c}, \tag{4.20}$$

where n_c is the total number of particles that are related to the cell; ΔV_c is the cell volume; $\boldsymbol{F}_{fp}{}^{i}$ is the fluid forces imposed on particle i, including all the terms given in Eq. (4.16).

4.2.3 Approach and Methodology

A Modified Lacey's Method

A modified Lacey's method was employed to calculate the mixing index of binary mixtures, taking into account the heterogeneous solid spatial distribution and particle size differences. When Lacey's method [16] is used in a numerical study, two issues need to be resolved including: heterogeneity of particle distribution in the domain due to presence of bubbles, and particle size difference rendering the inconsistency between the particle number and volume. To compensate for this heterogeneity of particle distribution Rhodes et al. [17] used adjustable sampling boxes with a fixed width and an adjustable height (in a two dimensional case the sampling boxes can be assumed to have an infinitely small depth). Rhodes' method allows for equal number of particles in each box to guarantee the same scrutiny level of scanning. The method has been successfully applied in a mono-sized particle system.

Meanwhile, Feng et al. [18] introduced the notion of equivalent particle number to handle particle size differences.

In this work, we adopted the adjustable sampling boxes proposed by Rhodes et al. [17] to compensate the heterogeneity of particle spatial distribution, and also used the equivalent particle number introduced by Feng et al. [18] to handle the inconsistency between the particle number and the particle volume.

The implementation of the method for calculation of mixing index is detailed as below. If the flotsam volume fraction in the sampling box is X_i, then the actual variance is calculated as,

$$S^2 = \frac{1}{N-1}\sum_{i=1}^{N}\left(X_i - \overline{X}\right)^2, \tag{4.21}$$

where N is the total number of sampling boxes; $\overline{X}$ is the mean volume fraction of flotsam over all sampling boxes, which is calculated by,

$$\overline{X} = \frac{1}{N}\sum_{i=1}^{N} X_i, \tag{4.22}$$

Then the mixing index is given as,

$$M = \frac{S_0^2 - S^2}{S_0^2 - S_{\mathrm{R}}^2}, \tag{4.23}$$

where S_0^2 and S_{R}^2 represent the variances in the two extreme states, completely segregated and well mixed, respectively. They are calculated by,

$$S_0^2 = \overline{X}\left(1-\overline{X}\right), \tag{4.24}$$

$$S_{\mathrm{R}}^2 = \frac{\overline{X}\left(1-\overline{X}\right)}{N_{\mathrm{pa}}}, \tag{4.25}$$

where N_{pa} is the average particle number over all sampling boxes, i.e.,

$$N_{\mathrm{pa}} = \frac{1}{N}\sum_{i=1}^{N} N_{\mathrm{p},i}, \tag{4.26}$$

$N_{\mathrm{p},i}$ is the actual equivalent particle number in the sampling box.

Before scanning the fluidized bed, the entire domain was divided evenly into a number of vertical columns with a width of w_{co}. The scanning was carried out in parallel on these columns starting from the bottom. To save the scanning time, an initial height was used for each sampling box. The box

height was then increased gradually with a constant incremental step until the number of particles contained in the sampling box reached the pre-set particle number N_s. The scanning process was looped consecutively along the column until the entire bed of particles was scanned and housed by sampling boxes. In this study, an initial box height of 1.5 r_L and a constant incremental step of 0.5 r_L were used, where r_L is the larger particle radius. An example of outputs from our post-processing code is illustrated in Figure 91. It should be noted that it is practically impossible to guarantee the particle number in each sampling box $N_{p,i}$ is exactly equal to N_s, as in the last incremental step the particles are always slightly more than the number gap to reach N_s. However, the standard error on particle number was found to be within 5%, resulting in a standard deviation of less than 0.01 on the mixing index.

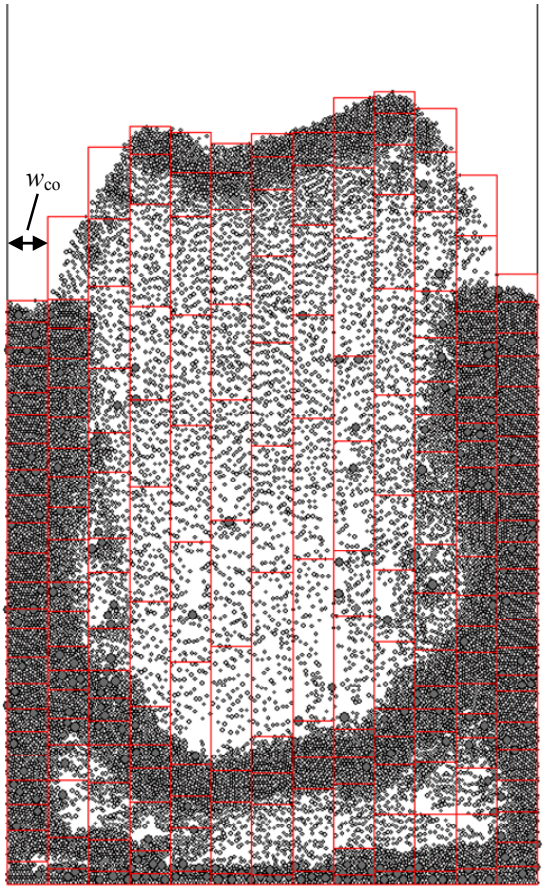

Figure 91: Adjustable sampling boxes for calculation of mixing index.

The exception to the abovementioned approach is the top boundary layer where the particle numbers are always smaller than the pre-set number N_s. In this case a margin value $N_{pm} = \varphi N_s$ was set to determine whether to include or disregard the sampling box. In other words, if $N_{p,i}$ is smaller than N_{pm}, the box will be disregarded; otherwise, it will be counted. Our sensitivity analysis (Table 9) however showed that the changes in mixing index results as a function of φ (0.2 – 1.0) were rather negligible (i.e. the standard deviation was less than 0.007). For the purpose of consistency the criteria for inclusion or disregarding of a sampling box in the top boundary layer was set at $\varphi = 0.9$.

Table 9: Influence of top sampling boxes on mixing index

φ	0.2	0.4	0.6	0.8	0.9	1.0
M	0.6559	0.6577	0.6587	0.6596	0.6606	0.6626

Numerical Simulation

An in-house code of a two dimensional (2D) CFD-DEM model was programmed to carry out numerical simulations in a rectangular computational domain with a width to height ratio of 1:10. As described earlier the correlation of Hoomans et al. [15] was used to calculate the 3D void fraction. Given that the numerical simulation of a full size fluidized bed is computationally expensive, the approach of using a smaller domain with periodic boundary conditions was adopted following the work of Kafui et al. [19]. In this approach however, the physical dimensions of the computational domain has to be carefully selected so the numerical results can effectively represent the bulk characteristics of the full size fluidized bed (i.e., the oxidation reactor of the CLAS system). A uniform inlet gas flow was imposed at the bottom of the bed, and the pressure-outlet boundary condition was used for the top side. The gas phase equations were solved by a semi-implicit method for pressure-linked equations revised (SIMPLER) [20-21]. In order to correctly capture particles contacts, the time step for particle phase was chosen to be substantially smaller than the fluid time step. The two-way coupling automatically adjusted the number of particle iterations carried out to match the CFD time step, such that,

$$\Delta t_{\mathrm{f}} = \sum_{N_{\mathrm{si}}} \Delta t_{\mathrm{s}} \,, \tag{4.27}$$

where Δt_{f} is the fluid time step; Δt_{s} is the particle time step, and N_{si} is the calculation steps of particle motion between two consecutive fluid time step.

The particle time step is dependent on the particle material properties and calculated by,

$$\Delta t_{\mathrm{s}} = \frac{2\pi\sqrt{m/k}}{n_{\mathrm{f}}}, \tag{4.28}$$

where m is the smallest particle mass, and k is the spring stiffness of particles; n_{f} is a constant and set to be 5 for all simulations. According to Tsuji et al. [22], the spring stiffness is a flexible parameter in the simulation of macroscopic hydrodynamics of fluidized beds. Kaneko et al. [23] varied the value of stiffness from 8 to 80, 000 N/m but could visually not observe any difference in the bubble dynamics of a gas-solid bubbling fluidized bed. Others (e.g. [24-26]) have reported similar findings. Here, the value of particle spring stiffness was set at 10 N/m. Selecting a small value for the spring stiffness improves the computational efficiency. The damping coefficient is determined by the spring stiffness and restitution coefficient of particles and calculated as [22],

$$\eta = -\frac{2\log(e)}{\sqrt{\pi^2 + \log^2(e)}}\sqrt{mk}\,, \tag{4.29}$$

e is the particle restitution coefficient. The other parameters for the simulation are listed in Table 10.

Table 10: Simulation conditions and parameters

Domain size, mm × mm	15 × 150 , 20 × 200
Cell size, mm × mm	1 × 1
Gas density, kg/m3	1.225
Gas viscosity, Pa·s	1.7894e-5
particle number	5 000 ~ 30 000
particle size, µm	
Species 1	116
Species 2	234, 278, 328, 393
particle density, kg/m^3	
Species 1	939, 2462,3287, 6949, 8057
Species 2	939
Mixture composition, %	
Weight fraction of species 1	10
Normal spring stiffness, N/m	
particle-particle	10
particle-wall	10
Tangential spring stiffness, N/m	
particle-particle	10
particle-wall	10
Restitution coefficient, -	
particle-particle	0.9
particle-wall	0.86
Sliding coefficient, -	
particle-particle	0.3
particle-wall	0.3

Experimental Study

The experimental data collected from the bench-scale cold-flow setup (see Figure 6) used in Section 4.1 was also employed for validation of the CFD-DEM modelling results. Figure 34 shows the experimental setup where two inter-connected fluidised beds reactors were used. This setup is a cold flow model of a 10kW$_{th}$ CLAS pilot-plant consisting of five major components namely the air reactor, riser, fuel reactor, two loop seals and a cyclone. The particle recirculation between the air and fuel reactors was implemented as the cyclone captured the particles passing through the riser and returned them to the fuel reactor. The fuel reactor was a fluidized bed with an inner diameter of 90 mm and height of 195 mm. Binary mixtures of glass beads and polyethylene particles (Table 11) were prepared by manual mixing with a stirrer in a large beaker. The CLAS system was loaded with the particle mixture (2 kg total inventory) and was run until steady state conditions were reached at a fixed solids recirculation rate. The experiments were then stopped by abruptly ceasing the air supply and particles in the fuel reactor were collected in a graduated cylindrical sample holder that is inserted at the bottom

of the reactor. The mixing index of experimental data was then quantified using the method described by a number of researchers. In this method the mixing index is defined as $M = X/X'$, where X is the concentration of glass beads particle at the top layer and X' is the overall average concentration of the glass beads particle in the bed.

Table 11: Particles properties in experiments

Parameter	Unit	Glass Ballotini	Polyethylene
Mean Diameter (arithmetic averaging)	μm	116	234, 278, 328, 393
Density	kg/m^3	2462	939
Terminal velocity[1]	m/s	0.63	0.87, 0.97, 1.21, 1.69
Minimum Fluidization Velocity[2]	m/s	0.013	0.0198, 0.028, 0.039, 0.055

1: calculated by the correlation of Harder and Levenspiel;
2: calculated by Ergun equation based on the packed bed voidage of 0.4.

4.2.4 Results and Discussion

A typical simulation of mixing process as a function of excess gas velocity is presented in Figure 35. It is worth noting that the excess gas velocity defined as superficial velocity minus minimum fluidisation velocity of the binary mixture is commonly used to describe the bubbling dynamics and hence the mixing/segregation behaviour in a bubbling fluidized bed. That is because according to the two-phase theory, the amount of gas in the excess of that required for the minimum fluidization is considered to flow through the bed as visible bubbles. For this reason, our results are presented in terms of the excess velocity instead of the superficial gas velocity. As Figure 92a shows, at t = 0 s, two particle species are closely packed in a completely segregated arrangement. As the air is injected, bubbles are formed in the central region carrying small particles upwards during their rise. Rising of bubbles renders the collapse of top layer which consists of large particles, pushing them to the sides (Figure 92b). Small particles that are entrained by rising bubbles encounter large particles that are falling. Large particles are only percolating the small particles layer where the local bed voidage is relatively great. When moving close to the top boundary of a bubble, large particles preferentially tend to fall down through the bubbles where the upward fluid velocity is at its minimum (Figure 92c). However, due to high fluid velocity around the rising bubbles, both particle species will be entrained and move upwards along the bubble sides. As such, re-circulation patterns are formed around the bubbles serving as the major mechanism which promotes solids mixing. The falling motion of large particles through the free space inside the bubbles and subsequent sinking of large particles to the bottom of the bed on the other hand is considered to be the main mechanism that leads to segregation of two solids species. At steady states some large particles assemble and rest at the bottom and the others are still fluidized in the bed (Figures 35e – 35g). As the gas velocity is much higher than the minimum fluidization velocity of the binary mixture (i.e. U_{ex} = 0.04 m/s), overall a good mixing is achieved.

A sensitivity analysis on post-processing calculation of mixing index using the modified Lacey's method developed in this study was performed. Specifically, sensitivity of model outputs in terms of mixing index to input parameters namely the width of adjustable sampling boxes and pre-set particle number were investigated.

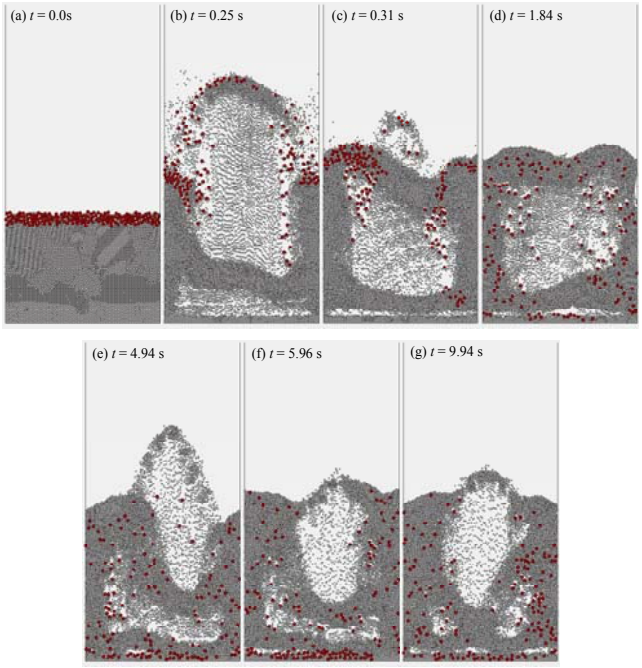

Figure 92: Mixing process with initial segregated particles arrangement (U_{ex} = 0.04 m/s, X_L=0.1, ρ_1 = 2462 kg/m^3, ρ_2 = 939 kg/m^3, d_1 = 116 µm, d_2 = 328 µm, A_D = 15 × 150 mm^2).

Figure 93 shows the effect of column width, w_{co}, on the evolution of mixing index. As it can be seen, a decrease in column width (i.e. from 1.5 to 0.75 mm) leads to a negligible change of less than 0.3% in mixing index, indicating that the mixing index is independent of the column width for column to domain width ratios between 1/20 and 1/10. Figure 93b shows the effect of scanning scrutiny level (i.e., the pre-set particle number in the sampling box) on the evolution of mixing index. For N_s ranging between 100 and 200, the variation in average mixing indexes is within 3.42%. However, for N_s = 50, the scrutiny level appears too small to meet the sampling requirement and as a result much lower mixing index was observed. For higher scrutiny levels (N_s = 300) the simulation result overestimates mixing index. This is because a greater scrutiny level entails a larger sampling box, which will drown out the heterogeneous distribution of discrete particles and subsequently result in a larger mixing index. In the extreme case where the sampling box size is equal to the bed size, the mixing index reaches the maximum value of 1. Based on the above test results, a column width of 1.5 mm and a scrutiny level of scanning with a fixed pre-set particle number of 100 were used to calculate the mixing index here.

Use of sampling boxes with adjustable heights is believed to play a key role in the above low sensitivity of mixing index to the size of sampling box. In support of this argument we have presented the sensitivity of mixing index to column width of fix-sized sampling boxes used in post-processing calculation of mixing index in conventional Lacey's and Feng et al.'s methods. As Figure 94 shows, when the width of sampling box reduces from 2.0 to 1.0 mm, the mixing index varies significantly from 0.83 to 0.52, indicating that in both conventional methods mixing index is very sensitive to the size of sampling box. Ignoring the influence of heterogeneous spatial distribution of particles induced by rising bubbles is considered to be responsible for such great sensitivities to the size of sampling box in conventional methods.

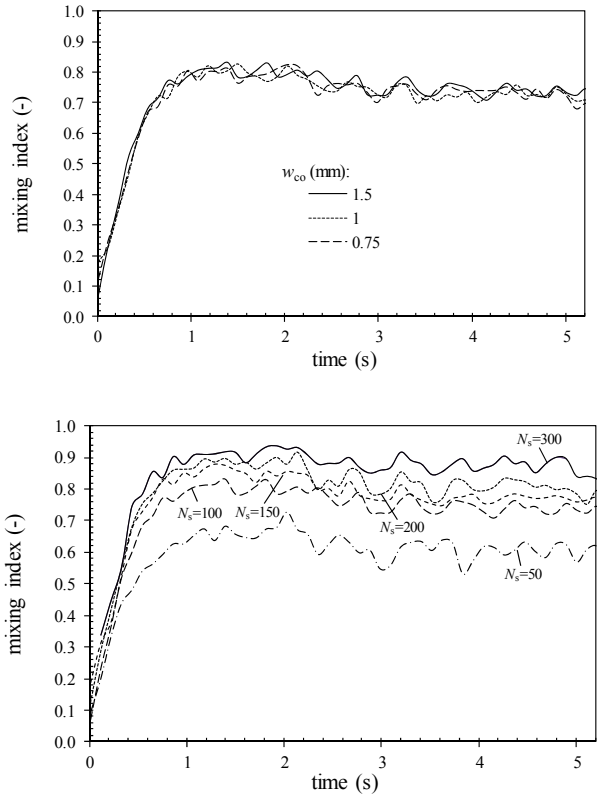

Figure 93: Influence of (a) vertical column width and (b) fixed particle number in each sampling box on mixing index (U_{ex} = 0.04 m/s, X_L = 0.1, ρ_1 = 2462 kg/m^3, ρ_2 = 939 kg/m^3, d_1 = 116 µm, d_2 = 328 µm, A_D = 15 × 150 mm^2).

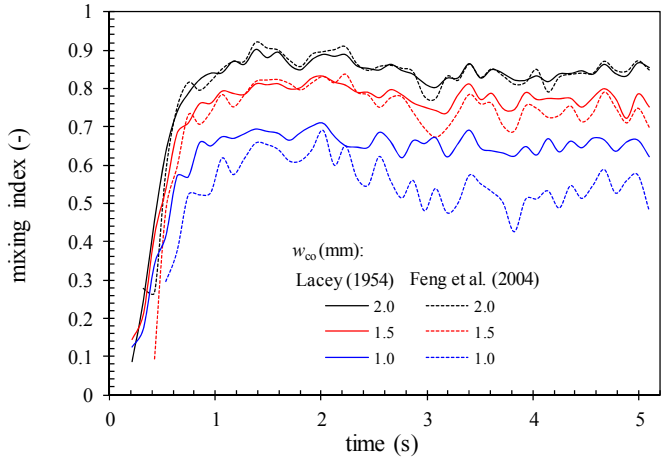

Figure 94: Influence of sampling box size on mixing index using conventional Lacey's and Feng's methods (U_{ex} = 0.04 m/s, X_L=0.1, ρ_1 = 2462 kg/m^3, ρ_2 = 939 kg/m^3, d_1 = 116 µm, d_2 = 328 µm, A_D = 15 × 150 mm^2).

Figure 95 illustrates the sensitivity of model predictions namely mixing index to domain size for binary mixtures. Two domain sizes namely 15 × 150 mm^2 and 20 × 200 mm^2 were examined. Whilst a slight deviation between the results at different domain sizes exists, the sensitivity of mixing index to the domain size under the examined conditions appears to be negligible. As shown earlier, the time-averaged mixing index at the quasi steady state (i.e. after about 7 s) changes from 0.81 to 0.8 when the domain size increases from 15×150 to 20×200 mm^2. Figure 96 shows the bed expansion behaviour in terms of the normalised bed height defined as the height of expanded bed to the initial static bed height (i.e. H/H_0) in both domains. It can be seen that as the domain increases by 1.7 times in size, the normalised bed height increases from 1.54 to 1.7 (i.e., 10%). Further investigation of the sensitivity of the model to the domain size is required. However, since the focus of the present study is on the mixing and segregation, the domain size of 20 × 200 mm^2 has thus been used in the simulation.

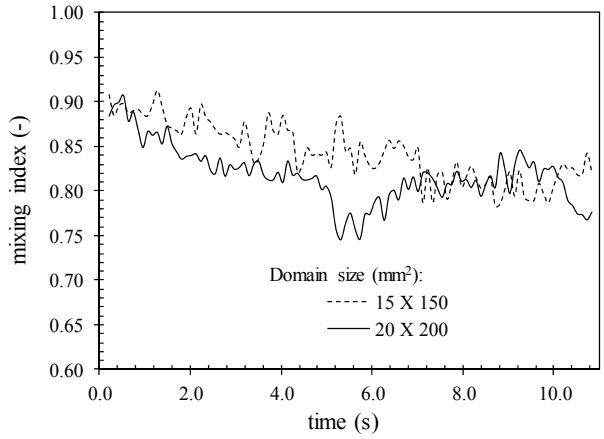

Figure 95: Sensitivity of mixing index to domain size (U_{ex} = 0.04 m/s, X_L=0.1, ρ_1 = 2462 kg/m^3, ρ_2 = 939 kg/m^3, d_1 = 116 µm, d_2 = 278 µm).

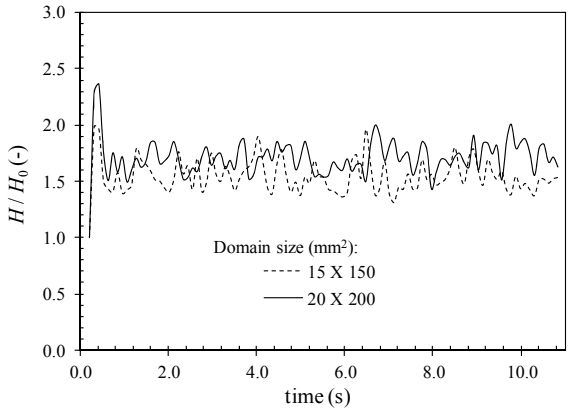

Figure 96: Sensitivity of bed expansion to domain size (U_{ex} = 0.04 m/s, X_L=0.1, ρ_1 = 2462 kg/m^3, ρ_2 = 939 kg/m^3, d_1 = 116 µm, d_2 = 278 µm).

Figure 97 shows the sensitivity of model predictions for mixing index to initial static bed height (at zero gas flow rate), which is represented by the dimensionless bed aspect ratio (i.e. H_0/D_t). Three cases with bed aspect ratios of 0.2, 0.4, and 0.7 were examined. As the aspect ratio increases the amplitude of

fluctuation in mixing index evolution curves reduces. This finding is in line with the results of Peeler and Huang [27] and Wu and Baeyens [28], who concluded that the bed aspect ratio is important only in shallow beds. In shallow beds, the bubble frequency increases and bubbles can quickly penetrate the bed increasing bubble splitting and coalescing rates [29]. As a result, the high fluctuation of mixing index is observed. On the contrast, in deep beds, the average bubble frequency is much less and subsequently the overall mixing index appears more stable.

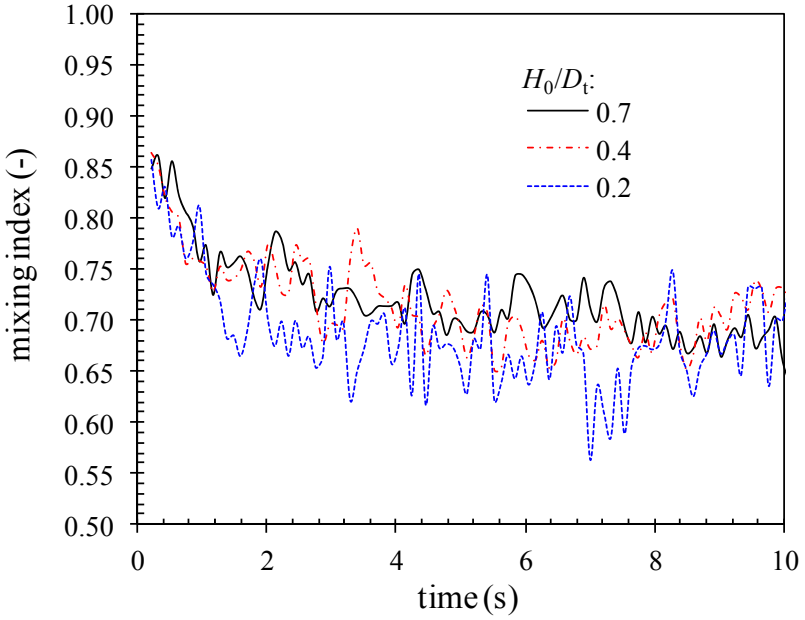

Figure 97: Sensitivity of mixing index to initial packed bed height (U_{ex} = 0.04 m/s, X_L=0.1, ρ_1 = 2462 kg/m^3, ρ_2 = 939 kg/m^3, d_1 = 116 µm, d_2 = 328 µm, A_D = 20 × 200 mm^2).

Figure 98 shows the sensitivity of the evolution of mixing index to initial particle spatial-arrangement. Two extreme cases namely a completely segregated with a mixing index close to zero and a randomly mixed particles with a mixing index close to one were simulated. As Figure 98 demonstrates, the evolutional trend lines of two cases converge after about 1 s indicating that the final mixing index results is independent of the initial particle positions. Although the initial particle spatial-arrangement influences the mixing process, it does not influence the final mixing status of binary mixtures. Indeed, the mixing status is determined primarily by particle properties (e.g. size and density) and operating conditions (e.g. excess gas velocity).

The effect of particle size ratio (i.e. diameter ratio of large to small particle species) on the mixing/segregation of binary mixtures was examined at an excess gas velocity of 0.04 m/s. In this study, the particle size ratio was increased by increasing the diameter of large particles whilst the size of small particles remained constant. The binary mixtures consisted of small particles with a diameter of 116 µm and a density of 2462 kg/m^3, and large particles with diameters of 234, 278, 328, and 393 µm and a density of 939 kg/m^3.

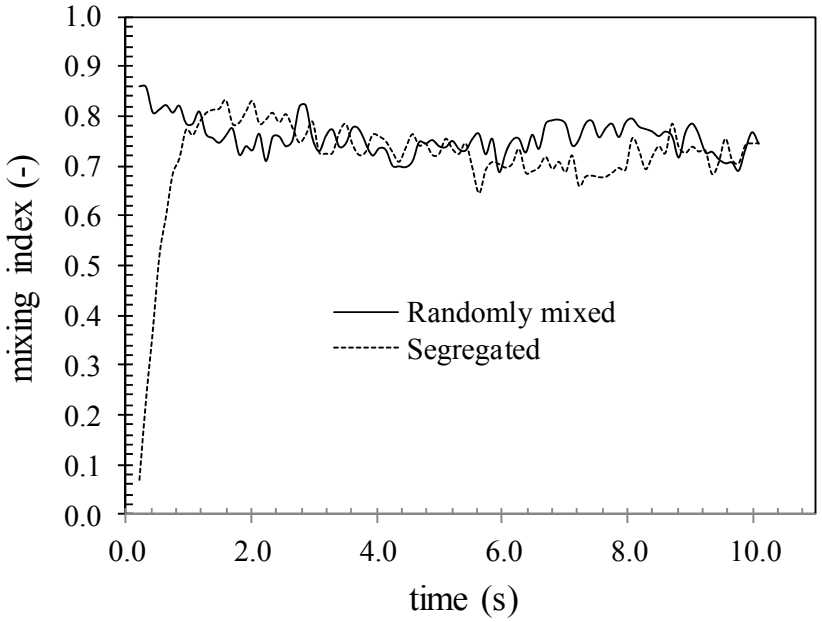

Figure 98: Sensitivity of mixing index to initial particle position (U_{ex} = 0.04 m/s, X_L=0.1, ρ_1 = 2462 kg/m^3, ρ_2 = 939 kg/m^3, d_1 = 116 µm, d_2 = 328 µm, A_D = 15 ×150 mm^2).

Figure 99 illustrates the particle mixed status at steady state as a function of particle size ratios. It can be seen that at a low particle size ratio (i.e. d_R = 2.0), the fluidized bed exhibits a typical bubbling fluidization regime where both particle species are fluidized. The mixture composition is almost the same over the entire domain as shown in Figure 99a. In such cases, the bubble frequency is high due to small particle size difference. The bubbles formed in the domain are relatively small and distributed in the bed irregularly with appreciable radial movement. Hence, a good mixing is observed. As the particle size ratio increases, particle segregation becomes more significant where large particles start to sink to the bottom forming stratified layers with non-uniform local mixture compositions. Moreover, small particles above the jetsam layer remain fully fluidized in a nearly slugging fluidization regime where bubbles coalesced frequently to form even larger bubbles.

Figure 100 shows the mixing index versus particle size ratio at steady state. The mixing index is the time averaging value of transient mixing indexes under steady state conditions. As Figure 43 illustrates an increase in particle size ratio decreases the mixing index. At small particle size ratios, the forces experienced by each particle are at the same level due to the comparable particle sizes. As a result, the trajectories of particles are very similar and good mixing is thus achieved. However, as the particle size ratio increases, the large particles segregate through the particle-lean space inside the bubbles and sink due to the out-of-balance forces (e.g. the gravitational force is dominant). These settled large particles serve as an extended gas distributor and subsequently small particles above the jetsam layer are fluidized more readily. Large bubbles formed under these conditions in turn increases the settling rate of other large particles resulting in a poor mixing.

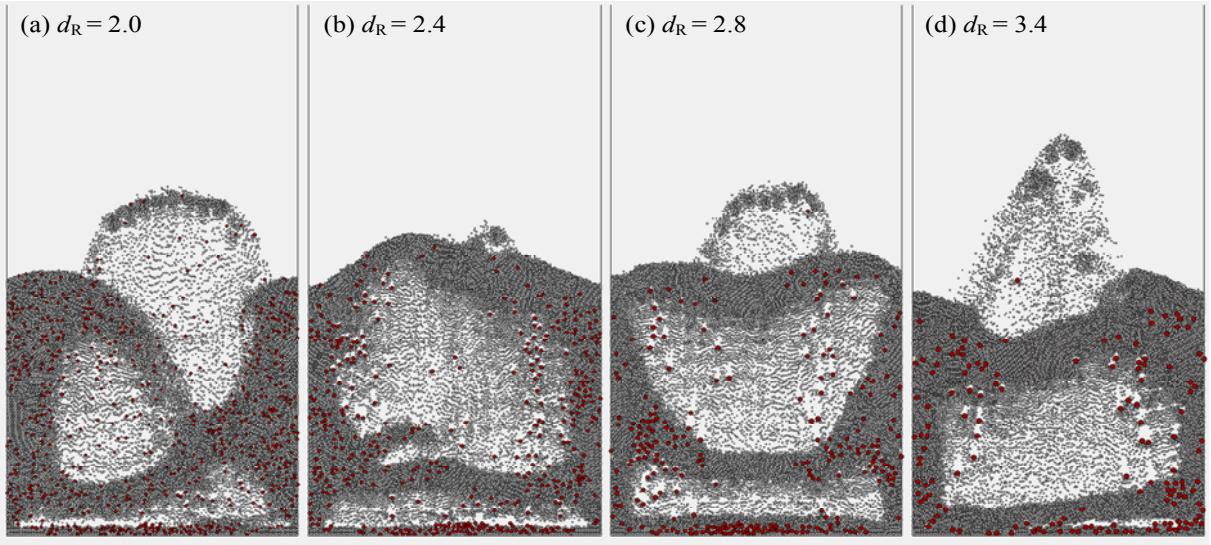

Figure 99: Snapshots of solids mixing status at different particle size ratios (t = 10.84 s, U_{ex} = 0.04 m/s, X_L=0.1, ρ_1 = 2462 kg/m^3, ρ_2 = 939 kg/m^3, A_D = 20 × 200 mm^2).

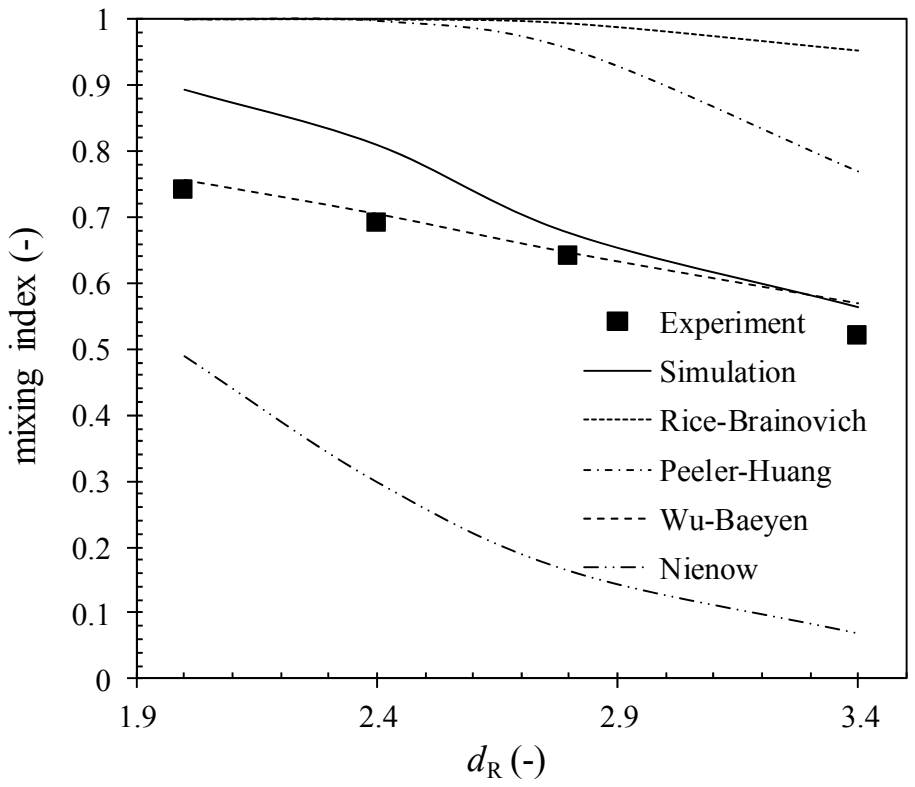

Figure 100: Influence of particle size ratio on mixing index (U_{ex} = 0.04 m/s, X_L=0.1, ρ_1 = 2462 kg/m^3, ρ_2 = 939 kg/m^3, A_D = 20 × 200 mm^2).

Figure 100 also shows the theoretical predictions by several existing empirical correlations. These correlations were originally formulated based on the experimental data of either equal density or equal size particulate systems. As Figure 100 shows, Nienow's correlation [30] developed for particles of equal size and different densities significantly underestimates mixing index predictions of our CFD/DEM Model. However, the modified version of Nienow's correlation by Rice and Brainovich [31] and Peeler and Huang [27] that is applicable for equal density systems, largely overestimates the mixing index predictions. The correlation proposed by Wu and Baeyens [28] for solids mixtures of equal density and different sizes provides the closest predictions to our simulation results especially at larger particle size ratios. The observed behaviour indicates that Wu and Baeyens' correlation could effectively capture the effect of change in the particle size ratio (whilst maintaining the density of the particles constant) on segregation and mixing behaviour.

Also shown in Figure 100 is the experimental data obtained in this work. It should be noted that these simulations of the batch fluidized bed were performed using the steady state conditions in experiments. Our experimental results showed that under steady state conditions, the composition of particles and the total solid mass in the oxidation reactor of the CLAS system remained unchanged for a given fluidisation velocity. Whilst the local gas-solid flow characteristics of the fuel reactor is expected to be affected by the solid circulation, the bulk behaviours such as mixing and segregation are expected to be independent of the solid circulating rate under steady state conditions. Therefore the qualitative comparison of the bulk characteristics of the simulated fluidised bed to those of the oxidation reactor of the CLAS system under steady state conditions has been conducted. It can be seen that the CFD/DEM model provides the same trend as that obtained in experiments, indicating the decreasing mixing index as the particle size ratio increases.

The effect of particle density ratio (i.e. density ratio of small to large particle species) on the mixing/segregation of binary mixture was examined at an excess gas velocity of 0.04 m/s. The particle density ratio was increased by increasing the density of small particles whilst the density of large particles remained constant. The binary mixtures consisted of small particles with a diameter of 116 μm and a density of 939, 2462, 3287, 4883, 6949 and 8075 kg/m^3, and large particles with diameter of 328 μm and a density of 939 kg/m^3.

Figure 101 shows the mixed status of binary mixtures at steady state with density ratios ranging from 1.0 to 8.6. It can be seen that when the density ratio is 1.0 (i.e. an equal density system) two stratified layers are formed with all large particles resting at the bottom as the jetsam while small particles are fluidized above the jetsam layer. Since the superficial velocity is much higher than the minimum velocity of small particles, a turbulent fluidization regime is observed with very changeable bubble size and irregular bubble shape and obvious bubble wakes (Figure 101a). As the density ratio increases, namely the density of small particles increases, the mixing is gradually improved with more large particles fluidized (Figures 101b – 101c). At a density ratio of 5.2, a very good mixing is achieved forming a uniform local mixture composition (Figure 101d). A further increase in the density ratio results in the so-called layer inversion phenomenon with the majority of large particles being fluidized and forming a layer at the upper region of fluidized bed whilst small particles sink to the bottom forming a jetsam layer (Figures 101e – 101f). Moreover, the bubble size becomes smaller as the density ratio increases at the excess gas velocity of 0.04 m/s. The larger bulk density at higher density ratios is believed to contribute to reducing the size of bubbles at a given excess gas velocity. It also appears that

the fluidization status of the bed is governed mainly by the particles above the bottom segregated layer resulting bin either slugging or bubbling fluidization regime.

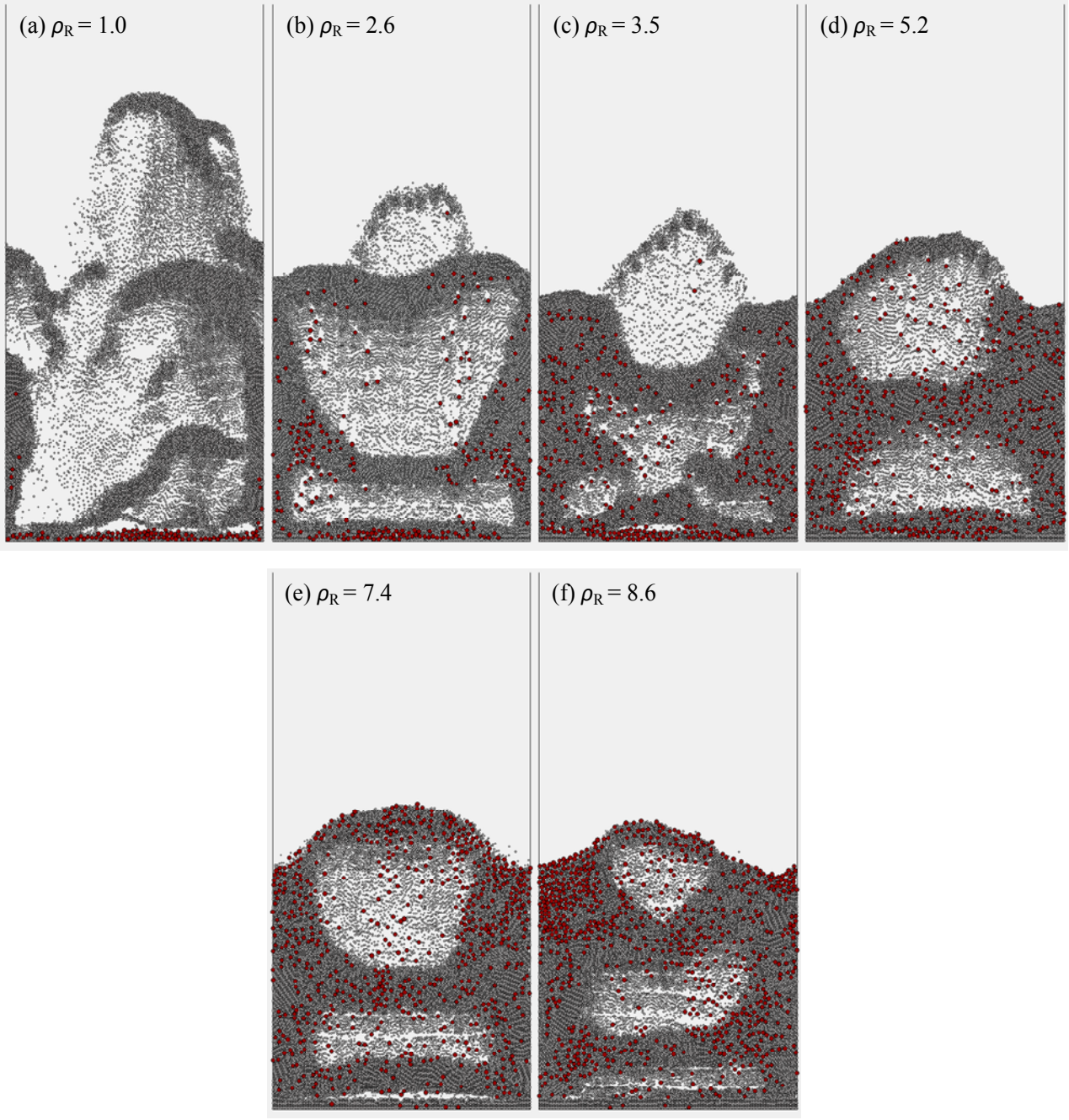

Figure 101: Snapshots of solids mixing status at different particle density ratios (t = 10.84 s, U_{ex} = 0.04 m/s, X_L=0.1, d_1 = 116 µm, d_2 = 328 µm, A_D = 20 × 200 mm^2).

Figure 102 shows the mixing index as a function of density ratio. As the density ratio increases from 2.6 to 8.6, the mixing index reaches the maximum value of 0.83 at ρ_R = 5.2 indicating very good mixing characteristics for the given conditions. This is despite the fact that the minimum fluidization velocity of small particle species at ρ_R = 5.2 (i.e., 0.025 m/s) is still smaller than that of the large one (i.e., 0.039 m/s). The reason for achieving an optimum mixing can be explained by the comparable slip velocities of two solid species (i.e. interstitial fluid velocity minus particle velocity). At ρ_R = 5.2 comparable slip velocities result in the same net forces acting on particles. Both small and large particle species are undergoing similar fluidized trajectories. Therefore, an equilibrium state of mixture can be achieved with optimum conditions for mixing. Increasing the density of small particles further, will increase the bulk density of the mixture, leading to smaller sized bubbles and lower local bed voidage, which in turn increase the average interstitial velocity. For larger particles with constant size and density, the increase in interstitial velocity renders the fluid hydrodynamic forces dominant over gravity and interparticle forces driving the large particles upwards. As a result these particles are floating above the bottom jetsam layer which mostly consists of the smaller and heavier particles.

Generally speaking, the existing correlations which were developed based on equal-size or equal-density systems are considered not to be applicable for prediction of layer inversion. A typical comparison between our simulation results and those of Wu-Baeyens' correlation [28] is presented in Figure 102. As shown in this figure, mixing index predictions of Wu-Baeyens' correlation exhibit a continuous decrease as the particle density ratio increases, while the simulation results show layer inversion phenomenon at ρ_R = 5.2. Clearly Wu-Baeyens' prediction did not exhibit a layer inversion behaviour for the binary mixture simulated in this study. This could be because there are two counter-acting phenomena as the density ratio increases: (i) de-mixing due to low bubble rising rate at greater mixture densities and (ii) mixing as the slip velocities of both species become closer by increasing the density ratio (when $\rho_R \leq 5.2$). Wu-Baeyens' correlation however only considers the effect of the former factor while ignoring the latter one.

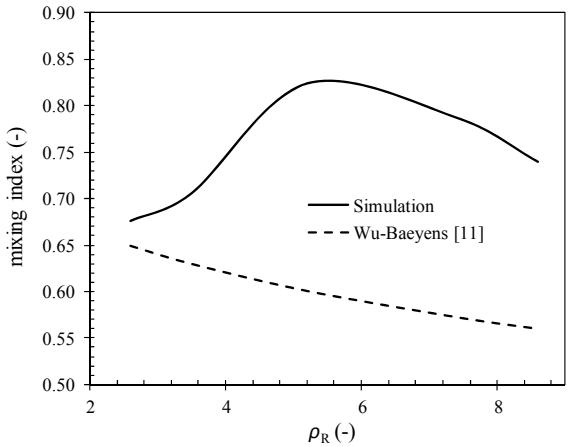

Figure 102: Influence of particle density ratio on mixing index (U_{ex} = 0.04 m/s, X_L=0.1, d_1 = 116 µm, d_2 = 328 µm).

The effect of excess gas velocity on mixing/segregation of binary mixture of particles was examined. The binary mixtures consisted of small particles with a diameter of 116 µm and a density of 2462

kg/m^3, and large particles with diameter of 328 µm and a density of 939 kg/m^3. Figure 46 illustrates the mixed status of binary mixtures under excess gas velocities ranging from 0.001 m/s to 0.07 m/s. The two phases flow pattern varies from bubbling to slugging fluidization regimes as the excess gas velocity increases. At low U_{ex}, most of the bubbles in the upper flotsam rich portion of the bed are small and rising slowly leading to poor mixing (Figure 103a). As the excess gas velocity increases, several behaviours are observed almost simultaneously. Firstly, the frequency of bubble initiation in the region just above the jetsam-rich portion increases and the bubbles in this area become larger in size. Subsequently, greater fraction of larger particles sinks forming a non-bubbling jetsam-rich layer which serves as an extended distributor. Secondly, bubble coalescence occurs, forming larger bubbles which rise to the surface at a greater rate. As a result, the amount of jetsam lifted in the growing wakes increases (Figure 103b). A further increase in $U_{ex,}$ enhances mixing as the majority of jetsam particles are carried away by the bubble wakes (Figures 103c – 103d). Whilst there is a distinct difference in fluidisation regime at high excess gas velocities (i.e. 0.04–0.07 m/s), the spatial distribution of large particles and local mixture composition remains the same (Figures 103e – 103h).

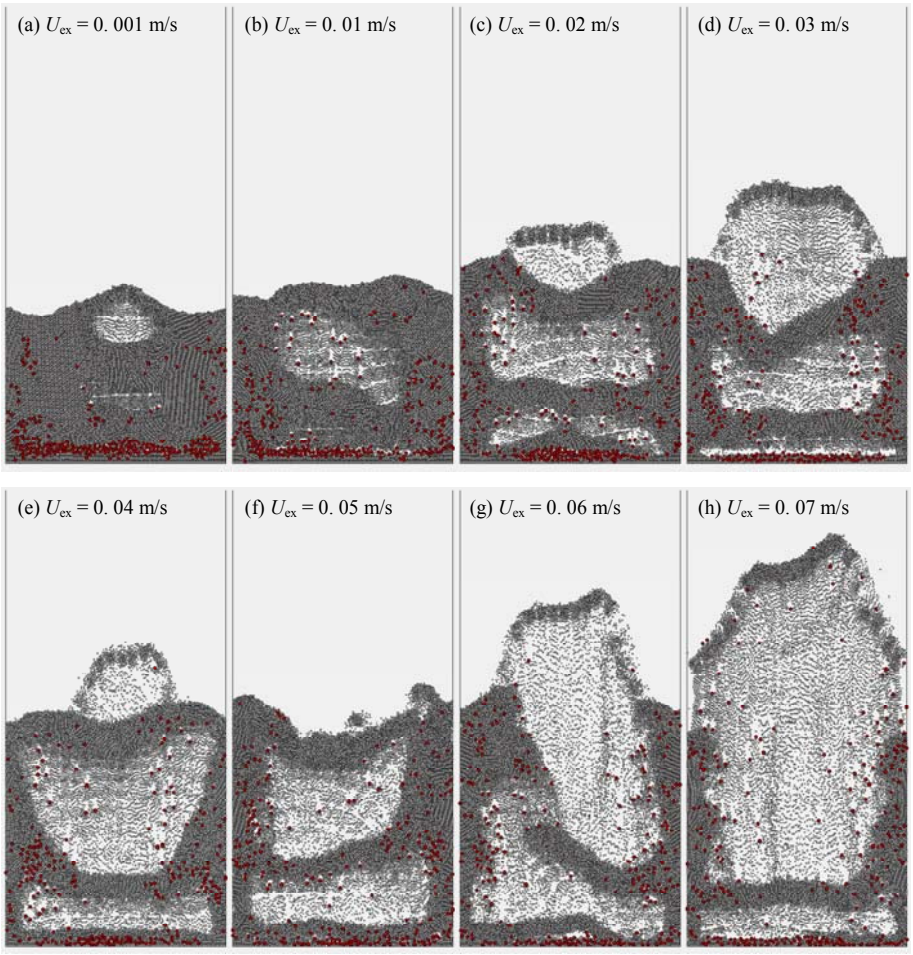

Figure 103: Snapshots of solids mixing status at different excess gas velocities (t = 10.84 s, X_L=0.1, ρ_1 = 2462 kg/m^3, ρ_2 = 939 kg/m^3, d_1 = 116 µm, d_2 = 328 µm, A_D = 20 × 200 mm^2).

Figure 104 shows the effect of excess gas velocity on mixing index at steady state. The Boltzmann function was used for fitting the simulation data. As Figure 104 shows, at superficial velocities just above the minimum fluidization velocity of mixture, the mixing index value is relatively small (e.g. 0.455 at U_{ex} = 0.001 m/s). This is mainly due to a low bubble frequency, low bubble rising rate as well as small bubble sizes. The small bubble size and slow bubble rising rate hinders the upward movement of jetsam in bubble wakes. This hindered upward movement of jetsam in competition to the segregation due to solids down-flow, makes it very difficult to maintain a high jetsam concentration in the upper region. As a result segregation dominates over the mixing and poor mixing results. As the excess gas velocity increases to 0.01 m/s, the bubble size increases and roughly half of the jetsam are carried upwards by the bubble wakes improving the mixing rapidly. As the excess gas velocity increases further, the amount of jetsam transported by bubble wakes increases remarkably in comparison to the rate of segregation through the down-flow of jetsam particles. The majority of jetsam particles are fluidized and the local mixture composition becomes relatively uniform, corresponding to a large mixing index. Any further increase in U_{ex} has little effect on the mixing index due to the counteracting behaviours namely the increasing frequency of bubble initiation and the increasing bubble rising rate. After U_{ex} increases to a certain point, the above two behaviours reach an equilibrium and no further change happens to the mixing status of binary mixture. The optimum conditions for mixing of binary mixtures appear to be a function of bubble size, bubble rising rate and bubbling dynamics (e.g., splitting and coalescing).

It is worth noting that the take-over velocity (U_{to}), defined as the critical superficial velocity at which the mixing index is equal to 0.5, is reached at very low U_{ex}. This is because the take-over velocity is a function of properties of the jetsam as well as the flotsam. Since particles are differing in both sizes and densities, the difference in particle fluidization hydrodynamics caused by particle size differences is offset by the difference in particle density. As such, the take-over velocity can be much smaller than equal-density or equal-size particulate systems.

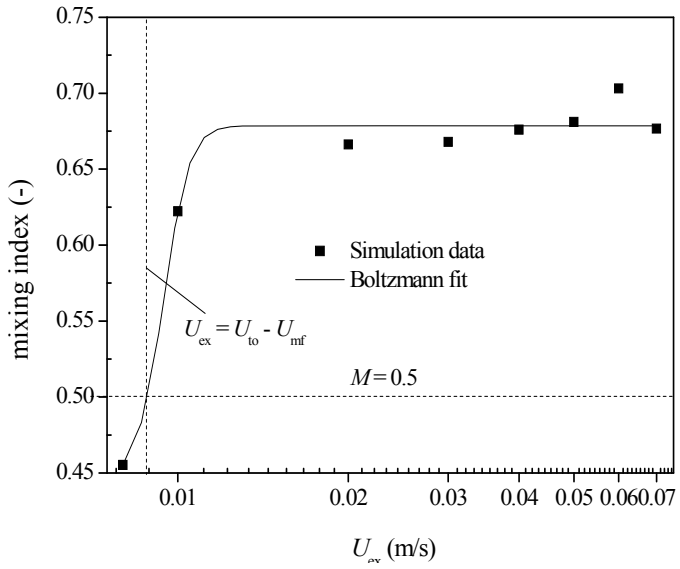

Figure 104: Influence of excess gas velocities on mixing index (X_L=0.1, ρ_1 = 2462 kg/m^3, ρ_2 = 939 kg/m^3, d_1 = 116 μm, d_2 = 328 μm, A_D = 20 × 200 mm^2).

Small domains with periodic boundary conditions have been used by other researchers to simulate gas-solid fluidized beds (e.g. [19]). The reasonable agreement between the CFD-DEM model predictions and the experimental data obtained in this study (Figure 100) is further supporting the above approach. However, it should be noted that there are a number of limitations associated with this approach namely (i) its applicability is limited to the conditions at which the wall effect is considered negligible, (ii) cannot be used when bubbles are comparable or larger in size than the domain width and (iii) only suited when information on bulk/average characteristics of the system are required. The relevance of these limitations to the presented simulations is discussed below.

Earlier studies have demonstrated that mixing and segregation in bubbling fluidized beds are closely related to bubble dynamics. It is also established that the wall effect is a function of tube-to-particle size ratio (e.g., [32-34]). A comprehensive study was conducted by Liu et al. (2008) to address the effect of confining walls on gas-solid fluidization behaviour using microsized particles (diameter: 96.4, 242.1 and 460.6 μm) in fluidized beds with inner diameters of 12, 20 and 32 mm. They found that the wall effect was only significant in the 12 mm bed. The result implies a critical tube-to-particle size ratio of 26 - 43. In this study, the particle size ranges between 116 and 393 μm. The tube-to-particle size ratio range is 229 – 776. Considering such large tube-to-particle size ratios, it is reasonable to assume that the wall effect is negligible.

Prior to commencing the simulations, the second criterion was checked by estimating the size of bubbles formed under the examined conditions using Choi et al. [35] bubble-growth model. Choi et al.'s model which correlates the bubble size to bubble volumetric flow rate and bubble dynamics (e.g., coalescence and splitting) has been successfully applied to beds of Geldart's group A, B and D particles and is expressed as,

$$\frac{\mathrm{d}\,d_\mathrm{b}}{\mathrm{d}\,h} = \frac{2.264 q_\mathrm{b} - f_\mathrm{s}^* d_\mathrm{b}/3}{U_\mathrm{sf} - U_\mathrm{mf} + 0.711\left(g d_\mathrm{b}\right)} \tag{4.30}$$

where U_sf and U_mf are the superficial and minimum velocities of particles, respectively. The volumetric bubble flux q_b is calculated by,

$$q_\mathrm{b} = U_\mathrm{sf} - \left(\frac{U_\mathrm{sf}}{U_\mathrm{mf}}\right)^{0.62} U_\mathrm{mf} \tag{4.31}$$

The average bubble splitting frequency f_s^* was determined by an empirical correlation that was developed based on the experimental data, expressed as,

$$f_\mathrm{s}^* = 6.47\times10^{-4}\left(\frac{U_\mathrm{sf}}{U_\mathrm{mf}}\right)^{0.454} \frac{g}{U_\mathrm{mf}} \tag{4.32}$$

In our simulations, Geldart's group B and A particles were used with gas superficial velocity varying between 0.013 – 0.083 m/s which corresponds to excess gas velocities of 0.00018 – 0.07 m/s. The correlation of Cheung et al. [36] was used to calculate U_mf of the binary mixture based on the size,

density and composition of each particle species. Figure 105 shows axial bubble size distribution at U_{ex} = 0.04, 0.05, 0.06 and 0.07 m/s, calculated using Choi et al.'s [35] model. It can be seen that the bubble size is 6.4 mm at h = 0.02 m for U_{ex} = 0.04 m/s, and is 12.7 mm at h = 0.03 m for U_{ex} = 0.07 m/s. These bubble sizes generated at the top of the bed under the examined conditions are smaller than the selected computational domain width (i.e., 20 mm), addressing the second limitation of the approach. It might be noted that the bubble size predicted by the numerical simulation appears larger than that predicted by Choi et al. model. The deviation can be attributed to the limitation of the Hoomans et al. correlation [15], which under-predicts the minimum fluidization velocity and subsequently leads to the over-prediction of the bubble size in the simulations. The third limitation is also addressed since the focus is on investigating the segregation and mixing behaviour of binary mixtures in terms of mixing index which is basically a bulk characteristic.

It should be noted that the model is unable to simulate the solid circulation near the wall. However since theoretically the wall effect is considered to be negligible, the influence of near wall solid circulation that is promoted by the wall effect on the bulk mixing/segregation behaviour is expected to be minor. Further validation of the model is necessary to investigate the extent to which these limitations affect the prediction of hydrodynamics of gas-solid fluidized beds. Finally, the 2D nature of the model appears to be the main factor leading to the observed deviation between the simulation predictions and the experimental results for the mixing index of binary mixtures of particles. The development of a 3D model which inherently addresses all of the above shortcomings is discussed in Chapter 7.

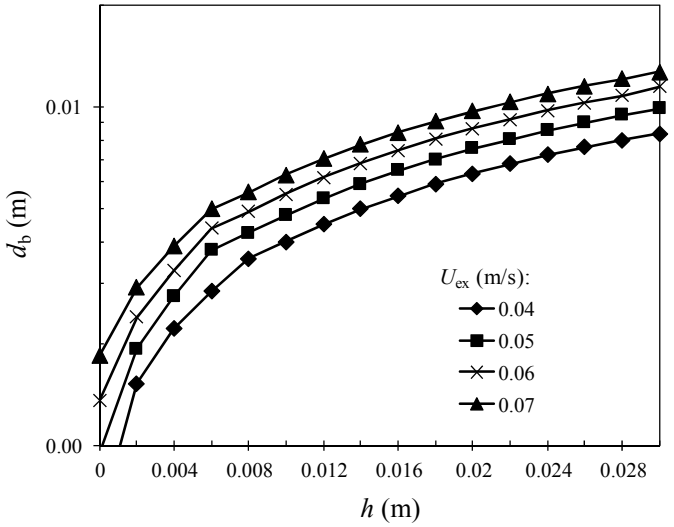

Figure 105: Axial distribution of bubble size under excess gas velocities of 0.04, 0.05, 0.06 and 0.07 m/s predicted by the bubble-growth model of Choi et al. [35].

4.2.5 Conclusions

An Eulerian-Lagarangian based model was developed to investigate the mixing/segregation behaviour of binary mixtures differing in both size and density. A modified Lacey's method was also employed to calculate mixing index taking into account both heterogeneous particle spatial distribution and particle

size differences. The approach for calculation of mixing index was found to exhibit very little dependency on the sampling cell size and the scrutiny level of scanning. The domain size was found to have little effect on the final mixing result. In shallow beds, a small mixing index was obtained with very large amplitude of fluctuation whilst the effect of bed height on mixing index was marginal in deep beds. The initial spatial-arrangement of particles played minor role in determining the final mixing status. It was found that as the size ratio of the binary mixture of particles increased, the mixing index decreased. Amongst different empirical formulas developed for the prediction of mixing index, the Wu-Baeyens predictions provided the closest result to the simulation data when the size ratio was changed. Reasonable qualitative agreement has been obtained between the simulation results and the experimental data. Layer inversion behaviour was observed when the density ratio varied from 1 to 8.4. The comparable slip velocities of two solid species were considered to be the main reason that gave rise to layer inversion. As the excess gas velocity increased, the mixing index increased rapidly at first and then plateaued after the excess gas velocity exceeded a certain value. Mixing can be achieved at a lower excess gas velocity for binary mixtures of different sizes and densities than in particulate systems with only size or density differences. Moreover, it appeared that the best mixing status of a binary mixture differing in both sizes and densities is a function of bubble size, bubble rising rate and bubbling dynamics (e.g., splitting and coalescing). It should be noted that the application of the 2D model developed in this study has several limitations. A comprehensive validation of the model is therefore needed to fully understand the extent of these limitations.

Chapter 5

PILOT-SCALE STUDIES ON REACTOR CONFIGURATION

5.1 MANIFOLD SWITCHING REACTOR (MSR) CONCEPT

The working principle of the manifold switching process is very simple. Unlike conventional chemical looping processes, in manifold switching the solid reactants are stationary. The process is carried out using two reactors operating in opposite modes, that is, one reactor undergoes oxidation while the other is under reduction. Once the solid reactants have been fully converted to products, the inlet gas streams are switched between oxidation (i.e. air) and reduction agents (e.g. steam, CO_2, flue gas, etc) to change the operating mode of the reactors. To avoid undesirable mixing of the oxidation and reduction agents a pulse of a swipe gas (e.g. He) is introduced to each reactor prior to every switching cycle.

Figure 106 schematically illustrates the evolution of the concentration and temperature fields within the MSR unit. As shown, initially the metal oxide particles are un-reacted since the sweep gas which is initially introduced into the reactor is non-reactive. As a result, the whole system is at a uniform initial temperature. Once the reactive gases are introduced into the MSR unit, heterogeneous reactions between particles and the gas begin and consequently a reaction front with a rate of W_1 propagates through the bed. Due to chemical reactions the bed temperature changes (see Figure 106b). This change leads to a difference between the bed and incoming gas temperatures, in turn, giving rise to a heat front which travels through the bed at a rate of W_2.

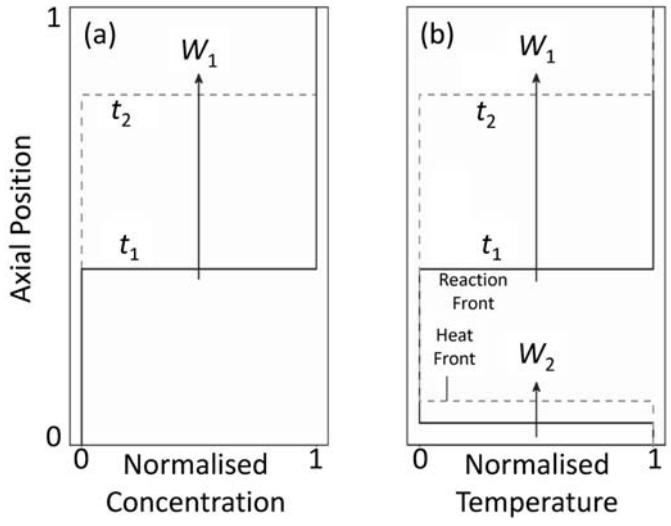

Figure 106: Schematic representation of the evolution of the normalised fields for (a) concentration of product gases and (b) bed temperature within a typical MSR unit.

5.2 EXPERIMENTAL METHODS & TECHNIQUES

5.2.1 Sample Preparation

Oxides of Cu(II) on silica support were employed in MSR experiments. The oxides were prepared by the wet impregnation method given that at the time when MSR experiments were underway we had not have master the spray drying method. The preparation of the metal oxide samples begun by the direct mixing of commercial CuO powders (Sigma-Aldrich) with silica powder at a 3:2 carrier/support weight ratio. Distilled water was then added to the carrier/support mix to form a paste. The paste was dried in an oven at 105^{o}C for 36 hours to free up the capillary water. The dry paste was then calcined for 5 hours under nitrogen in a high temperature furnace at a set temperature of 750^{o}C. The calcined sample was pulverised in a ball mill and sieved to a particle size range of 90-106 μm (mesh 170 < particle size < mesh 140[§]). The quality of the final products were evaluated using X-Ray fluorescence (XRF) and X-Ray Diffraction (XRD) methods to determine the distribution of metal active sites on the surface and within the carrier particles, respectively. The internal structure of samples were characterised by mercury porosimetry and BET (Brunauer-Emmer-Teller) surface area measurements. In particular, the thickness of platelike grains of the CuO layer was determined from the weight fraction of CuO in the sample and the active surface area data. Table 12 summarises the physical characteristics of the oxides prepared in the MSR study.

Table 12: Properties of CuO on alumina support

Property	Unit	CuO
Actual active metal oxide content	%wt	62
Molecular weight of the active metal oxide	kg kmol^{-1}	79.55
Solid density	kg m^{-3}	4200
Molar density of the active metal oxide	mol m^{-3}	32734
Particle size	μm	90 to 106
Porosity	--	0.6
BET specific surface area	m^2 g^{-1}	44
Grain size	m	--
Thickness of the metal oxide layer (CuO samples only)	m	1.22×10^{-8}

5.2.2 Procedure

The experimental setup shown in Figures 10-11 was employed to carry out a comprehensive set of MSR experiments. A total of 20 thermocouples were fitted along the length of both reactors so that the axial temperature distribution can be measured with a high degree of spatial resolution. Similarly, 10 iso-kinetic sampling ports were fitted to each reactor for collection of gaseous reactant and products

§ *ASTM-E11 standard*

along the reactor length at 1 min intervals. Collected gas samples were analysed using a micro-GC unit. The reactors were externally heated by two tube furnaces. Insulation materials were inserted between the furnace and reactor walls to minimise radial heat losses.

A typical experiment consisted of several redox (reduction / oxidation) cycles to allow the sample to stabilise. Typically the data set corresponding to the fifth redox cycle was used for determination of reaction data since the redox properties of the sample considerably deteriorated over the first few cycles until they reached a repeatable level at or on about the fifth cycle. The experimental procedure involved the following steps: (i) a charge of between 250 to 500 g of metal oxide was loaded into each reactor, (ii) the heating system was turned on and the reaction temperature was set to a pre-determined level, (iii) the reactor was then purged with nitrogen and the sample was heated under nitrogen at a rate of 100^{o}C/min, (iv) once the desired temperature was reached the nitrogen flow was turned off and instead the reacting gases were introduced, (v) the samples were then allowed to react with the gas mixture until the changes in the concentration of products at the outlet of each reactor diminished, (vi) at this point the flows of reacting gases were stopped and a purge of helium was introduced for about 10 s to avoid the mixing of air and reducing gas, (vii) steps iv to vi were repeated at least three times and the measurements of temperature distribution and product concentration corresponding to the final redox cycle (typically fifth cycle) were collected for further analysis.

5.3 RESULTS AND DISCUSSION

Figures 107 and 108 show the temporal and spatial distributions of the oxygen concentration and gas temperature in a MSR unit during a typical oxidation half cycle. From these figures the propagation of the reaction front can be easily observed. It is also clear from these figures that the oxidation reaction precedes at a sufficiently high rate. The reference to "sufficiently high" rates is made in the context of comparing the fixed-bed results presented in Milestone Report #1 and manifold switching results presented in Figure 20. For instance, it takes about 10 min (@95^{o}C) in the fixed-bed setup to reach a 100% oxidation conversion in the fixed-bed setup whereas in the MSR unit the same process takes about 4 min (Figure 107). Figure 108 in particular indicates that the high oxidation rate results in a relatively steep temperature front and that the temperature rise appears to be uniform over the reactor length. The shape of the temperature profiles over the regions where temperature is decreasing (e.g. axial positions between 0.7 and 1 m for the 4 min plot) is an indication of radial heat losses although our analyses confirm that the effect of such losses in the centre of the reactor in a given redox cycle is about ±8 which is quite negligible.

Figure 109 illustrates the temporal variation of the gas temperature at the reactor outlet for a complete oxidation half cycle. As can be seen, the temperature profile is not completely uniform when the oxidation half cycle begins primarily as a result of residual heat (i.e. preheating) from the previous reduction half cycle. A careful analysis of all experimental data has indicated to us that while such small temperature effects may be eventually levelled out, they usually lead to larger deviations from the desired temperature profiles and hence lower the overall effectiveness of the manifold switching process. These temperature effects can be cancelled out either by increasing the reactor length which effectively increases the residence time of the heat front in the bed, or by mild fluidisation of the particle bed for a relatively short period of time just after the completion of the proceeding half cycle.

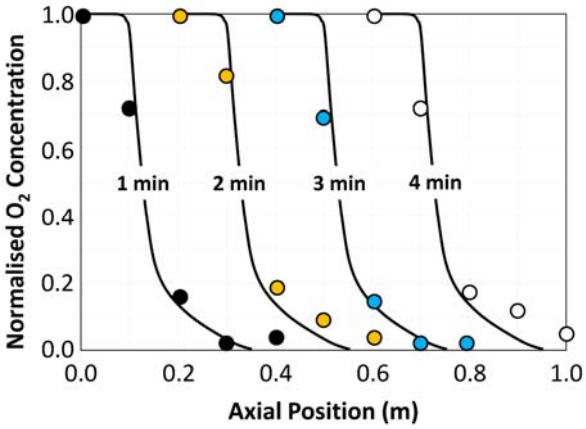

Figure 107: Temporal and spatial evolution of the normalised oxygen concentration within a typical MSR unit.

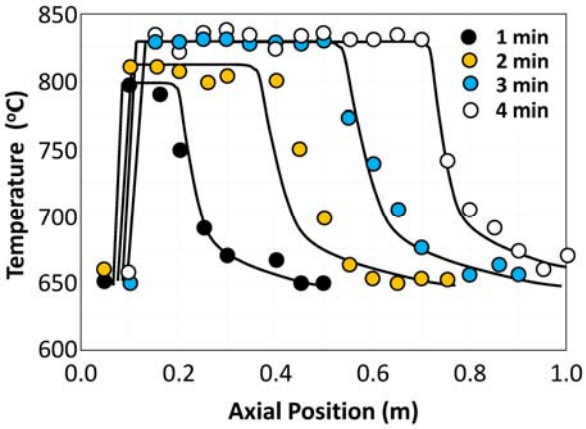

Figure 108: Temporal and spatial evolution of the temperature within a typical MSR unit.

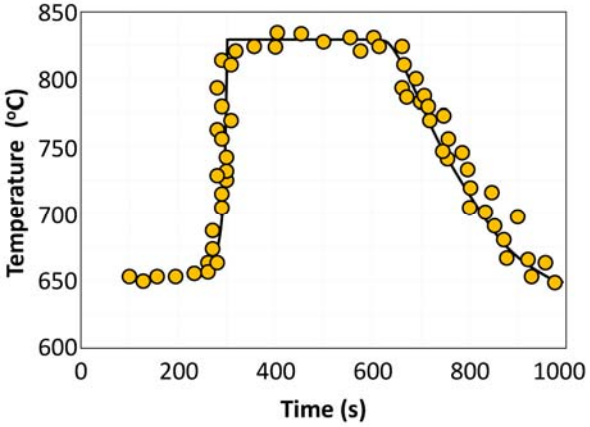

Figure 109: Variation of the reactor outlet temperature as a function of time within a typical MSR unit.

Figure 110 shows plots of maximum temperature rise (that is the difference between the initial and maximum temperatures at a given axial location in a typical reaction half cycle against reactor length for three different cases. The base case refers to results corresponding to a residence time of 15 min under standard operating conditions. However, in the "increased flow rate" case the volumetric flow rate of the incoming gas has been increased by a factor 5 (gas velocity was kept just below the minimum fluidisation velocity). All other parameters and variables for this case were identical to the base case. Similarly, in the "decreased reactivity" case the metal oxide particles were doped with a layer of inert material to lower their reactivity by a factor 2. Again, all other parameters and variables for this case were kept the same as the base case.

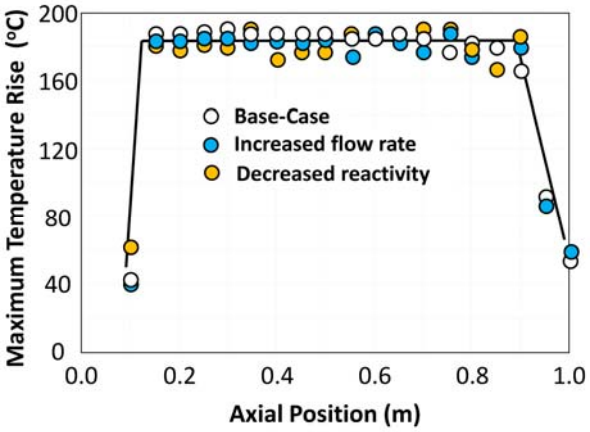

Figure 110: Plots of maximum temperature rise as a function of the axial position for a typical MSR unit.

The plots shown in Figure 110 indicate that maximum temperature rise is neither sensitive of to the gas flow rate nor reaction kinetics given that plots for all three cases are almost identical. This is perhaps the most important finding of MSR studies as it implies that the reactor temperature profile is not a function of reaction kinetics or gas flow rate, but only of the properties of gas and solid material. We have verified this finding through a simple analytical analysis which resulted in the following expression:

$$\Delta T = \frac{-\Delta H_{\mathrm{R}}}{\dfrac{C_{p,\mathrm{s}} M_{\mathrm{act}}}{w_{\mathrm{act}} \xi} - \dfrac{C_{p,\mathrm{g}} M_{\mathrm{O_2}}}{w_{\mathrm{g,O_2}}^{\mathrm{in}}}} \tag{5.1}$$

where

- ξ represents the ratio of the number of moles of gas and solid needed for the oxidation reaction
- w_{act} denotes weight fraction of the reactive material in the oxygen carrier
- $C_{p,s}$ and $C_{p,g}$ are the specific heats of solids and gas respectively
- $w_{g,O2}^{in}$ is weight fraction of the reactive component in the gas

- M_{act} and M_{O2} are molecular weights of reactive component of the solid and oxidation agent (air) respectively
- ΔH_R is the reaction enthalpy

From a process operation and safety point of view such independence from reaction kinetics and flow rate is very advantageous. Therefore, as long as the oxidation reaction is fast enough, any potential decrease of the activity of the oxygen carrier will not directly affect the reactor temperature and temperature rise. This suggests a system with high degree of stability and robustness to deal with an industrial level of variability.

5.4 CONCLUDING REMARKS

Unlike conventional chemical looping systems, in MSR based systems carrier particles are not circulated between the two reactor assemblies and the cycle is completed by switching over the reacting gases from one reactor assembly to the other. Each reactor, therefore, functions periodically as a fuel reactor and an air reactor. As a result the oxygen carrier particles are not subjected to cyclic moves from one reactor to another and, hence, their physical integrity can be maintained over a much larger of repeated redox cycles. This opens up a pathway for a much wider use of low mechanical strength yet highly effective oxygen carriers for chemical looping air separation. The experimental results presented in this report have certainly confirm the strengths of the manifold switching concept and demonstrated that the technique has no detrimental impact on the cyclic redox reactions between oxygen carrier particles and air. However, the use of packed beds in MSR units may lower the degree of mixing in the reactors and ultimately lead to formation of undesirable hot spots in the reactors. This however can be resolved if packed beds are periodically subjected to mild fluidisation.

Chapter 6

DETERMINATION OF SCALE-UP RULES

6.1 OVERVIEW

The term scale-up generally refers to the task of designing large-scale equipment based on the knowledge gained experimentally using a small-scale laboratory version of the equipment. The underlying principle of scale-up involves establishing the relationships that exist between different scales of the processing equipment. Such relationships are usually expressed in terms of a series of dimensionless numbers (i.e. size independent) that describe the processes involved in the operation of the equipment. These dimensionless numbers form the basis for scaling from one size to another. Some well-known examples of dimensionless numbers include the Reynold's number which describe the simple case of developed flow through tubes or Nusselt's number that is typically used to characterise the heat transfer process.

In practice, by maintaining a suitable set of dimensionless numbers constant during the conversion of small-scale information to the full-scale unit (assuming that both the small- and large-scale units are geometrically similar), one would be able to design the full-scale equipment from the small-scale information and/or data. As can be appreciated, the most important step in scale-up is to accurately determine the dimensionless numbers.

Given that from a hardware point of view CLAS and ICLAS processes are carried out using bubbling fluidised bed reactors, the dimensionless numbers required for scale-up have to be able to characterise both the hydrodynamics and chemical reaction processes taking place in fluidised beds.

However, scale-up of fluidised beds is a difficult and complex task because the hydrodynamics and chemical reaction phenomena are coupled through the heat and mass transfer processes as well as particle transport. For example it is well known that the bubble size does not change upon scale-up but reactor diameter does. As a result, flow characteristics (i.e. hydrodynamics) would be very different in the small and large reactor which, in turn, means the mixing, mass-transfer and heat transfer processes would be different (see Section 6.2 for more details). Because of these of scaling issues, the maximum scale-up factor of 100 is considered for bubbling fluidised beds.

6.2 MAIN CHALLENGES IN SCALING-UP FLUIDISED BED REACTORS

In a fluidised bed, the bed of solid particles is held in suspension by an upward flow of a fluidising agent (e.g. a gas such as air in the case of gas-solid fluidised beds). This establishes a liquid-like behaviour in the particle bed which is commonly referred to as fluidisation. In the case of bubbling fluidised beds, the fluidising agent forms pockets of gas (i.e. bubbles) which travel upwards through the

expanded particle bed. Today fluidised bed reactors, especially bubbling fluidised beds, are used in an extensive array of industrial applications ranging from the chemical, metallurgical and environmental to pharmaceutical sectors. The interest in fluidised bed reactors originates from their technical advantages over the other types of reactors such as fixed bed reactors. These advantages become particularly important in systems, such as CLAS and ICLAS, where reacting particles are suspended by the reactant gas (i.e. fluidising agent). The key advantages include: (i) large gas-solid interface area, (ii) excellent particle mixing and gas-solid contacting which not only enhances mass transfer, but also the heat transfer between particles and the gas as well as the heat transfer to the internal surfaces of the reactor such as reactor walls and heat exchanger tubes, (iii) nearly isothermal temperature distribution even for highly exothermal reactions, and (iv) a constant and low pressure drop in the bed which does not depend on the gas velocity; ensuring low-energy consumption and efficient reactor operation)

However, bubbling fluidised bed reactors also suffer from a number of technical shortcomings which impact upon their operations especially when beds with irregularly shaped and polydispersed particles are operated at high gas velocities and elevated temperatures and/or pressures (like in CLAS & ICLAS). These shortcomings which make it difficult to describe the processes / phenomena taking place within the fluidised bed reactor also make the task of scale-up complicated and challenging. The key challenges are:

- Scale Dependency of Design Parameters - One of the main challenges is the scale dependence of many important design parameters such as particle properties, mass/heat transfer and bubble growth. In particular the mass transfer of reacting gas from the bubble phase to the dense phase is highly scale-dependent. The key reasons for this scale dependence of fluidised bed parameters are wall-effects which play a more dominant role in the small-scale units than in the large-scale ones. Contact with the reactor wall affects both the particle and gas phases as well as their interaction with the bed.

- Bubble Phase Characteristics - Among the bubble phase features, the bubble size and rise velocity are considered to be amongst the most important design factors. But they strongly depend on the reactor scale. For this reason, slugging (when the bubble diameter becomes equal to the vessel diameter) is more likely to happen in small-scale units because the maximum stable bubble diameter is in the order of 15 to 30 cm. However, slugging starts if the bubble size is about 2/3 of the bed diameter. Therefore, in sufficiently large beds, slugging will not occur and hence the fluidisation in the large-scale unit will be significantly different from that observed in the small-scale unit. Due to wall effects though, the rise velocity of slugs would be about 50% lower than that of the bubbles of the same diameter. Therefore, the gas residence time in the bed is decreased and gas bypassing is increased ultimately lowering the chemical conversion rate and product yield. The reduced chemical conversion is particularly encountered with fast reactions which are often diffusion-controlled.

- Gas-Solid Mixing – It is well known that the solids mixing rate (i.e. the axial dispersion coefficient) is directly proportional to the bed diameter as well as to the bed aspect ratio H/D, the fines content and the superficial gas velocity. As a result, in small-scale reactors particles are usually moved upward in the wake of bubbles while in large-scale reactors toroidal shape structures are dominant. This difference between small and large-scale reactors in terms of gas-solid contacting pattern makes it difficult to match solids mixing in the scale-up.

6.3 SCALE-UP METHODOLOGY AND PROCEDURES

To overcome the scaling issues outlined above, in this project we devised and implemented a particular approach whereby "scale-up" rules are obtained using a range of experiments, theoretical and modelling results. Figure 111 shows the procedure for arriving at scale-up rules for air separation systems. As can be seen, the work leading to this outcome required a number of experimental setups which were discussed earlier in Chapter 2. In what follows, we describe the scale-up procedures employed here followed by the list of validated scale-up rules.

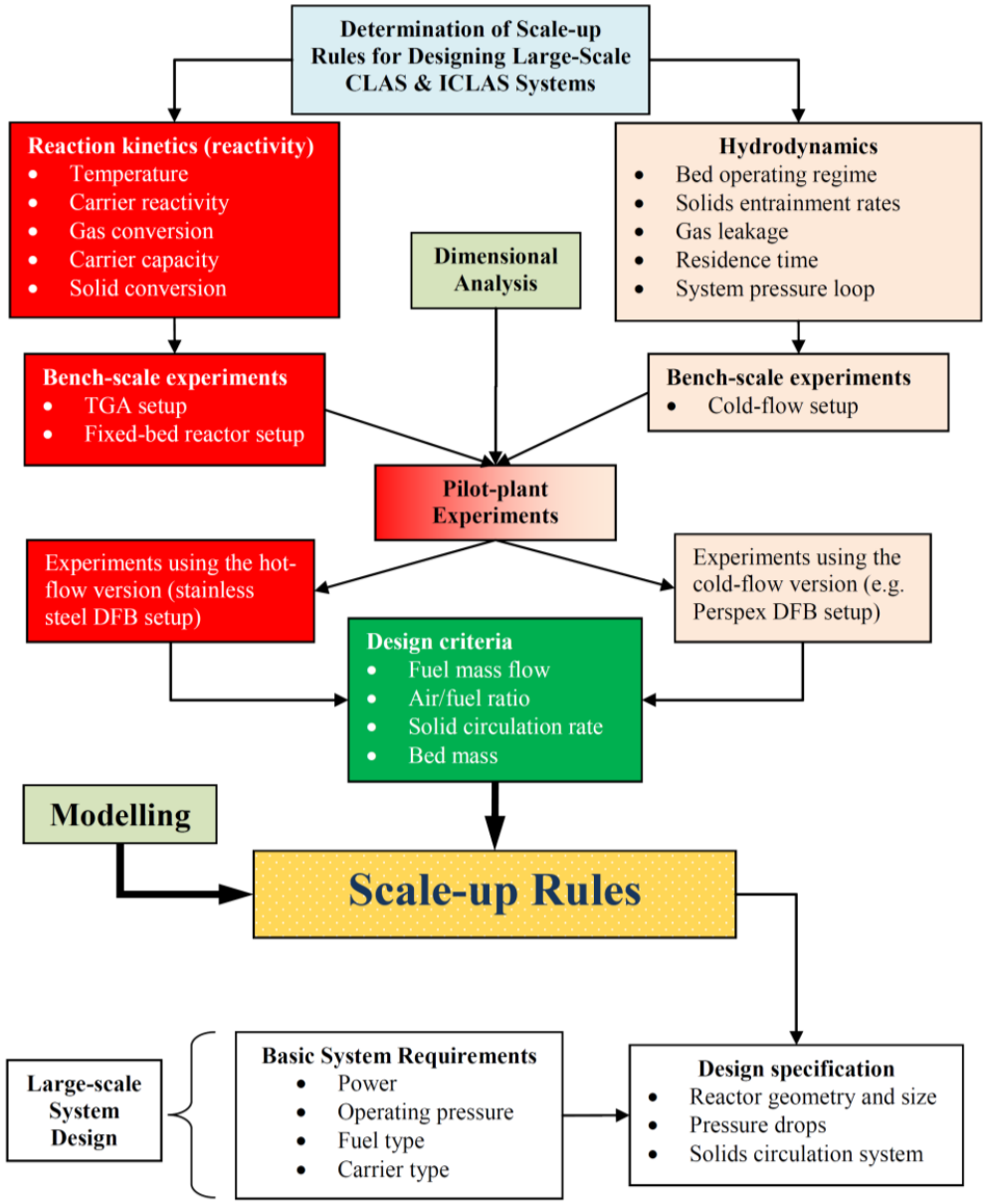

Figure 111: Flowchart of the procedure implemented in this project for determining scale-up rules.

Under the prerequisite that the reaction kinetics and reactivity of oxygen carrier particles are known, the procedure to a proper scale-up involves:

- Selections of the appropriate fluidisation regime and reactor type from reaction kinetics, reactivity and chemical conversion studies. This is the so-called screening procedure.
- Construct a cold-flow lab-scale reactor model (D~0.2 m) which is capable of answering questions of importance for the design of the industrial plant. Key questions include;
  - Particle attrition and entrainment
  - Solids feeding and discharge issues
  - Residence time distribution (RTD) studies
  - Effect of particle distribution
  - Solids flow and circulation
  - Solids separation and segregation
  - Gas bypassing
  - Gas leakage
- Built a pilot-scale prototype (D~0.2 - 0.5 m) which is an intermediate before full-scale plant
- Construct the either a full-scale plant (D>0.5 m) or a demonstration plant by using data and experience from the cold-flow model and the pilot-scale unit.

6.4 HYDRODYNAMIC SCALE-UP

Following the procedure outlined in the previous section, for hydrodynamic scale-up studies we first design and built a small-scale cold flow model described earlier in Section 2.1.1). The cold-flow model was then used in a comprehensive series of hydrodynamic studies (see Chapter 4) to answer the questions related to particle transport; including those listed above (see Section 6.3). Based on the knowledge gained from the cold-flow model and reactivity studies we then designed, built and commissioned a 10 kW_{th} pilot-plant prototype. This was achieved by dimensional analysis and using the approach suggested by Glicksman where by maintaining identical values of several key dimensionless parameters in bench- and pilot-scale units, the physical dimensions of the pilot-scale unit were calculated from those of the bench-scale setup. As outlined in Chapter 2, the key dimensionless parameters used in this analysis are:

$$\frac{u^2}{g.L},\ \frac{\rho_p}{\rho_f},\ \frac{\rho_p.u.d_p}{\eta^2},\ \frac{\rho_f.u.L}{\eta},\ \frac{G_s}{\rho_p.u},\ bed\_geometry,\ \Phi,\ PSD \qquad (2.1;\ \text{repeated here})$$

where u is superficial gas velocity, g the acceleration of gravity, L characteristic length, ρ_p particle density, ρ_f gas density, d_p particle diameter, η dynamic viscosity of the gas, G_s solid circulation rate, Φ particle sphericity, and PSD the particle size distribution.

The same dimensional analysis methodology was used to design the large-scale demonstration unit descried in Chapter 2. The validity of the scaling was assessed by comparing the experimental data collected from the large-scale unit against those obtained from the cold flow model.

The large-scale experimental campaign involved running a number of tests in the large-scale demonstration unit (Figure 14). In each test only the flow rate for the air reactor supply was systematically changed while the gas flow rate to the reduction reactor (or fuel reactor) and the both loop seals were kept at a constant flow rate. The measurements of the flow rates from were made by measuring the pressure difference across orifice plate mounted on the supply lines of the air reactor, reduction reactor and the loop seals.

The pressure profile in the demonstration unit was also accurately measured using a series of pressure transducers. The measurements were taken after 10-15 minutes from the start of the test (or scheduled changes in the air reactor flow rate) to ensure that the system reaches a stable and steady-state mode of operation. The pressure measurements were then taken at 5 s intervals for period of 2-3 minutes. The results of pressure profile measurements were compared with those obtained from the bench-scale cold-flow setup.

The initial particle loading (i.e. solid inventory) in all tests was the same and followed the distribution shown in Figure 112. The data shown in Figure 112 were estimated from the measurements of the particle bed dimensions in the demonstration unit and the physical properties of particles. Table 13 provides more details about the initial solid inventory.

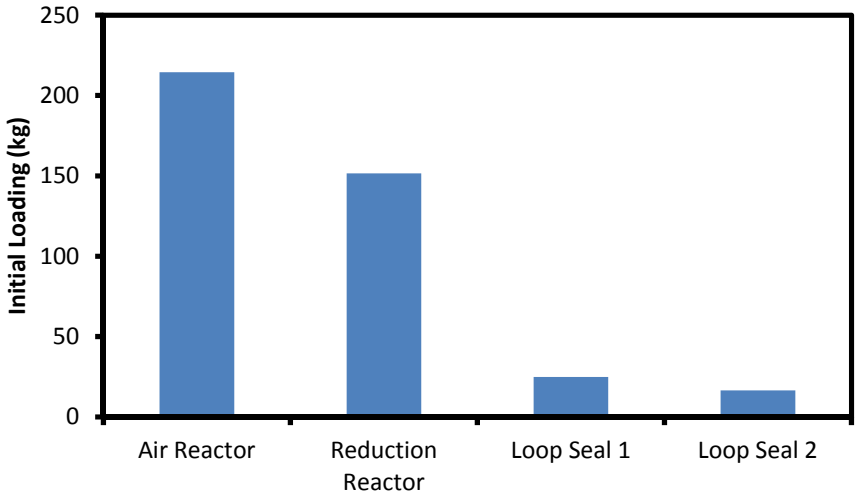

Figure 112: Initial particle loading in each component of the large-scale demonstration unit.

Table 13: Initial solid inventory calculations

Unit Operation	Bed Height (m)	Cross Sectional Area (m^2)	Bed Volume (m^3)	Particle Density (kg/m^3)	Void Fraction (assumed)	Solid Fraction	Solid Volume (m^3)	Inventory (kg)
Air Reactor	0.74	0.19625	0.1452	2462	0.4	0.6	0.08714	214.5
Reducer (fuel reactor)	0.33	0.10254	0.2475	2462	0.4	0.6	0.06152	151.5
Loop Seal (1)	0.21	0.08	0.0168	2462	0.4	0.6	0.01008	24.8
Loop Seal (2)	0.14	0.08	0.0112	2462	0.4	0.6	0.00672	16.5

Figure 113 shows a comparison of the pressure profiles for three different flow rates in the air reactor achieved by changing its inlet pressure between 37 and 41 kPa. As can be seen, the highest pressure is reached in the air reactor and for the range of inlet pressures studied here the pressure profiles are almost identical.

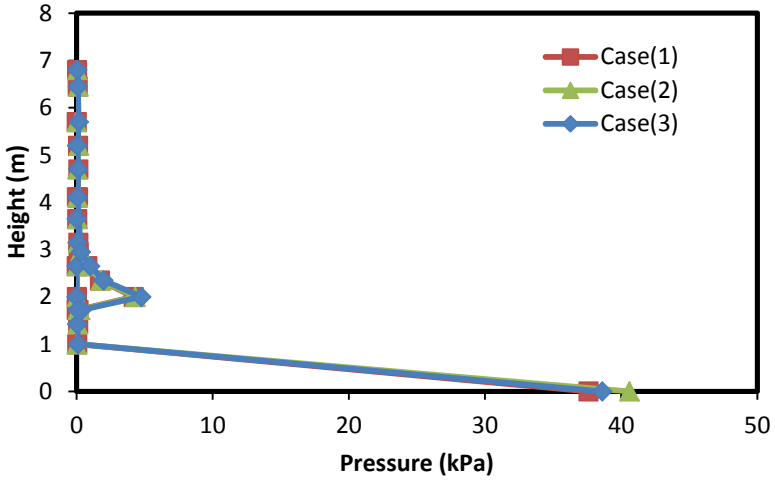

Figure 113: Pressure profiles for the demonstration plant for d_p= 120µm GB [Case1: P_{in}=37.6 kPa, Case2: P_{in}=40.60 kPa and Case3: P_{in}=38.60 kPa].

The profiles shown in Figure 113 very closely resemble the pressure profiles from the 10 kW_{th} pilot-plant (see Figure 114) although the magnitudes, as shown in Figure 115, are different due to scaling effect. However, by and large the results from the demonstration plant indicate that the overall behaviour and performance characteristics of the large-scale plant match those of the bench-scale cold-flow model and the pilot-plant. This verifies the validity of the dimensionless parameters (eq 2.1) used in the scaling up the bench-scale information and suggests that these dimensionless parameters can be considered as part of the set of scale-up rules (see Section 6.6).

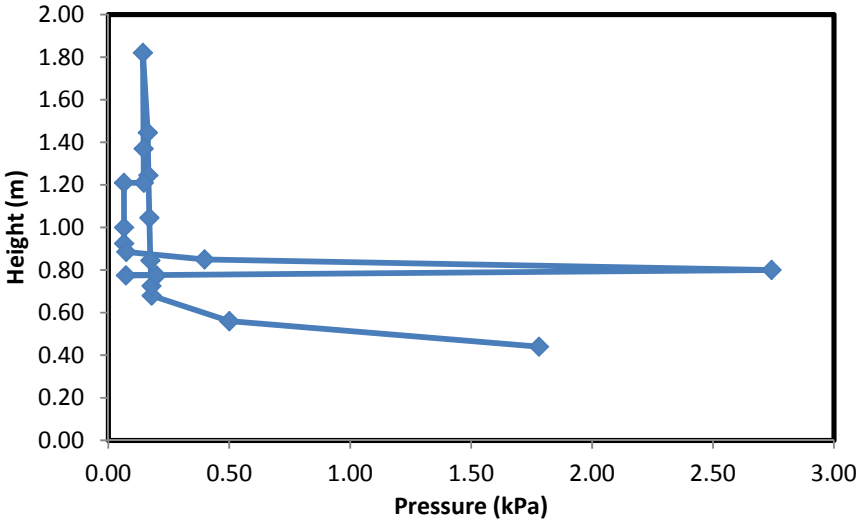

Figure 114: A typical pressure profile for the 10 kW_{th} pilot-plant prototype.

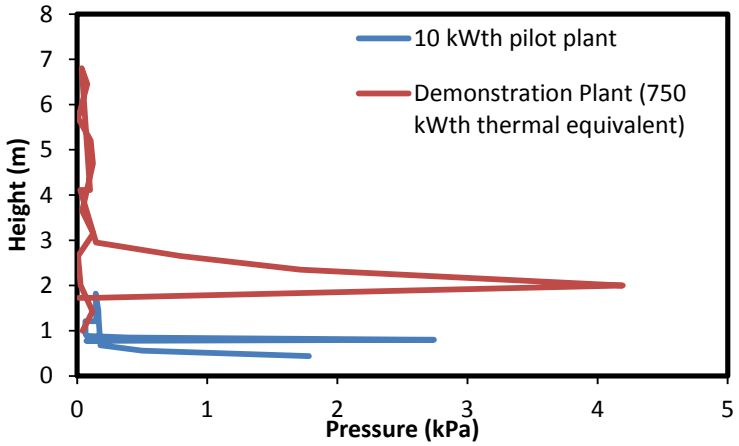

Figure 115: Comparison of pressure profiles of the demonstration unit and 10 kW_{th} pilot-plant.

6.5 CHEMICAL REACTION SCALE-UP

In addition to hydrodynamic similarity the chemical similarity (in terms of reactivity, selectivity and conversion) has to be considered in the scale-up of the bubbling fluidised bed reactors. Given that in reactive systems scaling always impacts upon the interactions among heat and mass transfer, kinetics and hydrodynamics processes, the chemical conversion and selectivity of reacting particles within such systems would also inevitably influenced by scaling. For instance, if during scale-up different particle sizes are used in the small- and large-scale models, the resultant full-scale unit may not operate according to the design specification because the intra-particle diffusion limitations might have been overlooked during scale-up studies. Therefore, in the scale-up of reacting systems the rate determining step of the process (i.e. reaction, convection, or diffusion) must be identified.

As far as the CLAS and ICLAS processes are concerned, the scale-up of the air reactor can be handled without any major difficulties since in this reactor a constant mean particle residence time is required for scale-up. The required particle residence time, in turn, can be easily determined from the reactivity data collected for various metal oxides in the 10 kW_{th} pilot-plant prototype.

From the reaction engineering point of view the main challenge in the scale-up of the CLAS and ICLAS processes is the reduction reactor. Similar conversions can only be achieved if the gas solid contacting is similar at different scales. While reaction rate constants and order of reaction are determined by reactivity tests, the required gas residence time is underpinned by the reactor mass. In this study constant gas residence time has been used as the key scaling parameter although for a more general case the mass transfer coefficient X (dimensionless interphase mass transfer) and the dimensionless reaction rate k* as proposed by Grace (1986) are suitable scale-up parameters.

In this study detailed assessments of the above scaling parameters for chemical reaction scale-up of the reduction reactor were carried out by a combined set of theoretical analysis and mathematical modelling (Chapter 7). These assessments verified the validity of the scaling parameters which are reported in Section 6.6.

6.6 SCALE-UP RULES

Given the material covered in Sections 6.4 and 6.5, the following set of scale-up rules (i.e. criteria) is proposed for scaling of the CLAS or ICLAS based processes:

Table 14: Scale-up Rules

Scaling Category	Scale-up Rule*	Description
Hydrodynamic Scaling	$\frac{U_0 \rho_g d_p}{\mu} = \text{constant}$	Reynolds number (ratio of inertial to viscous forces)
	$\frac{U_0^2}{gD} = \text{constant}$	Froude number (ratio of inertial to gravitational forces)
	$\frac{\rho_g}{\rho_p} = \text{constant}$	Gas to particle density ratio
	$\frac{D}{H} = \text{constant}$	Aspect ratio
	$\frac{d_p}{D} = \text{constant}$	Ratio of particle to reactor diameter
	$\phi = \text{constant}$	Particle sphericity ($0 \le \phi \le 1$)
	$psd = \text{constant}$	Particle size distribution
	Geometrical similarity in terms of shape and design	
Chemical Reaction Scaling	$\frac{\text{Air Flow Rate}}{\text{Solid Inventory}} = \text{constant}$	Air reactor
	$\frac{\text{Reducing Gas Flow Rate}}{\text{Solid Inventory}} = \text{constant}$	Reduction reactor
	$M^* = \text{constant}$	Reduction reactor
	$k^* = \text{constant}$	Reduction reactor

* where:

D ≡ Reactor characteristic diameter
d_p ≡ Mean average metal oxide particle diameter
g ≡ Gravitational acceleration
H ≡ Reactor characteristic height
k^* ≡ Dimensionless reaction rate constant
M^* ≡ Interphase mass transfer coefficient
U_0 ≡ Superficial gas velocity
ϕ ≡ Dynamic viscosity of the gas
μ ≡ Dynamic viscosity of the gas
ρ_g ≡ Gas density
ρ_p ≡ Particle density

Chapter 7

MATHEMATICAL MODELLING

7.1 OVERVIEW

As noted in Chapter 4, earlier in the project we developed a two-dimensional (2D) CFD-DEM model for investigating the particle transport issues such as segregation in CLAS / ICLAS systems. The model however lacked chemical reaction, energy balance and heat transfer sub-models and hence was more suited for examination of non-reacting systems like the bench-scale cold-flow setup. On the basis of the experience gained during the development of the 2D model, we also developed a three-dimensional (3D) CFD-DEM model for:

1. Studying the performance characteristics of reacting versions of the CLAS / ICLAS processes such as the 10 kW_{th} pilot-plant.

2. Assisting with the scale-up rule studies.

3. Assisting with the engineering design of CLAS / ICLAS processes particularly in regards to the sensitivity of the design geometry to inlet velocities for the reduction reactor, the air reactor and the loop seals.

The basis of the 3D hybrid model is a commercially available CFD-DEM software package called FLUENT. However, due to the limitation of the base FLUENT model for proper description of complex processes occurring within the CLAS / ICLAS systems, we have extensively modified the base model and incorporated a number of sub-models into the base model using the User Defined Subroutine (UDS) option available in FLUENT.

In the final version of this 3D hybrid model the solid phase (i.e. particles of the metal/metal oxides) is tracked using the discrete element method, while the fluid phase is described by the modified Navier-Stokes equation derived by replacing the point mechanical and fluid related variables with averaged values. The particle temperature is calculated by the energy balance equation considering the energy released or absorbed during the cyclic redox reactions of metal oxides. Similarly, the fluid temperature is calculated by applying the conservation of energy (1^{st} law of thermodynamics) with a heat source accounting for the convective heat transfer to and from particles.

The model has been validated by comparing the predicted solid circulation rate with the experimental data collected from the bench-scale cold-flow model as well as those from the 10 kW_{th} pilot-plant. The descriptions of the hybrid CFD-DEM model and its sub-models together with some of the predictions of the model are presented in the following sections.

7.2 DESCRIPTION OF THE 3D CFD-DEM MODEL

7.2.1 Governing Equations for the Fluid-Flow and Particle Transport

The gas-solid flow pattern in a typical CLAS / ICLAS system exhibits the characteristics of bubbling fluidisation regime, in which the local solid concentration is very high and the influence and the presence of particles on the gas flow cannot be neglected. The presence of solid particles in the two-phase flow is taken into account through the introduction of local void fraction and gas-solid interacting terms into the Navier-Stokes equations of the single phase flow. The local averaged continuity and momentum equations of the gas flow are:

$$\frac{\partial(\varepsilon\rho_{\mathrm{g}})}{\partial t}+\nabla\bullet(\varepsilon\rho_{\mathrm{g}}\mathbf{u}_{\mathrm{g}})=0 \tag{7.1}$$

$$\frac{\partial(\varepsilon\rho_{\mathrm{g}}\mathbf{u}_{\mathrm{g}})}{\partial t}+\nabla\bullet(\varepsilon\rho_{\mathrm{g}}\mathbf{u}_{\mathrm{g}}\mathbf{u}_{\mathrm{g}})=-\varepsilon\nabla p+\nabla\bullet(\varepsilon\boldsymbol{\tau}_{\mathrm{f}})+\mathbf{f}_{\mathrm{sg}}+\varepsilon\rho_{\mathrm{g}}\mathbf{g} \tag{7.2}$$

where ρ_{g} and $\mathrm{u_g}$ are fluid density and velocity, respectively. $\mathrm{f_{sg}}$ is the local mean particle-fluid interaction force, which is calculated based on the Newton's third law by,

$$\mathbf{f}_{\mathrm{sg}}=-\frac{1}{\Delta V_{\mathrm{c}}}\sum_{i=1}^{N_{\mathrm{p}}}\alpha_i\mathbf{f}_{\mathrm{f},i} \tag{7.3}$$

where N_{p} is the particle number inside the computational cell; ΔV_{c} is the cell volume; $\mathbf{f}_{\mathrm{f,i}}$ is the total fluid force and α_i is the volume fraction of particle i in the cell.

In a dense fluid-solid flow, a single particle is interacting with neighbouring particles, surrounding fluid and the geometry of computational domain. The equations describing the motion of particle i are:

$$m_i\frac{d\mathbf{v}_i}{dt}=\mathbf{f}_{\mathrm{c},i}+\mathbf{f}_{\mathrm{f},i}+m_i\mathbf{g}, \tag{7.4}$$

where m_i, I_i, v_i and w_i are mass, moment of inertia, translational and angular velocities of particle i, respectively. $\mathrm{f_{c,i}}$ is the total collision contact force. A soft-sphere model, specifically the linear spring-dashpot model [2-5], was employed in the present study to solve the contact mechanics.

7.2.2 Governing Equations for the Energy Balance, Heat Transfer and Chemical Reactions

The temperature of any individual particle is calculated by the following equation:

$$h(t+\Delta t)-h(t)=chtc\times s_p\times(T_f-T_p) \tag{7.5}$$

In which h represents the total enthalpy including the particle and the reacting gases. Particle enthalpy is calculated by summing the enthalpy of metal and its metal oxide.

$$h = h_{me} + h_{meoxide} + h_{gases} \tag{7.6}$$

Concentrations of gases at the initial time are set as the same with the flowing field concentrations. After the time step Δt, the composition of gases is determined from the conversion rate X which is calculated from the metal oxidation/reduction kinetics. The enthalpy of solids is calculated from the HSC manual as following:

$$h = aT + 5.0\times10^{-4}\times b\times T^2 - 10^5\times c/T + 10^{-6}\times d\times T^3/3.0 \tag{7.7}$$

In which a, b, c, d are the coefficients from the HSC manual. Finally the temperature field for the solid phase is determined iteratively using a standard iteration method.

7.3 NUMERICAL SIMULATIONS

7.3.1 Numerical Procedure

The hydrodynamics of an entire CLAS system has been simulated with the total solid inventory of 1 kg. The Phase Couple SIMPLE method was employed to solve the fluid flow field. Polyethylene particles with a density of 1150 kg/m^3 are used in the simulation. The average primary particle size is 200 μm and a parcel size of 2 mm is used in the simulation (i.e. one parcel is 10 primary particles). In total, 216 004 parcels are tracked in the simulation. The fluid time step (i.e., Δt_f) is 1e^{-3} s and the particle time step (i.e., Δt_s) is 1e^{-4} s. The inlet velocity of air reactor is 0.5 m/s, and the inlet velocity of fuel reactor is 0.07 m/s. The flow chart of the CFD-DEM two-way coupling simulation is shown in Figure 116.

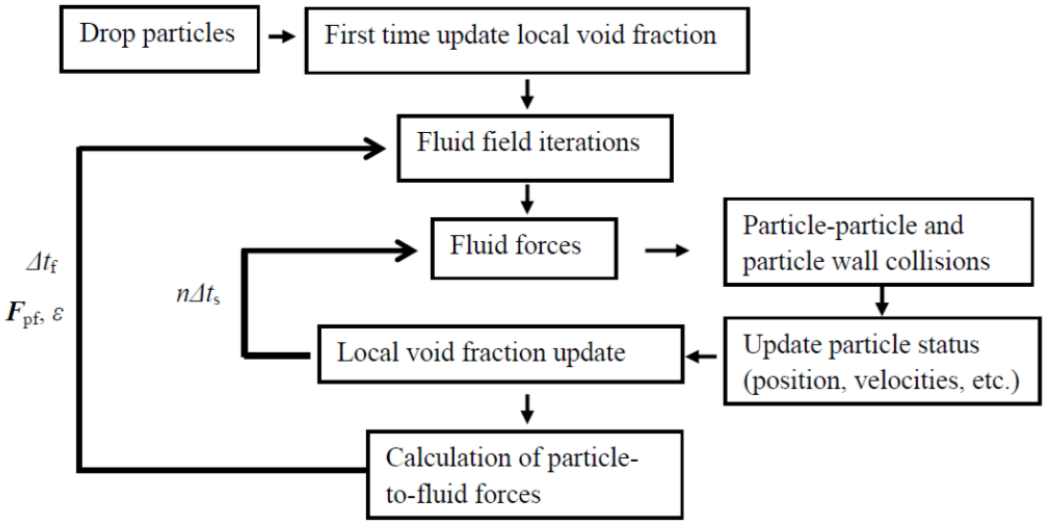

Figure 116: Flow chart of the CFD-DEM two way coupling.

7.3.2 Simulation Results

A series of experiments were carried out to verify the validity of simulation results. The experimental component of the investigation was carried out using the 10 kW_{th} pilot-plant. The apparatus consisted of five major components namely the air reactor, riser, reduction reactor, two loop seals and a cyclone. The air reactor was a vertical tube with an inner diameter of 80 mm and height of 300 mm connected to a riser with inner diameter of 40 mm and height of 1150 mm. A cyclone was used to capture the particles transported by the upward flow of the fluidising fluid through the riser and return them to the system. Two fluidised loop seals were used in the experimental setup with loop seal 1 located before the reduction reactor to prevent leakage of air to the fuel reactor and loop seal 2 located after the reduction reactor to prevent any leakage of fuel to the air reactor. The particles captured in the cyclone fell under the force of gravity to loop seal 1 and then fluidised to the reduction reactor. The reduction reactor with an inner diameter of 85 mm and height of 196 mm was operated at a range of 4-8 times the minimum fluidisation velocity of the mixture. Fluidisation was used to guarantee a smooth transport of particles through the loop seals. The air reactor could be operated at flow rates up to Q_{AR} = 200 L/min, while flow rates up to Q_{FR} = 50 L/min and Q_{LS} = 25 L/min could be reached in the reduction reactor and loop seals, respectively.

Figure 117 illustrates the predicted contour plots of oxygen concentration in the simulated 10 kW_{th} pilot-plant. As depicted, the highest oxygen concentration of about 21-22 vol% is observed at the inlet of the air reactor where fresh air enters the system and in the reduction reactor where oxygen carrier particles release their oxygen molecules during their reduction to a lower oxidation state. Elsewhere in the system the average oxygen concentration is about 5 vol%. Measurements of the oxygen concentration at the inlets of the air and reduction reactors are consistent with the predictions shown in Figure 117 and confirm their validity. These predictions also suggest that the concept of CLAS and/or ICLAS is technically viable and can be implemented using a pair of bubbling fluidised beds.

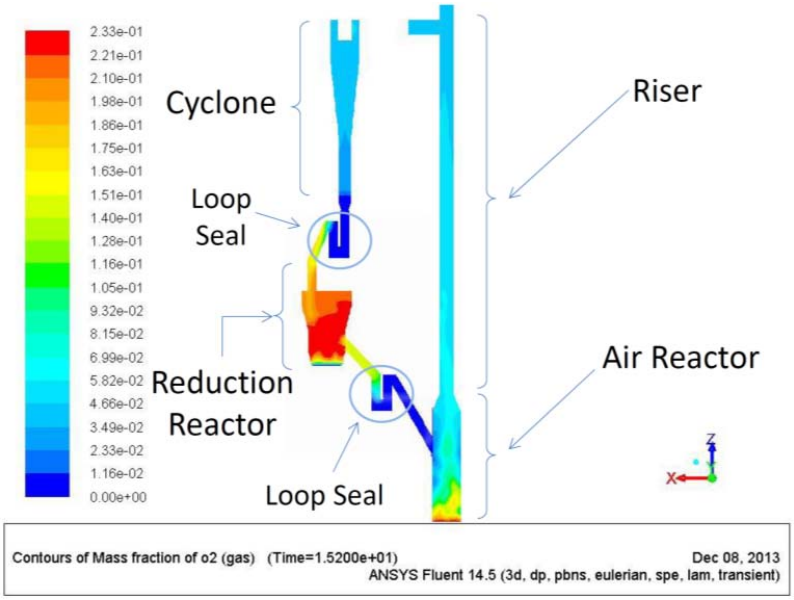

Figure 117: Contour plots of oxygen concentration in the simulated 10 kW_{th} pilot-plant.

For the case shown in Figure 117, the contour plots of N_2 and water are shown in Figures 118a and 118b, respectively. As can be seen, the nitrogen gas predominately exists in the air reactor / riser region and the model is capable of predicting this somewhat expected distribution of nitrogen quite well. In contrast the water mainly exists in the reduction reactor and regions around it including the loop seals. This primarily due to the fact that the simulation presented here is for a CLAS type process where steam is employed as a reducing agent to control and/or adjust the partial pressure of oxygen in the reduction reactor. Again the model is successfully predicting the spread of water (in the steam form) around the system.

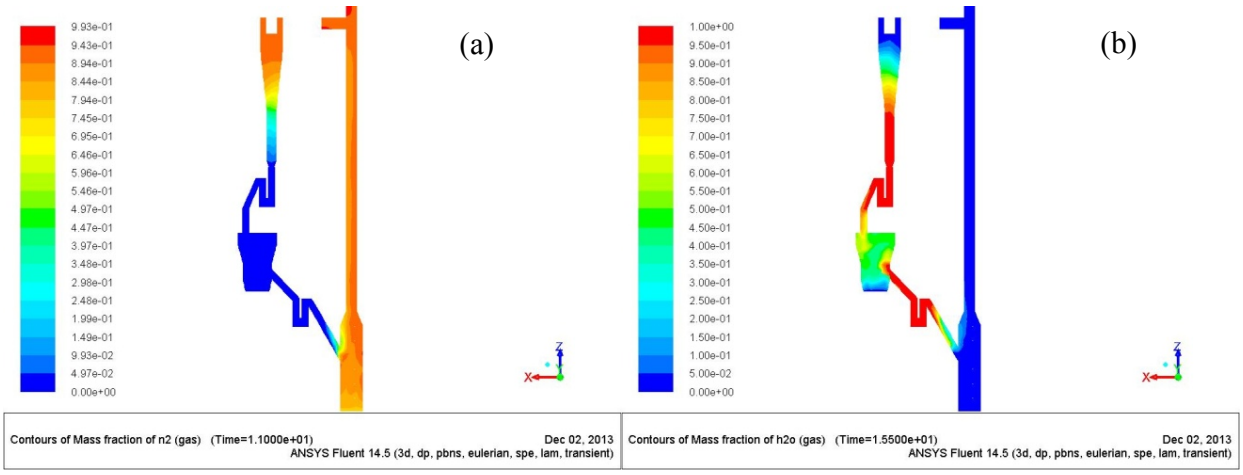

Figure 118: Contour plots of (a) N_2 and (b) water in the simulated 10 kW_{th} pilot-plant.

Figures 119a and 119b show typical contours of temperature and solids conversion in the 10 kW_{th} pilot-plant. There is a strong relationship between the solids conversion and temperature contours and the model (as evident by Figure 119) does a good job of predicting this relation.

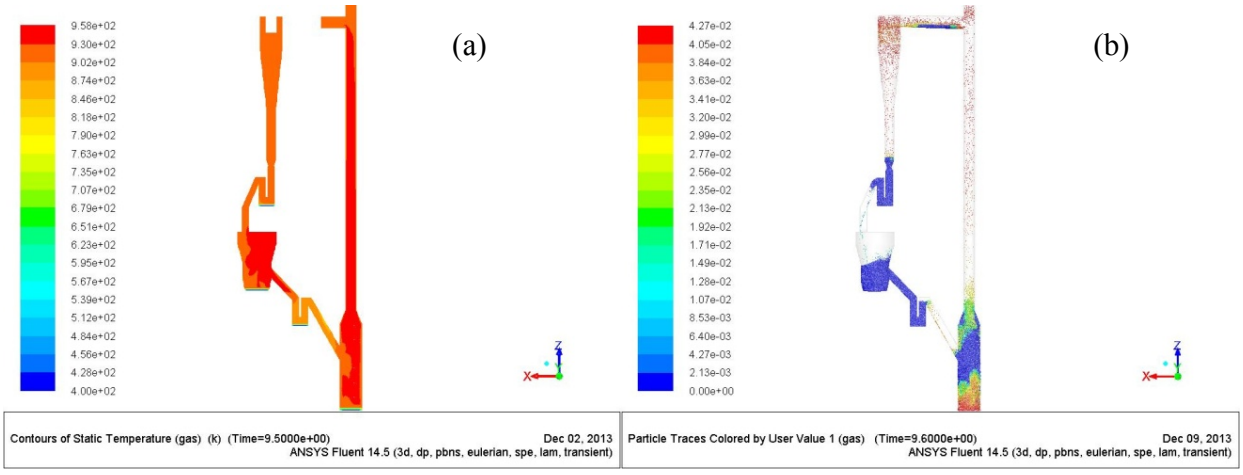

Figure 119: Contour plots of (a) temperature and (b) particle distribution in the simulated 10 kW_{th} pilot-plant.

Chapter 8

TECHNOECONOMIC ASSESSMENT

8.1 BACKGROUND

The most recent literature on oxy-fuel combustion [37] indicate that as a technology option for mitigation of GHG emissions in short to medium terms, oxy-fuel is particularly suited to older coal-fired power plants (> 20 years) where the capital cost is typically written off after 20 years and as such the retrofit costs can be covered over a longer period. As shown in Table 15 there are 8 major coal-fired power plants (capacity > 1 MW) in NSW with a combined capacity of 11.75 GW. Of these, six plants (Bayswater, Eraring, Liddell, Munmorah, Vales Point and Wallerawang) with a combined capacity of 10.2 GW have been in service for over 20 years and as such are particularly attractive for oxy-fuel option. Given the above, one of the key objectives of this study was to:

(i) Carry out a techno-economic assessment of the NSW fleet of coal-fired power plants for oxy-fuel conversion.

(ii) Determine the extent to which the economic viability of oxy-fuel operations is enhanced by integration of the chemical looping based air separation processes into such operations.

In this chapter the results of a techno-economic assessment for conversion of the above eight power plants to oxy-firing are presented. The assessment has been carried out at an elementary level mainly to evaluate the relative merits of various air separation processes when incorporated into oxy-fuel operations. As such the current techno-economic study focuses on the key question of: "*Is oxy-firing worth doing in NSW?*" rather than "*Can oxy-firing be done in NSW?*". The answer to the latter question requires a much more detailed feasibility study which is beyond the scope of the present investigation.

Furthermore, for an elementary study such as that outlined here it is necessary to assume that the transport and storage of CO_2 from the power plant to the sequestration site is feasible from both technical and economic points of view. It is also important to assume that for any given power plant the oxy-fuel retrofit is not limited by any space and layout limitations. Obviously these assumptions which are quite site-specific may not always be valid. However, recent studies of fleet retrofit potential suggest that a considerable number of existing coal-fired power plants around the world can be retrofitted for oxy-firing. Besides, it is essential to make such assumptions in a benchmarking exercise like that described here.

The details of the methodology and key findings from the present techno-economic assessment are provided in the proceeding sections. While a large number of case studies were examined, all possible combinations of interest could not be assessed. It should be highlighted that the assessment presented here was carried out using a spreadsheet based analysis toolkit developed in-house specifically for this

study. The spreadsheet model will be made available to staff at NSW Coal Innovation so that other scenarios of interest to the NSW government can be examined. Although it should be recognised that the model was primarily developed for internal use by the members of the research team and as a result no resources were devoted to develop a built-in user friendly interface and help facilities. Moreover, whilst the technical support after the release of the model is not guaranteed, the author and his team will do their best to provide a basic level of assistance.

8.2 METHODOLOGY

8.2.1 Overview

The techno-economic study summarised here was concerned with retrofitting the 8 major coal-fired power plants listed in Table 15 for oxy-firing operation. A number of relevant publications were used to establish an accurate database of technical information and cost components [38-46].The most important principle followed in the techno-economic assessment was to use a consistent and correct baseline. For this purpose several alternative retrofit configurations, differing only in ASU but otherwise identical, were considered for each plant. These were:

- *Base Case*: "business as usual" operation scenario for the existing plant (air-fired) with no carbon capture and storage (CCS).
- *Cryogenic Case:* Oxygen fired retrofit with a cryogenic type ASU and CCS.
- *ICLAS [S] Case:* Oxygen fired retrofit with an ICLAS (steam reduction) and CCS.
- *ICLAS [FG] Case:* Oxygen fired retrofit with an ICLAS (recycled flue gas reduction) and CCS.

The technical assessment for each plant comprised an investigation of the impact of both ASU and CPU (CO_2 processing unit) on the plant's performance characteristics. The impact was evaluated and expressed in terms of:

- Plant thermal efficiency
- Plant thermal efficiency penalty
- Electricity output penalty (EOP)
- Power requirement for oxygen production
- Power requirement for CPU

Similarly, in the economic assessment of technology options for the NSW fleet of coal-fired power plants, we considered Base-Case, Case 1, Case 2 and Case 3 scenarios outlined earlier. The economic assessment was evaluated and expressed in terms of:

- Power plant retrofit costs (i.e. capital cost)
- Operating costs
- Levelised cost of electricity
- Incremental cost of electricity relative to the Base-Case
- CO_2 abatement costs relative to the Base-Case

In addition to the above comparisons among various oxy-fuel alternatives, a series of bench-marking comparisons were also made between chemical looping based oxy-fuel options and a suite of other low emission technologies for renewable energy sources and fossil fuels.

8.2.2 Technical Assessment Methodology

Figure 120 illustrates the flowchart of the "*Technical Assessment Sub-model (TAS)*" developed by the research team to determine the technical aspects of oxy-fuel retrofit to the NSW coal-fired power plant fleet. The basic plant data for the NSW coal-fired power plants of interest were obtained from reference [45] and have been summarised in Table 15. The properties of the fuel (ultimate analysis) used in each power plant have also been summarised in Table 16. Moreover, the equations used in TAS to calculate various outputs and/or parameters have been listed in this section to provide the reader with a basic understanding of the science underlying TAS. The data used in calculations of the power demand for ASU were those obtained from the experimental components of the present study whereas the data for CPU power demand calculation were adopted from the literature for systems combining highest efficiencies and best practices [38-40; 46].

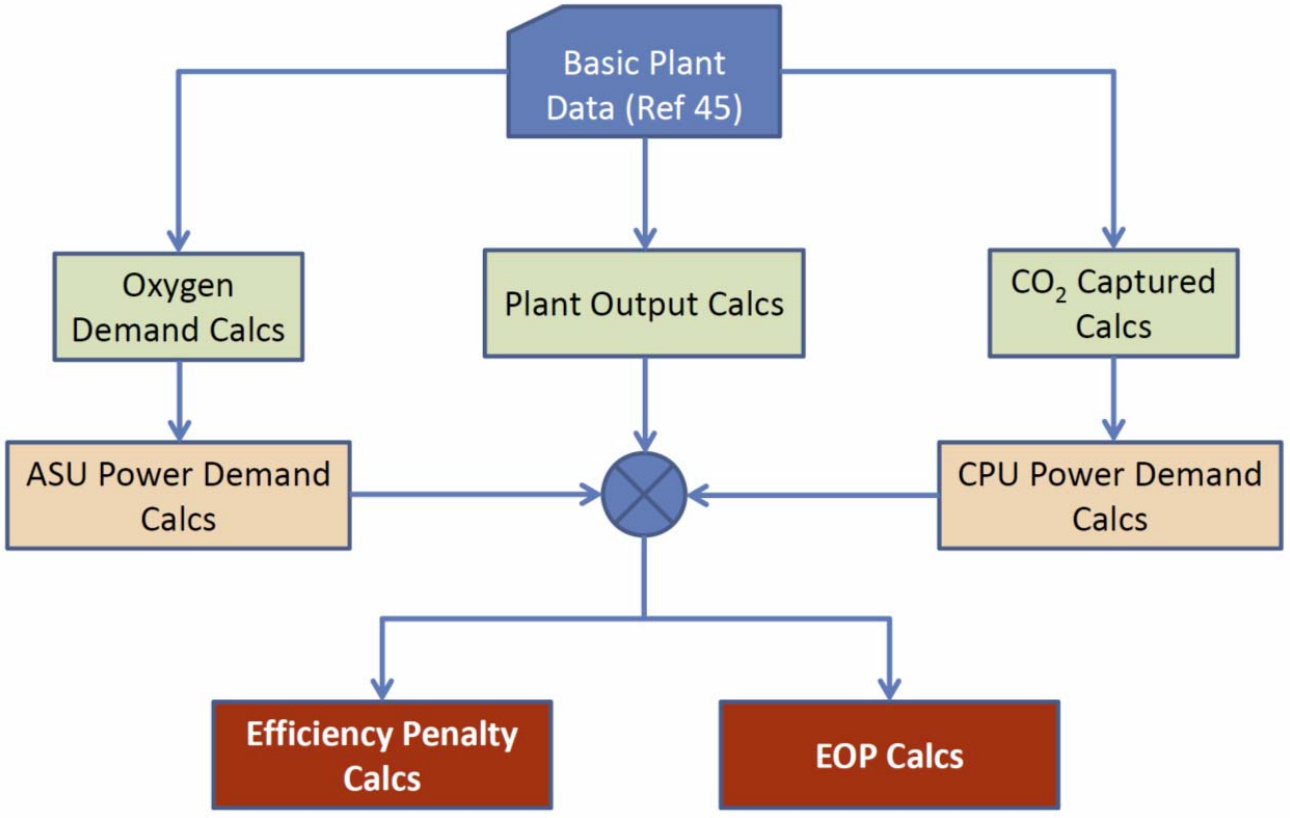

Figure 120: Flowchart of TAS.

Table 15: Basic plant data for 8 major coal-fired power plants in NSW [45]

	Bayswater	Eraring	Liddell	Mt Piper	Munmorah	Redbank	Vales Point B	Wallerawang
Operator	Macquarie Generation	Eraring Energy	Macquarie Generation	Delta Electricity.	Delta Electricity.	National Power	Delta Electricity.	Delta Electricity.
Commencement year	1984	1982	1971	1992	1969	2001	1978	1976
Boiler type**	PF	PF	PF	PF	PF	CFBC	PF	PF
Maximum capacity (MW)	2640	2640	2000	1320	600	150	1320	1000
Send out electricity (GWh)	15955	13859	8070	7921	226	1027	6671	5458
Number of units	4	4	4	2	2	1	2	2
Unit capacity (MW)	660	660	500	660	300	150	660	500
Condenser cooling	Natural draft cooling towers	Natural draft cooling towers	Custom built lake	Evap. cooling towers	Evap. cooling towers	Evap. cooling towers	Evap. cooling towers	Evap. cooling towers
Cooling medium	Fresh water (Hunter river)	Salt water (lake Macq.)	Fresh water (Hunter river)	Fresh water (Cox river)	Salt water (lake Mun mora)	Fresh water (Hunter river)	Salt water (lake Macq.)	Fresh water (Cox river)
Annual average thermal efficiency (HHV basis)	36.5%	36.4%	32.7%	37.2%	32.0%	32.0%	35.6%	33.2%
Fuel*	Coal	Coal	Coal	Coal	Coal	Coal tailing	Coal	Coal
Annual fuel consumption (Mt)	7.23	5.63	4.16	3.1	0.1	0.53	2.82	2.27
CO_2 emission rate (kg/MWh)	879	870	949	843	984	978	896	893

* See Table 16 for details

** PF → Pulverised Fuel ; CFBC → Circulating Fluidised Bed Combustor

Table 16: Fuel properties for 8 major coal-fired power plants in NSW [45]

	Bayswater	Eraring	Liddell	Mt Piper	Munmorah	Redbank	Vales Point B	Wallerawang
C (%)	53.5	59.0	49.7	59.3	63.6	51.8	58.2	59.1
H (%)	3.5	3.7	3.3	3.7	4.0	3.3	3.7	3.7
N (%)	1.2	1.2	1.1	1.4	1.2	2.2	1.2	1.3
S (%)	0.5	0.4	0.5	0.5	0.4	0.3	0.4	0.5
O (%)	6.4	6.6	6.3	6.1	7.3	5.4	6.3	5.8
Ash (%)	24.7	21.0	30.4	21.2	19.0	8.0	22.2	21.7
Moisture (%)	10.1	8.2	8.8	8.0	4.5	30.0	8.0	8.0
Calorific Value (MJ/kg)*	22.4	24.3	20.9	24.7	26.3	21.6	23.8	26.0

* HHV basis

Plant Output Calculations

$$TPO = \frac{SOE \times 1000}{OC} \tag{8.1}$$

$$OC = LF \times 365 \times 24 \tag{8.2}$$

where

TPO ≡ Typical plant output (MW)
SOE ≡ Send out electricity (GWh)
OC ≡ Operating capacity (h/year) calculated from Eq (8.2)
LF ≡ Load or capacity factor (assumed to be 85% in this study)

CO_2 Captured Calculations

$$CCO_2 = \frac{CE \times \left(CO_2ER \times 10^{-3}\right) \times \left(SOE \times 1000\right)}{10^6} \tag{8.3}$$

where

CCO_2 ≡ Captured CO_2 per year (Mt/yr)
CE ≡ Capture efficiency (assumed to be 90% in this study)
CO_2ER ≡ CO_2 emission rate (kg/MWh)

O_2 Demand Calculations

$$Q_{in} = \frac{SOE \times 1000}{(OC \times Eff)} \tag{8.4}$$

$$FCR = \frac{Q_{in}}{FCV} \tag{8.5}$$

$$CRR = FCR \times (C\%) \tag{8.6}$$

$$ORR = [FCR \times (O\%)]/2 \tag{8.7}$$

$$ODT_m = \left[FCR \times \frac{(MW_{O2})}{MW_C} \right] - ORR \tag{8.8}$$

$$ODA_m = ODT_m \times (1 + EX_{air}) \tag{8.9}$$

$$ODA_V = \left(\frac{ODA_m}{MW_{O2}} \right) \times \left(\frac{\overline{R}}{T_a \times P_a} \right) \times \left(\frac{1}{3600} \right) \tag{8.10}$$

where

CRR ≡ Rate of carbon release from fuel (kg/s)
Eff ≡ Plant's thermal efficiency
EX_{air} ≡ Excess air; assumed to be 1.5% in this study; see reference [41]
FCR ≡ Fuel consumption rate (kg/s)
FCV ≡ Fuel calorific value (MJ/kg)
MW_C ≡ Molecular weight of carbon (12 kg / kmol)
MW_{O2} ≡ Molecular weight of oxygen (32 kg / kmol)
ODA_m ≡ Actual oxygen demand on mass basis (kg/s)
ODA_V ≡ Actual oxygen demand on volumetric basis (m^3/h); assuming ideal gas behaviour
ODT_m ≡ Theoretical oxygen demand on mass basis (kg/s); assuming 100% combustion efficiency
ORR ≡ Rate of oxygen release from fuel (kg/s)
P_a ≡ Ambient Pressure (assumed to be 101.3 kPa in this study)
Q_{in} ≡ Total input thermal energy to the power plant (MW)
$\overline{R}$ ≡ Universal gas constant (8.314 $kJ.kmol^{-1}.K^{-1}$)
T_a ≡ Ambient temperature (assumed to be 22°C in this study)

ASU Power Demand Calculations

$$ASU_W = \frac{ODA_V \times SP}{1000} \tag{8.11}$$

$$SP_A = \begin{Bmatrix} (a) & 0.34 & kW/(m^3/h) \rightarrow Cryogenic;\ see\ \text{Ref [41]} \\ (b) & 0.18 & kW/(m^3/h) \rightarrow ICLAS\,[S];\ project\ data \\ (c) & 0.08 & kW/(m^3/h) \rightarrow ICLAS\,[FG];\ project\ data \end{Bmatrix} \tag{8.12}$$

where

ASU_W ≡ Air separation unit power demand (MW)
SP_A ≡ Specific power of the ASU in $kW.m^{-3}.h^{-1}$

CPU Power Demand Calculations

$$CPU_W = \left(\frac{SP_C}{1000}\right) \times \left(\frac{CCO_2 \times 10^6}{OC}\right) \tag{8.13}$$

where

CPU_W ≡ CO_2 processing unit power demand (MW)
SP_C ≡ Specific power of the CPU (assumed to be 135 kWh/tCO_2 captured; see Ref [42])

Efficiency Penalty Calculations

$$EP_A = Eff - \left(\frac{TPO - ASU_W}{Q_{in}}\right) \tag{8.14}$$

$$EP_C = Eff - \left(\frac{TPO - CPU_W}{Q_{in}}\right) \tag{8.15}$$

$$EP_T = EP_A + EP_C \tag{8.16}$$

where

EP_A ≡ Efficiency penalty due to ASU (%)
EP_C ≡ Efficiency penalty due to CPU (%)
EP_T ≡ Total efficiency penalty

Electricity Output Penalty Calculations

$$\%EOP = \left(\frac{ASU_W + CPU_W}{TPO}\right) \tag{8.17}$$

$$EOP = \left(\frac{\left[ASU_W + CPU_W \right] \times 1000 \times OC}{CCO_2 \times 10^6} \right) \tag{8.18}$$

where

$\%EOP \equiv$ Electricity penalty expressed as percentage of typical plant output (%)
$EOP \equiv$ Electricity penalty per tonne of CO_2 captured (kWh/tCO_2)

8.2.3 Economic Assessment Methodology

Figure 121 illustrates the flowchart of the "*Cost Assessment Sub-model (CAS)*" developed by the research team to determine the economic aspects of oxy-fuel retrofit to the NSW coal-fired power plant fleet. The basic cost data were obtained from references [38-43 and 46] and have been summarised in Tables 17-20. Moreover, the equations used in CAS to calculate various outputs and/or parameters have been listed in this section to provide the reader with a basic understanding of the underlying methodology particularly in respect to determination of the levelised cost of electricity.

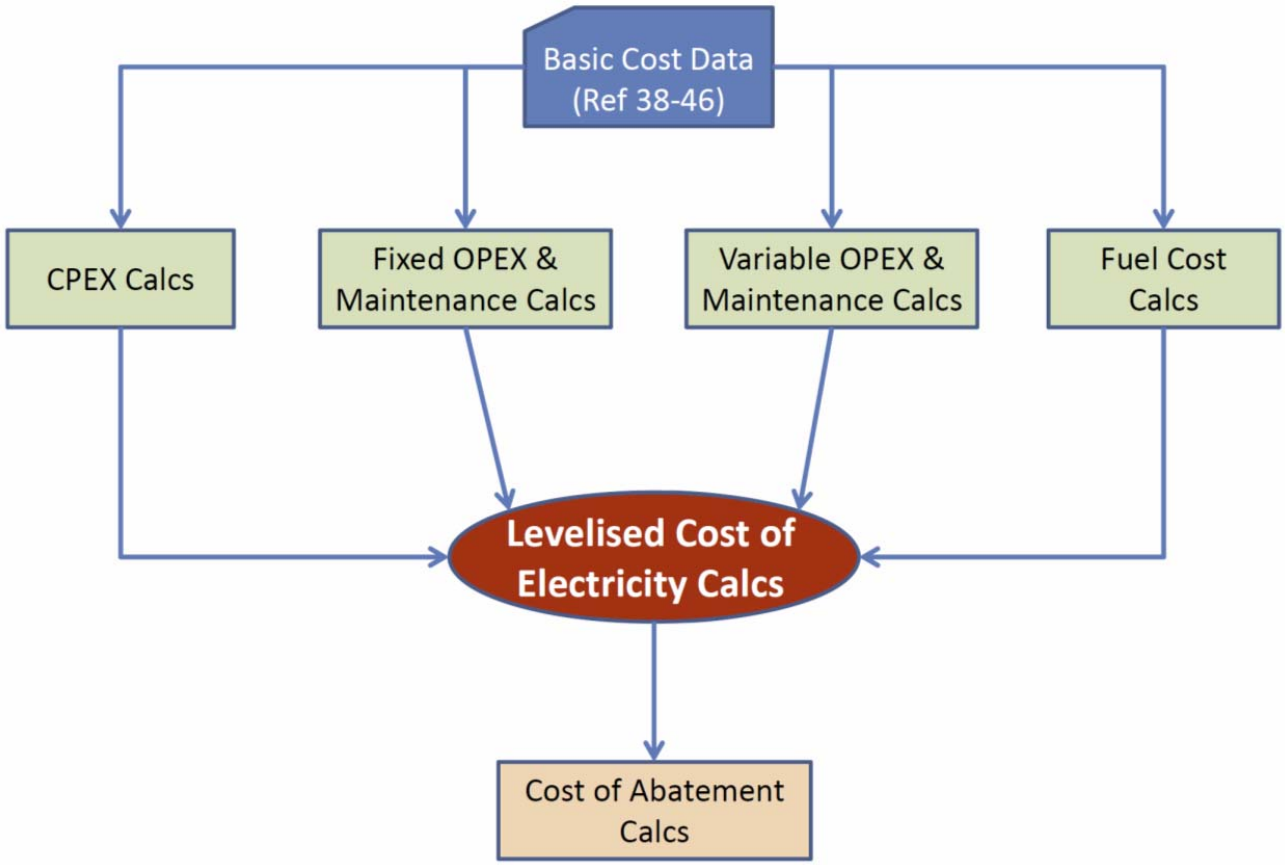

Figure 121: Flowchart of CAS.

Table 17 summarises the unit cost (expressed as A$ per kW of plant output unless otherwise specified) for various component of the retrofit work. Unit costs (see the second column from left) were expressed in terms of the value of dollar in 2009 and on the basis LHV of a reference coal (Table 18) used in Reference [38]. These figures have been adjusted in this study based on to 2014 dollar and HHV of the reference coal (see columns 3-5 of Table 17).

Table 17: Components of capital cost

Items	Unit cost based on LHV		Unit cost based on HHV		Notes
	(2009 $)*	(2014 A$)	(2009 $)	(2014 $)	
	$/kW	$/kW	$/kW	$/kW	
Coal handling system	129.8	122.1	115.3	108.5	
Coal prep and feed systems	44.7	42.1	39.7	37.4	
Feed water and miscellaneous BOP systems	159.2	149.8	159.2	149.8	
PC boiler and accessories	865.3	814.2	865.3	814.2	
ASU (cryogenic)	652.8	614.2	652.8	614.2	
ASU (cryogenic)		4917.2		4917.2	Unit costs per kW of ASU power demand
ASU (ICLAS [S])#		4300		4300	Unit costs per kW of ASU power demand
ASU (ICLAS [FG])#		3980		3980	Unit costs per kW of ASU power demand
Flue gas clean up	252.3	237.4	252.3	237.4	S&L models
Purification and Compression	287.5	270.5	287.5	270.5	
HRSG, ducting and stack	40.4	38.0	40.4	38.0	
Steam turbine generator	475.7	447.6	475.7	447.6	
Cooling water systems	114.5	107.7	114.5	107.7	
ASH/spent sorbent handling	46.3	43.6	46.3	43.6	Unit costs adjusted based on coal ash & sulphur content
Access electric plant	238.1	224.0	238.1	224.0	
I&C	48.5	45.6	48.5	45.6	

** References [38-40]*
 # Reference [43]; based on figures for catalytic cracking units in petrochemical plants and refineries

Table 18: Properties of reference coal used in determining unit costs listed in Table 17.

C (%)	49.83
H (%)	2.91
N (%)	0.71
S (%)	0.22
O (%)	13.87
Ash (%)	32.46
Moisture (%)	3.88
Calorific Value (MJ/kg); HHV	20.23

Table 19 shows the unit costs for fixed operating and maintenance cost items. The unit cost for operator labour was obtained assuming a labour rate of $60/hr and 13 operators per shift. The original unit costs from References [38-40] listed in the second column are in $/kWyr for the 2009 dollar. These unit costs have been adjusted for the 2014 dollar and have been also calculated on the basis of $ per MWh of plant output. For conversion from $/kWyr to $/MWh it was assumed that the capacity factor was 85% which according to Eq (8.2) equates to an operating capacity of OC = 7446 h/yr.

Table 19: Components of the fixed operating and maintenance cost

Item	2009 $/kWyr	2014 $/kWyr	2009 $/MWh	2014 $/MWh
Operator labour#	11.8	11.1	1.6	1.5
Maintenance cost	50.3	47.3	6.8	6.4
Admin. and support labour	0.96	0.9	0.1	0.1
Total	**63.1**	**59.3**	**8.5**	**8.0**

Table 20 summarises the variable operating and maintenance cost items primarily adopted from information provided in references [38-40]. With the exception of oxygen carriers cost, all other cost items are assumed to be the same for all alternative air separation options. Also the cost of oxygen carriers are based on information received from several vendors.

Table 20: Components of the variable operating and maintenance cost

Items	Cryogenic ($M/yr)	ICLAS [S] ($M/yr)	ICLAS [FG] ($M/yr)
Water	16.8	16.8	16.8
WT chem	12.9	12.9	12.9
Fabric filter bags and cages	2.4	2.4	2.4
Fly and bottom ash disposal	67.8	67.8	67.8
Oxygen carriers for ICLAS#	0	33.5	33.5
Total	99.9	133.4	133.4

Fuel Cost Calculations

$$UFC = UFC_R \times \left(\frac{FCV}{FCV_R} \right) \tag{8.19}$$

$$TFC = \left(UFC \times 1000 \right) \times \left(\frac{SOE}{10^6} \right) \tag{8-20}$$

$$FC = \left(TFC \times 10^6 \right) \times \left(FCV \times AFC \times 10^9 \right) \tag{8-21}$$

where

AFC	≡	Annual fuel consumption (Mt/yr)
FC	≡	Fuel cost per unit of energy content ($/MJ)
FCV	≡	Fuel calorific value (MJ/kg)
FC	≡	Fuel cost per unit of energy content ($/MJ)
TFC	≡	Total fuel cost per year ($/yr)
UFC	≡	Unit fuel cost in dollar per MWh of send out electricity ($/MWh)
R	≡	Subscript 'R' refers to the reference fuel described in Table 18

Levelised Cost of Electricity Calculations

If for simplicity it is assumed that the net output of the power plant, operating, maintenance and fuel costs are constant over the life of the plant, then the levelised cost of electricity can be calculated from the following set of equations:

$$LCOE = \left(\frac{\left(TCR \times FCF \right) + FOM}{NPO} \right) + VOM + CS + \left(HR \times FC \right) \tag{8.22}$$

$$FCF = \frac{r(1+r)^t}{(1+r)^t - 1} \tag{8.23}$$

$$NPO = TPO - ASU_W - CPU_W \tag{8.24}$$

$$HR = \frac{AFC \times FCV \times 10^9}{NPO \times OC} \tag{8.25}$$

where

CS	≡	Cost of CO_2 storage ($/t$CO_2$); assumed to be \$72/tCO_2 for NSW [46]
FCF	≡	Fixed charged factor calculated by Eq (8.23)
FOM	≡	Fixed operating and maintenance cost ($/yr); see Table 19

HR ≡ Net power plant heat rate (MJ/MWh); see Eq (8.25)
LCOE ≡ Levelised cost of electricity ($/MWh)
NPO ≡ Net power plant output (MW); see Eq (8.24)
r ≡ Rate of capital discharge (%); assumed to be 7% in this study [38-40]
t ≡ Power plant life (yr); assumed to be 25 yr in this study
TCR ≡ Total capital requirement ($); see Table 17
VOM ≡ Variable operating and maintenance cost ($/MWh); see Table 20

Cost of Abatement Calculations

$$COA = \left(\frac{LCOE - LCOE_{\text{Ref}}}{CO_{2\text{Ref}} - CO_{2Cap}} \right) \tag{8.26}$$

where

COA ≡ Cost of CO_2 abatement expressed as dollar per tonne of captured CO_2 ($/t$CO_2$)
CO_{2Av} ≡ CO_2 avoided (tCO_2/MWh)
Ref ≡ The subscript 'Ref" refers to business as usual case with no CCS

8.3 RESULTS AND DISCUSSION

8.3.1 Plant Technical Assessment

Oxygen Demand

Figure 122 shows the gross value of the oxygen demand (assuming 100% oxy-firing) for the 8 coal-fired power plants under investigation. Given that the gross oxygen demand is directly proportional to the plant capacity, it is not surprising that Bayswater requires about 1 million cubic meters of oxygen per hour whereas Munmorah only needs about 16000 cubic meters per hour.

However, the gross value of oxygen demand does not provide the whole picture because in addition to the plant capacity the oxygen demand is also related to the type of fuel consumed in the plant (note that the fuel carbon and oxygen contents as well as its calorific value influence the overall oxygen demand). For that reason and to have a better understanding of the oxygen demand, a normalised version of the information provided in Figure 122 is illustrated in Figure 123. This time though the oxygen demand is expressed in cubic meters of oxygen per MWh of the power plant output. As can be seen the normalised oxygen demand varies between 450 and 550 m^3/MWh for the coal-fired power plants in NSW. Interestingly, the normalised values shown in Figure 123 indicate that Bayswater has one the lowest normalised oxygen demand while Munmorah exhibits a very high demand. This confirms that the gross value of oxygen demand cannot be the sole factor in determining the oxygen demand for a given oxy-fuel retrofit. The normalised oxygen demand appears to be a better and more accurate indicator as it considers both the plant capacity and fuel type.

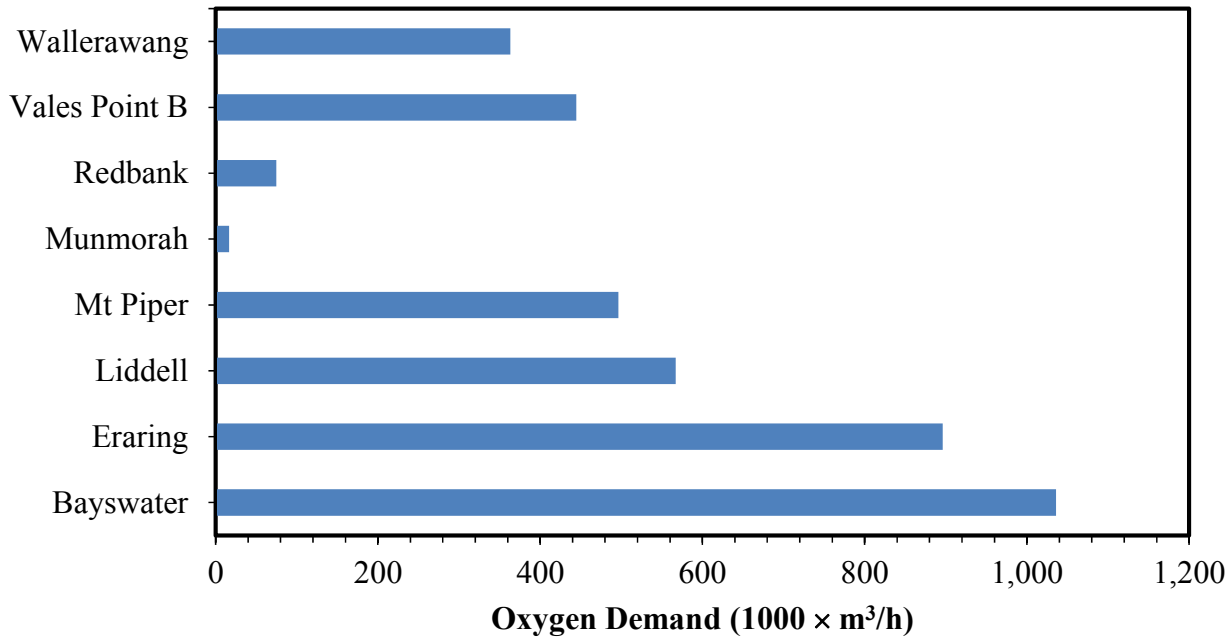

Figure 122: Bar char plots of gross oxygen demand for coal-fired power plants in NSW.

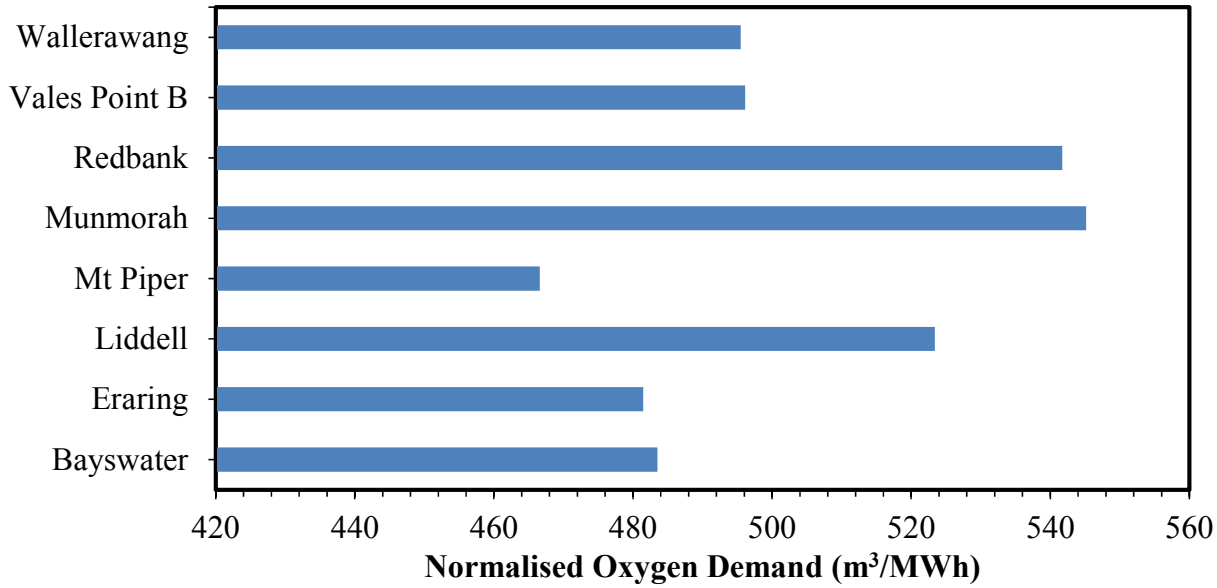

Figure 123: Bar char plots of normalised oxygen demand for coal-fired power plants in NSW.

CO_2 Avoided (Captured)

Figures 124 and 125 respectively present the gross and normalised values of CO_2 avoided (i.e. captured) by each NSW coal-fired power plant if modified and retrofitted for oxy-firing operation. The gross values (Figure 124) are expressed in million tonnes of CO_2 captured per year while the normalised values are expressed in tonnes of CO_2 avoided per unit of the original send out electricity

(i.e. before retrofit). As Figure 124 shows, the CO_2 avoided in gross terms vary from 0.2 to 13 Mt/yr for the NSW power plants under investigation. The combined value of CO_2 avoided for these power plants is about 47 Mt/yr which is equivalent to the annual GHG emissions from 9.5 million average cars (note that the total number of cars in Australia is about 13.5 million).

Similarly the normalised values of the CO_2 avoided vary between 0.78 and 0.88 tCO_2/MWh for the power plants considered in this study (see Figure 125). The Bayswater and Eraring power plants are standout cases here because they have relatively modest values of normalised CO_2 avoided (≈ 0.79 tCO_2/MWh) while in gross terms these two power plants can potentially achieve the highest levels of CO_2 captured in the state if retrofitted for oxy-firing operation (Figure 124).

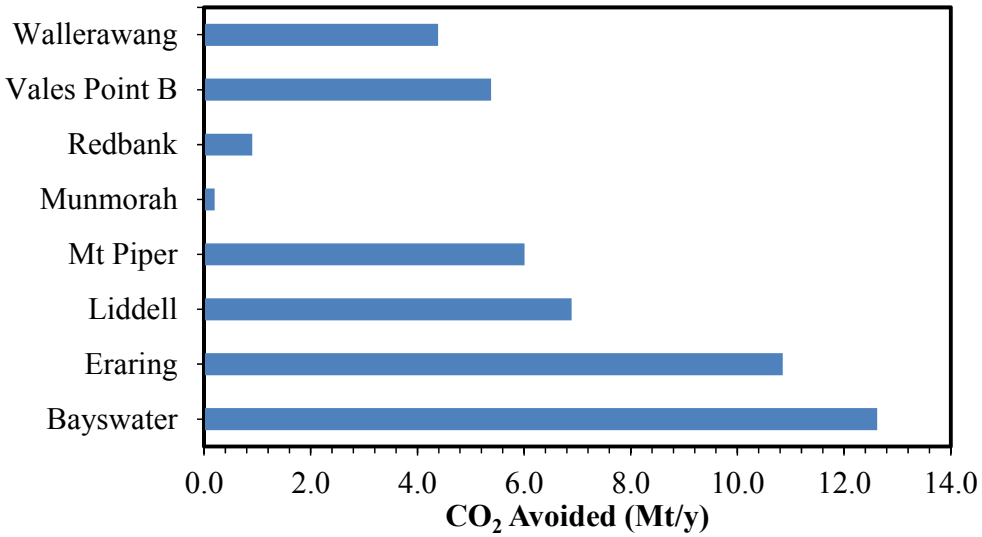

Figure 124: Bar char plots of gross CO_2 avoided for coal-fired power plants in NSW.

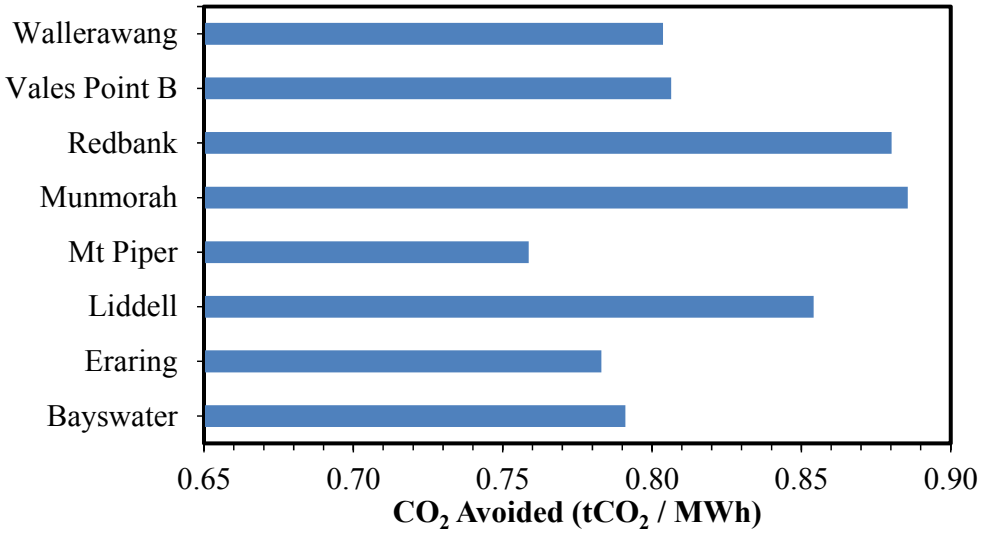

Figure 125: Bar char plots of normalised CO_2 avoided for coal-fired power plants in NSW.

Parasitic Power Losses Due to Oxy-Firing Retrofit

Figures 126 and 127 show the power demands of the ASU and CPU components of the oxy-firing retrofit for the 8 NSW coal-fired power plants. The ASU power demand for each plant has been calculated with the underlying assumption that the air separation unit is capable of delivering the relevant oxygen demand depicted in Figure 122. Similarly, the CPU power demand for each plant has been determined assuming that the CO2 quantities shown in Figure 124 ought to be avoided (captured). Also, as noted earlier it is assumed in the present analysis that all oxy-fuel options utilise the same CPU design and hence differ only in terms of the ASU design. For that reason Figure 127 shows only one option for the CPU component of each power plant while the cryogenic, ICLAS [S] and ICLAS [FG] options are considered in Figure 126 for the air separation component of the retrofit.

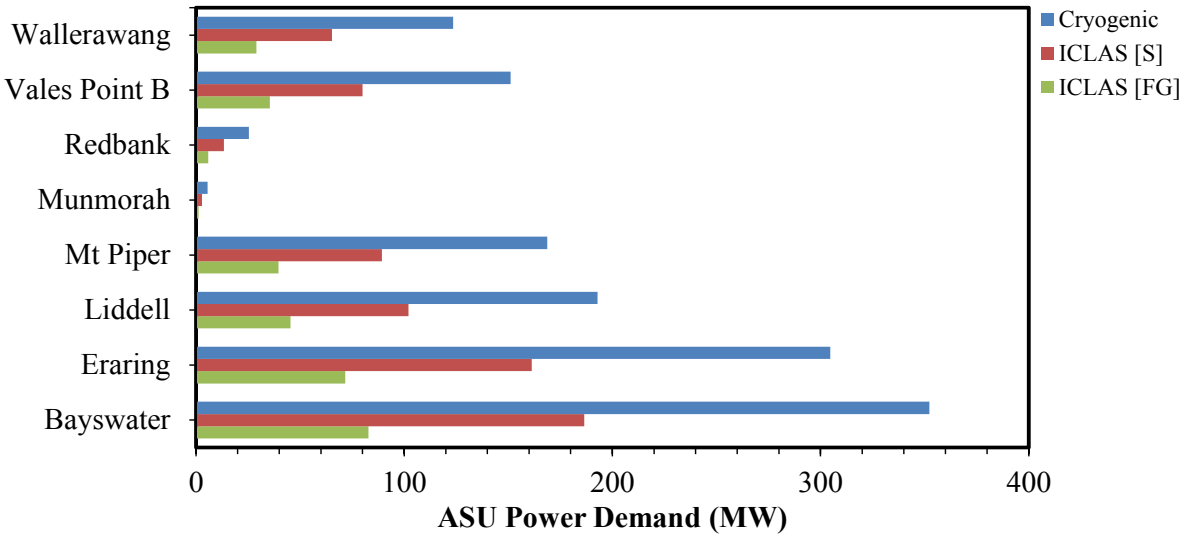

Figure 126: Bar char plots of ASU power demand for coal-fired power plants in NSW.

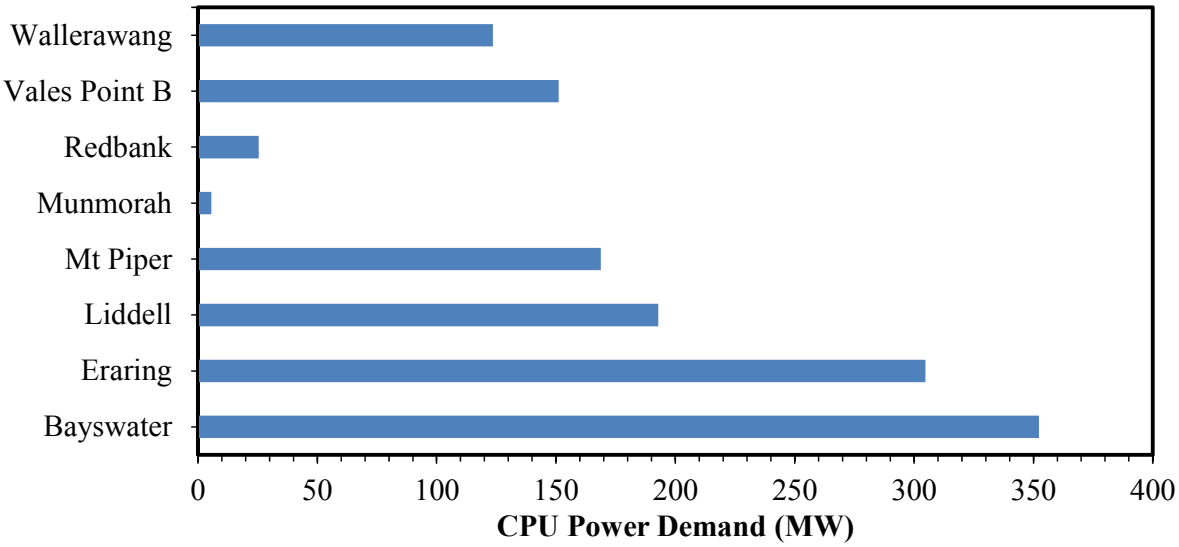

Figure 127: Bar char plots of CPU power demand for coal-fired power plants in NSW.

As shown in Figure 126 the deference in ASU power demands for cryogenic and ICLAS based designs is quite significant for each power plant studied here. In fact, the ratios of ICLAS [S] / cryogenic and ICLAS [FG] / cryogenic power demands for the ASU component are 0.53 and 0.24, respectively. Thus on average the ICLAS [S] process leads to 47% reduction in the ASU power demand when compared with a cryogenic based system whilst for the same operating conditions ICLAS [FG] lowers the ASU power demand by as much as 76% if it replaces a cryogenic based unit.

Figure 128 illustrates the bar chart plots of the combined parasitic load (i.e. sum of ASU and CPU power demands) for the NSW coal-fired power plants. As shown, there are significant losses of output power when a conventional plant is converted to oxy-firing operation. These losses are clearly much higher when a cryogenic based air separation unit is employed.

For benchmarking, the combined parasitic load for each power plant was normalised against its typical output and the results were summarised in Figure 129 and reported as "Plant capacity Loss". The formula used for normalisation was:

$$PCL = \left(\frac{CPL}{TPO} \right) \tag{8.27}$$

where

PCL ≡ Plant capacity loss (%)
CPL ≡ Combined parasitic load (MW)

It can be seen from this figure that when cryogenic air separation is employed the capacity loss can be as high as 30% of the plant output whereas the capacity loss can be progressively reduced to figures as low as 15% (i.e. 50% reduction in capacity loss) if an ICLAS [FG] type design is implemented.

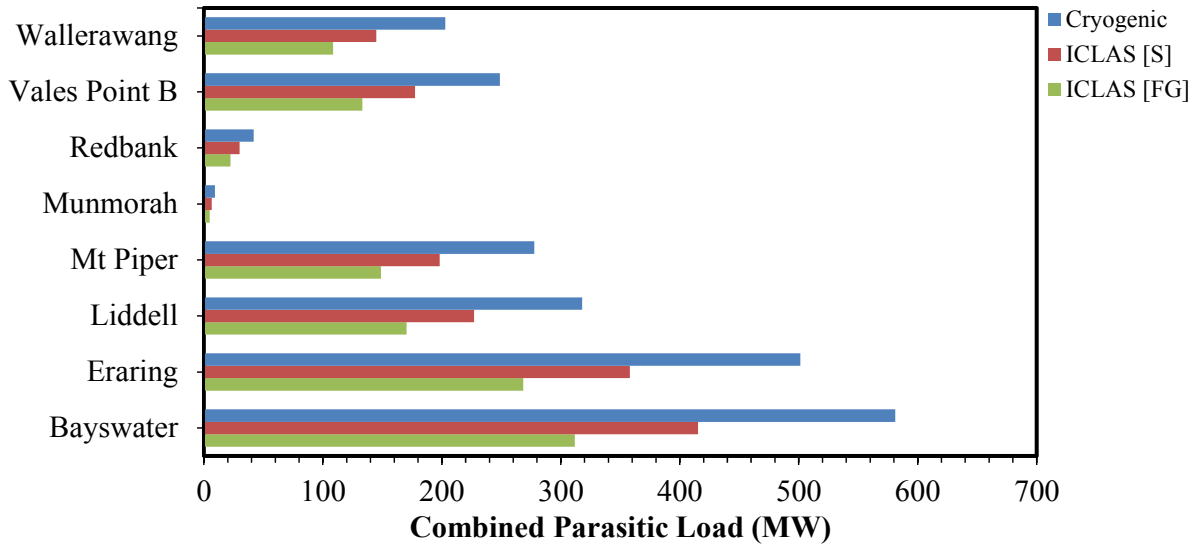

Figure 128: Bar char plots of combined parasitic load for coal-fired power plants in NSW.

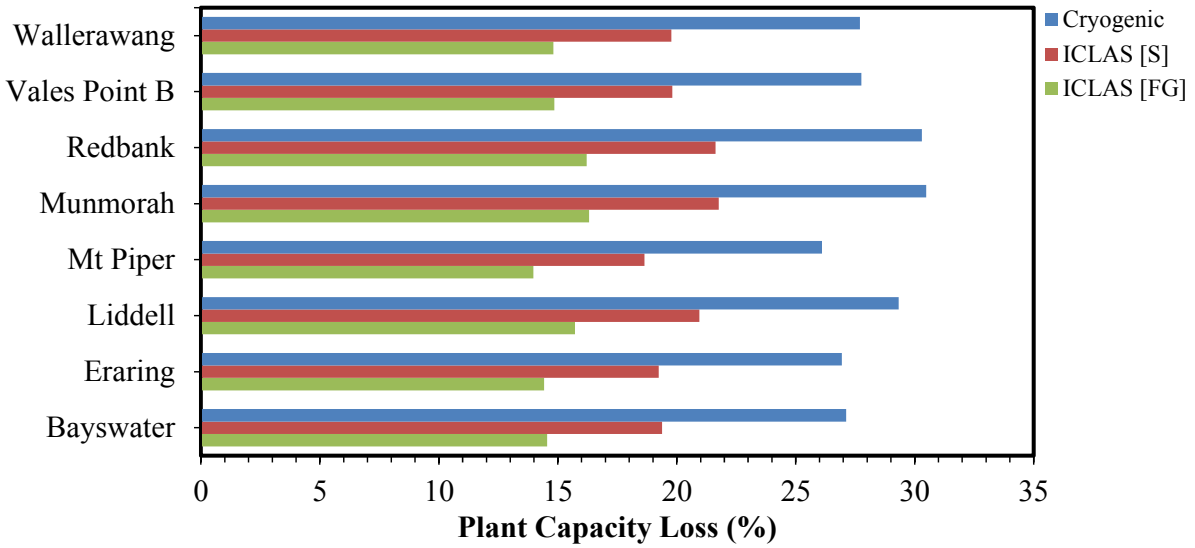

Figure 129: Bar char plots of plant capacity loss for coal-fired power plants in NSW.

Thermal Efficiency

Figure 130 depicts a comparison of power plant thermal efficiency for the four cases under investigation; that is: the base case; oxy-fuel with cryogenic air separation; oxy-fuel with ICLAS with steam reduction (ICLAS [S]) and finally oxy-fuel with flue gas reduction (ICLAS [FG]). As shown all three oxy-fuel options lower the plant thermal efficiency when compared with the business as usual case (i.e. base-case). However, both chemical looping based air separation processes considered here and in particular the ICLAS [FG] consistently lead to lower levels of efficiency loss.

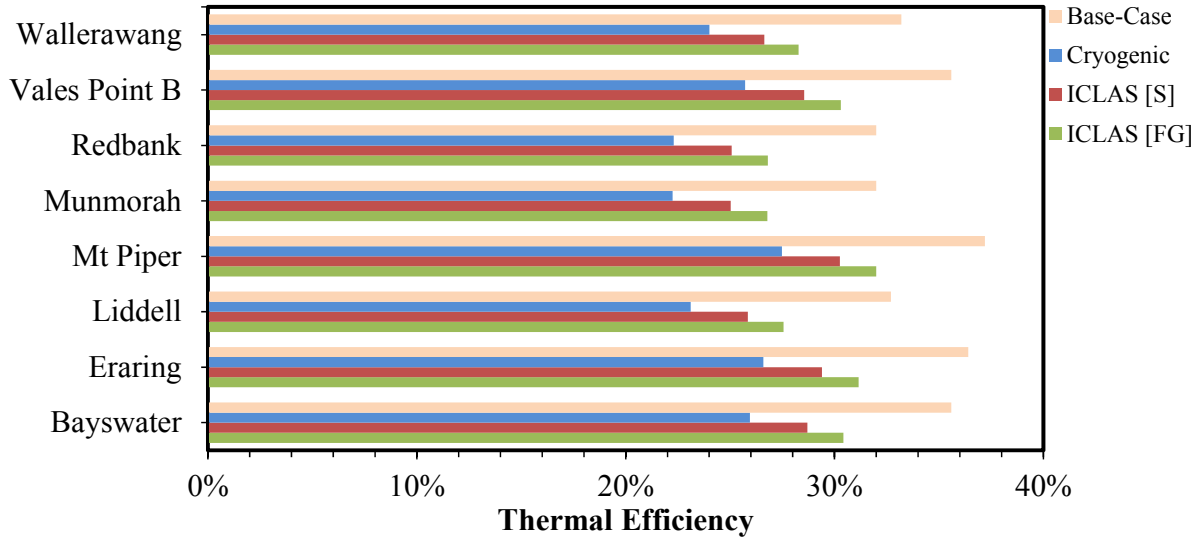

Figure 130: Bar chart plots of thermal efficiency for the NSW fleet of coal-fired power plants.

This is more evident in Figure 131 where the efficiency penalty (rather than the actual thermal efficiency) associated with the three different air separation options has been shown for the oxy-fuel conversion of the NSW coal-fired power plants (assuming the same CPU for all cases). As can be seen, the average efficiency penalty due to the implementation of the cryogenic option in NSW is about 10 percentage point which is quite consistent with figures reported in a number of recent studies [37]. The efficiency penalty of the power plant, however, can be significantly reduced by the introduction of chemical looping based air separation processes. As evident from Figure 131, the average efficiency penalty associated with ICLAS [S] is about 7.5% while that of the ICLAS [FG] is approximately 5%; representing a 50% reduction in efficiency losses when compared with the conventional cryogenic air separation option.

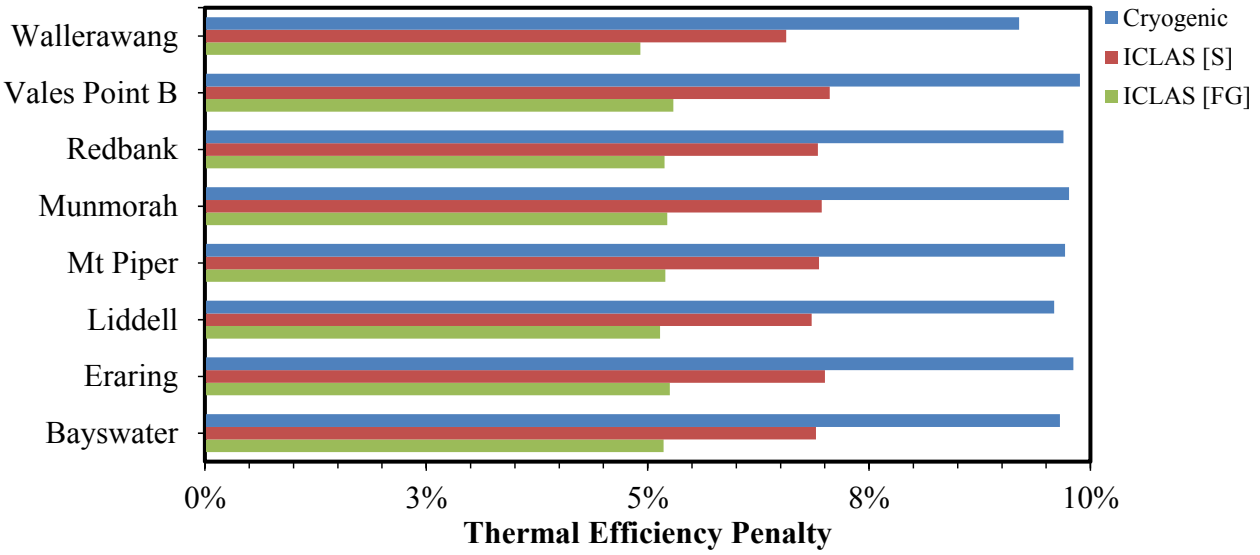

Figure 131: Bar chart plots of thermal efficiency penalty for the NSW fleet of coal-fired power plants.

The efficiency penalties shown in Figure 131 are primarily due to power demands of the ASU and CPU components of the oxy-fuel retrofit. The breakdown of the efficiency penalty in terms of its respective components is shown in Figure 132.

As this figure indicates, in the case of the cryogenic air separation the efficiency penalty due to the ASU approximately represents 61% of the total efficiency penalty whereas for ICLAS [S] and ICLAS [FG] the efficiency penalties associated with ASU respectively represent about 45% and 27% of the overall efficiency penalty. In other words, while for the cryogenic case the limiting unit in terms of the design of the retrofit plant is ASU, in the case of chemical looping based air separation processes and in particular ICLAS [FG], it is the CPU which underpins the efficiency losses rather than the ASU. This, as shown in the proceeding sections, leads to much lower operating and maintenance costs and results in significantly higher economic gains as more electricity can be exported compared with that associated with a cryogenic air separation component.

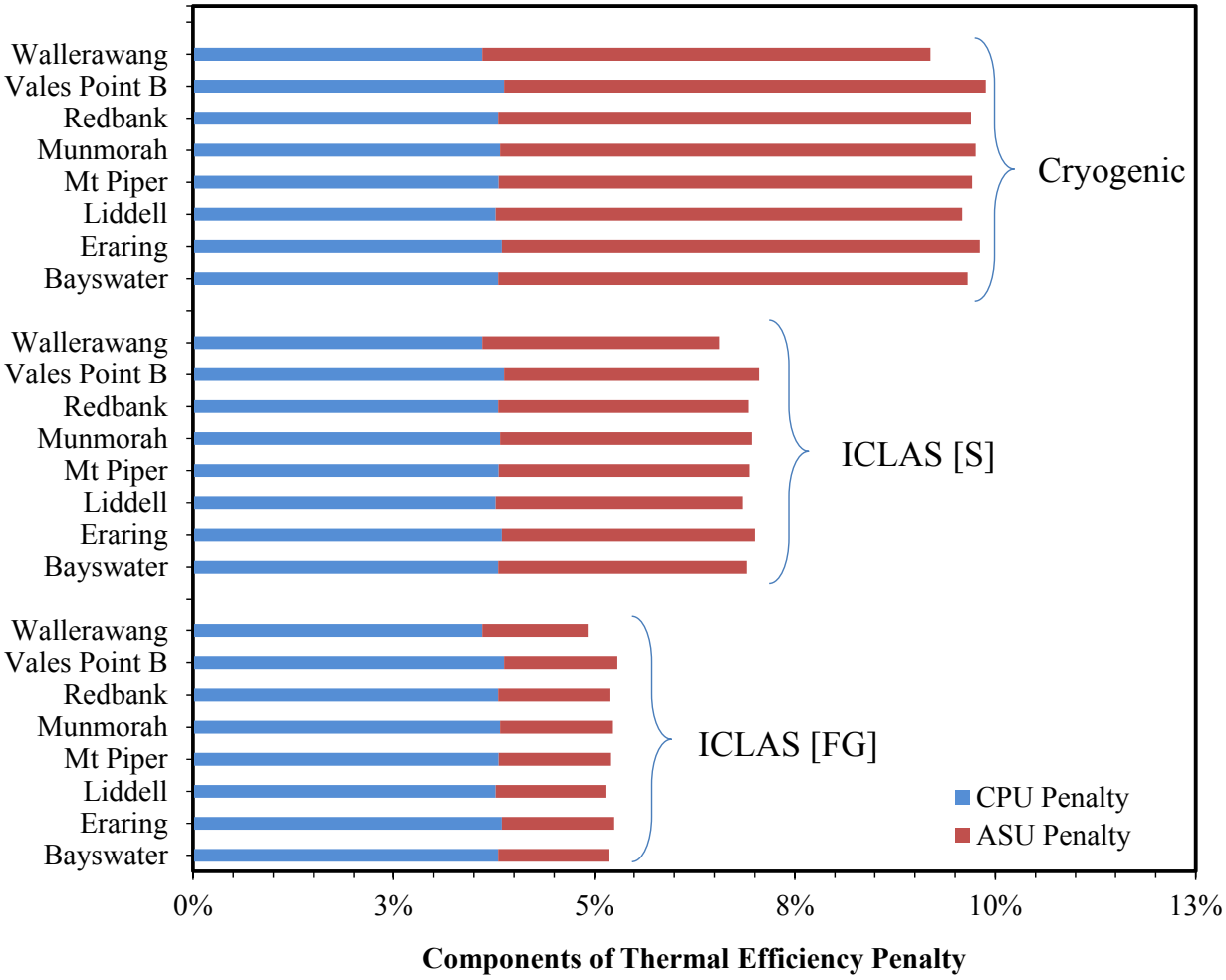

Figure 132: Bar chart plots of thermal efficiency penalty for the NSW fleet of coal-fired power plants as a function of efficiency penalty due to ASU and CPU power demands.

Electricity Output Penalty (EOP)

Electricity output penalty (EOP) is essentially another way of expressing the plant losses due to parasitic load. However, EOP is usually normalised by the amount of CO_2 avoided and as such is a measure of the effectiveness of the CO_2 capture technology. Figure 133 shows EOP for the eight coal-fired power plants that are being examined in this study. Yet again there is a clear difference between the results corresponding to the cryogenic and those related to chemical looping based air separation with ICLAS [FG] showing the lowest EOP figures for each power plant. Interestingly, the results appear to be independent of the power plant showing little variation from plant to plant. For instance, in the case of cryogenic air separation the EOP varies between 342.8 and 344.6 kWh/tCO_2 captured. Similarly, for the ICLAS [S] the EOP ranges from 245 t0 246 kWh/tCO_2 captured while ICLAS [FG]

varies over a much tighter range of EOP between 184 and 184.3 kWh/tCO_2 captured. The corresponding averages for the cryogenic, ICLAS [S] and ICLAS [FG] are 344.0, 245.6 and 184.2 kWh/tCO_2 captured, respectively.

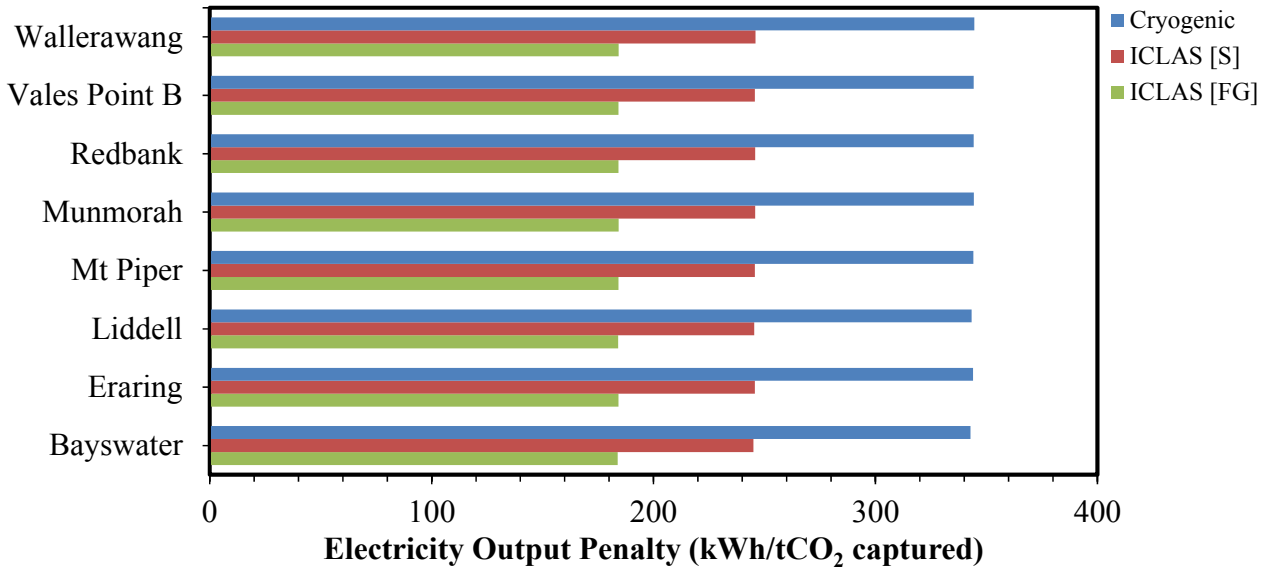

Figure 133: Bar chart plots of EOP for the NSW fleet of coal-fired power plants.

8.3.2 Plant Economic Assessment

Capital Cost

Figures 134 and 135 show the gross and normalised version of the capital cost for the oxy-firing retrofit of NSW coal-fired power plants. The data set used in the calculation of the capital cost was presented earlier in Table 17. As Figure 134 indicates, depending on the power plant specifications / features and the type of air separation technology selected, the gross capital cost varies between $70 million to about $6 billion. The highest capital cost is associated with the Bayswater plant and the lowest one corresponds to Munmorah.

The bar chart plots of the normalised capital cost (expressed in $ / kW of send out electricity) shown in Figure 135 reveal that the average cost of oxy-firing retrofit with a cryogenic type air separator is approximately $3,900/kW whereas the corresponding retrofit costs with ICLAS [S] and ICLAS [FG] options are $3,100/kW and $2,600/kW, respectively. Therefore, an ICLAS [FG] type design can potentially lead to 32% reduction in capital cost and as noted earlier to 50% reduction in efficiency penalties when compared with a cryogenic based design.

Interestingly, Bayswater which in gross terms represents the highest capital cost, in normalised terms features a close to average capital cost. The same trend by and large is exhibited by other large power

plants such as Eraring and Wallerawang while small plants such as Munmorah and Redbank post very high values for the normalised capital cost. This suggests that regardless of the air separation design, the oxy-firing retrofit is more economical and cost effective if implemented in coal-fired power plants with relatively high plant capacity (i.e. high MW output).

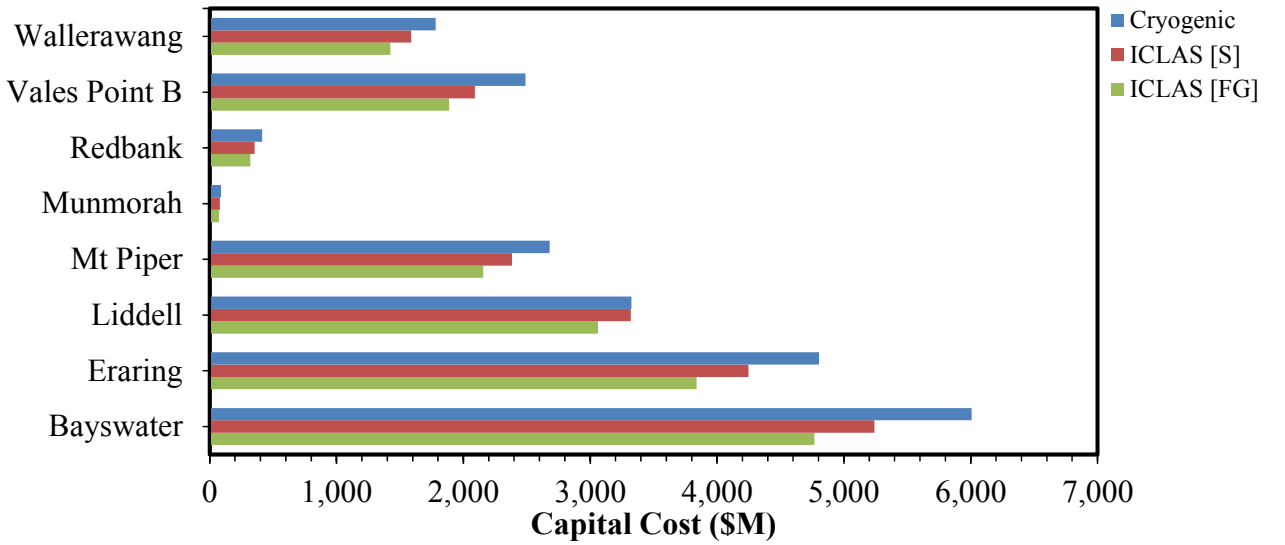

Figure 134: Bar chart plots of the gross capital cost for the retrofit of NSW fleet of coal-fired power plants.

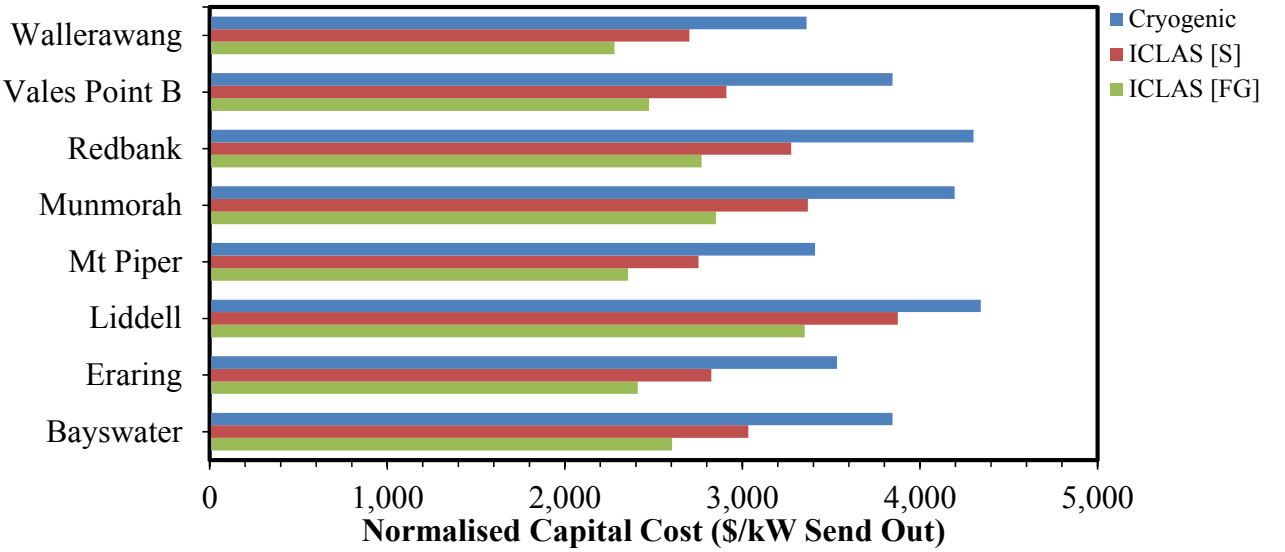

Figure 135: Bar chart plots of the normalised capital cost for the retrofit of NSW fleet of coal-fired power plants.

To gain a better insight into the impact of air separation unit on the capital cost the breakdown of capital cost items for the Bayswater power plant is shown in Figures 136 to 139. Figure 136 illustrates

the pie chart plot of the capital cost items for a cryogenic based design while Figures 136 and 138 show similar breakdowns of the capital cost for the ICLAS [S] and ICLAS [FG] designs. As can be seen in these figures in the case of the cryogenic design the ASU capital cost represents 26% of the total cost and is as high as that corresponding to the boiler modifications. For this configuration the capital cost of the CPU is as low as 9% of the overall cost.

However, for an ICLAS [S] type design (see Figure 137) the capital cost of the ASU: (i) only constitutes 15% of the overall cost, (ii) is comparable with the capital cost of the CPU, and (iii) is only one third of the capital cost associated with boiler modification.

For an ICLAS [FG] type design (see Figure 138) the capital cost of the ASU reduces even further to levels as low as 7% of the overall capital cost. In comparison the capital cost of the ICLAS [FG] component of the retrofit becomes one fifth of the boiler modification cost and as such for an ICLAS [FG] type design the capital cost of the ASU is no longer the limiting factor.

This is better shown in Figure 139 where the relative importance of the ASU and CPU capital costs are compared with respect to the combined cost of these items. For a cryogenic design (Figure 139a) the ASU unit costs almost 3 times more than the CPU whereas in the case of an ICLAS [S] design the relative cost of ASU to CPU becomes 1.5 (note: 60.4 / 39.6 ~ 1.5; see Figure 139b). This downward trend continues to the extent that for an ICLAS [FG] design the relative cost of ASU to CPU drops to 0.64 (note: 39 / 61 ~ 0.64; see Figure 139c).

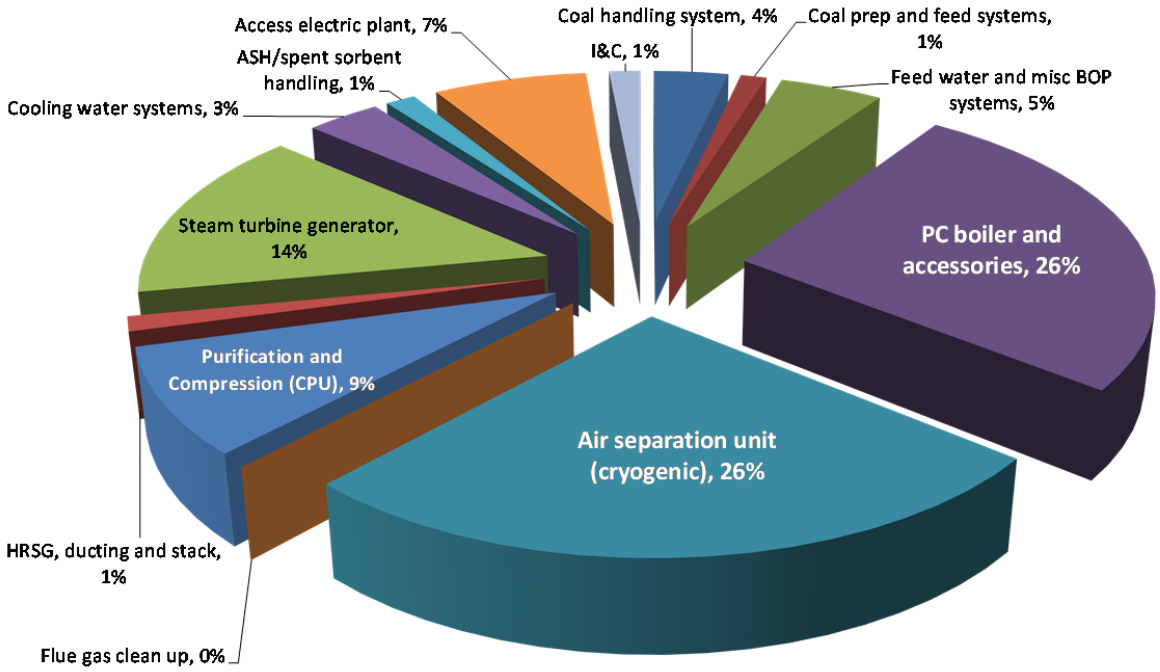

Figure 136: Breakdown of capital cost items for the Bayswater power plant (cryogenic option).

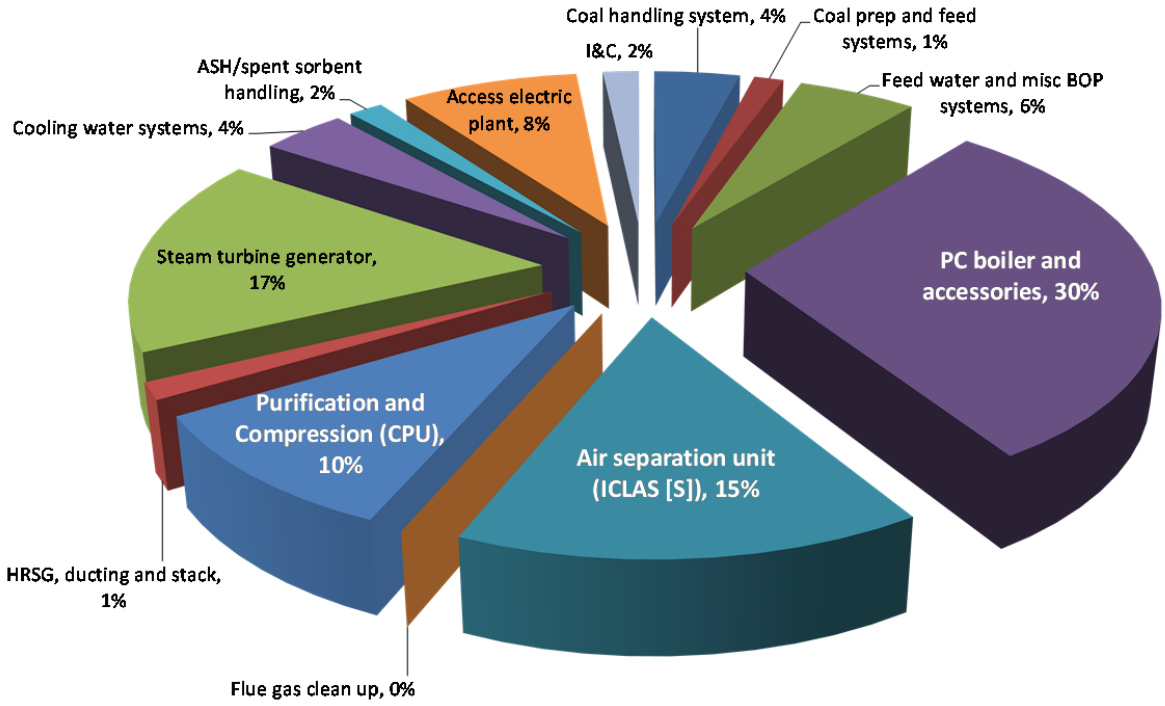

Figure 137: Breakdown of capital cost items for the Bayswater power plant (ICLAS [S] option).

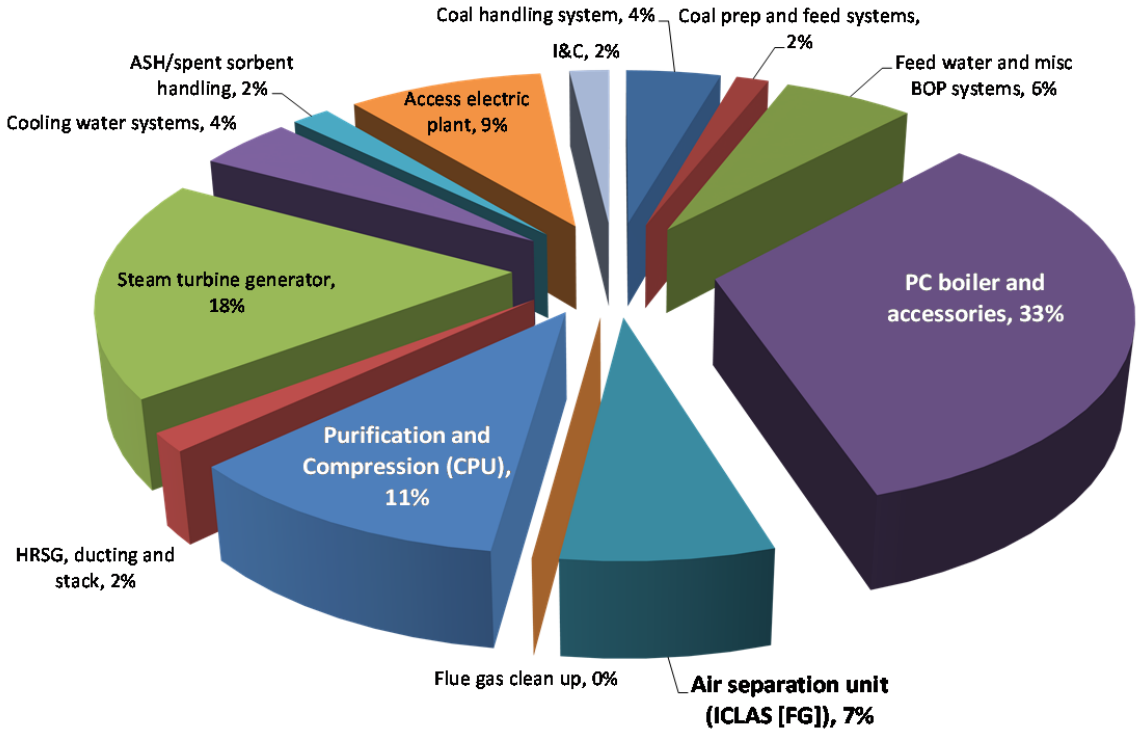

Figure 138: Breakdown of capital cost items for the Bayswater power plant (ICLAS [FG] option).

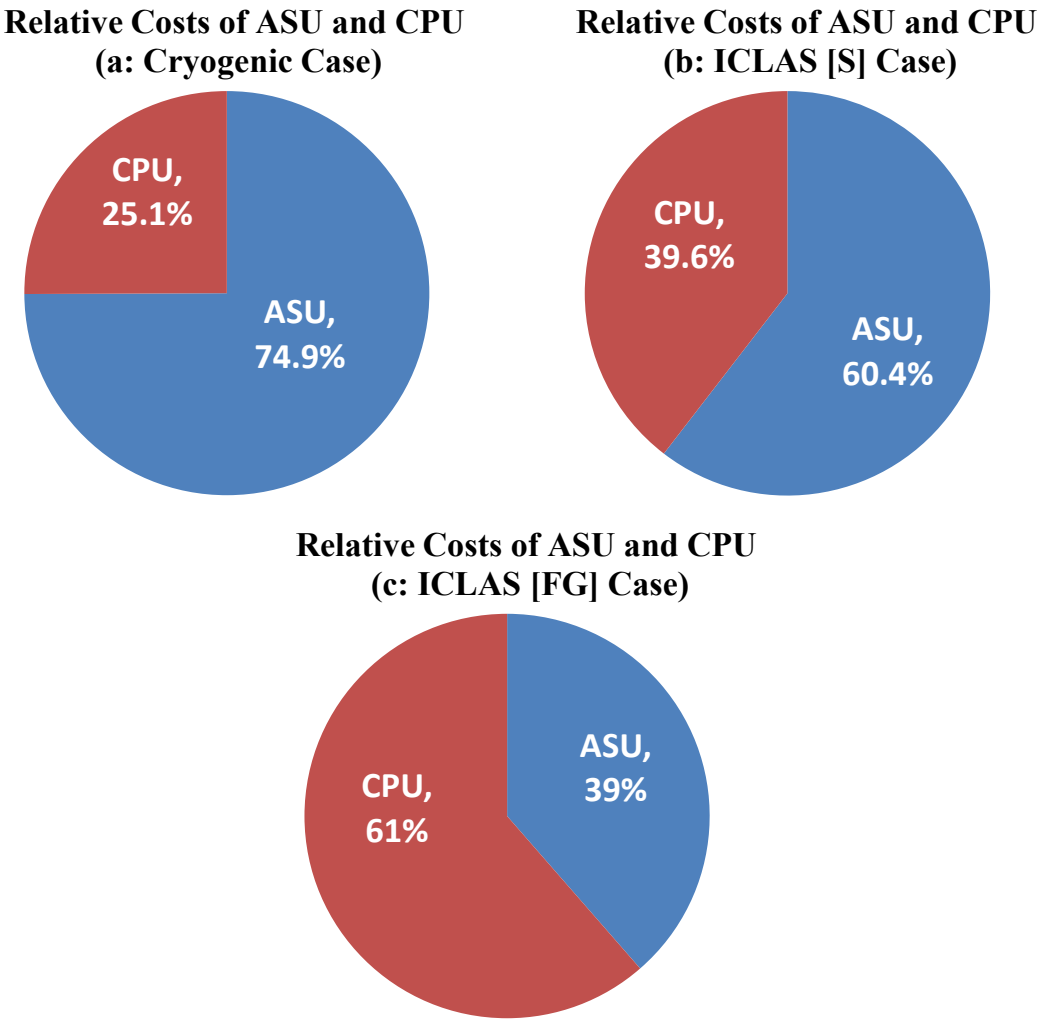

Figure 139: Relative costs of ASU and CPU with respect to their combined capital cost.

To put the capital cost estimates presented in this section into perspective, a benchmarking comparison was undertaken to compare the normalised capital cost for 22 different low emission technologies (both renewable and fossil fuel based) with the current results for oxy-firing retrofit of the NSW coal-fired power assets with a configuration involving ICLAS [FG] and CCS. The majority of data for the abovementioned low emission technologies were adopted from Reference [46]. The results of the benchmarking comparison have been summarised in Figure 140. As can be seen, the capital cost for an ICLAS [FG] based oxy-fuel retrofit in NSW, which ranges between $2,300/kW to $3,400/kW) is much cheaper than many of the technology options shown in Figure 140 (except open and combined gas turbine cycles) and is quite comparable with the more cost effective technologies such supercritical pulverised black coal, combined cycle gas turbine with CCS and wind (onshore). Notably, the capital cost estimates from this study are also much lower than the values presented in Figure 140 for oxy-fuel combustion of black coal. This is partly due to the lower capital and operating costs of the ICLAS [FG]

(note previous studies only considered oxy-fuel with cryogenic ASU) and partly due to the fact that there is no need for costly FGD (flue gas desulphurisation) units in NSW given the low sulphur content of the coal consumed in NSW.

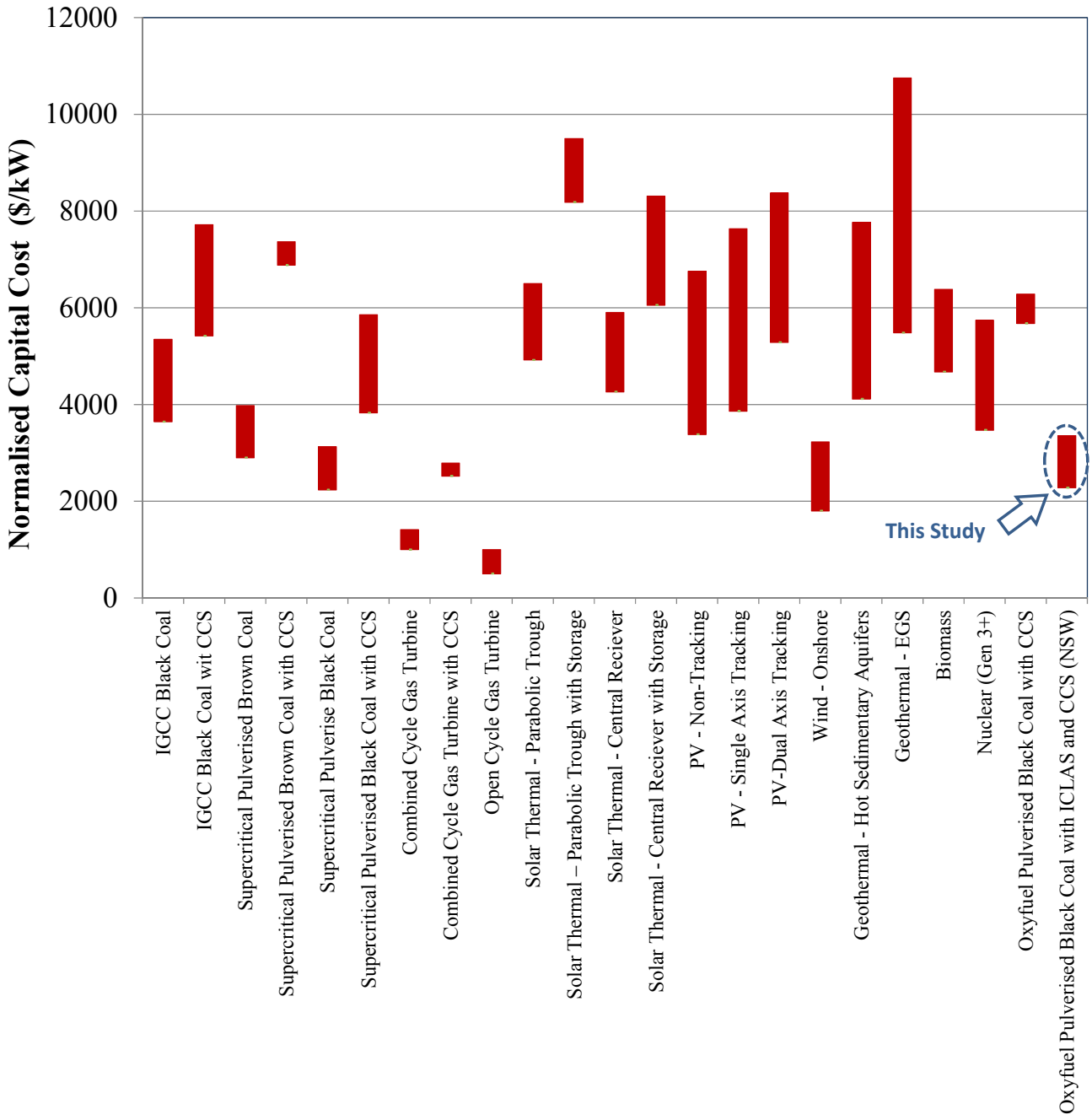

Figure 140: Benchmarking of the normalised capital cost for the NSW coal-fired power plants retrofitted for oxy-firing (with ICLAS [FG] and CCS) against the normalised capital cost for 22 alternative low emission technologies.

Levelised Cost of Electricity

Levelised cost of electricity (LCOE) is considered the most convenient measure of the overall competiveness of alternative power generation technologies. It represents the cost in real dollars (per kWh basis) of building and operating a power plant over an assumed life cycle. In simple terms, LCOE represents the minimum price of electricity at which a power plant generates enough revenue to pay for production cost and provide sufficient return to investors. Key inputs in calculating LCOE as noted in Section 8.2.3, include costs such as capital costs, fixed and variable operations and maintenance costs, fuel cost, financing costs, and an assumed utilisation rate for the power plant.

The LCOE for the coal-fired power plants under investigation in this study have been summarised in Figure 141. According to this figure the most expensive power plants as far as electricity generation is concerned are Munmorah and Redbank. The main reason for the observed trend is the small capacity of these plants and their relatively high values of normalised capital cost. In contrast, large capacity power plants such as Bayswater or Eraring post relatively modest LCOE (see Figure 141). It is evident from Figure 141 that yet again retrofit configurations with chemical looping based air separators and in particular ICLAS [FG] outperform those retrofits which incorporate cryogenic air separation. Based on Figure 141, the average value of LCOE for a cryogenic based oxy-fuel plant in NSW is $118/MWh whereas the average figures for the ICLAS [S] and ICLAS [FG] are $105/MWh and $95/MWh, respectively.

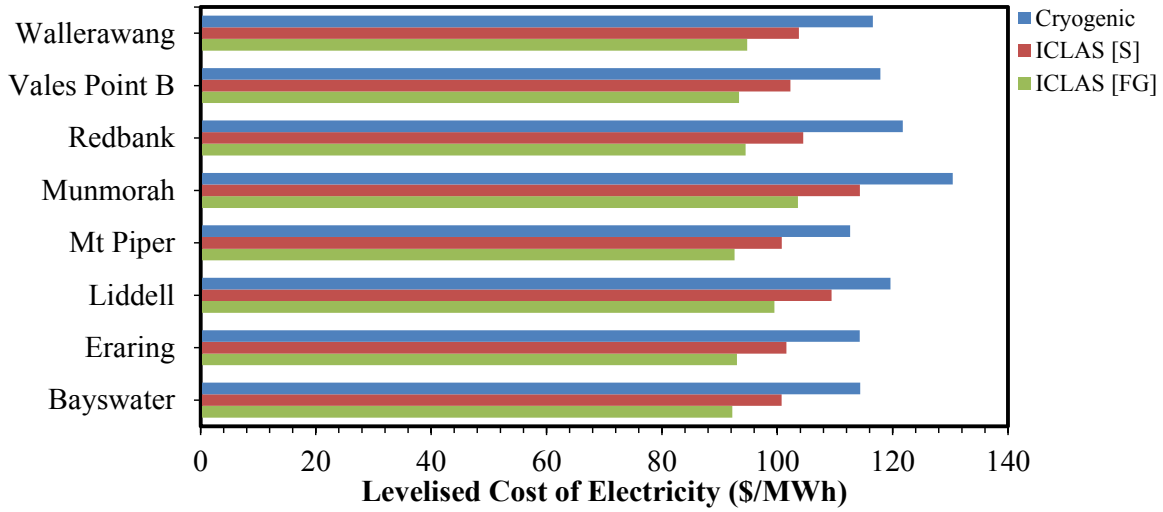

Figure 141: Bar charts of LCOE for NSW coal-fired power plants retrofitted for oxy-firing operation.

Similar to the benchmarking exercise discussed in the previous section and to put LCOE estimates presented in this section into perspective, a benchmarking comparison was undertaken to compare the LCOE for 23 different low emission technologies (both renewable and fossil fuel based technologies). The results are presented in Figure 142 where most of the data was adopted from Ref [46]. In this figure the results designated as "this study" correspond to oxy-fuel retrofits with ICLAS [FG] and CCS only. As can be seen, the LCOE for an ICLAS [FG] based oxy-fuel retrofit in NSW, which is about $100/MWh, is much cheaper than many of the technology options shown in Figure 140 and is quite

comparable with the more cost effective technologies such as supercritical pulverised fuel (black coal) and combined cycle gas turbine. Notably, the LCOE from this study is also much lower than the values presented in Figure 140 for oxy-fuel combustion of black coal. This is partly due to the lower capital and operating costs of the ICLAS [FG] and partly due to the fact that there is no need for costly FGD (flue gas desulphurisation) units in NSW given the low sulphur content of the coal used in NSW.

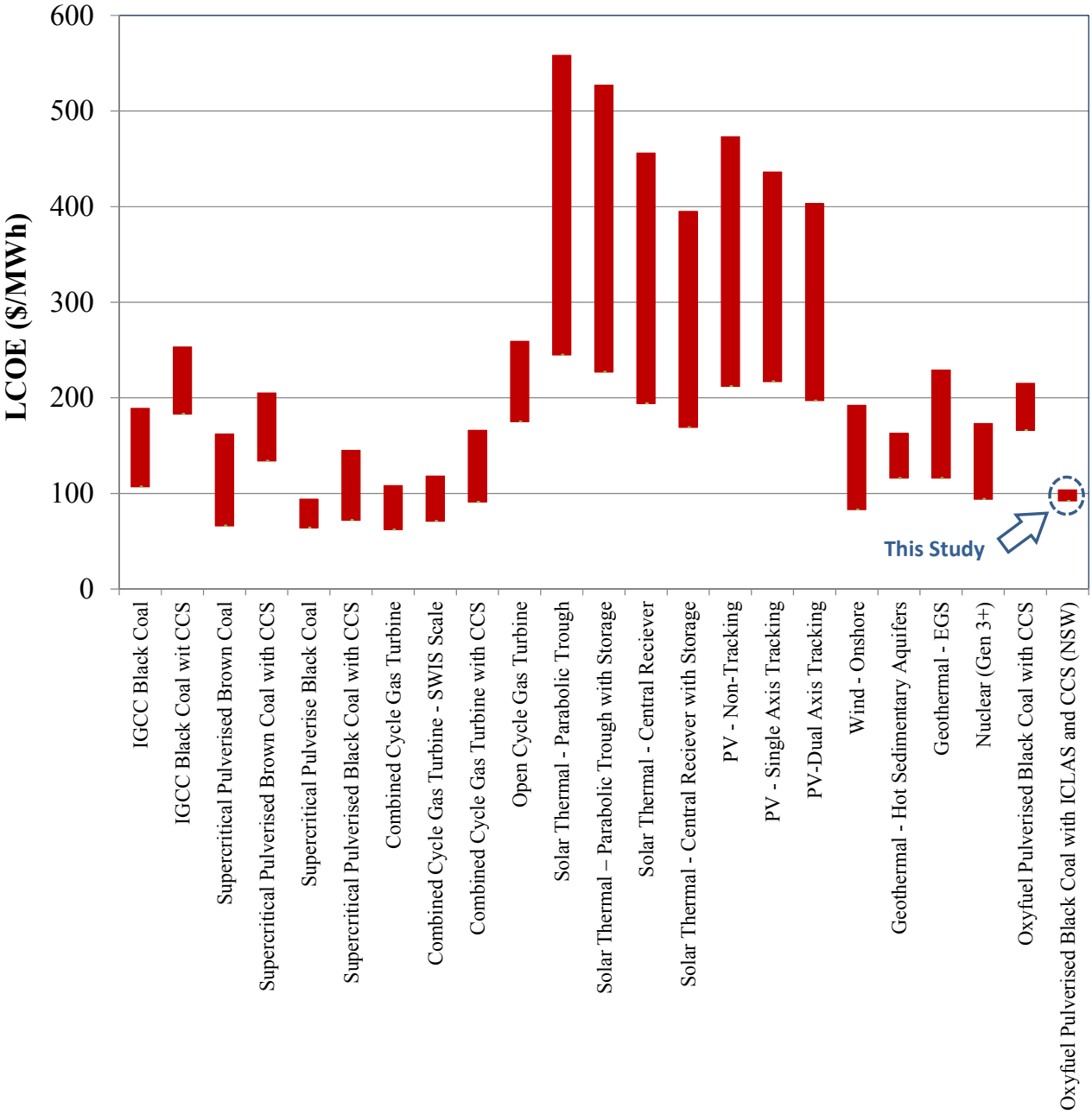

Figure 142: Benchmarking of the LCOE for the NSW coal-fired power plants retrofitted for oxy-firing (with ICLAS [FG] and CCS) against the LCOE for 22 alternative low emission technologies [46].

It should be highlighted that the average cost of electricity generation in NSW is currently about \$38/MWh [39]. Therefore, the rollout of oxy-fuel retrofits in the State will inevitably leads to higher generation cost. To understand the level and magnitude of such cost blowouts, the increase in the cost of electricity (Δ Cost of Electricity) due to oxy-fuel retrofit has been examined for the 8 power plants under investigation. The results have been summarised in Figure 143 and 144 where the increase in the production cost has been examined with and without carbon tax (a fixed value of \$23/tCO_2 was assumed). Clearly, regardless of the ASU design or the carbon price, significant increases in the generation cost of electricity are to be expected if oxy-fuel technology deployed across NSW. Although under the scenario of a carbon tax regime (Figure 144), the expected increases in the generation cost are more modest. Also, by and large, ICLAS [FG] results in much smaller levels of cost increase and as such is the most attractive option.

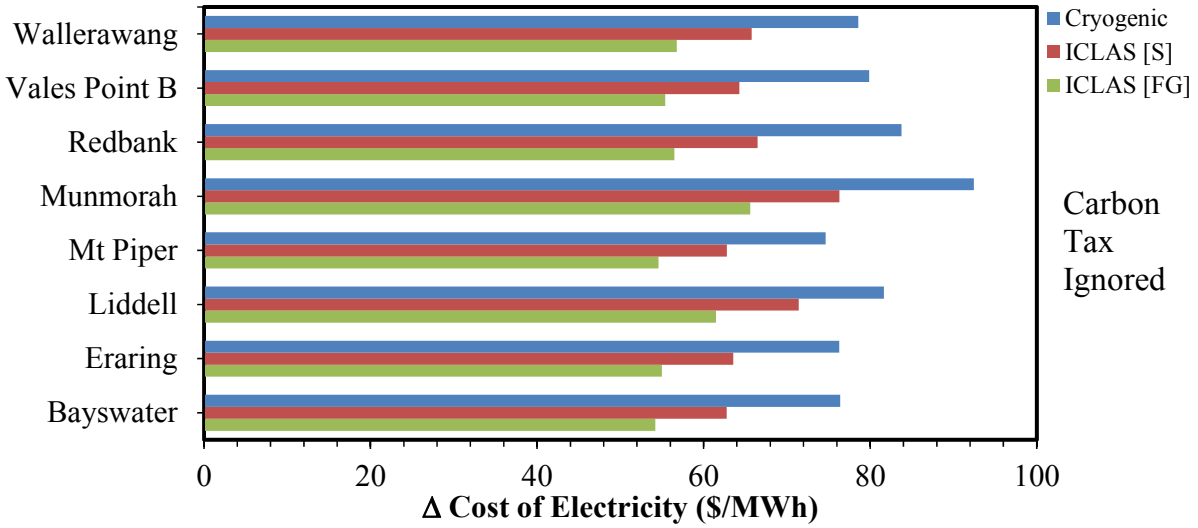

Figure 143: Bar char plot of rises in the cost of generating electricity (no carbon tax).

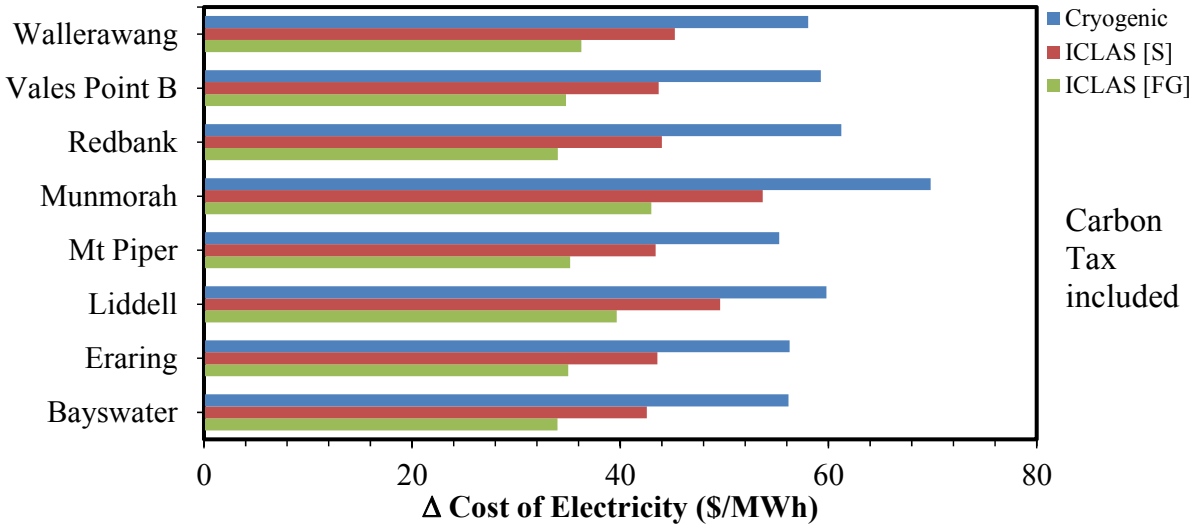

Figure 144: Bar char plot of rises in the cost of generating electricity (carbon tax included).

Cost of Abatement

The cost of abatement (COA) refers to the cost associated with the voluntary or compulsory removal of CO_2 from a generating plant. As described in Section 8.2.3, COA is expressed is expressed in $/tCO_2$ captured. The COA for NSW coal-fired power plants if retrofitted for oxy-firing operation are shown in Figures 145 and 146 as a function of ASU design under two scenarios of "no carbon tax" and "with carbon tax". Under the 'no carbon tax' scenario the cost of abatement ranges between $61/tCO_2$ and $85/tCO_2$ with averages of 81, 74 and 67 $/tCO_2$ for the cryogenic, ICLAS [S] and ICLAS [FG] designs, respectively. However, when carbon tax is included the cost of abatement drops to a range between $37/tCO_2$ and $64/tCO_2$ with averages of 60, 51 and 43 $/tCO_2$ for the cryogenic, ICLAS [S] and ICLAS [FG] designs, respectively.

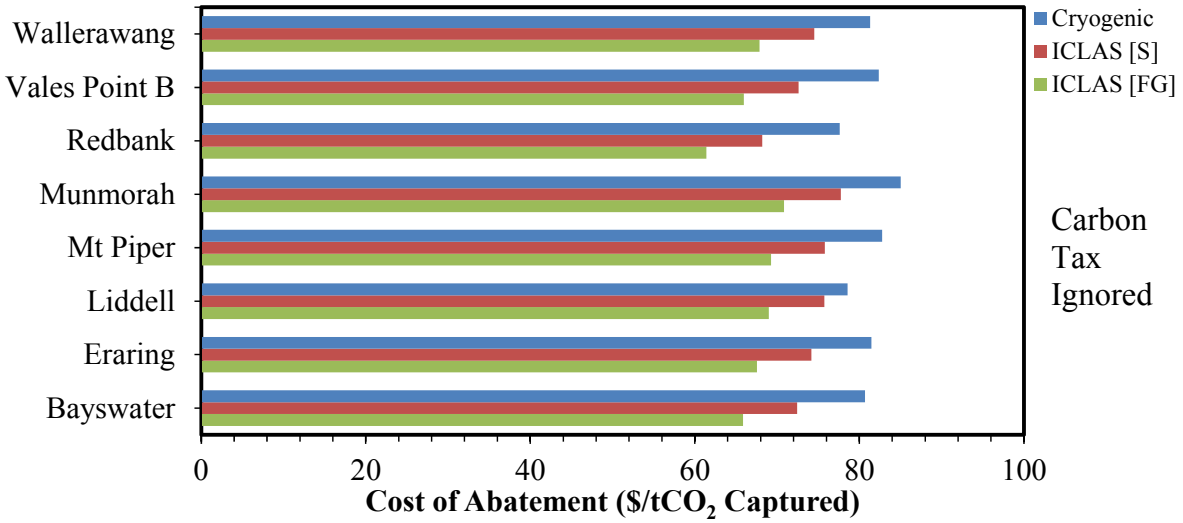

Figure 145: Bar char plot of cost of abatement for NSW coal-fired power plants (no carbon tax).

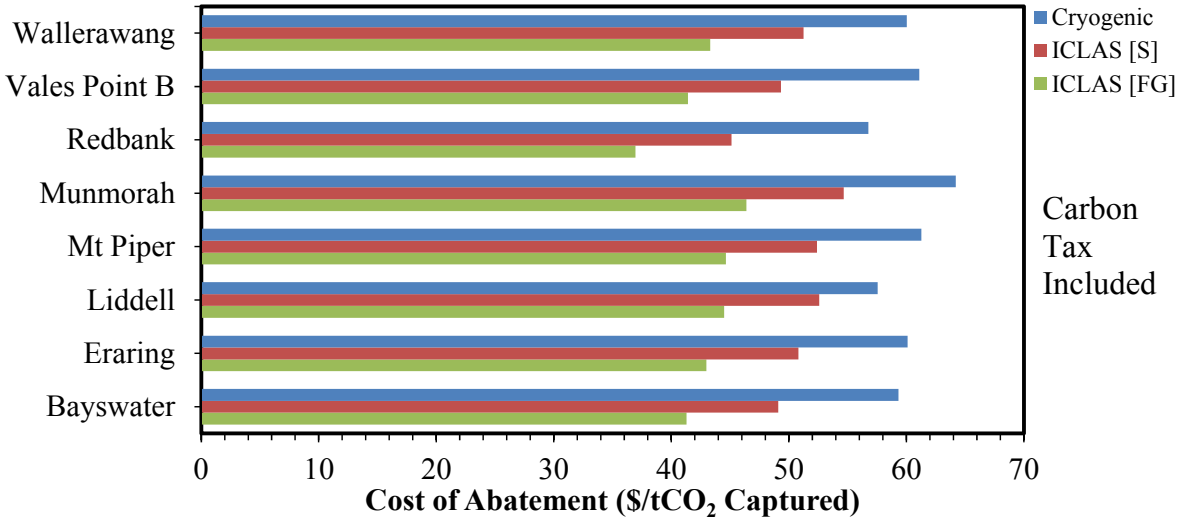

Figure 146: Bar char plot of cost of abatement for NSW coal-fired power plants (carbon tax included).

8.4 CONCLUSIONS

The following key conclusions can be drawn based on the results of the techno-economic analysis presented in this chapter:

- Broadly speaking and subject to the simplifying assumptions made in the present study, oxy-fuel conversion of the coal-fired power generation assets in NSW appears to be one of the most viable low emission options for the State provided that a chemical looping based design for air separation is employed.

- This, however, requires a detailed feasibility study for each power plant and more importantly further studies to demonstrate the effectiveness of the chemical looping based air separation at scale.

- Also, a range of suitable options ought to be identified and/or established for the storage and sequestration of CO_2 in NSW. Without a viable storage option, the rollout of oxy-fuel technology across NSW will not reach its full potential and will unlikely lead to any tangible outcome for the State or companies involved.

Chapter 9

LIFE CYCLE ASSESSMENT

9.1 BACKGROUND

Advitech Pty Limited (Advitech) was engaged by the University of Newcastle (UoN) to create a comparative Life Cycle Assessment (LCA) that would demonstrate the environmental performance of using Integrated Chemical Looping Air Separation (ICLAS) as part of a hypothetical state wide rollout of oxy-fuel technology to coal-fired power plants in NSW.

UoN has developed two innovative methods for oxygen refining process termed Chemical Looping Air Separation (CLAS), and Integrated Chemical Looping Air Separation (ICLAS). The latter method has been specifically designed to be used in O_2/CO_2 (oxy-fuel) combustion of coal. Both methods require a great deal less energy to refine oxygen than current methods (cryogenic distillation -CD) used to enable oxy-fuel combustion. Quantifying the total environmental performance of these approaches is of significant interest, as it demonstrates the benefit of the new methods over current practice. This LCA will also satisfy the requirements of an initial funding agreement of the research.

9.2 METHODOLOGY

This LCA is a comparative LCA of two types of coal fired power stations with Oxy-fuel combustion. The difference investigated is the air separation method which is by either Integrated Chemical Looping Air Separation (ICLAS [FG]) or by conventional methods of Cryogenic Distillation (CD). This comparison uses two measures to quantify environmental impact: Greenhouse gas emissions, in units of tonnes of Carbon Dioxide equivalent (tCO_2e), and embodied energy in units of Gigajoules (GJ).

The LCA model does not generate any new energy or emission factors for energy production, rather using the best assumptions, which is selecting the most realistic, as long as information is available to allow for this activity or source to be represented. Much of this work relies on various recent research papers and while all care has been undertaken to try to align boundary assumptions for the representative processes, some differences in these underlying studies may occur (especially where information published in other languages has been used in a translated version).

The LCA was set up according to the following international standards and protocols:

- ISO 14040:2006 and ISO14044:2006 (superseding ISO 14041, ISO 14042 and ISO 14043)
- Complying with PAS 2050 and GHG Protocol Life Cycle Accounting and Reporting Standard
- In accordance with the Japanese PCR (Product Category Rule) for Grid Electricity

This LCA was not performed for an Environmental Product Declaration (EPD), but the LCA includes enough detail that this could be completed at a later date if required.

As pointed out earlier this LCA comparison uses two measures to quantify environmental impact: Greenhouse gas emissions, in units of tonnes of Carbon Dioxide equivalent (tCO_2e), and embodied energy in units of Gigajoules (GJ). Outputs are also developed into useful KPIs for comparison. These are bases of per MWh, and per tonne of black coal.

Scenario Details from Journal Paper (Basis) of This Study

The scope of the LCA study is based upon the paper "Process Evaluation of an 865 MWe Lignite Fired O_2/CO_2 Power Plant (Andersson & Johnsson, [41])", which provides many details of the operation and sizing of a typical plant. The paper by these authors provides the following details:

- Net electrical output: 865 MWe
- Boiler size for CD oxy-fuel combustion: 2585 MWt
- Gross power production: 46%
- Internal electricity demand: 61 MWe (including benefits from process integration – feedwater preheating from flue gas)
- CD type ASU electrical demand: 181 MWe

Major Changes from Reference [41] Base Case Model

- Changed fuel feed from European lignite to Australian black coal
- Maintained identical electrical output to the grid in both ASU cases, and where ICLAS [FG] has provided a benefit, this resulted in requiring a smaller boiler due to a lower parasitic load of the air separation unit (ASU)
- No carbon capture and storage (CCS) occurs in this model (see also the next sub-section)

Major Assumptions

- The study assumes viable options for CO_2 storage for NSW will be found in the near future. However, because of the present uncertainty about these storage options, the LCA model ignores the storage and sequestration of CO_2 and mainly focuses on the power plant itself.
- Oxy-fuel feed requirement is 528,000 m^3/h of normal air
- Cryogenic distillation air separation has an energy demand of 0.35 $kW/m^3/h$; resulting in an ASU requiring 181 MWe
- ICLAS air separation has an energy demand of 0.15 $kW/m^3/h$; resulting in an ASU requiring 83 MWe (*It should be highlighted that according to project data the power demand of an ICLAS [FG] type air separator is about 0.08 $kW/m^3/h$ but in this LCA study a more conservative figure of 0.15 $kW/m^3/h$ was selected to represent the worst case scenario. While*

not reported here, additional LCA calculations were also carried out for power demands of 0.10 kW/m^3/h and 0.05 kW/m^3/h.)

- 0.33 kg of oxygen carrier (30%CuO,70%SiO2) produces 1 m^3 of normal air (project data)
- Based on a weighted basis of electricity produced in NSW, the hypothetical power station was located adjacent to Liddell and Bayswater power stations
- Based on proximity to electricity production, the metal substrate preparation was located in a nearby industrial zoned area in Mt Thorley (LOT 6 O'Hara Pl Mt Thorley NSW 2330)
- Copper and Silica for the substrate were assumed to be supplied and recycled in western Sydney (Parramatta)
- This study excludes decommissioning.

Minor Assumptions of This Study

- Power station construction materials are based on requiring a DeNOx unit, which may not be required in Australia (due to coal characteristics), this was used as most larger power stations (~500MWe) included in the study of Röder et al., (2004) were in Europe, which include these measures (and by using this assumption smaller estimates of material per MW capacity resulted, rather than lower sized power stations (~100MWe) without DeNOx units)
- Identical construction materials for both ASUs, while in reality ICLAS operates at atmospheric pressure, substantially lower than the CD type ASU pressures, which means there would be a net benefit of ICLAS [FG] requiring less materials (and associated safety equipment)
- The recharge rate of the oxygen carrier metal substrate is 20% replacement every 3 months
- Processed silica (SiO_2) was assumed to require the same energy and wastage of raw sand equivalent to metallurgical sand
- Recycling of copper has been calculated from excluding the mining and mineral processing components (metal production average only)

9.3 LCA CALCULATIONS

The LCA calculations were performed using the following flowcharts of inputs, components and outputs for the cryogenic and ICLAS processes, respectively. For details please refer to Appendix C.

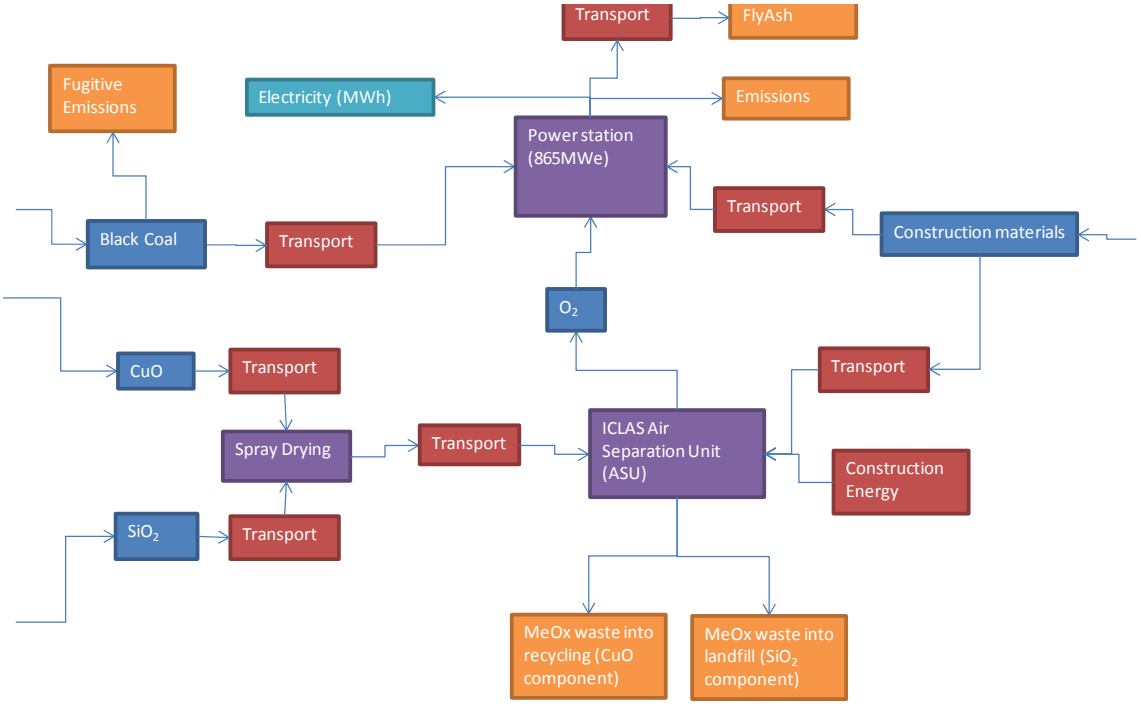

Figure 147: Flowchart of inputs, components and output for the ICLAS [FG] process.

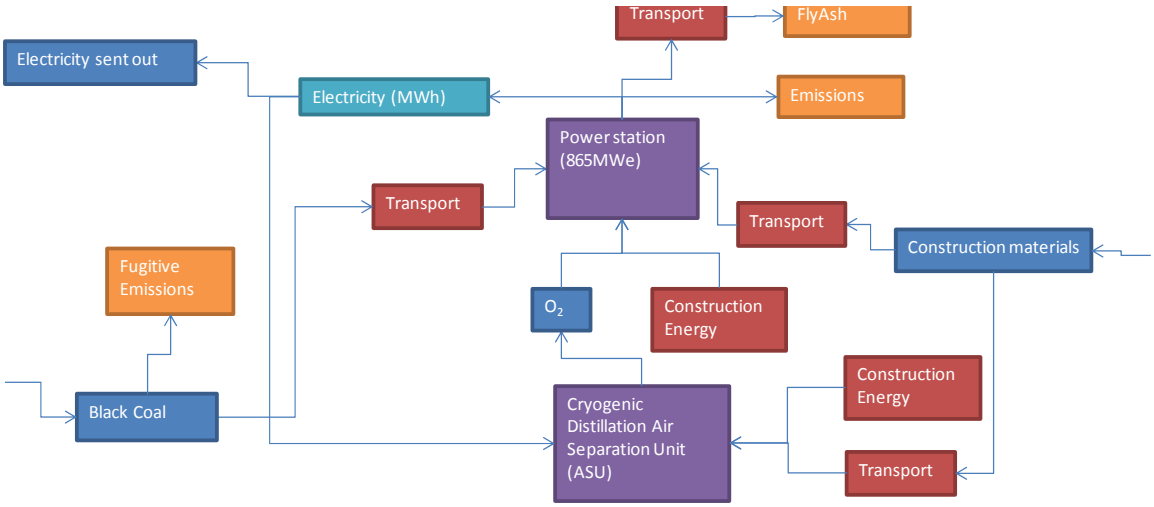

Figure 148: Flowchart of inputs, components and output for the cryogenic process.

9.4 RESULTS AND DISCUSSION

The model has allocated attributes for certain energy and emission sources. These are either 'initial' (once off such as construction emissions, initial ICLAS substrate charge for the ASU, etc.) or 'annual' energy and emissions (feed, ICLAS recharge, transport etc.), which are repeated for the life of the plant (here 20 years). This results in a widening gap of energy and emissions impact between scenarios. The resultant cumulative energy and emissions (and saving between the methods) at the end of the selected lifetime is usually what is used to gauge the benefit of one method over another. Analysing and investigating further breakdown of sources on an initial or annual basis is useful for understanding the main reasons why one method is better than the other (or for prioritising which type of impact is more important (energy – usually cost driven, or emissions – usually environmental or government regulator driven). But since we understand why the benefit occurs for ICLAS (due to reduction in feed for auxiliary power requirements), we do not need to go into further detail unless this is required for a particular purpose or if we are looking to reduce some of the smaller components further.

Figure 149 and Table 21 are the main output of the LCA for emissions and demonstrate the benefit of using ICLAS over conventional methods (cryogenic) for oxy-fuel combustion, which is roughly 14% less CO_2e emissions for identical production of electricity to the grid. This is for the full life cycle of 20 years.

Similarly, Figure 150 and Table 22 are the main output of the LCA for energy and demonstrate that over the 20 years life cycle of the plant about 8.5% less energy can be consumed if ICLAS is used instead of cryogenic air separation for oxy-fuel combustion.

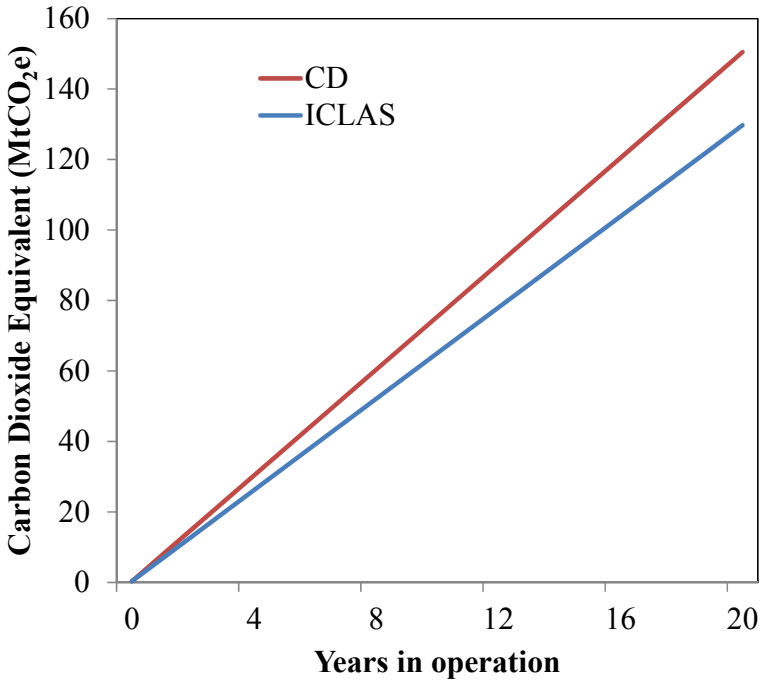

Figure 149: Emissions of both scenarios over the 20 year lifetime of the power plant.

Table 21: Emissions of both scenarios over the 20 year lifetime of the power plant (tabulated form)

Year	ICLAS Emissions (Million tonr	CD Emissions (Million tonnes of CO_2e)	% ICLAS of CD	Comments
0	0.36	0.36	100.70%	Before com
1	6.83	7.86	86.85%	
2	13.30	15.37	86.53%	
3	19.77	22.87	86.42%	
4	26.24	30.38	86.36%	
5	32.71	37.89	86.33%	
6	39.18	45.39	86.30%	
7	45.64	52.90	86.29%	
8	52.11	60.40	86.28%	
9	58.58	67.91	86.27%	
10	65.05	75.42	86.26%	
11	71.52	82.92	86.25%	
12	77.99	90.43	86.25%	
13	84.46	97.93	86.24%	
14	90.93	105.44	86.24%	
15	97.40	112.95	86.24%	
16	103.87	120.45	86.23%	
17	110.34	127.96	86.23%	
18	116.81	135.46	86.23%	
19	123.28	142.97	86.23%	
20	129.75	150.48	86.22%	

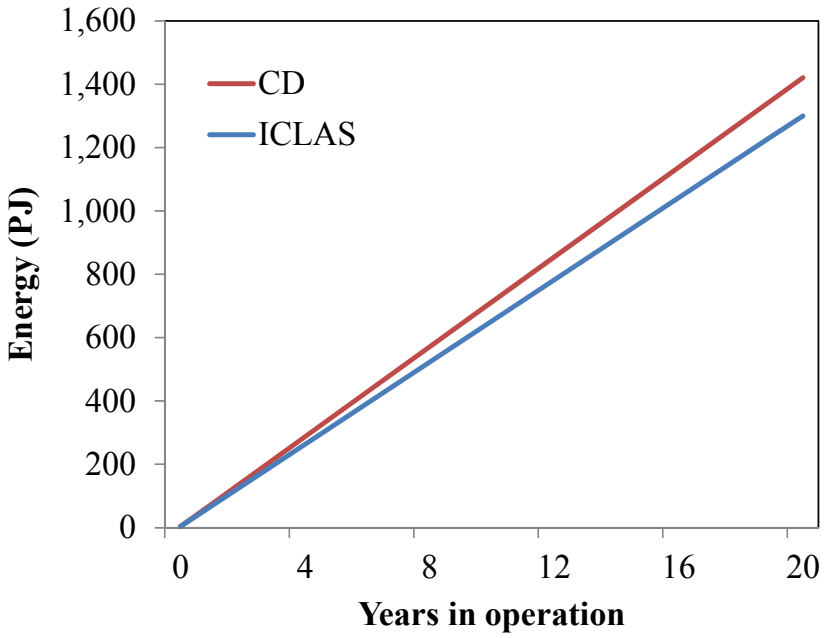

Figure 150: Energy of both scenarios over the 20 year lifetime of the power plant.

Table 22: Energy of both scenarios over the 20 year lifetime of the power plant (tabulated form)

Year	ICLAS Energy (PJ)	CD Energy (PJ)	% ICLAS of CD process	Comments
0	3.78	3.77	100.23%	Before commissioning (i.e. building
1	68.59	74.60	91.95%	
2	133.40	145.42	91.73%	
3	198.21	216.25	91.66%	
4	263.02	287.08	91.62%	
5	327.84	357.91	91.60%	
6	392.65	428.74	91.58%	
7	457.46	499.57	91.57%	
8	522.27	570.39	91.56%	
9	587.08	641.22	91.56%	
10	651.90	712.05	91.55%	
11	716.71	782.88	91.55%	
12	781.52	853.71	91.54%	
13	846.33	924.53	91.54%	
14	911.14	995.36	91.54%	
15	975.96	1,066.19	91.54%	
16	1,040.77	1,137.02	91.53%	
17	1,105.58	1,207.85	91.53%	
18	1,170.39	1,278.67	91.53%	
19	1,235.20	1,349.50	91.53%	
20	1,300.02	1,420.33	91.53%	

Figures 151 to 154 illustrate the breakdown of total emission and energy by source. Figure 152 is essentially the same as Figure 151 but has been resized (zoomed) so that the non-feed sources can be better distinguished. Similarly, Figures 153 and 154 show similar information but have different zooms. The main message from Figures 151 to 154 is that by far the largest model source for both scenarios is the black coal feed. This feed (on an annual basis) is far larger than any of the initial construction energy or emissions.

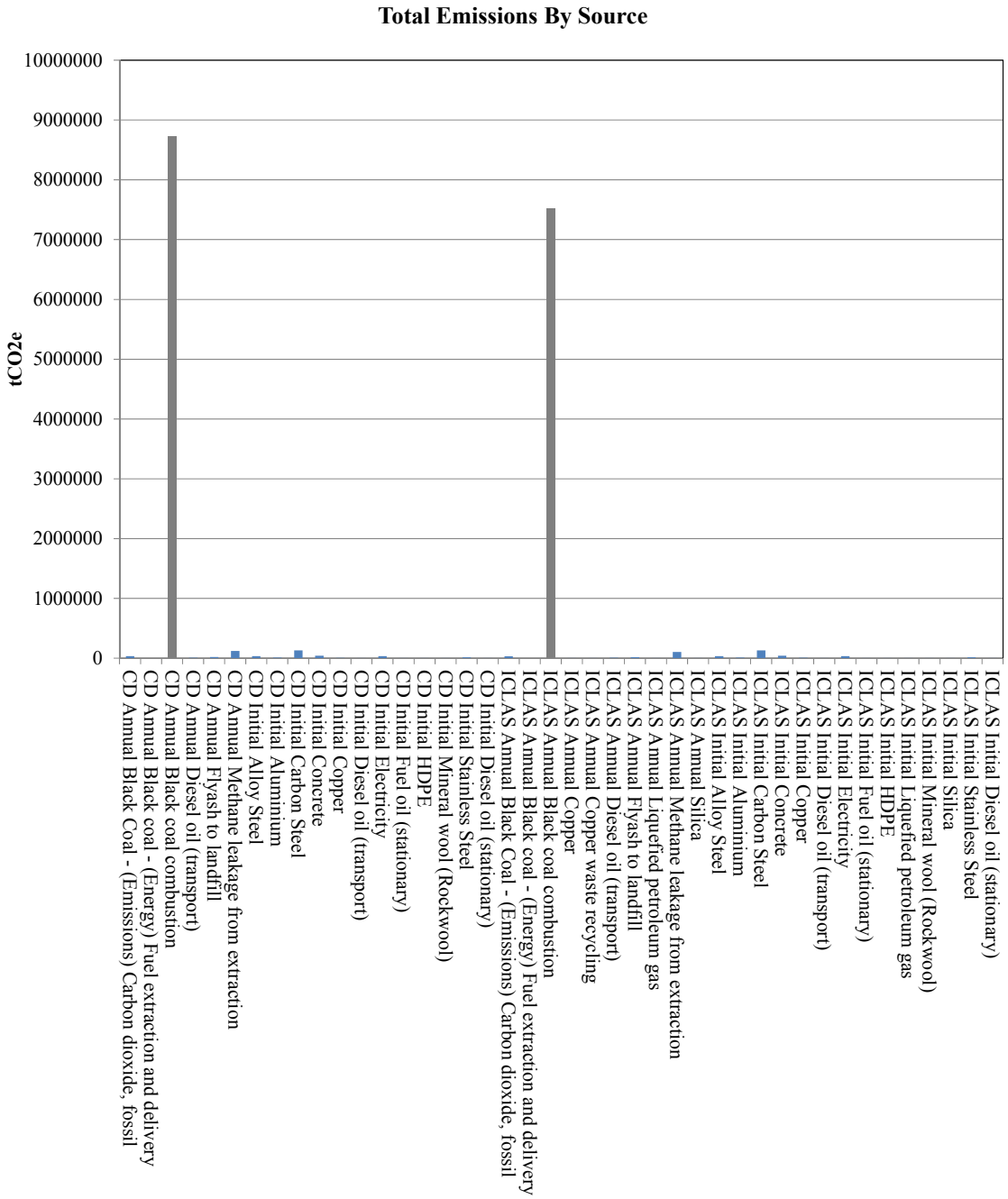

Figure 151: Emissions of all sources.

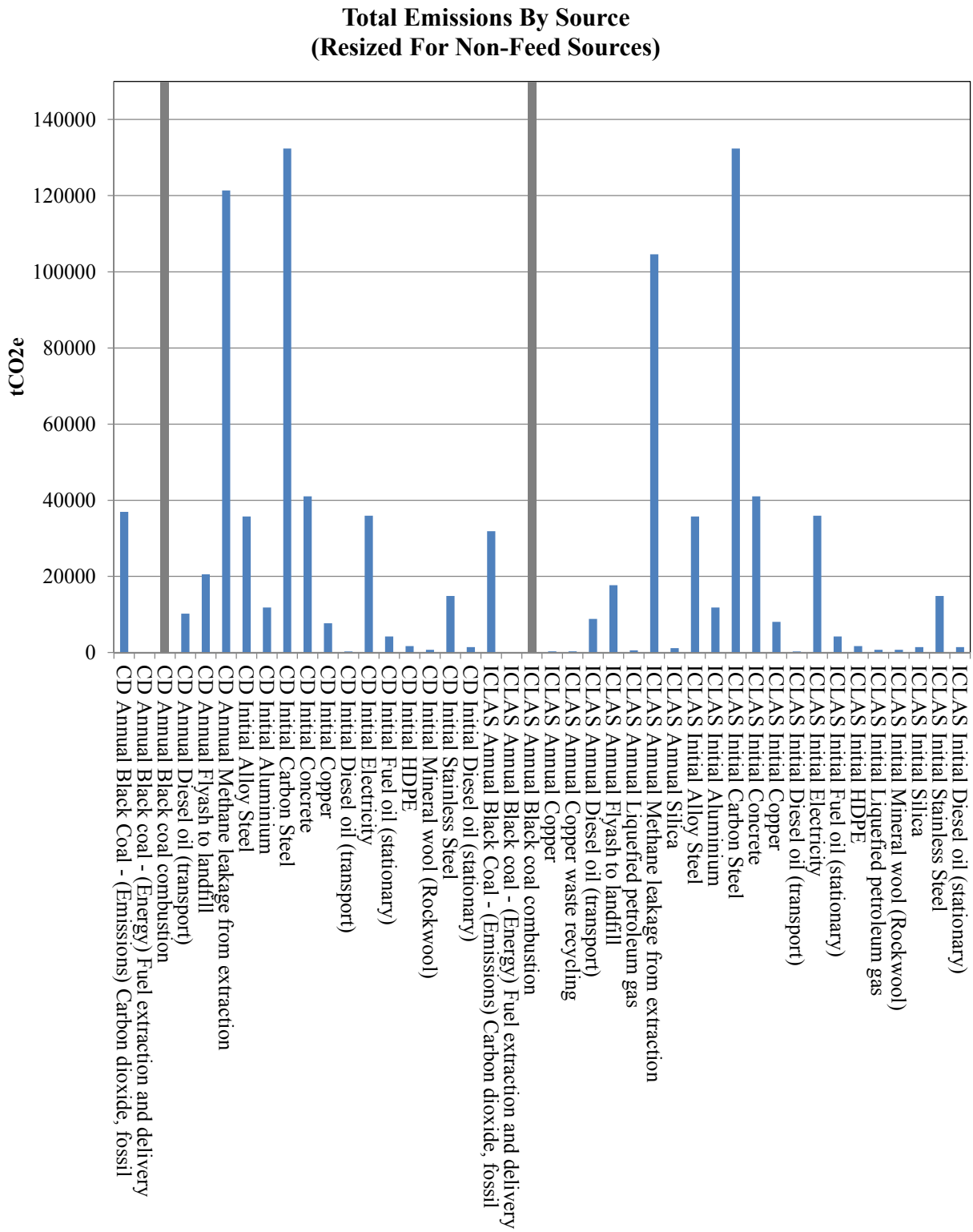

Figure 152: Emissions of all sources (resized for non-feed sources).

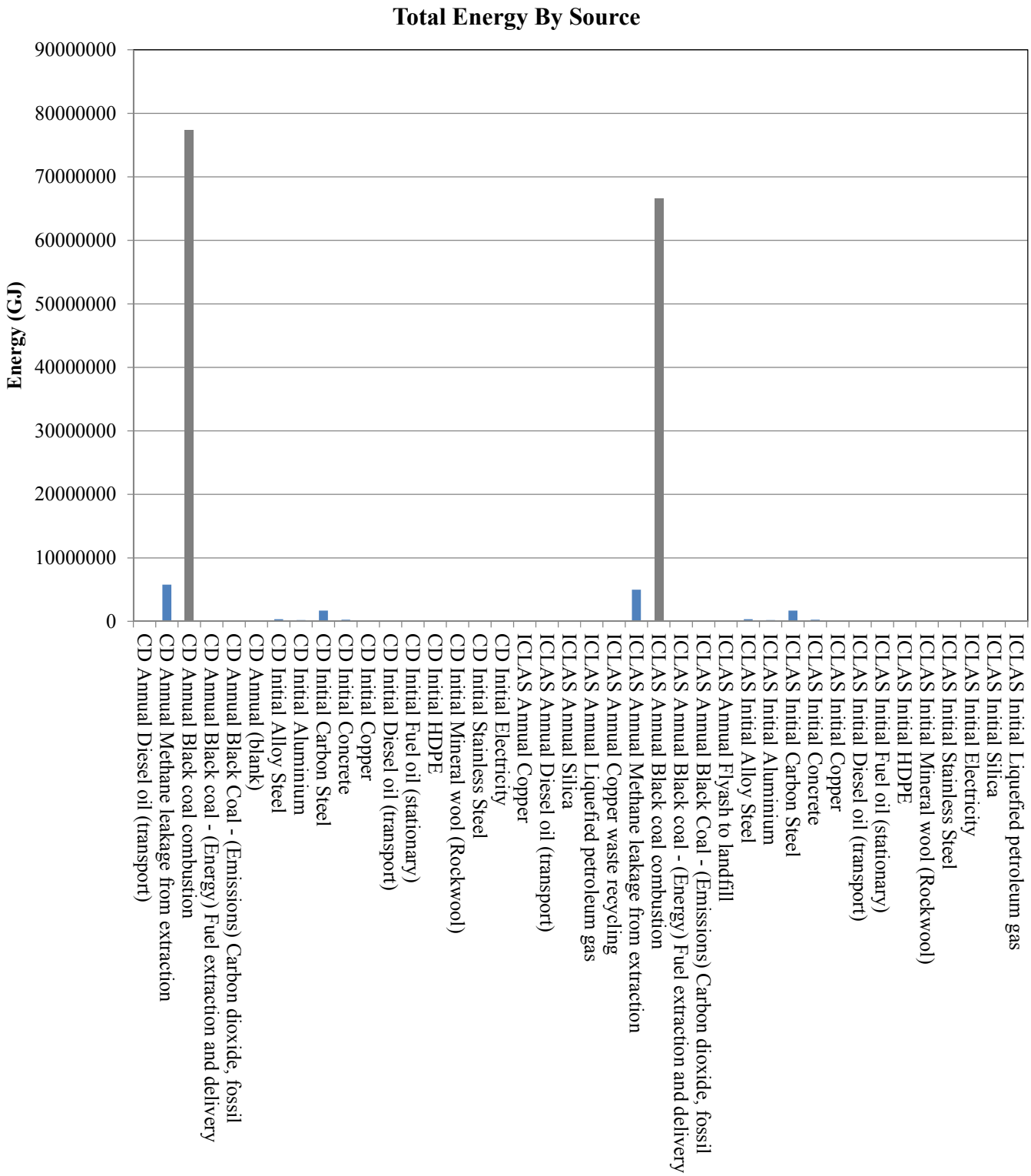

Figure 153: Energy of all sources.

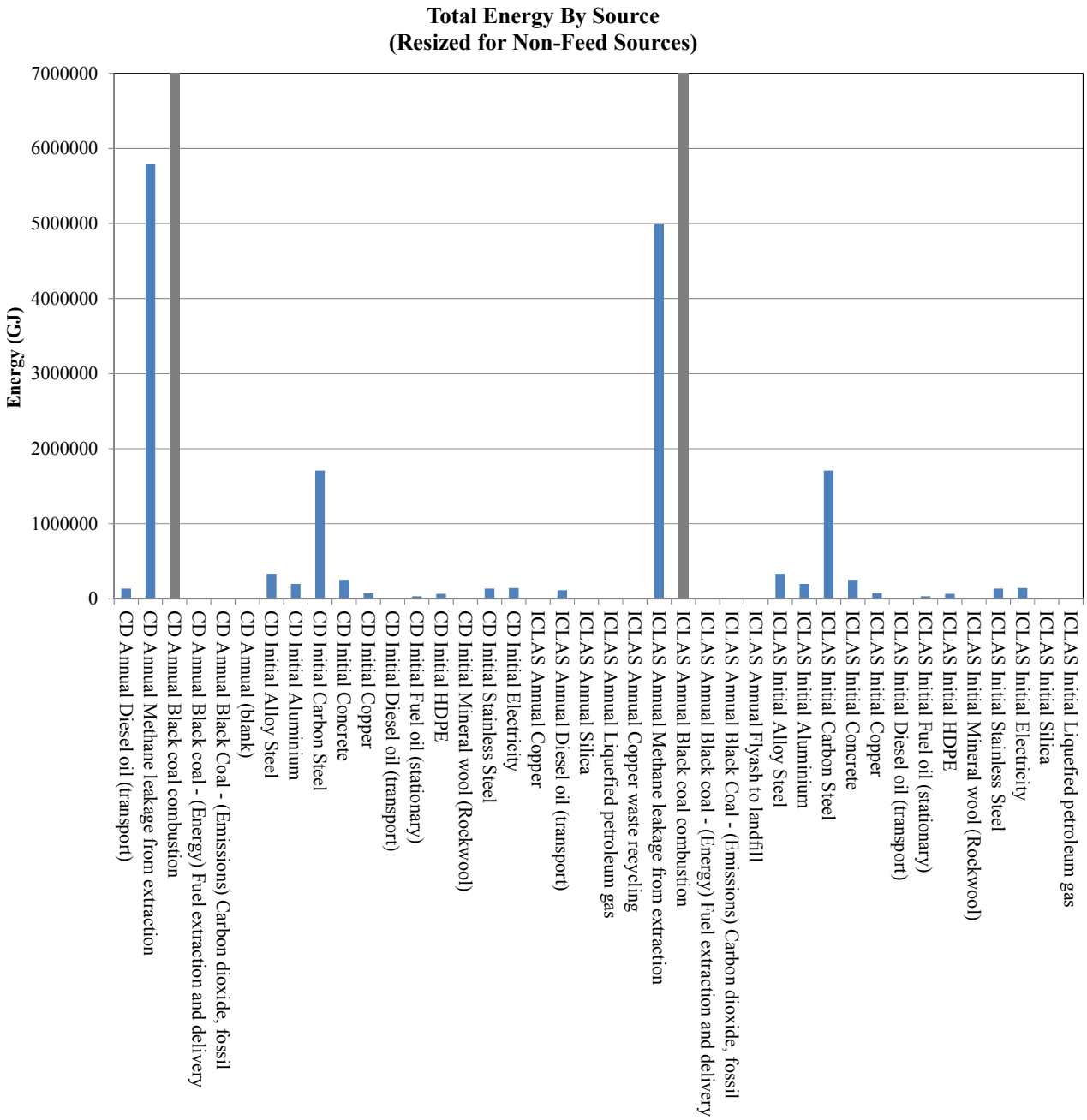

Figure 154: Energy of all sources (resized for non-feed sources).

Due to this dominance of impact of the coal feed, anything relating to this source has a large impact on the overall LCA. Since the ICLAS method substantially reduces the boiler size required (due to needing less auxiliary power) and hence feed, results in the fact that although there are additional set-up and operational processes occurring, that these sources are negligible, when compared to feed reduction amounts. See Figures 155 and 156 below for total annual emissions and energy, notably all non-feed components are barely visible.

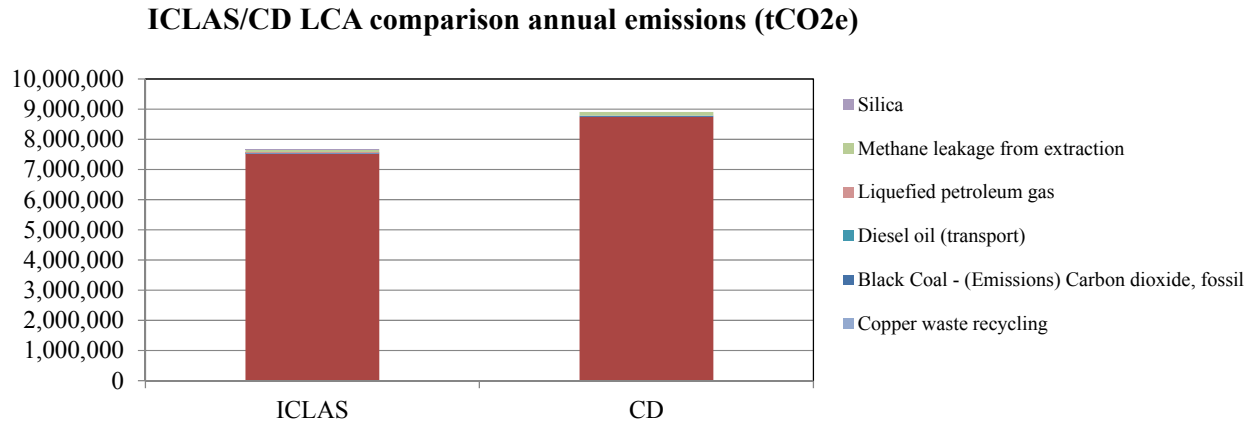

Figure 155: Comparison of all annual emissions for both scenarios of ICLAS and CD.

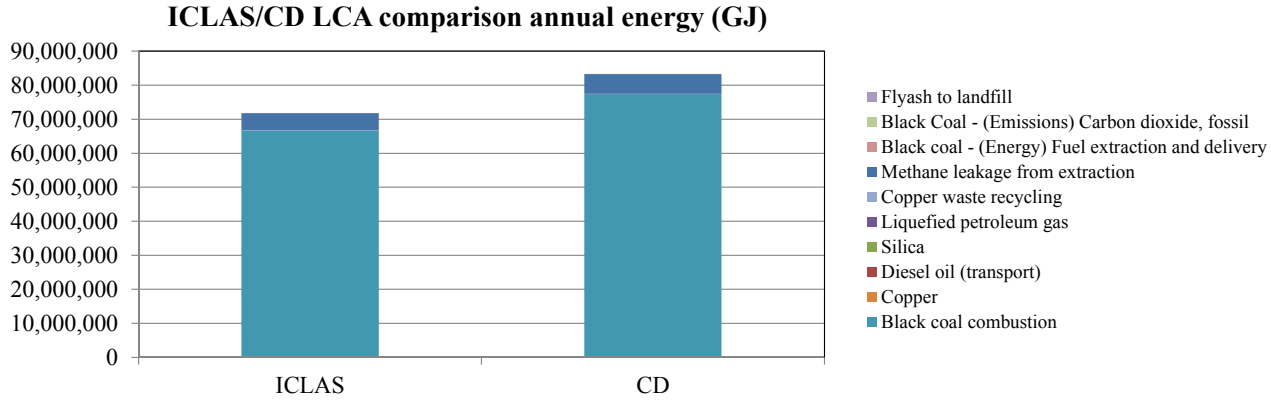

Figure 156: Comparison of all annual energy for both scenarios of ICLAS and CD.

LCA summary (base case):

Annual basis (emissions):	CD 7,505,948 tCO2e;	ICLAS 6,469,403 tCO2e
Annual basis (energy):	CD 70,828,125 GJ;	ICLAS 61,035,007 GJ
Annual basis ICLAS saving:	1,036,545 tCO2e (13.81%);	9,793,118 GJ (13.83%)
Initial basis (emissions):	CD 356,464 tCO2e;	ICLAS 358,971 tCO2e
Initial basis (energy):	CD 3,768,351 GJ;	ICLAS 3,776,938 GJ
Initial basis ICLAS saving:	-2,507 tCO2e (-0.70%)*;	-8,587 GJ (-0.23%)*

**(Negative above implies CD uses less initial energy and emissions)*

Lifetime basis (emissions): (MtCO2e - Million tonnes of Carbon Dioxide equivalent)	CD 150.48 MtCO2e;	ICLAS 129.75 MtCO2e
Lifetime basis (energy):	CD 1420.33 PJ;	ICLAS 1300.02 PJ
Lifetime basis ICLAS saving:	**20.73 MtCO2e (13.78%);**	**120.31 PJ (8.47%)**

KPIs:

EMISSIONS:

ICLAS	CD	
1,366.11	1,583.73	Total emissions (Million tCO2e)
10.5	12.2	tCO2e/MWh sent out

13.74% saving by using ICLAS

ENERGY:

13,689.82	14,953.04	Total energy (PJ)
105.5	115.2	GJ/MWh sent out

8.45% saving by using ICLAS

COAL:

45,968,674	53,352,782	tonnes of coal
0.35	0.41	tonne of coal/MWh sent out

13.84% saving by using ICLAS

9.5 CONCLUSIONS

The comparative LCA study demonstrated the domination of black coal feed as an energy and emissions source within the overall LCA. The large quantity of feed required results in the annual operational emissions to be far larger than that of power station set-up. This breakdown implies the importance of using the feed as efficiently as possible (on a tonne coal/MWh sent out to the grid basis) for optimal environmental performance (which is an intuitive outcome).

ICLAS can significantly achieve better performance than current methods (cryogenic distillation) by reducing the parasitic load required by the power station for oxy-fuel combustion. It should be noted that it may additionally have significant safety and cost benefits over current methods as well (while not explored in this study).

From the outset of this study, the benefit of the lower energy requirement for oxygen production indicated an improvement for energy and emissions, though it was unknown how the use of the metal substrate oxygen carrier (and associated processes and activities) may ameliorate this benefit. Due to the large contribution of black coal in operations, the use of the metal substrate oxygen carrier is negligible, contributing less than 1% additional energy and emissions in power station set-up (using conservative assumptions) and in the operational phase still showing a substantial benefit (over 13% reduction in carbon emissions equivalent) even when the ICLAS metal substrate processes and activities are included.

The use of ICLAS in place of cryogenic distillation could substantially reduce required energy and emissions. Using this study's model, it would be equivalent to saving:

- 120 PJ or over 33,300,000 MWh of embodied energy saved
- 20,700,000 tCO_2e (equivalent to taking almost 200,000 new passenger vehicles off the road for every year of the 20 year operation of the facility [using 5 metric tonnes of CO_2 equivalent per new passenger vehicle per year]).

Chapter 10

OVERALL CONCLUSIONS AND RECOMMENDATIONS FOR FUTURE RESEARCH

10.1 OVERALL CONCLUSION

The NSW Coal Innovation has generously funded the initial research and development stages of a novel chemical looping air separation (CLAS) technology for tonnage production of oxygen. This unique yet simple and cost effective technology has a particular application in oxy-fuel combustion and gasification of coal and, as detailed in this report, offers significant reductions in the energy and CO_2 emissions footprints of oxygen production. Our research efforts thus far have verified the validity of the CLAS concept and confirmed its superior capabilities over conventional cryogenic based air separation technologies.

However, while the potential for CLAS to achieve significantly lower overall costs compared to conventional ASU technologies remains (as highlighted by the Techno-economic study), further materials and process development efforts combined with a large-scale demonstration campaign are required before the CLAS process can be fully endorsed / accepted. This is the subject of our recommendation for future studies (see below).

10.2 RECOMMENDATIONS FOR FUTURE WORK

As noted in Section 10.1, through the project MOC10/1067 (this project) the research team at the University of Newcastle made considerable advances in fundamental understanding of the processes underpinning the operation of CLAS based systems and provided the scientific evidence to prove the concept. However, the scope of the project MOC10/1067 did not allow the research team to gain operational experience with a sufficiently large-scale working prototype of the CLAS process (i.e. a large-scale reacting version as opposed to the 7 m high cold-flow non-reacting version used in scale-up studies). This may represent a barrier against commercial deployment of the CLAS technology, hence, warranting a new and dedicated project. The team therefore recommends that a new research project to be undertaken to address this need.

The new project should focus on the development and field trials of a sufficiently large CLAS / ICLAS prototype (e.g. a 500 kW_{th} with a height of approximately 7-8 m) with the aim of taking the chemical looping air separation technology through its next phase of development and into pre-commercialisation stage. The specific objectives of the new project are:

- To gain operational experience with a large-scale CLAS prototype
- To establish the operational envelope of the CLAS process
- To expound application relevant standards for the design, construction, installation and verification of CLAS based systems for a diverse range of industry applications

Duration and Timeline for The New Project:

- The overall project duration is two years (i.e. 8 quarters)
- The first 4 quarters are dedicated to design and construction of the 500 kW_{th} CLAS / ICLAS prototype
- Quarter 5 has been allocated to commissioning of the prototype and troubleshooting
- Quarters 6 and 7 are allocated for field trials
- Quarter 8 is dedicated for analysis and consolidation of results as well as dissemination of findings

Indicative Budget for The New Project:

Heads of Expenditure	Year 1	Year 2	TOTAL ($)
Salaries: 1 x Postdoc (Level B/1 plus 31% on-cost)	$110,957	$110,957	$221,914
Equipment: Design, construction and commissioning of the 500 kW_{th} CLAS prototype	$600,000	$50,000	$650,000
Materials & Maintenance (metal oxides, gas, etc)	$8,000	$40,000	$48,000
Travel	$3,000	$3,000	$6,000
Other (safety consultants, particle analysis, etc)	$30,000	$10,000	$40,000
Sub-Total	$751,957	$213,957	$965,914
University Overheads (15% of Sub-Total)	$112,794	$32,094	$144,887
TOTAL	$864,751	$246,051	**$1,110,801**

Chapter 11

PROJECT ADMINISTRATION OVERVIEW

11.1 BUDGET AND ACTUAL SPEND

Total project funding (cash only):	$886,618
Actual spend (30 May 2014; cash only):	$970,230
Actual spend (NSW Coal Innovation share; cash only):	$886,618
Actual spend (the team share; cash only)*:	$83,612

** This expenditure is largely associated with the design and fabrication of the 7 m tall demonstration unit which was not in the original scope of the work but was deemed essential for the scale-up studies*

11.2 TIMELINE

Project official start date (awarded date):	23 Dec 2010
Project official end date:	22 Dec 2013
Project kick-off date (actual):	24 Jan 2011
Project completion date (actual):	21 March 2014
Final report submission:	30 May 2014

11.3 HUMAN RESOURCES

Name	Role	Funded by the Project?	Notes
Prof Behdad Moghtaderi	Project leader & Chief Investigator	N	
Prof Terry Wall	Chief Investigator	N	
Dr Elham Doroodchi	Researcher	N	
Dr Kalpit Shah	Researcher	Y	Partial salary support
Dr Caimao Luo	Researcher	Y	Partial salary support
Dr Zengbiao Peng	Researcher	Y	Partial salary support
Dr Jafar Zanganeh	Researcher	N	
Dr Ron Roberts	Technical support	N	
Hui Song	PhD student	Y	Partial salary and research support
Yusif Alghamdi	PhD student	Y	Research support only
Bernadette Shillington	Undergraduate student	Y	Research support only
Thomas Wilson	Undergraduate student	Y	Research support only
Shawn Columbus	Undergraduate student	Y	Research support only
Timothy Law	Undergraduate student	Y	Research support only
Neil Gardner	Technical support	N	

11.4 PROJECT MANAGEMENT

Meetings held in Newcastle or Visits by the Representatives of the Funding Body

- 29 Sept 2011
- 19 Jan 2012

Presentations

- B Moghtaderi, "A Novel Chemical Looping Based Air Separation Technology for Oxy-Fuel Combustion of Coal", NSW Low Emission Coal Summit, 8-9 June 2010.
- B Moghtaderi, "Progress Update: Chemical Looping Air Separation", NSW Coal Innovation Visit, Newcastle, 29 Sept 2011.
- B Moghtaderi, "Progress Update: Chemical Looping Air Separation", NSW Coal Innovation Visit, Newcastle, 19 Jan 2012.
- B Moghtaderi, "A Novel Chemical Looping Based Air Separation Technology for Oxy-Fuel Combustion of Coal", Presentation to the NSW Coal Innovation Board, Sydney, 15 Aug 2012.
- B Moghtaderi, "A Novel Chemical Looping Based Air Separation Technology for Oxy-Fuel Combustion of Coal", Presentation to the NSW Coal Innovation Board during their visit from Newcastle, 29 Oct 2012.
- B Moghtaderi, "Chemical Looping Air Separation", Presentation to the NSW Minister for Energy, 18 April 2013.

Reports

- 12 quarterly progress reports
- Milestone Report #1; 5 Jan 2012
- Milestone Report #2; 6 Jan 2013
- Final Report; 30 May 2014

11.5 PUBLICATIONS

Journal Publications

1. Peng Z, Doroodchi E, Alghamdi Y, Moghtaderi B, "Mixing and Segregation of solid Mixtures in Bubbling Fluidized Beds under Conditions Pertinent to the Fuel Reactor of a Chemical Looping System", *Powder Technology*, 235, 823-837, 2013.
2. Shah K, Moghtaderi B, Wall T, "Effect of Flue Gas Impurities on the Performance of a Chemical Looping Based Air Separation Process for Oxy-Fuel Combustion", *Fuel*, 103, 932-942, 2013.

3. Peng Z, Doroodchi E, Alghamdi Y, Moghtaderi B, "Mixing and Segregation of solid Mixtures in Bubbling Fluidized Beds under Conditions Pertinent to the Fuel Reactor of a Chemical Looping System", *Powder Technology*, 235, 823-837, 2013.
4. Shah K, Moghtaderi B, Zanganeh J, Wall T, "Integration Options for Novel Chemical Looping Air Separation (ICLAS) Process for Oxygen Production In Oxy-Fuel Coal Fired Power Plants", *Fuel*, In Press, Corrected Proof, Available online 29 January 2013.
5. Moghtaderi B, "Effects of Particle Cloud Extinction on Synthesis Gas Reduction of Metal Oxides in Chemical Looping Reactors", *Fuel*, 99, 262-270, 2012.
6. Moghtaderi B, "Review of the Recent Chemical Looping Process Developments for Novel Energy and Fuel Applications", *Energy Fuels*, 26(1), 5-40, 2012.
7. Shah K, Moghtaderi B, Wall T, "Selection of Suitable Oxygen Carriers for Chemical Looping Air Separation: A Thermodynamic Approach", *Energy & Fuels*, 26(4), 2038-2045, 2012.
8. Song H, Doroodchi E, Moghtaderi B, "Redox Characteristics of Fe-Ni/SiO_2 Bimetallic Oxygen Carriers in CO under Conditions Pertinent to Chemical Looping Combustion", *Energy & Fuels*, 26(1), 75-84, 2012.
9. Moghtaderi B, "Application of Chemical Looping Concept for Air Separation at High Temperatures", *Energy & Fuels*, 24, 190-198, 2010.

Refereed Conference Publications

10. Alghamdi Yf, Peng Z, Doroodchi E, Moghtaderi B, "CFD-DEM Simulation of Mixing and Segregation of Fluidized Binary Mixtures of Particles with Different Sizes and Densities", Proceedings of 21st International Conference on Fluidized Bed Combustion, Naples, Italy (2012)
11. Song H, Shah K, Doroodchi E, Moghtaderi B, "Thermogravimetric Analysis of NiO/SiO_2 Oxygen Carriers under CO/Air Environment for Chemical Looping Combustion", Australian Combustion Symposium 2011, Shoal Bay (2011)
12. Shah K, Moghtaderi B, Wall TF, "Chemical Looping Air Separation (CLAS) for Oxygen Production: Thermodynamic and Economic Aspects", Proceedings of the Australian Combustion Symposium 2011, Shoal Bay (2011)
13. Moghtaderi B, Song H, Doroodchi E, Wall TF, "Reactivity Analysis of Mixed Metal Oxides", 1st International Conference on Chemical Looping, IFP-Lyon, France, 17 - 19 March 2010.

REFERENCES

1. Moghtaderi B, Wall T, “Chemical Looping Oxygen Generation for Oxy-fuel Combustion and Gasification”, ANLEC-R&D, $296,000, 2011-2014.

2. Moghtaderi B, “Xstrata Chemical Looping Program”, Xstrata Coal, $450,000, 2011-2014.

3. Moghtaderi B and Song H, "Reduction Properties of Physically Mixed Metallic Oxide Oxygen Carriers in Chemical Looping Combustion", Energy & Fuels, 2010. 24(10): p. 5359-5368.

4. Song H, Doroodchi E, Moghtaderi B, "Redox Characteristics of Fe–Ni/SiO2 Bimetallic Oxygen Carriers in CO under Conditions Pertinent to Chemical Looping Combustion", Energy & Fuels, 2011. 26(1): p. 75-84.

5. Gayán, P., et al., Development of Cu-based oxygen carriers for Chemical-Looping with Oxygen Uncoupling (CLOU) process. Fuel, 2012. 96(0): p. 226-238.

6. Arjmand, M., et al., Prospects of Al_2O_3 and $MgAl_2O_4$-Supported CuO Oxygen Carriers in Chemical-Looping Combustion (CLC) and Chemical-Looping with Oxygen Uncoupling (CLOU). Energy & Fuels, 2011. 25(11): p. 5493-5502.

7. Leion, H., et al., Use of $CaMn_{0.875}Ti_{0.125}O_3$ as Oxygen Carrier in Chemical-Looping with Oxygen Uncoupling. Energy & Fuels, 2009. 23: p. 5276-5283.

8. Shulman, A., et al., Manganese/Iron, Manganese/Nickel, and Manganese/Silicon Oxides Used in Chemical-Looping With Oxygen Uncoupling (CLOU) for Combustion of Methane. Energy & Fuels, 2009. 23: p. 5269-5275.

9. Shulman, A., et al., Chemical - Looping with oxygen uncoupling using Mn/Mg-based oxygen carriers - Oxygen release and reactivity with methane. Fuel, 2011. 90(3): p. 941-950.

10. Mattisson, T., A. Jardnas, and A. Lyngfelt, Reactivity of some metal oxides supported on alumina with alternating methane and oxygen-application for chemical-looping combustion. Energy & Fuels, 2003. 17(3): p. 643-651.

11. L.E. Silbert, D. Ertaz, G.S. Grest, T.C. Halsey, D. Levine, S.J. Plimpton, Granular flow down an inclined phane: Bagnold scaling and rheology, Phys. Rev. E., 64 (2001) 051302.

12. O.R. Walton, R.L. Braun, Viscosity, granular-temperature, and stress calculations for shearing assemblies of inelastic, frictional disks, J. Rheol., 30 (1986) 949-981.

13. P.A. Cundall, O.D.L. Strack, A discrete numerical model for granular assemblies, Geotechnique, 29 (1979) 47-65.

14. B.H. Xu, A.B. Yu, Numerical simulation of the gas-solid flow in a fluidized bed by combining discrete particle method with computational fluid dynamics, Chem. Eng. Sci., 52 (1997) 2785-2809.

15. B.P.B. Hoomans, J.A.M. Kuipers, W.J. Briels, W.P.M. van Swaaij, Discrete particle simulation of bubble and slug formation in a two-dimensional gas-fluidised bed: a hard-sphere approach, Chem. Eng. Sci., 51 (1996) 99-118.

16. Y.Q. Feng, B.H. Xu, S.J. Zhang, A.B. Yu, P. Zulli, Discrete particle simulation of gas fluidization of particle mixtures, AIChE J., 50 (2004) 1713-1728.

17. M.J. Rhodes, X.S. Wang, M. Nguyen, P. Stewart, K. Liffman, Study of mixing in gas-fluidized beds using a DEM model, Chem. Eng. Sci., 56 (2001) 2859-2866.

18. P.M.C. Lacey, Developments in the theory of particle mixing, J.Appl.Chem. , 4 (1954) 257-268.

19. K.D. Kafui, C. Thornton, M.J. Adams, Discrete particle-continuum fluid modelling of gas–solid fluidised beds, Chem. Eng. Sci., 57 (2002) 2395-2410.

20. S.V. Patankar, D.B. Spalding, A calculation procedure for heat, mass and momentum transfer in three-dimensional parabolic flows, Int. J. Heat Mass Transfer, 15 (1972) 1787-1972.

21. S.V. Patankar, Numerical heat transfer and fluid flow, Hemisphere, Washington, 1980 (1980).

22. Y. Tsuji, T. Kawaguchi, T. Tanaka, Discrete particle simulation of two-dimensional fluidized bed, Powder Technol., 77 (1993) 79-87.

23. Y. Kaneko, T. Shiojima, M. Horio, DEM simulation of fluidized beds for gas-phase olefin polymerization, Chem. Eng. Sci., 54 (1999) 5809-5821.

24. J.M. Link, Development and validation of a discrete particle model of a spout-fluid bed granulator, Ph.D. Thesis, University of Twente, Enschede (2006).

25. C.R. Muller, S.A. Scott, D.J. Holland, B.C. Clarke, A.J. Sederman, J.S. Dennis, L.F. Gladden, Validation of a discrete element model using magnetic resonance measurements, Particuology, 7 (2009) 297-306.

26. T.W. Li, R. Garg, J. Galvin, S. Pannala, Open-source MFIX-DEM software for gas-solids flows: Part II — Validation studies, Powder Technol., 220 (2011) 138-150.

27. J.P.K. Peeler, J.R. Huang, Segregation of wide size range particle mixtures in fluidized bdes, Chem. Eng. Sci., 44 (1989) 1113-1119.

28. S.Y. Wu, J. Baeyens, Segregation by size difference in gas fluidized beds, Powder Technol., 98 (1998) 139-150.

29. M. Horio, A. Nonaka, A generalized bubble diameter correlation for gas-solid fluidized beds, AIChE J., 33 (1987) 1865-1872.

30. R.W. Rice, J.F. Brainovich, Mixing/segregation in two-and three-dimensional fluidized beds: binary systems of equidensity spherical particles, AIChE J., 32 (1986) 7-16.

31. A.W. Nienow, P.N. Rowe, L.Y.L. Cheung, A quantitative analysis of the mixing of two segregating powders of different density in a gas fluidised bed, Powder Technol., 77 (1978) 79-87.

32. B. Eisfeld, K. Schnitzlein, The influence of con"ning walls on the pressure drop in packed beds, Chem. Eng. Sci., 56 (2001) 4321-4329.

33. X.H. Liu, G.W. Xu, S.Q. Gao, Micro fluidized beds: Wall effect and operability, Chem. Eng. J., 137 (2008) 302-307.

34. T.W. Li, P. Gopalakrishnan, R. Garg, M. Shahnam, CFD–DEM study of effect of bed thickness for bubbling fluidized beds, Particuology, doi: 10.1016/j.partic.2012.02.006 (2012).

35. J.H. Choi, J.E. Son, S.D. Kim, Generalized model for bubble size and frequency in gas-fluidized beds, Ind. Eng. Chem. Res., 37 (1998) 2559-2564.

36. L. Cheung, A.W. Nienow, P.N. Rowe, Minimum fluidisation velocity of a binary mixture of different sized particles, Chem. Eng. Sci., 29 (1974) 1301-1303.

37. Wall TF, Liu Y, Spero C, Elliott LK, Khare S, Rathnam RK, et al., 'An overview on oxyfuel coal combustion: State of the art research and technology development', Chemical Engineering Research and Design, 87 1003-1016 (2009).

38. Dr Kalpit Shah, Dr Liza Elliott; Dr Reinholt Spörl, Mr Lawrence Belo and Professor Terry Wall; "Coal quality impacts and gas quality control in oxy-fuel technology for carbon capture and storage – cost impacts and coal value", A milestone report provided to Glencore as part of a research contract with the Xstrata Coal Low Emissions Research.

39. EPRI Australian electricity generation technology costs- Reference case 2010; Electric power research institute: 2010.

40. NETL, D. Pulverized coal oxycombustion power plants; DOE/NETL-2007/1291; National energy technology laboratory, 2007.

41. Energy Conversion and Management 47 (2006) 3487–3498.

42. Retrofitting CO2 Capture to Existing Power Plants; IEAGHG Report; Report 2011/02, May 2011.

43. Perry's Chemical Engineering Handbook; 7th Edition, 1997.

44. Toward A Common Method Of Cost Estimation For CO2 Capture And Storage At Fossil Fuel Power Plants, Global CCS Institute, March 2013.

45. CCSD Technology Assessment Report 58; A Life Cycle Assessment of the NSW Electricity Grid.

46. Australian Energy-Technology Assessment 2012; Australian Government, Bureau of Resources and Energy Economics, 2012 Report.

ACKNOWLEDGEMENTS

The author wishes to thank the members of the Chemical Looping Research group at the University of Newcastle (Dr Doroodchi, Dr Luo, Dr Peng, Dr Shah, Dr Zanganeh, Mr Alghamdi, Ms Paymooni, Mr Song and Mr Zhang) for their hard work and dedication as well as contributions to the present report. The author would also like to acknowledge the financial support provided to this project by the NSW government through the Coal Innovation NSW fund.

APPENDIX A: SEM AND XRD RESULTS

(1) SEM Images of mono species metal oxide oxygen carriers

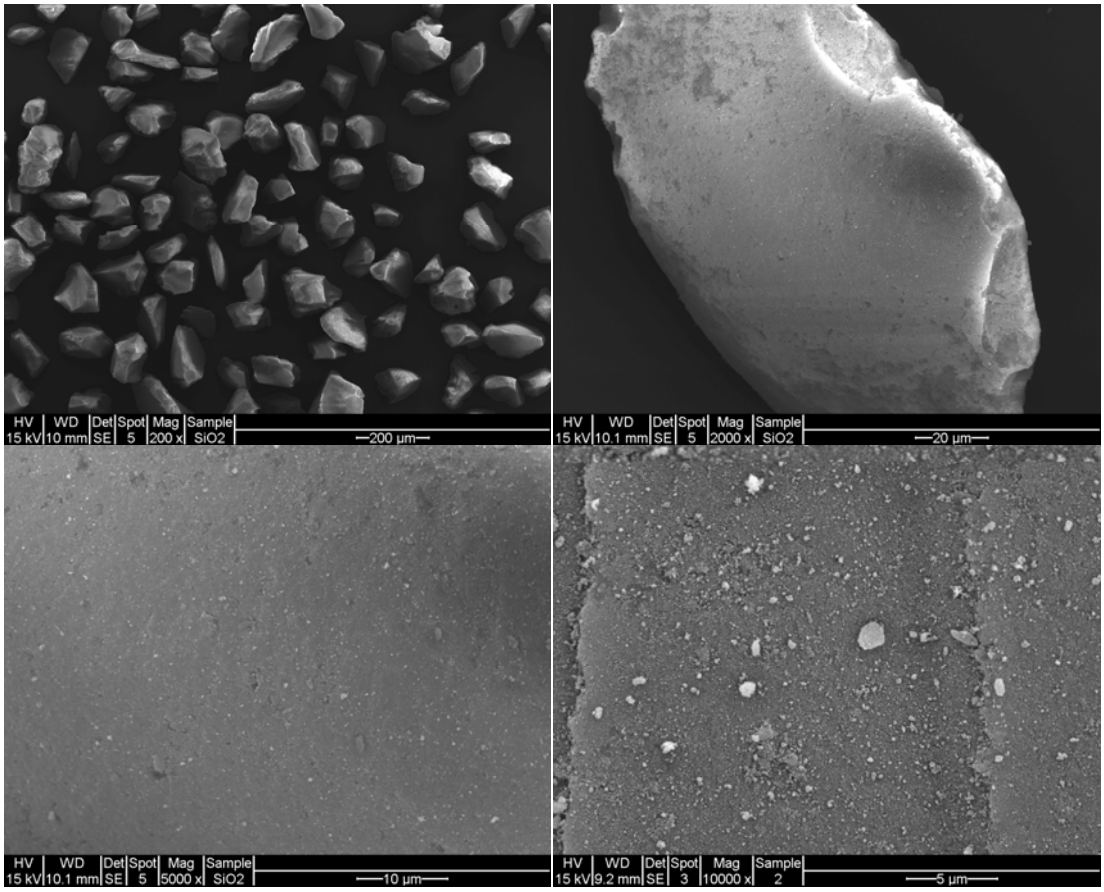

Figure A1. SiO_2 images at the magnification of 200X, 2000X, 5000X and 10000X.

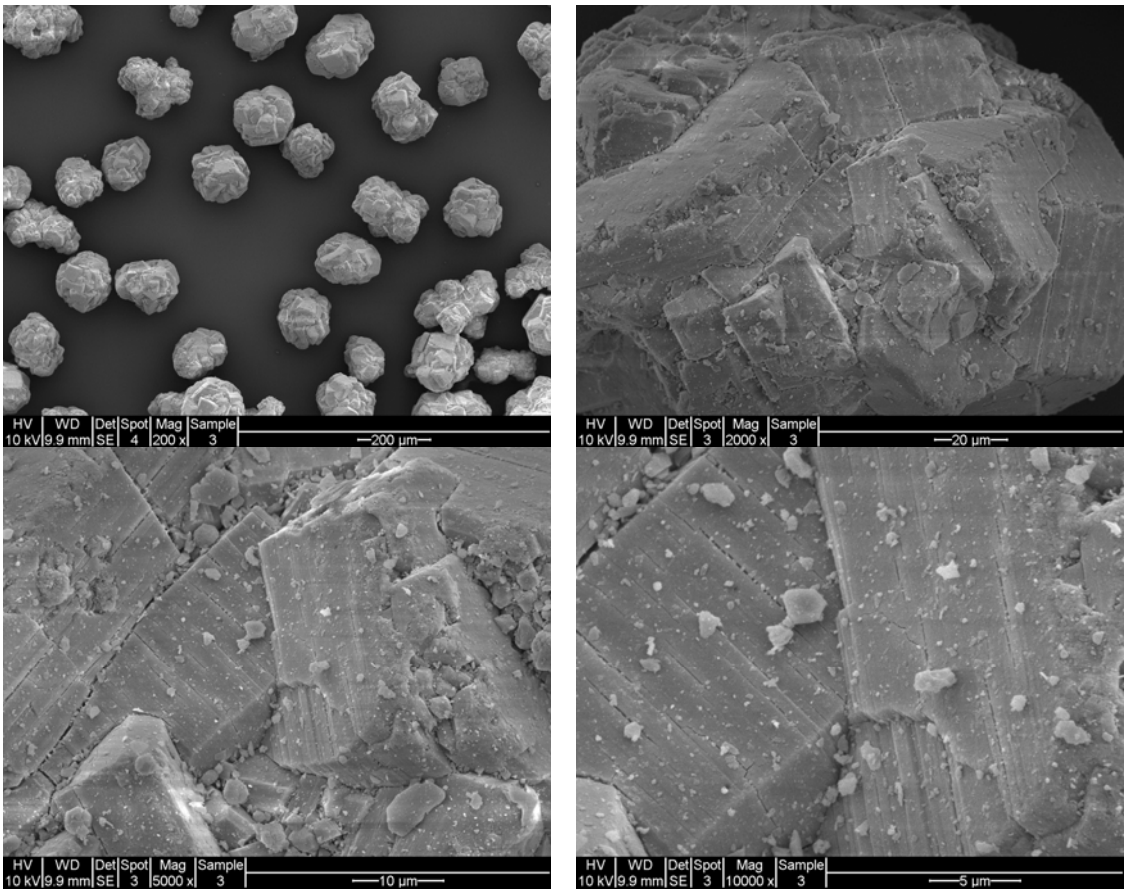

Figure A2. Al_2O_3 images at the magnification of 200X, 2000X, 5000X and 10000X.

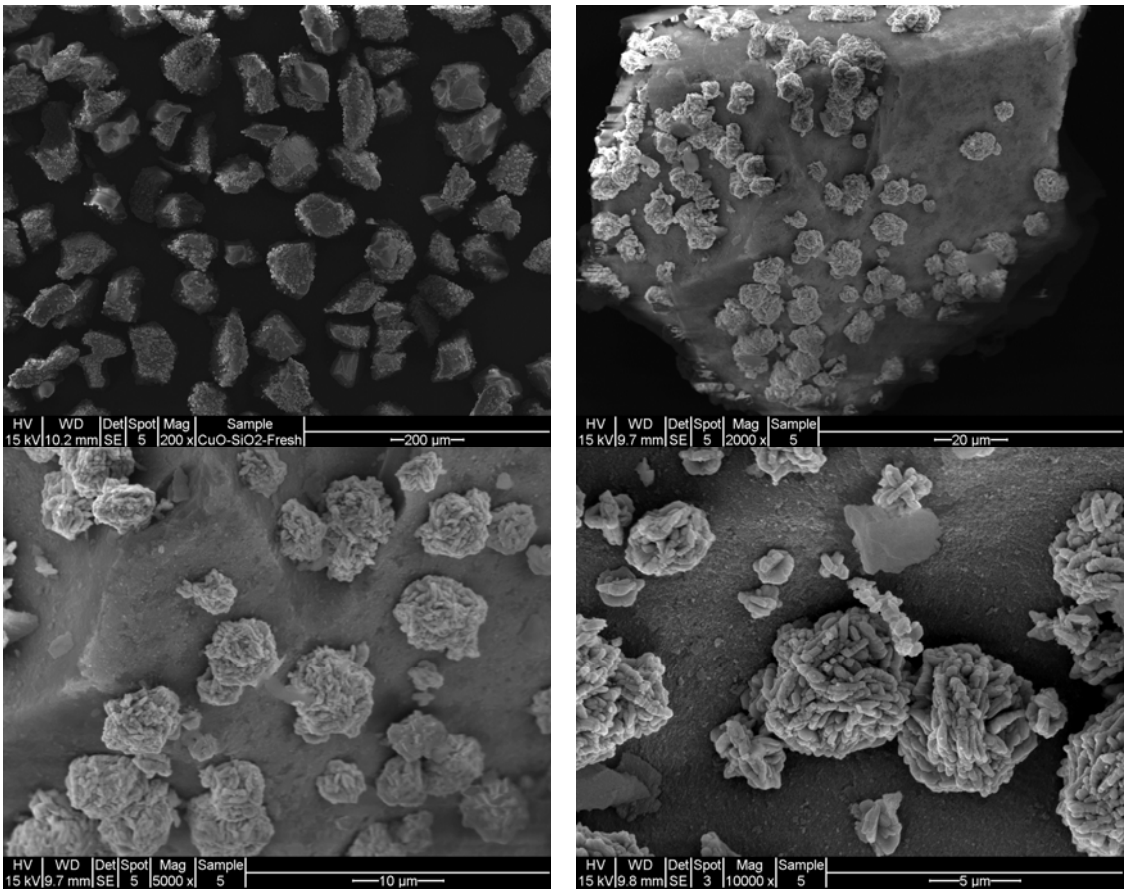

Figure A3. Fresh sample images of 30%CuO/SiO2 at the magnification of 200X, 2000X, 5000X and 10000X.

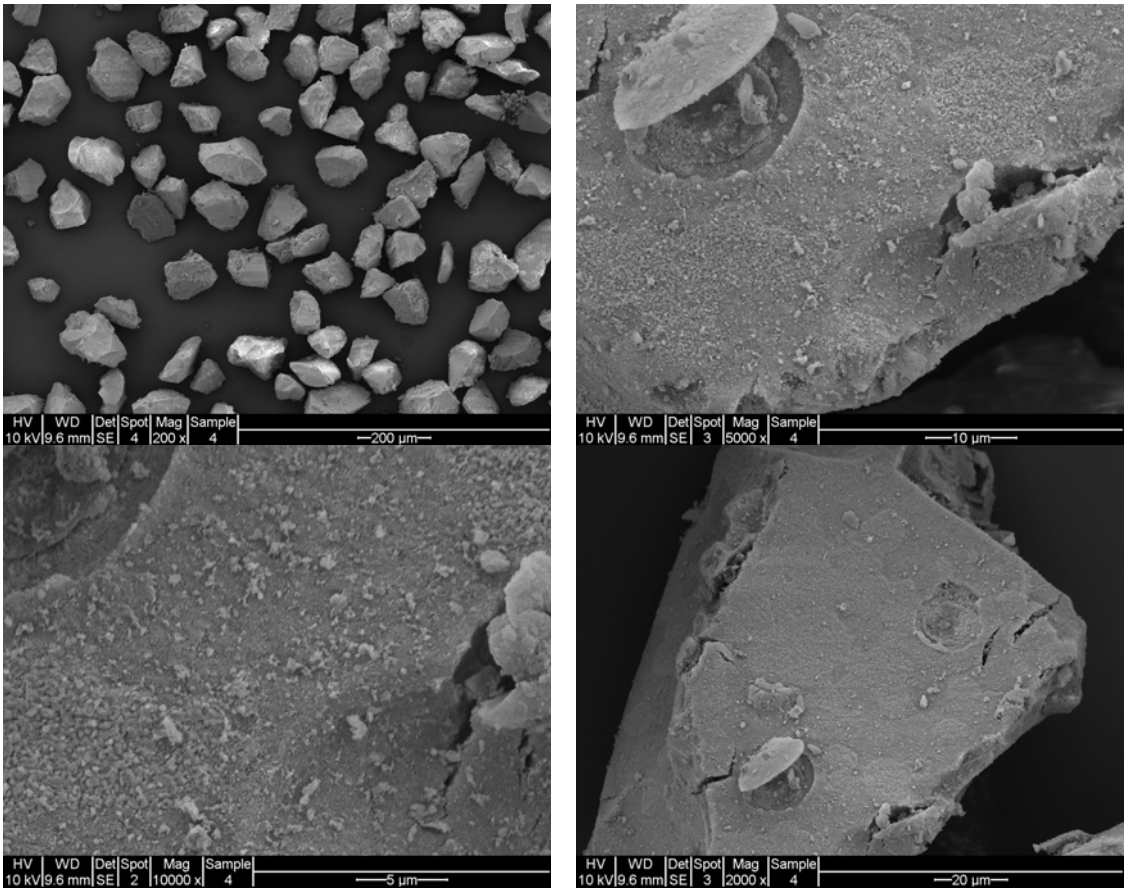

Figure A4. Sample images of 30%CuO/SiO_2 after 41 continuous desorption-sorption cycles test in TGA at 800^{o}C for the magnification of 200X, 2000X, 5000X and 10000X.

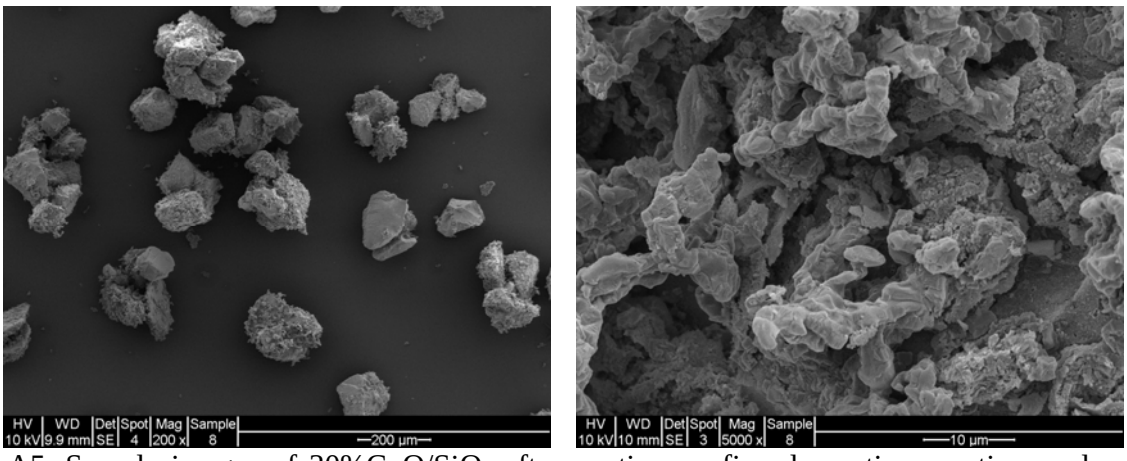

Figure A5. Sample images of 30%CuO/SiO_2 after continuous five desorption-sorption cycles test in TGA at 800 for the magnification of 200X and 5000X.

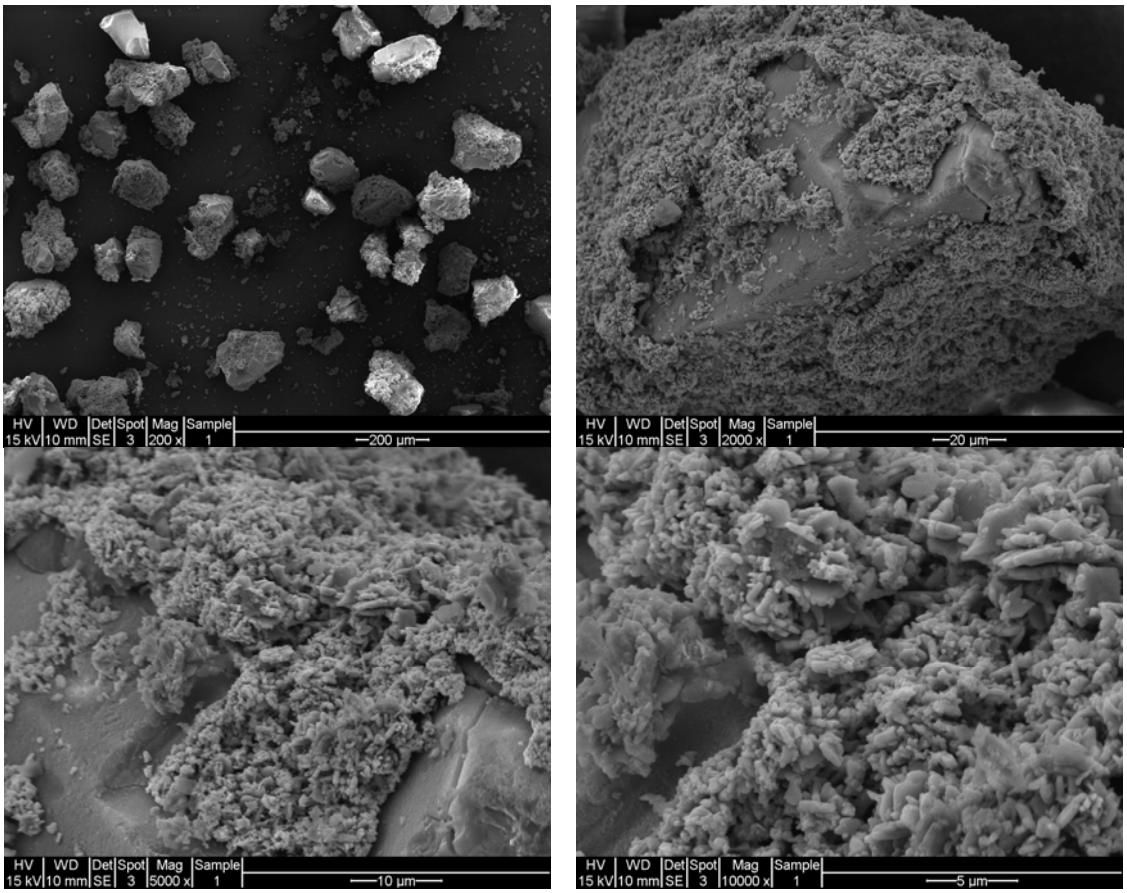

Figure A6. Fresh sample images of 60%CuO/SiO_2 at the magnification of 200X, 2000X, 5000X and 10000X.

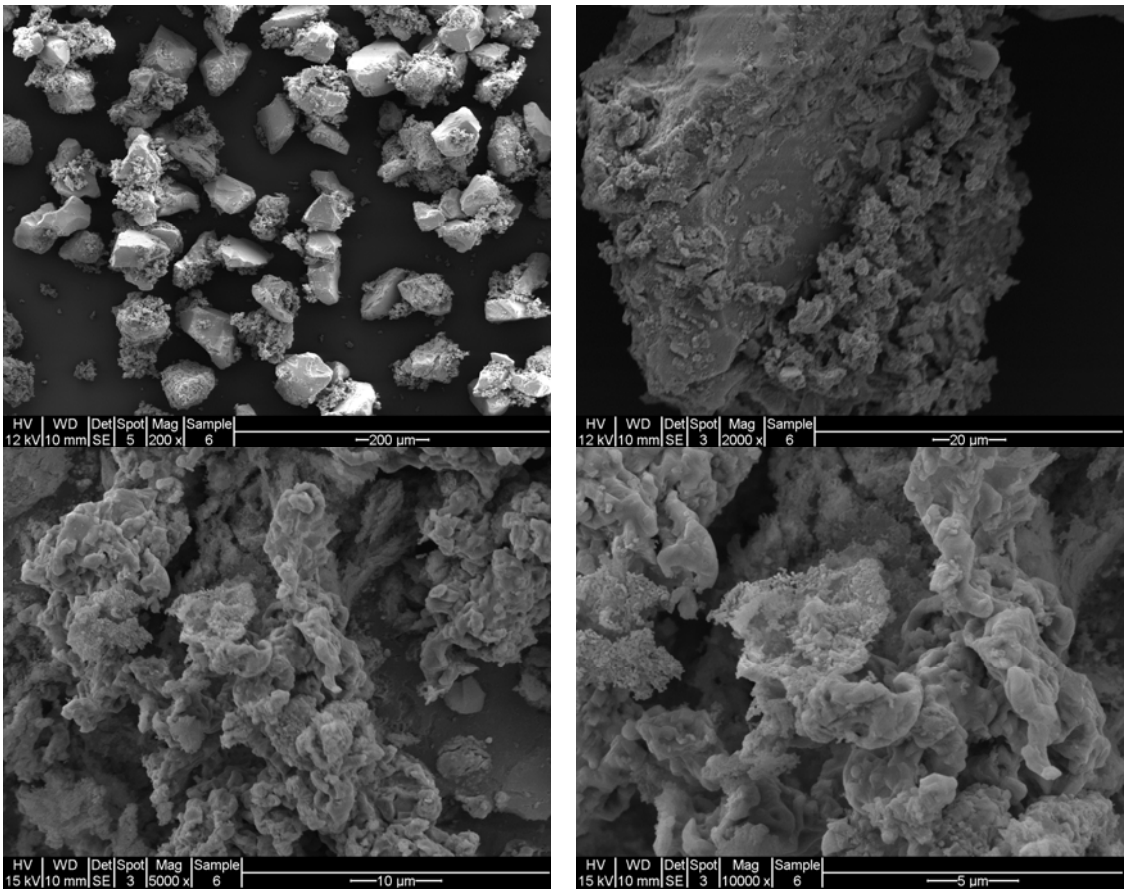

Figure A7. Sample images of 60%CuO/SiO_2 after 18 continuous desorption-sorption cycles test in TGA at 900^{o}C for the magnification of 200X, 2000X, 5000X and 10000X.

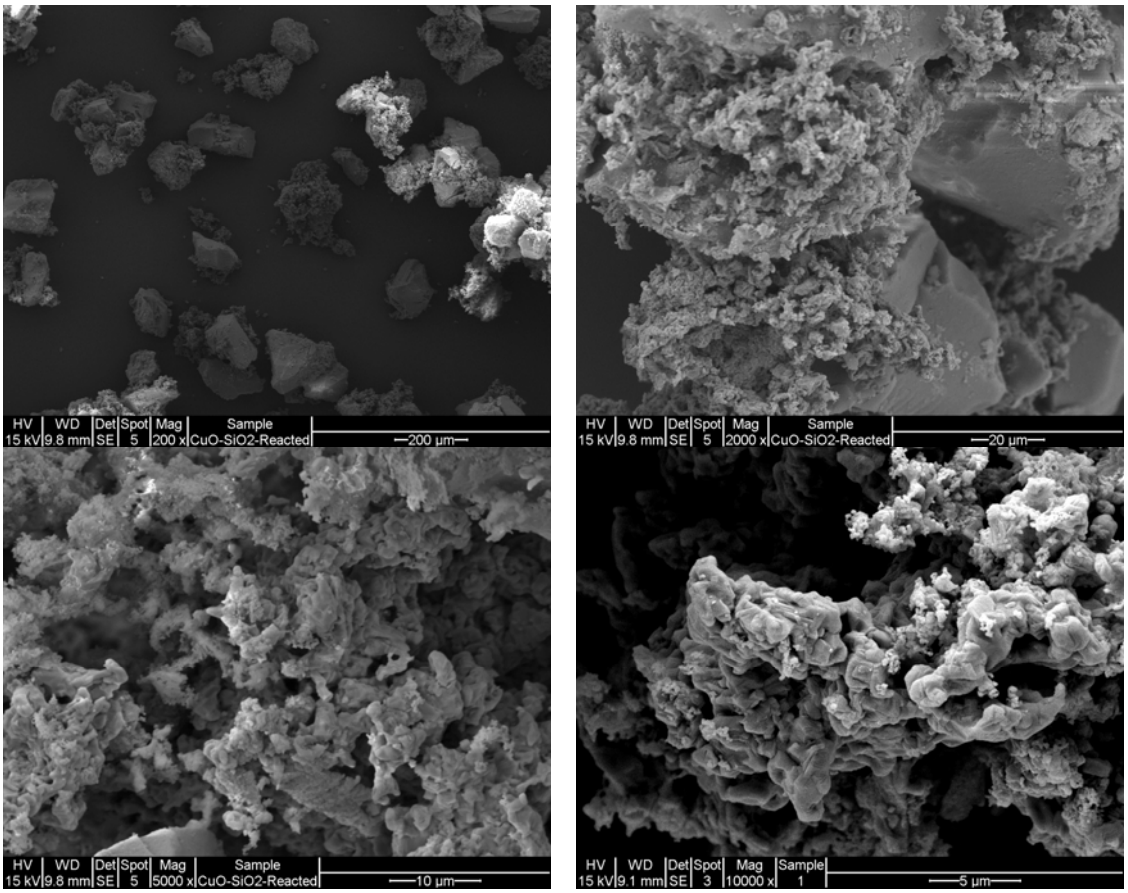

Figure A8. Sample images of 60%CuO/SiO_2 after 41 continuous desorption-sorption cycles test in TGA at 900^{o}C for the magnification of 200X, 2000X, 5000X and 10000X.

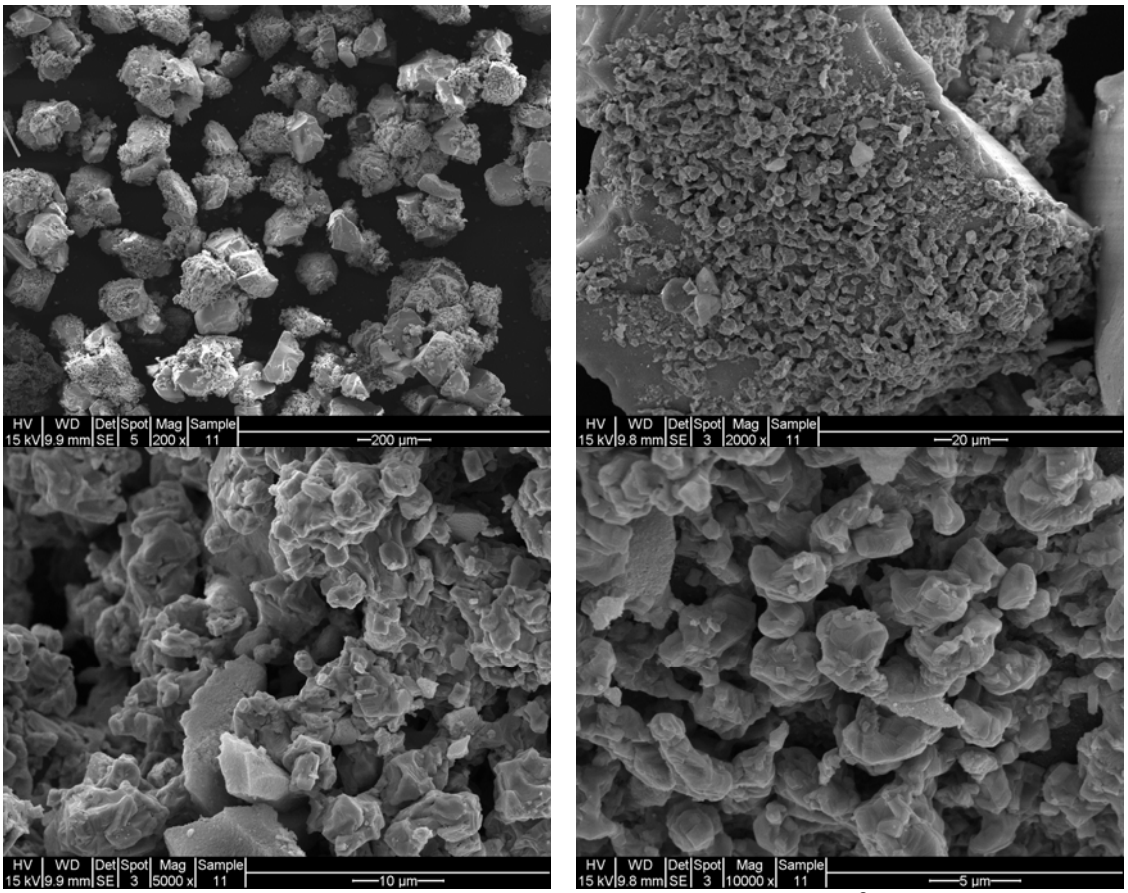

Figure A9. Sample images of 60%CuO/SiO_2 after packed-bed test at 800^{o}C for the magnification of 200X, 2000X, 5000X and 10000X.

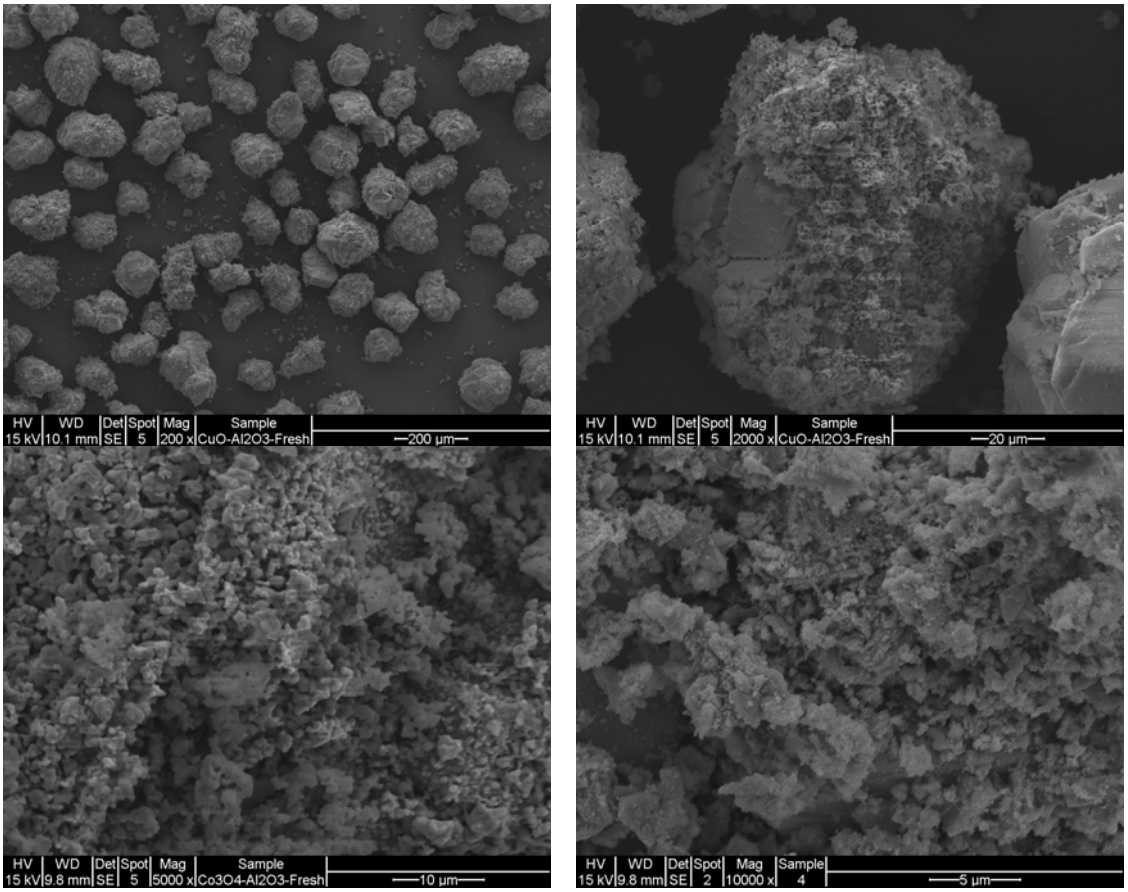

Figure A10. Fresh sample images of CuO/Al_2O_3 at the magnification of 200X, 2000X, 5000X and 10000X.

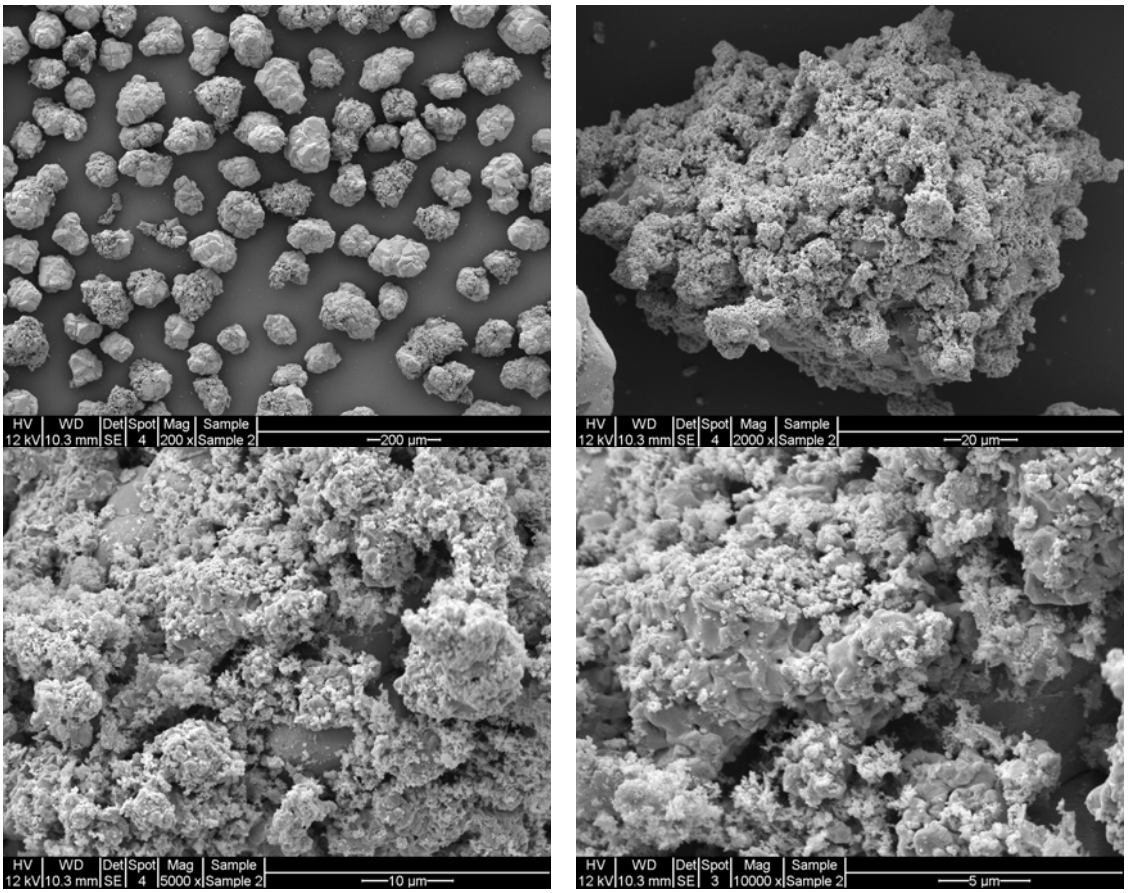

Figure A11. Sample images of CuO/Al_2O_3 after five continuous desorption-sorption cycles test in TGA at 800^{o}C for the magnification of 200X, 2000X, 5000X and 10000X.

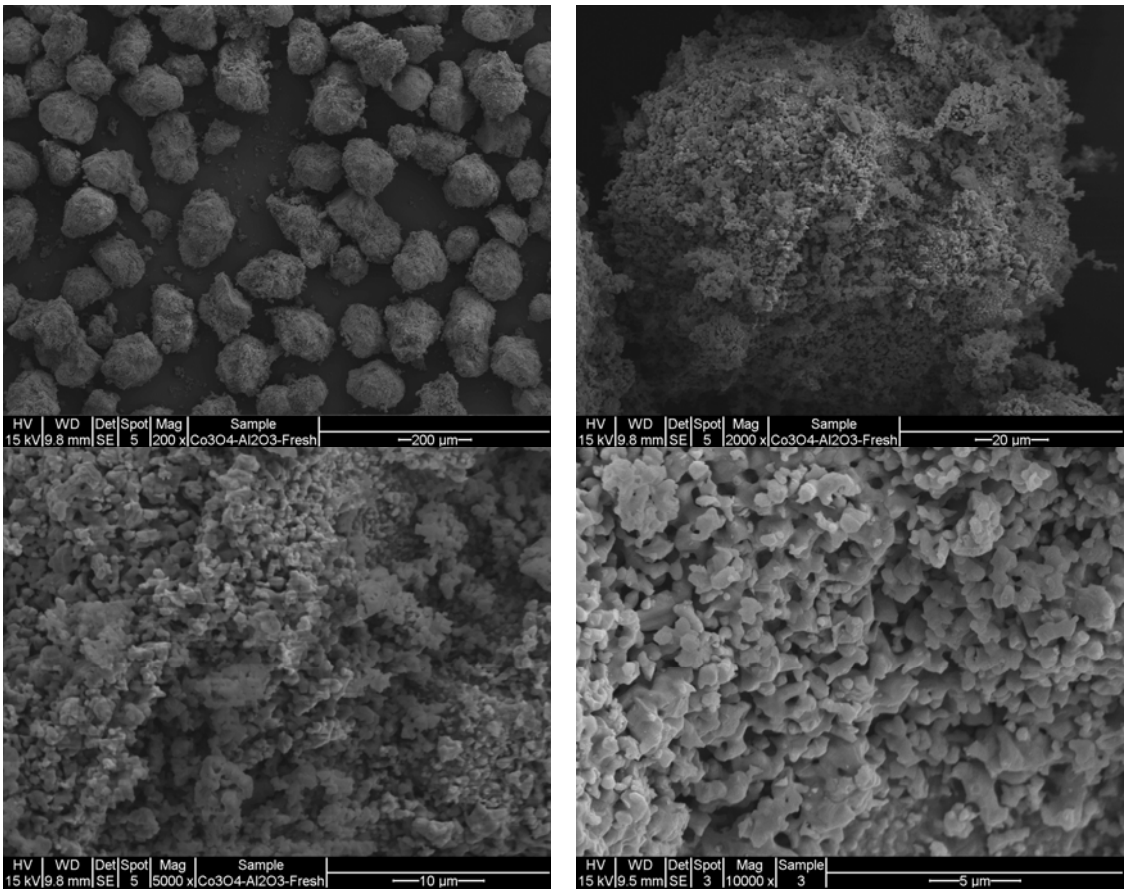

Figure A12. Fresh sample images of Co_3O_4/Al_2O_3 at the magnification of 200X, 2000X, 5000X and 10000X.

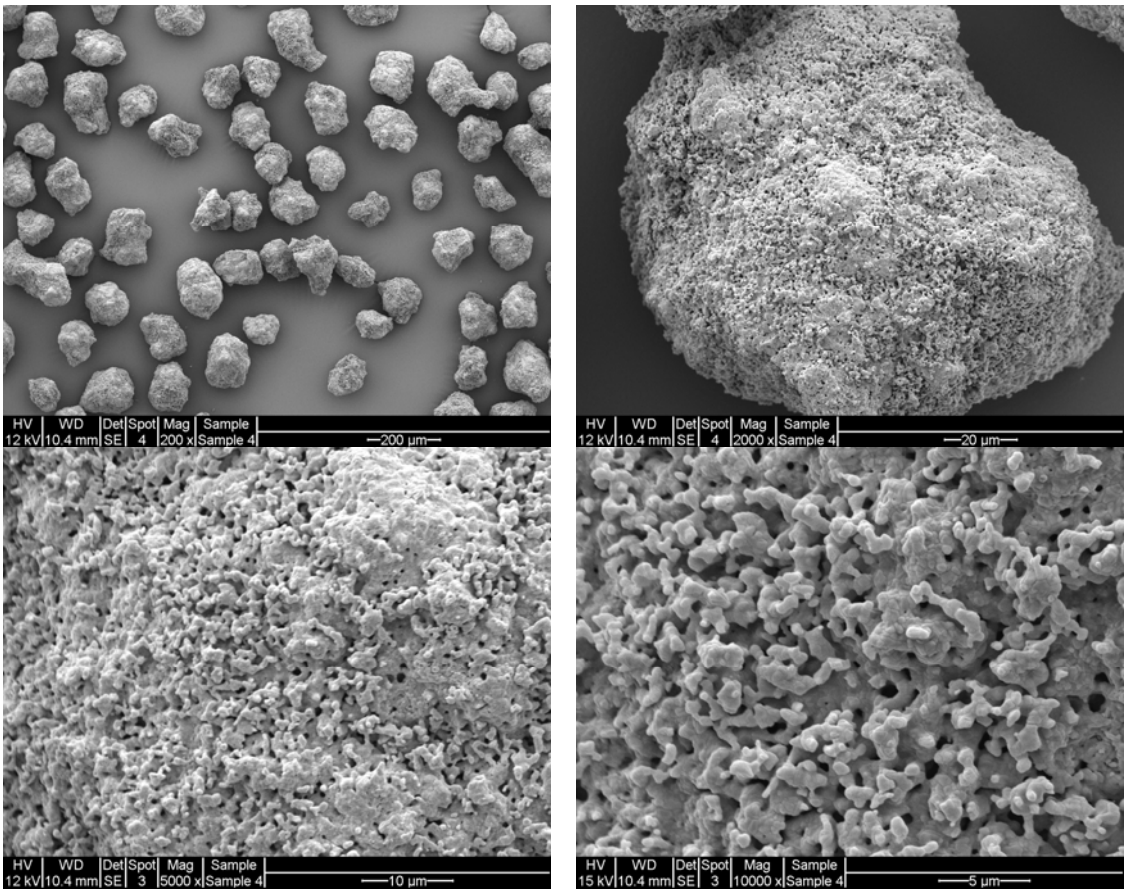

Figure A13. Sample images of Co_3O_4/Al_2O_3 after five continuous desorption-sorption cycles test in TGA at 800^{o}C for the magnification of 200X, 2000X, 5000X and 10000X.

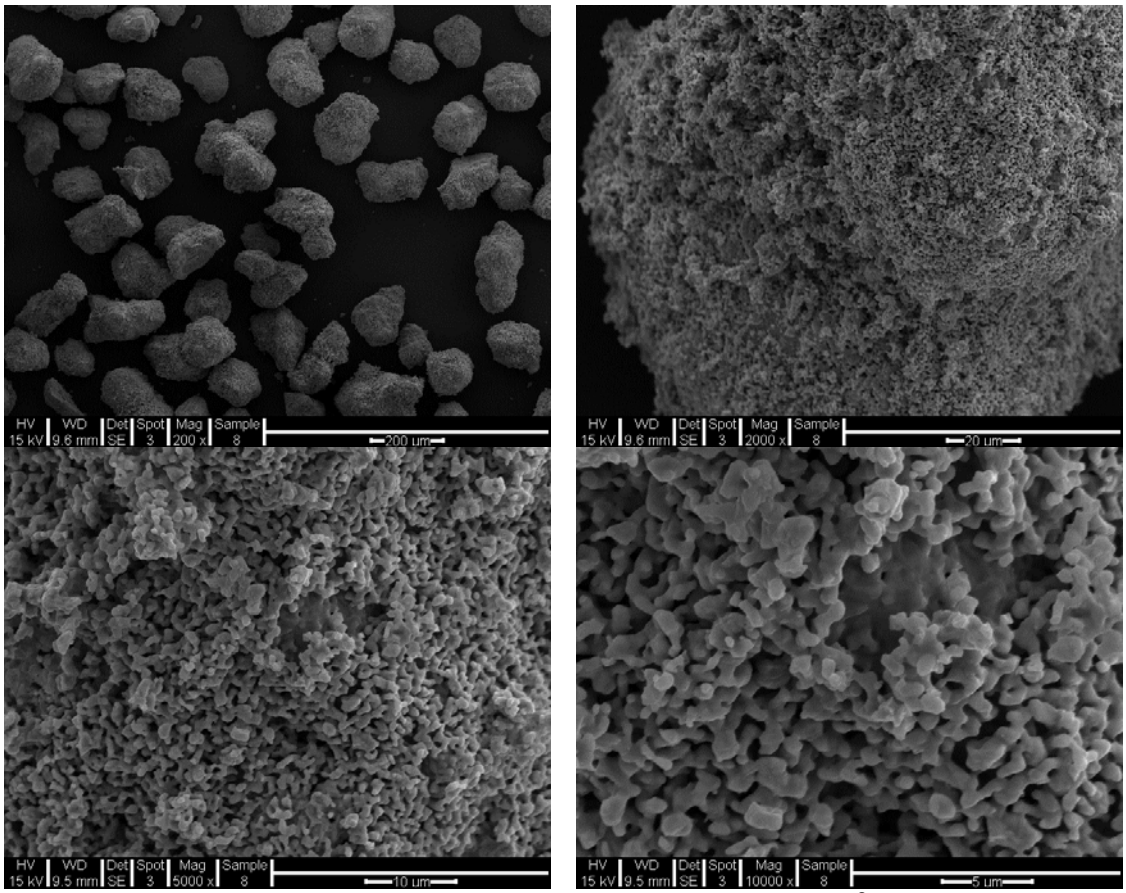

Figure A14. Sample images of Co_3O_4/Al_2O_3 after packed-bed test at 800^oC for the magnification of 200X, 2000X, 5000X and 10000X.

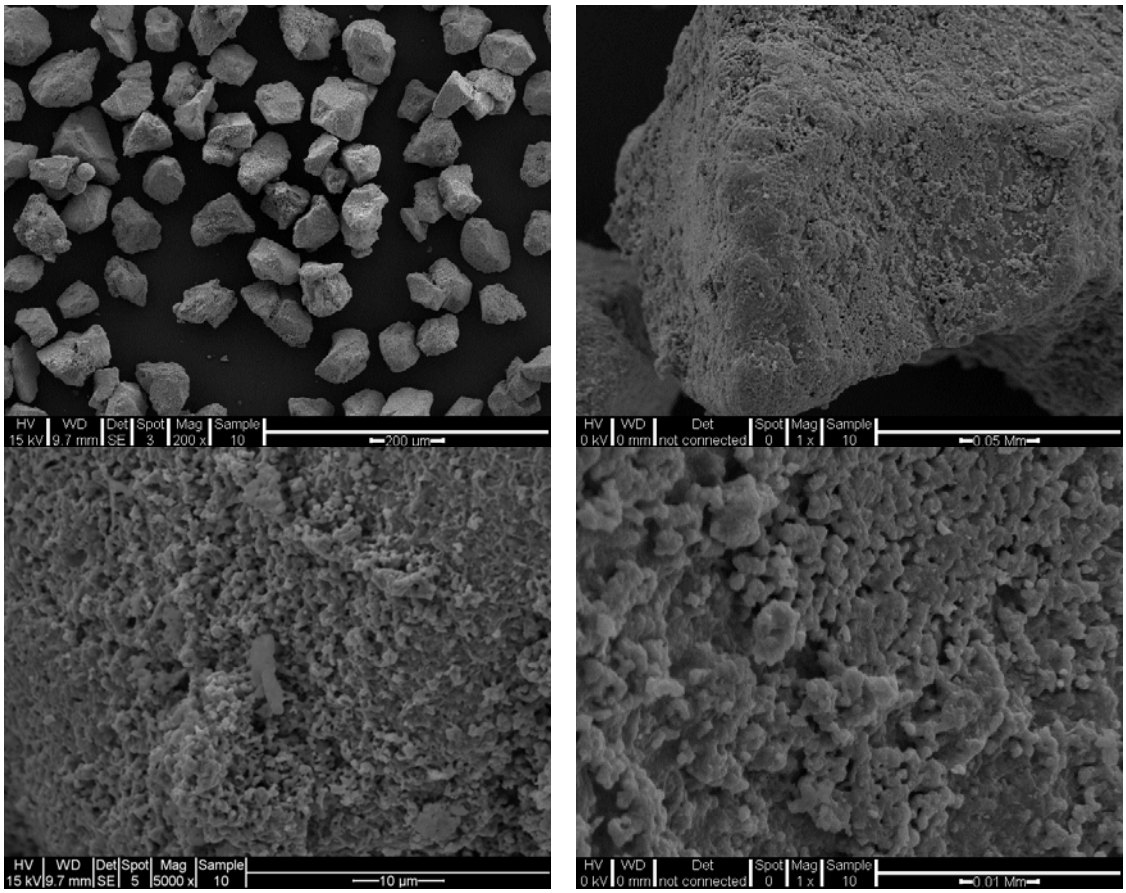

Figure A15. Fresh sample images of Co_3O_4/SiO_2 at the magnification of 200X, 2000X, 5000X and 10000X.

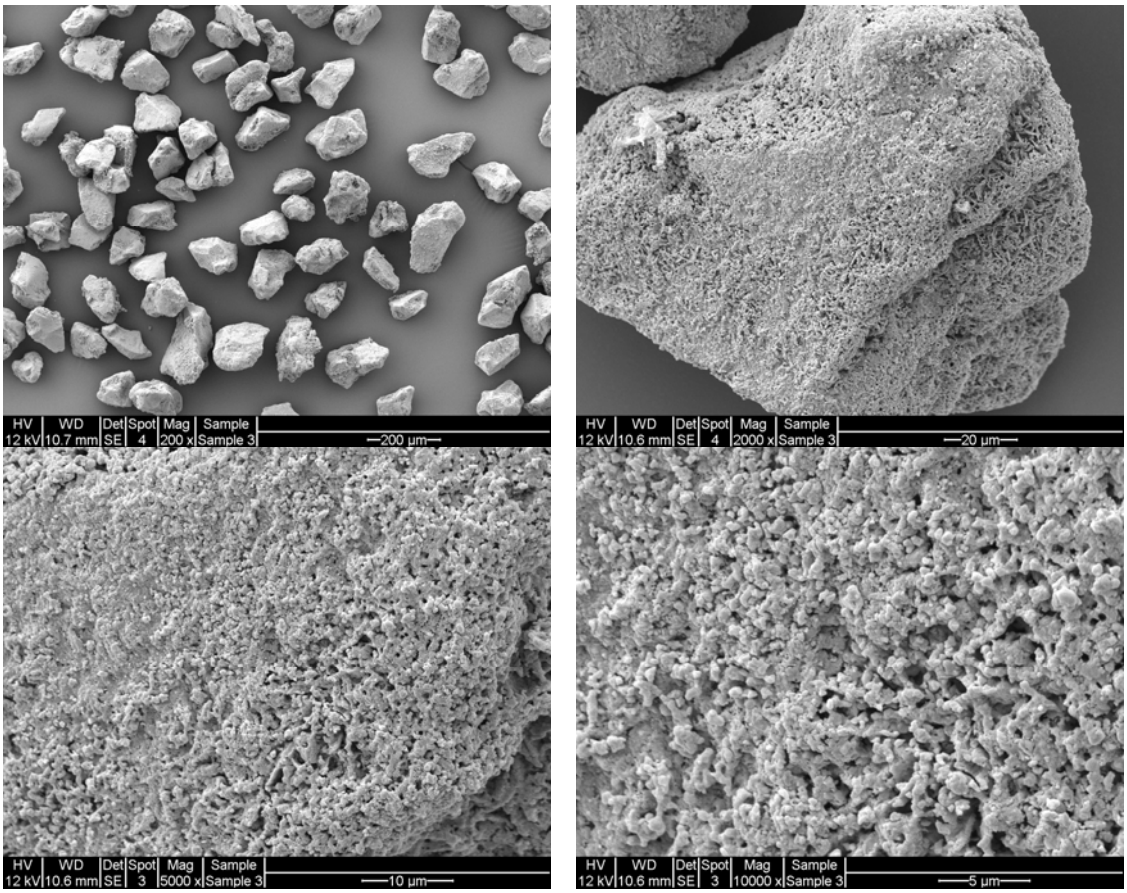

Figure A16. Sample images of Co_3O_4/SiO_2 after five continuous desorption-sorption cycles test in TGA at 800^{o}C for the magnification of 200X, 2000X, 5000X and 10000X.

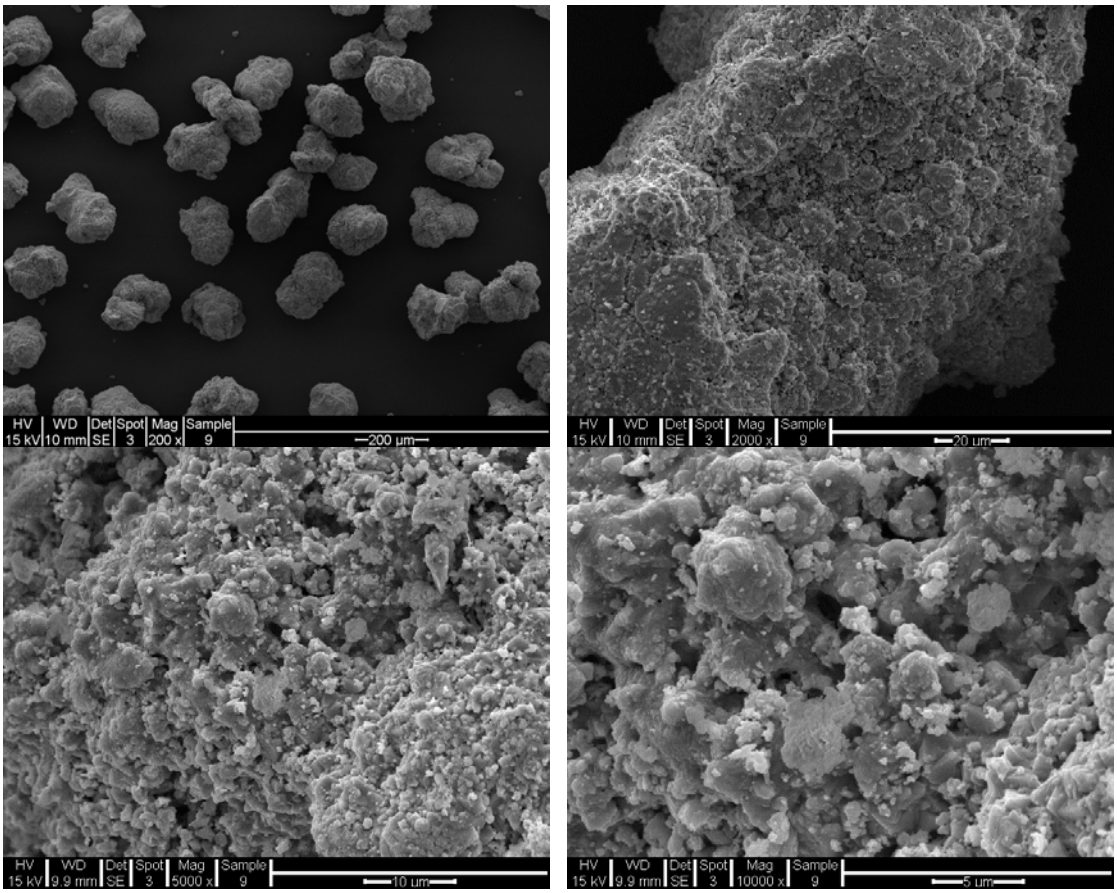

Figure A17. Fresh sample images of Mn_2O_3/Al_2O_3 at the magnification of 200X, 2000X, 5000X and 10000X.

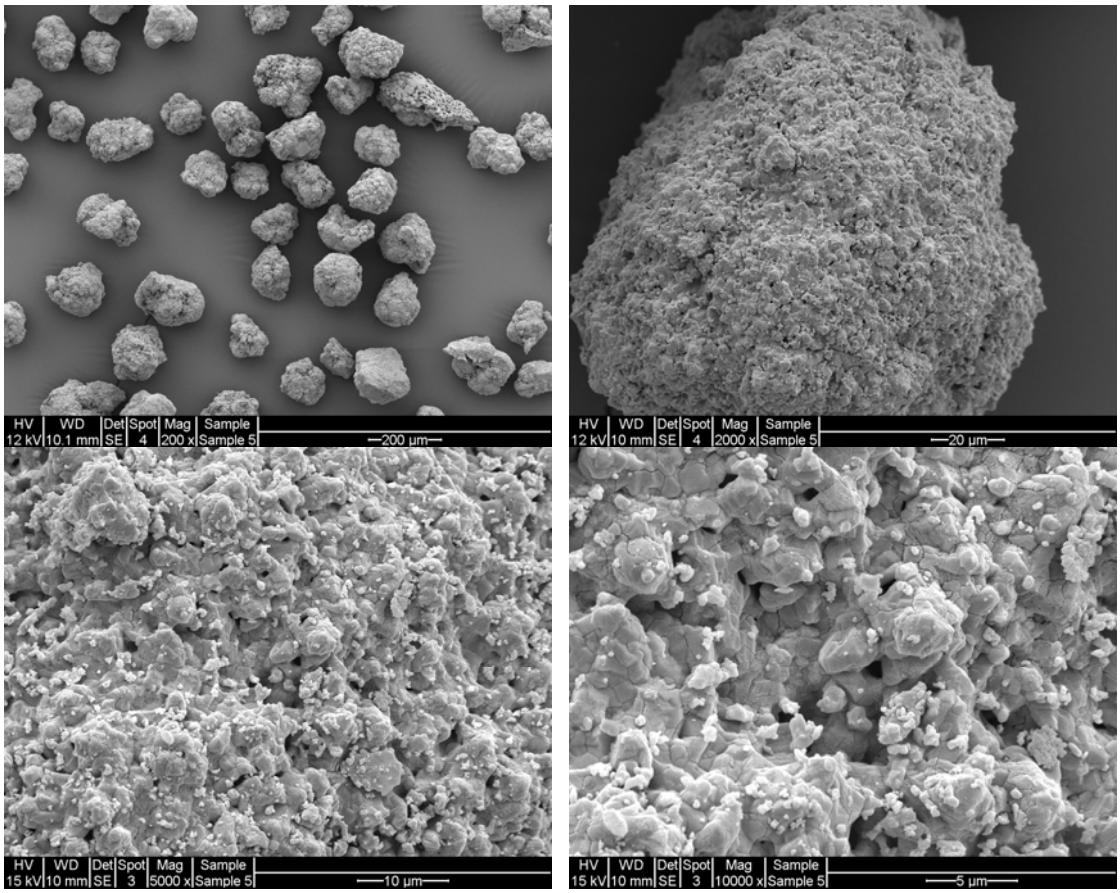

Figure A18. Sample images of Mn_2O_3/Al_2O_3 after five continuous desorption-sorption cycles test in TGA at 800^{o}C for the magnification of 200X, 2000X, 5000X and 10000X.

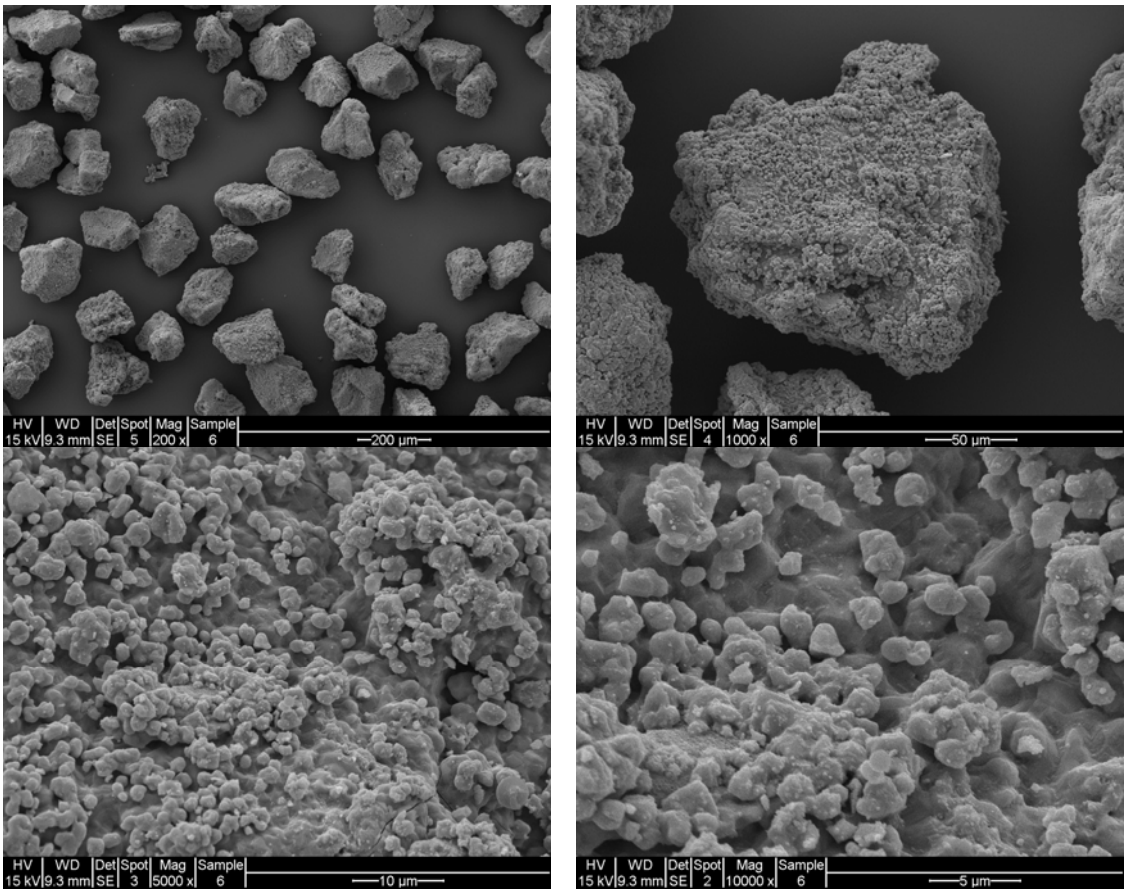

Figure A19. Fresh sample images of Mn_2O_3/SiO_2 at the magnification of 200X, 2000X, 5000X and 10000X.

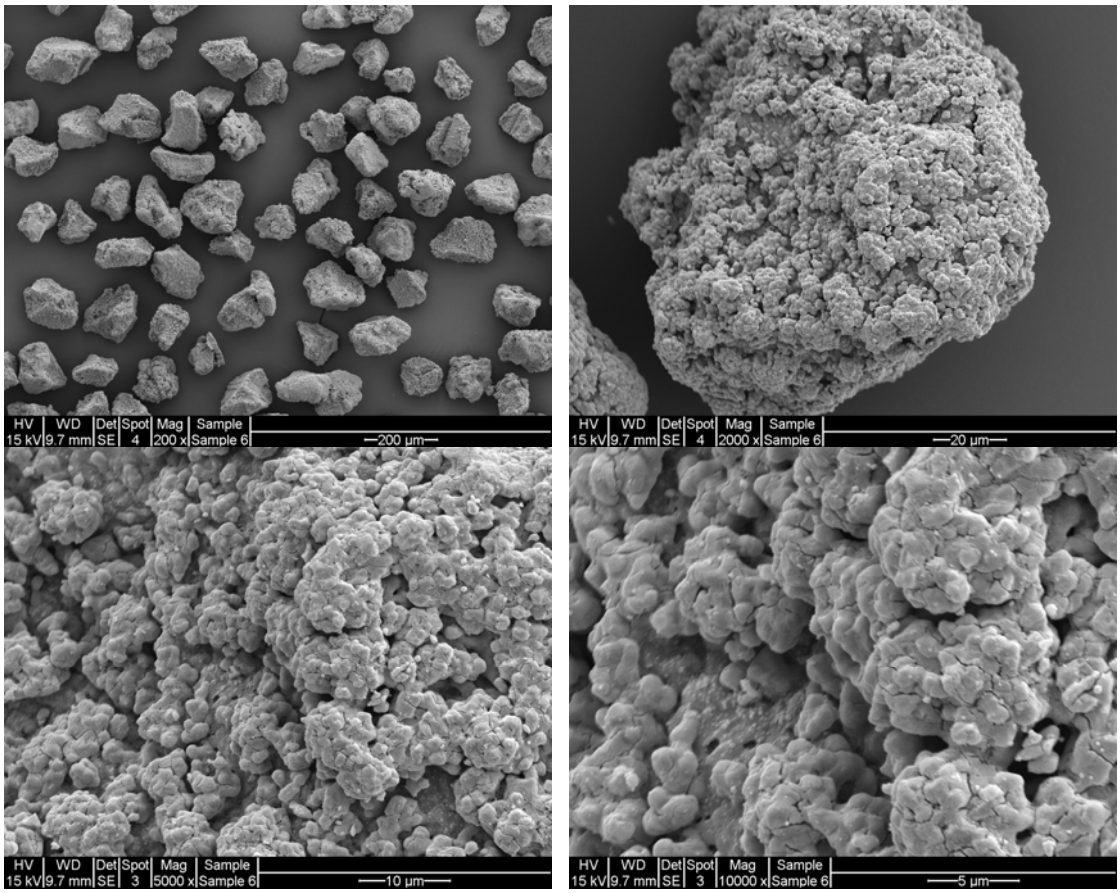

Figure A20. Sample images of Mn_2O_3/SiO_2 after five continuous desorption-sorption cycles test in TGA at 800^{o}C for the magnification of 200X, 2000X, 5000X and 10000X.

(2) SEM images of mixed metal oxides oxygen carriers

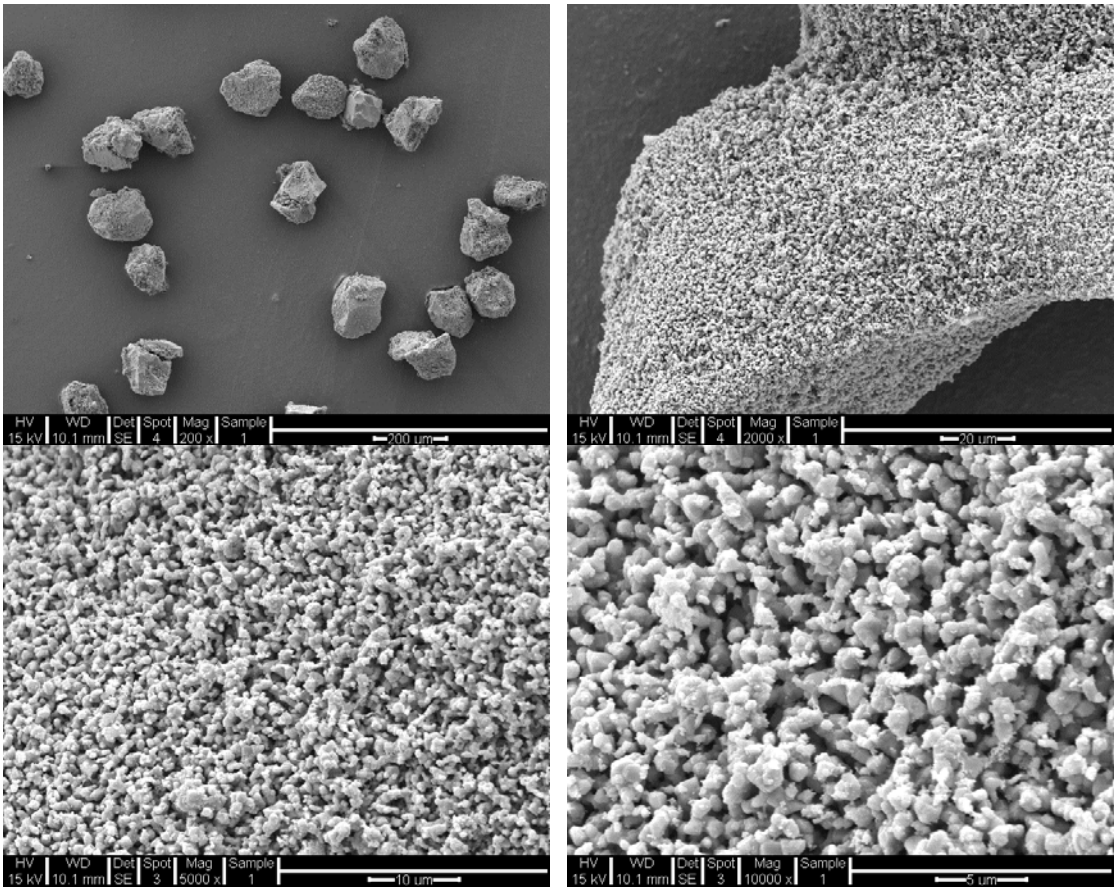

Figure A21. Fresh sample images of CuO-MgO-9-1/SiO_2 at the magnification of 200X, 2000X, 5000X and 10000X.

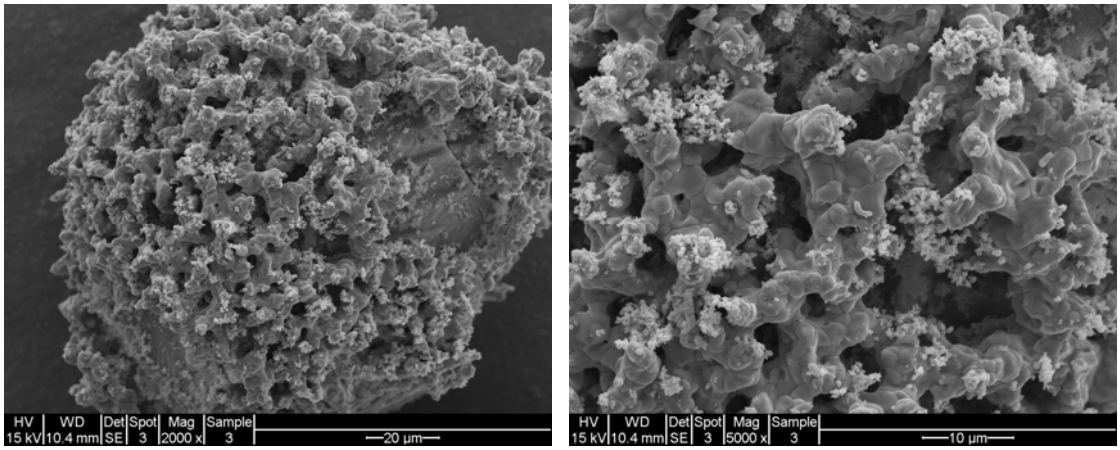

Figure A22. Sample images of CuO-MgO-9-1 /SiO_2 after 41 continuous desorption-sorption cycles test in TGA at 900^{o}C for the magnification of 2000X and 5000X.

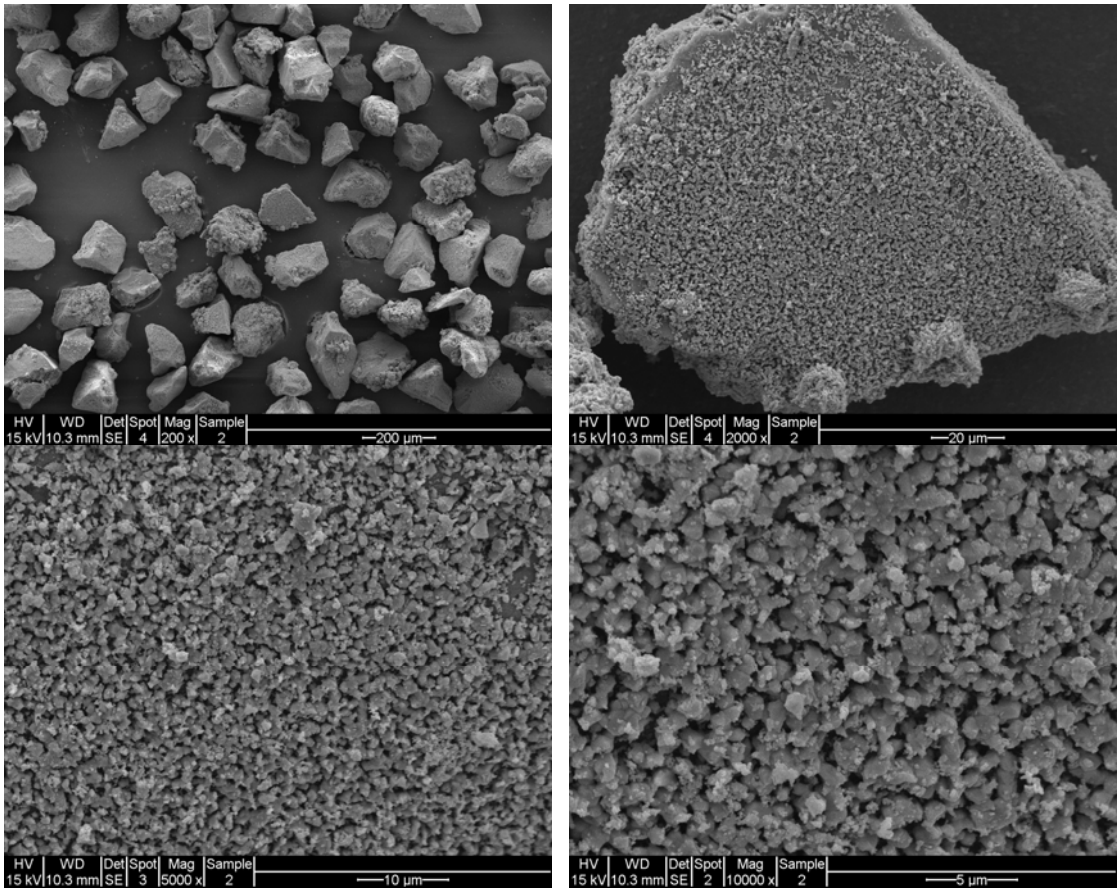

Figure A23. Fresh sample images of CuO-MgO-4-1/SiO_2 at the magnification of 200X, 2000X, 5000X and 10000X.

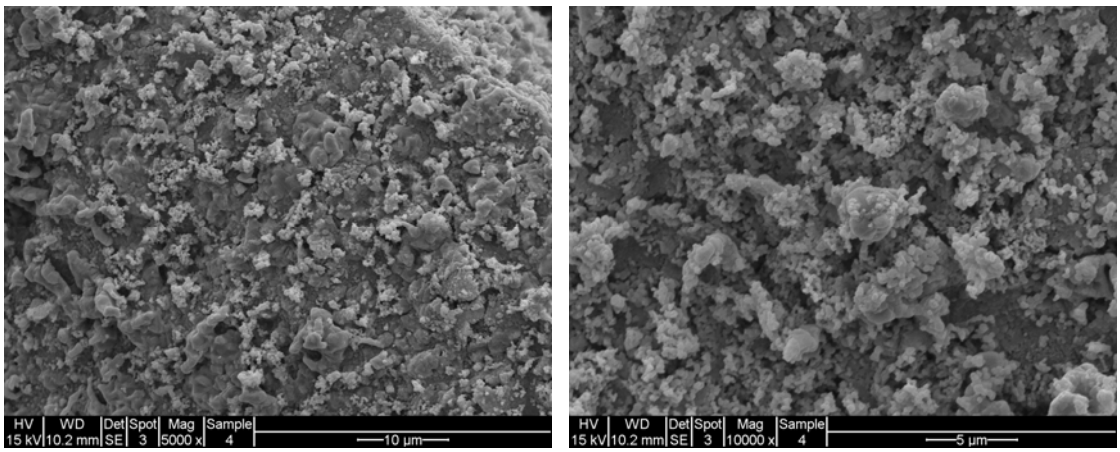

Figure A24. Sample images of CuO-MgO-4-1 /SiO_2 after 41 continuous desorption-sorption cycles test in TGA at 900^{o}C for the magnification of 5000X and 10000X.

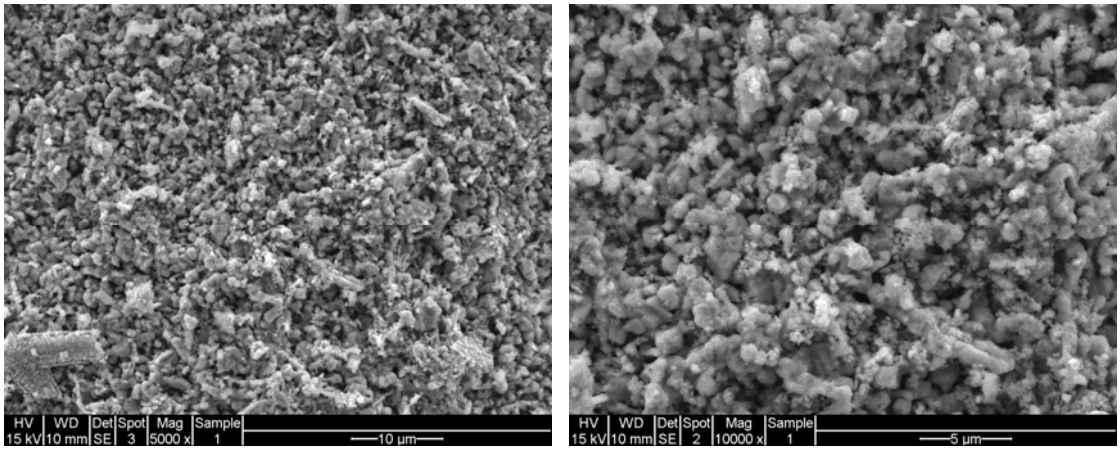

Figure A25. Fresh sample images of CuO-MgO-7-3/SiO_2 at the magnification of 5000X and 10000X.

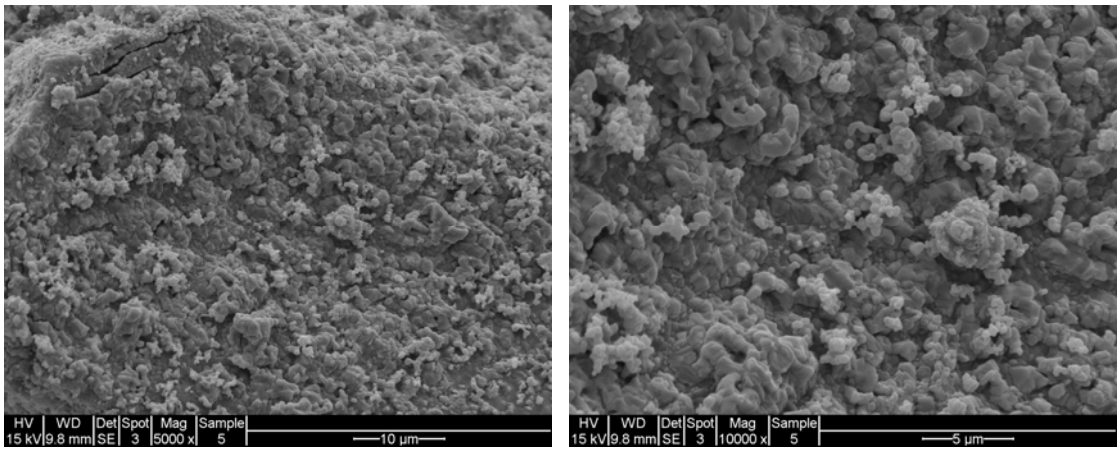

Figure A26. Sample images of CuO-MgO-7-3 /SiO_2 after 41 continuous desorption-sorption cycles test in TGA at 900^{o}C for the magnification of 5000X and 10000X.

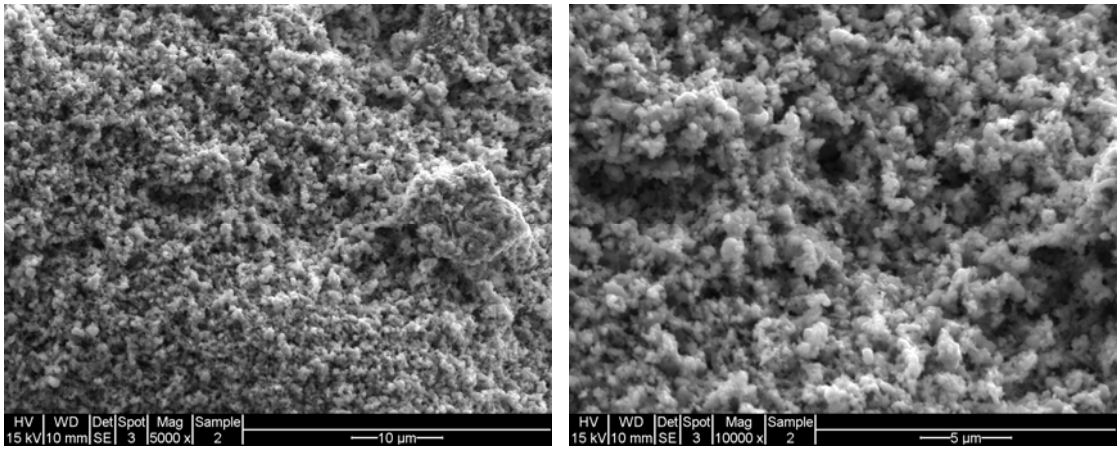

Figure A27. Fresh sample images of CuO-MgO-1-1/SiO_2 at the magnification of 5000X and 10000X.

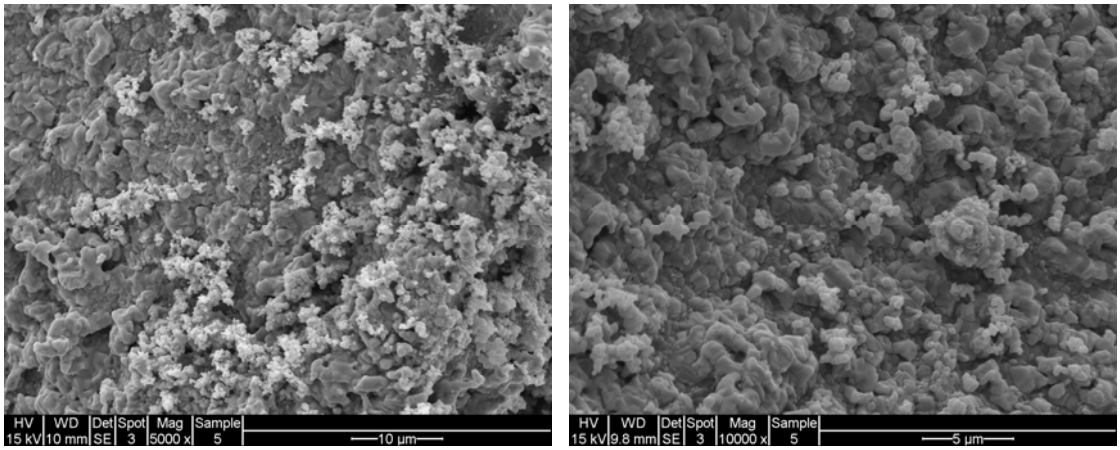

Figure A28. Sample images of CuO-MgO-1-1 /SiO_2 after 41 continuous desorption-sorption cycles test in TGA at 900^{o}C for the magnification of 5000X and 10000X.

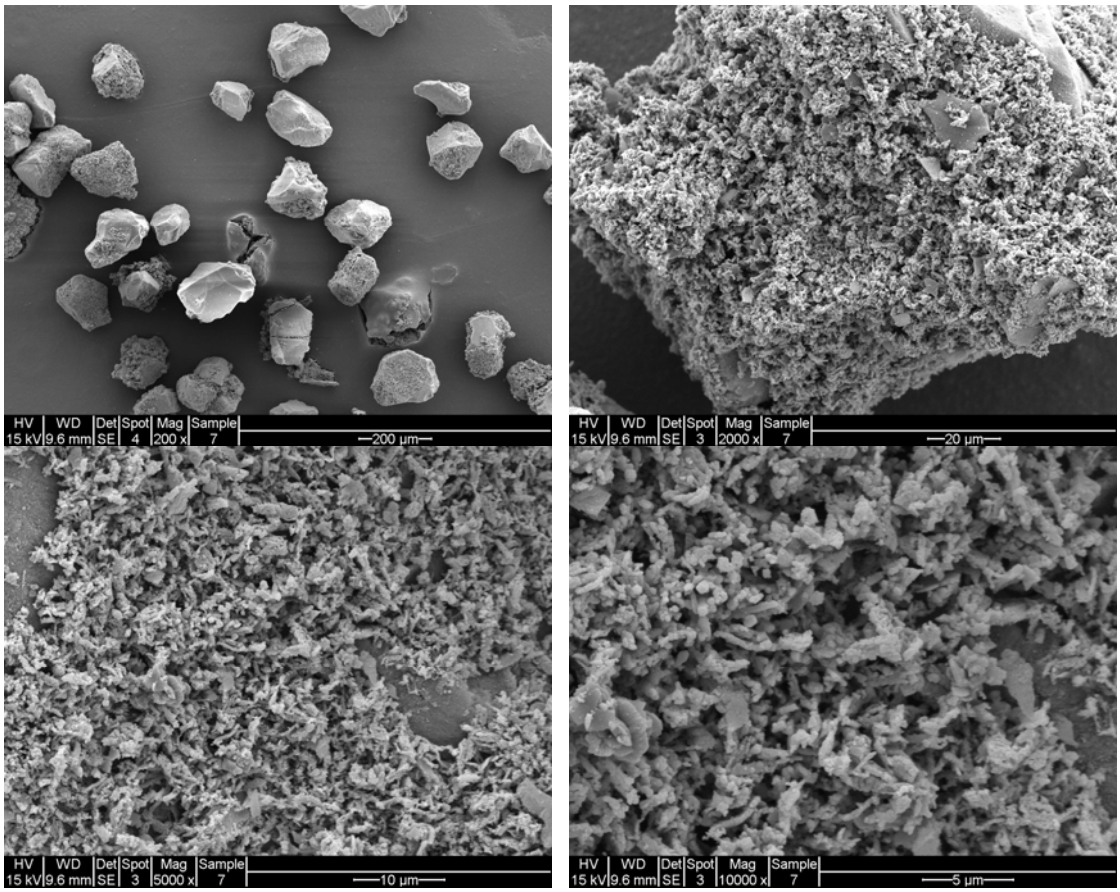

Figure A29. Fresh sample images of CuO-NiO-9-1/SiO_2 at the magnification of 200X, 2000X, 5000X and 10000X.

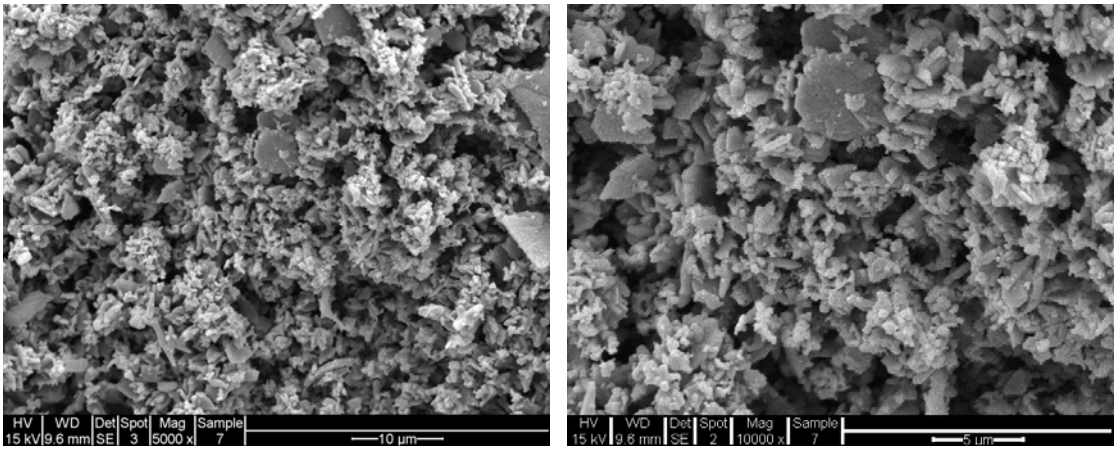

Figure A30. Sample images of CuO-NiO-9-1 /SiO_2 after 41 continuous desorption-sorption cycles test in TGA at 900^{o}C for the magnification of 5000X and 10000X.

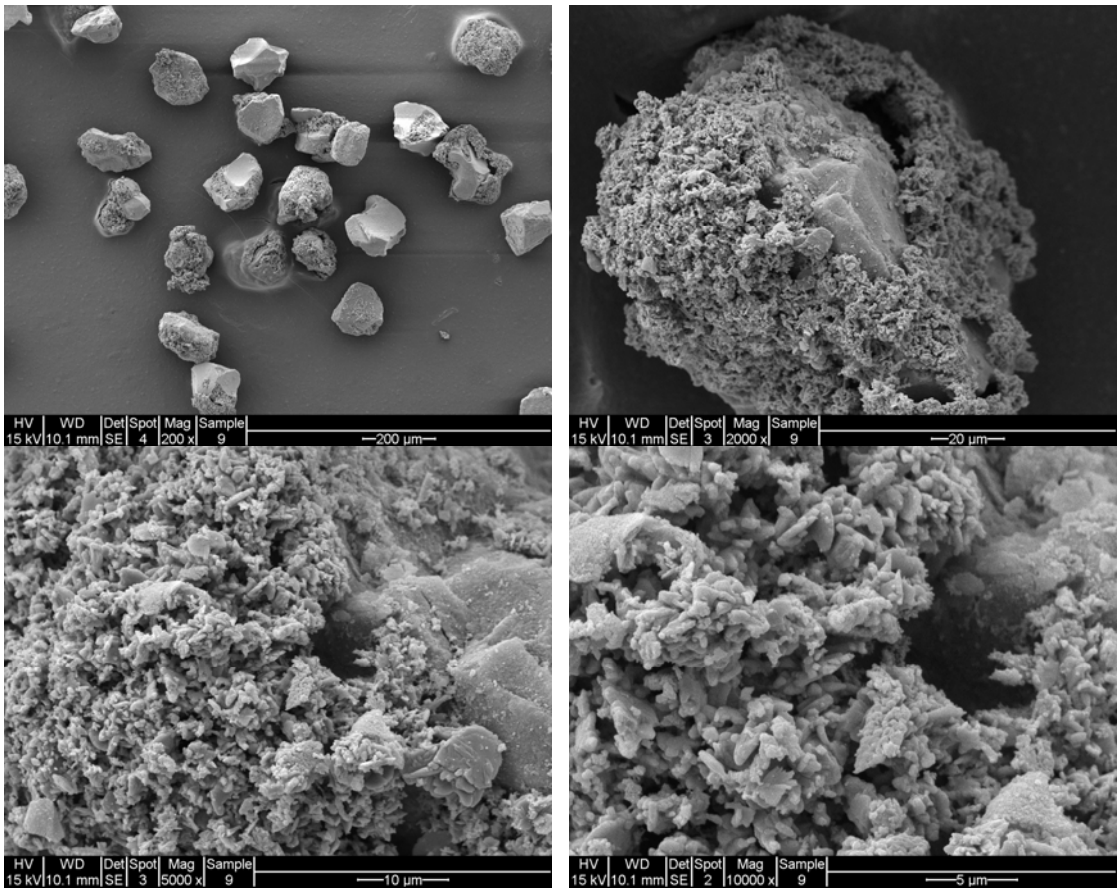

Figure A31. Fresh sample images of CuO-NiO-4-1/SiO_2 at the magnification of 200X, 2000X, 5000X and 10000X.

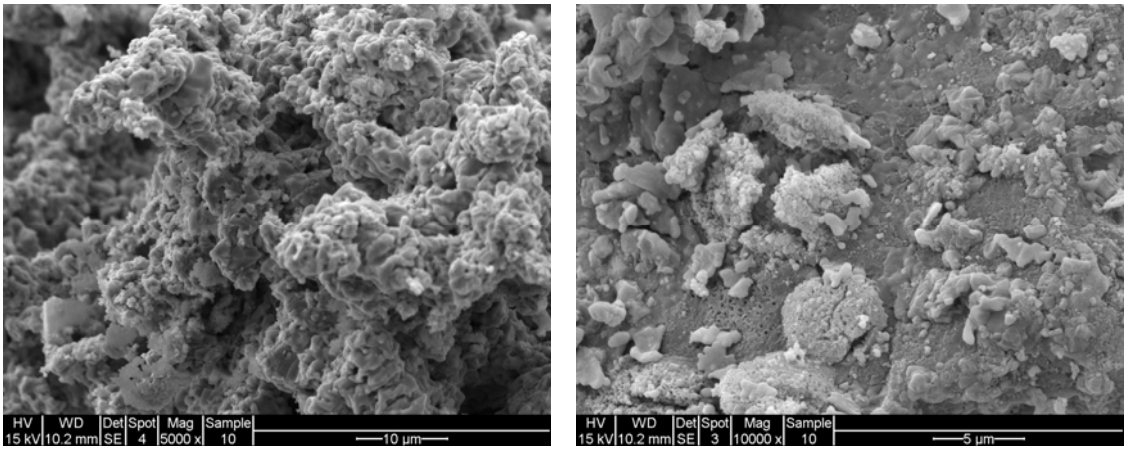

Figure A32. Sample images of CuO-NiO-4-1 /SiO_2 after 41 continuous desorption-sorption cycles test in TGA at 900^{o}C for the magnification of 5000X and 10000X.

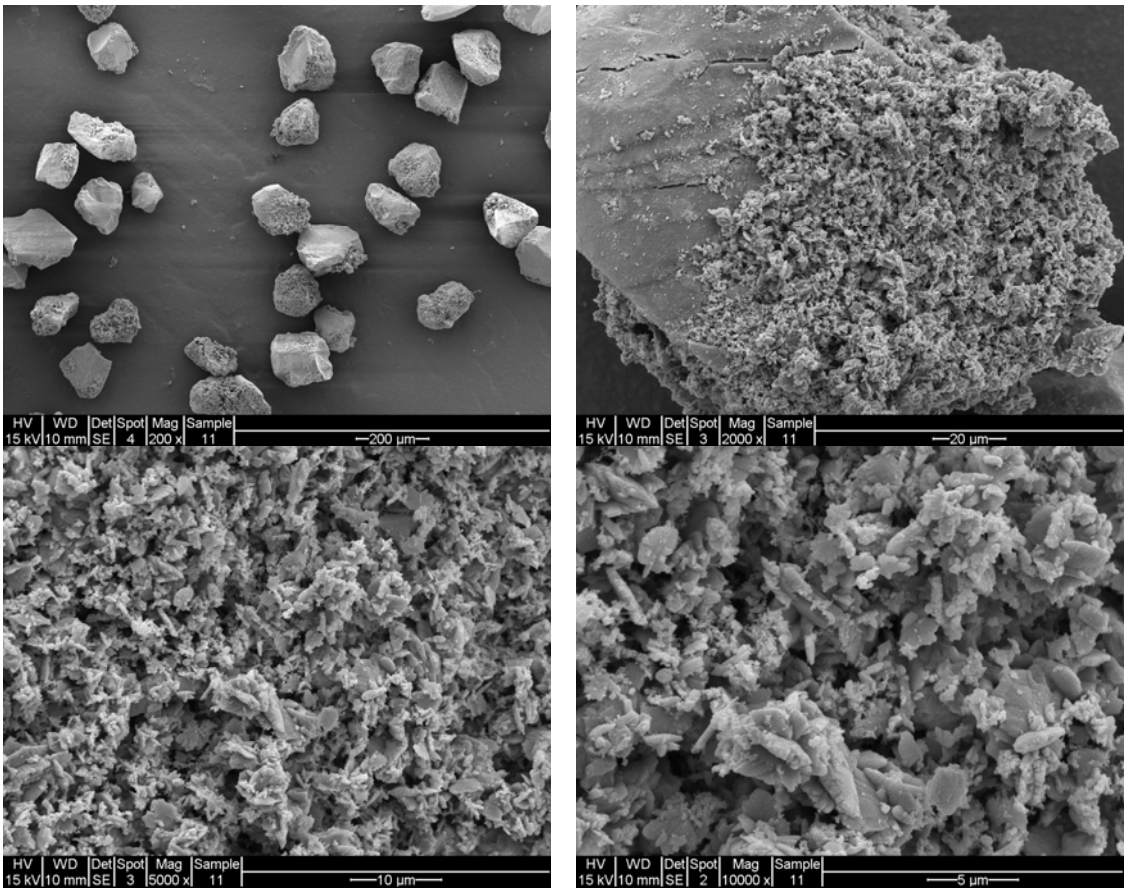

Figure A33. Fresh sample images of CuO-NiO-7-3/SiO_2 at the magnification of 200X, 2000X, 5000X and 10000X.

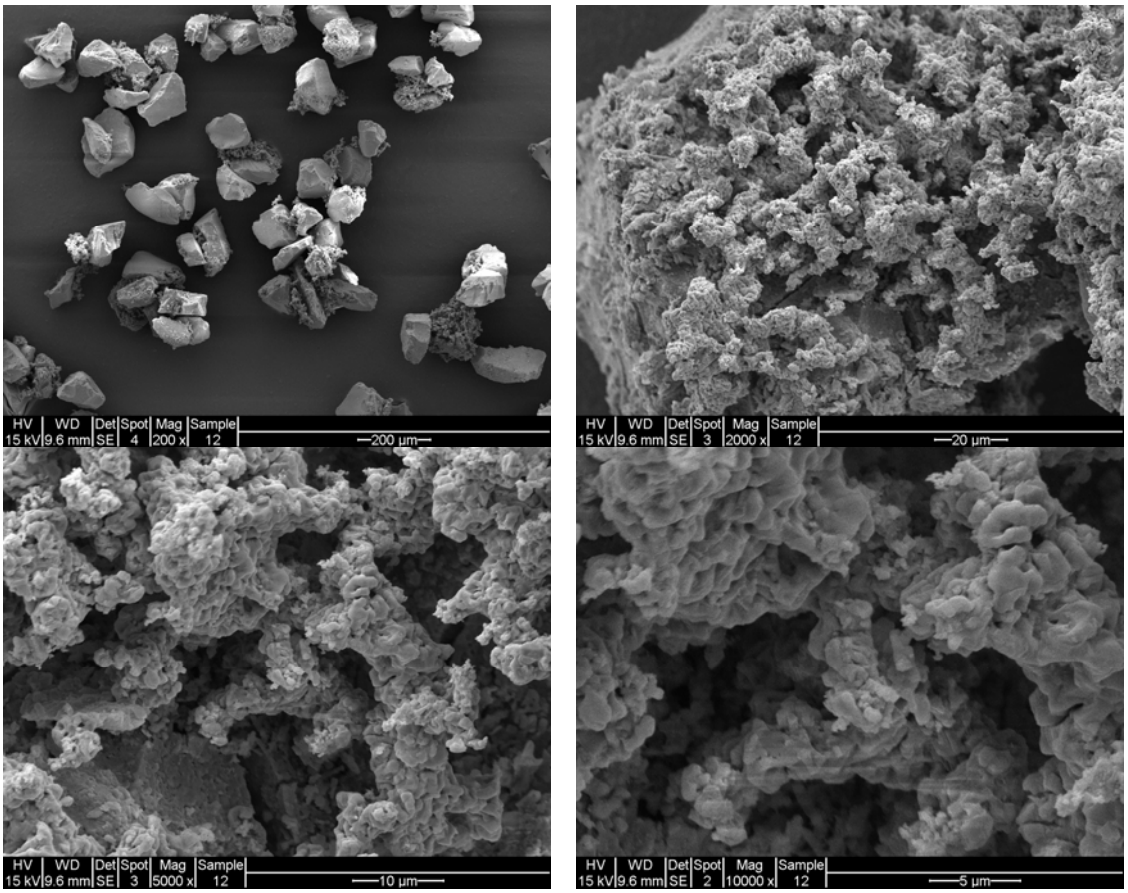

Figure A34. Sample images of CuO-NiO-7-3 /SiO_2 after 41 continuous desorption-sorption cycles test in TGA at 900^{o}C for the magnification of 200X, 2000X, 5000X and 10000X.

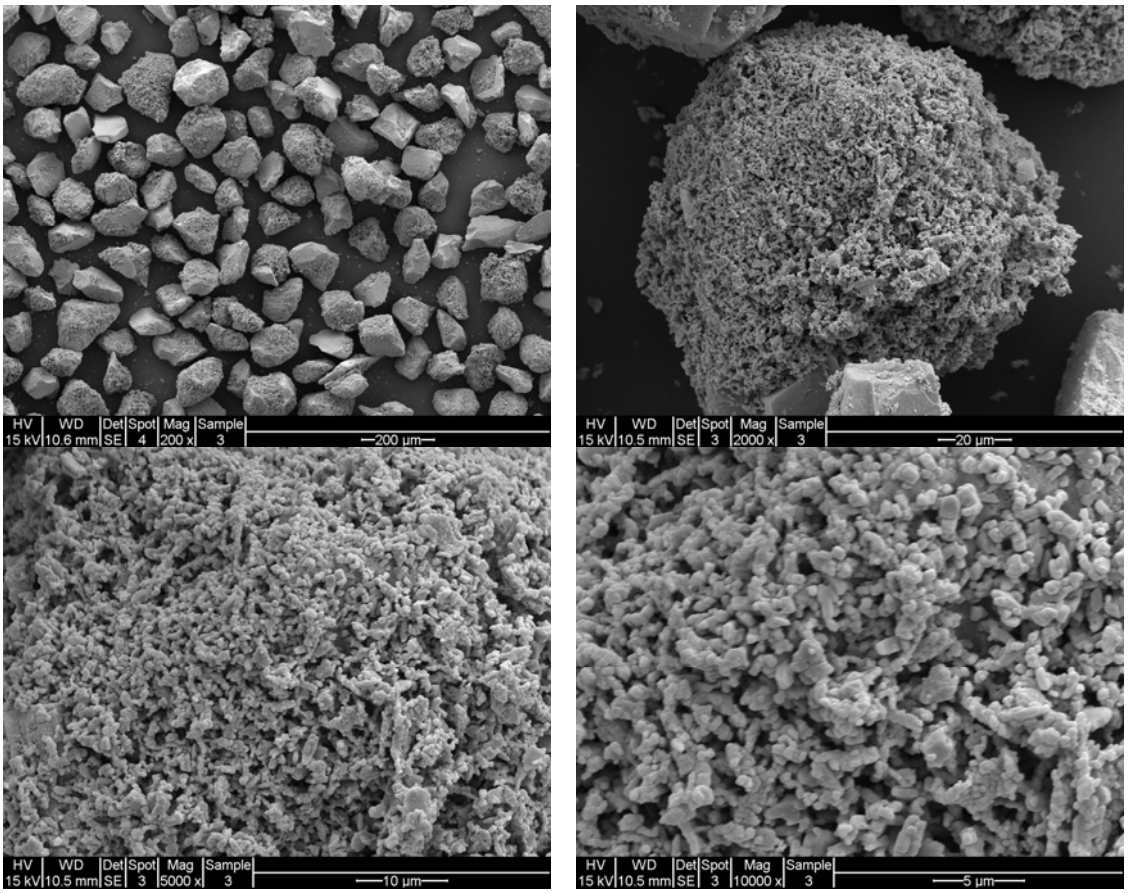

Figure A35. Fresh sample images of $CuO\text{-}Co_3O_4\text{-}9\text{-}1/SiO_2$ at the magnification of 200X, 2000X, 5000X and 10000X.

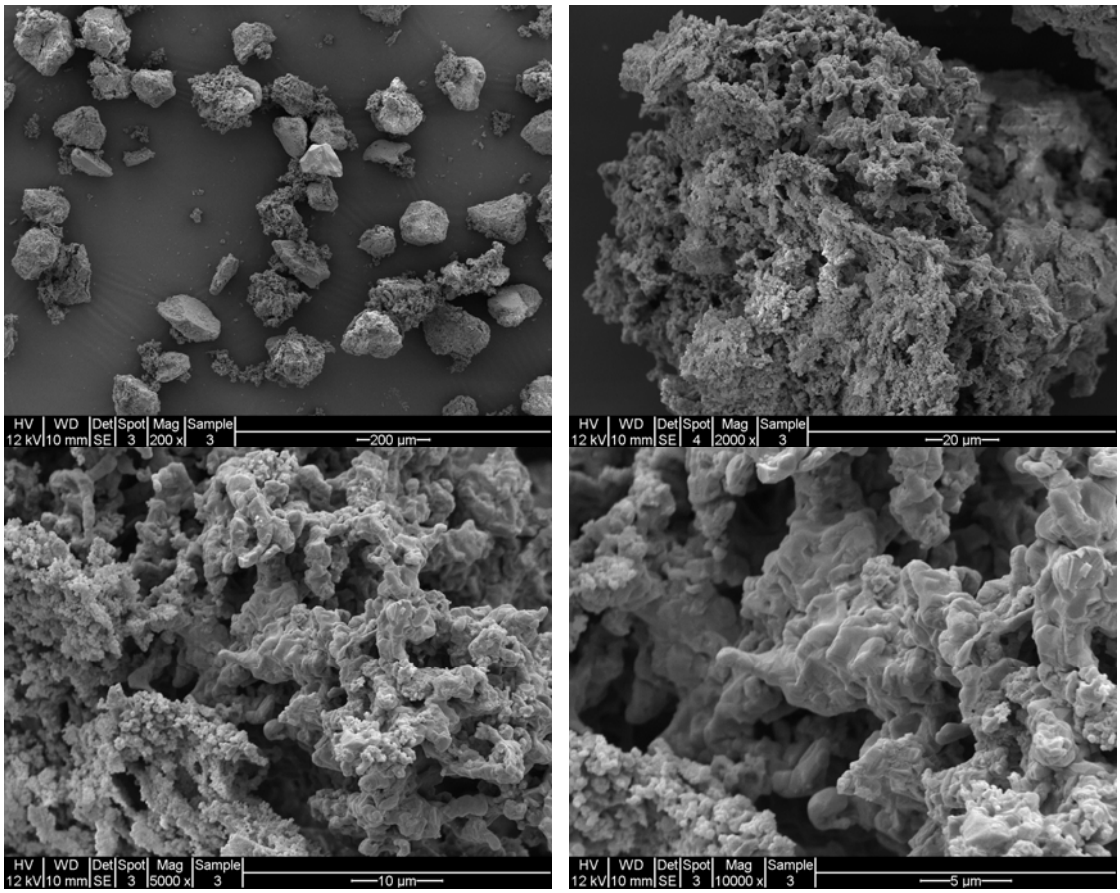

Figure A36. Sample images of CuO-Co_3O_4-9-1 /SiO_2 after 41 continuous desorption-sorption cycles test in TGA at 900^{o}C for the magnification of 200X, 2000X, 5000X and 10000X.

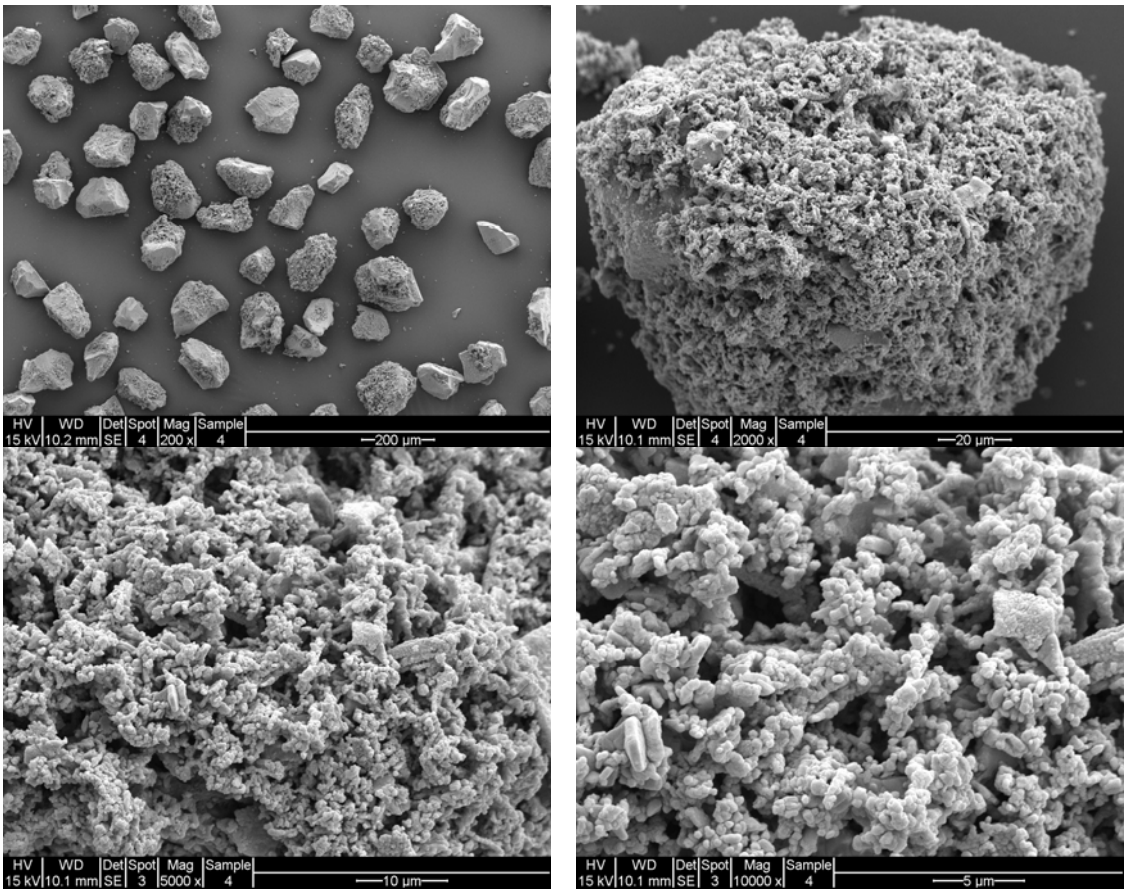

Figure A37. Fresh sample images of $CuO\text{-}Co_3O_4\text{-}4\text{-}1/SiO_2$ at the magnification of 200X, 2000X, 5000X and 10000X.

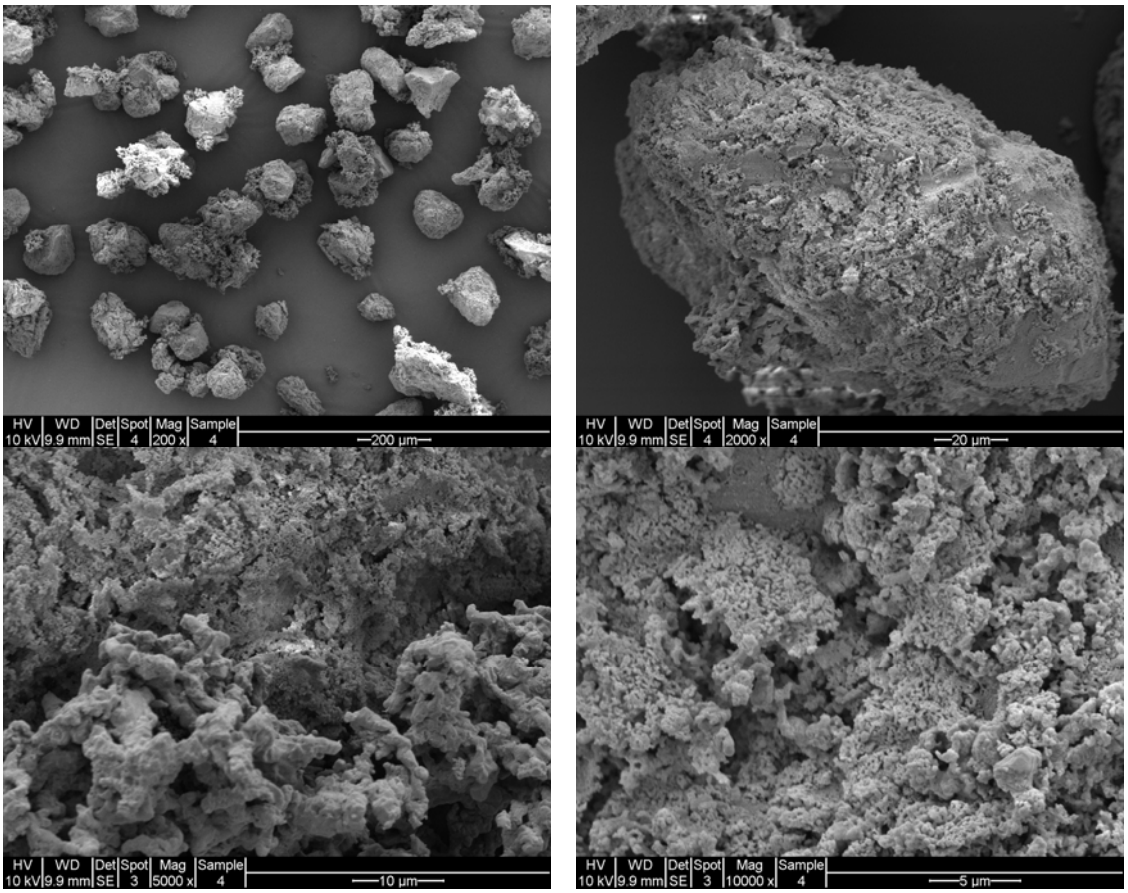

Figure A38. Sample images of $CuO\text{-}Co_3O_4$-4-1 /SiO_2 after 41 continuous desorption-sorption cycles test in TGA at 900^{o}C for the magnification of 200X, 2000X, 5000X and 10000X.

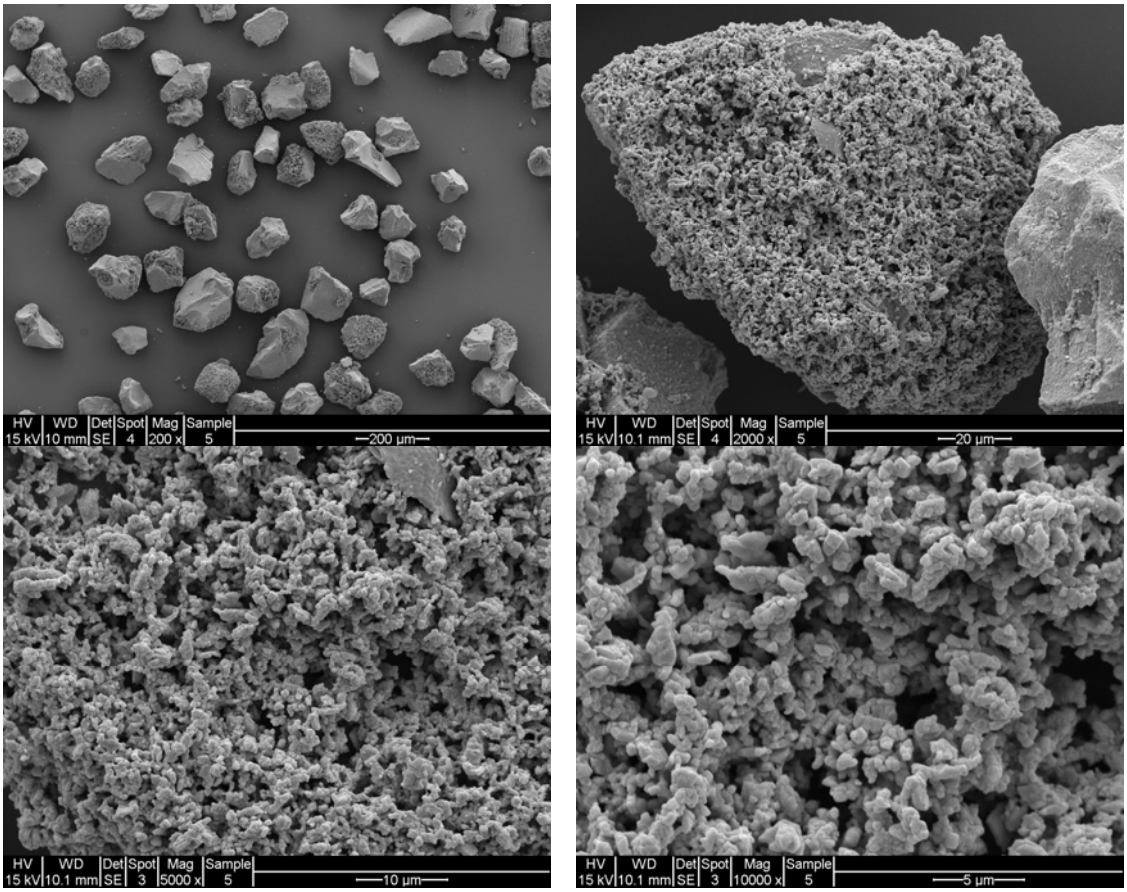

Figure A39. Fresh sample images of $CuO\text{-}Co_3O_4\text{-}7\text{-}3/SiO_2$ at the magnification of 200X, 2000X, 5000X and 10000X.

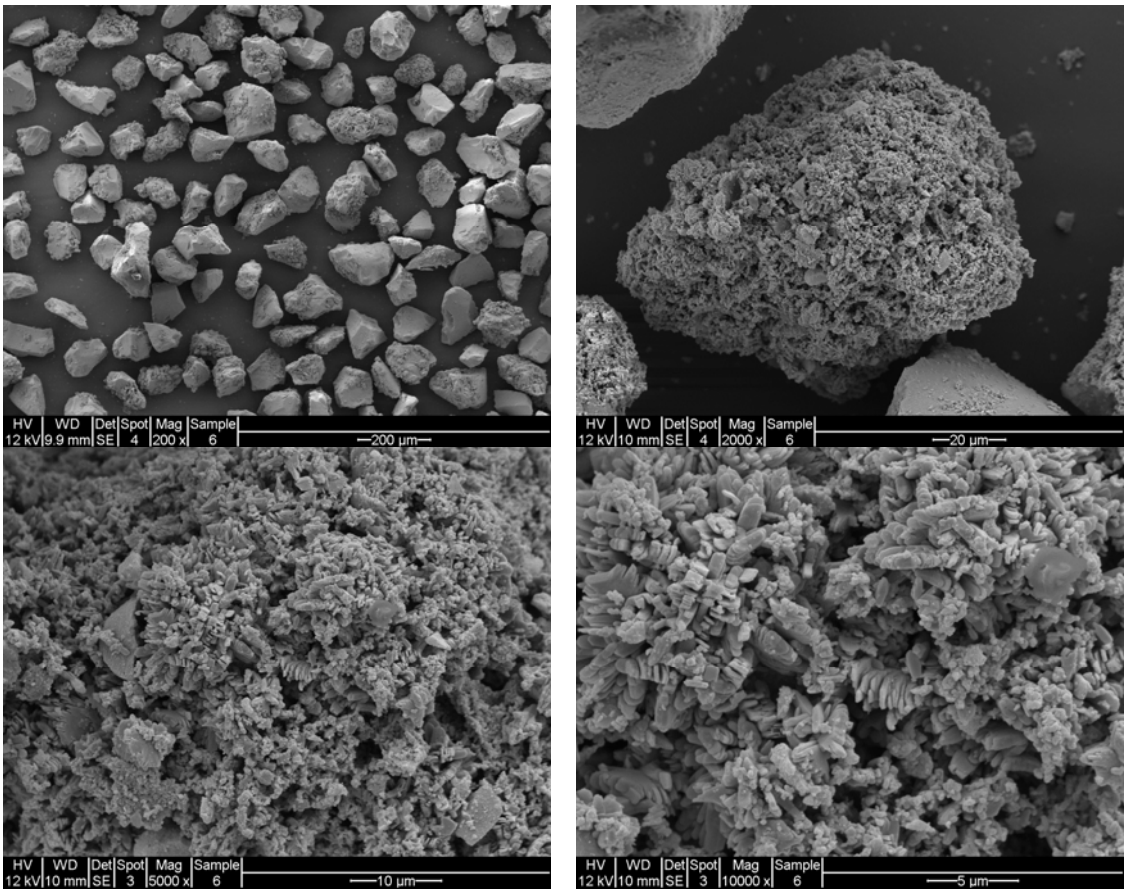

Figure A40. Fresh sample images of CuO-Fe_2O_3-4-1/SiO_2 at the magnification of 200X, 2000X, 5000X and 10000X.

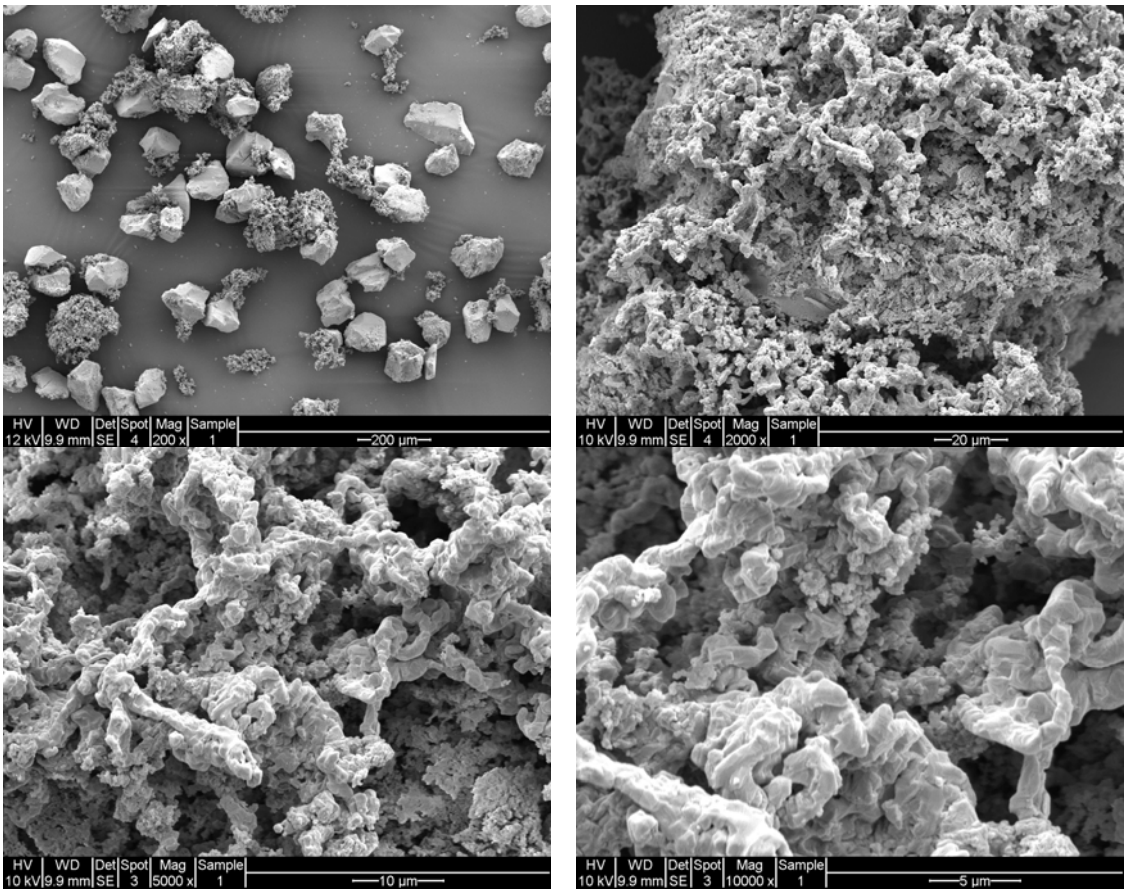

Figure A41. Sample images of CuO- Fe_2O_3-4-1 /SiO_2 after 41 continuous desorption-sorption cycles test in TGA at 900^{o}C for the magnification of 200X, 2000X, 5000X and 10000X.

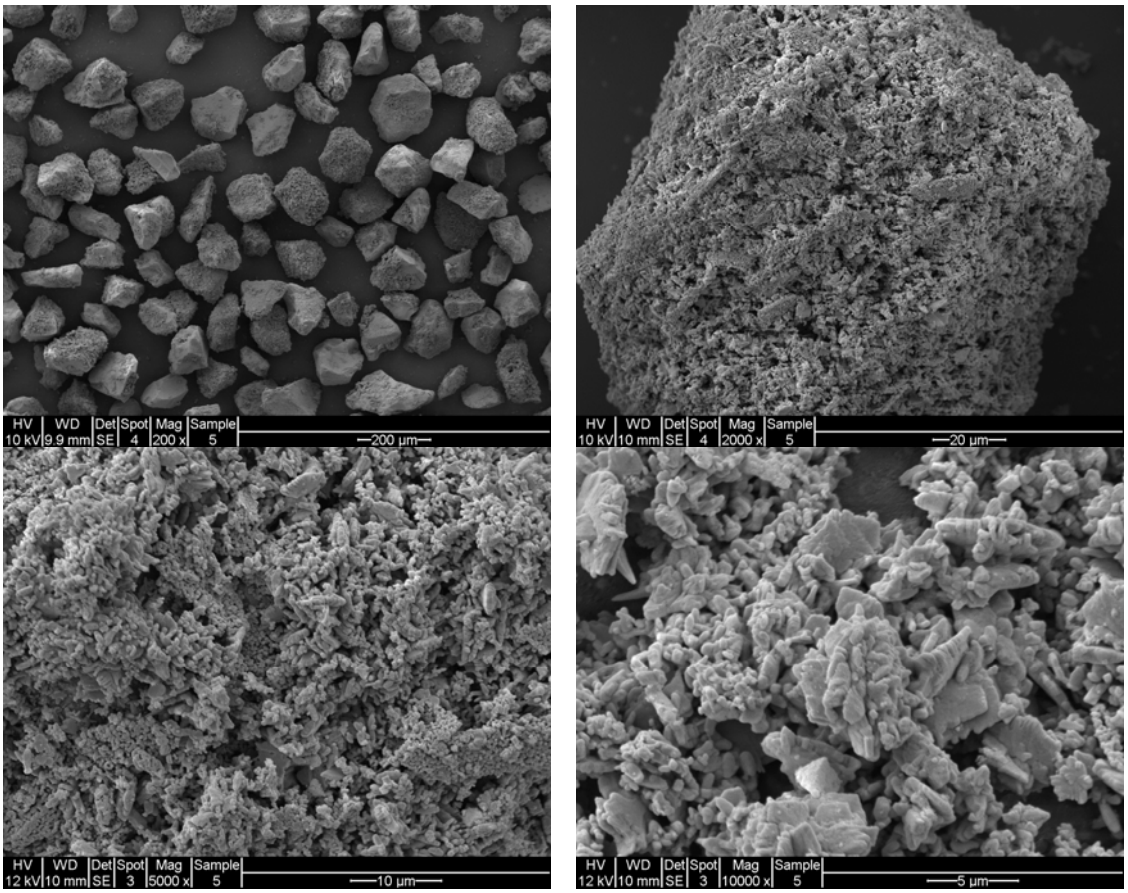

Figure A42. Fresh sample images of CuO-Mn_2O_3-4-1/SiO_2 at the magnification of 200X, 2000X, 5000X and 10000X.

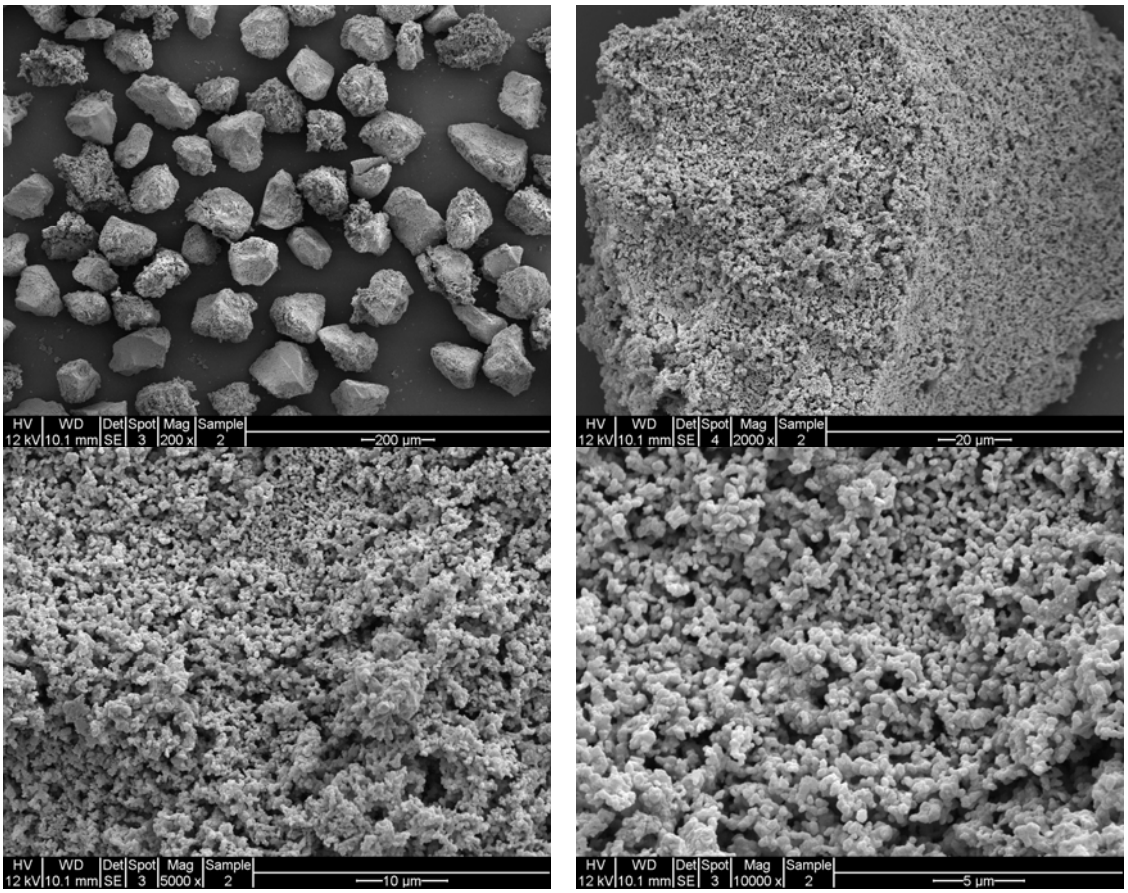

Figure A43. Sample images of CuO- Mn_2O_3-4-1 /SiO_2 after 41 continuous desorption-sorption cycles test in TGA at 900^{o}C for the magnification of 200X, 2000X, 5000X and 10000X.

(3) XRD patterns

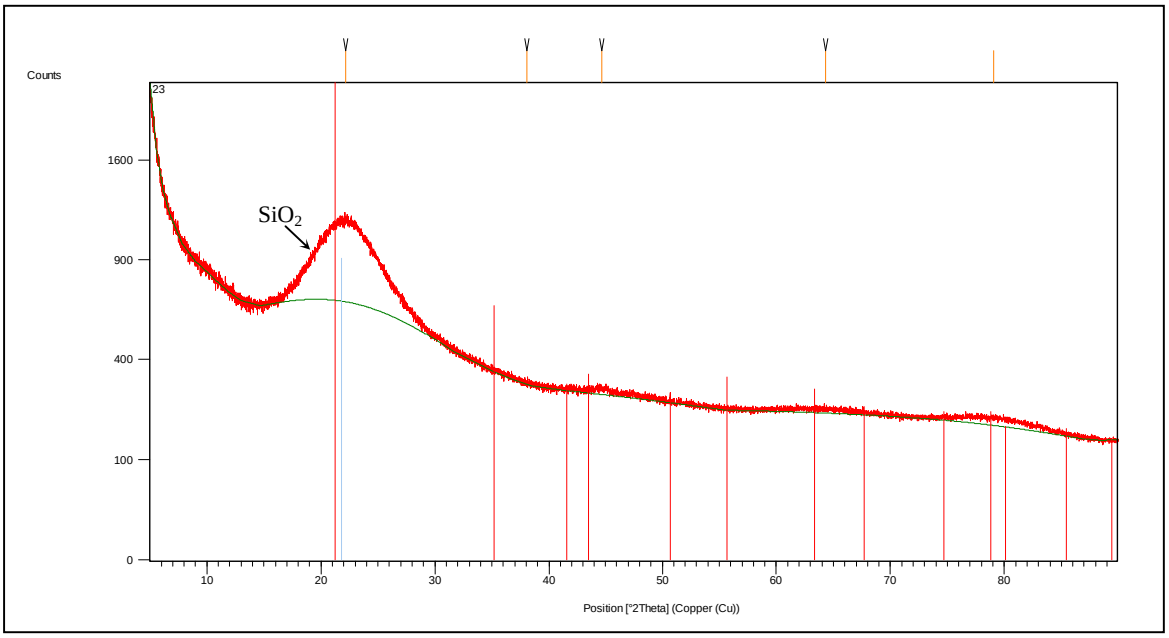

Figure A44. XRD pattern of SiO_2

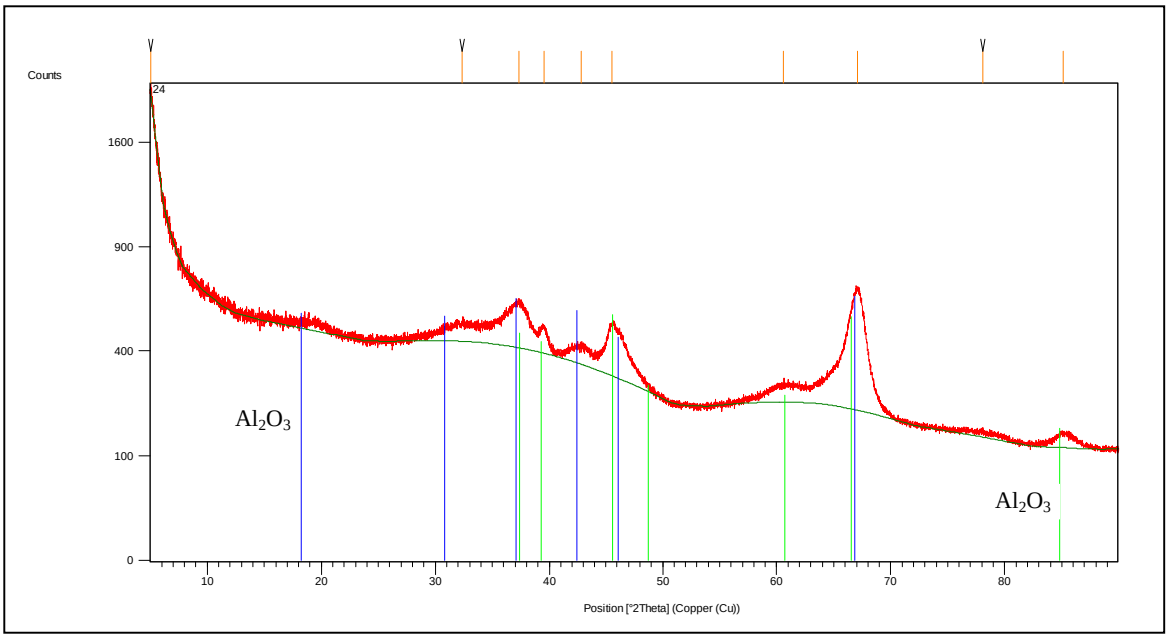

Figure A45. XRD pattern of Al_2O_3

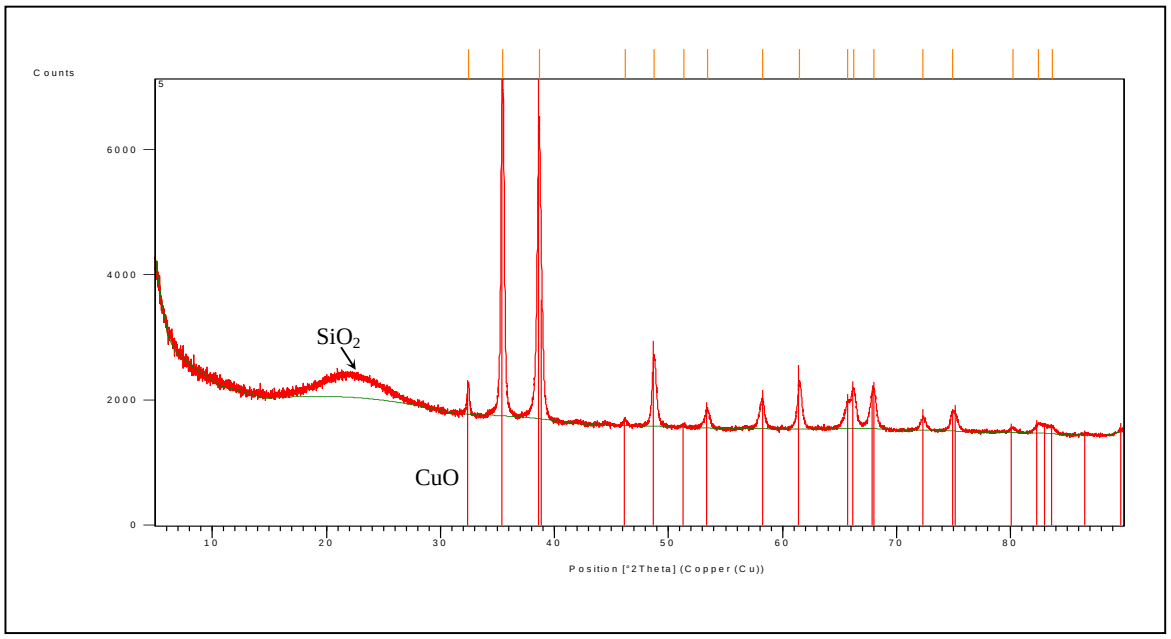

Figure A46. XRD pattern of CuO/SiO_2

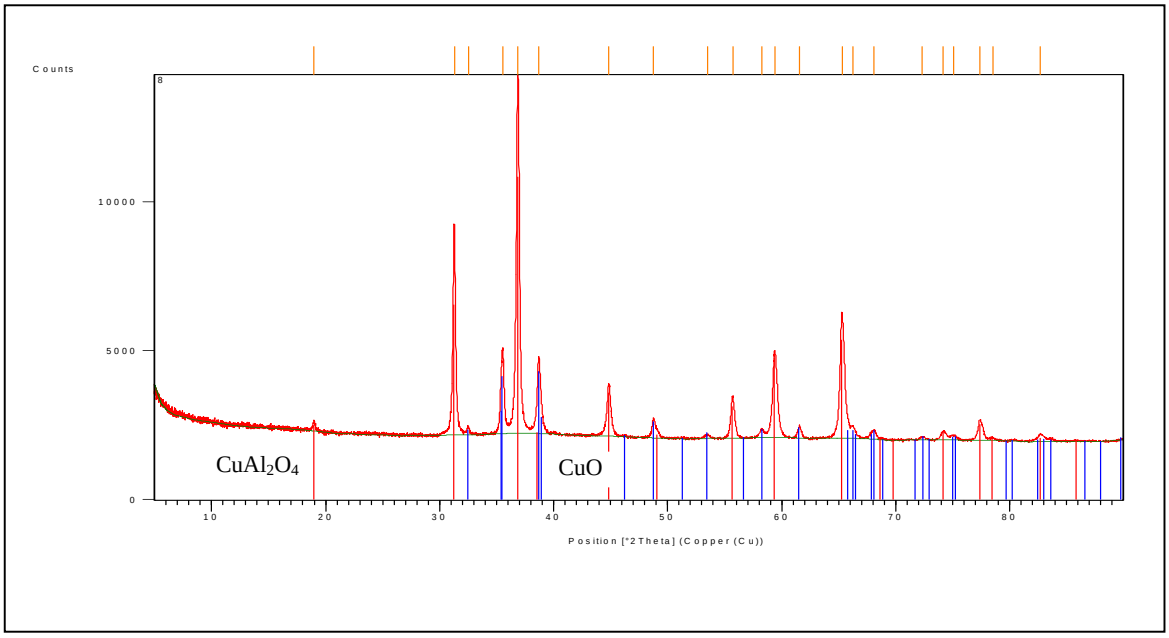

Figure A47. XRD pattern of CuO/Al_2O_3

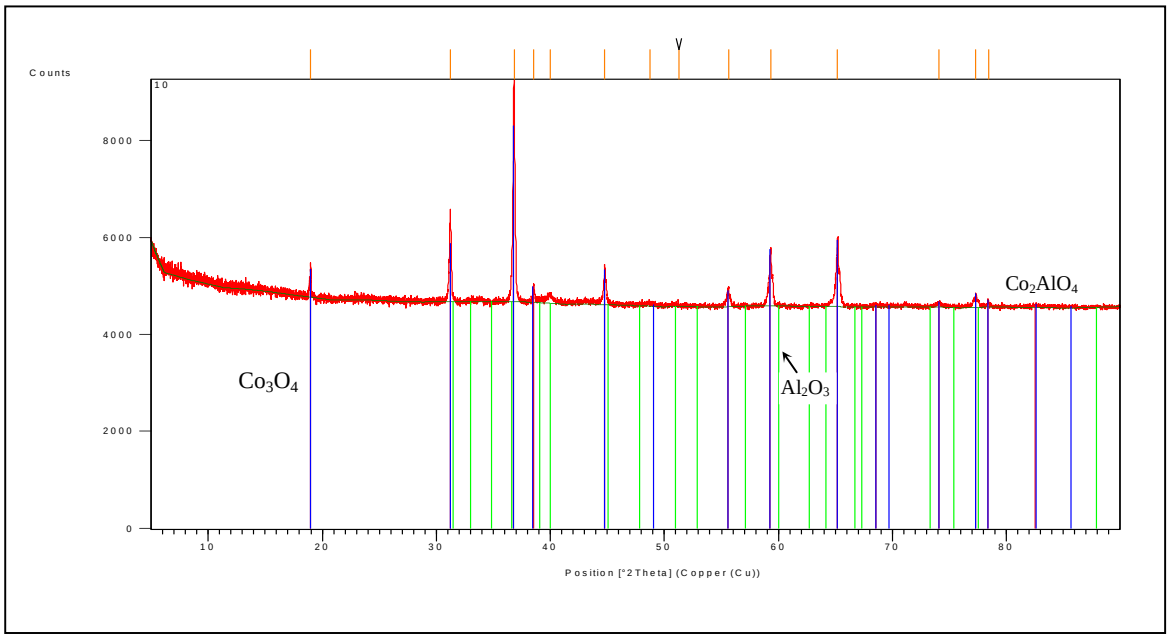

Figure A48. XRD pattern of Co_3O_4/Al_2O_3

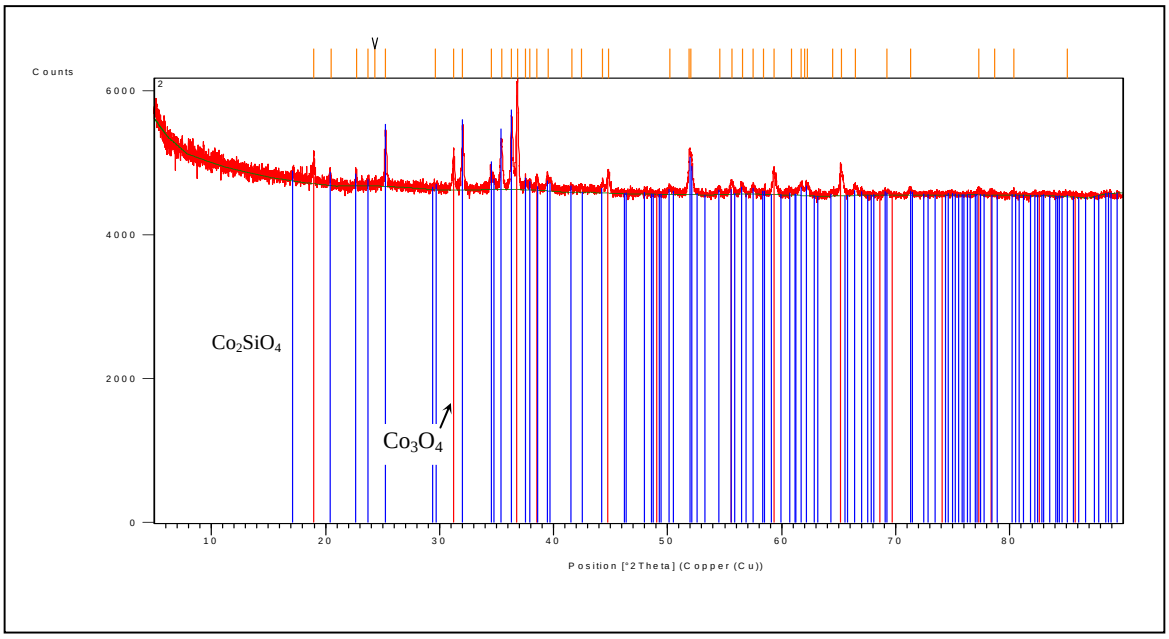

Figure A49. XRD pattern of Co_3O_4/SiO_2

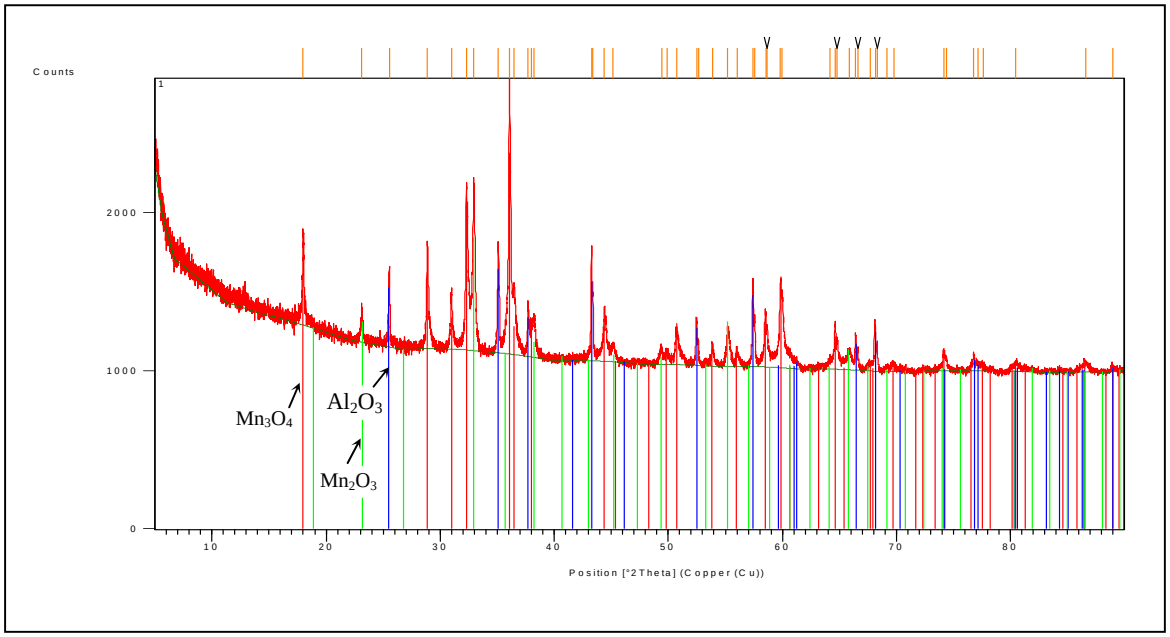

Figure A50. XRD pattern of Mn_2O_3/ Al_2O_3

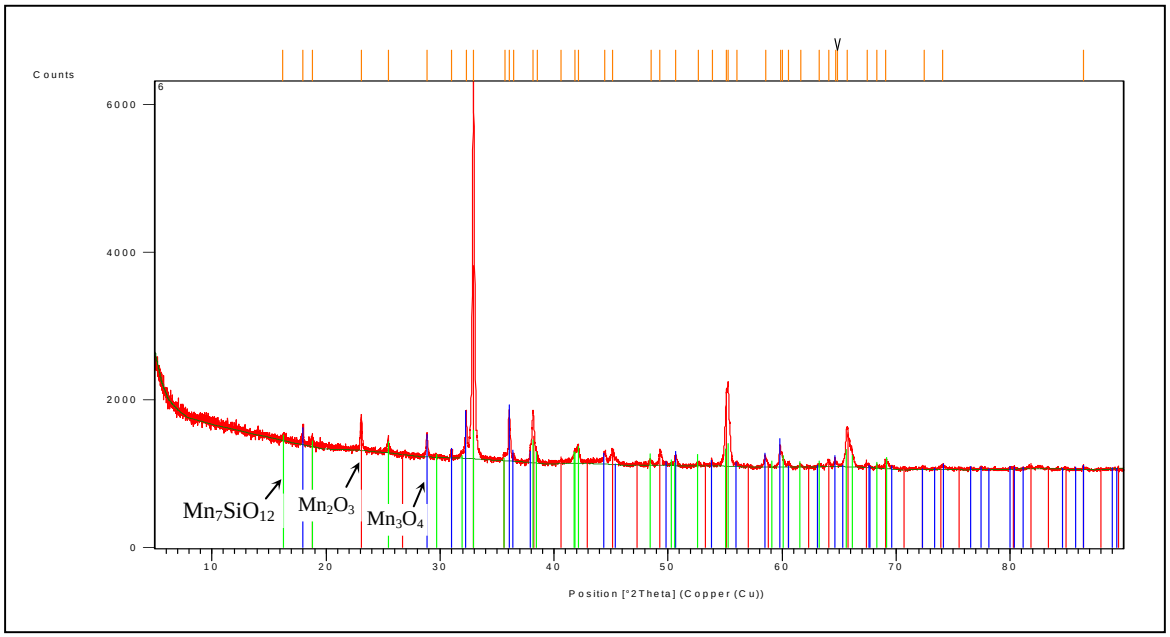

Figure A51. XRD pattern of Mn_2O_3/ SiO_2

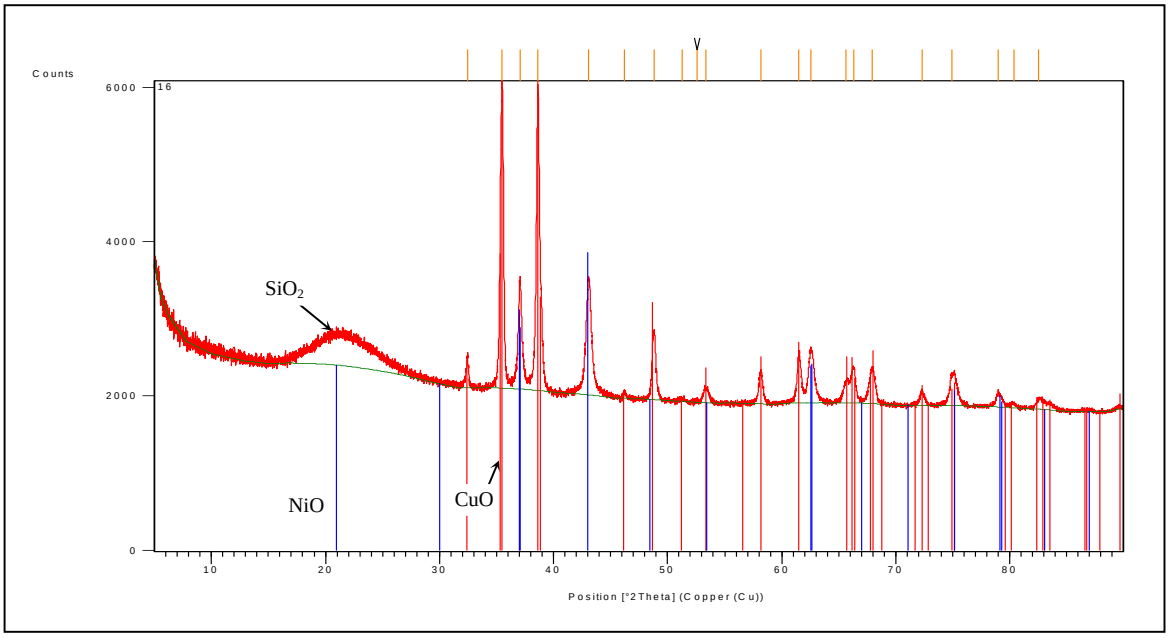

Figure A52. XRD pattern of CuO-NiO-9-1 / SiO_2

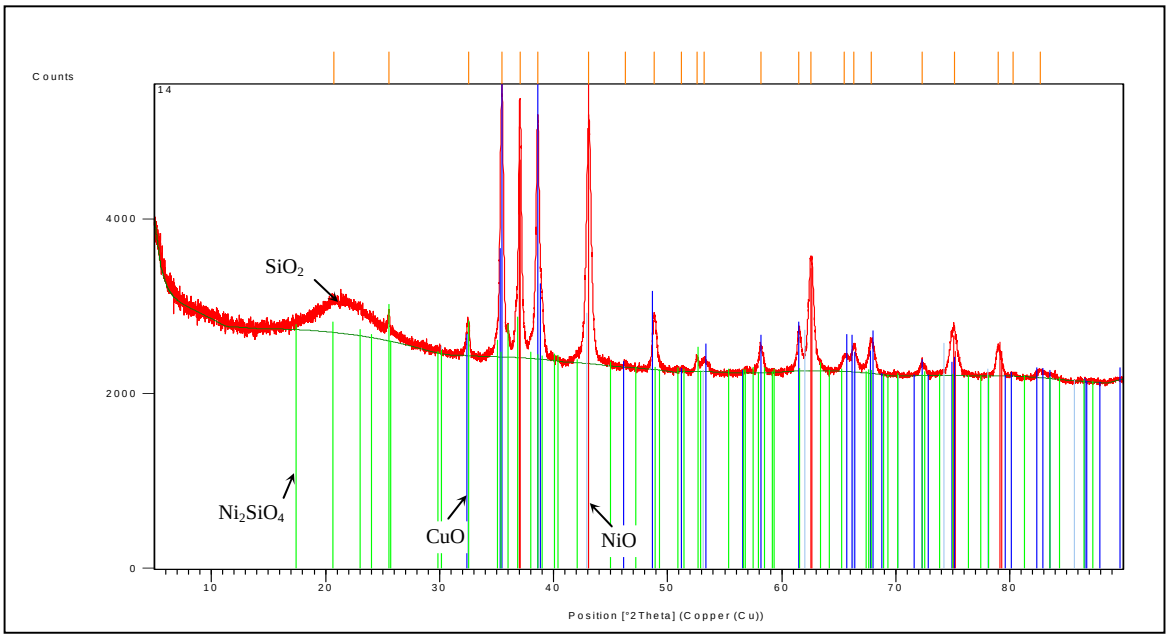

Figure A53. XRD pattern of CuO-NiO-4-1 / SiO_2

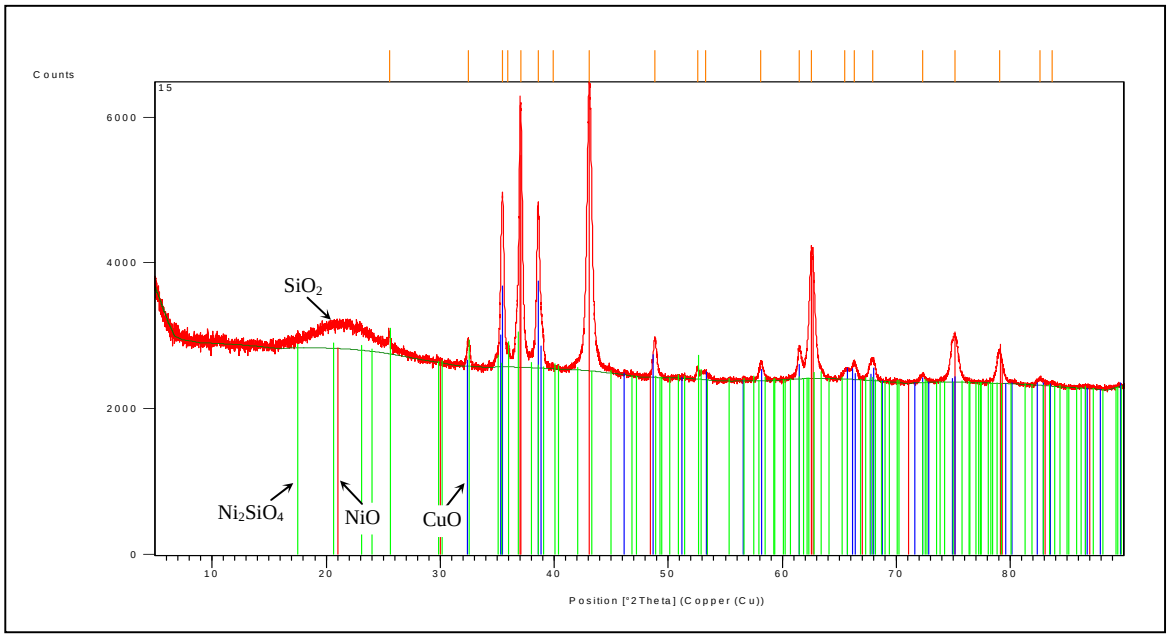

Figure A54. XRD pattern of CuO-NiO-7-3 / SiO_2

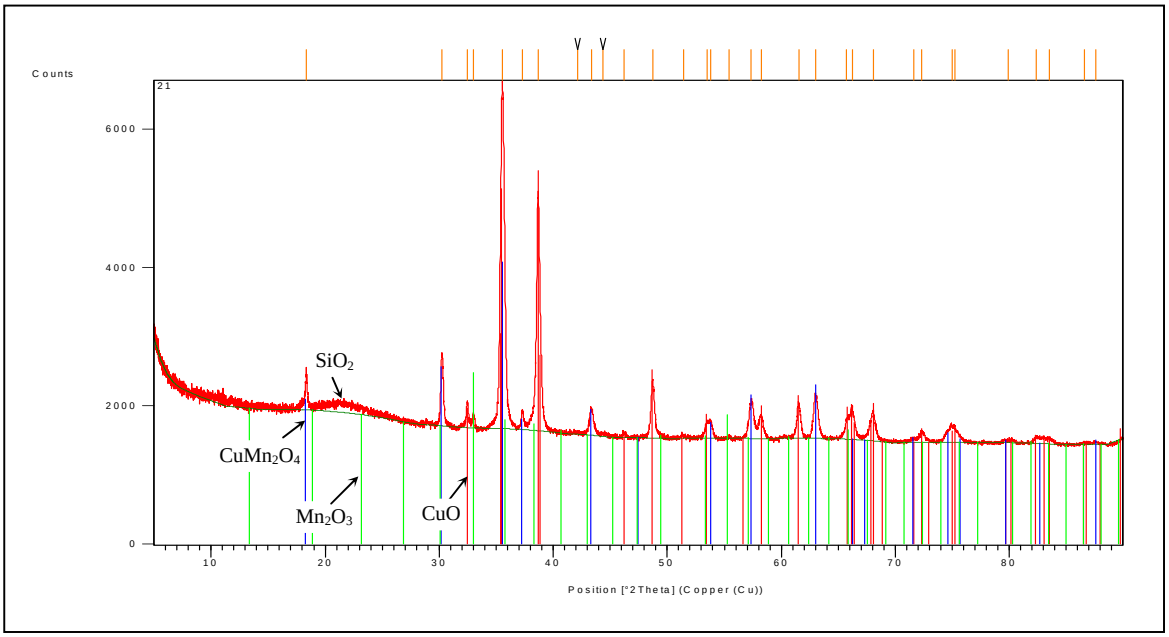

Figure A55. XRD pattern of CuO-Mn_2O_3-4-1 / SiO_2

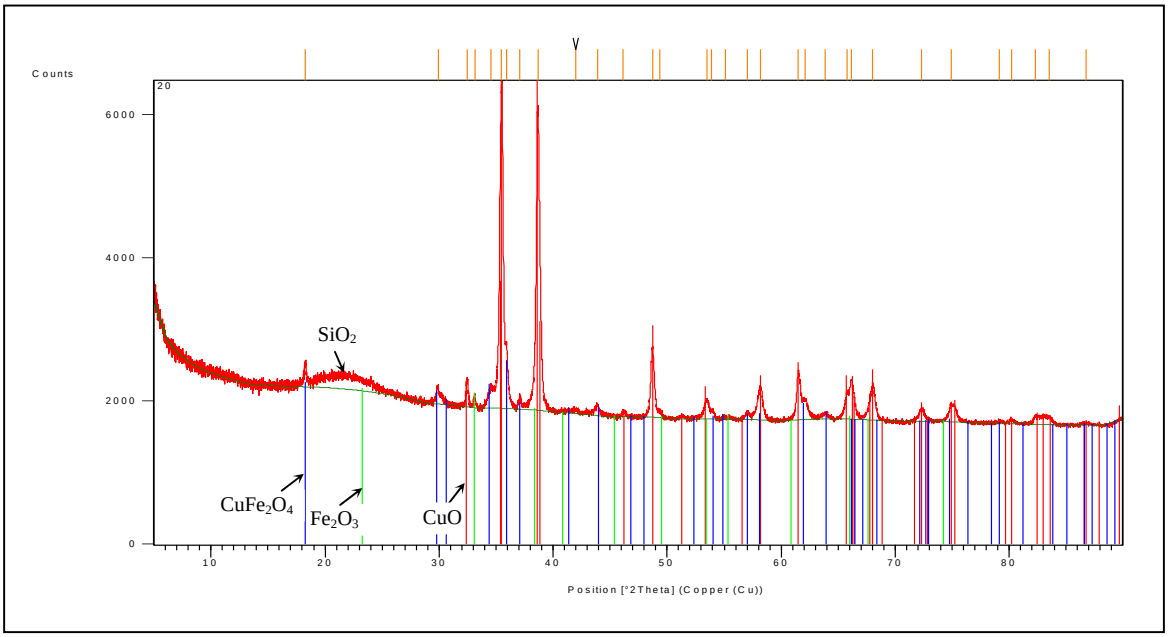

Figure A56. XRD pattern of CuO-Fe_2O_3-4-1 / SiO_2

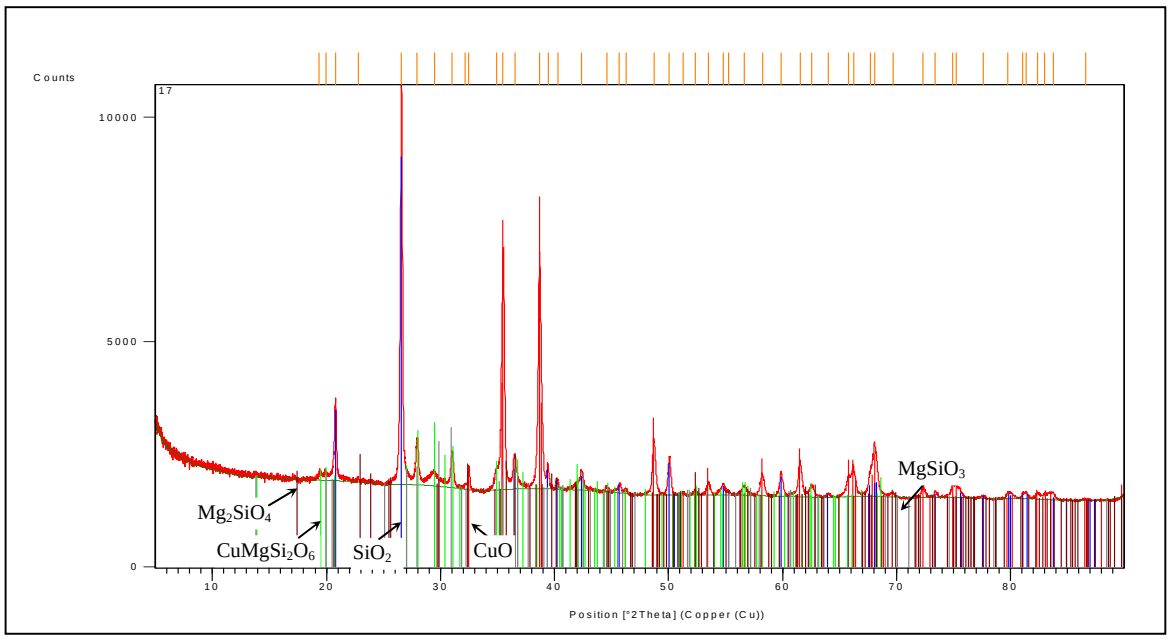

Figure A57. XRD pattern of CuO-MgO-9-1 / SiO_2

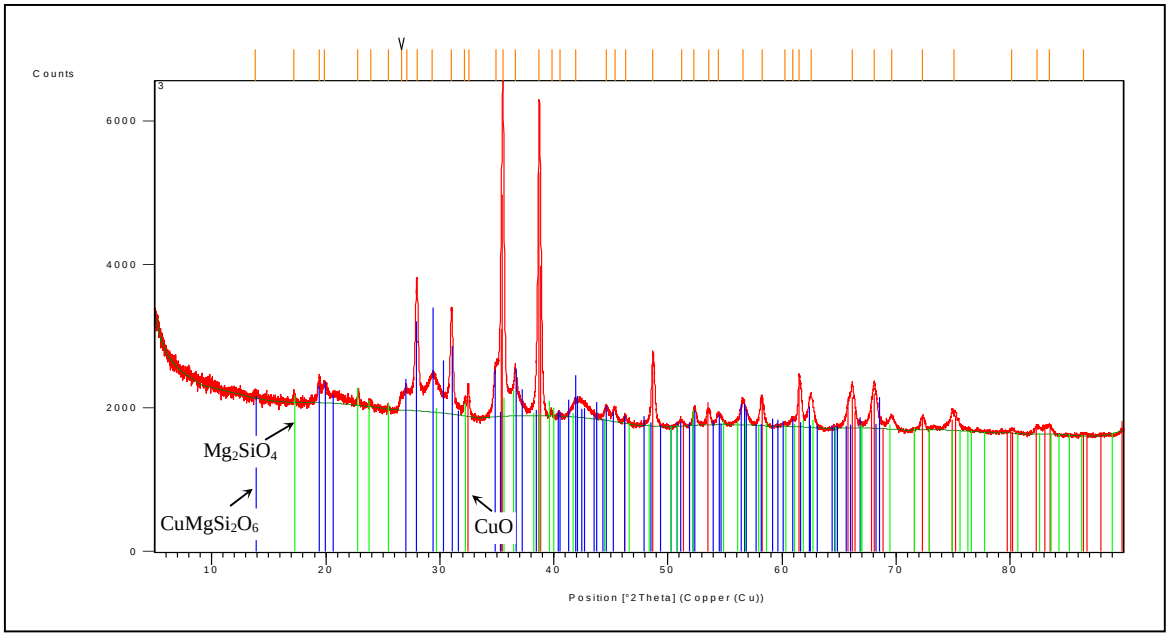

Figure A58. XRD pattern of CuO-MgO-4-1 / SiO_2

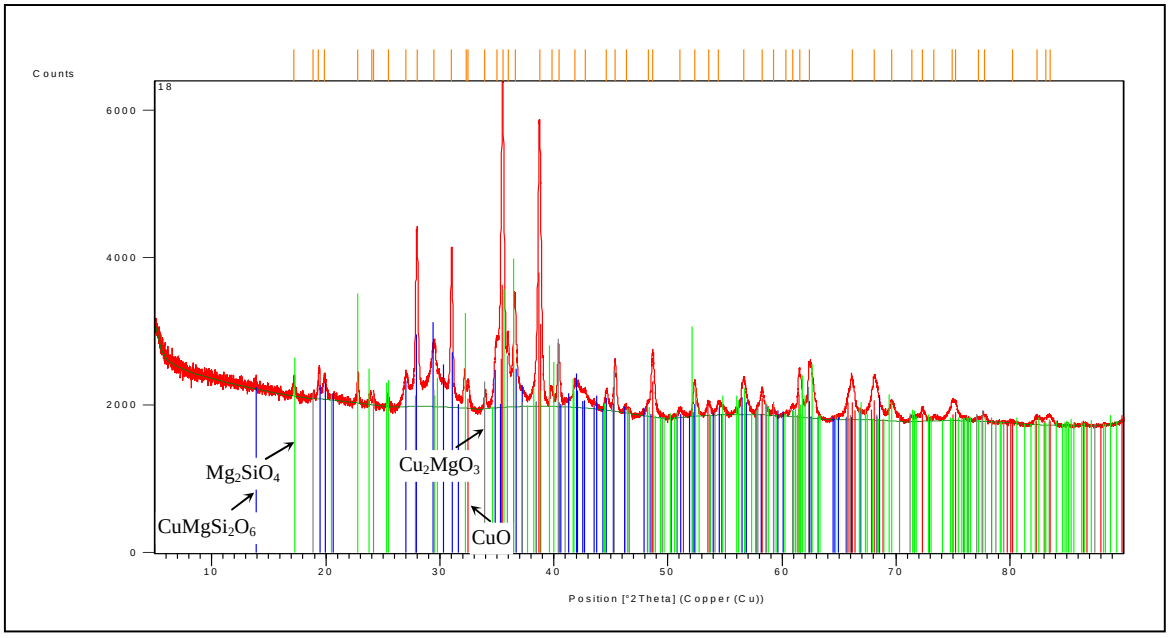

Figure A59. XRD pattern of CuO-MgO-7-3 / SiO_2

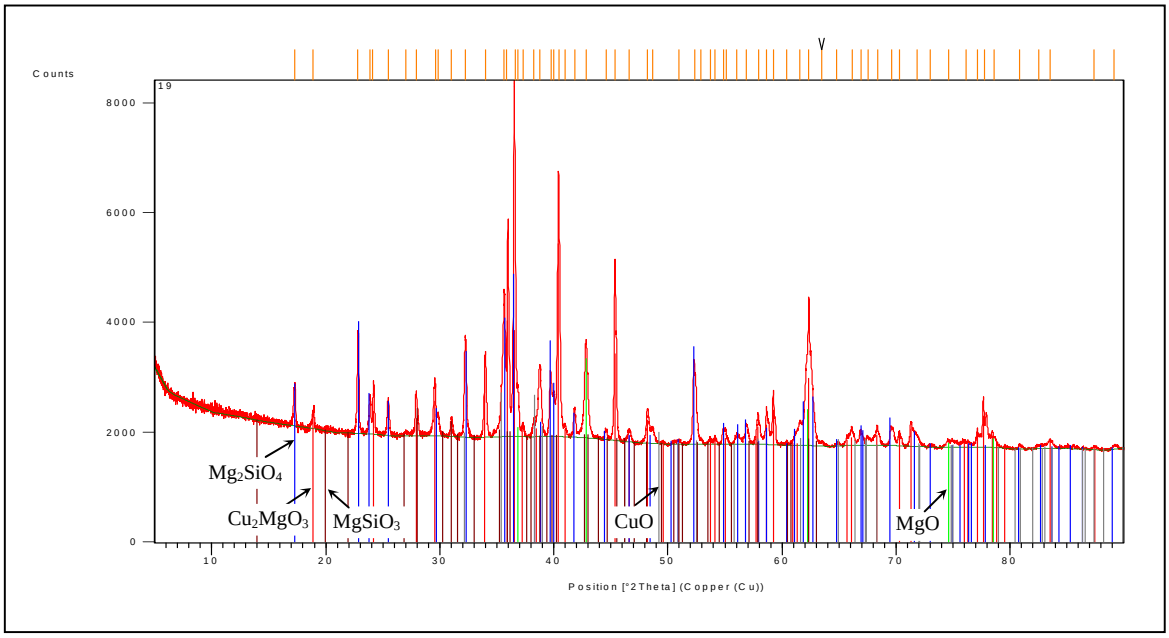

Figure A60. XRD pattern of CuO-MgO-1-1 / SiO_2

APPENDIX B: BIMETALLIC Cu-BASED RESULTS

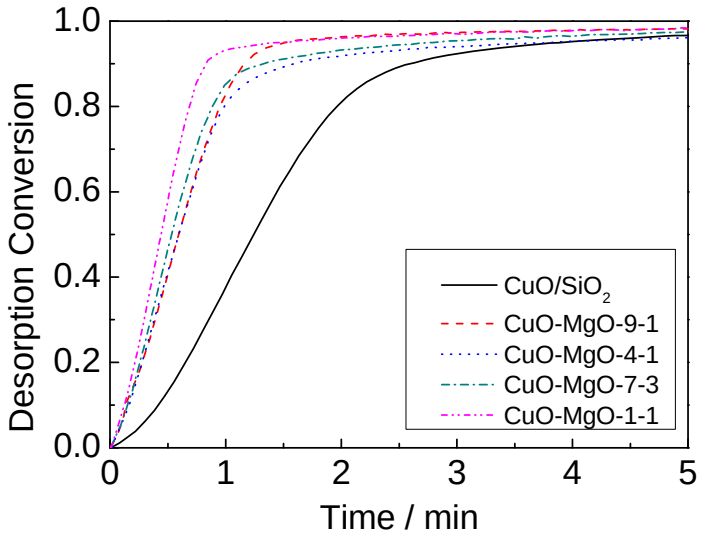

Figure B1: The effect of adding MgO and its weight ratio on oxygen desorption conversion of CuO/SiO_2 at 900°C.

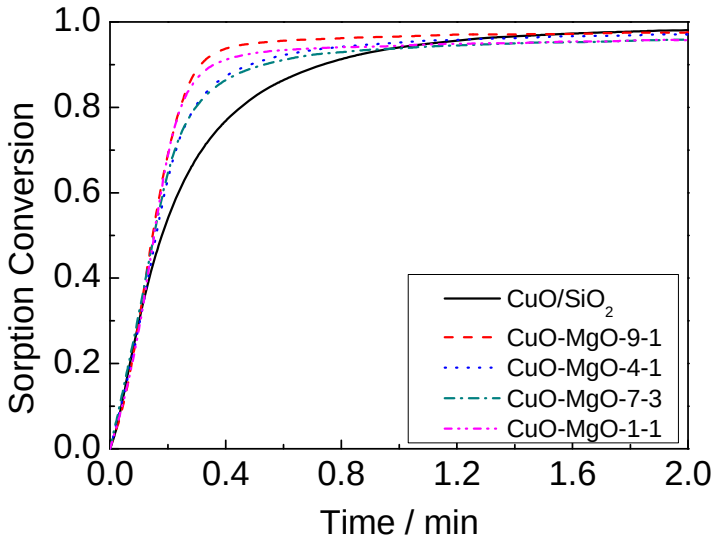

Figure B2: The effect of adding MgO and its weight ratio on oxygen sorption conversion of CuO/SiO_2 at 900°C.

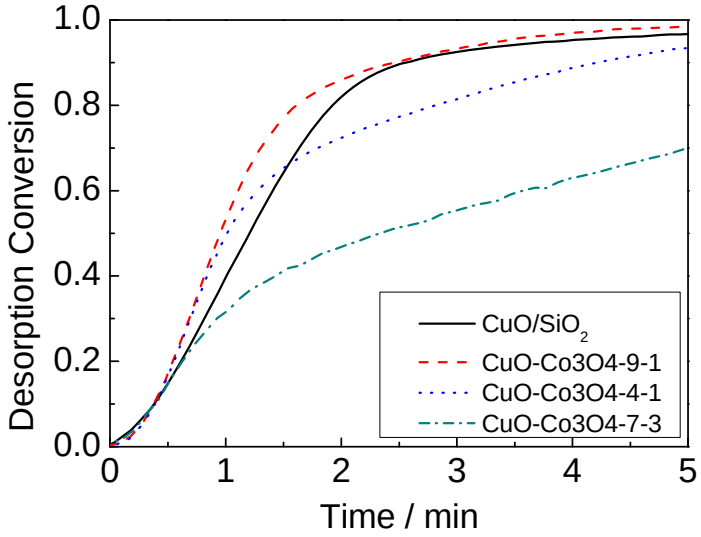

Figure B3: The effect of adding Co_3O_4 and its weight ratio on oxygen desorption conversion of CuO/SiO_2 at 900°C.

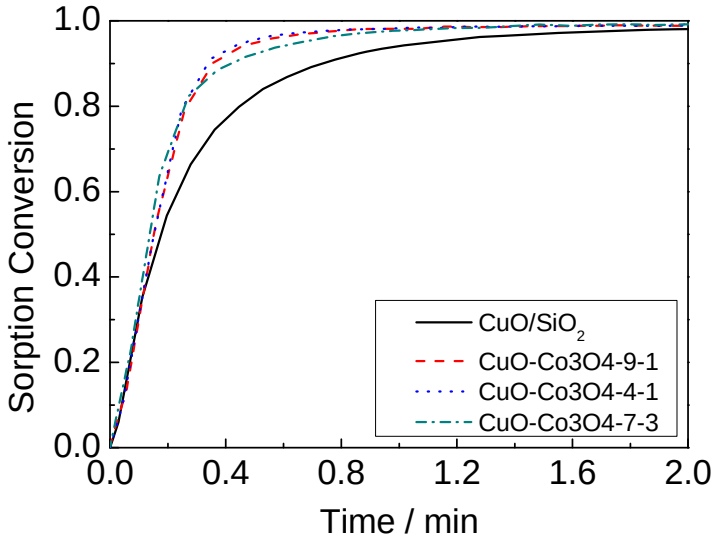

Figure B4: The effect of adding Co_3O_4 and its weight ratio on oxygen sorption conversion of CuO/SiO_2 at 900°C.

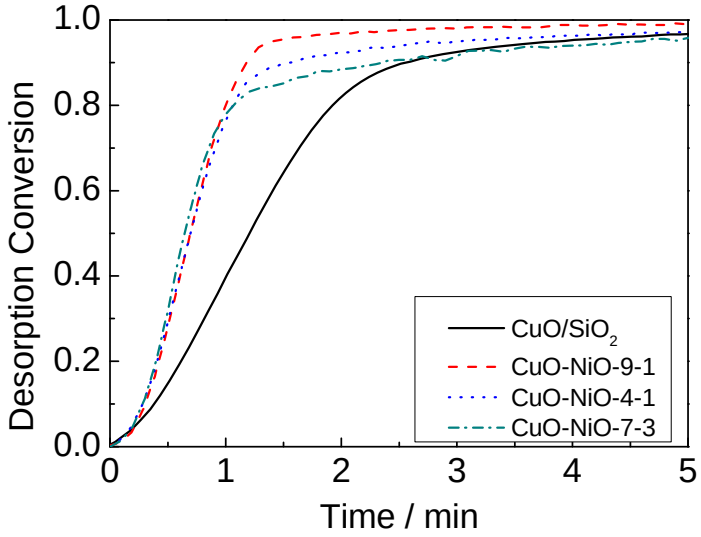

Figure B5: The effect of adding NiO and its weight ratio on oxygen desorption conversion of CuO/SiO_2 at 900°C.

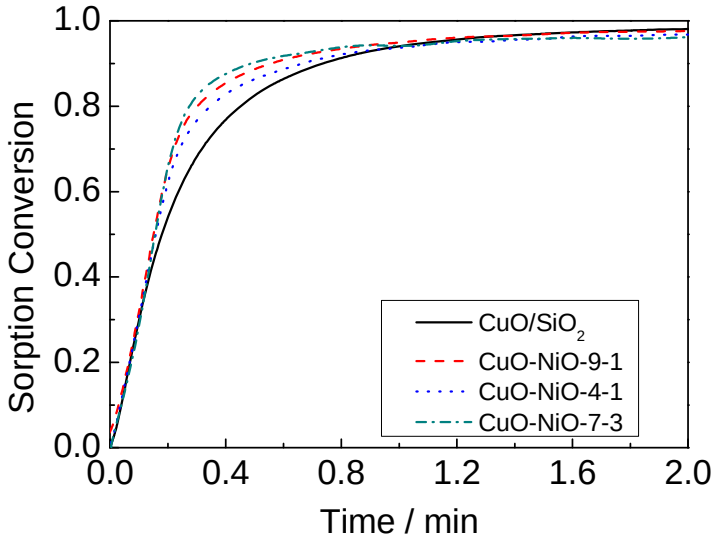

Figure B6: The effect of adding NiO and its weight ratio on oxygen sorption conversion of CuO/SiO_2 at 900°C.

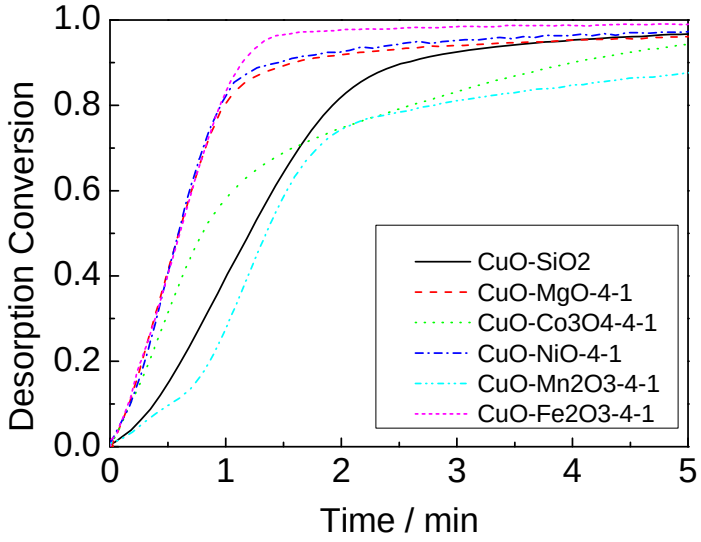

Figure B7: The effect of adding different metal oxides at 25 wt. % on oxygen desorption conversion of CuO/SiO_2 at 900^{o}C.

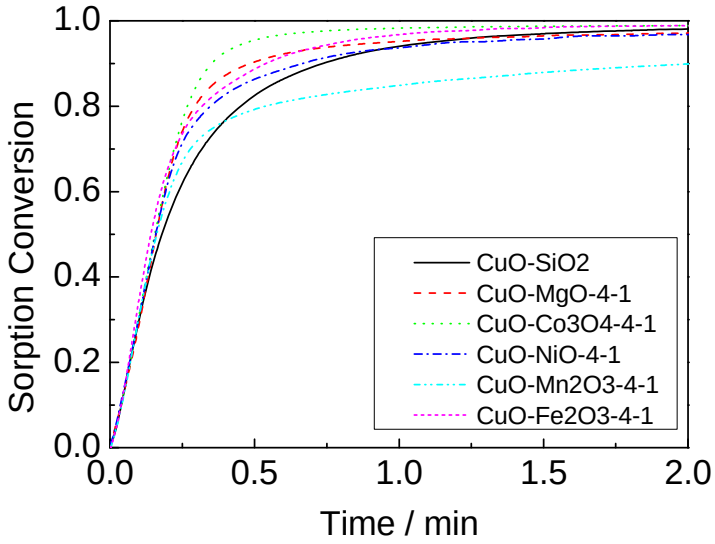

Figure B8: The effect of adding different metal oxides at 25 wt. % on oxygen sorption conversion of CuO/SiO_2 at 900^{o}C.

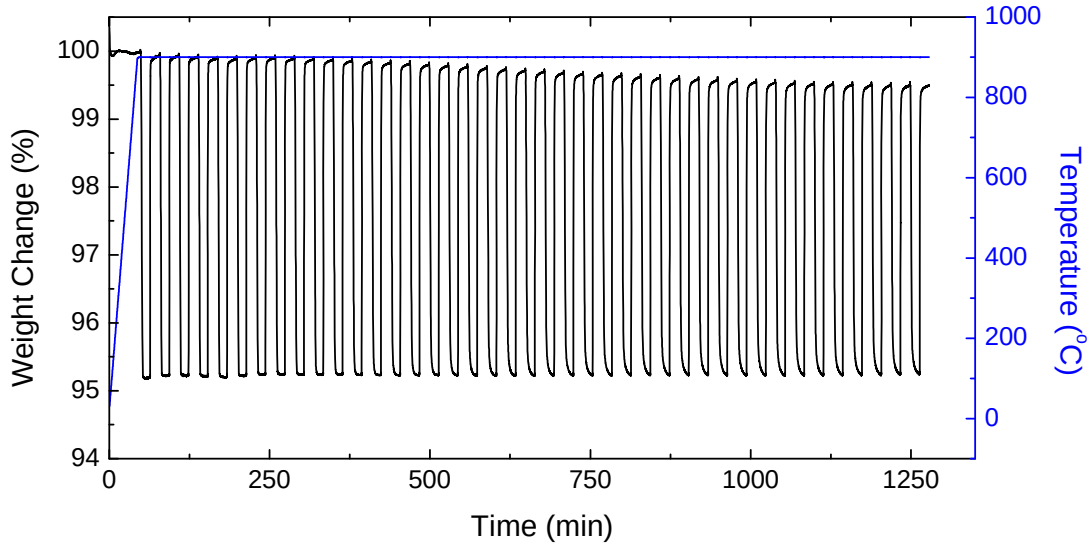

Figure B9: Weight change of 60 wt.%CuO/40 wt.%SiO_2 during 41 continuous oxygen desorption-sorption cycles in TGA at 900°C. Desorption time = 15min; Sorption time = 15min.

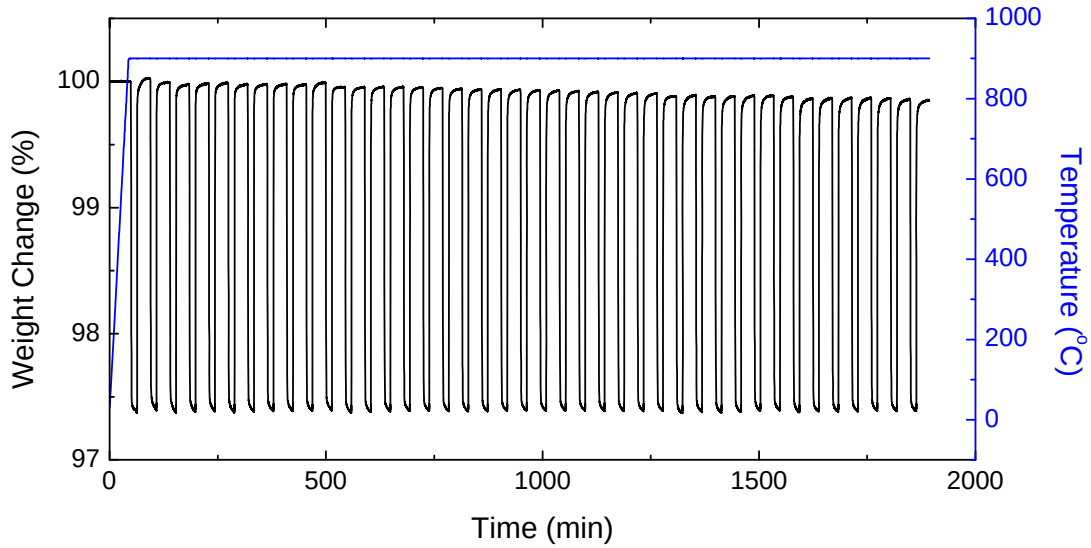

Figure B10: Weight change of CuO-MgO-9-1/SiO_2 during 41 continuous oxygen desorption-sorption cycles in TGA at 900°C. Desorption time = 15min; Sorption time = 30min.

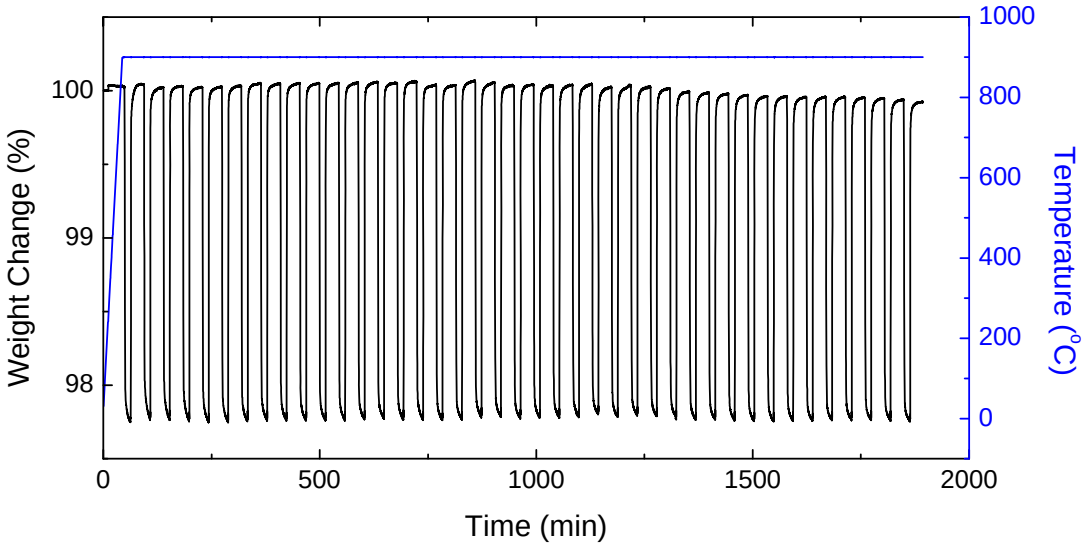

Figure B11: Weight change of CuO-MgO-4-1/SiO_2 during 41 continuous oxygen desorption-sorption cycles in TGA at 900°C. Desorption time = 15min; Sorption time = 30min.

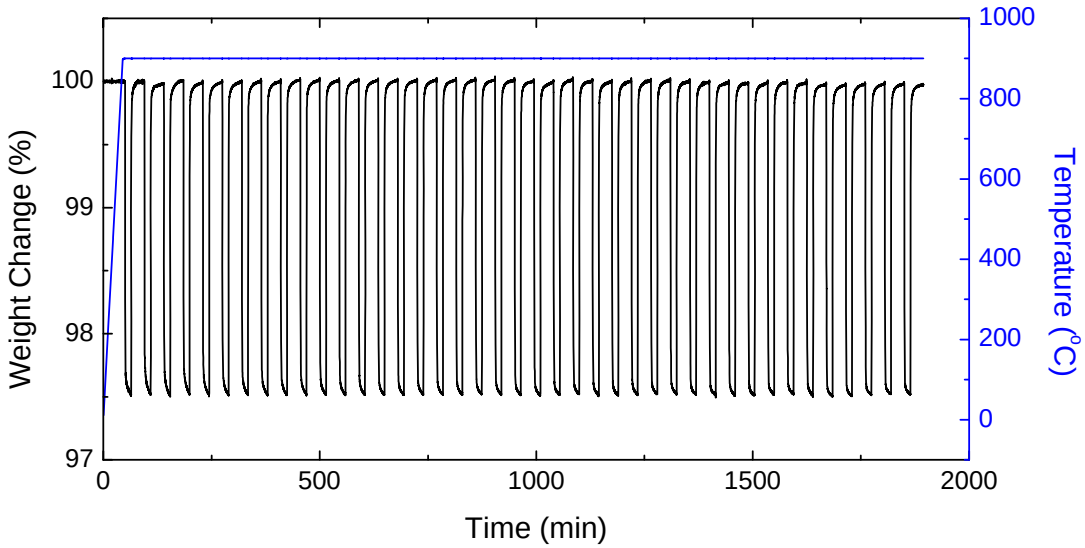

Figure B12: Weight change of CuO-MgO-7-3/SiO_2 during 41 continuous oxygen desorption-sorption cycles in TGA at 900°C. Desorption time = 15min; Sorption time = 30min.

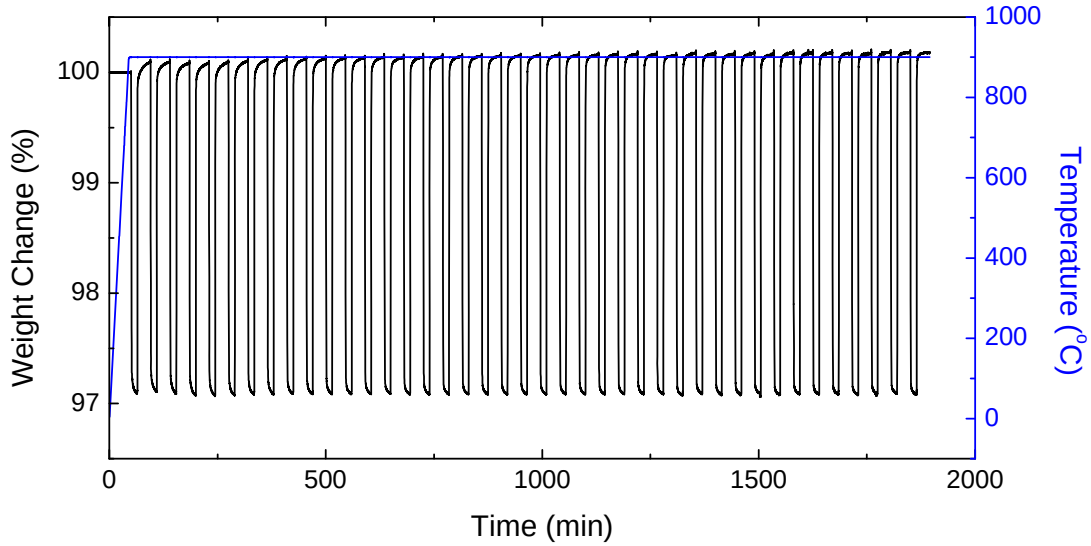

Figure B13: Weight change of CuO-MgO-1-1/SiO_2 during 41 continuous oxygen desorption-sorption cycles in TGA at 900°C. Desorption time = 15min; Sorption time = 30min.

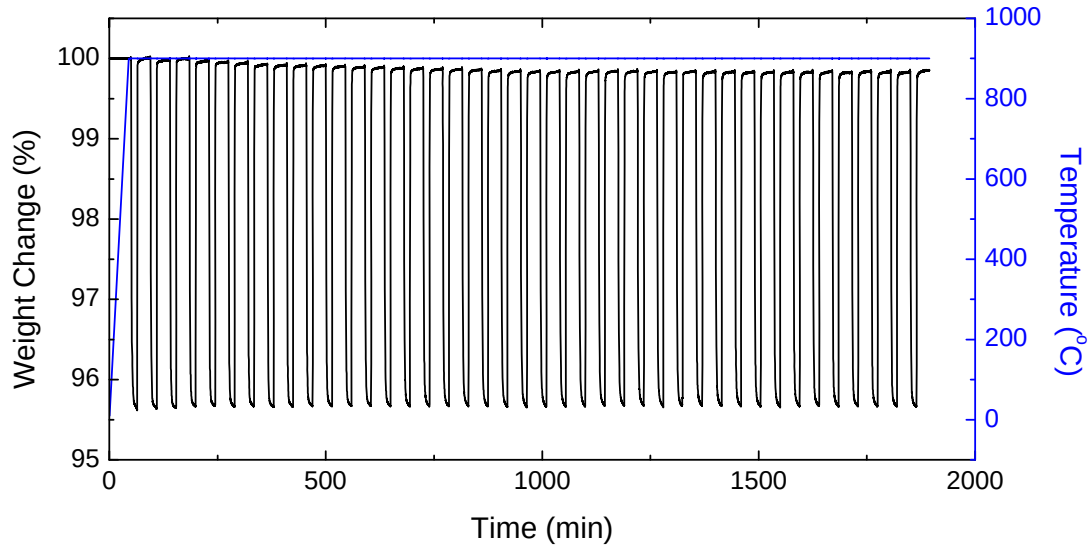

Figure B14: Weight change of CuO-Co_3O_4-9-1/SiO_2 during 41 continuous oxygen desorption-sorption cycles in TGA at 900°C. Desorption time = 15min; Sorption time = 30min.

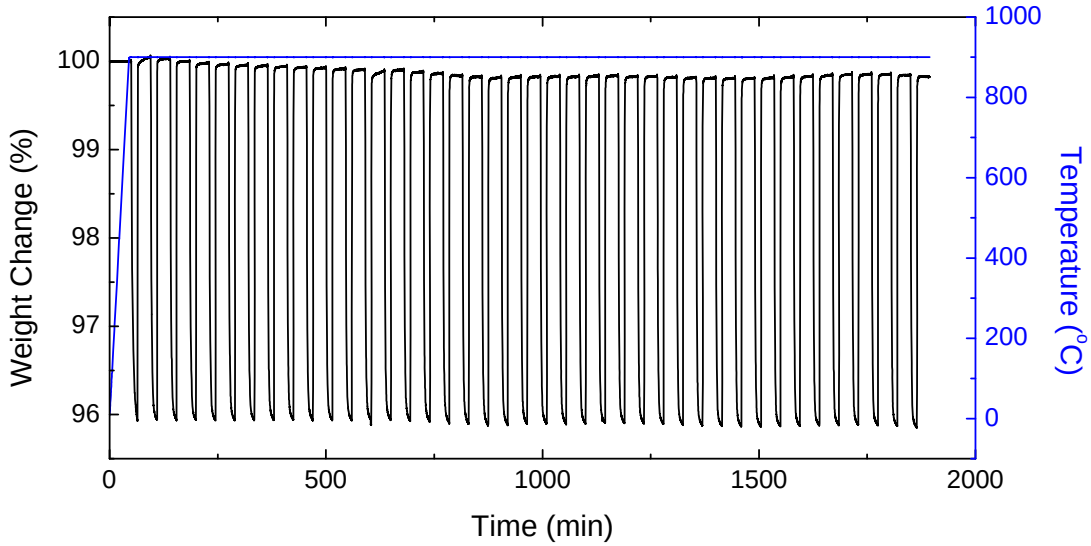

Figure B15: Weight change of CuO-Co_3O_4-4-1/SiO_2 during 41 continuous oxygen desorption-sorption cycles in TGA at 900°C. Desorption time = 15min; Sorption time = 30min.

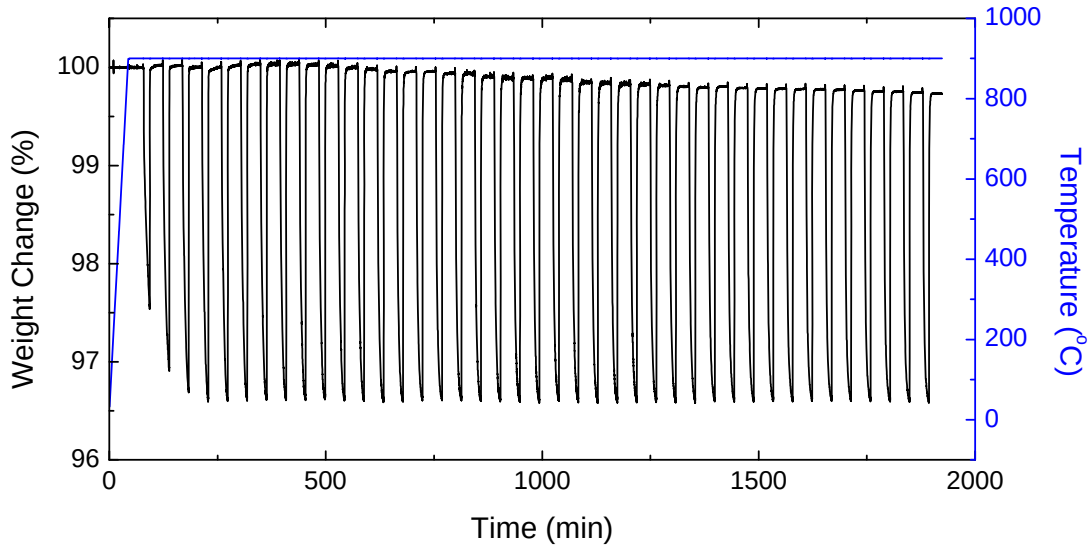

Figure B16: Weight change of CuO-Co_3O_4-7-3/SiO_2 during 41 continuous oxygen desorption-sorption cycles in TGA at 900°C. Desorption time = 15min; Sorption time = 30min.

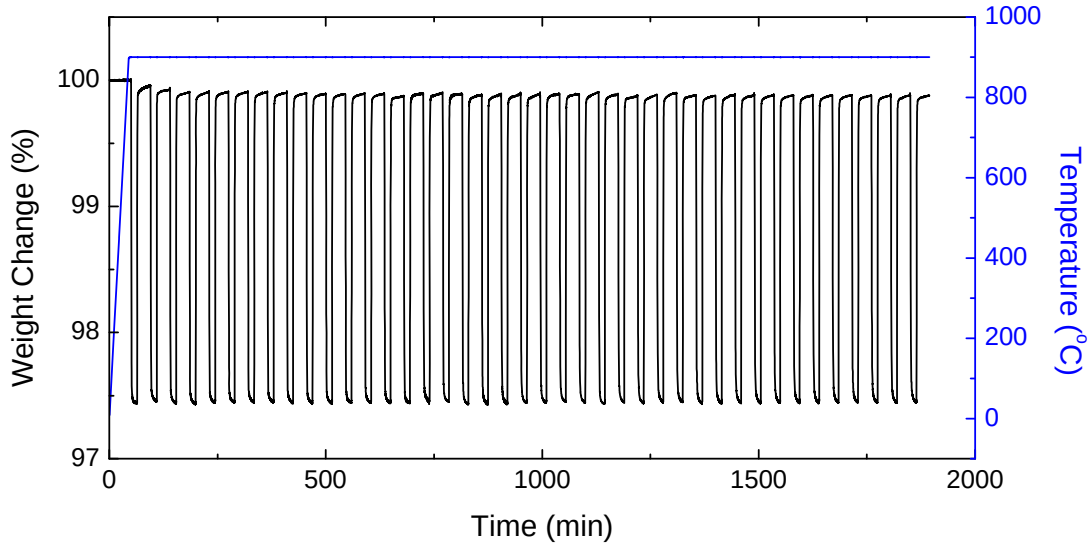

Figure B17: Weight change of CuO-NiO-9-1/SiO_2 during 41 continuous oxygen desorption-sorption cycles in TGA at 900°C. Desorption time = 15min; Sorption time = 30min.

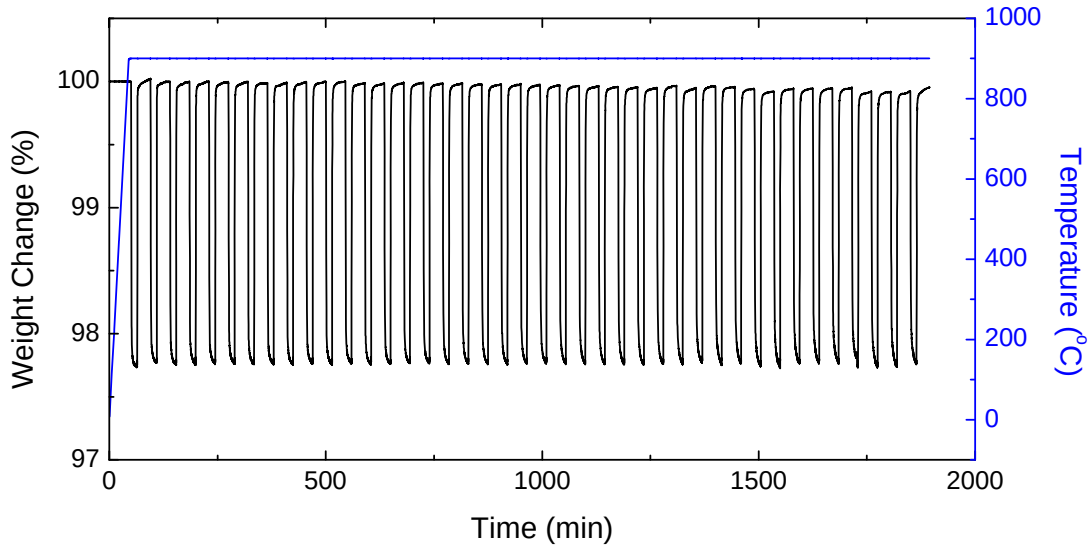

Figure B18: Weight change of CuO-NiO-4-1/SiO_2 during 41 continuous oxygen desorption-sorption cycles in TGA at 900°C. Desorption time = 15min; Sorption time = 30min.

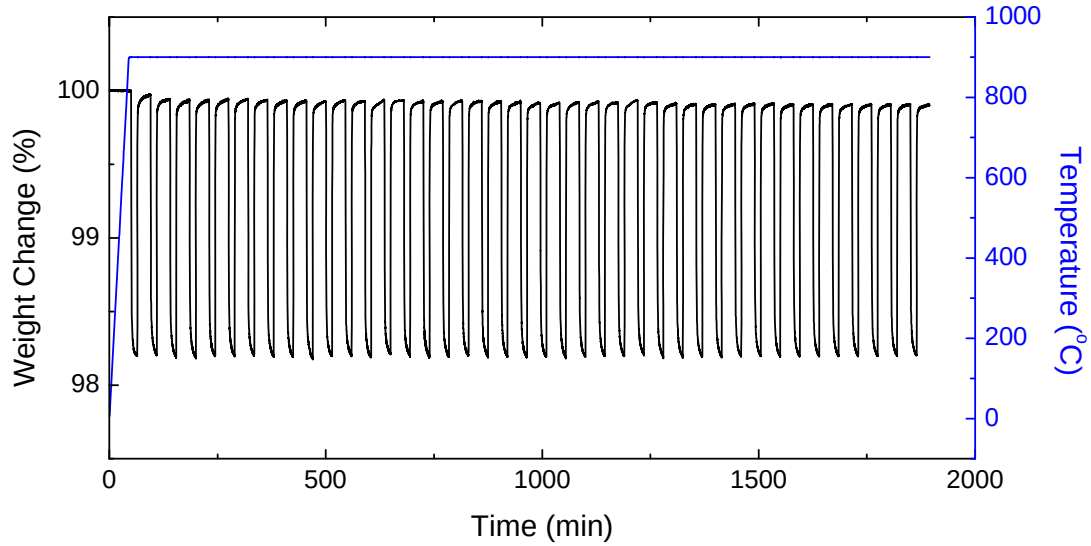

Figure B19: Weight change of CuO-NiO-7-3/SiO_2 during 41 continuous oxygen desorption-sorption cycles in TGA at 900°C. Desorption time = 15min; Sorption time = 30min.

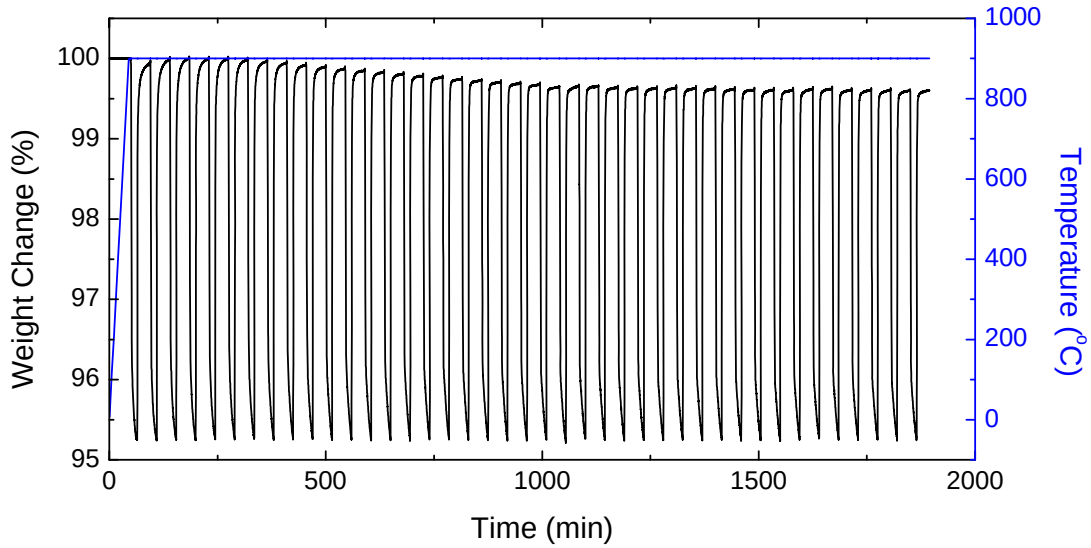

Figure B20: Weight change of CuO-Mn_2O_3-4-1/SiO_2 during 41 continuous oxygen desorption-sorption cycles in TGA at 900°C. Desorption time = 15min; Sorption time = 30min.

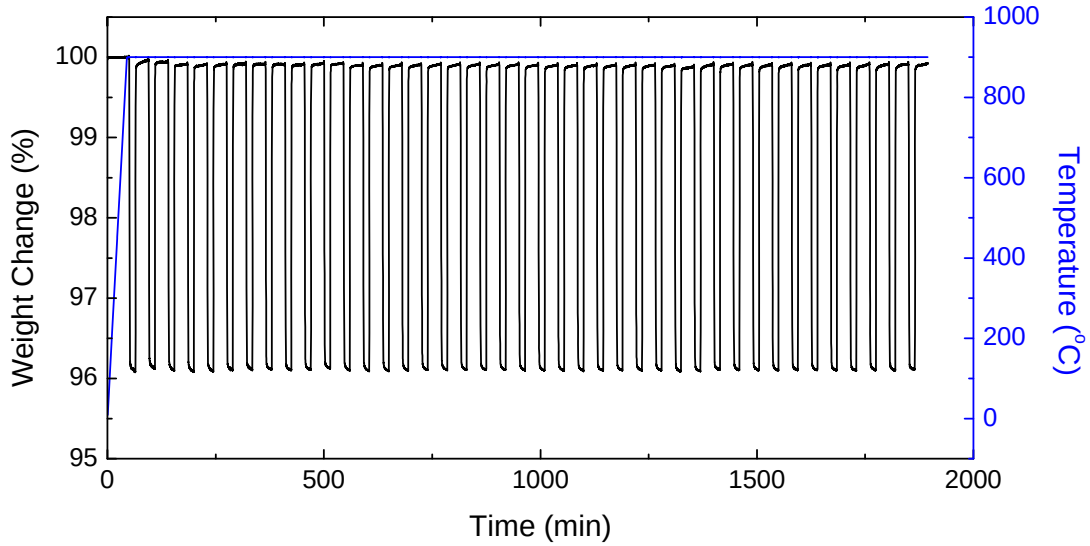

Figure B21: Weight change of CuO-Fe_2O_3-4-1/SiO_2 during 41 continuous oxygen desorption-sorption cycles in TGA at 900°C. Desorption time = 15min; Sorption time = 30min.

APPENDIX C: LCA CALCULATIONS

AIR SEPARATION UNIT SIZING

Oxygen demand

528,000 $Sm^3 O_2/h$

Power requirements of Oxygen production

Lower	0.34	$kW/h/Sm^3$	Cryogenic distillation
Upper	0.36	$kW/h/Sm^3$	Cryogenic distillation
	0.15	$kW/h/Sm^3$	ICLAS

Oxygen carrier (CuO/SiO_2)

0.33 kg CuO/SiO_2 (30:70) per 1Sm3 of $O_{2/h}$

Total Oxygen carrier required

174,240 kg

Power requirements

83368	kW/Sm^3	Allowing for additional production required due to 95% oxygen purity (see references and assumptions this page)
83	MW/Sm^3	

Oxygen carrier recharge (CuO/SiO_2)

Assume 20% every 3 months

3	months
20%	recharge
34,848	kg
139,392	kg p.a.

30%	CuO fraction
70%	SiO2 fraction

	Initial charge	recharge p.a.	recharge over lifetime	
CuO fraction	52,272	41,818	836,352	kg
SiO2 fraction	121,968	97,574	1,951,488	kg

The final power consumption of the Cyrogenic Distillation ASU with the above features becomes 181 MWe (Andersson & Johnsson 2005). Upper and lower boundary limits :

Power requirements of O2 production

179520	kW/Sm^3	For oxygen demand
190080	kW/Sm^3	For oxygen demand

Average	184800	kW/Sm^3
	184.8	MW/Sm^3

These calculations show that it is none of the above (upper/lower/average) that produce the exact ASU electricity demand. Therefore a weighted basis, so I will just pro rata energy requirements stated in paper (181MWe for the ASU).

Spray drying energy requirement

Assume energy and feed rate of example from "APV_Spray Dryer.pdf". This could vary substantially based on form and moisture content

Feed rate

40,090	kg/h
19,930	kW

Initial charge	recharge p.a.		
4.3	3.5	hrs	
86,620	69,296	kWh	
311.83	249.47	GJ	
12.13	9.71	kL	(Assuming worst case LPG - where Natural gas is not available, energy content in factors tab)

SIMULATING POWER STATION DETAILS

Based on the energy flow sankey diagram from Andersson & Johnsson (2006)

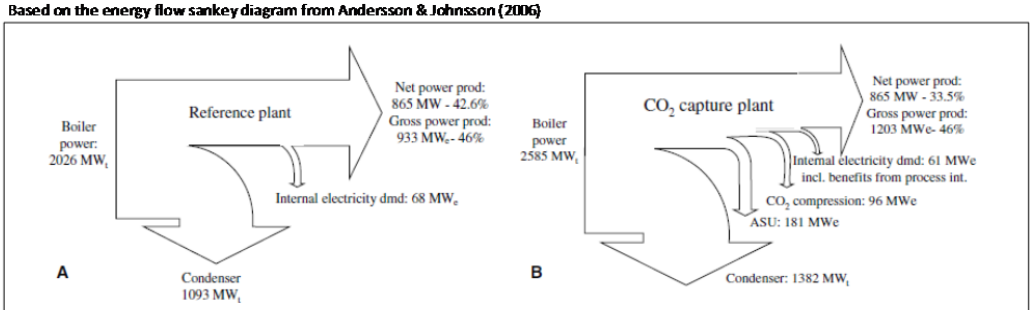

Fig. 4. Sankey diagrams of the reference power plant (A) and the CO_2 capture plant (B). The capture plant has the same power output as the reference power plant, scaled according to Eq. (1).

Setting up base case Andersson & Johnsson (2006) parameters

		Comment
865	MW_e	Net Power production
2	Generation units	Lippendorf type
2000	Commission year	
933	MW_e	Gross electricity output
2026	MW	Boiler power (2030 originally stated)
42.7%	Electricity net efficiency	
Raw lignite	Fuel	
677	kg/s	Stream flow
554/258.5	°C/bar	High pressure steam
583/49.7	°C/bar	intermediate pressure steam
0.038	bar	steam pressure at condenser discharge
	Standard reactor	
46%	efficiency	calculated
68	MW_e	Internal demand (61 with feedwater pre-heating from flue gas)
1093	MW_t	Condenser
2.0	GJ/s	feed requirement
193.0	kg/s	192.9524 0.083272 tonne/second
0.0105	GJ/kg	European lignite
10.5	MJ/kg	European lignite
8.99	MJ/kg	Australian lignite
24.33	MJ/kg or GJ/tonn	Australian black coal

No feedwater pre-heating from flue gas

	CD Oxy-fuel (without CO_2 capture)	
46%	gross efficiency	kept constant
865	MW_e	Net Power production (constant)
249	MW_e	Internal demand+ASU
2419.04	MW_t	Adjusted boiler power
1305.04	MW_t	Condenser

Power demand of oxy fuel with ICLAS

181	MW_e	CD hourly basis
83	MW_e	ICLAS hourly basis

Andersson & Johnsson 2006 (Table 2)

Proximate analysis [kg/kg] and fuel flow [kg/s] of the lignite

	Guarantee	Max wate	Max ash
Hi [MJ/kg]	10.5	9.7	9.7
C	0.2911	0.2917	0.2718
H	0.0247	0.0248	0.0231
O	0.0819	0.0821	0.0765
N	0.003	0.003	0.0028
S	0.0143	0.0143	0.0136
Cl	0.0001	0.0001	0.0001
F	0.00005	0.00005	0.00005
Ash	0.065	0.0541	0.085
Moisture	0.52	0.53	0.5276
Fuel flow	192.6	223.7	223.7

Andersson & Johnsson 2006 (Table 3)

Components	[kg/s]	[wt%]	[m3n/s]	[vol%]
H2O	176.4	38.4	222.3	60.4
CO2	253.9	55.3	130.2	35.4
SO2	6.7	1.5	2.3	0.6
O2	6.4	1.4	4.6	1.2
N2	0.6	0.2	0.5	0.2
Ar	14.6	3.2	8.3	2.2
Total	458.7	100	365.9	100

Design composition of the flue gas during O2/CO2 combustion

Andersson & Johnsson 2006 (Table 4)

	Reference plant			Oxy-fuel		
Emissions to air	mg/m3n	kg/h	kg/Mwhe	mg/m3n	kg/h	kg/Mwhe
SOx	<350	<1120	1.28	<6	<13	0.015
NOx	<145	<460	0.53	<141	<190	0.22
CO2	<235	<740,000	855.2	<4	<5000	5.8
Dust	<2	<6	0.007	<1	<1	0.001

From Table 3.1 (Australian Coal Characteristics) 2010 EPRI report

	Black Coal	Lignite	
Upper	24.82	9.92	MJ/kg
Lower	23.84	8.06	MJ/kg

No feedwater pre-heating from flue gas

	ICLAS Oxy-fuel (without CO_2 capture)	
46%	gross efficiency	kept constant
865	MW_e	Net Power production (constant)
151.3684	MW_e	Internal demand+ASU
2207.034	MW_t	Adjusted boiler power
1190.665	MW_t	Condenser

Including feedwater pre-heating from flue gas

1*

	CD Oxy-fuel (without CO_2 capture)	
46%	gross efficiency	kept constant
865	MW_e	Net Power production (constant)
242	MW_e	Internal demand+ASU (61MWe from Andersson & Johnsson, 2006)
2403.839	MW_t	Adjusted boiler power
1296.839	MW_t	Condenser

Including feedwater pre-heating from flue gas

2*

	ICLAS Oxy-fuel (without CO_2 capture)	
46%	gross efficiency	kept constant
865	MW_e	Net Power production (constant)
144.3684	MW_e	Internal demand+ASU (61MWe from Andersson & Johnsson, 2006)
2191.833	MW_t	Adjusted boiler power
1182.465	MW_t	Condenser

*The above scenarios are used in the feed scenarios, and for calculating the power station materials

Table 3-1
Australian Coal Characteristics

	Black Coal (Hunter Valley)	Brown Coal (Latrobe Valley)
Coal Composition		
Moisture	7.50	61.50
Carbon	60.18	26.31
Hydrogen	3.78	1.85
Nitrogen	1.28	0.23
Chlorine	0.00	0.00
Sulfur	0.43	0.15
Oxygen	5.63	9.16
Ash	21.20	0.80
Ash Mineral Analysis	N/A	N/A
Heating Value (as received)		
Higher MJ/kg (Btu/lb)	24.82 (10,679)	9.92 (4,269)
Lower MJ/kg (Btu/lb)	23.84 (10,257)	8.06 (3,466)

COAL FEED SCENARIOS

From Andersson & Johnsson 2006

- Each of the power plants has auxiliary components such as coal feeder, pulveriser, blower, pumps, cooling tower, ESP/FF etc. The internal electricity demand of 68 MWe is from such auxiliary equipment (ED: 61MWe where feedwater preheating with flue gas is undertaken). Though this depends on the design and manufacturing company, auxiliary power consumption is considered to
- CO2 capture plant costs include flue gas cleaning, CO2 compression and liquefaction in cold box. It is generally considered between 10-30% of the generated output.
- The recycling of flue gas is mainly to control the adiabatic flame temperature in the furnace which otherwise could reach to >2000 oC.

From Kalpit Shah

- Low sulphur coal can't reduce the auxiliary power demand of the power plant. The cost associated with flue gas cleaning in CO_2 circuit will be reduced for low sulphur coal somewhat, but not to a great extent. Therefore, I would use the same figures for the low sulphur Australian coal.

Assume: Australia with low sulphur coal does not reduce internal demand for FGD (taken to be 61 MW with flue gas integration)

1 *Including feedwater pre-heating from flue gas*

	CD Oxy-fuel (without CO_2 capture)	
46%	gross efficiency	kept constant
865	MW_e	Net Power production (constant)
242	MW_e	Internal demand+ASU
2404	MW_t	Adjusted boiler power
1297	MW_t	Condenser
2403.84	MJ/s	Feed requirement
267.39	kg/s	Australian lignite
98.80	kg/s	Australian black coal
411.20	kgs per MWh	Australian black coal
2.43	MWh per tonne	Australian black coal
2667639094	kg/yr	Australian black coal
2667639	t/yr	Australian black coal
2.67	Mt/yr	Australian black coal
53.35	Mt lifetime of plant	Australian black coal

2 *Including feedwater pre-heating from flue gas*

	ICLAS Oxy-fuel (without CO_2 capture)	
46%	gross efficiency	kept constant
865	MW_e	Net Power production (constant)
144	MW_e	Internal demand+ASU
2192	MW_t	Adjusted boiler power
1182	MW_t	Condenser
2192	MJ/s	Feed requirement
244	kg/s	Australian lignite
90	kg/s	Australian black coal
374.93	kgs per MWh	Australian black coal
2.67	MWh per tonne	Australian black coal
2432367354	kg/yr	Australian black coal
2,432,367	t/yr	Australian black coal
2.43	Mt/yr	Australian black coal
48.65	Mt lifetime of plant	Australian black coal

Assume plant availability from Andersson & Johnsson 2006

7500	7500 h/year
8760	all hours
85.62%	availability
20	Plant life (years)

ICLAS PROCESS SITE LOCATIONS

1. The centroid of power stations in NSW above 1000MWe, is in the National Park, therefore use a smaller number of largest power stations

Coal PS	Latitude	Longitude
1 Bayswater	-32.39605	150.94877
2 Eraring	-33.06223	151.52036
3 Liddell	-32.37086	150.97634
4 Mt Piper	-33.39339	149.9705
5 Munmorah	-33.21261	151.54215
6 Redbank	-32.58934	151.04617
7 Vales Point	-33.16055	151.54189
8 Wallerawang	-33.40268	150.08321

Drawing centroid

Bayswater	-32.39605	150.94877
Liddell	-32.37086	150.97634
Redbank	-32.58934	151.04617
Eraring	-33.06223	151.52036
Vales Point	-33.16055	151.54189
Munmorah	-33.21261	151.54215
Wallerawang	-33.40268	150.08321
Mt Piper	-33.39339	149.9705
Bayswater	-32.39605	150.94877

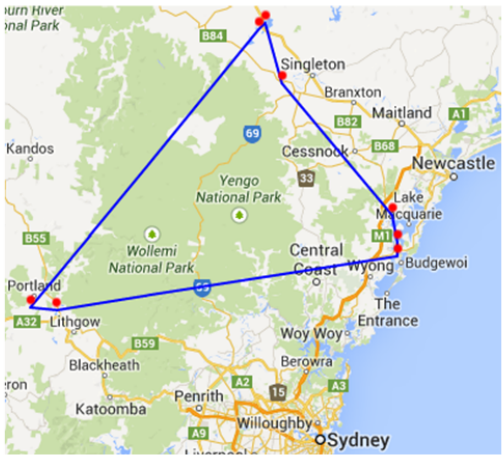

Power station	Location	Owner	Technology	Capacity
Appin Mine	Illawarra	EDL Group	CSM	56 MW
Bayswater	Hunter	Macquarie Generation	Steam/Coal	2720 MW
Blowering	Snowy	Snowy Hydro	Hydro	80 MW
Broadwater	North Coast	Delta Electricity	BaGasse	30 MW
Capital Wind Farm	Tarago	Renewable Power Ventures	Wind	141 MW
Condong	North Coast	Delta Electricity	BaGasse	30 MW
Colongra	Central Coast	Delta Electricity	OCGT	668 MW
Cullerin	Upper Lachlan	Origin Energy	Wind	30 MW
Eraring	Lower Hunter	Origin Energy	Steam/Coal	2880 MW
Gunning Wind Farm	Walwa	Acciona Energy	Wind	47 MW
Guthega	Snowy	Snowy Hydro	Hydro	60 MW
Liddell	Hunter	Macquarie Generation	Steam/Coal	2080 MW
Mount Piper	Central Coast	EnergyAustralia	Steam/Coal	1400 MW
Munmorah	North Coast	Delta Electricity	Steam/Coal	600 MW
Murray*	Snowy	Snowy Hydro	Hydro	1500 MW
Redbank	Hunter	Redbank Project	Coal Tailings	145 MW
Shoalhaven	Nowra	Origin Energy	Hydro	240 MW
Smithfield	Smithfield	Maruberi	Gas Cogen	160 MW
Tallawarra	Wollongong	TRUenergy	CCGT****	435 MW

2. Centroid of top 3 power stations by electrical production is heavily weighted to Hunter Valley. Assume adjacent to Bayswater and Liddell.

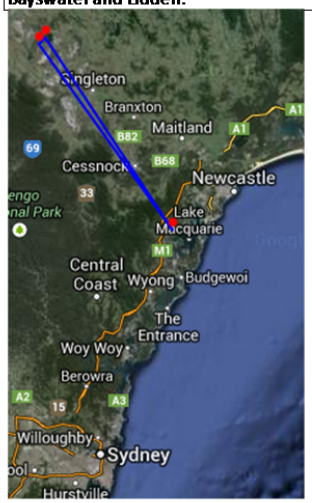

Liddell Station Road, Liddell, New South Wales

Checking zoning allowances for industrial zoning for oxygen carrier (metal substrate) production through spray drying

LOT 6 O'Hara
Pl
Mt Thorley
NSW 2330

-32.629687, 151.105493

S32° 37.7812', E151° 6.3296'

TRANSPORT CALCULATIONS

Coal Transport

	CD	ICLAS	
Total tonnes p.a.	2,667,639.09	2,432,367.35	**Assume Aust black coal**
Total tonnes lifetime	53,352,781.89	48,647,347.07	**Based on 20 year life**

Breakdown of Macquarie generation (Bayswater and Liddell) is supplied with the following breakdown:

Mac Gen total usage	13 **Mt/yr**		See references tab for sources of breakdown estimates
Wilpinjong	7-8 **Mt/yr**	58%	
Ravensworth	2-3 **Mt/yr**	19%	

The rest supplied by Mangoola and Mt Arthur (though no figures could be found).

		Therefore approximating p.a.		Therefore approximating total lifetime	
Assume:		CD tonnes	ICLAS tonnes	CD tonnes	ICLAS tonnes
Wilpinjong	50%	1,333,819.55	1,216,183.68	26,676,391	24,323,674
Mangoola	20%	533,527.82	486,473.47	10,670,556	9,729,469
Mt Arthur	20%	533,527.82	486,473.47	10,670,556	9,729,469
Ravensworth	10%	266,763.91	243,236.74	5,335,278	4,864,735

Calculate distances	**km one way**	**From**	**To**
Wilpinjong	187	**1434 Ulan-Wollar Rd, Wilpinjong NSW 2850**	**Liddell Station Road, Liddell, New South Wales**
Mangoola	46.4	**Mangoola Mine Entrance, Wybong, New South Wales**	**Liddell Station Road, Liddell, New South Wales**
Mt Arthur	22.2	**Thomas Mitchell Drive**	**Liddell Station Road, Liddell, New South Wales**
Ravensworth	12.1	**Hebden Rd, Ravensworth**	**Liddell Station Road, Liddell, New South Wales**

Assume all road, which is conservative (as they may install rail to facilitate power station)

AVERAGE RATE OF FUEL CONSUMPTION(c) *(litres per 100 kilometres)*

	2005	2006	2007	2010	2012
Passenger vehicles	11.7	11.4	11.5	11.3	11.1
Motor cycles	5.8	6.4	6.5	6.1	5.9
Light commercial vehicles	13.3	13.0	13.1	13.0	12.6
Rigid trucks	29.1	29.6	28.5	28.0	28.7
Articulated trucks	54.7	55.6	54.6	56.2	57.7
Non-freight carrying trucks	22.7	26.4	27.6	29.0	22.6
Buses	27.3	26.8	28.3	29.5	29.0
Total	**14.0**	**13.8**	**14.0**	**13.8**	**13.7**

(a) Data for 2005-07, 2010 are for 12 months ended 31 October. Data for 2012 are for 12 months ended 30 June.
(b) The survey is not designed to provide reliable estimates of inter-survey movements. See Explanatory Note 14.
(c) Calculated using the total fuel consumption divided by the total kilometres travelled.

From ABS motor vehicle survey 2012 (Use 57.7 l/100km)
Assume articulated trucks

Axle/axle group/gross	GML	CML	HML
25/6 metre B-double – 9 axle	62.5t	64.5t	68t

http://www.rms.nsw.gov.au/doingbusinesswithus/lgr/downloads/information/heavy-vehicles/mass_limits.html

47.5 **B-double truck capacity (tonnes)**

		Therefore approximating p.a.		Therefore approximating total lifetime	
		CD truckloads	ICLAS truckloads	CD truckloads	ICLAS truckloads
Wilpinjong		28,080.41	25,603.87	561,608.23	512,077.34
Mangoola		11,232.16	10,241.55	224,643.29	204,830.94
Mt Arthur		11,232.16	10,241.55	224,643.29	204,830.94
Ravensworth		5,616.08	5,120.77	112,321.65	102,415.47

	kilometres one way	Therefore approximating p.a.		Therefore approximating total lifetime		
		CD kms	ICLAS kms	CD kms	ICLAS kms	
Wilpinjong	**187**	10,502,073.91	9,575,846.21	210,041,478.16	191,516,924.27	Assume two way (empty return)
Mangoola	**46.4**	1,042,344.88	950,415.54	20,846,897.51	19,008,310.77	
Mt Arthur	**22.2**	498,708.11	454,724.68	9,974,162.17	9,094,493.52	
Ravensworth	**12.1**	135,909.19	123,922.72	2,718,183.84	2,478,454.31	
	Total	12,179,036.08	11,104,909.14	243,580,721.68	222,098,182.87	
	Diesel used (kl)	7,027.30	6,407.53	140,546.08	128,150.65	
	Diesel used (GJ)	271,253.93	247,330.76	5,425,078.55	4,946,615.15	

Table from NGA July 2013:

Transport equipment type	Fuel combusted	Energy content factor (GJ/kL unless otherwise indicated)	Emission factor kg CO_2-e/GJ (relevant oxidation factors incorporated)		
			CO_2	CH_4	N_2O
Heavy vehicles conforming to Euro design standards					
Euro iv or higher	Diesel oil	38.6	69.2	0.05	0.5
Euro iii	Diesel oil	38.6	69.2	0.1	0.5
Euro i	Diesel oil	38.6	69.2	0.2	0.5

Source: National Greenhouse and Energy Reporting (Measurement) Determination 2008 (Schedule 1).
Notes: All emission factors incorporate relevant oxidation factors (sourced from the DIICCSRTE's National Inventory Report).

Liquid Fuels combusted	EF for scope 3
	kg CO_2-e/GJ
Diesel oil	5.3

Transport of Oxygen Carrier (MeOx, CuO:SiO2)

From: LOT 6 O'Hara Pl Mt Thorley NSW 2330
To: Liddell Station Road, Liddell, New South Wales — 39.4 kms

Mt Thorley to power station

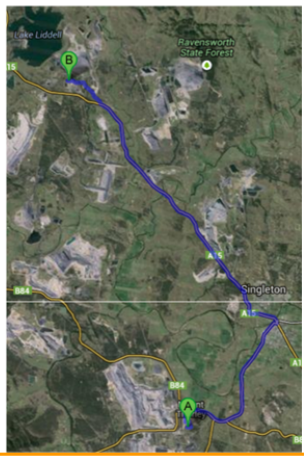

Initial charge	recharge p.a.	recharge over lifetime	
52272	41817.6	836352	CuO fraction
121968	97574.4	1951488	SiO2 fraction
174240	139392	2787840	kgs Total
174.24	139.392	2787.84	tonnes Total
4	4	80	truck trips
315.2	315.2	6304	kms
181.87	181.87	3637.41	L Diesel
0.18	0.18	3.64	kL Diesel
7.02	7.02	140.40	GJ Diesel

Assume two way (empty return)

Assume raw Cu, SiO2 from Sydney West (Parramatta) to LOT 6 O'Hara Pl Mt Thorley NSW 2330
198 kms

Initial charge	recharge p.a.	recharge over lifetime	
174240	139392	2787840	kgs Total
174	139	2788	tonnes Total
4	4	80	truck trips
1584	1584	31680	kms
913.97	913.97	18279.36	L Diesel
0.91	0.91	18.28	kL Diesel
35.28	35.28	705.58	GJ Diesel

Assume two way (empty return)

Assume transport back to parramatta for recycling

Transport of construction materials to site

Power Station construction materials

PS Concrete	216,250.00	t	216250
PS Carbon Steel	62,280.00	t	62280
PS Alloy Steel	6,228.00	t	6228
PS Stainless Steel	692.00	t	692
PS Copper	1,124.50	t	1124.5
PS Aluminium	519.00	t	519
PS Mineral wool (Rockwool)	648.75	t	648.75
PS RS, paint, rubber (as HDPE)	865.00	t	865
ASU Aluminium	658,845.00	kg	658845
ASU Steel, high alloyed	1,475,812.80	kg	1475812.8
ASU Steel, unalloyed	2,508,881.76	kg	2508881.76
ASU Concrete	1,644,477.12	kg	1644477.12
TOTAL	294,895.27	t	

Truck trips 6209 trips

Assume all material from Singleton
25.4 km

157708.6 total kms
90997.9 L Diesel
91.0 kL

Singleton to power station

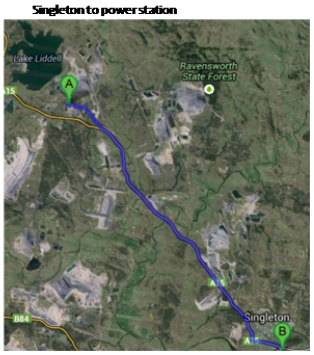

ENERGY AND EMISSION FACTORS

NGERnumber	Fuel combusted	CalcUnit	UnitSet	Energy content factor GJ/t	EF (kg CO2-e/GJ) CO2	CH4	N2O	Scope 3	Reference	Comments
1.0	Black coal combustion	t	UnitMass	24.3	88.2	0.03	0.2	24.3	NGA 2013, GJ/t from EPRI 2010 report (Hunter valley black coal)	
1.1	Black coal - (Energy) Fuel extr	t	UnitMass	2.32E-05	0	0	0	0.0	AUSCLI ("Black coal, NSW, at mine_System Process.xlsx")	
1.2	Black Coal - (Emissions) Carbc	t	UnitMass	0	13.84878	0	0	0.0	AUSCLI ("Black coal, NSW, at mine_System Process.xlsx")	

	Fuel combusted	CalcUnit	UnitSet	Energy content factor GJ/kL	CO2	CH4	N2O	Scope 3	Reference	Comments
40	Diesel oil (stationary)	kL	UnitVolume	38.6	69.2	0.1	0.2	5.3	NGA 2013	
41	Fuel oil (stationary)	kL	UnitVolume	39.7	72.9	0.03	0.2	5.3	NGA 2013	
44	Liquefied petroleum gas	kL	UnitVolume	25.7	59.6	0.1	0.2	5.0	NGA 2013	
54	Diesel oil (transport)	kL	UnitVolume	38.6	69.2	0.2	0.5	5.3	NGA 2013	
65	Diesel oil (post 2004)	kL	UnitVolume	38.6	69.2	0.01	0.6	5.3	NGA 2013	
68	Diesel oil (Euro iv or higher)	kL	UnitVolume	38.6	69.2	0.05	0.5	5.3	NGA 2013	
69	Diesel oil (Euro iii)	kL	UnitVolume	38.6	69.2	0.1	0.5	5.3	NGA 2013	
70	Diesel oil (Euro i)	kL	UnitVolume	38.6	69.2	0.2	0.5	5.3	NGA 2013	

	Fuel combusted	CalcUnit	UnitSet	Energy content factor GJ/kWh	Scope 2 (kg CO2-e/kWh)	Scope 3 (kg CO2-e/kWh)	Reference	Comments
77	Electricity	kWh	UnitElectricit	0.0036	0.87	0.19	NGA 2013 (NSW and ACT) - Latest Estimate (2011/2012)	

	Fuel combusted	CalcUnit	UnitSet	Energy content factor GJ/t	CO2 tCO2e/t*				Reference	Comments
100	Concrete	t	unitMass	1.17	0.188	0	0	0		
101	Carbon Steel	t	unitMass	26.2	2.03	0	0	0	ICE v2 2011. Non EU world typical (35.5% recycled) recycled content	
102	Alloy Steel	t	unitMass	53.7	5.738	0	0	0	Assumed 90% Carbon Steel, 10% Stainless steel (which is in line with assumptions of material incl	
103	Stainless Steel	t	unitMass	56.7	6.15	0	0	0	ICE v2 2011.	
104	Copper	t	unitMass	65.00	6.83	0	0	0	Average copper from Australia. A comparative life cycle assessment of copper production process	
105	Aluminium	t	unitMass	155	9.16	0	0	0	ICE v2 2011. General aluminium	
106	Mineral wool (Rockwool)	t	unitMass	16.8	1.12	0	0	0	ICE v2 2011.	
107	HDPE	t	unitMass	76.7	1.93	0	0	0	ICE v2 2011.	
108	Silica	t	unitMass	39.8187	11.67377	0	0	0	Assume MG silica, equivalent to 11000 kWh/t (11 kWh/kg) + 2.7kgs of sand (figures for sand from IC	
109	Copper waste recycling	t	UnitMass	64.90	6.78	0	0	0	Metal production of CSIRO, Norgate Australian LCA only (mining and mineral processing excluded)	
110	Methane leakage from extrac	t	UnitMass	2.17	0.0455	0	0	0	Assume (NSW open cut), from ISA nuclear report with fossil fuel in Australia summary	
111	Flyash to landfill	t	UnitMass	0	0.0363	0	0	0	US EPA's WARM (http://epa.gov/epawaste/conserve/tools/warm/Warm_Form.html) includes tran	
112	Flyash to recycling	t	UnitMass	0	-0.78925	0	0	0	US EPA's WARM (http://epa.gov/epawaste/conserve/tools/warm/Warm_Form.html)	

S	SourceLabel	SourceAmount	SourceUnit	GroupUn	Basis	Notes	NGERNu	EFLabelName	UnitSet	EmissionGrou	Energydirectly consumed
1	Black Coal	2432367.4 t		ICLAS	Annual	Main feedstock	1	Black coal combustion	UnitMass	Operations	y
2	Black Coal - extraction and delivery	2432367.4 t		ICLAS	Annual	Upstream energy	1.1	Black coal - (Energy) Fuel extraction and delivery	UnitMass	Operations	y
3	Black Coal - emissions from extraction and delivery	2432367.4 t		ICLAS	Annual	Upstream emissions	1.2	Black Coal - (Emissions) Carbon dioxide, fossil	UnitMass	Operations	y
4	Black Coal (Methane Leakage)	2432367.4 t		ICLAS	Annual	Assume (NSW open cut), from ISA nuclear	110	Methane leakage from extraction	UnitMass	Operations	n
5	Flyash to Landfill	515661.9 t		ICLAS	Annual	Calculated from 21.2% Ash from Hunter Va	111	Flyash to landfill	UnitMass	Operations	n
6	Coal Transport Diesel	6407.5 kL		ICLAS	Annual	Transport of main feedstock	54	Diesel oil (transport)	UnitVolume	Operations	y
7	Raw Copper	41817.6 kg		ICLAS	Annual	Operations component	104	Copper	unitMass	Operations	n
8	Raw Silica	97574.4 kg		ICLAS	Annual	Operations component	108	Silica	unitMass	Operations	n
9	Raw Copper & Silica transport Diesel	0.9 kL		ICLAS	Annual	Operations component	54	Diesel oil (transport)	UnitVolume	Operations	y
10	Copper & Silica spray drying	9.7 kL		ICLAS	Annual	Operations component	44	Liquefied petroleum gas	UnitVolume	Operations	n
11	CuO/SiO2 substrate transport Diesel	0.2 kL		ICLAS	Annual	Operations component	54	Diesel oil (transport)	UnitVolume	Operations	y
12	Raw Copper	52272.0 kg		ICLAS	Initial	Initial charge	104	Copper	unitMass	Construction	n
13	Raw Copper & Silica transport Diesel	0.9 kL		ICLAS	Initial	Initial charge	54	Diesel oil (transport)	UnitVolume	Construction	y
14	Copper & Silica spray drying	12.1 kL		ICLAS	Initial	Initial charge	44	Liquefied petroleum gas	UnitVolume	Construction	n
15	Raw Silica	121968.0 kg		ICLAS	Initial	Initial charge	108	Silica	unitMass	Construction	n
16	CuO/SiO2 substrate transport Diesel	0.2 kL		ICLAS	Initial	Initial charge	54	Diesel oil (transport)	UnitVolume	Construction	y
17	Concrete	216250.0 t		ICLAS	Initial	Power station construction	100	Concrete	unitMass	Construction	n
18	Carbon Steel	62280.0 t		ICLAS	Initial	Power station construction	101	Carbon Steel	unitMass	Construction	n
19	Alloy Steel	6228.0 t		ICLAS	Initial	Power station construction	102	Alloy Steel	unitMass	Construction	n
20	Stainless Steel	692.0 t		ICLAS	Initial	Power station construction	103	Stainless Steel	unitMass	Construction	n
21	Copper	1124.5 t		ICLAS	Initial	Power station construction	104	Copper	unitMass	Construction	n
22	Aluminium	519.0 t		ICLAS	Initial	Power station construction	105	Aluminium	unitMass	Construction	n
23	Mineral wool (Rockwool)	648.8 t		ICLAS	Initial	Power station construction	106	Mineral wool (Rockwool)	unitMass	Construction	n
24	KS, paint, rubber (as HDPE)	865.0 t		ICLAS	Initial	Power station construction	107	HDPE	unitMass	Construction	n
25	Aluminium	658845.0 kg		ICLAS	Initial	ASU construction	105	Aluminium	unitMass	Construction	n
26	Steel, high alloyed	1475812.8 kg		ICLAS	Initial	ASU construction, assume stainless steel	103	Stainless Steel	unitMass	Construction	n
27	Steel, unalloyed	2508881.8 kg		ICLAS	Initial	ASU construction, assume carbon steel	101	Carbon Steel	unitMass	Construction	n
28	Concrete	1644477.1 kg		ICLAS	Initial	ASU construction	100	Concrete	unitMass	Construction	n
29	Energy, electric	34259940.0 kWh		ICLAS	Initial	ASU construction	77	Electricity	UnitElectricity	Construction	y
30	Fuel oil, light	741.5 m3		ICLAS	Initial	ASU construction	41	Fuel oil (stationary)	UnitVolume	Construction	y
31	Construction material transport diesel	91.0 kL		ICLAS	Initial	Construction	54	Diesel oil (transport)	UnitVolume	Construction	y
32	Construction energy (electricity)	25240311.9 kWh		ICLAS	Initial	Power station construction	77	Electricity	UnitElectricity	Construction	y
33	Construction energy (diesel)	10088.7 kL		ICLAS	Initial	Power station construction	40	Diesel oil (stationary)	UnitVolume	Construction	y
34	Construction energy (fuel oil)	9809.1 kL		ICLAS	Initial	Power station construction	41	Fuel oil (stationary)	UnitVolume	Construction	y
35	CuO substrate recycling	41817.6 kg		ICLAS	Annual	Recycling process (SiO2 has no emissions,	109	Copper waste recycling	UnitMass	Operations	n
36	CuO/SiO2 substrate recycling transport diesel	0.9 kL		ICLAS	Annual	Waste/Recycling process	54	Diesel oil (transport)	UnitVolume	Operations	y
37	Black Coal	2667639.1 t		CD	Annual	Main feedstock	1	Black coal combustion	UnitMass	Operations	y
38	Black Coal - extraction and delivery	2667639.1 t		CD	Annual	Main feedstock	1.1	Black coal - (Energy) Fuel extraction and delivery	UnitMass	Operations	y
39	Black Coal	2667639.1 t		CD	Annual	Main feedstock	1.2	Black Coal - (Emissions) Carbon dioxide, fossil	UnitMass	Operations	y
40	Black Coal (Methane Leakage)	2667639.1 t		CD	Annual	Assume (NSW open cut), from ISA nuclear	110	Methane leakage from extraction	UnitMass	Operations	n
41	Flyash to Landfill	565539.5 t		CD	Annual	Calculated from 21.2% Ash from Hunter Va	111	Flyash to landfill	UnitMass	Operations	n
42	Coal Transport Diesel	7027.3 kL		CD	Annual	Transport of main feedstock	54	Diesel oil (transport)	UnitVolume	Operations	y
43	Concrete	216250.0 t		CD	Initial	Power station construction	100	Concrete	unitMass	Construction	n
44	Carbon Steel	62280.0 t		CD	Initial	Power station construction	101	Carbon Steel	unitMass	Construction	n
45	Alloy Steel	6228.0 t		CD	Initial	Power station construction	102	Alloy Steel	unitMass	Construction	n
46	Stainless Steel	692.0 t		CD	Initial	Power station construction	103	Stainless Steel	unitMass	Construction	n
47	Copper	1124.5 t		CD	Initial	Power station construction	104	Copper	unitMass	Construction	n
48	Aluminium	519.0 t		CD	Initial	Power station construction	105	Aluminium	unitMass	Construction	n
49	Mineral wool (Rockwool)	648.8 t		CD	Initial	Power station construction	106	Mineral wool (Rockwool)	unitMass	Construction	n
50	KS, paint, rubber (as HDPE)	865.0 t		CD	Initial	Power station construction	107	HDPE	unitMass	Construction	n
51	Aluminium	658845.0 kg		CD	Initial	ASU construction	105	Aluminium	unitMass	Construction	n
52	Steel, high alloyed	1475812.8 kg		CD	Initial	ASU construction, assume stainless steel	103	Stainless Steel	unitMass	Construction	n
53	Steel, unalloyed	2508881.8 kg		CD	Initial	ASU construction, assume carbon steel	101	Carbon Steel	unitMass	Construction	n
54	Concrete	1644477.1 kg		CD	Initial	ASU construction	100	Concrete	unitMass	Construction	n
55	Energy, electric	34259940.0 kWh		CD	Initial	ASU construction	77	Electricity	UnitElectricity	Construction	y
56	Fuel oil, light	741.5 m3		CD	Initial	ASU construction	41	Fuel oil (stationary)	UnitVolume	Construction	y
57	Construction material transport diesel	91.0 kL		CD	Initial	Construction	54	Diesel oil (transport)	UnitVolume	Construction	y
58	Construction energy (electricity)	25240311.9 kWh		CD	Initial	Power station construction	77	Electricity	UnitElectricity	Construction	y
59	Construction energy (diesel)	10088.7 kL		CD	Initial	Power station construction	40	Diesel oil (stationary)	UnitVolume	Construction	y
60	Construction energy (fuel oil)	9809.1 kL		CD	Initial	Power station construction	41	Fuel oil (stationary)	UnitVolume	Construction	y